

*Jim's Gamma
JK*

Multiphase Flow in Wells

James P. Brill

Floyd M. Stevenson Endowed Presidential Chair in Petroleum Engineering

Executive Director, Fluid Flow Projects

U. of Tulsa

and

Hemanta Mukherjee

Manager, Production Enhancement, West and South Africa

Schlumberger Oilfield Services

First Printing

**Henry L. Doherty Memorial Fund of AIME
Society of Petroleum Engineers Inc.**

**Richardson, Texas
1999**

Table of Contents

Chapter 1—Introduction	1
1.1 Scope	1
1.2 Objectives of Monograph	1
1.3 Organization of Monograph	1
1.4 Historical Background	2
1.5 Nomenclature and Units	4
Chapter 2—Single-Phase-Flow Concepts	5
2.1 Introduction	5
2.2 Conservation of Mass	5
2.3 Conservation of Momentum	5
2.4 Pressure-Gradient Equation	5
2.5 Flow in an Annulus	11
2.6 Conservation of Energy	13
Chapter 3—Multiphase-Flow Concepts	19
3.1 Introduction	19
3.2 Phase Behavior	19
3.3 Definition of Variables	20
3.4 Pressure Gradient	23
3.5 Flow Patterns	23
3.6 Liquid Holdup	24
3.7 Pressure-Traverse Computing Algorithm	26
3.8 Dimensional Analysis	27
Chapter 4—Multiphase-Flow Pressure-Gradient Prediction	28
4.1 Introduction	28
4.2 Pressure-Gradient Prediction	28
4.3 Evaluation of Wellbore Pressure-Gradient-Prediction Methods	56
4.4 Pressure-Gradient Prediction in Annuli	58
4.5 Evaluation of Annulus Liquid-Holdup and Pressure-Gradient-Prediction Methods	66
4.6 General Observations	67
Chapter 5—Flow Through Restrictions and Piping Components	70
5.1 Introduction	70
5.2 Description of Restrictions	70
5.3 Flow Through Chokes	70
5.4 Flow Through Piping Components	76
Chapter 6—Well Design Applications	78
6.1 Introduction	78
6.2 Vertical-Flow Performance	78
6.3 Inflow Performance	80
6.4 Production-Systems Analysis	86
6.5 Artificial Lift	91
6.6 Gas-Well Loading	92
6.7 Erosional Velocity	94
6.8 Special Problems	95
Appendix A—Nomenclature and SI Metric Conversion Factors	99
Appendix B—Fluid and Rock Properties	102
Appendix C—Vapor-/Liquid-Phase Equilibrium	135
Appendix D—Tubing and Casing Properties	145
Author Index	149
Subject Index	155

Chapter 1

Introduction

1.1 Scope

The accurate design of oil and gas well tubing strings requires the ability to predict flow behavior in the wells. Wells normally produce a mixture of gas and liquids, regardless of whether they are classified as oil wells or gas wells. This multiphase flow is significantly more complex than single-phase flow. However, the technology to predict multiphase-flow behavior has improved dramatically in the past decade. It is now possible to select tubing sizes, predict pressure drops, and calculate flow rates in wells with acceptable engineering accuracy. This chapter sets the stage for the monograph by describing the nature and occurrence of multiphase flow, and by presenting important historical events that have impacted on the development of modern multiphase-flow concepts.

The common occurrence of multiphase flow in wells can be discussed with the simplified production system shown in Fig. 1.1.

Fluids entering the wellbore from the reservoir can range from an undersaturated oil to a single-phase gas. Free water can accompany the fluids as a result of water coning, water flooding, or production of interstitial water. Alternatively, a free gas saturation in an oil reservoir can result in a gas/liquid mixture entering the well. Retrograde condensation can result in hydrocarbon liquids condensing in a gas condensate reservoir so that a gas/liquid mixture again enters the wellbore. Even when single-phase gas or liquid flow exists near the bottom of a well, multiphase flow can occur throughout most of the wellbore. This is a result of evolution of gas from oil or condensation of gas with reduction of pressure and temperature as the fluids flow up the well.

Although many of the wells drilled on land tend to be nearly vertical, wells drilled offshore and in other hostile environments, such as the Arctic, are normally directional or deviated. Inclination angles can vary from vertical near the surface to horizontal near the production zone. Flow rates of gas, oil, and water vary widely. Pipe diameters can be as small as 1 in. and as large as 9 in. Flow also can occur in a casing/tubing annulus. Depths can range from a few hundred feet to more than 20,000 ft. Pressures can be as low as a few atmospheres or as high as 20,000 psia. Temperatures can be above 400°F or approach the freezing point of water. Oil viscosities in wellbores can be less than 1 cp or greater than 10,000 cp.

Fluids entering the wellbore often flow through a complicated well completion region consisting of perforations, fractures, gravel pack, and other such items. The effect of this region must be included when coupling the well to the reservoir through inflow performance relationship (IPR) procedures. Most wells contain some type of well-control device that requires produced fluids to flow through a restriction. This can vary from a bottomhole choke to a

subsurface safety valve or a remotely controlled, variable-sized surface choke. Wells can be produced by artificial-lift mechanisms involving a submersible pump or gas injection.

The broad changes in flow variables encountered in producing wells have made the development of prediction methods much more difficult. Techniques that work for gas condensate wells do not necessarily work for oil wells. Assumptions that are valid for some wells are totally invalid for others.

1.2 Objectives of Monograph

Multiphase flow in pipes is not unique to the petroleum industry. The simultaneous flow of two or three phases in a single conduit is encountered in petrochemical plants, refineries, steam generators, automobile engines, storm sewers, nuclear reactors, and many other areas. Consequently, the technical literature in chemical, civil, mechanical, petroleum, and nuclear engineering all contain valuable contributions to multiphase flow in pipes. Unfortunately, each discipline uses different terminology, units, and nomenclature and is interested in different ranges of variables. An important objective of this monograph is to bring together the pertinent technology of all relevant disciplines into a single book that uses the nomenclature and units standardized by the Society of Petroleum Engineers.

Numerous methods have been proposed to predict multiphase flow in wells. Some are very general and others are applicable over a very narrow range of flow variables. Some are very empirical in nature and others make an attempt to model the basic phenomena encountered. It is vitally important that persons engaged in designing wells be aware of the limitations of all methods. Thus, a second objective of this monograph is to present the important methods to predict flow behavior in wells and to discuss their limitations and ranges of applicability.

Finally, engineers engaged in the design of wells should have a thorough understanding of the calculation procedures necessary to optimize their design calculations. This includes coupling the wells to both surface facilities and reservoirs. It also includes understanding computer algorithms, fluid physical properties, and mass transfer for multicomponent mixtures. A significant part of this monograph is devoted to these concepts.

1.3 Organization of Monograph

Predicting flow behavior when multiphase flow occurs in wells requires an understanding of concepts that are not a part of the curriculum in most engineering disciplines. Before multiphase-flow technology can be mastered, one must have an adequate knowledge of not only single-phase-flow fluid mechanics, thermodynamics,

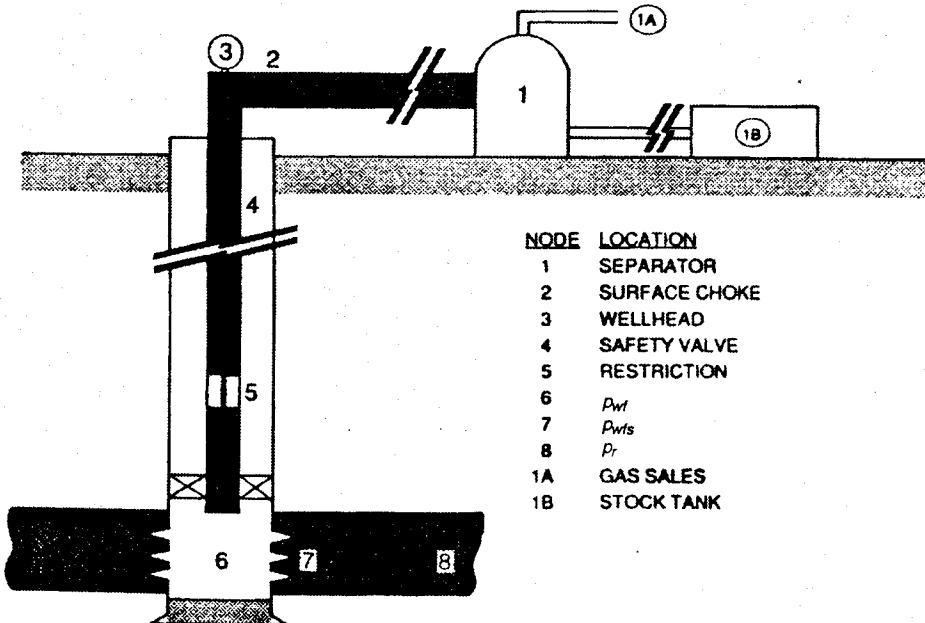


Fig. 1.1—Multiphase production system.¹

and heat transfer, but also vapor/liquid equilibrium (VLE) and fluid physical properties for multicomponent hydrocarbon systems. Thus, a significant part of this monograph will be devoted to a review of these important topics.

Chap. 1 clearly states the objectives of this monograph and describes the common occurrence of multiphase flow during the production and transportation of oil and gas. Some landmark publications are identified that have had a lasting influence on the understanding of the total system involved in flowing fluids from the reservoir to surface storage and processing facilities. Finally, a short discussion on nomenclature, unit conversion factors, and the SI (metric) unit system is included. Appendix A provides a complete Nomenclature and a list of conversion factors.

Basic theoretical concepts are presented in Chaps. 2 through 5. Chap. 2 concentrates on a review of important single-phase, steady-state-flow concepts for both Newtonian and non-Newtonian fluids and for gas. Included are brief reviews of conservation of mass and momentum and their use in the prediction of pressure gradients in both circular pipes and in annuli. Also included is the use of conservation of energy, thermodynamic principles, and heat transfer to predict fluid temperature behavior when hot fluids are produced from a reservoir, up the well, and through surface pipe.

Chap. 3 contains a description of the variables encountered in multiphase flow in pipes. Procedures are given for the use of black-oil and compositional models to predict mass transfer and in-situ volumetric flow rates. Techniques are presented to determine values for mixture variables. A detailed description of flow patterns for both circular pipes and annuli is given. The importance of liquid holdup and methods to measure this parameter are discussed. The standard computing algorithm for generating pressure and temperature vs. length traverses is presented. Appendices B and C contain methods to predict fluid physical properties and mass transfer for black-oil and compositional systems.

Chap. 4 contains a detailed description and evaluation of all commonly used correlations and mechanistic models to predict flow patterns and pressure gradients in wells.

Most wells contain some type of restriction for controlling flow rates and protecting downstream equipment. Chap. 5 contains a detailed description of critical and subcritical flow of single-phase and multiphase mixtures through chokes. Also included is a coverage of flow through piping components such as valves, elbows, and tees.

After mastering the material in Chaps. 2 through 5, the reader is prepared to address the many important practical applications encountered in multiphase flow in wells. Chap. 6 is devoted to the use

NODE	LOCATION
1	SEPARATOR
2	SURFACE CHOKE
3	WELLHEAD
4	SAFETY VALVE
5	RESTRICTION
6	P_w
7	P_{ws}
8	P_r
1A	GAS SALES
1B	STOCK TANK

of the material from Chaps. 2 through 5 in various well design applications. The concepts of production systems analysis or NODAL™ analysis are thoroughly described with examples. Applications include flowing, gas lift, and pumping wells. Production problems, such as predicting erosional velocities and unloading gas wells, also are given.

Although this monograph addresses only multiphase flow in wells, much of the material also is applicable to multiphase flow in near-horizontal flowlines and pipelines.

1.4 Historical Background

Gilbert² developed many of the concepts used today to analyze the well performance of flowing and gas-lift wells. He divided the production system into three distinct categories: inflow performance from the reservoir, vertical-lift performance in the well, and beam or choke performance. Graphical techniques were presented for coupling these categories to permit analysis of individual well problems. It is interesting to note that this same procedure is still followed today under the names of production systems analysis or NODAL™ analysis. However, the methods for describing the performance of each category have been vastly improved. Gilbert also presented a clear description of the unsteady flow behavior or "heading" that can exist in a well and showed how to minimize or eliminate the phenomenon. Nind³ expanded and clarified Gilbert's concepts.

The history of attempts to improve the prediction of vertical-lift performance for wells is especially interesting. Brill and Arirachakaran⁴ divided this history into three partially overlapping periods.

1.4.1 The Empirical Period (1950–75). Most early investigators used data obtained from laboratory test facilities, with a few using field data. These data usually included volumetric flow rates of gas and liquid, physical properties of each phase, pipe diameter and inclination angle, and pressures at the inlet and outlet of the pipe. In some cases, flow pattern was observed and liquid holdup was measured by use of quick-closing ball valves. Fluids were treated as homogeneous mixtures. However, gas and liquid phases were permitted to travel at different velocities, with slippage effects being accounted for through empirical liquid-holdup correlations. Empirical flow-pattern maps were used, often based on dimensionless groups. Steady-state, pressure-gradient equations were developed that were based on conservation of momentum and mass principles applied to the homogeneous mixtures. Frictional pressure losses relied on single-phase-flow equations, resulting in extensive use of mixture Reynolds numbers. Some investigators also used an empiri-

cal multiplicative factor to represent the increased friction resulting from the presence of a second phase.

The 1970's saw a trend in the petroleum industry to adopt some basic physical mechanisms already in use in other industries. This was especially true in the prediction of flow patterns and gas bubble-rise velocities in liquid columns. Two classic papers dealing with multiphase flow in horizontal pipes by Dukler and Hubbard⁵ and Taitel and Dukler⁶ clearly show that mechanistic models for slug flow and flow-pattern prediction already were available.

In general, the empirical period resulted in a collection of empirical correlations whose accuracy was limited by the lack of inclusion of basic physical mechanisms. Even when these mechanisms were partially included, their investigation was severely hampered by the unavailability of sufficiently accurate instrumentation and real-time data-acquisition systems.

1.4.2 The Awakening Years (1970–85). The empirical correlations used to predict pressure gradient, coupled with the introduction of the personal computer (PC) in the early 1980's, dramatically improved practical tools available to petroleum engineers. Techniques for numerically integrating the pressure gradient from one end of a pipe to the other were well understood, and virtually every major producing company had a computer program to predict pressure drop or flow rates for wells and pipelines. Procedures to connect wells to reservoirs through simple IPR techniques abounded. Brown⁷ presented the true concept of NODAL™ or production system analysis.

Unfortunately, it was quickly recognized that there were many problems with the methods available. Empirical flow-pattern maps were inadequate. Flow-pattern transitions, previously thought to be dependent mostly on flow rates (or superficial velocities), were found to be very sensitive to other parameters, especially inclination angle. An empirical liquid-holdup correlation for each flow pattern was equally inadequate. The assumption of a homogeneous mixture was oversimplified. It became clear that no matter how much data were gathered in either laboratory test facilities or from carefully tested field installations, the accuracy of the predictions could not improve without the introduction of more basic physical mechanisms.

Fortunately, progress in this area had already been made by the nuclear industry. Although the fluids used for these studies (steam and water) were trivial by comparison to those encountered in the petroleum industry, the methods used to formulate conservation equations were much more advanced.

1.4.3 The Modeling Period (1980–Present). Petroleum industry challenges in the 1980's required a much better understanding of multiphase-flow technology. This has been the modeling period. The increased cost of Arctic and offshore developments has justified increased spending. Millions of dollars were invested in multiphase flow through research consortiums in the U.S., Norway, France, and the U.K.

Investigators recognized that improved understanding of multiphase flow in pipes required a combined experimental and theoretical approach. Sophisticated test facilities were constructed that used new instrumentation for measuring important variables. Use of nuclear densitometers, ultrasonics, capacitance sensors, laser Doppler anemometers, and new high-speed photographic techniques abounded. PC-based data-acquisition hardware and software improved, permitting acquisition of large amounts of higher-quality data. Analysis of the data improved understanding of the complex dynamic mechanisms that exist during multiphase flow. This understanding was transformed into improved mechanistic models to better describe the physical phenomena occurring.

At the same time that improved experimental research was being conducted, efforts were expended to develop improved theoretical methods. The petroleum industry adopted the two-fluid modeling approach, pioneered by the nuclear industry, for the development of transient codes applicable to petroleum industry problems.^{8–11} This approach involves writing separate equations for each phase to describe conservation of mass, momentum, and energy. The resulting six-equation problem must be solved simultaneously with numerical simulation techniques. Various simplifications were found to be convenient, such as use of a single mixture-energy equation. Empirical

correlations and simplified closure relationships were still necessary for some parameters, such as interfacial friction factors, fraction of liquid entrained in the gas core for annular flow, and liquid holdup in a slug body. Improved correlations for these parameters became possible as a result of the experimental research being conducted.

The resulting transient codes are still being evaluated, but appear to be capable of simulating a variety of applications that are time-dependent. These include changes in inlet- or outlet-flow rates or pressures for pipelines and wellbores; pigging of pipelines; pipe blowdown, including burst pipe and leak detection; terrain slugging; and flow in pipelines with low velocities. Until recently, transient simulators have been much more difficult to use than steady-state programs. The magnitude and quality of required input data are much greater. Numerical instabilities are common, and simulations can require large amounts of computer time. In addition, results are more difficult to interpret than for steady-state flow. However, significant improvements have made transient simulators more user-friendly, and they will enjoy increased use in the future.

An important improvement in steady-state mechanistic models was the work to predict flow-pattern transitions for all inclination angles.^{6,8,12–16} This opened the door for improved models for each of the flow patterns, including the possibility of linking the various models through unified flow-pattern-transition criteria. Ozon *et al.*,¹⁷ Hasan and Kabir,¹⁸ Ansari *et al.*,¹⁹ Xiao *et al.*,²⁰ and Chokshi²¹ published combined or "comprehensive" mechanistic models. Their attempts to evaluate the models with field data confirm that the modeling approach is more accurate and precise than empirical correlations. Furthermore, it is now possible to continue improvement of these mechanistic models as experimental research is conducted on the basic mechanisms of multiphase flow.

Thus, the current state of the art in multiphase flow in pipes is the emergence of both two-fluid transient simulators and steady-state mechanistic models that more accurately describe the physical phenomena that occur. Transient simulators have the capability to analyze complex time-dependent problems but often suffer from convergence problems. The improved technology also carries an additional cost. Both the transient simulators and the mechanistic models are complex and require specialized training to understand and use. Interpretation of results is better carried out by engineers with a specialized background who are fully aware of any simplifying assumptions or limitations which have been included in the developments.

1.4.4 Role of Computers. The early computers were too slow and cumbersome to analyze individual well problems. However, they made it possible to develop generalized pressure-gradient curves that could be used with confidence, provided well characteristics were not significantly different than those used to develop the curves. Gradient curves were especially useful in the design of gas-lift installations. As computers became more powerful, affordable, easier to use, and more readily available, they gradually displaced gradient curves. Many companies developed versatile computer programs that rapidly analyze a broad variety of well characteristics along with the performance of all wells in a field. The availability of PC's and workstations has completed this evolution until today an engineer can perform in minutes analyses that would have taken months when Gilbert² first proposed the basic well-performance-evaluation procedures.

In addition to accelerated computing speeds, computers have played an equally important role in data-acquisition. The availability of fast computations and data transfer, mass storage devices, and vastly improved instrumentation has permitted vital research on the basic physical mechanisms that occur during multiphase flow in pipes. Methods are available today to measure such variables as local velocities and void fractions, interfacial phenomena between phases, and small changes in pressure and temperature. These measurements take advantage of how gas and liquid phases yield different values for such items as electrical capacitance and resistance, absorption of gamma rays and neutrons, sonic velocity, and optics.

Dramatic changes also are being made in user-friendly computer programs. There have been significant improvements in the design of graphical user interfaces, data integration, and knowledge-based expert systems. The result has been the emergence of commercial

computer programs that are not only easy to use, but also incorporate the very latest technology in a friendly, unintimidating manner. The faster computing speeds on PC's and engineering workstations also make possible a truly interactive, compositional-fluid-model approach for more precise calculations of mass transfer and fluid properties. This approach gives better pressure and temperature predictions and is more robust than the standard black-oil approach.

Also emerging is a trend for large standardized databases containing information ranging from drilling and completion records to well-test and production data. Soon it will be possible to access and cross-reference these databases with a well identification and to input data automatically into a multiphase-flow design program, thus dramatically reducing manual input requirements.

1.5 Nomenclature and Units

Much of the technology for multiphase flow in pipes was developed outside the petroleum industry. Consequently, there will be some confusion in nomenclature because many of the important publications have different nomenclature and terminology. Occasionally, it will be necessary to define new symbols or deviate from those recommended by the Society of Petroleum Engineers. As much as possible, this monograph uses the standard symbols adopted by the Society of Petroleum Engineers.²²

SI is the official abbreviation, *in all languages*, for the International System of Units (les Système International d'Unités). However, customary units²³ still are used frequently in many parts of the world, as well as throughout this monograph (except in Examples 4.9 and 4.10, which deal with mechanistic models that were developed on the basis of SI units). Appendix A presents customary units, along with factors to convert to the SI metric system of units.

References

1. Mach, J.M., Proano, E.A., and Brown, K.E.: "Application of Production System Analysis to Determine Completion Sensitivity in Gas Well Production," paper presented at the 1981 ASME Energy Sources Technical Conference and Exhibition, Houston, 18-22 January.
2. Gilbert, W.E.: "Flowing and Gas-Lift Well Performance," *Drill. & Prod. Prac.* (1954) 126.
3. Nind, T.E.W.: *Principles of Oil Well Production*, McGraw-Hill Book Co. Inc., New York City (1964).
4. Brill, J.P. and Arirachakaran, S.J.: "State of the Art in Multiphase Flow," *JPT* (May 1992) 538; *Trans., AIME*, **293**.
5. Dukler, A.E. and Hubbard, M.G.: "A Model for Gas-Liquid Slug Flow in Horizontal and Near Horizontal Tubes," *Ind. Eng. Chem. Fund.* (1975) **14**, 337.
6. Taitel, Y.M. and Dukler, A.E.: "A Model for Predicting Flow Regime Transitions in Horizontal and Near Horizontal Gas-Liquid Flow," *AIChE J.* (1976) **22**, 47.
7. Brown, K.E.: *The Technology of Artificial Lift Methods*, Petroleum Publishing Co., Tulsa, Oklahoma (1980) **2a**, **3a**, **3b**, and **4**.
8. Taitel, Y., Barnea, D., and Dukler, A.E.: "Modeling Flow Pattern Transitions for Steady Upward Gas-Liquid Flow in Vertical Tubes," *AIChE J.* (1980) **26**, 345.
9. Bendiksen, K.H. et al.: "The Dynamic Two-Fluid Model OLGA: Theory and Application," *SPEPE* (May 1991) 171; *Trans., AIME*, **291**.
10. Black, P.S. et al.: "Studying Transient Multi-Phase Flow Using the Pipeline Analysis Code (PLAC)," *J. Energy Res. Tech.* (March 1990) **112**, 25.
11. Pauchon, C. et al.: "A Comprehensive Mechanistic Model for Two-Phase Flow," *Proc.*, Sixth International Conference on Multi-Phase Production, Cannes, France (June 1993) 29.
12. Barnea, D., Shoham, O., and Taitel, Y.: "Flow Pattern Transition for Vertical Downward Two-Phase Flow," *Chem. Eng. Sci.* (1982) **37**, 741.
13. Barnea, D., Shoham, O., and Taitel, Y.: "Flow Pattern Transition for Downward Inclined Two-Phase Flow; Horizontal to Vertical," *Chem. Eng. Sci.* (1982) **37**, 735.
14. Barnea, D. et al.: "Gas Liquid Flow in Inclined Tubes: Flow Pattern Transition for Upward Flow," *Chem. Eng. Sci.* (1985) **40**, 131.
15. Barnea, D.: "Transition From Annular Flow and From Dispersed Bubble Flow—Unified Models for the Whole Range of Pipe Inclinations," *Int'l. J. Multiphase Flow* (1986) **12**, No. 5, 733.
16. Barnea, D.: "A Unified Model for Predicting Flow Pattern Transitions for the Whole Range of Pipe Inclinations," *Int'l. J. Multiphase Flow* (1987) **13**, No. 1, 1.
17. Ozon, P.M., Ferschneider, G., and Chwetzoff, A.: "A New Multiphase Flow Model Predicts Pressure and Temperature Profiles in Wells," paper SPE 16535 presented at the 1987 SPE Offshore Europe Conference, Aberdeen, 8-11 September.
18. Hasan, A.R. and Kabir, C.S.: "A Study of Multiphase Flow Behavior in Vertical Wells," *SPEPE* (May 1988) 263; *Trans., AIME*, **285**.
19. Ansari, A.M. et al.: "A Comprehensive Mechanistic Model for Upward Two-Phase Flow in Wellbores," *SPEPF* (May 1994) 143; *Trans., AIME*, **297**.
20. Xiao, J.J., Shoham, O., and Brill, J.P.: "A Comprehensive Mechanistic Model for Two-Phase Flow in Pipelines," paper SPE 20631 presented at the 1990 SPE Annual Technical Conference and Exhibition, New Orleans, 23-26 September.
21. Chokshi, R.N.: "Prediction of Pressure Drop and Liquid Holdup in Vertical Two-Phase Flow Through Large Diameter Tubing," PhD dissertation, U. of Tulsa, Tulsa, Oklahoma (1994).
22. *SPE Letter and Computer Symbols Standard for Economics, Well Logging and Formation Evaluation, Natural Gas Engineering, and Petroleum Reservoir Engineering*, SPE, Richardson, Texas (1986).
23. *The SI Metric System of Units and SPE Metric Standard*, SPE, Richardson, Texas (1984).

Chapter 2

Single-Phase-Flow Concepts

2.1 Introduction

The basis for virtually all computations involving fluid flow in pipes is conservation of mass, momentum, and energy. Application of these principles permits the calculation of changes in pressure and temperature with distance. In this chapter, the steady-state, pressure-gradient equation for single-phase flow in pipes is developed. Procedures to determine values of wall shear stress are reviewed, and example problems are solved to demonstrate the applicability of the pressure-gradient equation for both compressible and incompressible fluids. A review is presented of Newtonian and non-Newtonian fluid flow behavior in both circular pipes and in an annulus. The enthalpy-gradient equation also is developed and solved to obtain approximate equations that predict temperature changes during steady-state fluid flow. Of particular interest is the unique application to heat transmission in wellbores.

2.2 Conservation of Mass

Conservation of mass simply means that for a given control volume, such as a segment of pipe, the mass in, minus the mass out, must equal the mass accumulation.¹ For a constant-area duct,

$$\frac{\partial p}{\partial t} + \frac{\partial(\rho v)}{\partial L} = 0. \quad (2.1)$$

For steady-state flow, no mass accumulation can occur. Eq. 2.1 then becomes

$$\frac{\partial(\rho v)}{\partial L} = 0. \quad (2.2)$$

It is evident from Eq. 2.2 that steady-state flow also is characterized by $\rho v = \text{constant}$.

2.3 Conservation of Momentum

Application of Newton's first law to fluid flow in pipes requires that the rate of momentum out, minus the rate of momentum in, plus the rate of momentum accumulation in a given pipe segment must equal the sum of all forces on the fluids.¹ Fig. 2.1 defines the control volume and pertinent variables. Conservation of linear momentum can be expressed as

$$\begin{aligned} & \frac{\partial}{\partial t}(\rho v) + \frac{\partial}{\partial L}(\rho v^2) \\ &= -\frac{\partial p}{\partial L} - \tau \frac{\pi d}{A} - \rho g \sin \theta. \quad (2.3) \end{aligned}$$

2.4 Pressure-Gradient Equation

Combining Eqs. 2.2 and 2.3, and assuming steady-state flow to eliminate the rate of accumulation of linear momentum, gives

$$\rho v \frac{dv}{dL} = -\frac{dp}{dL} - \tau \frac{\pi d}{A} - \rho g \sin \theta. \quad (2.4)$$

Solving for the pressure gradient obtains

$$\frac{dp}{dL} = -\tau \frac{\pi d}{A} - \rho g \sin \theta - \rho v \frac{dv}{dL}, \quad (2.5)$$

which also frequently is called the mechanical energy balance equation. Thus, the steady-state, pressure-gradient equation is a result of applying the principles of conservation of mass and linear momentum.

Eq. 2.5 clearly shows that the steady-state pressure gradient is made up of three components. Thus

$$\left(\frac{dp}{dL} \right)_t = \left(\frac{dp}{dL} \right)_f + \left(\frac{dp}{dL} \right)_{el} + \left(\frac{dp}{dL} \right)_{acc}. \quad (2.6)$$

The first component in Eq. 2.5, described in greater detail in Eqs. 2.7 through 2.9, results from friction or shear stress at the pipe wall. Friction losses normally represent 5 to 20% of the total pressure drop in wells. The second term in Eq. 2.5 is the pressure gradient caused by elevation change (often called the hydrostatic head or elevation component). It is normally the predominant term in wells and contributes from 80 to 95% of the pressure gradient. The final component in Eq. 2.5 results from change in velocity (often called acceleration or the kinetic energy component). It is normally negligible and can become significant only if a compressible phase exists at relatively low pressures, such as in gas-lift wells near the surface.

For upward flow in a well, pressure always drops in the direction of flow. It is common to show the pressure drop as positive in the direction of flow. Eq. 2.5 must be multiplied by -1 to yield a positive pressure gradient.

Evaluation of the wall shear stress or friction losses can be accomplished by defining a dimensionless friction factor that is the ratio of the wall shear stress to the kinetic energy of the fluid per unit volume.¹ Thus,

$$f' = \frac{\tau}{\rho v^2/2}, \quad (2.7)$$

where f' = a Fanning friction factor. The Moody² friction factor, which is four times larger than the Fanning friction factor, is adopted throughout this monograph. Occasionally, such as for flow of non-

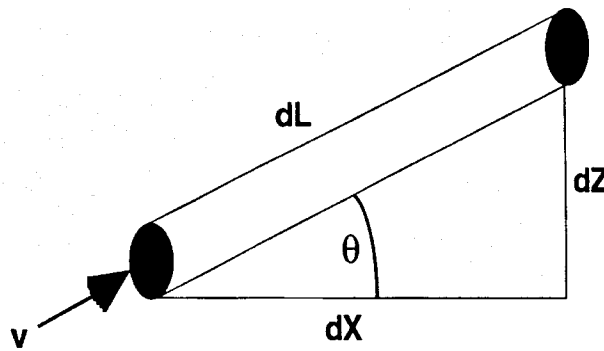


Fig. 2.1—Control volume.

Newtonian fluids and flow through annuli, Fanning friction factors are retained to preserve original equations. Eq. 2.7 can be solved for shear stress

$$\tau = f \frac{\rho v^2}{8} \quad (2.8)$$

Substituting Eq. 2.8 into Eq. 2.5, the frictional component of the pressure-gradient equation becomes

$$\left(\frac{dp}{dL} \right)_f = \left(f \frac{\rho v^2}{8} \right) \left(\frac{\pi d}{\pi d^2/4} \right) = \frac{f \rho v^2}{2d}, \quad (2.9)$$

which is often called the Darcy-Weisbach equation.³

Calculation of frictional pressure gradients requires the determination of values for friction factors. The procedure first requires an evaluation of whether the flow is laminar or turbulent. Laminar flow is considered to exist if the Reynolds number is less than 2,000. The Reynolds number is defined as

$$N_{Re} = \frac{\rho v d}{\mu} \quad (2.10)$$

2.4.1 Laminar Flow. For laminar flow, an analytical expression can be derived for the friction factor. The velocity profile for laminar flow can be integrated to yield the pressure gradient. This was done for flow in horizontal capillary tubes to give Eq. 2.11, which is the Poiseuille⁴ equation.

$$v = \frac{d^2}{32\mu} \left(\frac{dp}{dL} \right). \quad (2.11)$$

Because the pressure gradient in Eq. 2.11 results only from wall shear stresses or friction, the pressure gradient is identical to Eq. 2.9. Combining these equations gives

$$f = \frac{64\mu}{\rho v d} = \frac{64}{N_{Re}}. \quad (2.12)$$

2.4.2 Turbulent Flow. Our ability to predict flow behavior under turbulent-flow conditions is a direct result of extensive experimental studies of velocity profiles and pressure gradients. These studies have shown that both velocity profile and pressure gradient are very sensitive to characteristics of the pipe wall. A logical approach to defining friction factors for turbulent flow is to begin with the simplest case (i.e., the smooth-wall pipe), then proceed to the partially rough wall and finally to the fully rough wall.

Smooth pipe is seldom encountered in oil and gas production. However, laboratory studies often are conducted with glass or plastic pipes, which can approach smooth pipe. Numerous empirical equations have been proposed to predict friction factors for smooth pipe. The equations most often used, and their suggested ranges of applicability, are those of Drew *et al.*,⁵

$$f = 0.0056 + 0.5N_{Re}^{-0.32}, \quad (2.13)$$

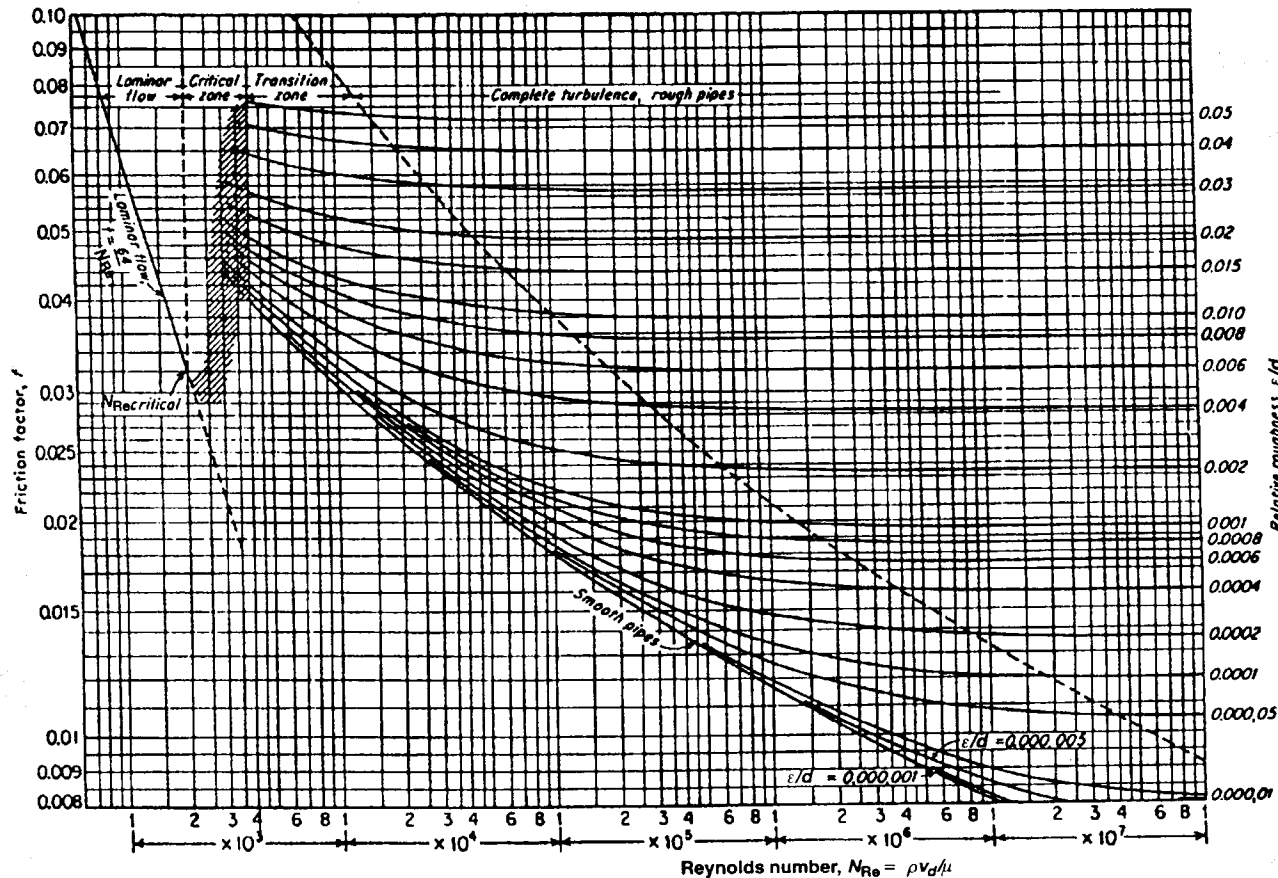


Fig. 2.2—Moody diagram.²

where

$$3,000 < N_{Re} < 3 \times 10^6,$$

and Blasius,⁶

$$f = 0.316N_{Re}^{-0.25}, \quad \dots \dots \dots \quad (2.14)$$

where

$$3,000 < N_{Re} < 10^5.$$

Although the Blasius equation is considered less accurate, it receives greater use because of its similarity to the laminar friction-factor equation. Both can be expressed in the form

$$f = CN_{Re}^n. \quad \dots \dots \dots \quad (2.15)$$

Normally, the inside wall of a pipe is not smooth. In turbulent flow, the roughness can have a significant effect on the friction factor and, thus, the pressure gradient. Wall roughness is a function of the pipe material, the method of manufacture, the age of the pipe, and the environment to which it is exposed.

From a microscopic sense, wall roughness is not uniform. Individual protrusions and indentations vary in height, width, length, shape, and distribution. The absolute roughness of a pipe, ϵ , is the mean protruding height of uniformly distributed and sized, tightly packed sand grains that would give the same pressure-gradient behavior as the actual pipe.

Dimensional analysis suggests that the effect of roughness does not result from its absolute dimensions, but rather from its dimensions relative to the inside diameter of the pipe, ϵ/d . In turbulent flow, the effect of wall roughness has been found to depend on both the relative roughness and the Reynolds number. If the laminar sublayer that exists within the boundary layer is sufficiently thick, the behavior is similar to a smooth pipe. The sublayer thickness is directly related to the Reynolds number.

Nikuradse's⁷ famous sand-grain experiments formed the basis for friction-factor data from rough pipes. His correlation for fully rough wall pipe is given as Eq. 2.16 and is still the best one available.

$$\frac{1}{\sqrt{f}} = 1.74 - 2 \log\left(\frac{2\epsilon}{d}\right). \quad \dots \dots \dots \quad (2.16)$$

The region in which f varies both with Reynolds number and relative roughness is called the transition region or partially rough wall. Colebrook⁸ proposed an empirical equation to describe the variation of f in the transition region. It has become the basis for modern friction-factor charts.

$$\frac{1}{\sqrt{f}} = 1.74 - 2 \log\left(\frac{2\epsilon}{d} + \frac{18.7}{N_{Re} \sqrt{f}}\right). \quad \dots \dots \dots \quad (2.17)$$

Note that Eq. 2.17 degenerates to Eq. 2.16 for large Reynolds numbers corresponding to fully developed turbulent or rough pipe flow. Solving Eq. 2.17 for f requires a trial-and-error process. Eq. 2.17 can be expressed as⁹

$$f_C = \left[1.74 - 2 \log\left(\frac{2\epsilon}{d} + \frac{18.7}{N_{Re} \sqrt{f_{est}}}\right) \right]^{-2}. \quad \dots \dots \dots \quad (2.18)$$

Values of f are estimated, f_{est} , and then calculated, f_C , until they agree to within an acceptable tolerance. A direct substitution procedure that uses the calculated value as the next assumed value results in convergence in only two or three iterations. The initial assumption can be obtained from one of the explicit smooth-pipe equations, or from explicit approximations to the Colebrook equation.

Numerous explicit approximations to the Colebrook equation have been proposed. Zigrang and Sylvester¹⁰ have given one of the most accurate and simple to use.

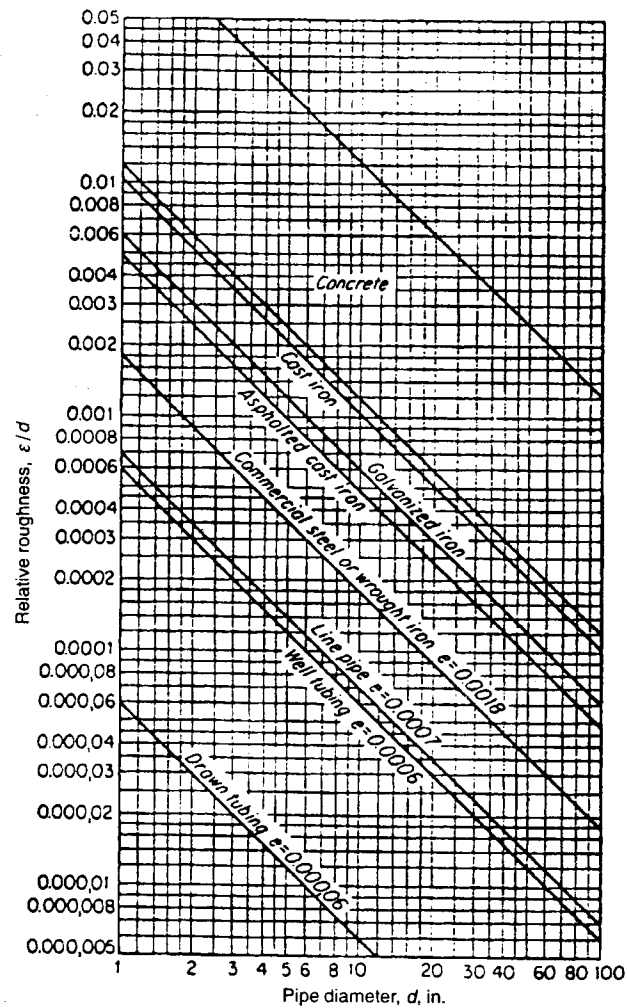


Fig. 2.3—Pipe roughness.²

$$\frac{1}{\sqrt{f}} = -2 \log\left[\frac{2\epsilon/d}{3.7} - \frac{5.02}{N_{Re}} \log\left(\frac{2\epsilon/d}{3.7} + \frac{13}{N_{Re}}\right)\right]. \quad \dots \dots \dots \quad (2.19)$$

In most cases, Eq. 2.19 can be used in lieu of Eq. 2.17.

Fig. 2.2 is a graph that shows the variations of friction factors with Reynolds number and relative roughness based on Eqs. 2.12 and 2.17.

It is important to emphasize that ϵ is not a physically measured property. Rather, it is the sand-grain roughness that would result in the same friction factor. The only way this can be done is to compare the behavior of a normal pipe with one that is sand-roughened. Moody² has done this and his results, given in Fig. 2.3, are still accepted values. However, these values should not be considered inviolate and could change significantly as a result of paraffin deposition, hydrates, erosion, or corrosion. If measured pressure gradients are available, a friction factor vs. Reynolds number relationship can be established and an effective relative roughness obtained from Fig. 2.2. Until it is again updated, this value of ϵ/d should be used for future predictions.

Initial values of roughness often are needed for design calculations. The recommended value for new tubing is $\epsilon = 0.00005$ ft. A common value used to generate pressure-gradient curves is 0.00015 ft. For tubing exposed to an environment that causes significant changes in roughness, "very dirty" pipe can have roughness values of 0.00075 ft.¹¹ For most wells, the friction component of the pressure gradient is small compared with the potential energy component. Consequently, approximate values for absolute roughness normally are sufficient.

Example 2.1—Single-Phase Liquid Pressure Drop. Calculate the pressure change in a water injection well. The following data are known.*

$$\begin{aligned} L &= 8,000 \text{ ft} \\ q_w &= 20,000 \text{ B/D} \\ \theta &= -90^\circ \\ \rho_w &= 62.4 \text{ lbm/ft}^3 \\ d &= 5.0 \text{ in.} \\ \mu_w &= 1.0 \text{ cp} \\ \varepsilon &= 0.00006 \text{ ft} \end{aligned}$$

The average velocity in the pipe is

$$v = \frac{(20,000)(5.615)}{\pi \left(\frac{5}{12}\right)^2 (86,400)} = 9.532 \text{ ft/sec.}$$

From Eq. 2.10, the Reynolds number is

$$N_{Re} = \frac{(62.4)(9.532)\left(\frac{5}{12}\right)}{\left(\frac{1.0}{1,488}\right)} = 3.688 \times 10^5.$$

Because $N_{Re} > 2,000$, flow is turbulent. The relative roughness for the pipe is

$$\frac{\varepsilon}{d} = \frac{(0.00006)}{\left(\frac{5}{12}\right)} = 0.000144.$$

From Eqs. 2.17, 2.19, or Fig. 2.2, $f = 0.0155$. Calculate the pressure gradient from Eqs. 2.5 and 2.9, neglecting acceleration effects

$$\begin{aligned} \frac{dp}{dL} &= \frac{-(0.0155)(62.4)(9.531)^2}{(2)\left(\frac{5}{12}\right)(32.2)} - \frac{(62.4)(32.2)[\sin(-90^\circ)]}{(32.2)} \\ &= -3.274 + 62.400 = 59.126 \text{ psf/ft} \\ &= -0.0227 + 0.4333 = 0.4106 \text{ psi/ft.} \end{aligned}$$

The pressure change is then

$$\begin{aligned} \Delta p &= (-0.0227 + 0.4333)(8,000) \\ &= -181.9 + 3,466.4 = 3,284.5 \text{ psi.} \end{aligned}$$

Note that the pressure change consists of a loss owing to friction of -181.9 psi and a gain from an elevation change of $+3,466.4$ psi.

2.4.3 Single-Phase Gas Flow. When a compressible fluid, such as gas, flows in a well, the density, velocity, and, consequently, the pressure gradient all vary with pressure. Cullender and Smith¹² developed the most widely used method to calculate flowing bottom-hole pressure in gas wells.

Neglecting kinetic energy, Eq. 2.5 can be written as

$$\frac{dp}{dL} = \frac{fpv^2}{2d} + \rho g \sin \theta. \quad \dots \quad (2.20)$$

For

$\rho = pM/ZRT$, $v = q/A$, $q = q_{sc}B_g$, and $B_g = p_{sc}TZ/T_{sc}p$.

Combining these expressions with Eq. 2.20 and separating variables gives

$$\frac{M}{R} \int_0^L dL = \int_{p_{wf}}^{p_{tf}} \frac{\frac{p}{ZT}}{\left(\frac{p}{ZT}\right)^2 g \sin \theta + C} dp, \quad \dots \quad (2.21)$$

*For examples in this monograph, the gravitational conversion constant, $g_c = 32.2 \text{ lbm ft/lbf sec}^2$, appears when problems are solved with customary units.

where

$$C = \frac{8p_{sc}^2 q_{sc}^2 f}{T_{sc}^2 \pi^2 d^5}.$$

Eq. 2.21 is applicable for any consistent set of units.

Substituting field units and integrating the left side of Eq. 2.21 gives

$$18.75\gamma_g L = \int_{p_{tf}}^{p_{wf}} I dp, \quad \dots \quad (2.22)$$

where

$$I = \frac{\frac{p}{ZT}}{0.001\left(\frac{p}{ZT}\right)^2 \sin \theta + F^2}, \quad \dots \quad (2.23)$$

$$F^2 = \frac{0.667f q_{sc}^2}{d^5}, \quad \dots \quad (2.24)$$

and p = psia, T = °R, q_{sc} = MMscf/D, d = in., and L = ft.

The right side of Eq. 2.22 cannot be integrated analytically without making assumptions about Z , T , and f . However, the trapezoidal rule for numerical integration can be applied by determining the value of I for each of any number of increments in p between p_{tf} and p_{wf} . Assuming the well can be divided into two halves for integration purposes—where only the intermediate value of pressure, that at the mid-depth, p_{mf} , is considered—Eq. 2.22 may be expressed as

$$\begin{aligned} 18.75\gamma_g L &= \frac{(p_{mf} - p_{tf})(I_{mf} + I_{tf})}{2} \\ &\quad + \frac{(p_{wf} - p_{mf})(I_{wf} + I_{mf})}{2}. \quad \dots \quad (2.25) \end{aligned}$$

Eq. 2.25 can be separated into two expressions, one for each half of the well.

Upper half:

$$18.75\gamma_g L/2 = (p_{mf} - p_{tf}) \frac{(I_{mf} + I_{tf})}{2}. \quad \dots \quad (2.26)$$

Lower half:

$$18.75\gamma_g L/2 = (p_{wf} - p_{mf}) \frac{(I_{wf} + I_{mf})}{2}. \quad \dots \quad (2.27)$$

While this method can be used with any number of steps, Cullender and Smith¹² demonstrated that the equivalent of four-step accuracy can be obtained with a two-step calculation if the Simpson's rule¹³ numerical-integration approach is used. The resulting equation is

$$18.75\gamma_g L = \left(\frac{p_{wf} - p_{tf}}{6}\right)(I_{wf} + 4I_{mf} + I_{tf}). \quad \dots \quad (2.28)$$

Use of the Cullender and Smith method to calculate flowing bottomhole pressures in gas wells can best be explained with an example problem.

Example 2.2—Single-Phase Gas Pressure Drop. With the following data, calculate the flowing bottomhole pressure in a gas well using the Cullender and Smith method with two increments.

$$\gamma_g = 0.75$$

$$L = 10,000 \text{ ft}$$

$$T_f = 245^\circ\text{F}$$

$$p_{tf} = 2,000 \text{ psia}$$

$$T_s = 110^\circ\text{F}$$

$$\varepsilon = 0.00007 \text{ ft}$$

$$d = 2.441 \text{ in.}$$

$$q_{sc} = 4.915 \text{ MMscf/D}$$

$$\bar{\mu} = 0.012 \text{ cp}$$

$$\theta = 90^\circ$$

Preliminary Calculations. Calculate f assuming a completely turbulent flow (fully rough wall). If flow is not completely turbulent, a Reynolds number calculated at surface conditions can be assumed to exist throughout the well. From Eqs. 2.16 and 2.24, $f=0.015$ and

$$F^2 = \frac{(0.667)(0.015)(4.915)^2}{(2.441)^5} = 0.00279.$$

Calculate I_{tf} (Eq. 2.23):

At $p_{tf}=2,000$ psia, $T=110^\circ\text{F}$, and $Z=0.71$,

$$\frac{p}{TZ} = \frac{2,000}{(570)(0.71)} = 4.942$$

and

$$I_{tf} = \frac{4.942}{(0.001)(4.942)^2 + 0.00279} = 181.60.$$

Upper Half of Well. Estimate p_{mf}^* (First Trial):

$$p_{mf}^* = p_{tf}(1 + 2.5 \times 10^{-5}L/2 \sin \theta)$$

$$= 2,000[1 + (2.5 \times 10^{-5})(5,000 \sin 90^\circ)]$$

$$= 2,250 \text{ psia.}$$

Calculate I_{mf} (Eq. 2.23):

At $p_{mf}^*=2,250$ psia, $T=110+67.5^\circ\text{F}$, and $Z=0.797$,

$$\frac{p}{TZ} = \frac{2,250}{(628)(0.797)} = 4.425$$

and

$$I_{mf} = \frac{4.425}{(0.001)(4.425)^2 + 0.00279} = 197.81.$$

Calculate p_{mf} (Eq. 2.26):

$$p_{mf} = p_{tf} + \frac{18.75\gamma_g L}{I_{mf} + I_{tf}} = 2,000 + \frac{(18.75)(0.75)(10,000)}{197.81 + 181.60}$$

$$= 2,000 + 371 + 2,371 \text{ psia (not close enough to } p_{mf}^*).$$

Estimate p_{mf}^* (Second Trial):

Select $p_{mf}^*=2,371$ psia.

Calculate I_{mf} (Eq. 2.23):

At $p_{mf}^*=2,371$ psia, $T=178^\circ\text{F}$, and $Z=0.796$,

$$\frac{p}{TZ} = \frac{2,371}{(638)(0.796)} = 4.669$$

and

$$I_{mf} = \frac{4.669}{(0.001)(4.669)^2 + 0.00279} = 189.88.$$

Calculate p_{mf} (Eq. 2.26):

$$p_{mf} = 2,000 + \frac{(18.75)(0.75)(10,000)}{189.88 + 181.60}$$

$$= 2,000 + 379 = 2,379 \text{ psia (not close enough to } p_{mf}^*).$$

Estimate p_{mf}^* (Third Trial):

Select $p_{mf}^*=2,379$ psia.

Calculate I_{mf} (Eq. 2.23):

At $p_{mf}^*=2,379$ psia, $T=178^\circ\text{F}$, and $Z=0.796$,

$$\frac{p}{TZ} = \frac{2,379}{(638)(0.796)} = 4.684$$

and

$$I_{mf} = \frac{4.684}{(0.001)(4.684)^2 + 0.00279} = 189.41.$$

Calculate p_{mf} (Eq. 2.26):

$$p_{mf} = 2,000 + \frac{(18.75)(0.75)(10,000)}{189.41 + 181.60} = 2,379 \text{ psia.}$$

Therefore, the pressure at the mid-point of the well is 2,379 psia. The value of p_{wf} is now calculated.

Lower Half of Well. Estimate p_{wf}^* (First Trial):

$$p_{wf}^* = p_{mf}(1 + 2.5 \times 10^{-5}L/2 \sin \theta)$$

$$= 2,379[1 + (2.5 \times 10^{-5})(5,000 \sin 90^\circ)]$$

$$= 2,676 \text{ psia.}$$

Calculate I_{wf} (Eq. 2.23):

At $p_{wf}^*=2,676$ psia, $T=245^\circ\text{F}$, and $Z=0.867$,

$$\frac{p}{TZ} = \frac{2,676}{(705)(0.867)} = 4.378$$

and

$$I_{wf} = \frac{4.378}{(0.001)(4.378)^2 + 0.00279} = 199.39.$$

Calculate p_{wf} (Eq. 2.27):

$$p_{wf} = p_{mf} + \frac{(18.75)(0.75)(10,000)}{199.39 + 189.41}$$

$$= 2,379 + 362 = 2,741 \text{ psia (not close enough to } p_{wf}^*).$$

Estimate p_{wf}^* (Second Trial):

Select $p_{wf}^*=2,741$ psia.

Calculate I_{wf} (Eq. 2.23):

At $p_{wf}^*=2,741$ psia, $T=245^\circ\text{F}$, and $Z=0.868$,

$$\frac{p}{TZ} = \frac{2,741}{(705)(0.868)} = 4.479$$

and

$$I_{wf} = \frac{4.479}{(0.001)(4.479)^2 + 0.00279} = 196.00.$$

Calculate p_{wf} (Eq. 2.27):

$$p_{wf} = 2,379 + \frac{(18.75)(0.75)(10,000)}{196.00 + 189.41} = 2,744 \text{ psia.}$$

This is close enough to the previously calculated value of 2,741 psia. Therefore, the flowing bottomhole pressure is 2,744 psia.

From Eq. 2.28, if the more accurate Simpson's rule numerical-integration approach is used, the flowing bottomhole pressure is predicted to be

$$p_{wf} = p_{mf} + \frac{(6)(18.75)(0.75)(10,000)}{181.60 + (4)189.41 + 196.00} = 2,743.2 \text{ psia.}$$

2.4.4 Non-Newtonian Fluids. The material presented previously is valid only for Newtonian fluids. However, fluids encountered in the petroleum industry often act as non-Newtonian fluids. These include many drilling muds; fluids, such as cement slurries, fracturing fluids, and spacers used during well-completion activities; polymers injected during EOR projects; crude oils at temperatures approaching the pour point; and many oil/water mixtures.

The design of piping systems for non-Newtonian fluids becomes complicated because the use of conventional friction-factor correlations is not directly applicable. These non-Newtonian fluids may assume any type of rheological behavior, depending on such factors as shear rate, temperature, and fluid composition. Fig. 2.4, from

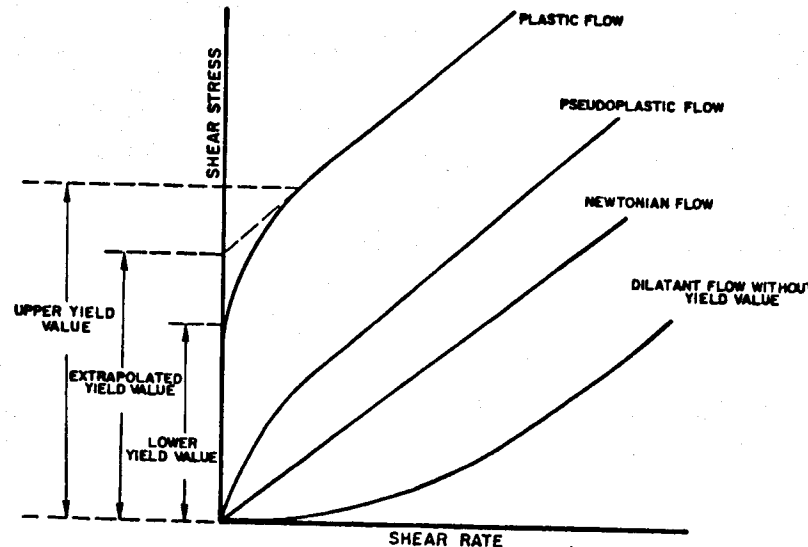


Fig 2.4—Rheological models.¹

Knudsen and Katz,¹ describes the types of rheological behavior that can be encountered.

Two methods commonly are used to design piping systems for the transport of oil/water mixtures. The first method treats the mixture as a Newtonian fluid with an apparent viscosity that can vary with water fraction. This method is covered in Chap. 3 because it can involve the combining of the viscosities from each phase to obtain a mixture viscosity. The second method treats the mixture as a non-Newtonian fluid and is based on the following assumptions¹⁴:

1. The mixture is homogeneous.
2. Slippage between phases is neglected. Thus, in-situ holdups are the same as their respective input volume fractions.
3. The rheological behavior of the oil/water dispersion system is suitably described by the Ostwald-de Waele power-law model.¹⁵

Power-Law Model. The power-law stress-strain relationship can be expressed as

$$\tau = K' \gamma^{n'} \quad (2.29)$$

If n' is unity, Eq. 2.29 will describe Newtonian behavior, and K' will be equal to the constant viscosity, μ . For a typical oil/water mixture, n' usually is less than unity, and Eq. 2.29 will describe pseudoplastic (shear thinning) behavior. It is also possible for an oil/water mixture to have n' greater than unity, resulting in dilatant (shear thickening) behavior. The type of behavior that a fluid system will follow normally is unknown but can be determined from laboratory experiments with an appropriate viscometer.

These tests must be conducted for a specified set of operating conditions: input water fraction, temperature, and droplet size distribution of the dispersed phase (or, indirectly, mixing speed). Once the fluid system is correctly characterized, the frictional pressure gradients for pipe flow in this particular oil/water dispersed system readily can be determined.

Generalized Reynolds Number. Metzner and Reed¹⁶ introduced the concept of a “generalized Reynolds number” for non-Newtonian flow. The usual Reynolds number definition is given in Eq. 2.10, which also can be written as

$$N_{Re} = \frac{\rho v d}{\tau_w} \left(\frac{8v}{d} \right). \quad (2.30)$$

where τ_w is the laminar wall shear stress, while the quantity, $8v/d$, is also the true shear rate at the pipe wall for a Newtonian fluid. Thus, the ratio, $[\tau_w/(8v/d)]$, corresponds to the Newtonian viscosity, μ .

For non-Newtonian flow, the relationship between the true shear rate and the apparent shear rate can be expressed as

$$\left(- \frac{dv}{dr} \right)_w = \left(\frac{3n' + 1}{4n'} \right) \left(\frac{8v}{d} \right), \quad (2.31)$$

where n' = the slope of a logarithmic plot of τ_w vs. $8v/d$, often called the flow-behavior index. From the same plot, the relationship of the tangential line to the laminar-flow curve can be written as

$$\tau_w = K' \left(\frac{8v}{d} \right)^{n'} \quad (2.32)$$

Combining Eqs. 2.30 and 2.32 gives

$$N_{Re_{M-R}} \frac{\rho v^{2-n'} d^{n'}}{8^{n'-1} K'} \quad (2.33)$$

and

$$\eta = K' \left(\frac{4n'}{3n' + 1} \right) \left(\frac{8v}{d} \right)^{n'-1}, \quad (2.34)$$

where $N_{Re_{M-R}}$ = the generalized Reynolds number, and η = apparent viscosity. Eqs. 2.33 and 2.34 clearly reduce to the normal Reynolds number and the Newtonian viscosity for a Newtonian fluid, when $n' = 1$ and $K' = \mu$.

Non-Newtonian Friction Factor. In general, the procedure for calculating friction factors for non-Newtonian fluids is similar to that for Newtonian fluids.

Laminar Flow. From Metzner and Reed,¹⁶ the Fanning friction factor for non-Newtonian laminar flow can be written as

$$f' = \frac{16}{N_{Re_{M-R}}} \quad (2.35)$$

Turbulent Flow—Smooth Pipes. Dodge and Metzner¹⁷ proposed this implicit friction-factor equation,

$$\sqrt{\frac{1}{f'}} = \frac{4.0}{n'^{0.75}} \log \left[N_{Re_{M-R}} f'^{(1-n'/2)} \right] - \frac{0.4}{n'^{1.2}} \quad (2.36)$$

Turbulent Flow—Rough Pipes. Govier and Aziz¹⁸ suggested this friction factor for power-law, pseudoplastic fluids flowing in rough pipes:

$$f' = f_{M-R} \left(\frac{f'_r}{f'_s} \right), \quad (2.37)$$

where f_{M-R} = the friction factor calculated from Eq. 2.36; f'_r = Newtonian flow Fanning friction factor for rough pipe, calculated at the same generalized Reynolds number; and f'_s = Newtonian

flow Fanning friction factor for smooth pipe, calculated at the same generalized Reynolds number. Szilas *et al.*¹⁹ obtained a similar result for pseudoplastic fluids from the following equation.

$$\sqrt{\frac{1}{f'}} = -4.0 \log \left[\frac{10^{-\beta/2}}{N_{Re,M-R}^{1/n'} (4f')^{(2-n')2n'}} + \frac{\epsilon}{3.71d} \right], \quad \dots \quad (2.38)$$

where

$$\beta = 1.51^{1/n'} \left(\frac{0.707}{n'} + 2.12 \right) - \frac{4.015}{n'} - 1.057. \quad \dots \quad (2.39)$$

Note that Eq. 2.38 is analogous to the Colebrook equation for Newtonian fluids given by Eq. 2.17, and also requires a trial-and-error solution procedure.

Fully Rough Wall Turbulence. Govier and Aziz¹⁸ recommended,

$$\sqrt{\frac{1}{f'}} = 4.06 \log d/2\epsilon + 6.0 - \frac{2.65}{n'}. \quad \dots \quad (2.40)$$

For Newtonian fluids, Eq. 2.40 essentially reduces to the von Karman equation,¹⁸

$$\sqrt{\frac{1}{f'}} = 4.06 \log d/2\epsilon + 3.36. \quad \dots \quad (2.41)$$

Frictional Pressure Gradient. Once the Fanning friction factor, f' , is determined for the particular system, the frictional pressure gradient can be calculated from

$$\left(\frac{dp}{dL} \right)_f = \frac{2f' \rho v^2}{d}. \quad \dots \quad (2.42)$$

K' and n' are clearly the two important parameters that will affect the frictional pressure-gradient calculation for a dispersion system. These two parameters can be determined experimentally with an appropriate viscometer.

Example 2.3—Non-Newtonian Oil/Water Mixture Pressure Drop. A horizontal pipe discharges an oil/water mixture at atmospheric pressure. Determine the inlet pressure required to maintain a constant volumetric flow rate of the dispersion for an input-water fraction of 20%. The following also are given:

$$q_m = 30 \text{ ft}^3/\text{sec}$$

$$d = 20 \text{ in.}$$

$$\epsilon = 0.001 \text{ ft}$$

$$L = 10,000 \text{ ft}$$

$$\rho_o = 53.74 \text{ lbm/ft}^3$$

$$\rho_w = 62.23 \text{ lbm/ft}^3$$

$$n' = 0.8589$$

$$K' = 7.1475 \times 10^{-3} \text{ lbf sec}^n/\text{ft}^2$$

Calculate the mixture density, using $\rho_m = \rho_o f_o + \rho_w f_w = 55.4 \text{ lbm/ft}^3$. For the given flow rate and water fraction, calculate the generalized Reynolds number,

$$N_{Re,M-R} \frac{\rho_m v_m^{n'-1} d^{n'}}{8^{n'-1} K'} = 9.97 \times 10^3.$$

The criterion for turbulent flow is considered to be $N_{Re,M-R} > 1,500$. For this example the flow regime is turbulent.

Using Eq. 2.37, compute the friction factor for turbulent flow of pseudoplastic fluids in rough pipes.

$$f' = f_{M-R} \left(\frac{f_s}{f_r} \right) = 0.007(1.006) \\ = 0.00704,$$

where f_{M-R} is given by Eq. 2.36, f_s is given by Eq. 2.14, and f_r is given by Eq. 2.17. Note that if Eq. 2.38 were used, the trial-and-error procedure would have given a f' value of 0.00676.

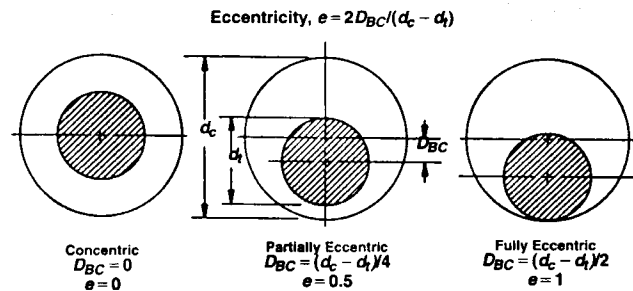


Fig. 2.5—Annuli configurations.²⁸

Calculate the pipe inlet pressure, p_1 .

$$p_1 = p_2 + 2f' \rho_m \frac{L}{d} v_m^2 = 205.9 \text{ psia.}$$

2.5 Flow in an Annulus

In the petroleum industry, flow in wells normally occurs in a tubing string. However, many oil wells with high production rates produce through the casing/tubing annulus. This trend is dictated by economics, multiple completions, and regulated production rates. Although few in number when compared with all producing wells, these "casing flow" wells account for a significant part of the world's oil production.

Other casing-flow applications are found in wells under various types of artificial lift. In sucker-rod pumping wells, a rod string is installed inside the tubing string to connect the prime mover unit on the surface to the pump at the bottom of the well. The fluids are pumped upward through the tubing-rod string annulus. Casing flow also can occur in gas well production. To remove or "unload" undesirable liquids that can accumulate at the bottom of these wells, a siphon tube often is installed inside the tubing string. The permanency of the siphon tube in the tubing string requires the fluids to flow upward through the tubing-string/siphon-tube annulus.

In the past, annuli have been treated based on the hydraulic diameter concept. The hydraulic diameter is four times the area for flow divided by the wetted perimeter. For annulus configurations,

$$d_h = d_c - d_t. \quad \dots \quad (2.43)$$

However, the hydraulic diameter is not always the most representative characteristic dimension for flow in an annulus. To determine appropriate characteristic dimensions, a clear understanding of flow in an annulus must be achieved.

An annulus is characterized by the existence of two circular pipes, where the flow occurs through the area bounded by the outer pipe inner wall and the inner pipe outer wall. Two geometrical parameters identify these configurations: the annulus pipe-diameter ratio, $K = d_t/d_c$, and the degree of eccentricity. The degree of eccentricity accounts for the displacement of the inner pipe center from the outer pipe center and is expressed by

$$e = \frac{2D_{BC}}{(d_c - d_t)}, \quad \dots \quad (2.44)$$

where d_t = outer diameter of the inner pipe (tubing), d_c = inner diameter of the outer pipe (casing), and D_{BC} = distance between the pipe centers. Annuli can have eccentricity values varying from zero to one. Fig. 2.5 shows cross sections of annuli with the same pipe-diameter-ratio value, K , and for eccentricities of 0.0, 0.5, and 1.0.

2.5.1 Friction Factor for Single-Phase Flow. For noncircular conduits, single-phase-flow friction factors often are determined through the application of the hydraulic-diameter concept. However, this concept is better suited for high degrees of turbulence.

For laminar flow, a rigorous treatment of the flow field is possible for any annulus configuration. Bird *et al.*¹⁵ gave analytical solutions for both the velocity profile and friction factor for a concentric annulus. Combining the developments by Heyda²⁰ and Snyder and

Goldstein,²¹ analytical solutions also can be found for these flow parameters for an eccentric annulus. These solutions are presented in a later section.

In turbulent flow, even for circular pipes, the mechanisms of turbulence are by no means fully understood. However, various semi-empirical and analytical models have been used successfully to predict the velocity distribution and pressure gradient. In noncircular configurations, where the transport phenomena are intrinsically more complex than for circular pipes, the formulation of an analytical model is even more complicated. Three ways have been used to predict the flow behavior of a turbulent-flow field in an annulus: empirical correlations, semi-empirical correlations, and application of universal velocity distributions.

Empirical correlations involve the application of curve-fitting techniques to experimental data to predict an overall flow quantity, such as friction factor. The resulting friction-factor correlations normally take the form of the Blasius-type expression, as given in Eq. 2.15 where C and n are determined empirically. Examples include the correlations of Knudsen and Katz,¹ and Dodge.²² Winkler²³ successfully used the Dodge correlation for flow in an annulus; however, he noted that this procedure did not take into account the annulus pipe-diameter ratio.

Semiempirical approaches involve the use of experimental data for turbulent flow in combination with characteristics of laminar flow in the same noncircular configuration. The Gunn and Darling²⁴ procedure is an example of this prediction category. Gunn and Darling concluded that the similarity existing between friction factors for circular and noncircular configurations in the laminar region is also accompanied by a similarity in the turbulent region. Using dimensional analysis, they showed that for turbulent flow in noncircular sections, the following functional dependency for friction factor exists.

$$f_{NC} = f_{NC} \left(N_{Re}, \frac{F_c}{F_{NC}} \right), \quad (2.45)$$

where F_c and F_{NC} are the so-called friction geometry parameters for the circular and noncircular configurations, respectively. At low Reynolds numbers, the friction factor is inversely proportional to the ratio F_c/F_{NC} . However, at high Reynolds numbers, the friction factor becomes independent of the F_c/F_{NC} ratio. At intermediate values of Reynolds numbers, the function given in Eq. 2.45 is established from suitable experimental data involving many noncircular types of configurations.

Newtonian Laminar Flow. The friction factor in laminar flow is determined from solution of the continuity equation, the equation of motion, and the Fanning equation. The solution is obtained for Newtonian, fully developed, steady-state, axial flow.

The Fanning equation can be written as

$$\Delta p = 2f' \frac{L}{d_h} \rho v^2, \quad (2.46)$$

and the Reynolds number is given by

$$N_{Re} = \frac{\rho v d_h}{\mu}. \quad (2.47)$$

The Fanning friction factor in circular pipes, f'_p , is given by

$$f'_p = \frac{F_p}{N_{Re}} = \frac{16}{N_{Re}}, \quad (2.48)$$

where F_p is a friction geometry parameter, having a constant value of 16 for pipe flow.

For a concentric annulus¹⁵

$$f'_{CA} = \frac{F_{CA}}{N_{Re}} = \frac{16}{N_{Re}} \frac{(1-K)^2}{\left[\frac{1-K^4}{1-K^2} - \frac{1-K^2}{\ln(1/K)} \right]}. \quad (2.49)$$

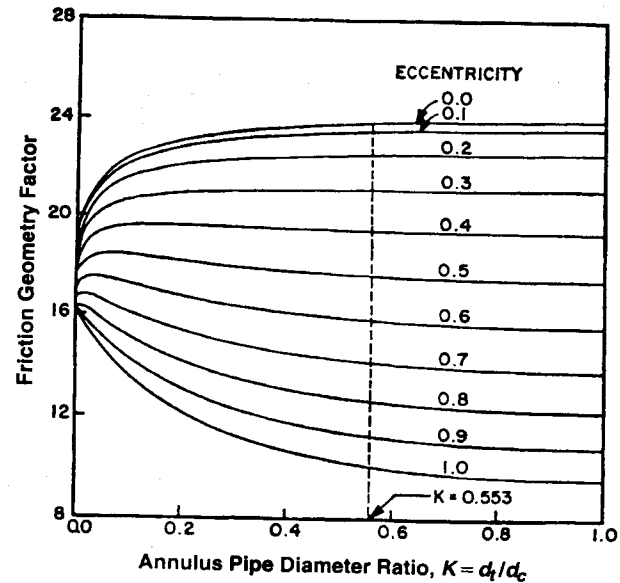


Fig. 2.6—Friction-geometry parameter in annuli and circular pipe (laminar single-phase flow at same Reynolds number).²⁸

Thus,

$$F_{CA} = F_{CA}(K) = \frac{16(1-K)^2}{\left[\frac{1-K^4}{1-K^2} - \frac{1-K^2}{\ln(1/K)} \right]}, \quad (2.50)$$

where f'_{CA} is the Fanning friction factor and F_{CA} is the friction-geometry parameter for a concentric annulus.

Through use of a bipolar coordinate system, Snyder and Goldstein²¹ presented an analytical solution for laminar flow in an eccentric annulus. Their solution was based on previous developments by Heyda²⁰ and El-Saden.²⁵ Redberger and Charles,²⁶ who presented a numerical solution for the problem, used the same technique. Applying the Fanning equation, it can be shown that

$$f'_{EA} = \frac{F_{EA}}{N_{Re}} = \frac{1}{N_{Re}} \frac{4(1-K)^2(1-K^2)}{\phi \sinh^4 \eta_0} \quad (2.51)$$

and

$$F_{EA} = F_{EA}(K, e) = \frac{4(1-K)^2(1-K^2)}{\phi \sinh^4 \eta_0}, \quad (2.52)$$

where

$$\begin{aligned} \phi &= (\cosh \eta_i - \cosh \eta_0)^2 \left(\frac{1}{\eta_i - \eta_0} - 2 \sum_{n=1}^{\infty} \frac{2n}{e^{2n\eta_i} - e^{2n\eta_0}} \right) \\ &\quad + \frac{1}{4} \left(\frac{1}{\sinh^4 \eta_0} - \frac{1}{\sinh^4 \eta_i} \right), \end{aligned} \quad (2.53)$$

$$\cosh \eta_i = \frac{K(1+e^2) + (1-e^2)}{2Ke}, \quad (2.54)$$

and

$$\cosh \eta_0 = \frac{K(1-e^2) + (1+e^2)}{2Ke}. \quad (2.55)$$

Although an infinite-series term is involved in Eq. 2.53, the number of terms can be truncated after several terms. As before, f'_{EA} is the Fanning friction factor and F_{EA} is the friction-geometry parameter for an eccentric annulus. Fig. 2.6 presents a plot of Eq. 2.52. Note that $K = 0$ for pipe flow, resulting in $F_{EA} = 16$, and that for fully concentric pipes ($e = 0$), F_{EA} approaches 24 as K approaches 1.0. This also corresponds to the analytical value for single-phase laminar

flow through parallel plates. For a fixed-diameter ratio, the friction-geometry parameter and, consequently, the friction factor decrease with an increase in the degree of eccentricity. Also, for a high degree of eccentricity, the friction-geometry parameter and, consequently, the friction factor are always smaller than for a circular pipe.

Finally, the error involved in predicting friction-factor values in annulus configurations by applying only the hydraulic-diameter concept and neglecting eccentricity can vary between 40 to 50%, depending on the annulus pipe-diameter ratio and the degree of eccentricity. This is demonstrated by the dashed line in Fig. 2.6, which represents the expected friction-geometry parameter values ($K = 0.553$) for the experimental facility used by Caetano *et al.*²⁷

Newtonian Turbulent Flow. Caetano *et al.* recommended the Gunn and Darling²⁴ procedure for turbulent flow because of its simplicity and good performance. The approach combines the behavior for friction factor in noncircular configurations, as given by Eq. 2.45, with a large amount of turbulent-flow data for many non-circular configurations. Combining the Gunn and Darling developments into a Nikuradse-type expression, the friction factor for concentric and eccentric annuli are predicted, respectively, from

$$\frac{1}{\left\{ f'_{CA} \left(\frac{F_p}{F_{CA}} \right)^{0.45 \exp[-(N_{Re} - 3,000)/10^6]} \right\}^{1/2}} = 4 \log \left[N_{Re} \left\{ f'_{CA} \left(\frac{F_p}{F_{CA}} \right)^{0.45 \exp[-(N_{Re} - 3,000)/10^6]} \right\}^{1/2} \right] - 0.4 \quad (2.56)$$

and

$$\frac{1}{\left\{ f'_{EA} \left(\frac{F_p}{F_{EA}} \right)^{0.45 \exp[-(N_{Re} - 3,000)/10^6]} \right\}^{1/2}} = 4 \log \left[N_{Re} \left\{ f'_{EA} \left(\frac{F_p}{F_{EA}} \right)^{0.45 \exp[-(N_{Re} - 3,000)/10^6]} \right\}^{1/2} \right] - 0.4. \quad (2.57)$$

In these equations, f' = Fanning friction factor and F = laminar-flow friction-geometry parameter presented earlier.

Non-Newtonian Laminar Flow. There is no available exact analytical solution for non-Newtonian laminar flow in an annulus. Haciislamoglu and Langlinais²⁸ developed a numerical model to analyze the flow behavior of yield/power-law fluids in concentric and eccentric annuli.

Concentric Annulus. The concentric annular flow of power-law fluids can be approximated closely by use of the less complex flow equations for a narrow slot.²⁹ The slot-flow approximation works well as long as $d_t/d_c > 0.3$. The relationship between true shear rate and apparent shear rate at the wall is expressed as

$$\left(-\frac{dv}{dr} \right)_w = \frac{4n' + 2}{4n'} \frac{8v}{d_c - d_t}, \quad (2.58)$$

where, n' = flow-behavior index.

The generalized Reynolds number concept also can be applied for an annular-flow geometry. The generalized Reynolds number is

$$N_{Re_{M-R}} \frac{\rho v^{2-n'} (d_c - d_t)^{n'}}{8^{n'-1} K'}, \quad (2.59)$$

where K' is a parameter related to the consistency index and is expressed by Eq. 2.60 for an annular geometry.

$$K' = K \left(\frac{4n' + 2}{4n'} \right)^{n'}. \quad (2.60)$$

Then, friction factor can be written as

$$f' = \frac{16}{N_{Re_{M-R}}}. \quad (2.61)$$

Therefore, with Eq. 2.62, the frictional pressure gradient for a concentric annulus can be calculated as

$$\left(\frac{dp}{dL} \right)_f = \frac{2f' \rho v^2}{d_c - d_t}. \quad (2.62)$$

Eccentric Annulus. Haciislamoglu and Langlinais²⁸ developed a correlation to predict frictional pressure losses of power-law fluids in an eccentric annulus. A correlating parameter, R , was defined as the ratio of frictional pressure losses in an eccentric annulus to those in a concentric annulus. The empirical correlation, which is valid for eccentricities from 0 to 0.95, pipe diameter ratios of 0.3 to 0.9, and flow-behavior indices, n' , of 0.4 to 1.0, is given by

$$R = 1 - 0.072 \frac{e}{n'} \left(\frac{d_t}{d_c} \right)^{0.8454} - 15e^2 \sqrt{n'} \left(\frac{d_t}{d_c} \right)^{0.1852} + 0.96e^3 \sqrt{n'} \left(\frac{d_t}{d_c} \right)^{0.2527}. \quad (2.63)$$

This correlation has a claimed accuracy of $\pm 5\%$. To predict the frictional pressure gradient in an eccentric annulus, the frictional pressure gradient in a concentric annulus is first calculated with Eq. 2.62. The corrected value for an eccentric annulus is then determined from

$$\left(\frac{dp}{dL} \right)_{FE} = \left(\frac{dp}{dL} \right)_{FC} R. \quad (2.64)$$

Non-Newtonian Turbulent Flow. There is no documented model to predict non-Newtonian turbulent flow in an annulus. However, an approach analogous to regular pipe flow can be postulated. The generalized Reynolds number for a concentric pipe can be used in the non-Newtonian pipe flow friction-factor correlations. Then, the Blasius equation can be used to calculate the frictional pressure gradient.

For an eccentric annulus, one might try to use the R correlation (Eq. 2.63) developed for laminar flow with a specific value of $d_t/d_c = 0.01$, as suggested by Sas-Jaworsky.³⁰ The frictional pressure gradient then can be obtained by use of the modified R for turbulent flow and a concentric annulus in Eq. 2.64.

2.6 Conservation of Energy

Application of energy conservation to fluid flow in pipes requires that in a given pipe segment the energy in, minus the energy out, plus the heat energy transferred to or from the surroundings must equal the rate of energy accumulation.¹⁵

$$\frac{\partial}{\partial t} (\rho e) = \frac{\partial}{\partial L} \left[\rho v \left(e + \frac{p}{\rho g_c J} \right) \right] + \frac{Q \pi d}{A}. \quad (2.65)$$

For steady-state flow, Eq. 2.65 reduces to

$$\frac{d}{dL} \left[\rho v \left(e + \frac{p}{\rho g_c J} \right) \right] = - \frac{Q \pi d}{A}. \quad (2.66)$$

The parameter J is the mechanical equivalent of heat and is necessary when dealing with customary units where mechanical energy and thermal energy have different units.

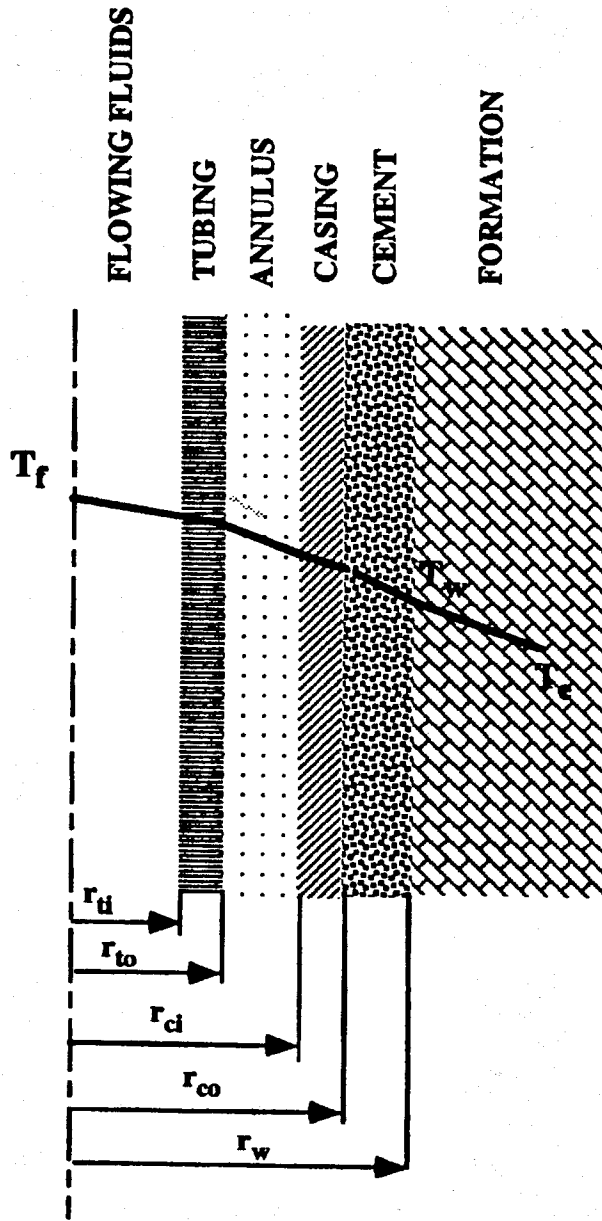


Fig. 2.7—Cross section of typical wellbore.³ (Reproduced with permission of the McGraw-Hill Cos.)

Expanding the left side of Eq. 2.66 yields

$$\rho v \frac{d}{dL} \left(e + \frac{p}{\rho g_c J} \right) + \left(e + \frac{p}{\rho g_c J} \right) \frac{d(\rho v)}{dL} = - \frac{Q\pi d}{A}. \quad (2.67)$$

In Eqs. 2.66 and 2.67, e is the intrinsic specific energy and is defined by

$$e = \frac{gL \sin \theta}{g_c J} + \frac{1}{2} \frac{v^2}{g_c J} + u. \quad (2.68)$$

Combining Eqs. 2.67 and 2.68 with Eq. 2.2 from conservation of mass principles yields

$$\rho v \frac{d}{dL} \left(\frac{gL \sin \theta}{g_c J} + \frac{1}{2} \frac{v^2}{g_c J} + u + \frac{p}{\rho g_c J} \right) = - \frac{Q\pi d}{A}. \quad (2.69)$$

Because specific enthalpy is defined as

$$h = u + \frac{p}{\rho g_c J}. \quad (2.70)$$

Eq. 2.69 can be expressed as

$$\rho v \frac{g \sin \theta}{g_c J} + \frac{\rho v v}{g_c J} \frac{dv}{dL} + \rho v \frac{dh}{dL} = - \frac{Q\pi d}{A}. \quad (2.71)$$

Finally, solving for the enthalpy gradient yields

$$\frac{dh}{dL} = - \frac{Q\pi d}{w} - \frac{v}{g_c J} \frac{dv}{dL} - \frac{g \sin \theta}{g_c J}. \quad (2.72)$$

The heat flux, Q , is defined in terms of overall heat-transfer coefficient and temperature difference between the fluids and the surroundings. Thus,

$$Q = U(T_f - T_e). \quad (2.73)$$

Eq. 2.72 clearly shows that the steady-state enthalpy-gradient equation is made up of three components. Thus,

$$\left(\frac{dh}{dL} \right)_t = \left(\frac{dh}{dL} \right)_{HT} + \left(\frac{dh}{dL} \right)_{acc} + \left(\frac{dh}{dL} \right)_{el}, \quad (2.74)$$

where

$$\left(\frac{dh}{dL} \right)_{HT} = - \frac{U\pi d(T_f - T_e)}{w}. \quad (2.75)$$

Because of the strong dependence of enthalpy and heat transfer on temperature, Eq. 2.72 is used to determine temperature change when fluids flow through pipes. Normally, the kinetic energy term is negligible. Therefore, for a horizontal pipe, an increase in fluid enthalpy equals the heat transferred to the fluid from the surroundings. Also, if no heat transfer occurs, an increase in elevation causes a decrease in enthalpy and a corresponding decrease in temperature.

2.6.1 Wellbore Heat Transfer. When hot reservoir fluids enter a wellbore and begin to flow to the surface, they immediately begin losing heat to the cooler surrounding rock. The surrounding rock gradually heats up, reducing the temperature difference and the heat transfer between the fluids and the rock. Eventually, for a constant-mass flow rate, the earth surrounding the well reaches a steady-state temperature distribution. Prediction of fluid temperatures in the wellbore as a function of depth and time is necessary to determine the fluid's physical properties and calculate pressure gradients.

Because of the high thermal conductivity and relatively small radial distance between the flowing fluids and the borehole wall, heat transfer in this region normally can be considered steady state. All heat lost by the fluids instantaneously flows through the wellbore and into the surrounding rock. An axial cross section of a typical wellbore is shown in Fig. 2.7. The following description of steady-state heat transfer in a wellbore would have to be modified for other types of completions.

Heat transfer within the tubing and in a fluid-filled annulus is primarily a result of convection. Heat transfer through the tubing and casing walls and through a cement-filled annulus between the casing and borehole wall primarily results from conduction.

Heat transfer resulting from conduction can be described by Fourier's equation in radial coordinates¹⁵

$$q = - 2\pi r \Delta L k \frac{\partial T}{\partial r}, \quad (2.76)$$

where q is the amount of heat flowing radially through a solid with thermal conductivity, k . Integration of Eq. 2.76 gives

$$T_2 - T_1 = \frac{q}{2\pi \Delta L} \frac{\ln(r_2/r_1)}{k_{1-2}}. \quad (2.77)$$

Heat transfer resulting from radial convection can be described by¹⁵

$$q = 2\pi r \Delta L h \Delta T, \quad \dots \dots \dots \quad (2.78)$$

where h = local convective-film coefficient.

If steady-state heat transfer occurs in the wellbore, q is constant. Expressions for temperature change through the wellbore can be developed from Eqs. 2.77 and 2.78 as follows.

For convection in the tubing,

$$T_f - T_u = \frac{q}{2\pi \Delta L} \frac{1}{r_u h_f}, \quad \dots \dots \dots \quad (2.79)$$

For conduction through the tubing wall,

$$T_u - T_{io} = \frac{q}{2\pi \Delta L} \frac{\ln\left(\frac{r_{io}}{r_u}\right)}{k_t}. \quad \dots \dots \dots \quad (2.80)$$

For convection through the casing/tubing annulus,

$$T_{io} - T_{ci} = \frac{q}{2\pi \Delta L} \frac{1}{r_{ci} h_{an}}. \quad \dots \dots \dots \quad (2.81)$$

For conduction through the casing,

$$T_{ci} - T_{co} = \frac{q}{2\pi \Delta L} \frac{\ln\left(\frac{r_{co}}{r_{ci}}\right)}{k_c}. \quad \dots \dots \dots \quad (2.82)$$

For conduction through the cement in the casing/borehole annulus,

$$T_{co} - T_w = \frac{q}{2\pi \Delta L} \frac{\ln\left(\frac{r_w}{r_{co}}\right)}{k_{cem}}. \quad \dots \dots \dots \quad (2.83)$$

Heat transfer into the surrounding rock is by heat conduction and is a transient process. The transient radial-heat-conduction equation is identical to the diffusivity equation encountered in transient well-test analysis.³¹ The infinite-reservoir, line-source solution is

$$T_w - T_e = \frac{q}{2\pi \Delta L} \frac{f(t)}{k_e}, \quad \dots \dots \dots \quad (2.84)$$

where T_e = the undisturbed geothermal earth temperature, $f(t)$, is given by

$$f(t) = \frac{1}{2} E_i\left(\frac{-r_w^2}{4\alpha t}\right), \quad \dots \dots \dots \quad (2.85)$$

and α = the earth thermal diffusivity defined as

$$\alpha = \frac{k_e}{\rho C}. \quad \dots \dots \dots \quad (2.86)$$

To monitor temperatures at the wellbore, the logarithmic approximation to the E_i solution is valid for times greater than 1 week.³² Thus, for $x < 0.0025$

$$E_i(-x) \approx \ln(x) + 0.5772 \quad \dots \dots \dots \quad (2.87)$$

and

$$f(t) = 0.405 + 0.5 \ln(t_{Dw}), \quad \dots \dots \dots \quad (2.88)$$

where

$$t_{Dw} = \frac{\alpha t}{r_w^2}. \quad \dots \dots \dots \quad (2.89)$$

Hasan and Kabir³³ showed that for typical reservoirs Eq. 2.88 can cause significant errors if applied to times less than 250 hours. They presented Eqs. 2.90 and 2.91 as simplified equations that, when used together, are valid for all times.

If $t_{Dw} \leq 1.5$,

$$f(t) = 1.1281 \sqrt{t_{Dw}} (1 - 0.3 \sqrt{t_{Dw}}). \quad \dots \dots \dots \quad (2.90)$$

If $t_{Dw} > 1.5$,

$$f(t) = [0.4063 + 0.5 \ln(t_{Dw})] \left(1 + \frac{0.6}{t_{Dw}}\right). \quad \dots \dots \dots \quad (2.91)$$

Hasan and Kabir³⁴ also stated that, in most cases of oil production, the temperature difference across the annulus is usually small and convective (natural) heat transfer becomes important. Unfortunately, the literature reports no work on natural convection in vertical annular geometry. Hasan and Kabir recommended using

$$h_{an} = \frac{0.049 (N_{Gr} N_{Pr})^{1/3} N_{Pr}^{0.074} k_{an}}{r_{io} \ln\left(\frac{r_{ci}}{r_{io}}\right)}, \quad \dots \dots \dots \quad (2.92)$$

where the Grashof number, N_{Gr} , reflects the extent of motion of the annulus fluid resulting from natural convection.

$$N_{Gr} = \frac{(r_{ci} - r_{io})^3 g \rho_{an}^2 \beta (T_{io} - T_{ci})}{\mu_{an}^2}. \quad \dots \dots \dots \quad (2.93)$$

The density of the heated fluid next to the tubing wall is less than the fluid next to the casing, creating a buoyancy force. The product of β (coefficient of thermal expansion) and the temperature difference is a measure of the density difference. The viscous force working against the buoyancy generates a circular motion of the fluid in the annulus. The Prandtl number, N_{Pr} , is a measure of the interaction between the hydrodynamic boundary layer and the thermal boundary layer and is defined as

$$N_{Pr} = \frac{\mu_{an} C_{P,an}}{k_{an}}. \quad \dots \dots \dots \quad (2.94)$$

Combining Eqs. 2.79 through 2.84 determines the total temperature change between the fluids and the undisturbed geothermal temperature of the surrounding rock.

$$T_f - T_e = \frac{q}{2\pi \Delta L} \left[\frac{1}{r_u h_f} + \frac{\ln\left(\frac{r_{io}}{r_u}\right)}{k_t} + \frac{1}{r_{ci} h_{an}} \right. \\ \left. + \frac{\ln\left(\frac{r_{co}}{r_{ci}}\right)}{k_c} + \frac{\ln\left(\frac{r_w}{r_{co}}\right)}{k_{cem}} + \frac{f(t)}{k_e} \right]. \quad \dots \dots \dots \quad (2.95)$$

A simple expression for the total heat loss from the fluids in the tubing can be estimated from Newton's law of cooling,¹⁵

$$q = 2\pi r_{io} \Delta L U \Delta T, \quad \dots \dots \dots \quad (2.96)$$

where U = an overall heat-transfer coefficient. Comparing Eqs. 2.95 and 2.96, it is evident that $(r_{io} U)^{-1}$ is the bracketed term in Eq. 2.95.

2.6.2 Temperature Prediction. Prediction of temperatures in wells requires application of conservation of mass, momentum, and energy principles. This can be accomplished by coupling the pressure-gradient and enthalpy-gradient equations given by Eqs. 2.5 and 2.72. The complexity of these equations prevents a rigorous analytical solution, but a numerical-solution procedure is given in Chap. 3. However, Sagar *et al.*,³⁵ Alves *et al.*,³⁶ and Hasan and Kabir³⁴ presented approximate analytical solutions. The Alves *et al.* formulation was for flow in pipes at any inclination angle. Their solution degenerates to equations presented by Ramey³² for the case of injection wells and by Coulter and Bardon³⁷ for the case of horizontal pipelines. Because the Alves *et al.* method involves fewer restrictive assumptions, it should yield more accurate predictions. Although numerous other publications have appeared, primarily pertaining to steam injection or producing wells, all are modifications to the Ramey method or to the calculation of heat-transfer coefficients. A summary of the Alves *et al.*³⁶ solution follows.

Because enthalpy is a state property, $h = h(p, T)$, a change in enthalpy can be calculated by considering effects of temperature and pressure separately. Thus,

$$\begin{aligned} dh &= \left(\frac{\partial h}{\partial T}\right)_p dT + \left(\frac{\partial h}{\partial p}\right)_T dp \\ &= C_p dT + \left(\frac{\partial h}{\partial p}\right)_T dp. \end{aligned} \quad (2.97)$$

Consider an isenthalpic process so that

$$dh = 0 = C_p dT + \left(\frac{\partial h}{\partial p}\right)_T dp,$$

or

$$\left(\frac{\partial h}{\partial p}\right)_T = -C_p \left(\frac{dT}{dp}\right)_h = -C_p \eta, \quad (2.98)$$

where η = the Joule-Thompson coefficient and represents isenthalpic cooling (or heating) by expansion. Combining Eqs. 2.97 and 2.98 gives

$$dh = C_p dT - C_p \eta dp. \quad (2.99)$$

Combining Eqs. 2.99 and 2.72 gives

$$\begin{aligned} C_p \frac{dT_f}{dL} - C_p \eta \frac{dp}{dL} &= \\ -\frac{g \sin \theta}{g_c J} - \frac{v}{g_c J dL} - \frac{U \pi d}{w} (T_f - T_e). \end{aligned} \quad (2.100)$$

Eq. 2.100 can be simplified to this differential equation.

$$\frac{dT_f}{dL} + \frac{T_f}{A} = \frac{T_e}{A} + \frac{1}{J \rho C_p} \frac{dp}{dL} \phi, \quad (2.101)$$

where

$$A = \frac{C_p w}{U \pi d} \quad (2.102)$$

and

$$\phi = \left[\frac{J \rho \eta C_p \frac{dp}{dL} - \frac{\rho g \sin \theta}{g_c} - \frac{\rho v}{g_c} \frac{dv}{dL}}{\frac{dp}{dL}} \right]. \quad (2.103)$$

If the surrounding temperature varies linearly with depth,

$$T_e = T_{ei} - g_G L \sin \theta, \quad (2.104)$$

where T_{ei} = surrounding temperature at the inlet of the pipe and is often taken as the reservoir temperature. The geothermal temperature gradient, g_G , typically varies from approximately 1.0 to 2.0°F/100 ft of vertical depth, depending on the thickness of the earth crust, presence of volcanic activity, and other such factors.

Combining Eqs. 2.101 and 2.104 yields a generalized differential equation that incorporates both the enthalpy- and pressure-gradient equations with no limiting assumptions. Thus,

$$\frac{dT_f}{dL} + \frac{T_f}{A} = \frac{T_{ei} - g_G L \sin \theta}{A} + \frac{1}{J \rho C_p} \frac{dp}{dL} \phi. \quad (2.105)$$

Eq. 2.105 can be integrated assuming constant values for U , C_p , η , g_G , θ , v , dv/dL , and dp/dL . The resulting solution is

$$\begin{aligned} T_f &= (T_{ei} - g_G L \sin \theta) + (T_i - T_{ei}) e^{-L/A} \\ &\quad + g_G \sin \theta A (1 - e^{-L/A}) + \frac{1}{J \rho C_p} \frac{dp}{dL} \phi A (1 - e^{-L/A}). \end{aligned} \quad (2.106)$$

Eq. 2.106 degenerates to all the more restrictive approximate analytical expressions to predict temperatures of fluids flowing in pipes.

For the case of horizontal flow, where $\theta = 0^\circ$, and neglecting acceleration effects, Eq. 2.103 simplifies to

$$\phi = J \rho \eta C_p \dots \quad (2.107)$$

and Eq. 2.106 degenerates to

$$T_f = T_{ei} + (T_i - T_{ei}) e^{-L/A} + \eta \frac{dp}{dL} A (1 - e^{-L/A}). \quad (2.108)$$

Eq. 2.108 is equivalent to the Coulter and Bardon³⁷ equation to predict temperatures in horizontal pipelines.

For an ideal gas, $\eta = 0$, and neglecting acceleration effects, Eq. 2.103 simplifies to

$$\phi = \left[\frac{-\rho g \sin \theta}{g_c} \right] \frac{\frac{dp}{dL}}{\frac{dp}{dL}} \dots \quad (2.109)$$

and Eq. 2.106 degenerates to

$$\begin{aligned} T_f &= (T_{ei} - g_G L \sin \theta) + (T_i - T_{ei}) e^{-L/A} \\ &\quad + g_G \sin \theta A (1 - e^{-L/A}) - \frac{g \sin \theta}{J g_c C_p} A (1 - e^{-L/A}), \end{aligned} \quad (2.110)$$

which is equivalent to the Ramey³² equation for an ideal gas. For the case of an incompressible liquid,

$$\eta = -\frac{1}{J C_p} \dots \quad (2.111)$$

and

$$\phi = \left[\frac{-\frac{dp}{dL} - \frac{\rho g \sin \theta}{g_c} - \frac{\rho v}{g_c} \frac{dv}{dL}}{\frac{dp}{dL}} \right] = \left[\frac{\frac{U \pi d}{w}}{\frac{dp}{dL}} \right]. \quad (2.112)$$

Neglecting friction, $\phi = 0$, and Eq. 2.106 degenerates to

$$\begin{aligned} T_f &= (T_{ei} - g_G L \sin \theta) + (T_i - T_{ei}) e^{-L/A} \\ &\quad + g_G \sin \theta A (1 - e^{-L/A}), \end{aligned} \quad (2.113)$$

which is equivalent to the Ramey expression for incompressible-liquid flow.

Comparison of Eqs. 2.106 and 2.113 shows that the Alves *et al.*³⁶ solution is actually the Ramey equation for single-phase liquid, plus a correction term. The correction term is a function of the total pressure gradient and the dimensionless parameter, ϕ . Analysis of this dimensionless coefficient can show when consideration of the correction term becomes important.

Calculation of flowing temperatures as a function of depth and time can be very tedious because of the complexity of the overall heat-transfer coefficient in Eq. 2.96. Shiu and Beggs³⁸ proposed an empirical correlation for A that was developed from a broad set of flowing-temperature surveys. The resulting equation is independent of time

$$A = 0.0149(w)^{0.5253}(d_{ii})^{-0.2904}(\gamma_{API})^{0.2608}(\gamma_g)^{4.4146}(\rho_L)^{2.9303}, \quad (2.114)$$

where w is in pounds per second, d_{ii} is in inches, and ρ_L is in pounds per cubic foot.

Eq. 2.106 is recommended when calculating temperature changes in wells flowing multiphase mixtures. It is first necessary to define several physical properties in terms of mixtures. These mixture properties are discussed in Chap. 3.

Example 2.4—Temperature Prediction Comparison. A single-phase oil flows up a tubing string that is cemented from top to bottom. Using Eq. 2.113 and the Shiu-Beggs correlation for A, calculate the wellhead temperature after the well has been flowing for 2 weeks. The following is given.

$$\begin{aligned}k_{cem} &= 0.42 \text{ Btu/hr-ft-}^{\circ}\text{F} \\k_s &= 25 \text{ Btu/hr-ft-}^{\circ}\text{F} \\k_e &= 1.4 \text{ Btu/hr-ft-}^{\circ}\text{F} \\k_o &= 0.08 \text{ Btu/hr-ft-}^{\circ}\text{F} \\C_{po} &= 0.65 \text{ Btu/lbm-}^{\circ}\text{F} \\a_e &= 0.04 \text{ ft}^2/\text{hr} \\q_o &= 5,000 \text{ bbl/D} \\T_R &= T_{bh} = T_{ei} = 200^{\circ}\text{F} \\\mu_o &= 1.0 \text{ cp} = 6.72 \times 10^{-4} \text{ lbm/ft-sec} \\r_{to} &= 2.750 \text{ in.} \\r_{ti} &= 2.446 \text{ in.} \\r_w &= 4.0 \text{ in.} \\\gamma_g &= 0.8 \\gG &= 0.015^{\circ}\text{F/ft} \\\gamma_{API} &= 30^{\circ}\text{API} \\L &= 10,000 \text{ ft} \\\theta &= 75^{\circ}\end{aligned}$$

1. Determine hf . The Dittus and Boelter equation³⁹ gives an acceptable correlation for the Nusselt number for turbulent flow ($N_{Re} > 10^4$) in the tubing when cooling is taking place

$$N_{Nu} = 0.023 N_{Re}^{0.8} N_{Pr}^{0.3}.$$

Reynolds Number:

$$v = \frac{(5,000 \text{ B/D})(5.615 \text{ ft}^3/\text{bbl})}{(86,400 \text{ sec/D})\pi \left(\frac{2.446 \text{ in.}}{12 \text{ in./ft}}\right)^2} = 2.489 \text{ ft/sec.}$$

$$\gamma_o = \frac{141.5}{131.5 + 30} = 0.876,$$

$$\rho_o = (0.876) \left(\frac{62.4 \text{ lbm}}{\text{ft}^3} \right) = 54.7 \frac{\text{lbm}}{\text{ft}^3},$$

and

$$N_{Re} = \frac{\rho v d}{\mu} = \frac{(54.7)(2.489)(4.892/12)}{6.72 \times 10^{-4}} = 8.259 \times 10^4.$$

Because $N_{Re} > 2,000$, flow is turbulent.

From Ref. 15, the Prandtl number is

$$N_{Pr} = \frac{\mu_o C_{po}}{k_o} = \frac{(6.72 \times 10^{-4})(3,600)(0.65)}{(0.08)} = 19.66.$$

Therefore,

$$N_{Nu} = \frac{h_f d_w}{k_o} = (0.023)(8.259 \times 10^4)^{0.8} (19.66)^{0.3} = 482.3$$

and

$$h_f = \frac{(482.3)(0.08)}{(4.892/12)} = 94.6 \text{ Btu/hr ft}^2\text{F.}$$

2. Determine reservoir time function, $f(t)$, from Eq. 2.89.

$$t_{Dw} = \frac{at}{r_w^2} = \frac{(0.04 \text{ ft}^2/\text{hr})(2 \text{ weeks})(168 \text{ hr/wk})}{(4.0/12)^2} = 120.96.$$

$$x = \frac{1}{4t_{Dw}} = \frac{1}{4(120.96)} = 0.0021.$$

Because $x < 0.0025$, Eq. 2.87 gives

$$f(t) = -\frac{1}{2} [\ln(0.0021) + 0.5772] = 2.794.$$

3. Determine heat-transfer coefficient using Eq. 2.95.

$$\begin{aligned}(r_{to} U)^{-1} &= \frac{1}{r_u h_f} + \frac{\ln\left(\frac{r_{to}}{r_u}\right)}{k_t} + \frac{\ln\left(\frac{r_w}{r_{to}}\right)}{k_{cem}} + \frac{f(t)}{k_e} \\&= \frac{12}{(2.446)(94.6)} + \frac{\ln\left(\frac{2.750}{2.446}\right)}{25.0} + \frac{\ln\left(\frac{4.0}{2.750}\right)}{0.42} + \frac{2.794}{1.4} \\&= 0.0519 + 0.0047 + 0.8921 + 1.9957 \\&= 2.9444 \text{ hr ft}^2\text{F/Btu.}\end{aligned}$$

4. Determine A

$$\begin{aligned}w &= \rho v A_p = (54.7)(2.489)\pi \left(\frac{2.446}{12.0}\right)^2 \\&= 17.77 \text{ lbm/sec} = 6.398 \times 10^4 \text{ lbm/hr.}\end{aligned}$$

From Eq. 2.102,

$$\begin{aligned}A &= \frac{(6.398 \times 10^4 \text{ lbm/hr})(0.65 \text{ Btu/lbm}^{\circ}\text{F})}{2\pi \left(\frac{2.750 \text{ in.}}{12 \text{ in./ft}}\right)(1.482 \text{ Btu/hr ft}^2\text{F})} \\&= 19,488 \text{ ft.}\end{aligned}$$

From Shiu-Beggs (Eq. 2.114),

$$\begin{aligned}A &= (0.0149)(17.77)^{0.5253} (4.892)^{-0.2904} (30)^{0.2608} \\&\quad \times (0.8)^{4.4146} (54.7)^{2.9303} \\&= (0.0149)(4.534)(0.631)(2.428)(0.373)(123,829) \\&= 4,783 \text{ ft.}\end{aligned}$$

5. Determine T_{wh} from Eq. 2.113.

$$\begin{aligned}T_{wh} &= [200.0 - (0.015)(10,000) \sin 75^{\circ}] + 0 \\&\quad + (0.015) \sin 75^{\circ} (19,488) (1 - e^{-10,000/19,488}) \\&= 200 - 144.9 + 113.3 \\&= 168.4^{\circ}\text{F.}\end{aligned}$$

From Shiu-Beggs (Eqs. 2.113 and 2.114),

$$\begin{aligned}T_{wh} &= [200.0 - (0.015)(10,000) \sin 75^{\circ}] + 0 \\&\quad + (0.015) \sin 75^{\circ} (4,783) (1 - e^{-10,000/4,783}) \\&= 200 - 144.9 + 60.7 \\&= 115.8^{\circ}\text{F.}\end{aligned}$$

References

1. Knudsen, J.G. and Katz, D.L.: *Fluid Dynamics and Heat Transfer*, McGraw-Hill Book Co. Inc., New York City (1958).
2. Moody, L.F.: "Friction Factors for Pipe Flow," *Trans., ASME* (1944) **66**, No. 8, 671.
3. Allen, T. Jr. and Ditzworth, R.L.: *Fluid Mechanics*, McGraw-Hill Book Co. Inc., New York City (1975).
4. Poiseuille, J.L.: *Compte Rendus* (1840) **11**, 961 and 1041; (1841) **12**, 112.
5. Drew, T.B., Koo, E.C., and McAdams, W.H.: *Trans., AIChE* (1930) **28**, 56.
6. Blasius, H.: *Z. Math. Phys.* (1908) **56**, 1.
7. Nikuradse, J.: *Forschungsheft* (1933) 301.

8. Colebrook, C.F.: "Turbulent Flow in Pipes With Particular Reference to the Transition Region Between the Smooth and Rough Pipe Laws," *J. Inst. Civil Eng.* (1939) **11**, 133.
9. Brill, J.P. and Beggs, H.D.: *Two-Phase Flow in Pipes*, U. of Tulsa, Tulsa, Oklahoma (1991).
10. Zigrang, D.J. and Sylvester, N.D.: "A Review of Explicit Friction Factor Equations," *J. Energy Res. Tech.* (June 1985) **107**, 280.
11. *Theory and Practice of the Testing of Gas Wells*, third edition, Energy Resources Conservation Board, Calgary (1975).
12. Cullender, M.H. and Smith, R.V.: "Practical Solution of Gas-Flow Equations for Wells and Pipelines With Large Temperature Gradients," *JPT* (December 1956) 281; *Trans., AIME*, **207**.
13. Burlington, R.S.: *Handbook of Mathematical Tables and Formulas*, fifth edition, McGraw-Hill Book Co. Inc., New York City (1973).
14. Martinez, A.E. et al.: "Prediction of Dispersion Viscosity of Oil/Water Mixture Flow in Horizontal Pipes," paper SPE 18221 presented at the 1988 SPE Annual Technical Conference and Exhibition, Houston, 2-5 October.
15. Bird, R.B., Stewart, W.E., and Lightfoot, E.N.: *Transport Phenomena*, John Wiley & Sons, New York City (1960).
16. Metzner, A.B. and Reed, J.C.: "Flow of Non-Newtonian Fluids—Correlation of the Laminar, Transition, and Turbulent-Flow Regions," *AICHE J.* (1955) **1**, 434.
17. Dodge, D.W. and Metzner, A.B.: "Turbulent Flow of Non-Newtonian Systems," *AICHE J.* (1959) **5**, 189.
18. Govier, G.W. and Aziz, K.: *The Flow of Complex Mixtures in Pipes*, Van Nostrand Reinhold Co., New York City (1972).
19. Szilas, A.P., Bobok, E., and Navratil, L.: "Determination of Turbulent Pressure Loss of Non-Newtonian Oil Flow in Rough Pipes," *Rheologica Acta* (1981) **20**, No. 5.
20. Heyda, J.F.: "A Green's Function Solution for the Case of Laminar Incompressible Flow Between Non-Concentric Circular Cylinders," *J. Franklin Inst.* (January 1959) **267**, 25.
21. Snyder, W.A. and Goldstein, G.A.: "An Analysis of Fully Developed Laminar Flow in an Accentric," *AICHE J.* (1965) **11**, 462.
22. Dodge, N.A.: "Friction Losses in Annular Flow," *ASME PN* (1964) 63-WA-11.
23. Winkler, H.W.: "Single- and Two-Phase Vertical Flow Through 0.996 x 0.625-Inch Fully Eccentric Plain Annular Configurations," PhD dissertation, U. of Texas, Austin, Texas (1968).
24. Gunn, D.J. and Darling, C.W.W.: "Fluid Flow and Energy Losses in Non Circular Conduits," *Trans., AIChE* (1963) **41**, 163.
25. El-Saden, M.R.: "Heat Conduction in an Eccentrically Hollow, Infinitely Long Cylinder with Internal Heat Generation," *J. Heat Transfer* (1961) **83**, 510.
26. Redberger, P.J. and Charles, M.E.: "Axial Laminar Flow in a Circular Pipe Containing a Fixed Eccentric Core," *Cdn. J. Chem. Eng.* (1962) **40**, 148.
27. Caetano, E.F., Shoham, O., and Brill, J.P.: "Upward Vertical Two-Phase Flow Through an Annulus. Part I: Single-Phase Friction Factor, Taylor Bubble-Rise Velocity and Flow-Pattern Prediction," *J. Energy Res. Tech.* (March 1992) **114**, 1.
28. Haciislamoglu, M. and Langlinais, J.: "Non-Newtonian Flow in Eccentric Annuli," *J. Energy Res. Tech.* (June 1990) **112**, 163.
29. Bourgoine, A.T. Jr. et al.: *Applied Drilling Engineering*, Textbook Series, SPE, Richardson, Texas (1991) **2**.
30. Sas-Jaworsky, A. II: "Coil Tubing Operations and Services—Part 4," *World Oil* (March 1992) 71.
31. Matthews, C.S. and Russell, D.G.: *Pressure Buildup and Flow Tests in Wells*, Monograph Series, SPE, Richardson, Texas (1967) **1**.
32. Ramey, H.J. Jr.: "Wellbore Heat Transmission," *JPT* (April 1962) 427; *Trans., AIME*, **225**.
33. Hasan, A.R. and Kabir, C.S.: "Heat Transfer During Two-Phase Flow in Wellbores: Part I—Formation Temperature," paper SPE 22866 presented at the 1991 SPE Annual Technical Conference and Exhibition, Dallas, 6-9 October.
34. Hasan, A.R. and Kabir, C.S.: "Aspects of Wellbore Heat Transfer During Two-Phase Flow," *SPEPF* (August 1994) 211.
35. Sagar, R., Doty, D.R., and Schmidt, Z.: "Predicting Temperature Profiles in a Flowing Well," *SPEPE* (November 1991) 441.
36. Alves, I.N., Alhanati, F.J.S., and Shoham, O.: "A Unified Model for Predicting Flowing Temperature Distribution in Wellbores and Pipelines," *SPEPE* (November 1992) 363.
37. Coulter, D.M. and Bardon, M.F.: "Revised Equation Improves Flowing Gas Temperature Prediction," *Oil & Gas J.* (26 February 1979) 107.
38. Shiu, K.C. and Beggs, H.D.: "Predicting Temperatures in Flowing Wells," *J. Energy Res. Tech.* (March 1980) **102**, 2.
39. Dittus, F.W. and Boelter, L.M.K.: *Pub. Eng.*, U. of California, Berkeley, California (1930) **2**, 443.

Chapter 3

Multiphase-Flow Concepts

3.1 Introduction

When two or more phases flow simultaneously in pipes, the flow behavior is much more complex than for single-phase flow. The phases tend to separate because of differences in density. Shear stresses at the pipe wall are different for each phase as a result of their different densities and viscosities. Expansion of the highly compressible gas phase with decreasing pressure increases the in-situ volumetric flow rate of the gas. As a result, the gas and liquid phases normally do not travel at the same velocity in the pipe. For upward flow, the less dense, more compressible, less viscous gas phase tends to flow at a higher velocity than the liquid phase, causing a phenomenon known as slippage. However, for downward flow, the liquid often flows faster than the gas.

Perhaps the most distinguishing aspect of multiphase flow is the variation in the physical distribution of the phases in the flow conduit, a characteristic known as flow pattern or flow regime. During multiphase flow through pipes, the flow pattern that exists depends on the relative magnitudes of the forces that act on the fluids. Buoyancy, turbulence, inertia, and surface-tension forces vary significantly with flow rates, pipe diameter, inclination angle, and fluid properties of the phases. Several different flow patterns can exist in a given well as a result of the large pressure and temperature changes the fluids encounter. Especially important is the significant variation in pressure gradient with flow pattern. Thus, the ability to predict flow pattern as a function of the flow parameters is of primary concern.

Analytical solutions are available for many single-phase-flow problems. Some were reviewed in Chap. 2. Even when empirical correlations were necessary (i.e., for turbulent-flow friction factors), the accuracy of prediction was excellent. The increased complexity of multiphase flow logically resulted in a higher degree of empiricism for predicting flow behavior. Many empirical correlations have been developed to predict flow pattern, slippage between phases, friction factors, and other such parameters for multiphase flow in pipes. Virtually all the existing standard design methods rely on these empirical correlations. However, since the mid-1970's, dramatic advances have taken place that improve understanding of the fundamental mechanisms that govern multiphase flow. These have resulted in new predictive methods that rely much less on empirical correlations.

This chapter introduces and discusses basic definitions for flow parameters unique to multiphase flow in pipes. Flow patterns are described in detail, including methods available to predict their occurrence. The pros and cons are presented for the use of empirical correlations based on dimensional analysis and dynamic similarity.

3.2 Phase Behavior

A complex mixture of hydrocarbon compounds or components can exist as a single-phase liquid, a single-phase gas, or as a two-phase mixture, depending on the pressure, temperature, and the composition of the mixture. Unlike a single component or compound, such as water or carbon dioxide, when two phases exist simultaneously a multicomponent mixture will exhibit an envelope rather than a single line on a pressure/temperature diagram. Fig. 3.1 gives a typical phase diagram for a multicomponent hydrocarbon system. The shapes and ranges of pressure and temperature for actual envelopes vary widely with composition.

Fig. 3.1 permits a qualitative classification of the types of reservoirs encountered in oil and gas systems. Typical oil reservoirs have temperatures below the critical temperature of the hydrocarbon mixture. Volatile oil and condensate reservoirs normally have temperatures between the critical temperature and the cricondentherm for the hydrocarbon mixture. Dry gas reservoirs have temperatures above the cricondentherm.

Many condensate fluids exhibit retrograde condensation, a phenomena in which condensation occurs during pressure reduction rather than with pressure increase, as for most gases. This abnormal or retrograde behavior occurs in a region between the critical point and the cricondentherm, bounded by the dewpoint curve above and a curve below formed by connecting the maximum temperature for each liquid volume percent.

As pressures and temperatures change, mass transfer occurs continuously between the gas and the liquid phases within the two-phase envelope of Fig. 3.1. All attempts to describe mass transfer assume that equilibrium exists between the phases. Two approaches have been used to simulate mass transfer for hydrocarbon systems: the "black-oil" or constant-composition model and the (variable) compositional model. Each is described in the following sections.

3.2.1 Black-Oil Model. The term black oil is a misnomer and refers to any liquid phase that contains dissolved gas, such as hydrocarbons produced from oil reservoirs. These oils are typically dark in color, have gravities less than 40°API, and undergo relatively small changes in composition within the two-phase envelope. A better description of the fluid system is a constant-composition model.

For black oils with associated gas, a simplified parameter has been defined to account for gas that dissolves (condenses) or evolves (boils) from solution in the oil. This parameter, R_g , can be measured in the laboratory or determined from empirical correlations. Appendix B gives a summary of available correlations. Because the black-oil model cannot predict retrograde condensation

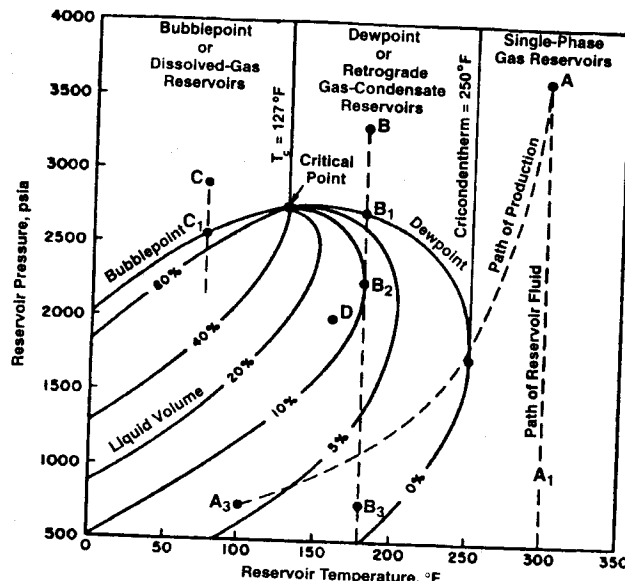


Fig. 3.1—Typical phase diagram.¹

phenomena, it should not be used for temperatures approaching the critical-point temperature.

A second parameter, called the oil formation volume factor, B_o , also has been defined to describe the shrinkage or expansion of the oil phase. Oil volume changes occur as a result of changes in dissolved gas and because of the compressibility and thermal expansion of the oil. Dissolved gas is by far the most important factor that causes volume change. Oil formation volume factor can be measured in the laboratory or predicted with empirical correlations given in Appendix B. Once the black-oil-model parameters are known, oil density and other physical properties of the two phases can be calculated. Appendix B gives methods to predict these properties.

When water also is present, solution gas/water ratio, R_{sw} , and water formation volume factor, B_w , can be defined. Appendix B also gives correlations for these parameters and physical properties of the water. The amount of gas that can be dissolved in water and the corresponding possible changes in water volume are much smaller than for gas/oil systems.

3.2.2 Compositional Model. For volatile oils and condensate fluids, vapor/liquid equilibrium (VLE) or "flash" calculations are more accurate to describe mass transfer than black-oil-model parameters. Appendix C provides a description of VLE calculations.

Given the composition of a fluid mixture or "feed," a VLE calculation will determine the amount of the feed that exists in the vapor and liquid phases and the composition of each phase. From these results, it is possible to determine the quality or mass fraction of gas in the mixture. Once the composition of each phase is known, it also is possible to calculate the interfacial tension and densities, enthalpies, and viscosities of each phase. Appendix C also gives methods to predict these properties.

VLE calculations are considered more rigorous than black-oil-model parameters to describe mass transfer. However, they also are much more difficult to perform. If a detailed composition is available for a gas/oil system, it is possible to generate black-oil parameters from VLE calculations. However, the nearly constant composition that results for the liquid phase and the increased computation requirements make the black-oil model more attractive for nonvolatile oils.

3.2.3 Volumetric Flow Rates. After mass transfer calculations are completed, it is possible to calculate the in-situ volumetric flow rates of each phase. For the black-oil model, volumetric flow rates are determined from

$$q_o = q_{o_{sc}} B_o, \quad \dots \dots \dots \quad (3.1)$$

$$q_w = q_{w_{sc}} B_w, \quad \dots \dots \dots \quad (3.2)$$

and

$$q_g = (q_{g_{sc}} - q_{o_{sc}} R_s - q_{w_{sc}} R_{sw}) B_g, \quad \dots \dots \dots \quad (3.3)$$

where B_g is derived from the engineering equation of state to be

$$B_g = p_{sc} ZT / p Z_{sc} T_{sc}. \quad \dots \dots \dots \quad (3.4)$$

Appendix B gives methods to predict gas compressibility, Z . For the compositional model, volumetric flow rates are calculated from

$$q_L = \frac{w_A(1 - x_g)}{\rho_L} \quad \dots \dots \dots \quad (3.5)$$

and

$$q_g = w_i x_g / \rho_g, \quad \dots \dots \dots \quad (3.6)$$

where x_g is the no-slip quality or gas mass fraction and is obtained from the results of a VLE calculation as follows,

$$x_g = \frac{VM_g}{VM_g + LM_L}. \quad \dots \dots \dots \quad (3.7)$$

If free water exists when the compositional model is used, the water flow rate must be added to q_L to account for all the liquid.

Example 3.1—Compositional-Model Flow Rates. A gas-condensate well is flowing at a rate of 500,000 lbm/D. At a given location in the pipe, a VLE calculation is performed on the gas composition, yielding

$$L = 0.05 \left(\frac{\text{mole liquid}}{\text{mole feed}} \right) V = 0.95 \left(\frac{\text{mole vapor}}{\text{mole feed}} \right),$$

$$M_L = 100 \left(\frac{\text{lbm}}{\text{mole liquid}} \right) M_{gV} = 20 \left(\frac{\text{lbm}}{\text{mole vapor}} \right),$$

and

$$\rho_L = 50 \text{ lbm/ft}^3 \quad \rho_g = 5.0 \text{ lbm/ft}^3.$$

From Eq. 3.7,

$$x_g = \frac{(0.95)(20.0)}{(0.95)(20.0) + (0.05)(100.0)}$$

$$= 0.792 \text{ lbm vapor/lbm mixture.}$$

With Eq. 3.5,

$$q_L = \frac{(500,000)(1 - 0.792)}{(86,400)(50)} = 0.024 \text{ ft}^3/\text{sec.}$$

With Eq. 3.6,

$$q_g = \frac{(500,000)(0.792)}{(86,400)(5.0)} = 0.917 \text{ ft}^3/\text{sec.}$$

3.3 Definition of Variables

When performing multiphase-flow calculations, single-phase-flow equations often are modified to account for the presence of a second phase. This involves defining mixture expressions for velocities and fluid properties that use weighting factors based on either volume or mass fractions. The choice of variables and weighting factors often depends on the predicted flow pattern. The following sections discuss each parameter.

3.3.1 Weighting Factors. When gas and liquid flow simultaneously up a well, the higher mobility of the gas phase tends to make the gas travel faster than the liquid. This is a result of the lower density and viscosity of the gas. Under steady-state conditions, this results in a re-

duced area fraction for the gas phase and an expanded area fraction for the liquid phase. Thus, slippage of gas past liquid results in larger in-situ liquid volume fractions than would be present if the two phases flowed at the same velocity. Liquid holdup can be defined as the fraction of a pipe cross section or volume increment that is occupied by the liquid phase. The difference in velocities of the gas and liquid phases can be estimated from a variety of equations developed from experimental data for a limited range of flow conditions. A more common procedure is to develop empirical correlations to predict liquid holdup, H_L , for a broad range of flow conditions.

For the case of equal phase velocities, or no-slip conditions, the volume fraction of liquid in the pipe can be calculated analytically from a knowledge of the in-situ volumetric flow rates given in the previous section. Thus,

$$\lambda_L = \frac{q_L}{q_L + q_g}, \quad (3.8)$$

where q_L is the sum of the oil and water flow rates for the black-oil model, or is given by Eq. 3.5 for the compositional model. If free water exists when the compositional model is used, the water flow rate must be added to the oil or condensate flow rate to account for all the liquid. Because the no-slip liquid holdup can be determined rigorously, it commonly is used as a correlating parameter to predict other multiphase-flow parameters, such as H_L .

When oil and water flow simultaneously in pipes, with or without gas, it is possible for slippage to occur between the oil and water phases. This type of slippage is normally small compared with the slippage that can occur between gas and liquid. However, slippage can be important when velocities are low, especially in horizontal wells where stratified flow can occur. Assuming no slippage, the oil fraction in a liquid phase is calculated from

$$f_o = \frac{q_o}{q_o + q_w}. \quad (3.9)$$

The water cut, f_w , based on in-situ rather than stock-tank flow rates, is simply $1 - f_o$.

3.3.2 Velocities. As described previously, the individual phase velocities normally are quite different. Only for the cases of the highly turbulent, dispersed-bubble-flow pattern and high-velocity, annular-flow pattern, in which the fluids exist as a homogeneous mixture, are the phase velocities essentially equal. For all other cases, significant slippage can occur between the gas and liquid. Under steady-state-flow conditions, slippage will result in a disproportionate amount of the slower phase being present at any given location in the well. The in-situ volume fraction of liquid, H_L , must be determined from empirical correlations or mechanistic models. Superficial velocities, which assume a given phase occupies the entire pipe area, are important correlating parameters. Thus,

$$v_{SL} = q_L/A_p \quad (3.10)$$

and

$$v_{Sg} = q_g/A_p. \quad (3.11)$$

A total or mixture velocity then can be defined as

$$v_m = \frac{q_L + q_g}{A_p} = v_{SL} + v_{Sg}. \quad (3.12)$$

If there were no slip between phases, both the gas and liquid would flow at the mixture velocity. Because of the slip between phases, the liquid typically flows at a velocity less than the mixture velocity, while the gas flows at a velocity greater than the mixture velocity. Time- and space-averaged velocities for each phase can be calculated from a knowledge of the time- and space-averaged liquid holdup obtained from the empirical correlations. Thus,

$$v_L = v_{SL}/H_L \quad (3.13)$$

and

$$v_g = \frac{v_{Sg}}{1 - H_L}. \quad (3.14)$$

A slip velocity can be defined as the difference between the actual phase velocities.

$$v_s = v_g - v_L. \quad (3.15)$$

A variety of other velocities are encountered in multiphase flow that pertain to flow mechanisms in specific flow patterns. Examples are rise velocities of small bubbles and larger bullet-shaped bubbles that often occur in bubble- and slug-flow patterns. Chap. 4 describes these in detail.

Example 3.2—Superficial Velocities: Black-Oil Model. An oil well is flowing 10,000 STBO/D with a producing gas/oil ratio of 1,000 scf/STBO or a gas-production rate of 10 MMscf/D. At a location in the tubing where the pressure and temperature are 1,700 psia and 180°F, calculate the in-situ volumetric flow rates and superficial velocities of the liquid and gas phases. Also calculate the mixture velocity and the no-slip liquid holdup. The following is known from the pressure/volume/temperature (PVT) example problem given in Appendix B.

$$\begin{aligned} B_o &= 1.197 \text{ bbl/STBO} \\ B_g &= 0.0091 \text{ ft}^3/\text{scf} \\ R_s &= 281 \text{ scf/STBO} \\ d &= 6.0 \text{ in.} \end{aligned}$$

$$A_p = \frac{\pi}{4} d^2 = \frac{\pi}{4} \left(\frac{6}{12} \right)^2 = 0.196 \text{ ft}^2.$$

With Eq. 3.1,

$$\begin{aligned} q_o &= \frac{(10,000 \text{ STBO/D})(1.197 \text{ bbl/STBO})(5.614 \text{ ft}^3/\text{bbl})}{86,400 \text{ sec/D}} \\ &= 0.778 \text{ ft}^3/\text{sec.} \end{aligned}$$

With Eq. 3.10,

$$v_{SL} = \frac{q_L}{A_p} = \frac{0.778}{0.196} = 3.97 \text{ ft/sec.}$$

With Eq. 3.3,

$$q_g = \frac{[10 \times 10^6 - (10,000)(281)](0.0091)}{86,400} = 0.757 \text{ ft}^3/\text{sec.}$$

With Eq. 3.11,

$$v_{Sg} = q_g/A_p = 0.757/0.196 = 3.86 \text{ ft/sec.}$$

With Eq. 3.12,

$$v_m = v_{SL} + v_{Sg} = 3.97 + 3.86 = 7.83 \text{ ft/sec.}$$

With Eq. 3.8,

$$\lambda_L = \frac{q_L}{q_L + q_g} = \frac{0.778}{0.778 + 0.757} = 0.507.$$

3.3.3 Fluid Properties. Regardless of whether the black-oil or the compositional model is used, it is possible to calculate the density and viscosity of each phase (oil, water, gas) and the gas/oil and gas/water surface tensions. A variety of methods have been used to define mixture fluid properties.

Oil/Water Mixture. For the black-oil-model case, and for the compositional-model case when free water exists, oil and water properties are combined under the assumption that there is no slippage between the oil and water.

$$\rho_L = \rho_o f_o + \rho_w f_w, \quad (3.16)$$

$$\sigma_L = \sigma_o f_o + \sigma_w f_w, \quad (3.17)$$

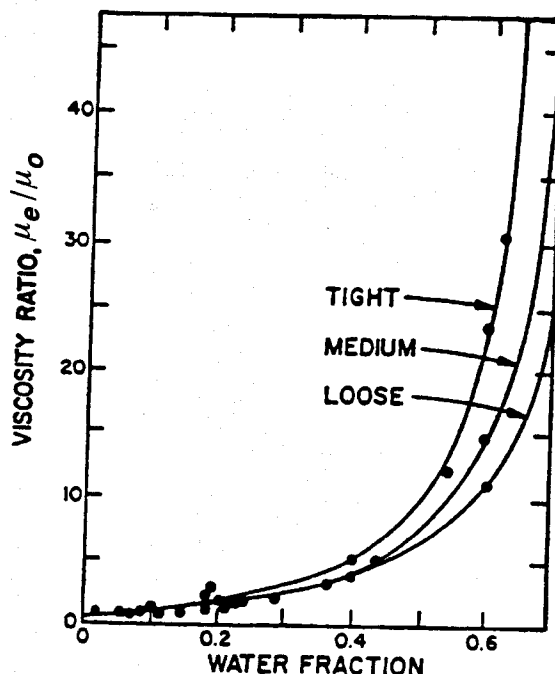


Fig. 3.2—Effect of water on emulsion viscosity.²

and

$$\mu_L = \mu_o f_o + \mu_w f_w \quad \dots \dots \dots \quad (3.18)$$

Studies have shown that Eq. 3.18 often is not valid for the viscosity of two immiscible liquids, such as oil and water. Chap. 2 presented a treatment of oil/water mixtures as a non-Newtonian fluid. An alternative approach is to treat the fluid as a Newtonian mixture with an apparent viscosity that, when used in the traditional Reynolds number expression, will yield an accurate friction factor from the Moody diagram shown in Fig. 2.2. Numerous studies have been published following this approach, beginning with the classical paper by Woelfin,² which predicted an exponential increase in mixture viscosity with increasing water fraction, as shown in Fig. 3.2.

The viscosity of a dispersion or emulsion has been found to depend mainly on the determination of which phase is continuous. The apparent liquid viscosity then will be governed primarily by the viscosity of the continuous phase, because this is the phase that predominates at the pipe wall where most of the friction losses occur. Other factors, such as the dispersed-phase viscosity and the droplet-size distribution of the dispersed phase, also are important.³

For some oil/water systems, the viscosity of the liquid mixture can be several times greater than the oil viscosity when the continuous phase is oil but the water fraction is approaching the point where an inversion of the dispersion or emulsion will occur.³ This increase has been attributed to two different causes: a deviation from Newtonian behavior near the inversion point, and an energy loss requirement to invert the mixture that is not accounted for in the conservation equations used. Thus, when a Newtonian-fluid flow model is used, the energy loss appears as an additional pressure loss that is seen as an increase in apparent viscosity. The inversion point of an oil/water mixture occurs at water fractions ranging from 0.2 to 0.5, with inversion taking place at lower water fractions when oil viscosities are high.³ Fig. 3.3 gives a plot that demonstrates this for experimental data from a variety of sources.³⁻⁷ Furthermore, by the use of surfactants, inversion can be accomplished at even lower water fractions.

Although Eq. 3.18 is the most common way to treat the apparent viscosity of an oil/water mixture, a more accurate method is to use the oil viscosity when oil is the continuous phase and the water viscosity when water is the continuous phase. Fig. 3.3 then could be used to estimate the water fraction at which inversion takes place. An even better alternative is to conduct flow tests on actual crudes

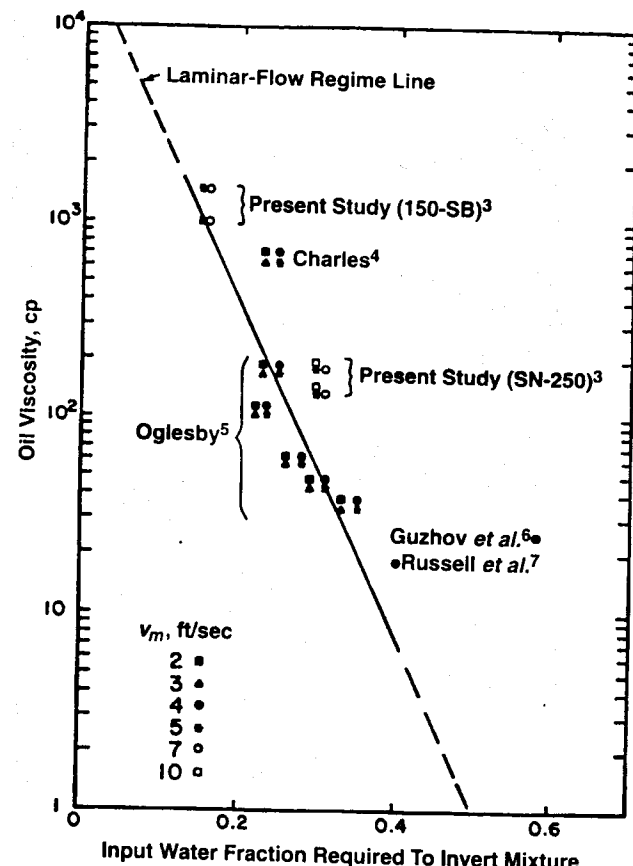


Fig. 3.3—Effect of oil viscosity on emulsion inversion.³

and water to determine the rheological characteristics and the probable inversion point.

Gas/Liquid Mixture. Numerous equations have been proposed to describe the physical properties of gas/liquid mixtures. In general, these equations are referred to as "slip" or "no-slip" properties, depending on whether H_L or λ_L is used as the volumetric weighting factor. Thus, for the case of two-phase viscosity,⁸

$$\mu_s = \mu_L H_L + \mu_g (1 - H_L) \quad \dots \dots \dots \quad (3.19)$$

or

$$\mu_s = (\mu_L^{H_L}) \times [\mu_g^{(1-H_L)}] \quad \dots \dots \dots \quad (3.20)$$

and

$$\mu_n = \mu_L \lambda_L + \mu_g (1 - \lambda_L) \quad \dots \dots \dots \quad (3.21)$$

Although Eq. 3.19 has never been used in multiphase-flow design correlations, Eq. 3.20 is used by the Hagedorn and Brown⁹ correlation described in Chap. 4. All other empirical correlations use Eq. 3.21.

The following expressions have been used to calculate multiphase-flow mixture densities.⁸

$$\rho_s = \rho_L H_L + \rho_g (1 - H_L) \quad \dots \dots \dots \quad (3.22)$$

$$\rho_n = \rho_L \lambda_L + \rho_g (1 - \lambda_L) \quad \dots \dots \dots \quad (3.23)$$

and

$$\rho_k = \rho_L \frac{\lambda_L^2}{H_L} + \rho_g \frac{(1 - \lambda_L)^2}{(1 - H_L)} \quad \dots \dots \dots \quad (3.24)$$

Eq. 3.24 contains the subscript k because it appears in the kinetic energy term for the specific case of a homogeneous-mixture, momentum-conservation equation.

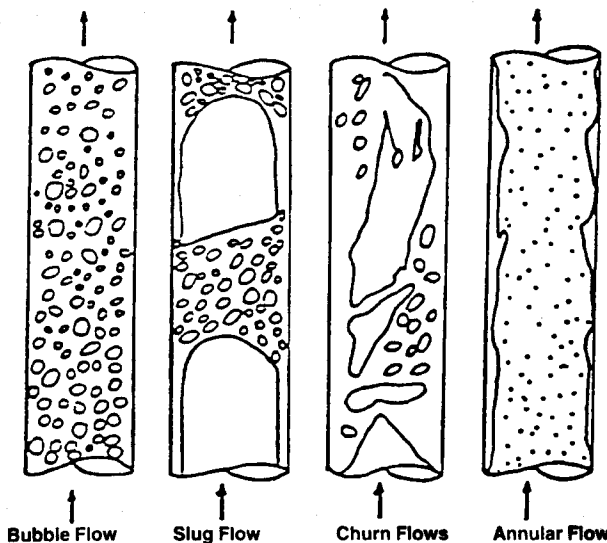


Fig. 3.4—Upward-vertical-flow patterns.¹⁰ (Reproduced with permission of American Inst. of Chemical Engineers.)

When performing temperature-change calculations for multiphase flow in wells, it is necessary to predict the enthalpy of the multiphase mixture. Most VLE calculation methods include a provision to predict the enthalpies of the gas and liquid phases. If enthalpies are expressed per unit mass, the enthalpy of a multiphase mixture can be calculated from

$$h = h_L(1 - x_g) + h_g x_g. \quad \dots \quad (3.25)$$

3.4 Pressure Gradient

The pressure-gradient equation derived in Sec. 2.3 for single-phase flow can be modified for multiphase flow by considering the fluids to be a homogeneous mixture. Thus,

$$\frac{dp}{dL} = \frac{f\rho_f v_f^2}{2d} + \rho_f g \sin \theta + \rho_f v_f \frac{dv_f}{dL}, \quad \dots \quad (3.26)$$

where the definitions for ρ_f and v_f can vary with different investigators. For vertical flow, $\theta = 90^\circ$, $\sin \theta = 1$, $dL = dZ$, and the equation can be written as

$$\left(\frac{dp}{dZ}\right)_t = \left(\frac{dp}{dZ}\right)_f + \left(\frac{dp}{dZ}\right)_{el} + \left(\frac{dp}{dZ}\right)_{acc}. \quad \dots \quad (3.27)$$

The pressure-drop component caused by friction losses requires evaluation of a two-phase friction factor. The pressure drop caused by elevation change depends on the density of the two-phase mixture which is usually calculated with Eq. 3.22. Except for conditions of high velocity, most of the pressure drop in vertical flow is caused by this component. The pressure-drop component caused by acceleration is normally negligible and is considered only for cases of high flow velocities.

Many methods have been developed to predict two-phase, flowing-pressure gradients. They differ in the manner used to calculate the three components of the total pressure gradient. Chap. 4 describes these methods.

3.5 Flow Patterns

Predicting the flow pattern that occurs at a given location in a well is extremely important. The empirical correlation or mechanistic model used to predict flow behavior varies with flow pattern. Brill and Beggs⁸ summarized numerous investigations that have described flow patterns in wells and that made attempts to predict when they occur.

Essentially all flow-pattern predictions are based on data from low-pressure systems, with negligible mass transfer between the

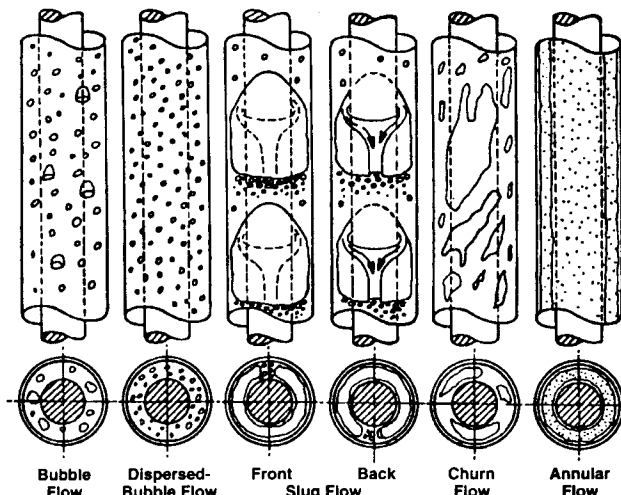


Fig. 3.5—Flow patterns in upward vertical flow through a concentric annulus.¹⁵

phases and with a single liquid phase. Consequently, these predictions may be inadequate for high-pressure, high-temperature wells, or for wells producing oil and water or crude oils with foaming tendencies. A consensus exists on how to classify flow patterns.

3.5.1 Flow-Pattern Classification in Wells. For upward multiphase flow of gas and liquid, most investigators¹⁰ now recognize the existence of four flow patterns: bubble flow, slug flow, churn flow, and annular flow. These flow patterns, shown schematically in Fig. 3.4, are described next. Slug and churn flow are sometimes combined into a flow pattern called intermittent flow. It is common to introduce a transition between slug flow and annular flow that incorporates churn flow. Some investigators^{11,12} have named annular flow as mist or annular-mist flow.

Bubble Flow. Bubble flow is characterized by a uniformly distributed gas phase and discrete bubbles in a continuous liquid phase. Based on the presence or absence of slippage between the two phases, bubble flow is further classified into bubbly and dispersed-bubble flows. In bubbly flow, relatively fewer and larger bubbles move faster than the liquid phase because of slippage. In dispersed-bubble flow, numerous tiny bubbles are transported by the liquid phase, causing no relative motion between the two phases.

Slug Flow. Slug flow is characterized by a series of slug units. Each unit is composed of a gas pocket called a Taylor bubble,^{13,14} a plug of liquid called a slug, and a film of liquid around the Taylor bubble flowing downward relative to the Taylor bubble. The Taylor bubble is an axially symmetrical, bullet-shaped gas pocket that occupies almost the entire cross-sectional area of the pipe. The liquid slug, carrying distributed gas bubbles, bridges the pipe and separates two consecutive Taylor bubbles.

Churn Flow. Churn flow is a chaotic flow of gas and liquid in which the shape of both the Taylor bubbles and the liquid slugs are distorted. Neither phase appears to be continuous. The continuity of the liquid in the slug is repeatedly destroyed by a high local gas concentration. An oscillatory or alternating direction of motion in the liquid phase is typical of churn flow.

Annular Flow. Annular flow is characterized by the axial continuity of the gas phase in a central core with the liquid flowing upward, both as a thin film along the pipe wall and as dispersed droplets in the core. At high gas flow rates more liquid becomes dispersed in the core, leaving a very thin liquid film flowing along the wall. The interfacial shear stress acting at the core/film interface and the amount of entrained liquid in the core are important parameters in annular flow.

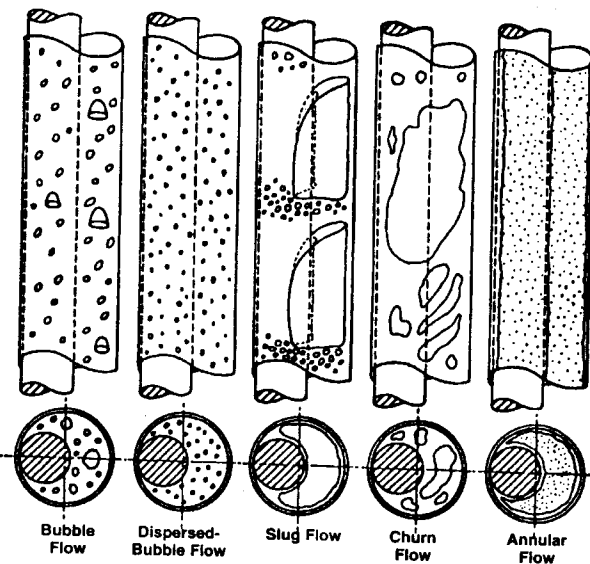


Fig 3.6—Flow patterns in upward vertical flow through a fully eccentric annulus.

3.5.2 Flow-Pattern Classification in Annuli. The experimental data collected by Caetano *et al.*¹⁵ reveal that, although the same flow patterns described for wellbores occur in annuli, their characteristics can be substantially different. Thus, it is essential to define the flow patterns in these configurations. Figs. 3.5 and 3.6 show flow patterns in concentric and fully eccentric annuli, respectively.

Bubble Flow. The gas phase is dispersed into small discrete bubbles in a continuous liquid phase, forming an approximately homogeneous flow through the annulus cross-sectional area. The discrete bubbles occur in two different shapes, namely spherical bubbles and cap bubbles. The spherical bubbles are very small, on the order of 3 to 5 mm diameter, compared with the annulus-cap bubbles, which are relatively larger but still always smaller than half of the configuration hydraulic diameter. The upward movement of the small spherical bubbles follows a zig-zag path, whereas the cap bubbles follow a straight path with a faster rise velocity. In a fully eccentric annulus, there is a tendency for the small bubbles and the cap bubbles to migrate into the widest gap of the annulus cross-sectional area. This causes a higher local void fraction relative to the cross-sectional average void fraction. At high liquid velocities, the mixture appears to flow at the same velocity with no slippage between the phases, regardless of the annulus geometry.

Slug Flow. This flow is characterized by large cap bubbles of gas moving upward, followed by liquid slugs that bridge the entire cross-sectional area and contain small spherically distributed gas bubbles. The large gas bubbles, which occupy almost the entire cross-sectional area of the annulus, are similar to the ones occurring in pipe flow and also are termed Taylor bubbles. The Taylor bubbles do not occupy the total cross-sectional area because they have a preferential channel through which most of the liquid ahead of the bubble flows backward (see Fig. 3.5). This preferential channel exists from the top to the bottom of the bubble and from the tubing wall to the casing wall. Because of the presence of this channel, no symmetry is observed for the Taylor bubble with respect to either vertical or horizontal planes. The liquid phase flows backward in the form of films, around the Taylor bubble, and through the preferential channel, wetting both the tubing and the casing walls. This tends to create a high turbulent region behind the Taylor bubble. Contrary to the concentric annulus case, for a fully eccentric annulus (see Fig. 3.6) the preferential liquid channel always is located where the pipe walls are in contact.

Churn Flow. The characteristics of churn flow are similar to those of pipe flow. There is no change in flow characteristics observed with the annulus configuration.

Annular Flow. The gas is a continuous phase flowing in the core of the annulus cross-sectional area. The liquid flows upward, partially as wavy films around the tubing and casing walls and partially in the form of tiny spherical droplets entrained in the gas core. The outer film that wets the casing wall is always thicker than the inner film flowing on the tubing wall.

Liquid accumulation near the pipe-wall contact point is an additional characteristic of annular flow in a fully eccentric annulus. This accumulation results from the merging of the casing and tubing liquid films, which probably happens as a result of the low local gas velocities.

Comparison among flow patterns occurring in upward vertical flow in a pipe and in an annulus reveals that the existence of an inner pipe in the annulus changes the characteristics of slug flow and annular flow. The Taylor bubbles in an annulus are not symmetric, having a preferential liquid flow channel through which most of the liquid phase is shed backward. Two films exist in the annular-flow pattern, one flowing around the tubing wall and one around the casing wall. These flow modifications seem to be a function of the pipe-diameter ratio and the eccentricity of the annulus.

3.5.3 Flow-Pattern Occurrence.

The following is a description of a typical sequence of flow patterns in an oil wellbore.

Starting with a flowing bottomhole pressure above the bubble-point pressure, only a liquid phase exists at the bottom. As the liquid flows upward, it experiences pressure decline resulting in the liberation of some of the gas dissolved in the liquid phase. The liberated gas appears as small bubbles in the continuous liquid phase, which characterizes the bubble-flow pattern. As the flow continues upward, further decrease in pressure and temperature occurs, resulting in gas expansion and the liberation of more solution gas from the oil phase. This creates more and larger bubbles that start coalescing with each other. The coalescence creates larger Taylor bubbles separated by the continuous liquid phase. The slug-flow pattern thus occurs. Further continuation of the upward motion of the flow into the region of lower pressure causes the expansion of Taylor bubbles along with the liberation of more gas from liquid slugs. This creates a chaotic two-phase flow, defined earlier as churn flow. The churn flow continues to exist until the gas flow rate is sufficiently high to push the liquid against the pipe wall. This characterizes the existence of annular flow.

Because of continuous changes in pressure, temperature, and mass transfer between the two phases, the flow pattern having a continuous liquid phase at the bottomhole can be completely transformed into a flow pattern with a continuous gas phase at the wellhead. Fig. 3.4 shows this progressive change of flow patterns.

After identifying the different flow patterns, tools are needed to predict their occurrence and flow behavior. This requires a thorough understanding of the mechanisms of each flow pattern. Ansari *et al.*¹⁶ used the best models for flow-pattern prediction and for flow-pattern behavior. They are discussed in Chap. 4.

3.5.4 Flow-Pattern Prediction. Methods to predict the occurrence of the various flow patterns in wells have fallen into two categories. Most early attempts were based on conducting experimental tests in small-diameter pipes at low pressures with air and water. Flow patterns were observed, and the values of various flow parameters at the transition between flow patterns were determined. Empirical flow-pattern maps were drawn that could be used to predict the transitions. Chap. 4 presents some of the more successful maps developed with this approach. The second method to predict flow patterns considers the basic mechanisms that are important in causing a flow-pattern change. This approach is not restricted to a narrow range of flow parameters and has proved to be highly successful. Chap. 4 presents mechanistic models for flow-pattern prediction.

3.6 Liquid Holdup

Sec. 3.3 discussed the interrelationships between gas and liquid phases traveling at different velocities (slippage). Eqs. 3.13 and 3.14 show the importance of liquid holdup in predicting velocities of each phase. Eqs. 3.19, 3.20, 3.22, and 3.24 show the importance of liquid

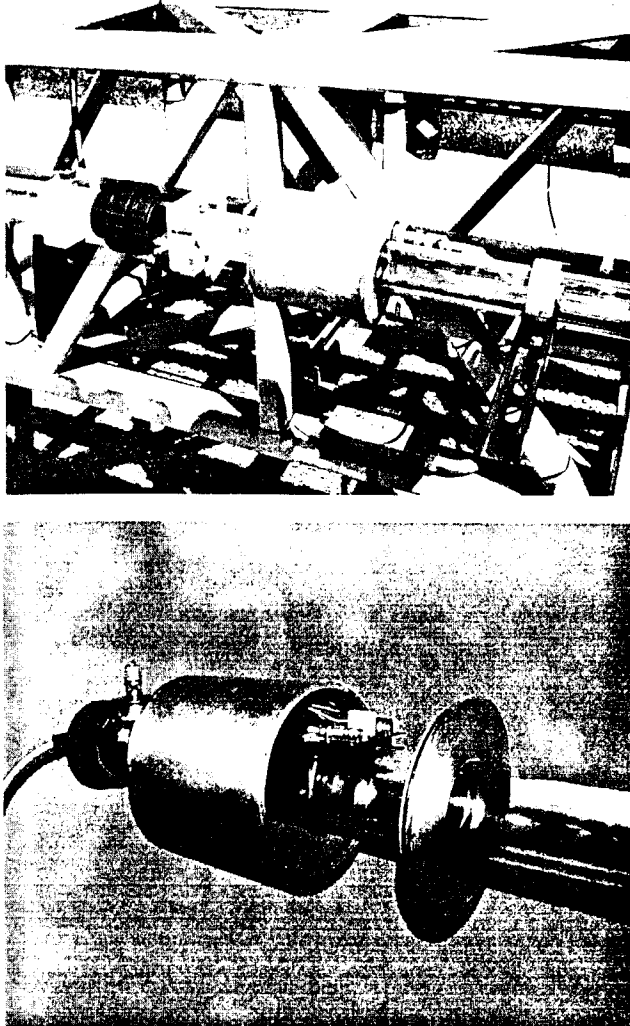


Fig 3.7—Capacitance sensor.

holdup in predicting the physical properties of gas/liquid mixtures. Sec. 2.3 discussed how the elevation component of the pressure-gradient equation for single-phase flow accounts for 80 to 95% of the total pressure gradient. The same will be true for multiphase flow in vertical pipes. Chap. 4 will show that Eq. 3.22 is very important in predicting multiphase-flow pressure gradients. Consequently, an accurate prediction of liquid holdup is normally the most important parameter in calculating multiphase-flow pressure drops in wells.

Chap. 4 presents several empirical correlations and mechanistic models to predict liquid holdup. Liquid-holdup measurements are required to develop and evaluate empirical correlations for predicting this important parameter. The most accurate method for measuring liquid holdup is to trap a representative sample of gas and liquid in a section of pipe and physically measure the volume fraction occupied by the liquid phase. This is commonly done by use of two quick-closing ball valves that can be operated simultaneously. A representative sample is much larger for intermittent flow (slug and churn) than for other flow patterns because of the nonuniform configuration of each phase. Because all slugs and Taylor bubbles have different lengths, it is necessary to trap several of each to obtain representative averages. Thus, the minimum distance between valves is dependent on the flow pattern. Vertical upflow of a multiphase mixture is known to stabilize fairly rapidly, so a meaningful measurement can be obtained after the mixture has flowed about 100 pipe diameters from the pipe inlet. However, the entrance length for other pipe-inclination angles is often much longer, especially for downward-inclined flow.

When quick-closing valves are used to measure liquid holdup, it often becomes necessary to obtain and average many measurements

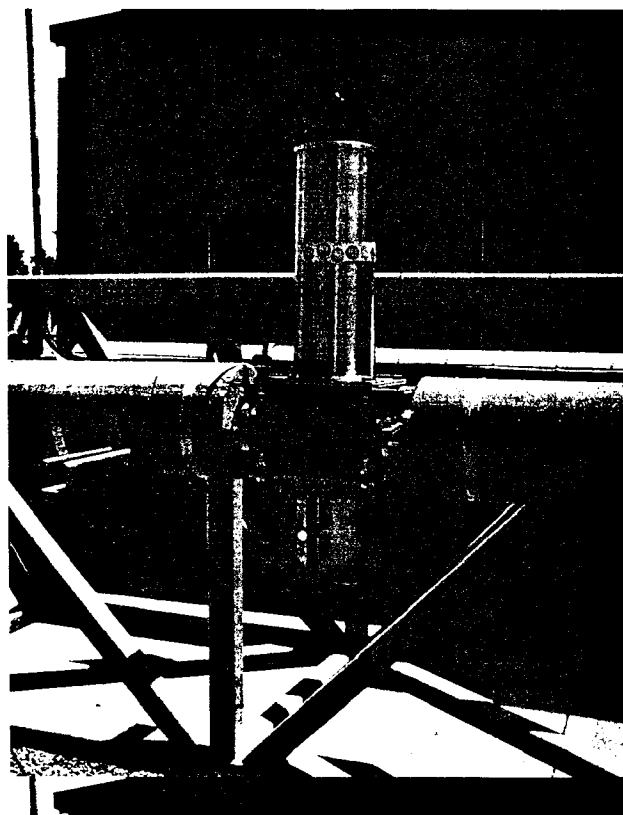


Fig 3.8—Nuclear densitometer.

to ensure accuracy and repeatability. This can result in a very time-consuming process. Also, the use of quick-closing valves in the field is not feasible. As a result, to measure liquid holdup continuously, many different methods have been tried, all of which rely on basic physics. These include laser-Doppler methods (light), ultrasonics (sound), gamma ray or neutron absorption (nuclear), and capacitance or resistance sensors (electricity). Two of the more commonly used methods are discussed next.

3.6.1 Capacitance Sensors. Capacitance sensors require the use of capacitor plates or rings to measure the dielectric constant of the two-phase mixture. This approach prohibits the use of a pipe or fluid that will conduct electricity. Thus, capacitance sensors cannot incorporate steel pipe or water as the liquid phase. For this reason, they are unsuitable for use in field operations. They have been used extensively in laboratory multiphase-flow experiments where PVC, acrylic, or glass pipe can be used, where the liquid phase can be a hydrocarbon mixture, such as Kerosene, and where the presence of water can be prevented.

Gregory and Mattar¹⁷ were the first to attempt to use capacitance sensors. They evaluated several designs and concluded that use of two helical capacitor plates, 180° out of phase, worked best. They also recommended specific dimensions and angles for the electrodes, depending on the pipe diameter.

Kouba *et al.*¹⁸ and Kouba¹⁹ developed a different design in which the electrodes were three equally-spaced rings. The center ring was the positive electrode, and the outer rings were ground-referenced. They showed that measurements with this design were as accurate as those with the helical sensors, and that the overall length of the sensor was much shorter, especially for larger-diameter pipe. Thus, the instantaneous liquid-holdup measurement would not be averaged over as long a pipe section. Butler *et al.*²⁰ further improved on the sensor and electronics design for capacitance sensors. **Fig. 3.7** is a photograph of a capacitance sensor.

In general, the electronics required to process the capacitance sensor poses difficulties. The difference in capacitance between a pipe full of air or natural gas vs. one full of a hydrocarbon liquid is

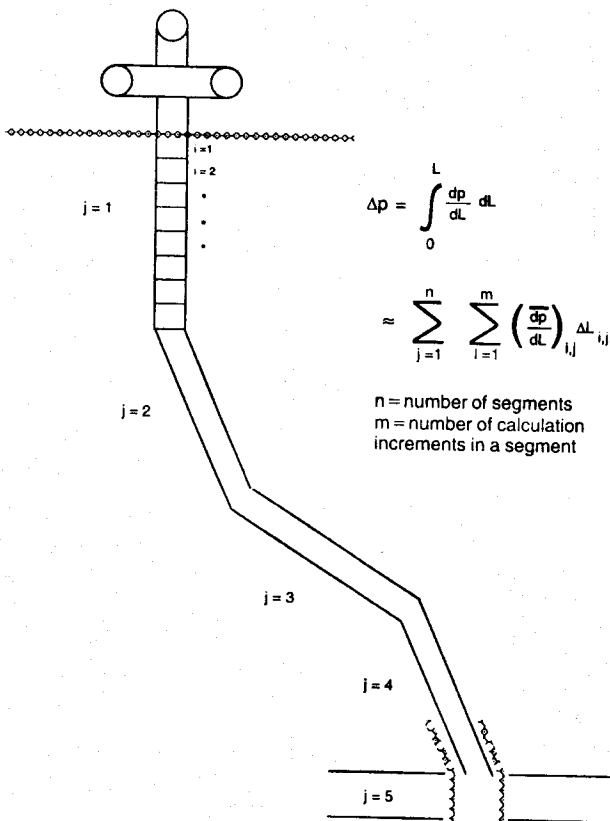


Fig. 3.9—Segmenting typical wellbore.

very small. As a result, such things as changes in humidity or minute concentrations of water in the liquid phase can cause significant measurement errors. In addition, Kouba *et al.* showed that dynamic calibration of the sensors was necessary because the capacitance measurement also was dependent on the location of the liquid phase within the sensor.

3.6.2 Nuclear Densitometers. Brill *et al.*²¹ used nuclear densitometers or gamma-ray absorption sensors to determine multiphase-flow behavior in large-diameter pipelines in the Prudhoe Bay field of Alaska. They used a pair of densitometers to measure the liquid holdup and the lengths of slugs and bubbles. Since then, these devices have been used to acquire data in many different field and laboratory tests. **Fig. 3.8** shows a nuclear densitometer.

Nuclear densitometers use a radioactive source that emits gamma rays. The source, often Cs¹³⁷, is contained in a lead-shielded cylinder for safety reasons to prevent the escape of gamma rays. When the top of the cylinder is removed, a cone of gamma rays is emitted. They pass through the pipe wall, through the fluids in the pipe, and through any insulation or other coatings around the pipe. Each of these media will absorb some of the gamma rays, depending in part on the density of the material. The number of gamma rays that successfully pass through all media can be counted and converted into an electrical signal. Because the major variable involved is the amount of liquid in the cone of gamma rays at a given time and the liquid phase absorbs more gamma rays than the less-dense gas phase, the electrical response is directly proportional to the liquid holdup.

Nuclear densitometers suffer from several disadvantages. Perhaps their greatest drawbacks are safety and governmental regulation. Gamma rays are potentially dangerous, although adequate measurements can be obtained with relatively small sources of radioactive material. The response time of the electronics is fairly long, typically on the order of 10 Hz, depending on the size and type of radioactive source and the method used to count the gamma rays. Thus, the measured lengths of rapidly moving slugs and bubbles may not always be as accurate as desired. Also, the measurement of liquid holdup can be sensitive to the location of the liquid in the pipe.

This limitation can be rectified partially by the use of multiple-beam gamma densitometers.

In spite of these deficiencies, nuclear densitometers have experienced increased use in the field. They are a nonintrusive instrument that can be attached to the outside of steel pipe and provide fairly accurate measurements of the volume fractions and flow patterns of the fluids inside the pipe.

3.7 Pressure-Traverse Computing Algorithm

When performing pressure-drop calculations, it is necessary to integrate the pressure gradient over the total length of the wellbore. Thus, the total pressure drop is

$$\Delta p = \int_0^L \left(\frac{dp}{dL} \right) dL. \quad \dots \dots \dots \quad (3.28)$$

For compressible and slightly compressible fluids, the pressure gradient from Eq. 3.26 varies throughout the pipe length. This is true for multiphase mixtures and even for crude oils above the bubble-point, in part because the temperature also varies throughout the wellbore. For oil and gas wells, the pressure gradient throughout the piping system will vary with pressure, temperature, and inclination angle. Pressure-drop or pressure-traverse calculations require that both the pressure-gradient equation and the enthalpy-gradient equation (Eq. 2.72) be coupled by use of a numerical algorithm.

Eqs. 2.5 and 2.105 constitute an initial-value problem with two coupled, ordinary differential equations in the variables p and T , respectively. All computer programs for performing steady-state, multiphase-flow, pressure-traverse calculations use what is often called a "marching algorithm." To solve this initial-value problem, start at either the top or bottom of a well and "march" to the other end, numerically integrating the pressure-gradient and enthalpy-gradient equations over short increments of pipe.

Fig. 3.9 shows a typical deviated wellbore that has been divided into five pipe segments, with a new segment resulting whenever a significant change occurs in inclination angle. New segments, or nodes, also would be required where there is a change in mass flow rate, where a pump is located, or where the pipe diameter or configuration changes. A change in mass flow rate would occur when a well is gas-lifted or when production from different zones is commingled.

Segments in Fig. 3.9 could be sufficiently long that there is a significant change in pressure gradient within a segment because of changes in such variables as densities, superficial and in-situ velocities, or even flow pattern. Thus, even for a pipe segment, it is necessary to divide the pipe into calculation increments within which the pressure gradient can be considered constant. The pressure drop then is determined by

$$\Delta p \approx \sum_{j=1}^n \sum_{i=1}^m \left(\frac{\overline{dp}}{dL} \right)_{i,j} \Delta L_{i,j}. \quad \dots \dots \dots \quad (3.29)$$

Fig. 3.10 gives a flow chart of the "marching algorithm" for a single pipe calculation increment for which p_i and T_i are known and p_{i+1} and T_{i+1} are to be calculated. A complete traverse is calculated by sequentially marching through all increments in all segments of the well.

The approximate analytical solutions to the enthalpy-gradient equation shown in **Fig. 3.10** were covered in Sec. 2.6. Note that the numerical integration of the enthalpy-gradient equation involves a trial-and-error solution for T_{i+1} for a guessed value of p_{i+1} . It also involves calculation of an average enthalpy gradient, and determination of the enthalpy of each phase and the mixture enthalpy at the end of the increment. Approximate analytical solutions for integrating the enthalpy-gradient equation normally are adequate and simplify the calculations significantly. The PVT-calculation box involves the determination of mass transfer between the phases and the densities, viscosities, and interfacial-surface tensions at the guessed average pressure and temperature in the increment. Appendices B and C provide procedures to perform these calculations.

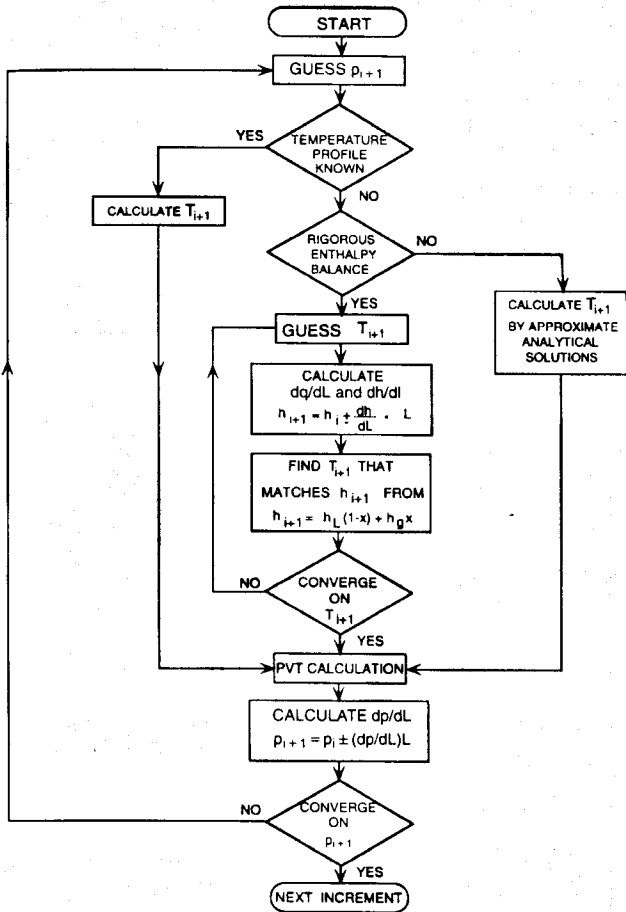


Fig. 3.10—Marching algorithm for a calculation increment.

Chap. 4 gives methods for calculating the pressure gradient at the guessed average pressure and temperature in the increment.

Commercial computer programs that perform production-systems-analysis calculations link the “marching algorithm” with reservoirs by use of inflow performance relationships that also account for various well-completion parameters. Depending on the analysis performed, calculations may be required in both upstream and downstream directions. Production systems analysis, often called NODALTTM analysis, involves a trial-and-error calculation that will match pressure and temperature conditions at a given node from both the upstream and the downstream system components. Chap. 6 gives a detailed analysis of production-design calculations.

3.8 Dimensional Analysis

The concept of using dimensional analysis and dynamic similarity has been very successful in designing experimental test facilities and analyzing data. Many of the accepted equations used in single-phase fluid flow and in heat-transfer calculations have been developed with these concepts. One example is the Colebrook²² equation for determining friction factor, which uses Reynolds number and relative roughness as dimensionless groups. The Dittus and Boelter²³ equation for convective film coefficient uses the Nusselt, Prandtl, and Reynolds numbers. Because of the increased complexity of multiphase flow over single-phase flow, it is not surprising that dimensional analysis also has been used extensively to develop predictive methods for multiphase flow.

In general, dimensionless analysis is used when there is insufficient understanding of the basic fundamentals that govern physical phenomena. The process involves preparing a list of all variables that might be important and using them to develop a collection of dimensionless groups following a procedure known as the Buckingham pi theorem.²⁴ When designing laboratory experiments, use of dimensionless groups helps ensure that small-scale tests can “scale up” to field applications.

It is not uncommon for initial predictive methods to rely heavily on empirical correlations based on dimensionless groups, only to be replaced by more fundamental equations as technology improves. This is certainly true for multiphase flow in wells. Duns and Ros¹¹ performed a dimensional analysis of multiphase flow through wells that is presented in Chap. 4. The dimensionless groups they developed have been used extensively by many other investigators when developing empirical correlations. Chap. 4 includes many of the early and widely accepted empirical correlations to predict flow pattern, friction factors, and liquid holdup. Chap. 4 also includes mechanistic models based on more fundamental concepts.

References

- Craft, B.C. and Hawkins, M.F.: *Applied Petroleum Reservoir Engineering*, second edition, Prentice-Hall Book Co. Inc., Englewood Cliffs, New Jersey (1991) 7.
- Woelfin, W.: “The Viscosity of Crude-Oil Emulsions,” *Drill. & Prod. Prac.* (1942) 148.
- Arirachakaran, S.J.: “An Experimental Study of Two-Phase Oil-Water Flow in Horizontal Pipes,” MS thesis, U. of Tulsa, Tulsa, Oklahoma (1983).
- Charles, M.E.: “Water Layer Speeds Heavy-Crude Flow,” *Oil & Gas J.* (26 August 1961) 59, 68.
- Oglesby, K.D.: “An Experimental Study on the Effects of Oil Viscosity, Mixture Velocity, and Water Fraction on Horizontal Oil-Water Flow,” MS thesis, U. of Tulsa, Tulsa, Oklahoma (1979).
- Guzhov, A.I. et al.: “Emulsion Formation During the Flow of Two Liquids in a Pipe,” *Neft Khoz* (August 1973) 8, 58 (in Russian).
- Russell, T.W.F., Hodgson, G.W., and Govier, G.W.: “Horizontal Pipeline Flow of Mixtures of Oil and Water,” *Cdn. J. Chem. Eng.* (1957) 37, 9.
- Brill, J.P. and Beggs, H.D.: *Two-Phase Flow in Pipes*, U. of Tulsa, Tulsa, Oklahoma (1991).
- Hagedorn, A.R. and Brown, K.E.: “Experimental Study of Pressure Gradients Occurring During Continuous Two-Phase Flow in Small-Diameter Vertical Conduits,” *JPT* (April 1965) 475; *Trans., AIME*, **234**.
- Taitel, Y.M., Barnea, D., and Dukler, A.E.: “Modeling Flow Pattern Transitions for Steady Upward Gas-Liquid Flow in Vertical Tubes,” *AICHE J.* (1980) 26, 345.
- Duns, H. Jr. and Ros, N.C.J.: “Vertical Flow of Gas and Liquid Mixtures in Wells,” *Proc., Sixth World Pet. Cong.*, Tokyo (1963) 451.
- Aziz, K., Govier, G.W., and Fogarasi, M.: “Pressure Drop in Wells Producing Oil and Gas,” *J. Cdn. Pet. Tech.* (July–September 1972) 11, 38.
- Dumitrescu, D.T.: “Stromung an Einer Luftblase im Senkrechten Rohr,” *Z Agnew. Math. Mech.* (1943) 23, 139.
- Davies, R.M. and Taylor, G.: “The Mechanics of Large Bubbles Rising Through Extended Liquids and Through Liquids in Tubes,” *Proc., Royal Soc., London* (1949) **200A**, 375.
- Caetano, E.F., Shoham, O., and Brill, J.P.: “Upward Vertical Two-Phase Flow Through an Annulus, Part I: Single-Phase Friction Factor, Taylor Bubble-Rise Velocity and Flow-Pattern Prediction,” *J. Energy Res. Tech.* (March 1992) **114**, 1.
- Ansari, A.M. et al.: “A Comprehensive Mechanistic Model for Two-Phase Flow in Wellbores,” *SPEPF* (May 1994) 143; *Trans., AIME*, **297**.
- Gregory, G.A. and Mattar, L.: “An In-Situ Volume Fraction Sensor for Two-Phase Flows of Non-Electrolytes,” *J. Cdn. Pet. Tech.* (April–June 1973) **12**, 48.
- Kouba, G.E., Shoham, O., and Brill, J.P.: “A Nonintrusive Flowmetering Method for Two-Phase Intermittent Flow in Horizontal Pipes,” *SPEPE* (November 1990) 373.
- Kouba, G.E.: “Dynamic Calibration of Two Types of Capacitance Sensors Used in Measuring Liquid Holdup in Two-Phase Intermittent Flow,” *Proc., 32nd ISA Intl. Instrumentation Symposium*, Seattle (May 1986) 479.
- Butler, R.T., Chen, X., and Brill, J.P.: “Ratio-Arm Bridge Capacitance Transducer for Two-Phase Flow Measurements,” paper presented at the 1995 ISA Intl. Instrumentation Symposium, Aurora, Colorado, 7–11 May.
- Brill, J.P. et al.: “Analysis of Two-Phase Flow Tests in Large-Diameter Flow Lines in Prudhoe Bay Field,” *SPEJ* (June 1981) 363.
- Colebrook, C.F.: “Turbulent Flow in Pipes With Particular Reference to the Transition Region Between the Smooth and Rough Pipe Laws,” *J. Inst. Civil Eng.* (1939) **11**, 133.
- Dittus, F.W. and Boelter, L.M.K.: *Pub. Eng.*, U. of California, Berkeley, California (1930) **2**, 443.
- Allen, T. Jr. and Ditzworth, R.L.: *Fluid Mechanics*, McGraw-Hill Book Co. Inc., New York City (1975).

Chapter 4

Multiphase-Flow Pressure-Gradient Prediction

4.1 Introduction

The pressure-gradient equation for single-phase flow in pipes was developed in Chap. 2, by use of the principles of conservation of mass and linear momentum. The same principles are used to calculate pressure gradient for multiphase flow in pipes. However, the presence of an additional phase makes the development much more complicated. Sec. 1.4 gives the historical background of methods used to predict multiphase-flow phenomena.

Early investigators treated multiphase flow as a homogeneous mixture of gas and liquid. This approach did not recognize that gas normally flows faster than liquid. The nonslip approach tended to underpredict pressure drop because the volume of liquid predicted to exist in the well was too small.

Improvements to the no-slip methods used empirical liquid-holdup correlations to account for slippage between the phases. Although liquid holdup and friction effects were often dependent on the flow pattern predicted by empirical flow-pattern maps, in general these methods still treated the fluids as a homogeneous mixture.

Unfortunately, treating the fluids as a homogeneous mixture is often unrealistic, resulting in poor predictions of flow behavior. A trend to improve flow-behavior predictions has emerged that is a compromise between the empirical correlations and the two-fluid approach. This is the phenomenological or mechanistic modeling approach, in which basic laws of physics are used to model the more important flow phenomena, including flow-pattern prediction. The mechanistic modeling approach still requires use of some empiricism, but only to predict specific flow mechanisms or closure relationships.

This chapter presents methods to predict pressure gradients. Also presented are modifications that improve accuracy, along with attempts to evaluate the various methods.

4.2 Pressure-Gradient Prediction

The methods used to predict pressure gradient can be classified as empirical correlations and mechanistic models.

4.2.1 Empirical Correlations. The empirical correlations to be discussed in this chapter can be placed in one of three categories:

Category "a." No slip, no flow pattern consideration. The mixture density is calculated based on the input gas/liquid ratio. That is, the gas and liquid are assumed to travel at the same velocity. The only correlation required is for the two-phase friction factor. No distinction is made for different flow patterns.

Category "b." Slip considered, no flow pattern considered. A correlation is required for both liquid holdup and friction factor. Because the liquid and gas can travel at different velocities, a method must be provided to predict the portion of the pipe occupied by liquid at any location. The same correlations used for liquid holdup and friction factor are used for all flow patterns.

Category "c." Slip considered, flow pattern considered. Not only are correlations required to predict liquid holdup and friction factor, but methods to predict which flow pattern exists are necessary. Once the flow pattern is established, the appropriate holdup and friction-factor correlations are determined. The method used to calculate the acceleration pressure gradient also depends on flow pattern.

The following list gives the published empirical correlations for vertical upward flow and the categories in which they belong.

Method	Category
Poettmann and Carpenter ¹	a
Baxendell and Thomas ²	a
Fancher and Brown ³	a
Hagedorn and Brown ⁴	b
Gray ⁵	b
Asheim ⁶	b
Duns and Ros ⁷	c
Orkiszewski ⁸	c
Aziz <i>et al.</i> ⁹	c
Chierici <i>et al.</i> ¹⁰	c
Beggs and Brill ¹¹	c
Mukherjee and Brill ¹²	c

It is important to recognize that only the methods of Beggs and Brill¹¹ and Mukherjee and Brill¹² were developed for angles other than vertical upward flow. Consequently, these two methods also are applicable to injection wells and hilly terrain pipelines. The other methods should be used with caution to predict pressure gradients in directional wells and should not be used for injection wells with multiphase flow. Descriptions of these methods follow, together with example problems for most methods.

Category "a." The three methods considered in this category differ only in the friction-factor correlation. In each method, field data based on Eq. 4.1 were used to calculate friction factors. For vertical flow of a homogeneous no-slip mixture, Eq. 3.26 can be expressed as

$$\frac{dp}{dz} = \frac{f \rho_n v_m^2}{2d} + \rho_n g. \quad \dots \dots \dots \quad (4.1)$$

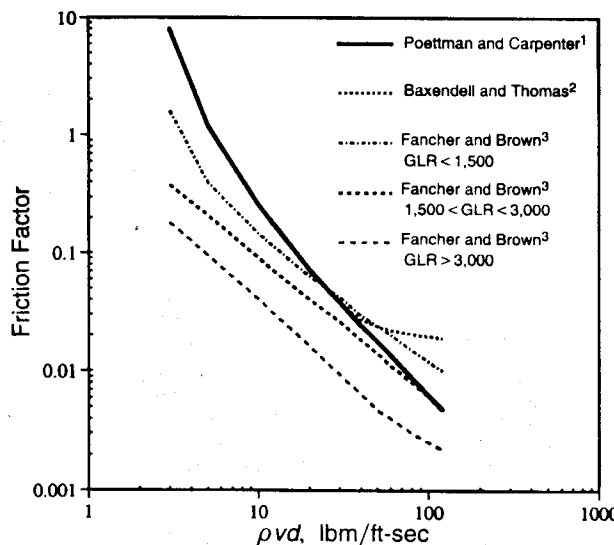


Fig. 4.1—Category “a” friction-factor correlations.

Fig. 4.1 shows the friction-factor correlations developed for the methods of Poettmann and Carpenter,¹ Baxendell and Thomas,² and Fancher and Brown.³ Because the numerator of the Reynolds number is not dimensionless, units must be specified for the abscissa in Fig. 4.1; those units are in lbm/ft·sec.

For interpolation purposes, the three curves for gas/liquid ratio in the Fancher and Brown correlation can be considered to represent gas/liquid ratios of 1,500, 2,250, and 3,000 scf/STBL.

Category “a” methods no longer should be used to predict multiphase-flow pressure gradients in wells. They can yield satisfactory results only for high-flow-rate wells for which the flow pattern would be dispersed-bubble flow. A no-slip condition characterizes the dispersed-bubble-flow pattern.

Example 4.1—Using the Poettmann and Carpenter Method, Calculate the Vertical, Multiphase-Flow Pressure Gradient for Example 3.2.

Given: $\rho_L = 47.61 \text{ lbm/ft}^3$ and $\rho_g = 5.88 \text{ lbm/ft}^3$.

1. Determine no-slip mixture density:

$$\rho_n = \rho_L \lambda_L + \rho_g (1 - \lambda_L)$$

$$= (47.61)(0.507) + (5.88)(0.493)$$

$$= 27.04 \text{ lbm/ft}^3.$$

2. Determine friction factor:

$$\rho_n v_m d = (27.04)(7.83)(0.5) = 105.86 \text{ lbm/(ft·sec)}.$$

From Fig. 4.1, $f = 0.0068$.

3. Determine total pressure gradient:

$$\begin{aligned} \frac{dp}{dz} &= \rho_n + \frac{f \rho_n v_m^2}{2 g_c d} = 27.04 + \frac{(0.0068)(27.04)(7.83)^2}{2(32.174)(0.5)} \\ &= 27.04 + 0.35 = 27.39 \text{ psf/ft} \\ &= 0.190 \text{ psi/ft}. \end{aligned}$$

Category “b.” Three methods are presented in this category. Hagedorn and Brown⁴ is a generalized method developed for a broad range of vertical two-phase-flow conditions. The Gray method⁵ is

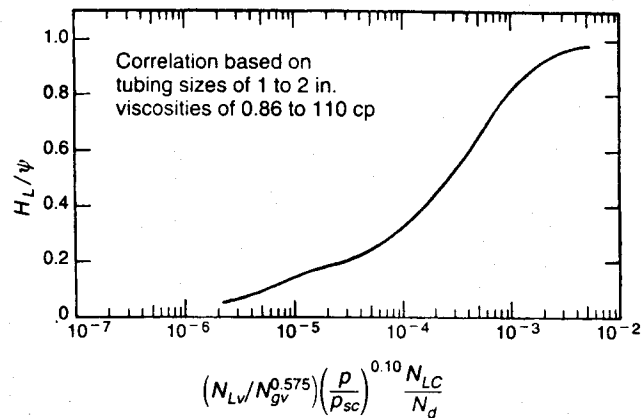


Fig. 4.2—Hagedorn and Brown⁴ correlation for H_L/ψ .

a specialized one developed for use with vertical gas wells that also produce condensate fluids and/or free water. The Asheim⁶ method uses MONA, a computer program based on a method that incorporates some basic mechanisms but also permits the adjustment of empirical parameters to fit available pressure measurements.

Hagedorn and Brown Method. The Hagedorn and Brown⁴ method is based on data obtained from a 1,500-ft-deep vertical experimental well. Air was the gas phase, and four different liquids were used: water and crude oils with viscosities of about 10, 30, and 110 cp. Tubing with 1.0, 1.25, and 1.5 in. nominal diameters were used. These data represent some of the most extensive large-scale tests ever reported. However, it is important to recognize that Hagedorn and Brown did not measure liquid holdup. Rather, they developed a pressure-gradient equation that, after assuming a friction-factor correlation, permitted the calculation of pseudo liquid-holdup values for each test to match measured pressure gradients. Thus, the values used to develop a liquid-holdup correlation were not true measures of the portion of pipe occupied by liquid.

Hagedorn and Brown developed this pressure-gradient equation for vertical multiphase flow

$$\frac{dp}{dz} = \frac{f \rho_n^2 v_m^2}{2 \rho_s d} + \rho_s g + \frac{\rho_s \Delta(v_m)}{2 dz}. \quad (4.2)$$

Liquid-Holdup Prediction. A liquid-holdup value must be determined to calculate the pressure-gradient component that results from a change in elevation. To correlate the pseudo liquid-holdup values, Hagedorn and Brown used four dimensionless groups proposed by Duns and Ros.⁷

Liquid velocity number:

$$N_{L_V} = v_{SL} \sqrt[4]{\frac{\rho_L}{g \sigma_L}}. \quad (4.3)$$

Gas velocity number:

$$N_{g_V} = v_{Sg} \sqrt[4]{\frac{\rho_L}{g \sigma_L}}. \quad (4.4)$$

Pipe diameter number:

$$N_d = d \sqrt{\frac{\rho_L g}{\sigma_L}}. \quad (4.5)$$

Liquid viscosity number:

$$N_L = \mu_L \sqrt[4]{\frac{g}{\rho_L \sigma_L^3}}. \quad (4.6)$$

These groups can be modified to include constants that make them dimensionally consistent when common oilfield units are used. Thus,

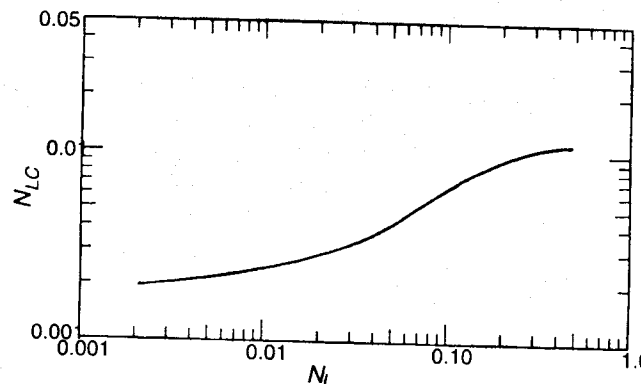


Fig. 4.3—Hagedorn and Brown⁴ correlation for N_{LC} .

$$N_{L_v} = 1.938 v_{SL} \sqrt[4]{\frac{\rho_L}{\sigma_L}},$$

$$N_{g_v} = 1.938 v_{Sg} \sqrt[4]{\frac{\rho_L}{\sigma_L}},$$

$$N_d = 120.872 d \sqrt{\frac{\rho_L}{\sigma_L}},$$

and

$$N_L = 0.15726 \mu_L \sqrt[4]{\frac{1}{\rho_L \sigma_L^3}},$$

where v_{SL} is in feet per second, v_{Sg} is in feet per second, ρ_L is in pounds per cubic foot, σ is in dynes per centimeter, μ_L centipoise, and d is in feet.

Fig. 4.2 shows the correlation for liquid holdup divided by a secondary correction factor, ψ . The abscissa requires a value of N_{LC} , which is correlated with N_L in Fig. 4.3. Fig. 4.4 shows the secondary correction-factor correlation. Once a value for liquid holdup has been determined from Figs. 4.2 through 4.4, the slip density can be calculated from Eq. 3.22.

Friction-Factor Prediction. Hagedorn and Brown assumed that two-phase friction factors could be predicted in the same way as single-phase friction factors. Thus, f is obtained from the single-phase Moody diagram in Fig. 2.2 for a given relative roughness and a two-phase Reynolds number defined as

$$N_{Re} = \frac{\rho_n v_m d}{\mu_s}, \quad (4.7)$$

where μ_s is defined in Eq. 3.20.

Acceleration Term. The pressure gradient resulting from acceleration is given by

$$\left(\frac{dp}{dZ} \right)_{acc} = \frac{\rho_s \Delta(v_m^2)}{2dZ}, \quad (4.8)$$

where

$$\Delta(v_m^2) = v_{m1}^2 - v_{m2}^2.$$

and 1, 2 designate downstream and upstream ends of a calculation increment, respectively.

If E_k is defined as

$$E_k = \frac{dZ}{dp} \left(\frac{dp}{dZ} \right)_{acc} = \frac{\rho_s \Delta(v_m^2)}{2dp}, \quad (4.9)$$

the total pressure gradient can be calculated from

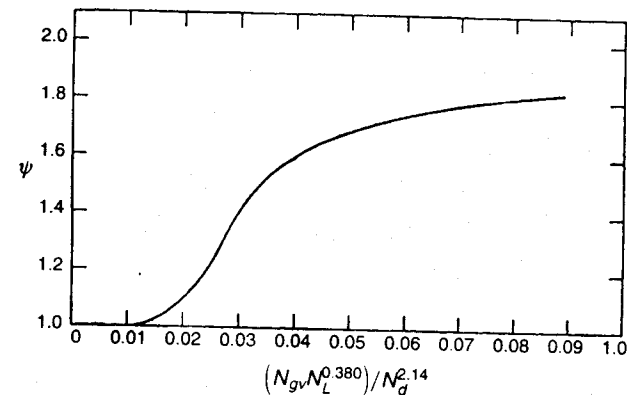


Fig. 4.4—Hagedorn and Brown⁴ correlation for ψ .

$$\frac{dp}{dZ} = \frac{\left(\frac{dp}{dZ} \right)_{el.} + \left(\frac{dp}{dZ} \right)_f}{1 - E_k} \quad (4.10)$$

Modifications. Over the years, several modifications have been proposed to improve the Hagedorn and Brown pressure-gradient predictions.

In conversations with Hagedorn, he suggested the first modification when he found that the correlation did not predict accurate pressure gradients for bubble flow. He suggested that, if the Griffith and Wallis¹³ criteria predicted the occurrence of bubble flow, the Griffith¹⁴ bubble-flow method should be used to predict pressure gradient. This approach is part of the Orkiszewski⁸ method, presented later.

The second modification is much more significant and is possibly a result of Hagedorn and Brown correlating pseudo liquid-holdup values rather than measured ones. Liquid-holdup values obtained from Figs. 4.2 through 4.4 are often less than no-slip holdup values. This is physically impossible because, for upward multiphase flow, liquid cannot travel faster than the gas phase. When this incorrect prediction occurs, the liquid-holdup value must be replaced with one that is physically possible. The approach normally used is to proceed with the no-slip liquid holdup. No attempt has been made to investigate whether this problem is peculiar to a specific range of variables.

The third common modification is to use the Duns and Ros⁷ method, if their mist- or transition-flow patterns are predicted to occur. There is no physical justification for this modification. It is used primarily to make the entire Hagedorn and Brown method a Category "c" method. Because the Duns and Ros method is presented later in this section, it is not described here.

A fourth modification often used is to replace the acceleration pressure-gradient component given by Eq. 4.8 with that proposed by Duns and Ros. Eq. 4.8 was not used by Hagedorn and Brown to analyze their data and is known to overpredict acceleration affects.

In summary, the modified Hagedorn and Brown method is a combination of several methods. The original Hagedorn and Brown method is used only for the slug region, as predicted by Griffith and Wallis and Duns and Ros, and then only if a physically possible liquid-holdup value is found.

Example 4.2—Using the Modified Hagedorn and Brown Method, Calculate the Vertical, Multiphase-Flow Pressure Gradient for Example 3.2.

Given: $\mu_o = 0.97$ cp, $\sigma_o = 8.41$ dynes/cm, $\mu_g = 0.016$ cp, and $\epsilon = 0.00006$ ft.

- Determine Duns and Ros dimensionless groups:

$$N_{L_v} = 1.938 v_{SL} \left(\frac{\rho_L}{\sigma_L} \right)^{1/4}$$

$$= (1.938)(3.97) \left(\frac{47.61}{8.41} \right)^{0.25} = 11.87,$$

$$N_{gv} = 1.938 v_{sg} \left(\frac{\rho_L}{\sigma_L} \right)^{1/4}$$

$$= (1.938)(3.86) \left(\frac{47.61}{8.41} \right)^{0.25} = 11.54,$$

$$N_d = 120.872 d \sqrt{\frac{\rho_L}{\sigma_L}}$$

$$= (120.872) \left(\frac{6}{12} \right) \sqrt{\left(\frac{47.61}{8.41} \right)} = 143.8,$$

and

$$N_L = 0.15726 \mu_L \left(\frac{1}{\rho_L \sigma_L^3} \right)^{1/4}$$

$$= (0.15726)(0.97) \left[\frac{1}{(47.61)(8.41)^3} \right]^{0.25} = 0.0118.$$

2. Determine liquid holdup:

From Fig. 4.3, $N_{LC} = 0.0024$.

From Fig. 4.2, the abscissa, a , is

$$\begin{aligned} a &= \frac{N_{Lg} N_{LC}}{N_{gv}^{0.575} N_d} \left(\frac{P}{P_{sc}} \right)^{0.1} \\ &= \frac{(11.87)(0.0024)}{(11.54)^{0.575} (143.8)} \left(\frac{1,700}{14.7} \right)^{0.1} \\ &= 7.81 \times 10^{-5} \end{aligned}$$

$$\therefore \frac{H_L}{\psi} = 0.3.$$

From Fig. 4.4, the abscissa, a , is

$$\begin{aligned} a &= \frac{N_{gv} N_L^{0.380}}{N_d^{2.14}} \\ &= \frac{(11.42)(0.0118)^{0.380}}{(143.8)^{2.14}} \\ &= 5.1 \times 10^{-5} \end{aligned}$$

$$\therefore \psi = 1.0$$

and

$$H_L = \frac{H_L}{\psi} \psi = (0.3)(1.0) = 0.3.$$

3. Check validity of H_L :

Because $H_L < \lambda_L$, set $H_L = \lambda_L = 0.507$.

4. Calculate slip density:

$$\begin{aligned} \rho_s &= \rho_L H_L + \rho_g (1 - H_L) \\ &= (47.61)(0.507) + (5.88)(1 - 0.507) \\ &= 27.04 \text{ lbm/ft}^3. \end{aligned}$$

5. Determine friction factor:

From Eq. 3.19,

$$\begin{aligned} \mu_s &= (0.97)^{0.507} (0.016)^{(1-0.507)} \\ &= 0.13 \text{ cp.} \end{aligned}$$

From Eq. 4.7,

$$\begin{aligned} N_{Re} &= \frac{(1,488)(27.04)(7.83)(0.5)}{0.13} \\ &= 1.21 \times 10^6 \end{aligned}$$

and

$$\frac{\varepsilon}{d} = \left(\frac{0.00006}{0.5} \right) = 0.00012.$$

From Fig. 2.2 or Eq. 2.17, $f = 0.0135$.

6. Determine pressure gradient, neglecting kinetic energy effects:

From Eq. 4.2,

$$\begin{aligned} \frac{dp}{dz} &= \frac{(0.0135)(27.04)^2 (7.83)^2}{(2)(27.04)(32.174)(0.5)} + (27.04) \frac{(32.174)}{(32.174)} \\ &= 0.70 + 27.04 = 27.74 \text{ psf/ft} \\ &= 0.193 \text{ psi/ft.} \end{aligned}$$

7. If calculations had been made with the incorrect liquid-holdup value of 0.3, the pressure gradient would have been 0.14 psi/ft.

Gray Method. Gray developed a method to determine the pressure gradient in a vertical gas well that also produces condensate fluids or water.⁵ A total of 108 well-test-data sets were used to develop the empirical correlations. Of these data sets, 88 were obtained on wells reportedly producing free liquids. The authors cautioned use of the method for velocities higher than 50 ft/sec, nominal diameters greater than 3.5 in., condensate/liquid loadings above 50 bbl/MMscf, and water/liquid loadings above 5 bbl/MMscf.

Gray proposed this equation to predict the pressure gradient for two-phase flow in vertical gas wells.

$$\frac{dp}{dz} = \frac{f \rho_n v_m^2}{2d} + \rho_s g - \rho_n^2 v_m^2 \frac{d}{dz} \left(\frac{1}{\rho_n} \right). \quad (4.11)$$

Liquid-Holdup Prediction. From a dimensional analysis and selected laboratory tests, three dimensionless groups of variables were selected to correlate liquid holdup.

$$N_v = \frac{\rho_n^2 v_m^4}{g \sigma_L (\rho_L - \rho_g)}, \quad (4.12)$$

$$N_D = \frac{g(\rho_L - \rho_g)d^2}{\sigma_L}, \quad (4.13)$$

and

$$R = \frac{v_{SL}}{v_{sg}}. \quad (4.14)$$

The resulting correlation developed to predict liquid holdup was given as

$$H_L = 1 - \frac{1 - e^{\left\{ -2.314 \left[N_v \left(1 + \frac{205.0}{N_D} \right) \right]^B \right\}}}{R + 1}, \quad (4.15)$$

where

$$B = 0.0814 \left[1 - 0.0554 \ln \left(1 + \frac{730R}{R+1} \right) \right]. \quad (4.16)$$

Gray suggested this expression for σ_L in Eqs. 4.12 and 4.13 when both condensate and water are present.

$$\sigma_L = \frac{f_o \sigma_o + 0.617 f_w \sigma_w}{f_o + 0.617 f_w}. \quad (4.17)$$

Gray stated that the liquid holdup in condensate wells often tends to be smaller than in oil wells producing at comparable gas/liquid ratios. This probably arises from natural time lags in the flashing and condensing processes, and also from the lower average interfacial surface tension in condensing systems compared with flashing black-oil systems. The formulation of Eq. 4.15 is such that the liquid holdup is ordinarily very near to the no-slip holdup.

Friction-Factor Prediction. The effect of liquid holdup on friction loss can be interpreted as a variation in wall roughness from that ordinarily experienced in single-phase, dry-gas flow. Gray proposed that friction factors for wet-gas wells were wholly dependent on a pseudo-wall-roughness factor because flow is normally in the fully-developed turbulent region. Friction factors can be obtained from the Moody diagram (Fig. 2.2) or from Eq. 2.16 for completely turbulent flow. The pseudo-wall-roughness, ϵ' , was correlated with a modified Weber number, similar to that used in the Duns and Ros⁷ method for mist flow. Defining a roughness variable,

$$\epsilon' = \frac{28.5\sigma_L}{\rho_n v_m^2}, \quad (4.18)$$

then, for $R \geq 0.007$,

$$\epsilon = \epsilon' \quad (4.19)$$

and, for $R < 0.007$,

$$\epsilon = \epsilon_g + \frac{R(\epsilon' - \epsilon_g)}{0.0007}, \quad (4.20)$$

with the restriction that $\epsilon \geq 2.77 \times 10^{-5}$. ϵ_g is the absolute wall roughness for single-phase gas flow. It is noteworthy that the correlation finally adopted includes both the effects of unusually high apparent roughness observed in certain laboratory test conditions and the effects of low apparent roughness in certain field systems.

Asheim Method. The Asheim⁶ method, or MONA, is independent of flow pattern, but does permit the selection of three empirical parameters for either the bubble- or slug-flow patterns. Once selected, however, these parameters must be used for all multiphase-flow calculations. The method can be used in conjunction with a history-matching procedure to adjust the three empirical parameters and minimize computation errors.

The pressure gradient is determined from

$$\frac{dp}{dL} = \frac{f \rho_n v_m^2}{2d} + \rho_s g \sin \theta. \quad (4.21)$$

Liquid-Holdup Determination. The gas and liquid velocities can be determined from

$$v_L = \frac{q_L}{A_L} = \frac{v_{SL}}{H_L} \quad (4.22)$$

and

$$v_g = \frac{q_g}{A_g} = \frac{v_{Sg}}{1 - H_L}. \quad (4.23)$$

Eqs. 4.22 and 4.23 can be combined to give

$$H_L = \frac{A_L}{A_L + A_g} = \frac{\frac{v_{SL}}{v_L}}{\frac{v_{SL}}{v_L} + \frac{v_{Sg}}{v_g}}. \quad (4.24)$$

Eq. 4.25 gives the functional relationship assumed between the gas- and liquid-phase velocities.

$$v_g = a_1 v_L + a_2. \quad (4.25)$$

Using Eqs. 4.22 and 4.25 to eliminate the gas- and liquid-phase velocities in Eq. 4.24 gives

$$H_L = \frac{\left[(v_{Sg} + a_1 v_{SL} - a_2)^2 + 4a_1 a_2 v_{SL} \right]^{0.5}}{2a_2} - \frac{v_{Sg} + a_1 v_{SL} - a_2}{2a_2}. \quad (4.26)$$

Two limiting cases must be defined to make the holdup expression complete. When the constant-slip term, a_2 , (buoyancy) is zero, the holdup becomes

$$H_L|_{a_2=0} = \frac{a_1 v_{SL}}{v_{Sg} + a_1 v_{SL}}. \quad (4.27)$$

When the liquid superficial velocity approaches zero, the flow situation may correspond to gas bubbling through stagnant liquid. The holdup for this case is found by rearranging Eq. 4.26 to obtain

$$H_L|_{v_{SL} \rightarrow 0^+} = 1 - \frac{v_{Sg}}{a_2}. \quad (4.28)$$

Friction-Factor Determination. This two-phase friction-factor correlation was used in Eq. 4.21.

$$f = a_3 f_n \frac{\rho_n}{\rho_k}, \quad (4.29)$$

where ρ_k is defined in Eq. 3.24. The wall friction factor, f_n , is determined from Fig. 2.2 for a no-slip Reynolds number defined by

$$N_{Re_n} = \frac{\rho_n v_m d}{\mu_n}. \quad (4.30)$$

Parameter Values. For slug flow, the normal values of the three parameters are $a_1 = 1.2$, $a_2 = 0.35 \sqrt{gd}$, and $a_3 = 1.0$. For homogeneous flow the normal values of the three parameters are $a_1 = 1.0$, $a_2 = 0$, and $a_3 = 1.0$. Asheim showed that, by selecting either slug flow or homogeneous flow, the three parameters can be adjusted for an optimized fit of field data.

Category "c." The methods considered in this category differ in how they predict flow pattern and how, for each flow pattern, they predict liquid holdup and the friction and acceleration pressure-gradient components. For vertical flow of a homogeneous slip mixture, Eq. 3.26 can be expressed as

$$\frac{dp}{dZ} = \left(\frac{dp}{dZ} \right)_f + \rho_s g + \left(\frac{dp}{dZ} \right)_{acc}. \quad (4.31)$$

Duns and Ros Method. The Duns and Ros⁷ method is a result of an extensive laboratory study in which liquid holdup and pressure gradients were measured. About 4,000 two-phase-flow tests were conducted in a 185-ft-high vertical-flow loop. Pipe diameters ranged from 1.26 to 5.60 in. and included two annulus configurations. Most of the tests were at near-atmospheric conditions with air for the gas phase and liquid hydrocarbons or water as the liquid phase. Liquid holdup was measured by use of a radioactive-tracer technique. A transparent section permitted the observation of flow pattern. For each of three flow patterns observed, correlations were developed for friction factor and slip velocity, from which liquid holdup can be calculated.

Duns and Ros performed the first dimensional analysis of two-phase flow in pipes. They identified 12 variables that were potentially important in the prediction of pressure gradient. Performing a dimensional analysis of these variables resulted in nine dimensionless groups, or π terms. Through a process of elimination, four of the

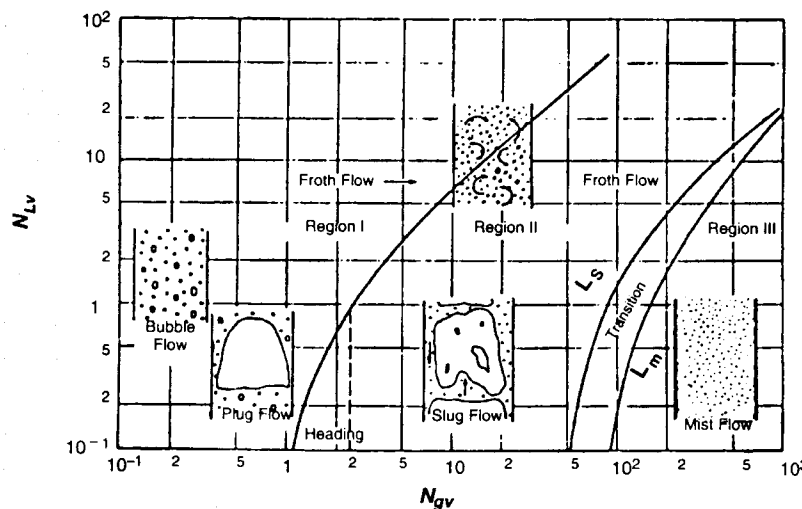


Fig. 4.5—Duns and Ros⁷ flow-pattern map.

groups were identified as being important and were used to select the range of variables in the experimental program. Eqs. 4.3 through 4.6 gave these four groups.

Flow-Pattern Prediction. Fig. 4.5 shows the flow-pattern map developed by Duns and Ros. They identified four separate regions for computation purposes, Regions I through III and a transition region. Fig. 4.5 illustrates the actual flow patterns existing in each region. Duns and Ros also identified the heading region as a fifth region, but this is now considered part of Region II. In this monograph, we will refer to Regions I through III as bubble, slug, and mist flow, respectively.

The flow-pattern transition boundaries are defined as functions of the dimensionless groups N_{gv} and N_{Lv} . For these transition boundaries, Duns and Ros proposed these equations.

Bubble/slug boundary:

$$N_{gv_{B/S}} = L_1 + L_2 N_{Lv}, \quad \dots \dots \dots \quad (4.32a)$$

where L_1 and L_2 are functions of N_d , as shown in Fig. 4.6.

Slug/transition boundary:

$$N_{gv_{S/Tr}} = 50 + 36N_{Lv}. \quad \dots \dots \dots \quad (4.32b)$$

Transition/mist boundary:

$$N_{gv_{Tr/M}} = 75 + 84N_{Lv}^{0.75}. \quad \dots \dots \dots \quad (4.32c)$$

Liquid-Holdup Prediction. Duns and Ros chose to develop empirical correlations for a dimensionless slip-velocity number, S , rather than for liquid holdup. S is defined in a similar way to the gas- and liquid-velocity numbers given by Eqs. 4.3 and 4.4. Thus,

$$S = v_s \sqrt{\frac{\rho_L}{g\sigma_L}} \quad \dots \dots \dots \quad (4.33)$$

or, in field units,

$$S = 1.938 v_s \sqrt{\frac{\rho_L}{\sigma_L}}. \quad \dots \dots \dots \quad (4.34)$$

The slip velocity was defined by Eq. 3.15 and, when combined with Eqs. 3.13 and 3.14, yields a quadratic equation for obtaining H_L .

$$v_s = v_g - v_L = \frac{v_{sg}}{1 - H_L} - \frac{v_{SL}}{H_L}, \quad \dots \dots \dots \quad (4.35)$$

or

$$H_L = \frac{v_s - v_m + \sqrt{(v_m - v_s)^2 + 4v_s v_{SL}}}{2v_s}. \quad \dots \dots \dots \quad (4.36)$$

The following procedure is used to calculate the elevation component of the pressure gradient.

1. Calculate the dimensionless slip velocity, S , using the appropriate correlation. The correlations for S are different for each flow pattern and are given later.
2. Solve Eq. 4.33 or 4.34 for the slip velocity.
3. Calculate the liquid holdup from Eq. 4.35 or 4.36.
4. Calculate the slip density from Eq. 3.22,

$$\rho_s = \rho_L H_L + \rho_g (1 - H_L). \quad \dots \dots \dots \quad (3.22)$$

5. Calculate the elevation component of the pressure gradient, as given in Eq. 4.31.

Bubble Flow. Bubble flow exists if $N_{gv} < N_{gv_{B/S}}$. For bubble flow, the dimensionless slip-velocity number is given by

$$S = F_1 + F_2 N_{Lv} + F_3 \left(\frac{N_{gv}}{1 + N_{Lv}} \right)^2, \quad \dots \dots \dots \quad (4.37)$$

where F_1 and F_2 are given in Fig. 4.7. They are functions of the liquid velocity number, N_L . F_3 can be obtained from

$$F_3' = F_3 - \frac{F_4}{N_d}, \quad \dots \dots \dots \quad (4.38)$$

where F_3 and F_4 also are obtained from Fig. 4.7.

The friction pressure-gradient component for bubble flow is given by

$$\left(\frac{dp}{dz} \right)_f = \frac{f \rho_L v_{SL} v_m}{2d}. \quad \dots \dots \dots \quad (4.39)$$

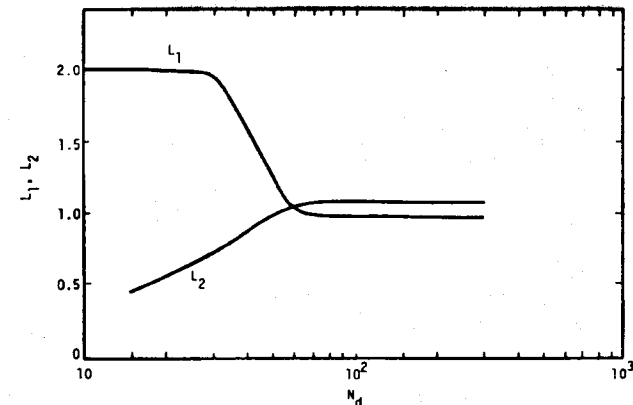


Fig. 4.6—Duns and Ros⁷ bubble/slug transition parameters.

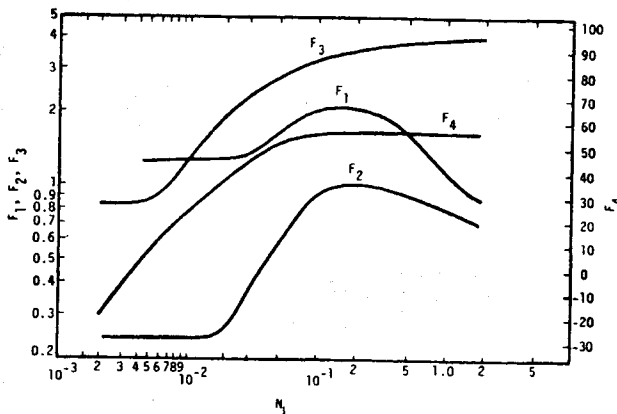


Fig. 4.7—Duns and Ros⁷ bubble-flow, slip-velocity parameters.

From experimental data, Duns and Ros developed this equation for f :

$$f = f_1 \frac{f_2}{f_3} \quad \dots \dots \dots \quad (4.40)$$

The friction factor is governed mainly by f_1 , which is obtained from a Moody diagram (Fig. 2.2) as a function of a Reynolds number for the liquid phase.

$$N_{Re_L} = \frac{\rho_L v_{SL} d}{\mu_L} \quad \dots \dots \dots \quad (4.41)$$

The factor f_2 in Eq. 4.40 is a correction for the in-situ gas/liquid ratio and is given in Fig. 4.8. The factor f_3 is considered by Duns and Ros as a second-order correction factor for both liquid viscosity and in-situ gas/liquid ratio. It becomes important for kinematic viscosities greater than approximately 50 cSt and is given by

$$f_3 = 1 + \frac{f_1}{4} \sqrt{\frac{v_{Sg}}{50v_{SL}}} \quad \dots \dots \dots \quad (4.42)$$

Duns and Ros considered the acceleration component of the pressure gradient to be negligible for bubble flow.

Slug Flow. Slug flow exists if $N_{gv_{B/S}} < N_{gv} < N_{gv_{S/T}}$. For slug flow, the dimensionless slip-velocity number is

$$S = (1 + F_5) \frac{(N_{gv})^{0.982} + F_6}{(1 + F_7 N_{Lv})^2}, \quad \dots \dots \dots \quad (4.43)$$

where F_5 , F_6 , and F_7 are given in Fig. 4.9 as functions of the liquid viscosity number, N_L , and

$$F'_6 = 0.029 N_d + F_6. \quad \dots \dots \dots \quad (4.44)$$

The friction pressure-gradient component for slug flow is calculated exactly the same way as for bubble flow. Also, the acceleration component for slug flow is considered negligible.

Mist Flow. Mist flow exists if $N_{gv} > N_{gv_{Tr/M}}$. Duns and Ros assumed that, at high gas flow rates, the liquid is transported mainly as small droplets. The result is nearly a no-slip condition between the phases. Thus, $S = 0$, $v_s = 0$, and $H_L = \lambda_L$. The mixture density for use in the elevation component of the pressure gradient then is calculated from Eq. 3.23.

Friction in the mist-flow pattern originates from the shear stress between the gas and the pipe wall. Thus, the friction component of the pressure gradient is determined from

$$\left(\frac{dp}{dZ} \right)_f = \frac{f \rho_g v_{Sg}^2}{2d}. \quad \dots \dots \dots \quad (4.45)$$

Because there is no slip, the friction factor is obtained from a Moody diagram (Fig. 2.2) as a function of a Reynolds number for the gas phase.

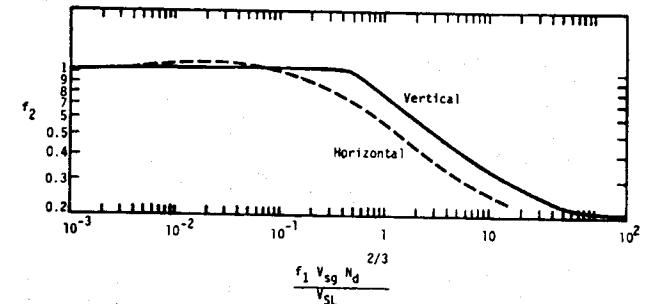


Fig. 4.8—Duns and Ros⁷ bubble-flow, friction-factor parameter.

$$N_{Re_g} = \frac{\rho_g v_{SL} d}{\mu_g} \quad \dots \dots \dots \quad (4.46)$$

Duns and Ros noted that the wall roughness for mist flow is the thickness of the liquid film that covers the pipe wall. Waves on the film cause an increased shear stress between the gas and the film that, in turn, can cause the greatest part of the pressure gradient. These waves result from the drag of the gas deforming the film in opposition to the surface tension. This process is affected by liquid viscosity and also is governed by a form of the Weber number

$$N_{We} = \frac{\rho_g v_{Sg}^2 \epsilon}{\sigma_L} \quad \dots \dots \dots \quad (4.47)$$

This influence was accounted for by making N_{We} a function of a dimensionless number containing liquid viscosity,

$$N_\mu = \frac{\mu_L^2}{\rho_L \sigma_L \epsilon} \quad \dots \dots \dots \quad (4.48)$$

Fig. 4.10 shows the functional relationship, where the coordinates are N_{We} vs. $N_{We} N_\mu$.

The value of roughness may be very small, but the relative roughness never becomes smaller than the value for the pipe itself. At the transition to slug flow, the waviness of the film may become large, with the crests of opposite waves touching and forming liquid bridges. Then ϵ/d approaches 0.5. Between these limits, ϵ/d can be obtained from equations developed from Fig. 4.10.

$$N_{We} N_\mu \leq 0.005; \frac{\epsilon}{d} = \frac{0.0749 \sigma_L}{\rho_g v_{Sg}^2 d} \quad \dots \dots \dots \quad (4.49)$$

and

$$N_{We} N_\mu > 0.005; \frac{\epsilon}{d} = \frac{0.3713 \sigma_L}{\rho_g v_{Sg}^2 d} (N_{We} N_\mu)^{0.302}, \quad \dots \dots \dots \quad (4.50)$$

where d is in feet, v_{Sg} is in feet per second, ρ_g is in pounds per cubic foot, and σ_L is in dynes per centimeter.

Values of f for the mist-flow pattern can be found for $\epsilon/d > 0.05$ from this extrapolation of the Moody diagram.

$$f = 4 \left\{ \frac{1}{\left[4 \log_{10} \left(0.27 \frac{\epsilon}{d} \right) \right]^2} + 0.067 \left(\frac{\epsilon}{d} \right)^{1.73} \right\} \quad \dots \dots \dots \quad (4.51)$$

As the wave height of the film on the pipe wall increases, the actual area available for gas flow decreases because the diameter open to flow of gas is now $d - \epsilon$. Duns and Ros suggested that the friction component of the pressure gradient could be refined by replacing d

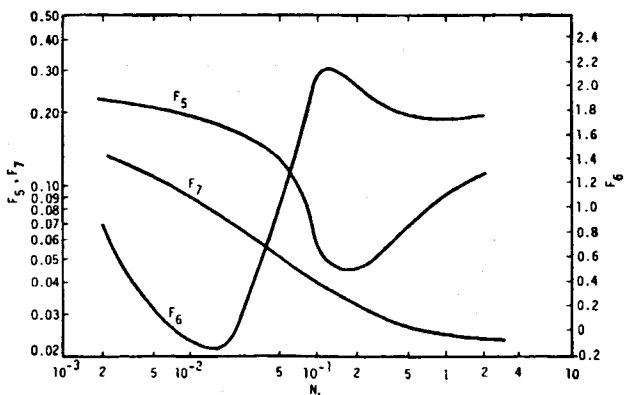


Fig. 4.9—Duns and Ros⁷ slug-flow, slip-velocity parameters.

with $d - \varepsilon$ and v_{Sg} with $v_{Sg} d^2 / (d - \varepsilon)^2$ throughout the calculations. This results in a trial-and-error procedure to determine ε .

In mist flow, acceleration often cannot be neglected as it was in bubble and slug flow. The acceleration component of the pressure gradient can be approximated by

$$\left(\frac{dp}{dz} \right)_{acc} = \frac{v_m v_{Sg} \rho_n}{p} \left(\frac{dp}{dz} \right). \quad (4.52)$$

Beggs and Brill¹¹ provided a derivation of Eq. 4.52. If we define a dimensionless kinetic energy, E_k , as

$$E_k = \frac{v_m v_{Sg} \rho_n}{p}, \quad (4.53)$$

the total pressure gradient can be calculated from

$$\left(\frac{dp}{dz} \right)_t = \frac{\left(\frac{dp}{dz} \right)_{el} + \left(\frac{dp}{dz} \right)_f}{1 - E_k}. \quad (4.54)$$

The dimensionless kinetic energy term, E_k , is related to the sonic velocity of a two-phase mixture. E_k is similar to the Mach number for compressible flow. Sonic conditions are reached when the Mach number becomes 1.0. When this occurs in a pipe, a "shock" is established, across which the pressure gradient is infinite. Eq. 4.54 will predict the same result if E_k becomes 1.0. Unfortunately, Eq. 4.53 can incorrectly yield E_k values greater than 1.0.

Transition Region. The transition region exists if $N_{gv_{S/Tr}} < N_{gv} < N_{gv_{Tr/M}}$. If this region is predicted, Duns and Ros suggested linear interpolation between the flow-pattern boundaries, $N_{gv_{S/Tr}}$ and $N_{gv_{Tr/M}}$ to obtain the pressure gradient. This will require a calculation of pressure gradients with both slug-flow and mist-flow correlations. The pressure gradient in the transition region then is calculated from

$$\left(\frac{dp}{dz} \right)_t = A \left(\frac{dp}{dz} \right)_{slug} + (1 - A) \left(\frac{dp}{dz} \right)_{mist}, \quad (4.55)$$

where

$$A = \frac{N_{gv_{Tr/M}} - N_{gv}}{N_{gv_{Tr/M}} - N_{gv_{S/Tr}}}. \quad (4.56)$$

Increased accuracy was claimed in the transition region if the gas density used in the mist-flow pressure-gradient calculation was modified to be

$$\rho'_g = \frac{\rho_g N_{gv}}{N_{gv_{Tr/M}}}, \quad (4.57)$$

where ρ'_g = gas density calculated at the given conditions of pressure and temperature. This modification accounts for some of the liquid being entrained in the gas.

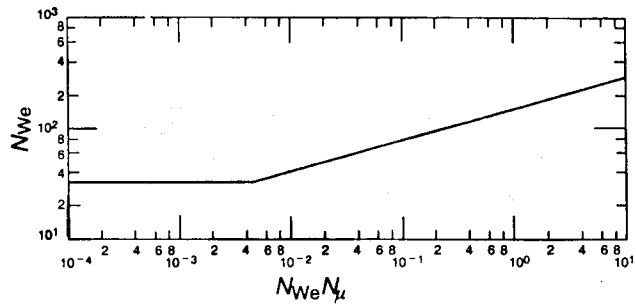


Fig. 4.10—Duns and Ros⁷ mist-flow, film-thickness correlation.

Modifications. Two proprietary modifications of the Duns and Ros method have been developed but are not available in the literature. The first, known as the Ros field method, involved modifications based on carefully obtained data from 17 high-GOR vertical oil wells.

In a joint Mobil-Shell study undertaken between 1974 and 1976, a modification resulted in the Moreland-Mobil-Shell method (MMSM). In this study, 40 vertical oil wells, including the 17 used in the Ros field method, and 21 directional wells were selected as the basis for the modifications. The MMSM method includes liquid-holdup correlations derived from the data for bubble and slug flow that are simpler in form than those used in the original Duns and Ros method. Possible discontinuities at flow-pattern-transition boundaries also were removed.

Example 4.3—Using the Duns and Ros Method, Calculate the Vertical, Multiphase-Flow Pressure Gradient for Example 3.2.

Given: $\mu_o = 0.97$ cp, $\sigma_o = 8.41$ dynes/cm, $\mu_g = 0.016$ cp, and $\varepsilon = 0.00006$ ft.

1. Determine the flow pattern:

From Fig. 4.5, Region I (froth or bubble).

Verification.

From Fig. 4.6, $L_1 = 1.0$; $L_2 = 1.1$,

$$N_{gv_{B/S}} = L_1 + L_2 N_{L_v}, \\ = 1.0 + (1.1)(11.87) = 14.06$$

and

$$N_{gv} = 11.54 < N_{gv_{B/S}}$$

∴ bubble flow exists.

2. Determine liquid holdup:

From Fig. 3.12, $F_1 = 1.2$, $F_2 = 0.24$, $F_3 = 1.3$, and $F_4 = 26.5$.

From Eq. 4.38,

$$F_3' = 1.3 - \frac{(26.5)}{(143.8)} = 1.116.$$

From Eq. 4.37 for bubble flow,

$$S_1 = 1.2 + (0.24)(11.87) + (1.116) \left(\frac{11.54}{1 + 11.87} \right)^2 \\ = 4.946.$$

From Eq. 4.35,

$$v_s = \frac{(4.946)}{(1.938) \left(\frac{47.61}{8.41} \right)^{0.25}} = 1.655 \text{ ft/sec.}$$

From Eq. 4.36,

$$H_L = \frac{1.655 - 7.83 + \sqrt{(7.83 - 1.655)^2 + (4)(1.655)(3.97)}}{(2)(1.655)} \\ = 0.559.$$

3. Determine friction factor:
From Eq. 4.41,

$$N_{Re_L} = \frac{(1,488)(47.61)(3.97)(0.5)}{(0.97)} = 1.45 \times 10^5$$

and

$$\frac{\varepsilon}{d} = \frac{0.00006}{0.5} = 0.00012.$$

From Fig. 2.2 or Eq. 2.17, $f_1 = 0.0175$.
From Fig. 4.8,

$$\begin{aligned} \frac{f_1 v_{sg} N_d^{2/3}}{4 v_{SL}} &= \frac{(0.0175)(3.86)(143.8)^{2/3}}{(4)(3.97)} \\ &= 1.17 \times 10^{-1} \\ \therefore f_2 &= 1.0. \end{aligned}$$

From Eq. 4.42,

$$f_3 = 1 + \frac{(0.0175)}{4} \sqrt{\frac{3.86}{(50)(3.97)}} = 1.0006.$$

From Eq. 4.40,

$$f = (0.0175) \frac{(1.0)}{(1.0006)} = 0.0175.$$

4. Determine pressure gradient, neglecting kinetic energy effects:
From Eqs. 4.31, 3.22, and 4.39,

$$\begin{aligned} \frac{dp}{dz} &= \frac{(0.0175)(47.61)(3.97)(7.83)}{(2)(32.174)(0.5)} \\ &+ [(47.61)(0.559) + (5.88)(1 - 0.559)] \frac{(32.174)}{(32.174)} \\ &= 0.80 + 29.21 = 30.01 \text{ psf/ft} \\ &= 0.208 \text{ psf/ft}. \end{aligned}$$

Orkiszewski Method. Orkiszewski⁸ tested several published correlations with field data and concluded that none was sufficiently accurate for all flow patterns. He then selected what he considered to be the most accurate correlations for bubble and mist flow and proposed a new correlation for slug flow. The slug-flow correlation was developed with the Hagedorn and Brown⁴ data. Orkiszewski selected the Griffith and Wallis^{13,14} method for bubble flow and the Duns and Ros⁷ method for mist flow.

Flow-Pattern Prediction. Orkiszewski used the Duns and Ros flow-pattern transitions for the boundaries between slug flow and mist flow, including the transition region between them. Eqs. 4.32b and 4.32c defined these. For the boundary between bubble flow and slug flow, he chose these criteria established by Griffith and Wallis.

Bubble/slug transition:

$$\lambda_{g_{B/S}} = L_B, \quad (4.58)$$

where

$$L_B = 1.071 - 0.2218 \frac{v_m^2}{d}, \quad (4.59)$$

and v_m = ft/sec, v_{sg} = ft/sec, d = ft, and L_B is constrained algebraically to be ≥ 0.13 .

Bubble Flow. Bubble flow exists if $\lambda_g = 1 - \lambda_L \leq \lambda_{g_{B/S}}$. The liquid holdup for bubble flow is determined from

$$H_L = 1 - \frac{1}{2} \left[1 + \frac{v_m}{v_s} - \sqrt{\left(1 + \frac{v_m}{v_s}\right)^2 - 4 \frac{v_{sg}}{v_s}} \right], \quad (4.60)$$

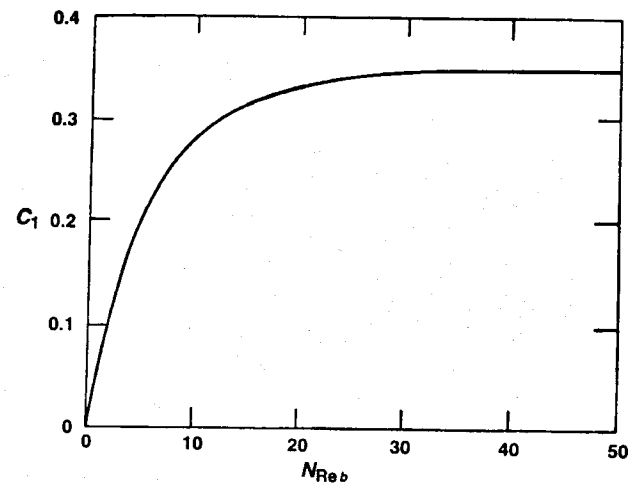


Fig. 4.11—Griffith and Wallis¹³ C_1 correlation.

which is equivalent to Eq. 4.36 for the Duns and Ros correlation. Orkiszewski adopted the Griffith¹⁴ suggestion that 0.8 ft/sec is a good approximation of an average v_s . In Sec. 4.2.2 we will show that v_s is a function of the gas and liquid densities and surface tension. The liquid holdup determined from Eq. 4.60 then is used to calculate slip density with Eq. 3.22, which in turn is used to calculate the elevation component of the pressure gradient.

The friction pressure-gradient component for bubble flow is given by

$$\left(\frac{dp}{dz} \right)_f = \frac{\rho_L (v_{SL}/H_L)^2}{2d}. \quad (4.61)$$

The friction factor is obtained from a Moody diagram (Fig. 2.2) as a function of relative roughness and Reynolds number for the liquid phase,

$$N_{Re} = \frac{\rho_L (v_{SL}/H_L) d}{\mu_L}. \quad (4.62)$$

The acceleration pressure-gradient component for bubble flow was considered negligible.

Slug Flow. Slug flow exists if $\lambda_g > \lambda_{g_{B/S}}$, and $N_{gv} < N_{gv_{S/T}}$. The slip density is calculated from

$$\rho_s = \frac{\rho_L (v_{SL} + v_b) + \rho_g v_{sg}}{v_m + v_b} + \rho_L \Gamma. \quad (4.63)$$

Orkiszewski developed Eq. 4.63 by performing mass and volume balances on a typical slug unit consisting of a Taylor bubble¹⁵ and a liquid slug. A similar Griffith and Wallis development neglected the presence of a liquid film around the Taylor bubble and the possibility of liquid droplets being entrained in the Taylor bubble. Consequently, Orkiszewski proposed the last term in Eq. 4.63 to account for the distribution of liquid in these regions. This modification was meant to extend the Griffith and Wallis work to include the high-velocity-flow range.

Griffith and Wallis correlated the bubble-rise velocity, v_b , by the relationship

$$v_b = C_1 C_2 \sqrt{gd}, \quad (4.64)$$

where C_1 and C_2 are expressed in Figs. 4.11 and 4.12 as functions of N_{Re_b} and N_{Re_L} .

$$N_{Re_b} = \frac{\rho_L v_b d}{\mu_L} \quad (4.65)$$

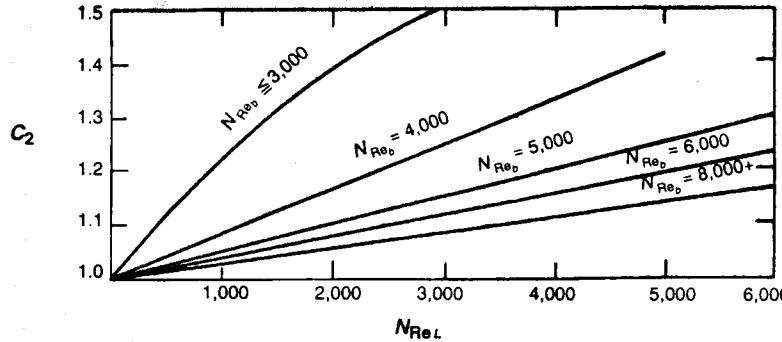


Fig. 4.12—Griffith and Wallis¹³ C_2 correlation.

TABLE 4.1—ORKISZEWSKI⁸ LIQUID DISTRIBUTION COEFFICIENT EQUATIONS

Continuous Liquid Phase	Value of v_m (ft/sec)	Equation for Γ
Water	<10	4.72
Water	>10	4.73
Oil	<10	4.74
Oil	>10	4.75

and

$$N_{Re_L} = \frac{\rho_L v_m d}{\mu_L} \quad (4.66)$$

Fig. 4.12 was extrapolated so that v_b could be evaluated at higher liquid Reynolds numbers. When C_2 cannot be read from Fig. 4.12, v_b can be calculated from this set of equations.

When $N_{Re_b} \leq 3,000$,

$$v_b = (0.546 + 8.74 \times 10^{-6} N_{Re_L}) \sqrt{gd} \quad (4.67)$$

When $N_{Re_b} \geq 8,000$,

$$v_b = (0.35 + 8.74 \times 10^{-6} N_{Re_L}) \sqrt{gd} \quad (4.68)$$

When $3,000 < N_{Re_b} < 8,000$,

$$v_b = \frac{1}{2} \left(v_{bs} + \sqrt{v_{bs}^2 + \frac{13.59 \mu_L}{\rho_L \sqrt{d}}} \right) \quad (4.69)$$

where

$$v_{bs} = (0.251 + 8.74 \times 10^{-6} N_{Re_L}) \sqrt{gd} \quad (4.70)$$

Because v_b and N_{Re_b} are interrelated, determination of v_b requires an iterative procedure when using Figs. 4.11 and 4.12 or Eqs. 4.67 through 4.70. The procedure follows.

1. Estimate a value of v_b . A good first guess is

$$v_b = 0.5 \sqrt{gd} \quad (4.71)$$

2. Calculate N_{Re_b} using the value of v_b from Step 1.
3. Calculate v_b using Eq. 4.64 or Eqs. 4.67 through 4.70.
4. Compare the values of v_b obtained in Steps 1 and 3. If they are not sufficiently close, use the value in Step 3 as the next guess and go to Step 1. Continue until convergence is achieved. This procedure will converge in one step if the new value of N_{Re_b} does not result in a change among Eqs. 4.67 through 4.70.

Orkiszewski used the data of Hagedorn and Brown to calculate and correlate the liquid distribution coefficient, Γ . Orkiszewski did not define criteria to establish which liquid phase is the continuous phase when both oil and water are present. Fig. 3.3 can be used for this purpose. Table 4.1 identifies liquid distribution coefficient equations. Depending on the continuous liquid phase and the value of the mixture velocity, the value of Γ is calculated from one of these expressions.

$$\begin{aligned} \Gamma = & \frac{0.013 \log \mu_L}{d^{1.38}} - 0.681 + 0.232 \log v_m \\ & - 0.428 \log d, \quad \dots \dots \dots \quad (4.72) \end{aligned}$$

$$\begin{aligned} \Gamma = & \frac{0.045 \log \mu_L}{d^{0.799}} - 0.709 - 0.162 \log v_m \\ & - 0.888 \log d, \quad \dots \dots \dots \quad (4.73) \end{aligned}$$

$$\begin{aligned} \Gamma = & \frac{0.0127 \log(\mu_L + 1)}{d^{1.415}} - 0.284 + 0.167 \log v_m \\ & + 0.113 \log d, \quad \dots \dots \dots \quad (4.74) \end{aligned}$$

and

$$\Gamma = \frac{0.0274 \log(\mu_L + 1)}{d^{1.371}} + 0.161 + 0.569 \log d + X, \quad \dots \dots \dots \quad (4.75)$$

where

$$X = - \log v_m \left[\frac{0.01 \log(\mu_L + 1)}{d^{1.571}} + 0.397 + 0.63 \log d \right] \quad (4.76)$$

and μ_L is in centipoise, d is in feet, and v_m is in feet per second. The value of Γ is constrained by these limits.

If $v_m < 10$,

$$\Gamma \geq -0.065 v_m \quad \dots \dots \dots \quad (4.77)$$

and,

if $v_m > 10$,

$$\Gamma \geq -\frac{v_b}{v_m + v_b} \left(1 - \frac{\rho_s}{\rho_L} \right) \quad (4.78)$$

Because the equation pairs do not necessarily meet at $v_m = 10$ ft/sec, these constraints are supposed to eliminate pressure discontinuities between equations for Γ . Fig. 4.13 shows the discontinuities can be significant. A method to eliminate them is described in the next section.

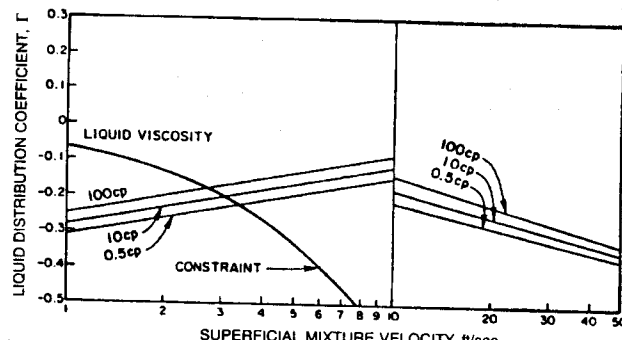


Fig. 4.13—Liquid distribution coefficient discontinuities.¹⁶

The friction pressure-gradient component for slug flow is

$$\left(\frac{dp}{dz}\right)_f = \frac{f\rho_L v_m^2}{2d} \left[\left(\frac{v_{SL} + v_b}{v_m + v_b} \right) + \Gamma \right], \quad (4.79)$$

where f is obtained from the Moody diagram (Fig. 2.2) by use of the Reynolds number given by Eq. 4.66. The acceleration pressure-gradient component for slug flow was considered negligible.

Orkiszewski recommended the Duns and Ros method if either mist flow or the transition region between mist flow and slug flow is predicted.

Modifications. The Orkiszewski method can cause a convergence problem in the computing algorithm, described in Sec. 3.7, for calculating pressure vs. depth traverses in wells. The problem results from discontinuities between Eqs. 4.72 and 4.73 for water as the continuous liquid phase, and between Eqs. 4.74 and 4.75 for oil as the continuous phase. Brill¹⁶ showed that the constraints given by Eqs. 4.77 and 4.78 are ineffective in eliminating the pressure discontinuities that result from the use of either pair of equations. Triggia* suggested that coefficients in Eqs. 4.73, 4.75, and 4.76 be modified so that the slopes of these curves are retained but the discontinuities are eliminated. This solves the convergence problem but also may affect the accuracy of results. The resulting equations for water and oil, respectively, were

$$\begin{aligned} \Gamma &= \frac{0.013 \log \mu_L}{d^{1.38}} - 0.287 - 0.162 \log v_m \\ &\quad - 0.428 \log d \end{aligned} \quad (4.80)$$

and

$$\begin{aligned} \Gamma &= \frac{0.0127 \log(\mu_L + 1)}{d^{1.415}} - 0.117 + 0.113 \log d \\ &\quad + C(1.0 - \log v_m), \end{aligned} \quad (4.81)$$

where

$$C = \frac{0.01 \log(\mu_L + 1)}{d^{1.571}} + 0.397 + 0.63 \log d. \quad (4.82)$$

The liquid distribution coefficient also can become too large a negative number for high flow rates corresponding to large values of v_m . When this occurs, Eq. 4.63 can become less than the no-slip mixture density. A second modification in the Orkiszewski correlation is to replace ρ_s with ρ_n when this occurs. It also becomes necessary to replace Eq. 4.79 for the friction pressure-gradient component. A logical replacement is

$$\left(\frac{dp}{dz}\right)_f = \frac{f\rho_n v_m^2}{2d}, \quad (4.83)$$

where f is obtained from the Moody diagram (Fig. 2.2) by use of a Reynolds number given by

$$N_{Re} = \frac{\rho_n v_m d}{\mu_n}. \quad (4.84)$$

*Personal communication with A. Triggia, Petrobras S.A., Rio de Janeiro (1984).

Example 4.4—Using the Orkiszewski Method, Calculate the Vertical, Multiphase-Flow Pressure Gradient for Example 3.2.

Given: $\mu_o = 0.97$ cp, $\mu_g = 0.016$ cp, $\sigma_o = 8.41$ dynes/cm, and $\epsilon = 0.00006$ ft.

1. Determine flow pattern:

From Eqs. 4.58 and 4.59,

$$\lambda_{g_{B/S}} = 1.071 - (0.2218) \frac{(7.83)^2}{(0.5)} = -26.1.$$

Because $-26.1 < 0.13$, set $\lambda_{g_{B/S}} = 0.13$.

$$\lambda_g = 1 - 0.507 = 0.493 > \lambda_{g_{B/S}}$$

∴ flow pattern is not bubble flow.

From Eq. 4.32,

$$N_{gv_{S/T_r}} = 50 + (36)(11.84) = 476.2.$$

Because $N_{gv} = 11.54 < 476.2$,

Flow pattern is slug flow.

2. Determine slip density:

From Eq. 4.66,

$$N_{Re_L} = \frac{(1,488)(47.61)(7.83)(0.5)}{0.97} = 2.86 \times 10^5$$

∴ Fig. 4.12 cannot be used.

$$\text{Guess } v_b = 0.5 \sqrt{gd} = (0.5) \sqrt{(32.174)(0.5)}$$

$$= 2.0 \text{ ft/sec.}$$

From Eq. 4.65,

$$N_{Re_b} = \frac{(1,488)(47.61)(2.0)(0.5)}{0.97} = 7.3 \times 10^4.$$

From Eq. 4.68,

$$\begin{aligned} v_b &= [(0.35) + (8.74 \times 10^{-6})(2.86 \times 10^5)] \sqrt{(32.174)(0.5)} \\ &= 11.43 \text{ ft/sec.} \end{aligned}$$

From Eq. 4.65,

$$N_{Re_b} = \frac{(1,488)(47.61)(11.43)(0.5)}{0.97} = 4.17 \times 10^5.$$

Because $N_{Re_b} > 8,000$,

$v_b = 11.43$ ft/sec is correct.

From Eq. 4.74,

$$\begin{aligned} \Gamma &= \frac{(0.0127) \log(0.97 + 1.0)}{d^{1.415}} - 0.284 \\ &\quad + (0.167) \log(7.83) + (0.113) \log(0.5) \\ &= -0.159. \end{aligned}$$

From Eq. 4.77,

$$\text{Is } -0.159 \geq -(0.065)(7.97) = -0.518?$$

Yes. Therefore, $\Gamma = -0.159$.

From Eq. 4.63,

$$\begin{aligned}\rho_s &= \frac{(47.61)(3.97 + 11.43) + (5.88)(3.86)}{7.83 + 11.43} + (47.61)(-0.159) \\ &= 39.25 - 7.57 \\ &= 31.68 \text{ lbm/ft}^3.\end{aligned}$$

3. Determine friction factor:

$$N_{Re_L} = 2.85 \times 10^5$$

and

$$\frac{\varepsilon}{d} = \frac{0.00006}{0.5} = 0.00012.$$

From Fig. 2.2 or Eq. 2.17, $f = 0.0158$.

4. Determine pressure gradient:

From Eqs. 4.31, 4.63, and 4.79,

$$\begin{aligned}\frac{dp}{dz} &= \frac{(0.0158)(47.61)(7.83)^2}{(2)(32.174)(0.5)} \left[\left(\frac{3.97 + 11.43}{7.83 + 11.43} \right) + (-0.159) \right] \\ &\quad + (31.68) \left(\frac{32.174}{32.174} \right) \\ &= 0.92 + 31.68 = 32.60 \text{ psf/ft} \\ &= 0.226 \text{ psi/ft.}\end{aligned}$$

Aziz et al. Method. The Aziz et al.⁹ method uses many of the fundamental mechanisms that form the basis of modern mechanistic models.

Flow-Pattern Prediction. Fig. 4.14 shows the flow-pattern map used by Aziz et al. and first presented by Govier et al.¹⁷ Eqs. 4.85 and 4.86 define the coordinates

$$N_x = v_{sg} \left(\frac{\rho_g}{0.0764} \right)^{1/3} \left[\left(\frac{72}{\sigma_L} \right) \left(\frac{\rho_L}{62.4} \right) \right]^{1/4} \quad (4.85)$$

and

$$N_y = v_{sl} \left[\left(\frac{72}{\sigma_L} \right) \left(\frac{\rho_L}{62.4} \right) \right]^{1/4}. \quad (4.86)$$

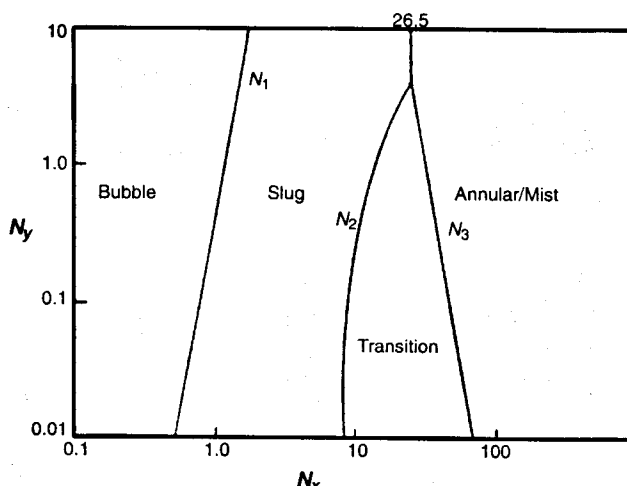


Fig. 4.14—Aziz et al.⁹ flow-pattern map. (Reproduced with permission of the Petroleum Soc.)

The bracketed terms in Eqs. 4.85 and 4.86 are attempts to validate the flow-pattern map for fluids other than air and water. For an air/water system at atmospheric conditions, the coordinates are the superficial velocities of each phase.

These equations represent the flow-pattern transitions in Fig. 4.14.

$$N_1 = 0.51(100N_y)^{0.172}, \quad (4.87)$$

$$N_2 = 8.6 + 3.8N_y, \quad (4.88)$$

and

$$N_3 = 70(100N_y)^{-0.152}, \quad (4.89)$$

where v_{SL} is in feet per second, v_S is in feet per second, ρ_g is in pounds per cubic feet, ρ_L is in pounds per cubic feet, and σ_L is in dynes per centimeter.

Bubble Flow. Bubble flow exists if $N_x < N_1$. Liquid holdup for bubble flow is calculated from

$$H_L = 1 - \frac{v_{sg}}{v_{bf}}, \quad (4.90)$$

where v_{bf} is the rise velocity of small gas bubbles in a flowing liquid. This velocity can be predicted from

$$v_{bf} = 1.2v_m + v_{bs}, \quad (4.91)$$

where the first term is the approximate velocity of the fluid mixture, accounting for the nonuniform velocity and bubble concentration profiles across the cross section, and v_{bs} is the rise velocity of a continuous swarm of small bubbles in a static liquid column. v_{bs} can be predicted from

$$v_{bs} = 1.41 \left[\frac{\sigma_L g(\rho_L - \rho_g)}{\rho_L^2} \right]^{1/4}. \quad (4.92)$$

The friction component of the pressure gradient is determined from

$$\frac{dp}{dz} = \frac{f \rho_s v_m^2}{2d}, \quad (4.93)$$

where ρ_s is determined from Eq. 3.22 and f is obtained from Fig. 2.2 or Eq. 2.17 for a Reynolds number given by

$$N_{Re} = \frac{\rho_L v_m d}{\mu_L}. \quad (4.94)$$

The acceleration component of the pressure gradient was considered to be negligible for bubble flow.

Slug Flow. Slug flow exists if $N_1 < N_x < N_2$ for $N_y < 4$ or $N_1 < N_x < 26.5$ for $N_y \geq 4$.

The liquid holdup for slug flow also is calculated from Eqs. 4.90 and 4.96. For slug flow, however, the bubble-rise velocity in a static liquid column is based on a Taylor bubble.¹⁵ Aziz et al. state that

$$v_{bs} = C \sqrt{\frac{gd(\rho_L - \rho_g)}{\rho_L}}, \quad (4.95)$$

where C was given by Wallis¹⁸ as

$$C = 0.345 \left[1 - e^{-0.029N_v} \right] \left[1 - e^{\left(\frac{3.37 - N_E}{m} \right)} \right]. \quad (4.96)$$

and

$$N_E = \frac{gd^2(\rho_L - \rho_g)}{\sigma_L}, \quad (4.97)$$

$$N_v = \frac{\sqrt{d^3 g \rho_L (\rho_L - \rho_g)}}{\mu_L}, \quad (4.98)$$

and m is determined from

N_v	m
≥ 250	10
$250 > N_v > 18$	$69N_v^{-0.35}$
≤ 18	25

The friction pressure-gradient component for slug flow is determined from

$$\left(\frac{dp}{dZ}\right)_f = \frac{\rho_L H_L v_m^2}{2d} \quad \dots \dots \dots (4.99)$$

The friction factor is obtained from a Moody diagram (Fig. 2.2) as a function of relative roughness and a Reynolds number given by

$$N_{Re} = \frac{\rho_L v_m d}{\mu_L} \quad \dots \dots \dots (4.100)$$

The acceleration pressure-gradient component was considered negligible for slug flow.

Mist Flow. Mist flow exists when $N_x > N_3$ for $N_y < 4$ or $N_x > 26.5$ for $N_y > 4$. Aziz *et al.* recommended the Duns and Ros mist-flow method be used to calculate pressure gradient for this flow pattern.

Transition Region. The transition region exists when $N_2 < N_x < N_3$ for $N_y < 4$. In Fig. 4.14, note that the transition region does not exist for $N_y > 4$. When the transition region is predicted, the pressure gradients must be calculated with both the slug-flow and mist-flow equations. To obtain the pressure gradient, linear interpolation is performed, similar to the procedure described in the Duns and Ros method. Thus,

$$\frac{dp}{dZ} = A \left(\frac{dp}{dZ} \right)_{slug} + (1 - A) \left(\frac{dp}{dZ} \right)_{mist} \quad \dots \dots \dots (4.101)$$

where

$$A = \frac{N_3 - N_x}{N_3 - N_2} \quad \dots \dots \dots (4.102)$$

Modifications. Al-Najjar and Al-Sooof¹⁹ showed that improved results could be obtained with the Aziz *et al.* method if the flow-pattern map in Fig. 4.14 was replaced with the Duns and Ros map in Fig. 4.5. Their conclusion was based on a comparison of the predicted and measured pressure drops for 80 tests on 15 flowing wells in Iraq, as well as on data of Poettmann and Carpenter¹ and Orkiszewski.⁸ The wells from Iraq were flowing primarily through a casing/tubing annulus.

Example 4.5—Using the Aziz *et al.* Method, Calculate the Vertical, Multiphase-Flow Pressure Gradient for Example 3.2.

Given: $\mu_o = 0.97$ cp, $\mu_g = 0.016$ cp, $\sigma_o = 8.41$ dynes/cm, and $\epsilon = 0.00006$ ft.

1. Determine flow pattern:

From Eqs. 4.85 and 4.86,

$$N_x = 3.86 \left(\frac{5.88}{0.0764} \right)^{1/3} \left[\left(\frac{72}{8.41} \right) \left(\frac{47.61}{62.4} \right) \right]^{1/4} = 26.25$$

and

$$N_y = 3.97 \left[\left(\frac{72}{8.41} \right) \left(\frac{47.61}{62.4} \right) \right]^{1/4} = 6.35.$$

From Fig. 4.14, slug flow exists.
Verification.

$$N_1 = 0.51[(100)(6.35)]^{0.172} = 1.55$$

for $N_y \geq 4$, $1.55 < 26.25 < 26.5$.

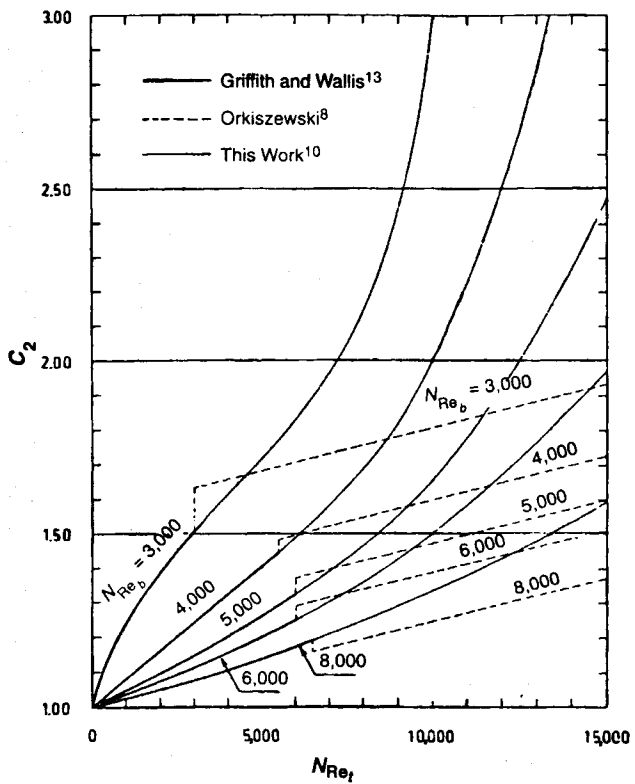


Fig. 4.15—Chierici *et al.*¹⁰ C_2 correlation.

2. Determine liquid holdup:

From Eq. 4.98,

$$N_v = \frac{\sqrt{(0.5)^3 (32.174) (47.61) (47.61 - 5.88)}}{(0.97/1,488)} \\ = 1.371 \times 10^5$$

$$\therefore m = 10.$$

From Eq. 4.97,

$$N_E = \frac{(32.174)(0.5)^2 (47.61 - 5.88)}{(8.41/454)} \\ = 1.812 \times 10^4.$$

From Eq. 4.96,

$$C = 0.345 \left[1 - e^{(-0.029N_v)} \right] \left[1 - e^{\left(\frac{3.37 - N_E}{10} \right)} \right] \\ = 0.345.$$

From Eq. 4.95,

$$v_{bs} = (0.345) \sqrt{\frac{(32.174)(0.5)(47.61 - 5.88)}{47.61}}$$

$$= 1.295 \text{ ft/sec.}$$

From Eq. 4.91,

$$v_{bf} = (1.2)(7.83) + 1.295 = 10.69 \text{ ft/sec.}$$

From Eq. 4.90,

$$H_L = 1 - \frac{3.86}{10.69} = 0.639.$$

3. Determine friction factor:

$$N_{Re} = \frac{(1,488)(47.61)(7.83)(0.5)}{(0.97)} = 2.86 \times 10^5$$

and

$$\frac{\varepsilon}{d} = \frac{0.00006}{0.5} = 0.00012.$$

From Fig 2.2 or Eq. 2.17, $f = 0.0158$.

4. Determine pressure gradient:

$$\begin{aligned} \frac{dp}{dz} &= \frac{(0.0158)(47.61)(0.639)(7.83)^2}{(2)(32.174)(0.5)} \\ &+ [(47.61)(0.639) + (5.88)(1 - 0.639)] \frac{(32.174)}{(32.174)} \\ &= 0.92 + 32.55 = 33.47 \text{ psf/ft} \\ &= 0.232 \text{ psi/ft.} \end{aligned}$$

Chierici et al. Method. The Chierici *et al.*¹⁰ method to predict flow pattern and to calculate liquid holdup and pressure gradient in the bubble-, transition-, and mist-flow regions is identical to that of Orkiszewski. The only difference is in the slug-flow region. Thus, only slug-flow treatment is presented.

Slug Flow. The Chierici *et al.* slug-flow treatment is almost identical to that of Aziz *et al.* Liquid holdup is determined from

$$H_L = 1 - \frac{v_{sg}}{v_m + v_b}, \quad \dots \quad (4.103)$$

where

$$v_b = C_1 C_2 \sqrt{gd}. \quad \dots \quad (4.104)$$

C_1 is obtained from Fig. 4.11 as a function of the bubble Reynolds number and is essentially 0.35 for all cases. Values of C_2 can be obtained from Fig. 4.15 for liquid Reynolds numbers less than 6,000. For this range, Fig. 4.15 is identical to Fig. 4.12 used by Orkiszewski. Chierici *et al.* show in Fig. 4.15 that the extrapolation equations proposed by Orkiszewski in Eqs. 4.67 through 4.70 can result in discontinuities. From earlier work by Nicklin *et al.*,²⁰ Chierici *et al.* proposed that for liquid Reynolds numbers greater than 6,000,

$$C_2 = \frac{1}{1 - 0.2 \frac{v_m}{v_b}}. \quad \dots \quad (4.105)$$

Curves based on Eq. 4.105 for extrapolation also are plotted in Fig. 4.15 and show no discontinuities.

Combining Eqs. 4.104 and 4.105 gives

$$v_b = 0.2v_m + 0.35\sqrt{gd}. \quad \dots \quad (4.106)$$

The resulting prediction of liquid holdup essentially is identical to that of Aziz *et al.*

The pressure-gradient friction component is identical to that of Aziz *et al.*, and the acceleration component is neglected for slug flow.

Example 4.6—Using the Chierici *et al.* Method, Calculate the Vertical, Multiphase-Flow Pressure Gradient for Example 3.2.

Given: $\mu_o = 0.97$ cp, $\mu_g = 0.016$ cp, $\sigma_o = 8.41$ dynes/cm, and $\varepsilon = 0.00006$ ft.

1. Determine flow pattern:

Orkiszewski predicted slug flow.

2. Determine liquid holdup:

From Eq. 4.106,

$$\begin{aligned} v_b &= (0.2)(7.83) + (0.35)\sqrt{(32.174)(0.5)} \\ &= 2.97 \text{ ft/sec.} \end{aligned}$$

From Eq. 4.103,

$$H_L = 1 - \frac{(3.86)}{(7.83 + 2.97)} = 0.642.$$

3. Determine friction factor:

$$N_{Re} = \frac{(1,488)(47.61)(7.83)(0.5)}{(0.97)} = 2.86 \times 10^5$$

and

$$\frac{\varepsilon}{d} = \frac{0.00006}{0.5} = 0.00012.$$

From Fig 2.2 or Eq. 2.17, $f = 0.0158$.

4. Determine pressure gradient:

$$\begin{aligned} \frac{dp}{dz} &= \frac{(0.0158)(47.61)(0.642)(7.83)^2}{(2)(32.174)(0.5)} \\ &+ [(47.61)(0.642) + (5.88)(1 - 0.642)] \frac{(32.174)}{(32.174)} \\ &= 0.92 + 32.67 = 33.59 \text{ psf/ft} \\ &= 0.233 \text{ psi/ft.} \end{aligned}$$

Beggs and Brill Method. The Beggs and Brill¹¹ method was the first one to predict flow behavior at all inclination angles, including directional wells. Their test facility was 1- and 1.5-in. sections of acrylic pipe, 90 ft long. The pipe could be inclined at any angle from the horizontal. The fluids were air and water. For each pipe size, liquid and gas rates were varied so that, when the pipe was horizontal, all flow patterns were observed. After a particular set of flow rates was established, the inclination of the pipe was varied through the range of angles so that the effect of angle on holdup and pressure gradient could be observed. Liquid holdup and pressure gradient were measured at angles from the horizontal of 0° , $\pm 5^\circ$, $\pm 10^\circ$, $\pm 15^\circ$, $\pm 20^\circ$, $\pm 35^\circ$, $\pm 55^\circ$, $\pm 75^\circ$, and $\pm 90^\circ$. The correlations were developed from 584 measured tests.

Beggs and Brill proposed the following pressure-gradient equation for inclined pipe.

$$\frac{dp}{dL} = \frac{\frac{f\rho_n v_m^2}{2d} + \rho_s g \sin \theta}{1 - E_k}, \quad \dots \quad (4.107)$$

where E_k is given by Eq. 4.53 and

$$\rho_s = \rho_L H_{L(\theta)} + \rho_g [1 - H_{L(\theta)}]. \quad \dots \quad (4.108)$$

Flow-Pattern Prediction. Fig. 4.16 illustrates the horizontal-flow patterns considered by Beggs and Brill. On the basis of observed flow patterns for horizontal flow only, they prepared an empirical map to predict flow pattern. Their original flow-pattern map has been modified slightly to include a transition zone between the segregated- and intermittent-flow patterns.²¹ Fig. 4.17 shows both the original and the modified (dashed lines) flow-pattern maps.

Beggs and Brill chose to correlate flow-pattern transition boundaries with no-slip liquid holdup and mixture Froude number, given by

$$N_{Fr} = \frac{v_m^2}{gd}. \quad \dots \quad (4.109)$$

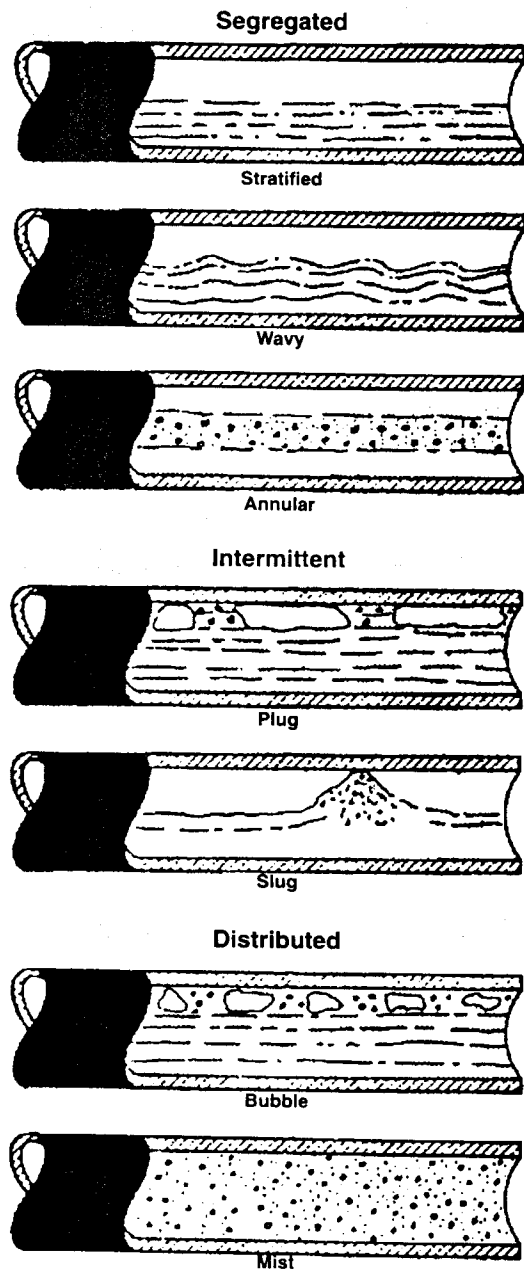


Fig. 4.16—Beggs and Brill¹¹ horizontal-flow patterns.

The equations for the modified flow-pattern transition boundaries are

$$L_1 = 316\lambda_L^{0.302}, \quad \dots \quad (4.110)$$

$$L_2 = 0.000925\lambda_L^{-2.468}, \quad \dots \quad (4.111)$$

$$L_3 = 0.10\lambda_L^{-1.452}, \quad \dots \quad (4.112)$$

and

$$L_4 = 0.5\lambda_L^{-6.738}. \quad \dots \quad (4.113)$$

The following inequalities are used to determine the flow pattern that would exist if the pipe were horizontal. This flow pattern is a correlating parameter and, unless the pipe is horizontal, gives no information about the actual flow pattern.

Segregated.

$$\lambda_L < 0.01 \text{ and } N_{Fr} < L_1$$

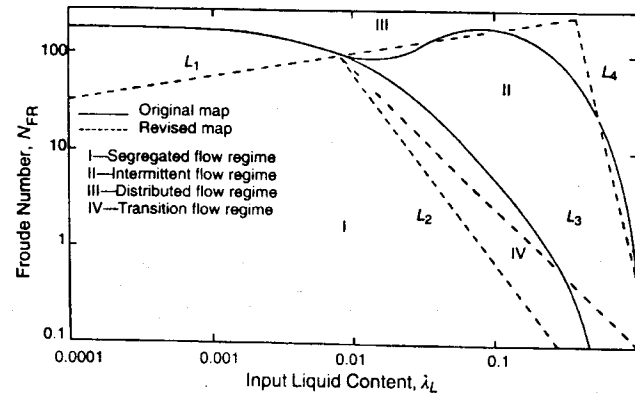


Fig. 4.17—Beggs and Brill²¹ horizontal-flow-pattern map.

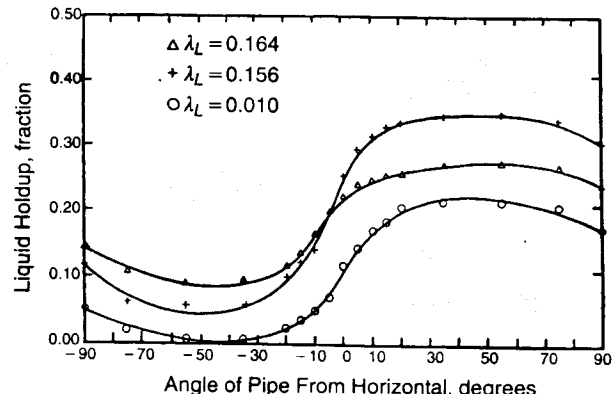


Fig. 4.18—Effect of inclination angle on liquid holdup.¹¹

or

$$\lambda_L \geq 0.01 \text{ and } N_{Fr} < L_2$$

Transition.

$$\lambda_L \geq 0.01 \text{ and } L_2 \leq N_{Fr} \leq L_3$$

Intermittent.

$$0.01 \leq \lambda_L < 0.4 \text{ and } L_3 < N_{Fr} \leq L_1$$

or

$$\lambda_L \geq 0.4 \text{ and } L_3 < N_{Fr} \leq L_4$$

Distributed.

$$\lambda_L < 0.4 \text{ and } N_{Fr} \geq L_1$$

or

$$\lambda_L \geq 0.4 \text{ and } N_{Fr} > L_4.$$

Liquid-Holdup Prediction. Different correlations for liquid holdup were developed for three horizontal-flow patterns. The liquid holdup that would exist if the pipe were horizontal is first calculated and then corrected for the actual pipe-inclination angle. Fig. 4.18 shows the variation of liquid holdup with pipe inclination for three of their tests. The liquid holdup was a maximum at about +50° from horizontal and a minimum at approximately -50°. For high flow rates corresponding to what now is called dispersed-bubble flow, liquid holdup essentially was independent of inclination angle.

The same equations are used to calculate liquid holdup for all flow patterns. However, the empirical coefficients are different for each flow pattern.

The liquid holdup that would exist if the pipe were horizontal is calculated first from

$$H_{L(0)} = \frac{a\lambda_L^b}{N_{Fr}^c}, \quad \dots \quad (4.114)$$

TABLE 4.2—BEGGS AND BRILL¹¹ EMPIRICAL COEFFICIENTS FOR HORIZONTAL LIQUID HOLDUP

Flow Pattern	<i>a</i>	<i>b</i>	<i>c</i>
Segregated	0.980	0.4846	0.0868
Intermittent	0.845	0.5351	0.0173
Distributed	1.065	0.5824	0.0609

with the restriction that $H_{L(0)} \geq \lambda_L$. The coefficients *a*, *b*, and *c* are determined from Table 4.2 for the appropriate horizontal-flow pattern.

Eq. 4.115 gives the liquid holdup corrected for the effect of inclination angle.

$$H_{L(\theta)} = H_{L(0)}\Psi. \quad \dots \quad (4.115)$$

The factor to correct liquid holdup for the effect of pipe inclination is given by

$$\Psi = 1.0 + C[\sin(1.8\theta) - 0.333 \sin^3(1.8\theta)], \quad \dots \quad (4.116)$$

where θ is the actual angle of the pipe from horizontal and *C* is defined by

$$C = (1.0 - \lambda_L) \ln(e\lambda_L^f N_{Fr}^g N_{Fr}^h), \quad \dots \quad (4.117)$$

with the restriction that $C \geq 0$. The coefficients *e*, *f*, *g*, and *h* are determined from Table 4.3 for the appropriate horizontal-flow pattern.

When the flow pattern falls in the transition region, the liquid holdup must be interpolated between the segregated and intermittent liquid-holdup values as

$$H_{L(\theta)_{Tr}} = AH_{L(\theta)_{Seg}} + (1 - A)H_{L(\theta)_{Int}}, \quad \dots \quad (4.118)$$

where

$$A = \frac{L_3 - N_{Fr}}{L_3 - L_2}. \quad \dots \quad (4.119)$$

Friction-Factor Prediction. The two-phase friction factor is calculated from

$$f = f_n(f/f_n). \quad \dots \quad (4.120)$$

The normalizing friction factor, f_n , is determined from the smooth pipe curve on the Moody diagram (Fig. 2.2) or from Eqs. 2.12 or 2.13 by use of a Reynolds number defined as

$$N_{Re} = \frac{\rho_n v_m d}{\mu_n} \quad \dots \quad (4.121)$$

and μ_n is obtained from Eq. 3.21.

The ratio of the two-phase friction factor to the normalizing friction factor was correlated with the Beggs and Brill experimental data, resulting in

$$f/f_n = e^s, \quad \dots \quad (4.122)$$

where

$$s = \frac{\ln y}{-0.0523 + 3.182 \ln y - 0.8725(\ln y)^2 + 0.01853(\ln y)^4} \quad \dots \quad (4.123)$$

and

$$y = \frac{\lambda_L}{[H_{L(\theta)}]^2}. \quad \dots \quad (4.124)$$

Eq. 4.123 contains discontinuities for y values of about 2.63×10^{-4} and 1.016. It is unlikely that the discontinuity at the smaller value of y would ever be encountered. However, it is necessary that $s = 0$ for $y = 1.0$ to ensure that the correlation degenerates

TABLE 4.3—BEGGS AND BRILL¹¹ EMPIRICAL COEFFICIENTS FOR *C*

Flow Pattern	<i>e</i>	<i>f</i>	<i>g</i>	<i>h</i>
Segregated uphill	0.011	-3.7680	3.5390	-1.6140
Intermittent uphill	2.960	0.3050	-0.4473	0.0978
Distributed uphill	No correction: $C=0; \Psi=1$			
All patterns downhill	4.700	-0.3692	0.1244	-0.5056

to single-phase liquid flow. For *s* that is used when $1 < y < 1.2$, Beggs and Brill introduced this correlation

$$s = \ln(2.2y - 1.2). \quad \dots \quad (4.125)$$

Modifications. Two modifications to the Beggs and Brill correlation frequently are used. Payne *et al.*²² experimented with a 2-in.-diameter flow loop constructed with Schedule 40 line pipe that was more than 500 ft long and contained three hills, each with inclination angles of about $\pm 10^\circ$ from horizontal. Carefully metered mixtures of natural gas and water were flowed through the pipe at pressures between 400 and 500 psia. Liquid holdup was measured in all uphill and downhill sections by use of quick-closing ball valves.

Payne *et al.* found that the Beggs and Brill method underpredicted friction factors. Because the Beggs and Brill method was based on data obtained in smooth pipe, Payne *et al.* recommended that the normalizing friction factor, f_n , be obtained from the Moody diagram (Fig. 2.2) or from Eq. 2.17 for an appropriate value of relative roughness. This change improved the pressure-drop predictions for the Beggs and Brill method for rough pipes.

Payne *et al.* also found that the Beggs and Brill method overpredicted liquid holdup in both uphill and downhill flow. On the basis of their limited data, Payne *et al.* recommended these constant correction factors to improve liquid-holdup values.

If $\theta > 0$,

$$H_{L(\theta)} = 0.924H_{L(0)}. \quad \dots \quad (4.126)$$

If $\theta < 0$,

$$H_{L(\theta)} = 0.685H_{L(0)}. \quad \dots \quad (4.127)$$

However, the resulting liquid holdup for $\theta > 0^\circ$ should not be less than λ_L . The original Beggs and Brill method has been found to overpredict pressure drops in producing wells. Consequently, improved results should be obtained if the Payne *et al.* liquid-holdup correction factor is applied for wells.

Example 4.7—Using the Beggs and Brill Method, Calculate the Vertical, Multiphase-Flow Pressure Gradient for Example 3.2.

Given: $\mu_o = 0.97$ cp, $\mu_g = 0.016$ cp, $\sigma_o = 8.41$ dynes/cm, and $\varepsilon = 0.00006$ ft.

1. Determine flow pattern:

From Eq. 4.109,

$$N_{Fr} = \frac{(7.83)^2}{(32.174)(0.5)} = 3.81.$$

From Fig 4.17 for $\lambda_L = 0.507$, the horizontal-flow pattern is intermittent.

2. Determine liquid holdup:

From Eq. 4.114,

$$H_{L(0)} = \frac{(0.845)(0.507)^{0.5351}}{(3.81)^{0.0173}} = 0.574.$$

From Eq. 4.117,

$$C = (0.493) \ln [2.96(0.507)^{0.305} (11.87)^{-0.4473} (3.81)^{0.0978}]$$

$$= -0.048 < 0.$$

Therefore,

$$C = 0, \Psi = 1.0, \text{ and } H_{L(90)} = H_{L(0)} = 0.574.$$

Apply Payne *et al.* correction factor:

$$H_{L(90)} = (0.924)(0.574) = 0.530.$$

3. Determine friction factor:

From Eq. 3.21,

$$\mu_n = (0.97)(0.507) + (0.016)(0.493) = 0.50 \text{ cp.}$$

From Eq. 4.121,

$$N_{Re} = \frac{(1,488)(27.04)(7.83)(0.5)}{(0.50)} = 3.15 \times 10^5.$$

From Fig. 2.2 for $\varepsilon/d = 0.00012$, $f_n = 0.0155$.

From Eq. 4.124,

$$y = \frac{(0.507)}{(0.530)^2} = 1.805.$$

From Eq. 4.123,

$$s = (0.591)/[-0.0523 + 3.182(0.591)]$$

$$- 0.8725(0.591)^2 + 0.01853(0.591)^4]$$

$$= 0.3873.$$

From Eq. 4.122,

$$\frac{f}{f_n} = e^{(0.3873)} = 1.473.$$

Therefore, $f = (1.473)(0.0155) = 0.0228$.

4. Determine pressure gradient:

$$\frac{dp}{dL} = \frac{(0.0228)(27.04)(7.83)^2}{(2)(32.174)(0.5)}$$

$$+ [(47.61)(0.53) + (5.88)(0.47)] \frac{(32.174)}{(32.174)} \sin(90^\circ)$$

$$= 1.17 + 28.00 = 29.17 \text{ psf/ft}$$

$$= 0.203 \text{ psi/ft.}$$

Mukherjee and Brill Method. The Mukherjee and Brill¹² method was initiated in an attempt to overcome some of the limitations of the Beggs and Brill method and to take advantage of new instrumentation developed to measure liquid holdup. Their test facility consisted of an inverted U-shaped, 1.5-in. nominal ID steel pipe. The closed end of the U-shaped pipe could be raised or lowered to permit flow at any angle from 0° to $\pm 90^\circ$ from the horizontal. Each leg of the U was 56-ft long with 22-ft entrance lengths and 32-ft test sections on both uphill and downhill sides. A transparent section in each leg allowed for flow-pattern observations and permitted the use of capacitance sensors to measure liquid holdup. Fluids were air and kerosene or lube oil. Approximately 1,000 pressure-drop meas-

TABLE 4.4—MUKHERJEE AND BRILL¹² EMPIRICAL COEFFICIENTS FOR LIQUID HOLDUP

	Uphill	Downhill Stratified	Downhill Other
C_1	-0.380113	-1.330282	-0.516644
C_2	0.129875	4.808139	0.789805
C_3	-0.119788	4.171584	0.551627
C_4	2.343227	56.262268	15.519214
C_5	0.475686	0.079951	0.371771
C_6	0.288657	0.504887	0.393952

urements and more than 1,500 liquid-holdup measurements were obtained for a broad range of gas and liquid flow rates.

Flow-Pattern Prediction. For each oil phase tested, flow-pattern maps were drawn on log-log scales with dimensionless gas and liquid velocity numbers as the coordinates. The transition curves were drawn on each map. These curves then were fitted with nonlinear regression equations. Two transitions were fitted for upflow. The bubble/slug transition was found to be linear at 45° with the axes and was best fit by Eq. 4.128.

$$N_{Lv_{BS}} = 10^x, \quad \dots \quad (4.128)$$

where

$$x = \log N_{gv} + 0.940 + 0.074 \sin \theta$$

$$- 0.855 \sin^2 \theta + 3.695 N_L. \quad \dots \quad (4.129)$$

The slug/(annular/mist) transition was identical for horizontal and all upflow and downflow angles. However, liquid viscosity had a significant effect on this transition. Increased liquid viscosity accelerates the transition from slug to annular/mist flow. Eq. 4.130 describes this transition.

$$N_{gv_{SM}} = 10^{(1.401 - 2.694 N_L + 0.521 N_L^{0.329})}. \quad \dots \quad (4.130)$$

In downflow and horizontal flow, the bubble/slug transition is described by

$$N_{gv_{BS}} = 10^y, \quad \dots \quad (4.131)$$

where

$$y = 0.431 - 3.003 N_L - 1.138 (\log N_{gv}) \sin \theta$$

$$- 0.429 (\log N_{gv})^2 \sin \theta + 1.132 \sin \theta. \quad \dots \quad (4.132)$$

This transition generates a family of curves for different inclination angles and liquid viscosities. In horizontal flow, this transition becomes a function of viscosity only and is a vertical straight line.

Eq. 4.133 gives the downflow and horizontal stratified-flow boundary.

$$N_{Lv_{ST}} = 10^z, \quad \dots \quad (4.133)$$

where

$$z = 0.321 - 0.017 N_{gv} - 4.267 \sin \theta - 2.972 N_L$$

$$- 0.033 (\log N_{gv})^2 - 3.925 \sin^2 \theta. \quad \dots \quad (4.134)$$

In downflow at higher liquid rates, bubble-/slug-flow transition occurs as gas velocities increase at a fixed liquid velocity. At lower liquid rates, bubble-/stratified-flow transition occurs below inclination angles of -30° . From 0° to -30° at lower rates, however, bubble flow did not occur for the range of flow parameters considered.

Fig. 4.19 gives a flow chart to predict flow patterns by use of these flow-pattern transition equations. The subscripts *BS*, *SM*, and *ST* in Eqs. 4.128, 4.130, 4.131, and 4.133 and in Fig. 4.19 represent the bubble/slug, slug/(annular/mist), and the stratified transitions, respectively.

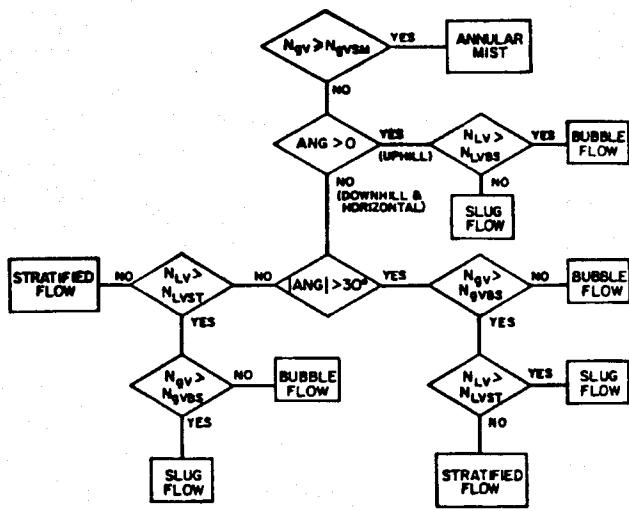


Fig. 4.19—Flow chart to predict Mukherjee and Brill¹² flow-pattern transitions.

Liquid-Holdup Prediction. The liquid-holdup data were correlated with an equation of the form

$$H_L = \exp \left[\left(C_1 + C_2 \sin \theta + C_3 \sin^2 \theta + C_4 N_L^2 \right) \left(\frac{N_{gv}^{C_5}}{N_{L_v}^{C_6}} \right) \right]. \quad (4.135)$$

Three different sets of coefficients were developed for Eq. 4.135. One set is for uphill and horizontal flow; one set is for downhill stratified flow; and the third set is for other downhill-flow patterns. Table 4.4 gives the coefficients.

Bubble and Slug Flow. The pressure gradient for bubble flow and slug flow is determined from

$$\frac{dp}{dL} = \frac{\frac{f \rho_s v_m^2}{2d} + \rho_s g \sin \theta}{1 - E_k}, \quad (4.136)$$

where

$$E_k = \frac{\rho_s v_m v_g}{\rho}. \quad (4.137)$$

The friction factor is obtained from a Moody diagram (Fig. 2.2) or Eq. 2.17 for an appropriate relative roughness and a Reynolds number given by

$$N_{Re} = \frac{\rho_n v_m d}{\mu_n}, \quad (4.138)$$

where μ_n is obtained from Eq. 3.21.

Annular Flow. The pressure gradient for annular flow is determined from Eq. 4.137 and

$$\frac{dp}{dL} = \frac{\frac{f \rho_n v_m^2}{2d} + \rho_s g \sin \theta}{1 - E_k}. \quad (4.139)$$

Mukherjee and Brill developed an empirical expression for the friction factor that depends on liquid holdup. Liquid holdup first is calculated from Eq. 4.135 and appropriate coefficients from Table 4.4. A ratio of holdup values then is calculated as

$$H_R = \frac{\lambda_L}{H_L}, \quad (4.140)$$

and a friction-factor ratio, f_R , is interpolated from Table 4.5. A no-slip friction factor, f_n , is obtained from a Moody diagram (Fig. 2.2)

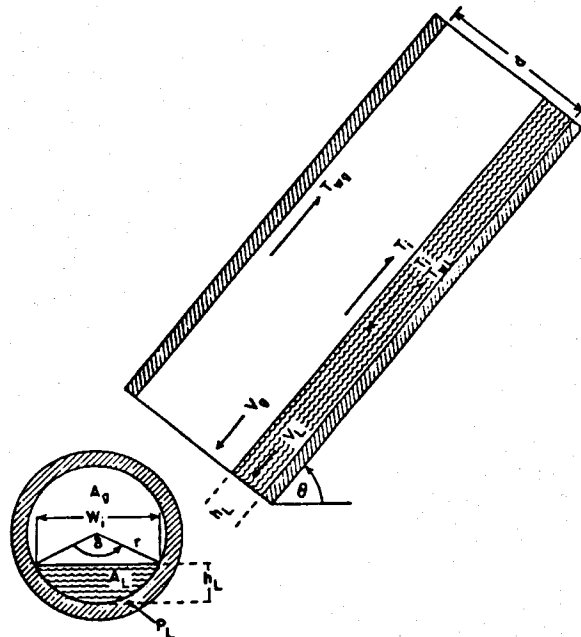


Fig. 4.20—Control volume for stratified flow.¹²

TABLE 4.5—MUKHERJEE AND BRILL¹² ANNULAR-FLOW FRICTION-FACTOR RATIOS

f_R	H_R
1.00	0.01
0.98	0.20
1.20	0.30
1.25	0.40
1.30	0.50
1.25	0.70
1.00	1.00
1.00	10.00

or Eq. 2.17 for an appropriate relative roughness and a Reynolds number given by Eq. 4.138. Then,

$$f = f_n(f_R). \quad (4.141)$$

Stratified Flow. It is likely that stratified flow will occur only in highly deviated or horizontal wells. Mukherjee and Brill chose a separated-flow or two-fluid approach to develop a pressure-gradient-prediction method. Fig. 4.20 gives a control volume that defines all variables for this approach.

A steady-state momentum balance on the gas and liquid phases yields Eqs. 4.142 and 4.143, respectively.

$$A_g \frac{dp}{dL} = -(\tau_{wg} P_g + \tau_i W_i) - \rho_g A_g g \sin \theta \quad (4.142)$$

and

$$A_L \frac{dp}{dL} = -(\tau_{wl} P_L + \tau_i W_i) - \rho_L A_L g \sin \theta. \quad (4.143)$$

Either equation can be used to calculate pressure gradient. Mukherjee and Brill chose Eq. 4.142. To eliminate the effect of interfacial forces in large-diameter pipes, they suggested the addition of Eqs. 4.142 and 4.143 to obtain Eq. 4.144.

$$A \frac{dp}{dL} = -(\tau_{wg} P_g + \tau_{wl} P_L) - (\rho_g A_g + \rho_L A_L) g \sin \theta. \quad (4.144)$$

Mukherjee and Brill concluded that, for most cases involving stratified flow, liquid holdup is sufficiently small. W_i is then small compared with P_g . Consequently, Eq. 4.142 becomes

$$\frac{dp}{dL} = -\tau_{wg} \frac{P_g}{A_g} - \rho_g g \sin \theta. \quad \dots \dots \dots \quad (4.145)$$

From simple geometrical considerations based on Fig. 4.20, it can be shown that δ , A_L , A_g , P_L , and P_g are all related to h_L and d . The relations are

$$\delta = 2 \cos^{-1} \left(1 - 2 \frac{h_L}{d} \right), \quad \dots \dots \dots \quad (4.146)$$

$$H_L = \left(\frac{A_L}{A} \right) = \frac{1}{2\pi} (\delta - \sin \delta), \quad \dots \dots \dots \quad (4.147)$$

$$P = P_L + P_g, \quad \dots \dots \dots \quad (4.148)$$

and

$$P_g = \left(1 - \frac{\delta}{2\pi} \right) P, \quad \dots \dots \dots \quad (4.149)$$

where δ is in radians. Hydraulic diameters for the gas and liquid phases also can be defined by

$$d_{hg} = d \frac{[2\pi - (\delta - \sin \delta)]}{2\pi - \delta + 2 \sin \frac{\delta}{2}} \quad \dots \dots \dots \quad (4.150)$$

and

$$d_{hL} = d \frac{(\delta - \sin \delta)}{\delta + 2 \sin \frac{\delta}{2}}. \quad \dots \dots \dots \quad (4.151)$$

Govier and Aziz²³ suggested that the wall shear stresses can be evaluated approximately by assuming single-phase flow to occur in the cross section occupied by a given phase. With these assumptions, these relations result.

$$\tau_{wL} = \frac{f_L \rho_L v_L^2}{2g} \quad \dots \dots \dots \quad (4.152)$$

and

$$\tau_{wg} = \frac{f_g \rho_g v_g^2}{2g}, \quad \dots \dots \dots \quad (4.153)$$

where f_L and f_g = Moody friction factors based on Reynolds numbers defined by

$$N_{Re_L} = \frac{\rho_L v_L d_{hL}}{\mu_L}, \quad \dots \dots \dots \quad (4.154)$$

$$N_{Re_g} = \frac{\rho_g v_g d_{hg}}{\mu_g}, \quad \dots \dots \dots \quad (4.155)$$

$$v_L = \frac{v_{SL}}{H_L}, \quad \dots \dots \dots \quad (4.156)$$

and

$$v_g = \frac{v_{Sg}}{1 - H_L}. \quad \dots \dots \dots \quad (4.157)$$

Use the following steps to obtain the pressure gradient for stratified flow.

1. Calculate H_L on the basis of Eq. 4.135.
2. Solve Eq. 4.147 iteratively for δ . A value of 0.001 is a good initial guess for δ . A_L also is calculated from Eq. 4.147.
3. Solve Eq. 4.146 for h_L/d . Calculate d_{hg} and d_{hL} from Eqs. 4.150 and 4.151.
4. Knowing δ and P , P_g and P_L are calculated from Eqs. 4.148 and 4.149.

5. Solve Eqs. 4.152 and 4.153 for τ_{wL} and τ_{wg} .

6. Calculate the pressure gradient from Eq. 4.144 for large-diameter pipes or Eq. 4.145 for smaller-diameter pipes.

Example 4.8—Using the Mukherjee and Brill Method, Calculate the Vertical, Multiphase-Flow Pressure Gradient for Example 3.2.

Given: $\mu_o = 0.97$ cp, $\mu_g = 0.016$ cp, $\sigma_o = 8.41$ dynes/cm, and $\epsilon = 0.00006$ ft.

1. Determine flow pattern:

From Eq. 4.130,

$$N_{gv_{S/M}} = 10^{(1.401 - 2.694(0.0118) + 0.521(11.87)^{0.329})}. \quad \dots \dots \dots \quad (4.130)$$

$$= 350.8.$$

$N_{gv} = 11.54 < 350.8$. Therefore, flow pattern is not annular/mist. Angle $> 0^\circ$. Therefore, from Eqs. 4.128 and 4.129,

$$\begin{aligned} x &= \log(11.54) + 0.940 + 0.074 \sin(90^\circ) \\ &\quad - 0.855 \sin^2(90^\circ) + 3.695(0.0118) \\ &= 1.2648. \end{aligned}$$

$$N_{Lv_{B/S}} = 10^{1.2648}$$

$$= 18.40.$$

$N_{Lv} = 11.87 < 18.4$. Therefore, flow pattern is slug flow.

2. Determine liquid holdup:

From Eq. 4.135 for uphill coefficients,

$$H_L = \exp \left\{ \left[\frac{-0.3801 + (0.1299) \sin(90^\circ) + (-0.1198 \sin^2(90^\circ)) + (2.343)(0.0118)^2}{(11.54)^{0.4757} / (11.87)^{0.2887}} \right] \right\} = 0.560.$$

3. Determine friction factor:

From Eq. 4.138,

$$N_{Re} = \frac{1,488(27.10)(7.83)(0.5)}{(0.5)} = 3.15 \times 10^5.$$

From Fig. 2.2 for $\epsilon/d = 0.00012$, $f = 0.0155$.

4. Determine pressure gradient:

From Eq. 4.136,

$$\begin{aligned} \frac{dp}{dL} &= \frac{(0.0155)[(47.6)(0.56) + (5.88)(0.44)](7.83)^2}{2(32.174)(0.5)} \\ &\quad + [(47.6)(0.56) + (5.88)(0.44)][(\sin 90^\circ) \frac{(32.174)}{(32.174)}] \\ &= 0.864 + 29.249 = 30.113 \text{ psf/ft} \\ &= 0.209 \text{ psi/ft}. \end{aligned}$$

4.2.2 Mechanistic Models. Most mechanistic models that predict two-phase-flow behavior in pipes are for an isolated mechanism, such as flow pattern, film thickness, or rise velocity of gas bubbles in liquid columns. Although several methods predict flow behavior for a single flow pattern, in this monograph we discuss only those that predict flow behavior for all flow patterns. Specifically, we describe the methods of Ansari *et al.*²⁴ and Hasan and Kabir.²⁵⁻²⁷

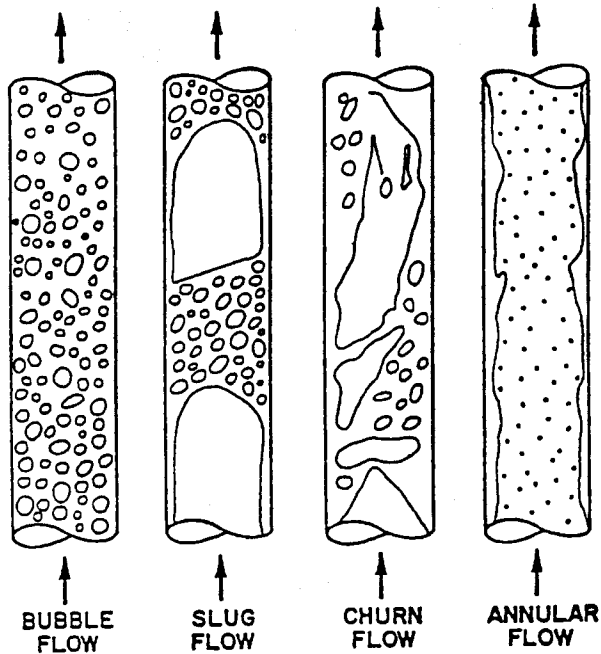


Fig. 4.21—Flow patterns in upward two-phase flow.³⁰ (Reproduced with permission of the American Inst. of Chemical Engineers.)

The models first predict the existing flow pattern and then calculate the flow variables by taking into account the actual mechanisms of the predicted flow pattern.

Two mechanistic models,^{28,29} currently in the review process for possible publication in journals, are not described in this monograph. In addition, OLGA and TACITE are commercial computer programs that include proprietary steady-state mechanistic models. Because of their proprietary nature, details of the models are not included in this monograph.

Ansari et al. Method. Ansari *et al.*²⁴ formulated a comprehensive mechanistic model for upward, vertical two-phase flow. This study was conducted as part of the Tulsa U. Fluid Flow Projects (TUFFP). Although the pressure-gradient equations imply that the model can be used for deviated wells, no attempt was made to account for the effect of inclination angle on the mechanisms considered. Because of the model's complexity and because it was developed with SI units, the development and examples also are presented in SI units.

Flow-Pattern Prediction. Taitel *et al.*³⁰ presented the basic work on mechanistic modeling of flow-pattern transitions for upward two-phase flow. They identified four distinct flow patterns and then formulated and evaluated the transition boundaries among them. Fig. 4.21 shows the four flow patterns: bubble flow, slug flow, churn flow, and annular flow.

Barnea *et al.*³¹ modified these transitions to extend the applicability of the Taitel *et al.* model to inclined flows. Barnea³² combined flow-pattern-prediction models applicable to different inclination-angle ranges into one unified model. On the basis of these studies, flow patterns can be predicted by defining transition boundaries among bubble, slug, and annular flows.

Bubble/Slug Transition. Taitel *et al.* gave the minimum diameter for which bubble flow occurs as

$$d_{\min} = 19.01 \left[\frac{(\rho_L - \rho_g)\sigma_L}{\rho_L^2 g} \right]^{1/2} \quad (4.158)$$

For larger pipe sizes, the basic transition mechanism for bubbly to slug flow is coalescence of small gas bubbles into large Taylor bubbles.¹⁵ Experimentally, this was found to occur at a void fraction

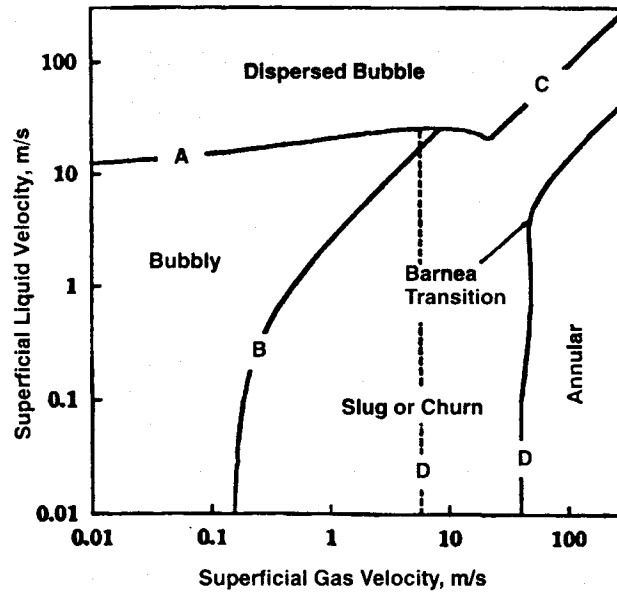


Fig. 4.22—Typical flow-pattern map for wellbores.²⁴

of about 0.25. With 0.25, the transition can be expressed in terms of superficial and slip velocities as

$$v_{Sg} = 0.25v_s + 0.333v_{SL}, \quad (4.159)$$

where v_s = slip or bubble-rise velocity given by Harmathy³³ as

$$v_s = 1.53 \left[\frac{g\sigma_L(\rho_L - \rho_g)}{\rho_L^2} \right]^{1/4} \quad (4.160)$$

This is shown as Transition B in Fig. 4.22.

At high liquid rates, turbulent forces break down large gas bubbles into small ones, even at void fractions greater than 0.25. This yields the Barnea³² transition to dispersed-bubble flow as

$$2 \left[\frac{0.4\sigma_L}{(\rho_L - \rho_g)g} \right]^{1/2} \left(\frac{\rho_L}{\sigma_L} \right)^{3/5} \left(\frac{f}{2d} \right)^{2/5} (v_{SL} + v_{Sg})^{1/2} = \\ 0.725 + 4.15 \left(\frac{v_{Sg}}{v_{Sg} + v_{SL}} \right)^{0.5}, \quad (4.161)$$

where f is obtained from the Moody diagram (Fig. 2.2) for a no-slip Reynolds number. This is shown as Transition A in Fig. 4.22.

At high gas velocities this transition is governed by the maximum packing of bubbles to give coalescence. Scott and Kouba³⁴ concluded that this occurs at a void fraction of 0.76, giving the transition for no-slip dispersed-bubble flow as

$$v_{Sg} = 3.17v_{SL} \quad (4.162)$$

This is shown as Transition C in Fig. 4.22.

Transition to Annular Flow. The transition criterion for annular flow is based in part on the gas-phase velocity required to prevent fall back of the entrained liquid droplets in the gas stream. This gives the transition as

$$v_{Sg} = 3.1 \left[\frac{g\sigma_L(\rho_L - \rho_g)}{\rho_g^2} \right]^{1/4} \quad (4.163)$$

and is shown as the left Transition D in Fig. 4.22.

Barnea³² proposed additional transition criteria that considered the effects of film thickness. One effect is the bridging of the gas

core by a thick liquid film at high liquid rates. Another effect is the instability of the liquid film, which causes a downward flow of the film at low liquid rates. The bridging mechanism is governed by the minimum liquid holdup required to form a liquid slug.

$$H_{LF} > 0.12. \quad \dots \quad (4.164)$$

H_{LF} is the fraction of the pipe cross section occupied by the liquid film, assuming no entrainment in the core. To account for the effect of liquid entrainment in the gas core, Eq. 4.164 was modified as

$$\left(H_{LF} + \lambda_L \frac{A_C}{A} \right) > 0.12, \quad \dots \quad (4.165)$$

where, from geometric considerations, H_{LF} can be expressed in terms of the dimensionless film thickness, $\underline{\delta} = \delta/d$, as $H_{LF} = 4\underline{\delta}(1-\underline{\delta})$. The dimensionless film thickness can be calculated by solving a dimensionless combined-momentum equation.

$$Y_M = \frac{Z}{(1 - H_{LF})^{2.5} H_{LF}} - \frac{1}{H_{LF}^3} X_M^2, \quad \dots \quad (4.166)$$

where Z is determined from either Eq. 4.221 or 4.222. X_M and Y_M , the modified Lockhart and Martinelli³⁵ parameters,³⁶ are

$$X_M = \sqrt{\frac{B(dp/dL)_{SL}}{(dp/dL)_{SC}}}, \quad \dots \quad (4.167)$$

$$Y_M = \frac{g \sin \theta (\rho_L - \rho_g)}{(dp/dL)_{SC}}, \quad \dots \quad (4.168)$$

and $B = (1 - F_E)^2 (f_F/f_{SL})$. Other parameters are defined in the annular-flow model. The film instability mechanism also can be expressed in terms of the modified Lockhart and Martinelli³⁵ parameters.³⁶

$$Y_M = \frac{2 - 1.5H_{LF}}{H_{LF}^3(1 - 1.5H_{LF})} X_M^2. \quad \dots \quad (4.169)$$

Annular flow exists if the two Barnea criteria are satisfied and if v_{sg} is greater than that at the transition given by Eq. 4.163. First, Eq. 4.165 is used to determine the first criterion for annular flow. If annular flow is predicted, then Eq. 4.169 must be solved implicitly for $\underline{\delta}_{min}$. If $\underline{\delta}_{min}$ is greater than $\underline{\delta}$, the second criterion for annular flow is satisfied. Eq. 4.169 can be solved for $\underline{\delta}_{min}$ by use of a Newton-Raphson approach. Eq. 4.169 is first expressed as

$$F(\underline{\delta}_{min}) = Y_M - \frac{2 - 1.5H_{LF}}{H_{LF}^3(1 - 1.5H_{LF})} X_M^2 \quad \dots \quad (4.170)$$

and

$$F'(\underline{\delta}_{min}) = \frac{1.5H_{LF} X_M^2}{H_{LF}^3(1 - 1.5H_{LF})} + \frac{(2 - 1.5H_{LF}) X_M^2 H_{LF} (3 - 5.5H_{LF})}{H_{LF}^3 (1 - 1.5H_{LF})^2}. \quad \dots \quad (4.171)$$

The minimum dimensionless film thickness then is determined iteratively from

$$\underline{\delta}_{min,j+1} = \underline{\delta}_{min,j} - \frac{F(\underline{\delta}_{min,j})}{F'(\underline{\delta}_{min,j})}. \quad \dots \quad (4.172)$$

A good initial guess is $\underline{\delta}_{min} = 0.25$. In Fig. 4.22, the right Transition D is a result of applying the two Barnea film thickness criteria.

Flow-Behavior Prediction. Ansari *et al.*²⁴ presented physical models to predict flow behavior in each flow pattern. This resulted in separate models for bubble flow, slug flow, and annular flow.

Churn flow was not modeled because of its complexity, but was treated as a part of slug flow.

Bubble-Flow Model. The bubble-flow model is based primarily on the work by Caetano³⁷ for flow in an annulus. The two bubble-flow patterns, dispersed-bubble flow and bubbly flow, were considered separately in developing the model.

Because of the uniform distribution of gas bubbles in the liquid and the lack of slippage between the two phases, dispersed-bubble flow was approximated as a pseudo-single phase. With this simplification, the two-phase parameters can be expressed as

$$\rho_{TP} = \rho_L \lambda_L + \rho_g (1 - \lambda_L), \quad \dots \quad (4.173)$$

$$\mu_{TP} = \mu_L \lambda_L + \mu_g (1 - \lambda_L), \quad \dots \quad (4.174)$$

and

$$v_{TP} = v_m = v_{SL} + v_{sg}. \quad \dots \quad (4.175)$$

For bubbly flow, slippage is considered by taking into account the bubble-rise velocity relative to the mixture velocity. Assuming a turbulent velocity profile for the mixture, with the rising bubble concentrated more at the center than along the wall of the pipe, the slippage velocity can be expressed as

$$v_s = v_g - 1.2v_m. \quad \dots \quad (4.176)$$

Eq. 4.160 gave Harmathy's³³ expression for bubble-rise velocity. To account for the effect of bubble swarm, Zuber and Hench³⁸ modified the expression as

$$v_s = 1.53 \left[\frac{g \sigma_L (\rho_L - \rho_g)}{\rho_L^2} \right]^{1/4} H_L^{n'}, \quad \dots \quad (4.177)$$

where the value of n' varies from one study to another. Ansari *et al.* found that a value of 0.5 for n' gave the best results. Combining Eqs. 4.176 and 4.177 yields

$$1.53 \left[\frac{g \sigma_L (\rho_L - \rho_g)}{\rho_L^2} \right]^{1/4} H_L^{0.5} = \frac{v_{sg}}{1 - H_L} - 1.2v_m. \quad \dots \quad (4.178)$$

This is an implicit equation for the actual holdup for bubbly flow. Two-phase-flow parameters then can be calculated from

$$\rho_{TP} = \rho_L H_L + \rho_g (1 - H_L) \quad \dots \quad (4.179)$$

and

$$\mu_{TP} = \mu_L H_L + \mu_g (1 - H_L). \quad \dots \quad (4.180)$$

The two-phase pressure gradient for bubbly and dispersed-bubble flow is composed of two components. Thus,

$$\left(\frac{dp}{dL} \right) = \left(\frac{dp}{dL} \right)_{el} + \left(\frac{dp}{dL} \right)_f. \quad \dots \quad (4.181)$$

The elevation pressure gradient is

$$\left(\frac{dp}{dL} \right)_{el} + \rho_{TP} g \sin \theta. \quad \dots \quad (4.182)$$

The friction component is

$$\left(\frac{dp}{dL} \right)_f + \frac{f_{TP} \rho_{TP} v_{TP}^2}{2d}, \quad \dots \quad (4.183)$$

where f_{TP} is obtained from a Moody diagram (Fig. 2.2) for a Reynolds number defined by

$$N_{Re_{TP}} = \frac{\rho_{TP} v_{TP} d}{\mu_{TP}}. \quad \dots \quad (4.184)$$

Because bubble flow is dominated by a relatively incompressible liquid phase, there is no significant change in the density of the flow-

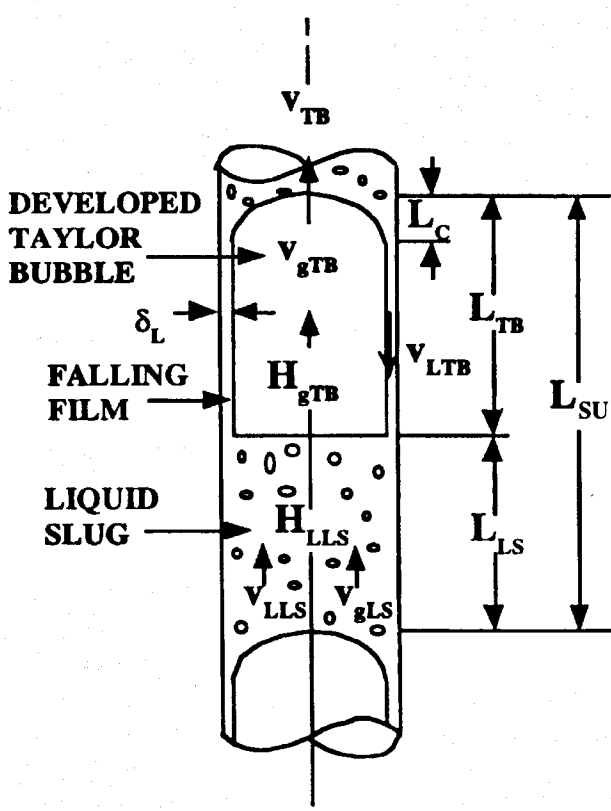


Fig. 4.23—Slug-flow schematic.²⁴

ing fluids. The fluid velocity is nearly constant, resulting in essentially no pressure drop from acceleration. Therefore, the acceleration pressure gradient is negligible compared with the other pressure-gradient components.

Slug-Flow Model. Fernandes *et al.*³⁹ presented the first complete physical model for slug flow. Sylvester⁴⁰ developed a simplified version using a correlation for slug void fraction. Both studies assumed a fully developed slug flow.

For a fully developed slug unit, as shown in Fig. 4.23, overall gas and liquid mass balances, respectively, are given by

$$v_{sg} = \beta v_{gTB}(1 - H_{LTB}) + (1 - \beta)v_{gLS}(1 - H_{LLS}) \quad \dots \dots \dots \quad (4.185)$$

and

$$v_{sg} = (1 - \beta)v_{LLS}H_{LLS} - \beta v_{LTB}H_{LTB}, \quad \dots \dots \dots \quad (4.186)$$

where

$$\beta = \frac{L_{TB}}{L_{SU}}. \quad \dots \dots \dots \quad (4.187)$$

Mass balances for steady-state liquid and gas transfer between the liquid slug and the Taylor bubble, respectively, are

$$(v_{TB} - v_{LLS})H_{LLS} = [v_{TB} - (-v_{LTB})]H_{LTB} \quad \dots \dots \dots \quad (4.188)$$

and

$$(v_{TB} - v_{gLS})(1 - H_{LLS}) = (v_{TB} - v_{gTB})(1 - H_{LTB}). \quad \dots \dots \dots \quad (4.189)$$

The Taylor-bubble-rise velocity is equal to the centerline velocity plus the Taylor-bubble-rise velocity in a stagnant liquid column.

$$v_{TB} = 1.2v_m + 0.35 \left[\frac{gd(\rho_L - \rho_g)}{\rho_L} \right]^{\frac{1}{2}}. \quad \dots \dots \dots \quad (4.190)$$

Similarly, the velocity of the gas bubbles in the liquid slug is

$$v_{gLS} = 1.2v_m + 1.53 \left[\frac{gd(\rho_L - \rho_g)}{\rho_L^2} \right]^{\frac{1}{2}} H_{LLS}^{0.5}, \quad \dots \dots \dots \quad (4.191)$$

where the second term on the right side represents the bubble-rise velocity, as defined in Eq. 4.177.

The velocity v_{LTB} of the falling film around the Taylor bubble can be correlated with the film thickness, δ_L by use of the Brotz⁴¹ expression,

$$v_{LTB} = \sqrt{196.7g\delta_L}, \quad \dots \dots \dots \quad (4.192)$$

where δ_L is the constant film thickness for fully developed slug flow. From geometrical considerations, v_{LTB} can be expressed in terms of the Taylor-bubble void fraction to give

$$v_{LTB} = 9.916 \left[gd(1 - \sqrt{H_{gTB}}) \right]^{\frac{1}{2}}. \quad \dots \dots \dots \quad (4.193)$$

The liquid-slug void fraction can be obtained from the correlation developed by Sylvester,⁴⁰ who used data from Fernandes *et al.*³⁹ and Schmidt.⁴²

$$H_{gLS} = \frac{v_{sg}}{0.425 + 2.65v_m}. \quad \dots \dots \dots \quad (4.194)$$

Eqs. 4.185, 4.186, 4.188 through 4.191, 4.193, and 4.194 can be solved iteratively to obtain the following eight unknowns that define the fully developed slug-flow model: β , H_{LTB} , H_{gLS} , v_{gTB} , v_{LTB} , v_{gLS} , v_{LLS} , and v_{TB} . Vo and Shoham⁴³ showed that these eight equations can be combined algebraically to give

$$\begin{aligned} & (9.916 \sqrt{gd}) (1 - \sqrt{1 - H_{LTB}})^{0.5} H_{LTB} \\ & - v_{TB}(1 - H_{LTB}) + \bar{A} = 0, \quad \dots \dots \dots \quad (4.195) \end{aligned}$$

where

$$\bar{A} = H_{gLS}(v_{TB} - v_{gLS}) + v_m. \quad (4.196)$$

With v_{TB} and H_{gLS} given by Eqs. 4.190 and 4.194, respectively, \bar{A} can be determined readily from Eq. 4.196. Eq. 4.195 can be solved for H_{LTB} by use of an iterative-solution method. Defining the left side of Eq. 4.195 as $F(H_{LTB})$,

$$\begin{aligned} F(H_{LTB}) &= (9.916 \sqrt{gd}) (1 - \sqrt{1 - H_{LTB}})^{0.5} H_{LTB} \\ & - v_{TB}(1 - H_{LTB}) + \bar{A}. \quad \dots \dots \dots \quad (4.197) \end{aligned}$$

The derivative of Eq. 4.197 with respect to H_{LTB} yields

$$\begin{aligned} F'(H_{LTB}) &= v_{TB} + (9.916 \sqrt{gd}) \\ & \times (1 - \sqrt{1 - H_{LTB}})^{0.5} \\ & + \frac{H_{LTB}}{4 \sqrt{1 - H_{LTB}(1 - \sqrt{1 - H_{LTB}})}}. \quad \dots \dots \dots \quad (4.198) \end{aligned}$$

Eqs. 4.197 and 4.198 suggest that the Newton-Raphson approach can be incorporated easily to determine H_{LTB} , the root of Eq. 4.197. Vo and Shoham also showed that, if a root exists in the interval of (0,1), the root is unique. Thus,

$$H_{LTB_{j+1}} = H_{LTB_j} - \frac{F(H_{LTB_j})}{F'(H_{LTB_j})}. \quad \dots \dots \dots \quad (4.199)$$

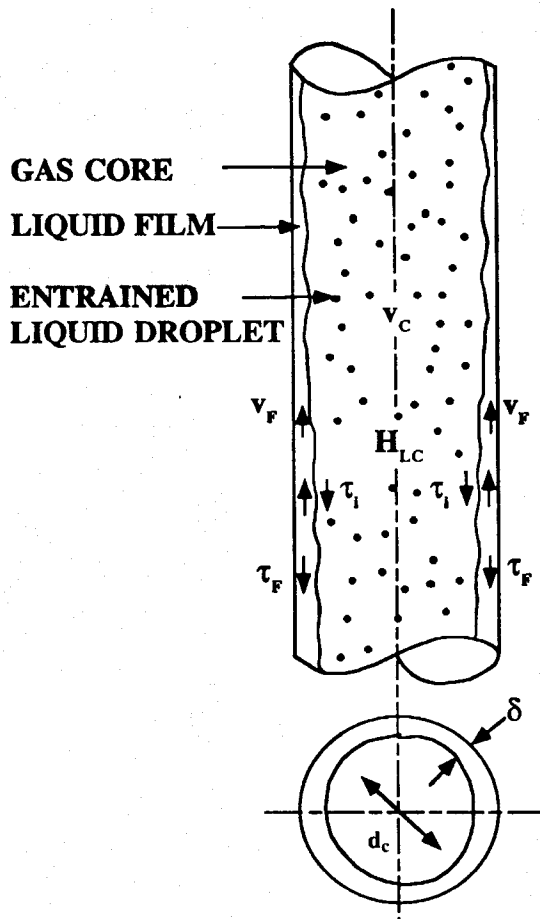


Fig. 4.24—Annular-flow schematic.²⁴

To determine all slug-flow variables, use this step-by-step procedure.

1. Calculate v_{TB} , v_{gLS} , and H_{gLS} from Eqs. 4.190, 4.191, and 4.194.
2. Using Eqs. 4.196 through 4.199, determine H_{LTB} . A good initial guess is $H_{LTB} = 0.15$.
3. Solve Eq. 4.193 for v_{LTB} . Note that $H_{gTB} = 1 - H_{LTB}$.
4. Solve Eq. 4.188 for v_{LLS} . Note that $H_{LLS} = 1 - H_{gLS}$.
5. Solve Eq. 4.191 for v_{gLS} .
6. Solve Eq. 4.189 for v_{gTB} .
7. Solve either Eq. 4.185 or 4.186 for β .
8. Assuming that $L_{LS} = 30d$, calculate L_{SU} and L_{TB} from the definition of β .

For fully developed slug flow, the elevation component of the pressure gradient occurring across a slug unit is given by

$$\left(\frac{dp}{dL}\right)_{el} = [(1 - \beta)\rho_{LS} + \beta\rho_g]g \sin \theta, \quad (4.200)$$

where

$$\rho_{LS} = \rho_L H_{LLS} + \rho_g(1 - H_{LLS}). \quad (4.201)$$

Eq. 4.200 assumes that the liquid film around the Taylor bubble does not contribute to the elevation component. Friction losses were assumed to occur only across the liquid slug and are neglected along the Taylor bubble. Therefore, the friction component of the pressure gradient is

$$\left(\frac{dp}{dL}\right)_f = \frac{f_{LS}\rho_{LS}v_m^2}{2d}(1 - \beta), \quad (4.202)$$

where f_{LS} is obtained from a Moody diagram (Fig. 2.2) for a Reynolds number defined by

$$N_{Re_{LS}} = \frac{\rho_{LS}v_md}{\mu_{LS}}. \quad (4.203)$$

For fully developed slug flow, Ansari *et al.*²⁴ assumed that the acceleration component of the pressure gradient can be neglected.

McQuillan and Whalley⁴⁴ introduced the concept of developing slug flow during their study of flow-pattern transitions. In developing slug flow, the length of the cap at the top of the Taylor bubble is a significant portion of the total length of the Taylor bubble. The film thickness varies throughout the Taylor-bubble region. Ansari *et al.* presented a detailed description of the complex equations to predict flow behavior for developing slug flow. Barnea⁴⁵ contends that failure to consider the developing slug region can result in significant pressure-drop-prediction errors. However, pipe in producing wells is so long that only minor errors should result if the entire slug-flow region is treated as fully developed flow. Consequently, this monograph does not address the developing slug region.

Annular-Flow Model. Wallis¹⁸ discussed the hydrodynamics of annular flow and presented the classic correlations for entrainment and interfacial friction as functions of film thickness. Hewitt and Hall-Taylor⁴⁶ gave a detailed analysis of the mechanisms involved in annular flow. All subsequent models were based on this approach.

Fig. 4.24 shows a fully developed annular flow. Conservation of momentum applied separately to the core and the film yields, for the core and the film, respectively,

$$A_C \left(\frac{dp}{dL} \right)_C - \tau_i S_i - \rho_C A_C g \sin \theta = 0 \quad (4.204)$$

and

$$A_F \left(\frac{dp}{dL} \right)_F + \tau_i S_i - \tau_F S_F - \rho_L A_F g \sin \theta = 0. \quad (4.205)$$

The core is considered a homogeneous mixture of gas and entrained liquid droplets flowing at the same velocity. Thus,

$$\rho_C = \rho_L \lambda_{LC} + \rho_g(1 - \lambda_{LC}), \quad (4.206)$$

where

$$\lambda_{LC} = \frac{F_E v_{SL}}{F_E v_{SL} + v_{Sg}}. \quad (4.207)$$

F_E is the fraction of the total liquid entrained in the core. Wallis¹⁸ determined it empirically as

$$F_E = 1 - \exp[-0.125(v_{crit} - 1.5)], \quad (4.208)$$

where

$$v_{crit} = 10,000 \frac{v_{Sg} \mu_g}{\sigma_L} \left(\frac{\rho_g}{\rho_L} \right)^{1/2}. \quad (4.209)$$

The shear stress in the film can be expressed as

$$\tau_F = f_F \rho_L \frac{v_F^2}{8}, \quad (4.210)$$

where f_F is obtained from a Moody diagram (Fig. 2.2) for a Reynolds number defined by

$$N_{Re_F} = \frac{\rho_L v_F d_{HF}}{\mu_L}, \quad (4.211)$$

where

$$v_F = \frac{q_L(1 - F_E)}{A_F} = \frac{v_{SL}(1 - F_E)}{4\delta(1 - \delta)} \quad (4.212)$$

and

$$d_{HF} = 4\delta(1 - \delta)d. \quad (4.213)$$

This gives

$$\tau_F = \frac{f_F}{8} (1 - F_E)^2 \rho_L \left[\frac{v_{SL}}{4\delta(1 - \delta)} \right]^2. \quad (4.214)$$

Eq. 4.214 reduces to

$$\tau_F = \frac{d}{4} \frac{(1 - F_E)^2}{[4\delta(1 - \delta)]^2} f_{SL} \left(\frac{dp}{dL} \right)_{SL}, \quad (4.215)$$

where the superficial liquid-friction-pressure gradient is given by

$$\left(\frac{dp}{dL} \right)_{SL} = \frac{f_{SL} \rho_L v_{SL}^2}{2d}, \quad (4.216)$$

where f_{SL} = the friction factor based on superficial liquid velocity and can be obtained from a Moody diagram (Fig. 2.2) for a Reynolds number defined by

$$N_{Re_{SL}} = \frac{\rho_L v_{SL} d}{\mu_L}. \quad (4.217)$$

For the shear stress at the interface,

$$\tau_i = \frac{f_i \rho_C v_C^2}{8}, \quad (4.218)$$

where

$$v_C = \frac{v_{SC}}{(1 - 2\delta)^2} \quad (4.219)$$

and

$$f_i = f_{SC} Z, \quad (4.220)$$

where Z = a correlating factor relating interfacial friction to the film thickness. On the basis of the performance of the model, Ansari *et al.* found that the Wallis expression for Z works well for thin films or high entrainments, whereas the Whalley and Hewitt⁴⁷ expression works well for thick films or low entrainments. Thus,

$$Z = 1 + 300\delta \text{ for } F_E > 0.9 \quad (4.221)$$

and

$$Z = 1 + 24 \left(\frac{\rho_L}{\rho_g} \right)^{1/3} \delta \text{ for } F_E < 0.9. \quad (4.222)$$

Combining Eqs. 4.218 through 4.220 yields

$$\tau_i = \frac{d}{4} \frac{Z}{(1 - 2\delta)^4} \left(\frac{dp}{dL} \right)_{SC}. \quad (4.223)$$

The superficial friction-pressure gradient in the core is given by

$$\left(\frac{dp}{dL} \right)_{SC} = \frac{f_{SC} \rho_C v_{SC}^2}{2d}, \quad (4.224)$$

where f_{SC} is obtained from a Moody diagram (Fig. 2.2) for a Reynolds number defined by

$$N_{Re_{SC}} = \frac{\rho_C v_{SC} d}{\mu_{SC}}, \quad (4.225)$$

$$v_{SC} = F_E v_{SL} + v_{Sg}, \quad (4.226)$$

and

$$\mu_{SC} = \mu_L \lambda_{LC} + \mu_g (1 - \lambda_{LC}). \quad (4.227)$$

The pressure gradient for annular flow can be calculated by substituting the above equations into Eqs. 4.204 and 4.205. Thus,

$$\left(\frac{dp}{dL} \right)_C = \frac{Z}{(1 - 2\delta)^5} \left(\frac{dp}{dL} \right)_{SC} + \rho_C g \sin \theta. \quad (4.228)$$

and

$$\left(\frac{dp}{dL} \right)_F = \frac{(1 - F_E)^2}{64\delta^3(1 - \delta)^3} f_{SL} \left(\frac{dp}{dL} \right)_{SL}$$

$$- \frac{Z}{2\delta(1 - \delta)(1 - 2\delta)^3} \left(\frac{dp}{dL} \right)_{SC} + \rho_L g \sin \theta. \quad (4.229)$$

The basic unknown in Eqs. 4.228 and 4.229 is the dimensionless film thickness, δ . The pressure gradients in the core and film must be the same. An implicit equation for δ can be obtained by equating Eqs. 4.228 and 4.229, giving

$$\frac{Z}{4\delta(1 - \delta)(1 - 2\delta)^5} \left(\frac{dp}{dL} \right)_{SC} - (\rho_L - \rho_C) g \sin \theta - \frac{(1 - F_E)^2}{64\delta^3(1 - \delta)^3} f_{SL} \left(\frac{dp}{dL} \right)_{SL} = 0. \quad (4.230)$$

To simplify this equation, Ansari *et al.* used the dimensionless approach developed by Alves *et al.*³⁶ This approach defines the following dimensionless groups in addition to using the previously defined modified Lockhart and Martinelli parameters, X_M and Y_M .

$$\phi_C^2 = \frac{(dp/dL)_C - g\rho_L \sin \theta}{(dp/dL)_{SC}} \quad (4.231)$$

and

$$\phi_F^2 = \frac{(dp/dL)_F - g\rho_L \sin \theta}{(dp/dL)_{SC}}. \quad (4.232)$$

Eq. 4.230 then reduces to

$$Y_M - \frac{Z}{4\delta(1 - \delta)[1 - 4\delta(1 - \delta)]^{2.5}} + \frac{X_M^2}{[4\delta(1 - \delta)]^3} = 0. \quad (4.233)$$

Eq. 4.233 can be solved iteratively by use of the Newton-Raphson approach to obtain δ . If Eq. 4.233 is $F(\delta)$, the derivative of Eq. 4.233 with respect to δ yields

$$\begin{aligned} F'(\delta) = & \frac{Z[4(1 - 2\delta)]}{[4\delta(1 - \delta)]^2 [1 - 4\delta(1 - \delta)]^{2.5}} \\ & - \frac{Z'}{4\delta(1 - \delta)[1 - 4\delta(1 - \delta)]^{2.5}} \\ & - \frac{2.5Z[4(1 - 2\delta)]}{4\delta(1 - \delta)[1 - 4\delta(1 - \delta)]^{3.5}} \\ & - \frac{3X_M^2[4(1 - 2\delta)]}{[4\delta(1 - \delta)]^4}. \end{aligned} \quad (4.234)$$

Then,

$$\underline{\delta}_{j+1} = \underline{\delta}_j - \frac{F(\underline{\delta}_j)}{F'(\underline{\delta}_j)}. \quad (4.235)$$

Once δ is known, the dimensionless groups ϕ_F and ϕ_C can be obtained from the following forms of Eqs. 4.228 and 4.229, respectively.

$$\phi_C^2 = \frac{Z}{(1 - 2\delta)^5} \quad (4.236)$$

and

$$\phi_F^2 = \frac{(1 - F_E)^2}{[1 - (1 - 2\delta)^2]^2} f_{SL}$$

$$\times \left\{ \frac{\frac{Z}{(1-2\delta)^5} - Y_M}{\frac{Z}{(1-2\delta)^5} - Y_M [1 - (1-2\delta)^2]} \right\} \quad \dots \dots \quad (4.237)$$

Because the pressure gradient in the film and core must be the same, the total pressure gradient can be obtained from either Eq. 4.231 or 4.232. Thus,

$$\left(\frac{dp}{dL} \right)_T = \left(\frac{dp}{dL} \right)_C = \phi_C^2 \left(\frac{dp}{dL} \right)_{SC} + g\rho_C \sin \theta \quad \dots \dots \quad (4.238)$$

or

$$\left(\frac{dp}{dL} \right)_T = \left(\frac{dp}{dL} \right)_F = \phi_F^2 \left(\frac{dp}{dL} \right)_{SL} + g\rho_L \sin \theta. \quad \dots \dots \quad (4.239)$$

Ansari *et al.* neglected the acceleration pressure gradient for annular flow. Lopes and Dukler⁴⁸ found that, except for a limited range of high liquid flow rates, the acceleration component resulting from the exchange of liquid droplets between the core and the film is negligible.

Example 4.9—Using the Ansari *et al.* Mechanistic Model, Calculate the Vertical, Multiphase-Flow Pressure Gradient for Example 3.2.

Given: $\epsilon = 0.00006$ ft = 1.83×10^{-2} m, $d = 6.0$ in. = 0.1524 m, $v_{SL} = 3.97$ ft/sec = 1.208 m/s, $v_{SG} = 3.86$ ft/sec = 1.173 m/s, $\rho_L = 47.61$ lbm/ft³ = 761.7 kg/m³, $\rho_g = 5.88$ lbm/ft³ = 94.1 kg/m³, $\sigma_L = 8.41$ dynes/cm = 8.41×10^{-3} kg/s², $\mu_L = 0.97$ cp = 0.97×10^{-3} Pa·s, $\mu_g = 0.016$ cp = 0.016×10^{-3} Pa·s.

Flow-Pattern Determination.

1. Check dispersed-bubble transition boundary (Eq. 4.161):

$$2 \left[\frac{(0.4)8.41 \times 10^{-3}}{(761.7 - 94.1)9.81} \right]^{1/2} \left(\frac{761.7}{8.41 \times 10^{-3}} \right)^{3/5} \left[\frac{1.49 \times 10^{-2}}{(2)(0.1524)} \right]^{2/5} \\ \times (1.208 + 1.173)^{1.2} = 0.725 + 4.15 \left(\frac{1.173}{1.208 + 1.173} \right)^{0.5} \\ \times 1.144 \neq 3.636.$$

Then, flow pattern is not dispersed bubble.

2. Check annular-flow transition boundary:

From Eq. 4.163,

$$v_{SG_{Ann}} = 3.1 \left[\frac{(9.8)(8.41 \times 10^{-3})(761.7 - 94.1)}{(94.1)^2} \right]^{1/4} \\ = 0.87 \text{ m/s.}$$

Although $v_{SG} = 1.173 > 0.87$ gives the annular-flow pattern, also check the Barnea transition criteria.

From Eq. 4.209,

$$v_{crit} = 10,000 \frac{(1.173)(0.016 \times 10^{-3})}{(8.41 \times 10^{-3})} \left(\frac{94.1}{761.7} \right)^{0.5} = 7.84 \text{ m/s.}$$

The entrainment fraction is calculated from Eq. 4.208.

$$F_E = 1 - \exp[-0.125(7.84 - 1.5)] = 0.547.$$

From Eq. 4.207,

$$\lambda_{LC} = \frac{(0.547)(1.208)}{(0.547)(1.208) + 1.173} = 0.36$$

The core density and viscosity are obtained from Eqs. 4.206 and 4.227, respectively, as

$$\rho_C = (761.7)(0.36) + (94.1)(1 - 0.36) = 334.4 \text{ kg/m}^3$$

and

$$\mu_{SC} = \frac{(0.97)(0.36) + (0.016)(1 - 0.36)}{1,000}$$

$$= 0.36 \times 10^{-3} \text{ Pa}\cdot\text{s.}$$

The superficial core velocity from Eq. 4.226 is

$$v_{SC} = (0.547)(1.208) + 1.173 = 1.834 \text{ m/s.}$$

From Eq. 4.225,

$$N_{Re_{SC}} = \frac{(334.4)(1.834)(0.1524)}{(0.36 \times 10^{-3})} = 260,000$$

and relative roughness is

$$\epsilon/d = \frac{1.83 \times 10^{-5}}{0.524} = 1.2008 \times 10^{-4}.$$

Then, the flow is turbulent.

From Fig. 2.2,

$$f_{SC} = 0.0152.$$

Similarly, from Eq. 4.217 the film Reynolds number is

$$N_{Re_{LS}} = \frac{(761.7)(1.208)(0.1524)}{(0.97 \times 10^{-3})} = 144,565$$

and the friction factor from Fig. 2.2 for a relative roughness of 1.2008×10^{-4} is

$$f_{SL} = 0.01708.$$

The superficial gas-core and liquid-film pressure gradients are determined from Eqs. 4.224 and 4.216 as

$$\left. \frac{dp}{dL} \right|_{SC} = \frac{(0.01708)(334.4)(1.8344)^2}{2(0.1524)} = 63.13 \text{ Pa/m}$$

and

$$\left. \frac{dp}{dL} \right|_{SL} = \frac{(0.0152)(761.7)(1.208)^2}{2(0.1524)} = 55.43 \text{ Pa/m.}$$

Assuming that $f_F/f_{SL} \approx 1$, the modified Lockhart and Martinelli parameters can be estimated from Eqs. 4.167 and 4.168 as

$$X_M = \sqrt{(1 - 0.547)^2 \frac{(55.43)}{(63.13)}} = 0.784,$$

$$X_M^2 = 0.615,$$

and

$$Y_M = (9.81) \frac{(761.7 - 334.4)}{(63.13)} = 66.34.$$

Because $F_E = 0.547$, using Eq. 4.222 yields

$$Z = 1 + (24) \left(\frac{741.7}{94.1} \right)^{1/3} \underline{\delta}.$$

Substituting X_M , Y_M , Z , and $H_{LF} = 4\underline{\delta}(1 - \underline{\delta})$ into Eq. 4.166 gives

$$66.34 - \frac{1 + 48.19\underline{\delta}}{4\underline{\delta}(1 - \underline{\delta})[1 - 4\underline{\delta}(1 - \underline{\delta})]^{2/5}} \\ + \frac{1}{[4\underline{\delta}(1 - \underline{\delta})]^{2/5}} 0.615 = 0.$$

Solving the above equation for δ , $\delta \approx 0.1265$. Therefore, $\delta = (0.1265) \times (0.1524) = 0.0193$ m and $H_{LF} = (4)(0.1265)(1 - 0.1265) = 0.442$. With the criterion from Eq. 4.165,

$$\left\{ 0.442 + (0.36) \frac{[0.1524 - 2(0.1524)(0.1265)]^2}{(0.1524)^2} \right\} > 0.12$$

$$0.72 > 0.12.$$

Thus, the liquid film holdup is sufficient to bridge the pipe, and annular flow does not exist.

3. Check bubbly flow existence:

With Eq. 4.158, the minimum pipe diameter at which bubbly flow can exist is

$$d_{\min} = 19.01 \left[\frac{(761.7 - 94.1)(8.4 \times 10^{-3})}{(761.7)^2(9.81)} \right]^{0.5}$$

$$= 0.0189 \text{ m} < 0.1524 \text{ m} = d.$$

Then, bubbly flow can exist.

4. Check bubble/slug transition:

From Eq. 4.160,

$$v_s = 1.53 \left[\frac{(9.81)(761.7 - 94.1)}{(761.7)^2} (8.41 \times 10^{-3}) \right]^{0.25}$$

$$= 0.151 \text{ m/s.}$$

From Eq. 4.159, the superficial liquid velocity at the transition is

$$v_{SL,t} = 3[1.173 - (0.25)(0.151)(\sin 90^\circ)] = 3.4 \text{ m/s}$$

and

$$v_{SL,t} = 3.4 \text{ m/s} > v_{SL} = 1.208 \text{ m/s.}$$

The flow pattern is then slug flow.

Slug-Flow Modeling.

The step-by-step procedure described in the discussion of the slug-flow model is followed to determine all slug-flow variables.

1. Calculate v_{TB} , H_{gLS} , and v_{gLS} from Eqs. 4.190, 4.191, and 4.194 as

$$v_{TB} = (1.2)(2.381) + (0.35) \left[\frac{(9.81)(0.1524)(761.7 - 94.1)}{(761.7)} \right]^{0.5}$$

$$= 3.258 \text{ m/s.}$$

$$H_{gLS} = \frac{1.173}{0.425 + (2.65)(2.881)} = 0.1742,$$

and

$$v_{gLS} = 1.2(2.381) + (0.151)(0.826)^{0.5} = 2.994 \text{ m/s.}$$

2. Using Eqs. 4.196 through 4.199, determine H_{LTB} . A good initial guess is $H_{LTB} = 0.15$.

$$\bar{A} = (0.1742)(3.258 - 2.994) + 2.381 = 2.427,$$

$$F(H_{LTB}) = \left[9.916 \sqrt{(9.81)(0.1524)} \right] \left(1 - \sqrt{1 - 0.15} \right)^{0.5} 0.15$$

$$- 3.258(1 - 0.15) + 2.427$$

$$= 0.1658,$$

$$F'(H_{LTB}) = 3.258 + \left[9.916 \sqrt{(9.81)(0.1524)} \right]$$

$$\times \left[\left(1 - \sqrt{1 - 0.15} \right)^{0.5} \right. \\ \left. + \frac{0.15}{4 \sqrt{(1 - 0.15)(1 - \sqrt{1 - 0.15})}} \right] \\ = 8.4383,$$

and

$$H_{LTB} = 0.15 - \frac{0.1658}{8.4383} = 0.13.$$

With the calculated H_{LTB} as the new guess for H_{LTB} ,

$$F(H_{LTB}) = \left[9.916 \sqrt{(9.81)(0.1524)} \right] \left(1 - \sqrt{1 - 0.13} \right)^{0.5} 0.13$$

$$- 3.258(1 - 0.13) + 2.427$$

$$= 0.00132,$$

$$F'(H_{LTB}) = 3.258 + \left[9.916 \sqrt{(9.81)(0.1524)} \right]$$

$$\times \left[\left(1 - \sqrt{1 - 0.13} \right)^{0.5} \right. \\ \left. + \frac{0.13}{4 \sqrt{(1 - 0.13)(1 - \sqrt{1 - 0.13})}} \right] \\ = 8.031,$$

and

$$H_{LTB} = 0.13 - \frac{0.00132}{8.031} = 0.1298.$$

The difference between the guessed and the calculated values of H_{LTB} is very small. Therefore, $H_{LTB} \approx 0.13$.

3. Solve Eq. 4.193 for v_{LTB} :

Note that $H_{gTB} = 1 - H_{LTB}$.

$$H_{gTB} = 1 - 0.13 = 0.87$$

and

$$v_{LTB} = 9.916 \left[(9.81)(0.1524) \left(1 - \sqrt{0.87} \right) \right]^{0.5} = 3.144 \text{ m/s.}$$

4. Solve Eq. 4.188 for v_{LLS} :

Note that $H_{LLS} = 1 - H_{gLS}$.

$$H_{LLS} = 1 - 0.174 = 0.826,$$

$$(3.258 - v_{LLS})0.826 = (3.258 + 3.1445)0.13,$$

and

$$v_{LLS} = 2.25 \text{ m/s.}$$

5. Solve Eq. 4.189 for v_{gTB} :

$$(3.258 - 2.994)(1 - 0.826) = (3.258 - v_{gTB})(1 - 0.13)$$

and

$$v_{gTB} = 3.205 \text{ m/s.}$$

6. Solve Eq. 4.185 for β :

$$1.173 = (1 - \beta)(2.994)(1 - 0.826) + \beta(3.205)(1 - 0.13)$$

and

$$\beta = 0.287.$$

7. Assuming $L_{LS} = 30d$, calculate L_{SL} and L_{TB} from the definition of β :

$$L_{LS} = 30(0.1524) = 4.57 \text{ m,}$$

$$(0.287)(4.57) = (1 - 0.287)(L_{TB}),$$

and

$$L_{TB} = 1.84 \text{ m.}$$

8. Elevation component of pressure gradient:

From Eq. 4.201,

$$\rho_{LS} = (761.7)(0.826) + (94.1)(1 - 0.826) = 654.4 \text{ kg/m}^3.$$

From Eq. 4.200,

$$\begin{aligned} \left(\frac{dp}{dL}\right)_{el} &= [(1 - 0.287)(654.4) + (0.287)(94.1)](9.81) \sin 90^\circ \\ &= 4,779.2 \text{ Pa/m.} \end{aligned}$$

9. Friction component of pressure gradient:

$$\begin{aligned} \mu_{LS} &= (0.97 \times 10^{-3})(0.826) + (0.016 \times 10^{-3})(1 - 0.826) \\ &= 8.04 \times 10^{-4} \text{ Pa} \cdot \text{s.} \end{aligned}$$

From Eq. 4.203,

$$N_{Re_{LS}} = \frac{(645.4)(2.381)(0.1524)}{(8.04 \times 10^{-4})} = 291,284.$$

Turbulent flow exists.

From Fig. 2.2,

$$\left.\begin{aligned} \epsilon/d &= 1.2 \times 10^{-4} \\ N_{Re_{LS}} &= 291,284 \end{aligned}\right\} \rightarrow f_{LS} \approx 0.0166.$$

From Eq. 4.202,

$$\begin{aligned} \left(\frac{dp}{dL}\right)_f &= \frac{(0.0166)(645.4)(2.381)^2}{2(0.1524)}(1 - 0.287) \\ &= 142.0 \text{ Pa/m.} \end{aligned}$$

10. Total pressure gradient:

$$\begin{aligned} \left(\frac{dp}{dL}\right)_T &= 4,779.2 + 142.0 \\ &= 4,921.2 \text{ Pa/m} \\ &= 4.921 \text{ kPa/m} \\ &= 0.218 \text{ psi/ft.} \end{aligned}$$

Hasan and Kabir Method. Hasan and Kabir²⁵⁻²⁷ also developed a mechanistic model to predict pressure gradients in wellbores.

Flow-Pattern Prediction. To model flow-pattern transitions, Hasan and Kabir adapted an approach very similar to that of Taitel *et al.*³⁰ Hasan and Kabir^{25,26} identified the same four flow patterns shown in Fig. 4.21: bubble flow, slug flow, churn flow, and annular flow.

Bubble/Slug Transition. Transition from bubble flow (the condition of small bubbles dispersed throughout the flow cross section) to slug flow (when the bubble becomes large enough to fill the entire cross section) requires agglomeration or coalescence. Bubbles, other than very small ones, generally follow a zigzag path when rising through a liquid. This results in collisions among bubbles, with the consequent bubble agglomeration and formation of larger bubbles,⁴⁹ which increases with an increase in the gas flow rate. Hasan *et al.*⁴⁹ reported that a transition to slug flow is expected at a void fraction of 0.25. By use of a drift-flux concept, the transition then can be expressed by Eq. 4.240.

$$v_{sg} = \frac{\sin \theta}{4 - C_o} (C_o v_{SL} + v_s). \quad (4.240)$$

C_o is the flow coefficient given by Eq. 4.241.

$$C_o = \begin{cases} 1.2 & \text{if } d < 0.12 \text{ m or if } v_{SL} > 0.02 \text{ m/s} \\ 2.0 & \text{if } d > 0.12 \text{ m and if } v_{SL} < 0.02 \text{ m/s} \end{cases}. \quad (4.241)$$

The Harmathy³³ expression, Eq. 4.160, is used for the slip or bubble-rise velocity. Transition to slug flow takes place at superficial gas velocities greater than that given by Eq. 4.240.

The terminal rise velocity of small bubbles given by Eq. 4.160 is dependent on fluid properties but independent of pipe diameter. However, the rise velocity of a Taylor bubble,²⁶

$$v_{TB} = 0.35 \sqrt{gd \frac{(\rho_L - \rho_g)}{\rho_L}} \sqrt{\sin \theta} (1 + \cos \theta)^{1/2}, \quad (4.242)$$

is dependent on the pipe diameter. When $v_{TB} > v_s$, the nose of the Taylor bubble sweeps the smaller bubbles ahead of it. However, when $v_{TB} < v_s$, which is possible in smaller-diameter pipes, the rising smaller bubbles approach the back of the Taylor bubble, coalesce with it, increase its size, and ultimately cause a transition to slug flow.

Dispersed-Bubble Transition. When large bubbles are dispersed into small bubbles at high liquid rates, transition to slug flow is inhibited, even though the gas void fraction exceeds 0.25. For the transition to dispersed-bubble flow, Taitel *et al.*³⁰ proposed

$$v_m^{1.12} = 4.68d^{0.48} \left[\frac{g(\rho_L - \rho_g)}{\sigma_L} \right]^{0.5} \left(\frac{\sigma_L}{\rho_L} \right)^{0.6} \left(\frac{\rho_L}{\mu_L} \right)^{0.08} \quad (4.243)$$

When the gas void fraction exceeds 0.52, bubble coalescence cannot be prevented and transition to either slug, churn, or annular flow must occur.

Slug/Churn Transition. The Barnea and Brauner^{50,51} model predicts the slug/churn transition. They argued that the transition from slug to churn flow occurs when the liquid slug trailing a Taylor bubble attains the maximum possible void fraction of 0.52, as given by Eq. 4.243. In other words, this transition boundary is a locus of constant mixture velocity values, v_m , where the turbulent intensity is maintained at the same level as that in dispersed-bubble flow.

Annular-Flow Transition. The transition criterion given by Eq. 4.163 also is used in the Hasan and Kabir mechanistic model to predict the transition to annular flow. Eq. 4.163 suggests that this transition criterion is independent of the liquid flow rate.

Flow-Behavior Prediction. The total pressure gradient in two-phase flow can be written as the sum of the gravitation or hydrostatic head (dp/dL_{el}), friction (dp/dL_f) and acceleration (dp/dL_{acc}) components. Thus,

$$\begin{aligned} \left(\frac{dp}{dL}\right)_t &= \left(\frac{dp}{dL}\right)_{el} + \left(\frac{dp}{dL}\right)_f + \left(\frac{dp}{dL}\right)_{acc} \\ &= \rho_s g \sin \theta + \frac{f v_m^2 \rho_s}{2d} + \rho_s v_m \frac{dv_m}{dL}, \end{aligned} \quad (4.244)$$

where

$$\rho_s = \rho_g(1 - H_L) + \rho_L H_L. \quad (4.245)$$

In general, the acceleration component can be neglected during all but the annular-flow pattern. Eq. 4.245 suggests that an accurate estimation of the liquid holdup is essential when computing the elevation component. This component accounts for most of the pressure drop occurring in the bubble- and slug-flow patterns. Because of the different hydrodynamics in each flow pattern, estimations of holdup, H_L , in-situ mixture density, ρ_m , and friction factor, f , are made separately.

Bubble and Dispersed-Bubble Flow. In bubble and dispersed-bubble flow the expression for holdup, H_L , is

$$H_L = 1 - \frac{v_{sg}}{C_o v_m + v_s}, \quad (4.246)$$

where C_o and v_s are given by Eqs. 4.241 and 4.160, respectively. To estimate total pressure gradient, Eq. 4.244 can be used with the mixture density calculated from the liquid holdup estimated with Eq. 4.246. The friction component can be computed by treating the multiphase mixture as a homogeneous fluid. Friction factor, f , can be determined from the Moody diagram (Fig. 2.2) for a Reynolds number defined as

$$N_{Re_m} = \frac{\rho_L v_m d}{\mu_L}. \quad (4.247)$$

This was recommended by Govier and Aziz²³ because ρ_L/μ_L would not be too different from ρ_m/μ_m , and the contribution of the friction component to the total pressure gradient is very small.

Slug and Churn Flow. The drift-flux model of Eq. 4.246 also was applied in slug flow, but with different values for C_o and v_s given by $C_o = 1.2$ and

$$v_s = 0.35 \left(gd \frac{\rho_L - \rho_g}{\rho_L} \right)^{0.5} \sqrt{\sin \theta} (1 + \cos \theta)^{1.2}. \quad (4.248)$$

It was recommended that the equations developed for slug flow also be used for the churn-flow pattern. However, because of the chaotic flow nature that tends to make the gas concentration profile flat, it is suggested that a value of 1.15 be used for C_o rather than a value of 1.2 used for the slug-flow pattern. As in bubble flow, the total pressure gradient can be obtained by Eq. 4.244 by use of Eqs. 4.246 and 4.248. The estimation of the friction component presents some difficulty because some of the liquid flows downward in a film around the Taylor bubble while most of the liquid flows upward in the liquid slug. Wallis¹⁸ suggested that the wall shear stress around the vapor bubble be ignored. With this assumption, the friction pressure gradient becomes

$$\left(\frac{dp}{dL}\right)_f = \frac{f v_m^2 \rho_L H_L}{2d}. \quad (4.249)$$

The product $\rho_L H_L$ is very nearly equal to ρ_m for low-pressure systems, indicating the similarity in evaluating the friction terms in slug and bubble flow. The contribution of the friction component is no longer negligible but is still small (typically 10% of the total gradient). Acceleration, however, is small and can be neglected.

Annular Flow. In annular flow, it is appropriate to estimate the liquid holdup in the central core rather than for the entire pipe cross

section. The liquid holdup for the core, λ_{LC} , is given by Eq. 4.207. Steen and Wallis⁵² suggested that, when the liquid film is fully turbulent, the liquid entrainment can be obtained as a unique function of the critical vapor velocity from

$$\left\{ \begin{array}{l} F_E = 0.0055 v_{crit}^{2.86} \text{ if } v_{crit} < 4 \\ F_E = 0.857 \log_{10} v_{crit} - 0.20 \text{ if } v_{crit} > 4 \end{array} \right\}, \quad (4.250)$$

where v_{crit} is defined by Eq. 4.209.

In annular flow, fine liquid droplets flow in the gas core with a velocity the same as the gas phase while a thin liquid film creeps up the pipe wall. Thus, the friction pressure drop pertains to the gas interacting with the wavy liquid film. The friction pressure gradient, which is a large component of the total pressure gradient for annular flow, can be written as

$$\left(\frac{dp}{dL}\right)_f = \frac{f_C \rho_C}{2d} \left(\frac{v_{sg}}{1 - \lambda_{LC}} \right)^2, \quad (4.251)$$

where

$$f_C = 0.046 \left(\frac{\rho_g v_{sg} d}{\mu_g} \right)^{-0.2} (1 + 75 \lambda_{LC}) \quad (4.252)$$

and

$$\rho_C = \frac{v_{sg} \rho_g + v_{SL} \rho_L F_E}{v_{sg} + v_{SL} F_E}. \quad (4.253)$$

The liquid holdup in the core can be given by this simple equation from Wallis¹⁸

$$\lambda_{LC} = (1 + X^{0.8})^{-0.378}, \quad (4.254)$$

where X , the Lockhart and Martinelli³⁵ parameter, is defined in terms of the gas mass fraction, x_g , and fluid properties as

$$X = \left(\frac{1 - x_g}{x_g} \right)^{0.9} \sqrt{\frac{\rho_g}{\rho_L}} \left(\frac{\mu_L}{\mu_g} \right)^{0.1}. \quad (4.255)$$

In the case of annular flow, the gas void fraction is for the channel volume not occupied by the liquid film. Hence, the gas mass fraction calculation should include the entrained liquid droplets.

Example 4.10—Using the Hasan and Kabir Mechanistic Model, Calculate the Vertical, Multiphase-Flow Pressure Gradient for Example 3.2.

Given: $\epsilon = 0.00006 \text{ ft} = 1.83 \times 10^{-5} \text{ m}$, $d = 6.0 \text{ in.} = 0.1524 \text{ m}$, $v_{SL} = 3.97 \text{ ft/sec} = 1.208 \text{ m/s}$, $v_{sg} = 3.86 \text{ ft/sec} = 1.173 \text{ m/s}$, $\rho_L = 47.61 \text{ lbm/ft}^3 = 761.7 \text{ kg/m}^3$, $\rho_g = 5.88 \text{ lbm/ft}^3 = 94.1 \text{ kg/m}^3$, $\sigma_L = 8.41 \text{ dynes/cm} = 8.41 \times 10^{-3} \text{ kg/s}^2$, $\mu_L = 0.97 \text{ cp} = 0.97 \times 10^{-3} \text{ Pa} \cdot \text{s}$, $\mu_g = 0.016 \text{ cp} = 0.016 \times 10^{-3} \text{ Pa} \cdot \text{s}$.

Flow-Pattern Determination.

1. Check bubble/slur transition (Eq. 4.240):

$$\begin{aligned} v_s &= 1.53 \left[\frac{(9.81)(8.41 \times 10^{-3})(761.7 - 94.1)}{(761.7)^2} \right]^{0.25} \\ &= 0.151 \text{ m/s}, \end{aligned}$$

$$C_o = 1.2,$$

and

$$v_{sg_{B/S}} = \left(\frac{1}{4 - 1.2} \right) [(1.2)(1.208) + 0.151] = 0.572.$$

Because $v_{sg} > v_{sg_{B/S}}$, bubble flow does not exist.

TABLE 4.6—RANGE OF DATA IN TUFFP WELL DATA BANK²⁴

Source	Nominal Diameter (in.)	Oil Rate (STB/D)	Gas Rate (Mscf/D)	Oil Gravity (°API)
Old TUFFP Databank*	1 to 8	0 to 10,150	1.5 to 10,567	9.5 to 70.5
Govier and Fogarasi ⁵⁴	2 to 4	8 to 1,600	114 to 27,400	17 to 112
Asheim ⁶	2 ^{7/8} to 6	720 to 27,000	740 to 55,700	35 to 86
Chierici <i>et al.</i> ¹⁰	2 ^{7/8} to 5	0.3 to 69	6 to 27,914	8.3 to 46
Prudhoe Bay	5.5 to 7	600 to 23,000	200 to 110,000	24 to 86

*Includes data from Poettmann and Carpenter,¹ Fancher and Brown,³ Baxendell and Thomas,² Orkiszewski,⁸ Hagedorn,⁵⁵ Espanol,⁵⁶ Messulam,⁵⁷ Camacho,⁵⁸ and field data from several oil companies.

2. Check dispersed-bubble transition boundary (Eq. 4.243):

$$v_m^{1.12} = (4.68)(0.1524)^{0.48} \left[\frac{(9.81)(761.7 - 94.1)}{8.4 \times 10^{-3}} \right]^{0.5} \\ \times \left(\frac{8.41 \times 10^{-3}}{761.7} \right)^{0.6} \left(\frac{761.7}{0.97 \times 10^{-3}} \right)$$

or $v_{mDB} = 4.401 > 2.381$. Therefore, neither dispersed-bubble nor churn flow exist. The flow pattern is slug.

Slug-Flow Modeling.

For slug flow, $C_o = 1.2$.

1. Calculate slip velocity (Eq. 4.248):

$$v_s = 0.35 \left[(9.81)(0.1524) \frac{(761.7 - 94.1)}{761.7} \right]^{0.5} \\ \times \sqrt{\sin 90^\circ} (1 + \cos 90^\circ)^{1.2} \\ = 0.401 \text{ m/s.}$$

2. Calculate holdup (Eq. 4.246) and slip density (Eq. 4.245):

$$H_L = 1 - \frac{1.173}{(1.2)(2.38) + 0.401} = 0.64$$

and

$$\rho_s = (761.7)(0.64) + (94.1)(0.36) = 521.4 \text{ kg/m}^3.$$

3. Elevation component of pressure gradient:

From Eq. 4.244,

$$\left(\frac{dp}{dL} \right)_{el} = (521.4)(9.81) \sin 90^\circ = 5,115 \text{ Pa/m.}$$

4. Friction component of pressure gradient:

From Eq. 4.247,

$$N_{Re_{LS}} = \frac{(761.7)(2.381)(0.1524)}{(0.97 \times 10^{-3})} = 284,942.$$

Turbulent flow exists.

From Fig. 2.2,

$$\left. \begin{aligned} \epsilon/d &= 1.2 \times 10^{-4} \\ N_{Re_{LS}} &= 284,942 \end{aligned} \right\} \rightarrow f \approx 0.0166.$$

From Eq. 4.249,

$$\left(\frac{dp}{dL} \right)_f = \frac{(0.0166)(2.381)^2(761.7)(0.64)}{2(0.1524)} \\ = 150.5 \text{ Pa/m.}$$

5. Total pressure gradient:

$$\left(\frac{dp}{dL} \right)_t = 5,115 + 150.5 \\ = 5,265.5 \text{ Pa/m} \\ = 5.266 \text{ kPa/m} \\ = 0.233 \text{ psi/ft.}$$

4.3 Evaluation of Wellbore Pressure-Gradient-Prediction Methods

The pressure drop in a well can be calculated with the computing algorithm described in Sec. 3.7. This requires that the profile of the well is known, that a pressure-gradient-prediction method is specified, that sufficient information is available to predict pressure/volume/temperature (PVT) relationships, and that adequate information is available to calculate fluid temperatures as a function of depth. Each requirement is a potential source of error when calculating pressure drop.

A common error in deviated wells is to not use accurate well profiles in the marching algorithm. Many times the profile is unknown and vertical flow is incorrectly assumed.

Black-oil-model PVT calculations, which include the prediction of mass transfer and fluid physical properties of the gas and liquid phases, can be highly inaccurate under many real applications. For example, bubblepoint pressures calculated from different black-oil models can have errors in excess of 50%. Depending on the depths of wells, this can lead to serious errors in pressure-drop calculations. PVT property correlations often incorrectly predict the part of a well in which single-phase flow occurs. This in turn can lead to very contradictory results when evaluating pressure-gradient-prediction methods with different PVT correlations.

When using empirical correlations or mechanistic models to predict pressure gradient, another common source of errors is the frequent absence of reality checks, such as ensuring that the calculated liquid holdup always exceeds the no-slip holdup for upward flow. Correlations that have been modified normally include reality checks. Correlations that have not been modified, such as Duns and Ros,⁷ Mukherjee and Brill,¹² and Aziz *et al.*⁹ may be vulnerable to such programming inadequacies.

With this introduction, an evaluation of six commonly used correlations and two mechanistic models was performed by Ansari *et al.*^{24,53} The pressure-drop predictions from applying each correlation and model by use of the computing algorithm described in Sec. 3.7 were compared with measured data in a well databank developed at TUFFP. The databank contained 1,712 well cases with a wide range of data, as shown in Table 4.6.

4.3.1 Criteria for Comparison With Data. Evaluation of the correlations and models with the databank was based on these statistical parameters.

TABLE 4.7—RELATIVE PERFORMANCE FACTORS²⁴

	EDB	VW	DW	VNH	ANH	AB	AS	VS	SNH	VSNH	AAN
<i>n</i>	1,712	1,086	626	755	1,381	29	1,052	654	745	387	70
Ansari	0.700	1.121	1.378	0.081	0.000	0.143	1.295	1.461	0.112	0.142	0.000
HagBr	0.585	0.600	0.919	0.876	0.774	2.029	0.386	0.485	0.457	0.939	0.546
Aziz	1.312	1.108	2.085	0.803	1.062	0.262	1.798	1.764	1.314	1.486	0.214
DunsRos	1.719	1.678	1.678	1.711	1.792	1.128	2.056	2.028	1.852	2.296	1.213
HasKa	1.940	2.005	2.201	1.836	1.780	0.009	2.575	2.590	2.044	1.998	1.043
BegBr	2.982	2.908	3.445	3.321	3.414	2.828	2.883	2.595	3.261	3.282	1.972
Orkis	4.284	5.273	2.322	5.838	4.688	1.226	3.128	3.318	3.551	4.403	6.000
MukBr	4.883	4.647	6.000	3.909	4.601	4.463	5.343	5.140	4.977	4.683	1.516

EDB = entire data bank; VW = vertical well cases; DW = deviated well cases; VNH = vertical cases without Hagedorn and Brown data; ANH = all well cases without Hagedorn and Brown data; AB = all well cases with 75% bubble flow; AS = all well cases with 100% slug flow; VS = vertical well cases with 100% slug flow; SNH = all well cases with 100% annular flow; VSNH = all vertical well cases with 100% slug flow without Hagedorn and Brown data; AAN = all well cases with 100% annular flow; Ansari = Ansari *et al.* model; HagBr = Hagedorn and Brown correlation; Aziz = Aziz *et al.* correlation; DunsRos = Duns and Ros correlation; HasKa = Hasan and Kabir model; BegBr = Beggs and Brill correlation; Orkis = Orkiszewski correlation; and MukBr = Mukherjee and Brill correlation.

$$E_1 = \left(\frac{1}{n} \sum_{i=1}^n e_{ri} \right) \times 100, \quad (4.256)$$

where

$$e_{ri} = \frac{\Delta p_{icalc} - \Delta p_{imeas}}{\Delta p_{imeas}}. \quad (4.257)$$

E_1 indicates the overall trend of the performance relative to the measured pressure drop.

$$E_2 = \left(\frac{1}{n} \sum_{i=1}^n |e_{ri}| \right) \times 100. \quad (4.258)$$

E_2 indicates an average of how large the errors are.

$$E_3 = \sqrt{\frac{(e_{ri} - E_1)^2}{n-1}}. \quad (4.259)$$

E_3 indicates the degree to which the errors are scattered about their average percent error.

$$E_4 = \left(\frac{1}{n} \sum_{i=1}^n e_i \right), \quad (4.260)$$

where

$$e_i = \Delta p_{icalc} - \Delta p_{imeas}. \quad (4.261)$$

E_4 indicates the overall trend independent of the measured pressure drop.

$$E_5 = \sqrt{\frac{(e_i - E_4)^2}{n-1}}. \quad (4.262)$$

E_5 also is independent of the measured pressure drop and indicates the magnitude of the average error.

$$E_6 = \sqrt{\frac{(e_i - E_4)^2}{n-1}}. \quad (4.263)$$

E_6 indicates the scattering of the errors about their average error.

4.3.2 Comparison Method. The correlations and models used for the comparison were a modified Hagedorn and Brown,⁴ Duns and Ros,⁷ Orkiszewski⁸ with the Triggia* correction, Beggs and Brill¹¹ with the Payne *et al.*²² correction, Mukherjee and Brill,¹² Aziz *et al.*,⁹ Ansari *et al.*,²⁴ and Hasan and Kabir.^{25,26} The evaluation was accomplished by a comparison of the statistical parameters. The

evaluation also involved the use of a relative performance factor F_{rp} , which was defined by

$$\begin{aligned} F_{rp} = & \frac{|E_1| - |E_{1\min}|}{|E_{1\max}| - |E_{1\min}|} + \frac{E_2 - E_{2\min}}{E_{2\max} - E_{2\min}} \\ & + \frac{E_3 - E_{3\min}}{E_{3\max} - E_{3\min}} + \frac{|E_4| - |E_{4\min}|}{|E_{4\max}| - |E_{4\min}|} \\ & + \frac{E_5 - E_{5\min}}{E_{5\max} - E_{5\min}} + \frac{E_6 - E_{6\min}}{E_{6\max} - E_{6\min}}. \quad (4.264) \end{aligned}$$

The minimum and maximum possible values for F_{rp} are 0 and 6, indicating the best and worst performances, respectively. Table 4.7 gives an evaluation of the methods in terms of F_{rp} with the best value for each column being boldfaced.

4.3.3 Overall Evaluation. An overall evaluation first was performed by use of the entire databank, resulting in Col. 1 of Table 4.7. The performance also was checked for vertical well cases only (Col. 2) and for deviated well cases only (Col. 3). To make the evaluation unbiased with respect to the methods, a second database was created that excluded 331 sets of data from the Hagedorn and Brown study. For this reduced databank, Col. 4 shows the results for all vertical well cases. Col. 5 shows the results for combined vertical and deviated well cases.

4.3.4 Evaluation of Individual Flow-Pattern Models. Performance of individual flow-pattern models is based on sets of data that are dominant in one particular flow pattern, as predicted by the transitions described by Ansari *et al.*²⁴ To have an adequate number of cases for the bubble-flow-pattern database, cases with bubble flow predicted over 75% of the well length were considered. These results are shown in Col. 6. Cols. 7 through 10 give results for cases predicted to have slug flow over 100% of the well length. The cases used for Cols. 7 and 8 were selected from the entire databank, whereas the cases used for Cols. 9 and 10 were selected from the reduced databank. Col. 11 gives results for those cases in the total databank that were predicted to be in annular flow for 100% of the well length. The performance of the Ansari *et al.* model for annular flow is significantly better than all other methods.

Ansari *et al.* concluded that the overall performance of their model was better than all other methods. However, the overall performances of the Hagedorn and Brown, Aziz *et al.*, Duns and Ros, and Hasan and Kabir methods are comparable. For the latter three methods, this can be attributed to the use of flow mechanisms. The excellent performance of the Hagedorn and Brown correlation can be explained only by the extensive data that were used in its development

*Personal communication with A. Triggia, Petrobras S.A., Rio de Janeiro (1984).

and modifications that have been made to the correlation. In fact, when the data without Hagedorn and Brown are considered, the Ansari *et al.* model performed best (Cols. 4 and 5). Although the Hagedorn and Brown correlation performed better than the others for deviated wells, none gave satisfactory results (Col. 3).

Only 29 cases satisfied the bubble-flow criteria. The Hasan and Kabir model gave the best predictions for these cases. When the Hagedorn and Brown data are included (Cols. 7 and 8), their method exceeds the performance of the Ansari *et al.* slug-flow model. The Ansari *et al.* model performed best when Hagedorn and Brown data are excluded for both all well cases and all vertical well cases (Cols. 9 and 10).

For annular flow, the Ansari *et al.* model is significantly better than all other methods (Col. 11).

Pucknell *et al.*⁵⁹ compared predicted pressure drops with measured pressure drops for 246 data sets collected from eight fields, including a gas and gas-condensate field. None of these data was used in the development of the pressure-gradient-prediction methods. They reached four specific conclusions.

- Despite the development of new mechanistic models, no single method gives accurate predictions of bottomhole flowing pressures in all fields.

- Traditional methods to predict pressure drops, such as that of Duns and Ros, give good results in oil wells, but can give very poor results in gas wells. The new mechanistic models give reasonable results in both oil and gas wells.

- Overall, the Ansari *et al.* mechanistic model gives the best results of all the methods evaluated. In oil wells, 62% of the pressure drops were predicted with errors of less than $\pm 6\%$. In gas wells, 68% of the pressure drops were calculated within $\pm 15\%$. These conclusions were derived from deviated wells with larger tubing sizes, typical of North Sea wells.

- The Ansari *et al.* and Hasan and Kabir models behave no better than many of the traditional methods in predicting erroneous discontinuities. Reliable convergence is desirable in any multiphase-flow model. The Ansari *et al.* model performed only as well as existing methods, but the Hasan and Kabir model performed somewhat better.

Salim and Stanislav⁶⁰ compared methods that describe the flow of gas/liquid mixture in wells with more than 189 data sets collected from five different sources. Most of their field data were taken from wells that exhibited the annular/mist-flow pattern. They concluded that the empirical correlations by Orkiszewski and Duns and Ros appeared to be less efficient than mechanistic models.

Clearly, evaluation of pressure-gradient-prediction methods to calculate pressure drop in wells is a difficult task. In this context, we strongly recommend that users exercise careful judgment based on evaluation of actual measured data to select a particular method.

4.4 Pressure-Gradient Prediction in Annuli

In the past, correlations were the most common procedure to predict liquid holdup and pressure gradient for multiphase flow in an annulus. These correlations were developed empirically from experimental data. Most correlations make predictions without taking into account the existing flow pattern. The predictions either have applied correlations originally developed for flow in pipes by use of the hydraulic diameter concept or have applied correlations developed from data obtained from two-phase flow in an annulus. Baxendell,⁶¹ Gaither *et al.*,⁶² Angel and Welchon,⁶³ and Winkler⁶⁴ presented empirical correlations for the prediction of pressure gradients in annuli. Except for the Winkler correlation, which primarily is for slug-flow conditions, all are flow-pattern independent. Ros⁶⁵ proposed a method to predict both liquid holdup and pressure gradient on the basis of dimensional analysis and experimental data. None of these empirical correlations can be considered general or comprehensive, nor do they capture the complex flow behavior that occurs when gas and liquid flow simultaneously in an annulus.

The use of mechanistic models to predict multiphase-flow behavior in annuli is a recent trend, similar to their use in predicting regular pipe flow. Caetano *et al.*^{66,67} and Hasan and Kabir⁶⁸ presented mechanistic models to predict flow behavior when gas and liquid si-

multaneously flow upward in an annulus. Each is described in following sections.

4.4.1 Caetano *et al.* Method. Caetano *et al.*^{66,67} conducted a combined experimental and theoretical study of upward, gas/liquid, two-phase flow in vertical concentric and fully eccentric annuli. The experimental part of the study involved flowing air with either water or kerosene up a vertical annulus. The experimental study included the establishment of flow-pattern definitions, determination of flow-pattern-transition boundaries, development of flow-pattern maps, and measurements of average volumetric liquid holdup and average pressure gradient for several tests in each flow pattern. The theoretical part included development of flow-pattern-prediction models and the formulation of models for each flow pattern to predict average volumetric liquid holdup and pressure gradient. Caetano *et al.* used Fanning friction factors throughout the study. They are preserved here to retain consistency with the original work.

Flow-Pattern-Transition Prediction. The models proposed to predict flow-pattern transitions in an annulus are similar to those proposed by Ansari *et al.*²⁴ for circular pipes.

Bubble-Slug-Flow Transition. The minimum equiperiphery diameter for which bubble flow occurs is

$$d_{EP} = 19.7 \sqrt{\frac{(\rho_L - \rho_g) \sigma_L}{g \rho_L^2}}, \quad (4.265)$$

where d_{EP} is the equiperiphery diameter defined by

$$d_{EP} = d_c + d_t \quad (4.266)$$

and d_c and d_t are the inside casing diameter and the outside tubing diameter, respectively.

For equiperiphery diameters larger than this, transition to slug flow was found experimentally to occur at average gas void-fraction values of 0.20 for flow through a concentric annulus and 0.15 for flow through a fully eccentric annulus. Thus, the Taitel *et al.*³⁰ model was modified for the bubble/slug transition in an annulus by use of values of the gas void fraction measured at this transition. The resulting equations for the transition then can be expressed by

$$v_{sg} = \frac{v_{SL}}{4.0} + 0.306 \left[\frac{(\rho_L - \rho_g) g \sigma_L}{\rho_L^2} \right]^{1/4} \quad (4.267)$$

and

$$v_{sg} = \frac{v_{SL}}{5.67} + 0.230 \left[\frac{(\rho_L - \rho_g) g \sigma_L}{\rho_L^2} \right]^{1/4} \quad (4.268)$$

Eqs. 4.267 and 4.268 constitute the criteria for the bubble/slug transition boundary at low liquid flow rates in concentric and fully eccentric annuli, respectively.

Transition to Dispersed-Bubble Flow. At high superficial liquid velocities, the Barnea³² criterion for transition to dispersed-bubble flow was modified with the hydraulic-diameter concept. The transition from either bubble or slug flow to dispersed-bubble flow then becomes

$$2 \left[\frac{0.4 \sigma_L}{(\rho_L - \rho_g) g} \right]^{1/2} \left(\frac{\rho_L}{\sigma_L} \right)^{3/5} \left(\frac{2f}{d_h} \right)^{2/5} (v_{SL} + v_{sg})^{1.2} \\ = 0.725 + 4.15 \left(\frac{v_{sg}}{v_{sg} + v_{SL}} \right)^{0.5}, \quad (4.269)$$

where the hydraulic diameter is defined by

$$d_h = d_c - d_t. \quad (4.270)$$

f' is the Fanning friction factor evaluated for the homogenous mixture flowing in either the concentric or eccentric annulus, as given by Eqs. 2.56 and 2.57, respectively.

For a uniform bubble-size distribution and a cubic lattice packing, 0.52 is the maximum allowable gas void fraction under dispersed-bubble conditions. Higher values of void fraction will cause transition to slug flow. Applying this criterion to slip flow yields this transition boundary to dispersed-bubble flow for gas void fractions of 0.52.

$$v_{sg} = 1.083v_{sl} + 0.796 \left[\frac{(\rho_L - \rho_g)g\sigma_L}{\rho_L^2} \right]^{1/4}. \quad (4.271)$$

Transition to Annular Flow. For pipe flow, Taitel *et al.*³⁰ suggested that the mechanism causing transition to annular flow is related to the minimum gas velocity necessary to transport upward the largest liquid droplet entrained in the gas core. The required minimum gas velocity is determined from a balance between gravity and drag forces acting on the largest stable droplet. The transition is given by Eq. 4.163.

Flow-Behavior Prediction. Mechanistic models were developed to predict flow behavior for all flow patterns in annuli configurations. This includes bubble, dispersed bubble, slug, and annular flow. Each model is presented.

Bubble Flow. The basic concept for modeling the bubble-flow pattern is the slippage that takes place between the gas and the liquid phases, given by

$$v_s = v_g - v_L = \frac{v_{sl}}{H_L} - \frac{v_{sg}}{1 - H_L}. \quad (4.272)$$

Eq. 4.177 gave the rise velocity of a single gas bubble in a bubble-swarm medium. The bubble-swarm index, $n' = 0.5$, determined experimentally and used in the model, agrees with the value used by Ansari *et al.*²⁴

Combining Eqs. 4.272 and 4.177 and rearranging yields

$$\frac{H_L^{n'+2} - H_L^{n'+1} + \frac{(v_{sl} + v_{sg})H_L}{1.53 \left[\frac{(\rho_L - \rho_g)g\sigma_L}{\rho_L^2} \right]^{1/4}}}{\frac{v_{sl}}{1.53 \left[\frac{(\rho_L - \rho_g)g\sigma_L}{\rho_L^2} \right]^{1/4}}} = 0, \quad (4.273)$$

which is an implicit equation for the liquid holdup, H_L .

The total pressure gradient for steady-state flow consists of three components,

$$\left(\frac{dp}{dL} \right) = \left(\frac{dp}{dL} \right)_{el} + \left(\frac{dp}{dL} \right)_f + \left(\frac{dp}{dL} \right)_{acc}. \quad (4.274)$$

These components are referred to as elevation, friction, and convective acceleration, respectively.

Successful modeling of two-phase-flow pressure gradient requires analyzing each pressure-gradient component as a function of the existing flow pattern. The elevation component is evaluated rigorously through the slip density, ρ_s , based on the in-situ liquid holdup. Thus, the elevation component is

$$\left(\frac{dp}{dL} \right)_{el} = \rho_{TP}g, \quad (4.275)$$

where

$$\rho_{TP} = \rho_L H_L + \rho_g(1 - H_L) \quad (4.276)$$

and the in-situ liquid holdup, H_L , is given by Eq. 4.273.

The acceleration pressure gradient in bubble flow is normally negligible. Thus,

$$\left(\frac{dp}{dL} \right)_{acc} = 0. \quad (4.277)$$

The friction-pressure-gradient component for annuli configurations is given by

$$\left(\frac{dp}{dL} \right)_f = \frac{4f'}{d_h} \rho_{TP} \frac{v_m^2}{2}, \quad (4.278)$$

where the mixture velocity, v_m , is

$$v_m = v_{sl} + v_{sg}. \quad (4.279)$$

The Fanning friction factor, f' , is determined by the method presented in Chap. 2 for annuli configurations. The Reynolds number for bubble flow is defined by

$$N_{Re_{TP}} = \frac{\rho_{TP} v_m d_h}{\mu_{TP}}. \quad (4.280)$$

The mixture viscosity, μ_{TP} , is

$$\mu_{TP} = \mu_L \lambda_L + \mu_g(1 - \lambda_L), \quad (4.281)$$

where the no-slip liquid holdup, λ_L , is given by

$$\lambda_L = \frac{v_{sl}}{v_{sl} + v_{sg}}. \quad (4.282)$$

Combining Eqs. 4.274, 4.275, 4.277, and 4.278, the total pressure gradient for bubble flow is

$$\left(\frac{dp}{dL} \right) = \rho_{TP}g + \frac{4f'}{d_h} \rho_{TP} \frac{v_m^2}{2}. \quad (4.283)$$

Dispersed-Bubble Flow. The model for dispersed-bubble flow is based on the no-slip, homogeneous nature of this flow pattern. Therefore, Eq. 4.283 also can be used for dispersed-bubble flow by replacing liquid holdup in Eq. 4.276 with no-slip liquid holdup, λ_L , as given by Eq. 4.282.

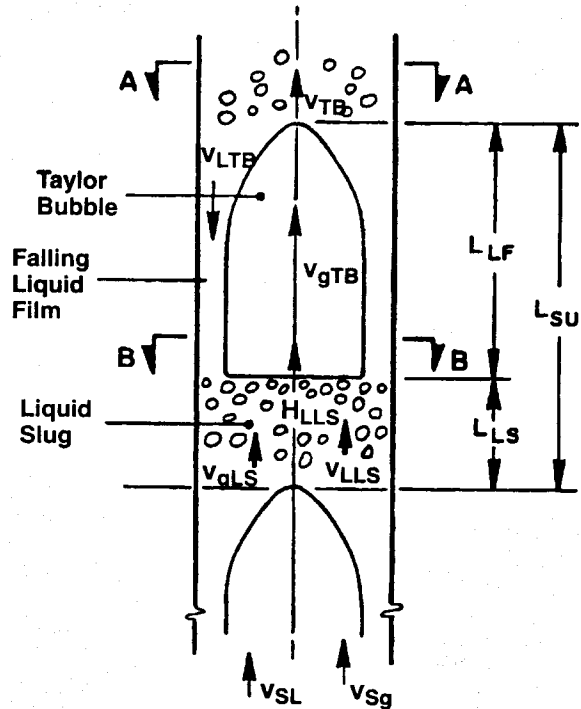
Slug Flow. Caetano *et al.* developed a hydrodynamic model for slug flow in annuli that considers two possible configurations. The first configuration is for fully developed Taylor-bubble flow and occurs when the bubble cap length is negligible compared with the total liquid film length. Under this condition, the film thickness reaches a constant terminal value, which can be used as the average thickness for the entire film zone. The second configuration is for a developing Taylor bubble, which consists of only a cap bubble. For this case, the film thickness varies continuously along the film zone and cannot be assumed constant.

The model developed for the case of a constant film thickness constitutes a simplified form of the model developed by Fernandes *et al.*³⁹ for upward vertical pipe flow. Caetano *et al.* extended the model using characteristics observed for slug flow in annuli. For the case of a cap bubble with varying film thickness, the model follows the approach of McQuillan and Whalley,⁴⁴ who studied the transition from bubble to slug flow. However, as discussed previously, pipes encountered in producing wells are so long that to treat the entire slug-flow region as fully developed flow should introduce only minor errors. Therefore, a model for the developing Taylor-bubble region is not included in this monograph.

Fig. 4.25 shows the physical model for fully developed slug flow. The figure shows a slug unit, consisting of a Taylor-bubble and a film region, followed by a liquid slug. Also given are the lengths, velocities, and holdup values corresponding to the different regions of the slug unit. Chap. 3 gave a descriptive representation of slug flow in an annulus.

Taylor-Bubble Translational Velocity. Caetano *et al.* found that the rise velocity of a Taylor bubble can be predicted by using the equiperipheral-diameter concept. Thus, the translational velocity of the Taylor bubble is

$$v_{TB} = 1.2v_M + 0.345\sqrt{g(d_c + d_i)}. \quad (4.284)$$



- v_{SL}** = superficial liquid velocity
 v_{Sg} = superficial gas velocity
 v_{LLS} = in-situ liquid velocity in liquid slug
 v_{gLS} = in-situ gas velocity in liquid slug
 v_{LTB} = in-situ liquid velocity in liquid film
 v_{gTB} = in-situ gas velocity in Taylor bubble
 v_{TB} = Taylor-bubble transitional velocity
 H_{LLS} = liquid holdup in liquid slug
 L_{LS} = length of liquid slug
 L_{LF} = length of liquid film
 L_{SU} = length of slug unit

Fig. 4.25—Fully developed slug flow.⁶⁷

Mass Balance in Slug and Film Zone. A mass balance on the liquid phase between Planes A-A and B-B of Fig. 4.25 yields

$$(v_{TB} - v_{LLS})H_{LLS} = (v_{TB} + v_{LTB})H_{LTB}, \quad \dots \quad (4.285)$$

where v_{LTB} , the in-situ liquid velocity in the film surrounding the Taylor bubble, is considered positive for downward flow. H_{LTB} is the liquid holdup at a cross section that contains the terminal film thickness.

Similarly, a mass balance for the gas phase yields

$$(v_{TB} - v_{gLS})(1 - H_{LLS}) = (v_{TB} + v_{gTB})(1 - H_{LTB}). \quad \dots \quad (4.286)$$

Liquid-Slug Zone. The liquid and gas phases in the liquid-slug zone are assumed to behave like bubble flow. Following Barnea and Brauner,⁵⁰ Caetano *et al.* proposed that the liquid holdup in the slug zone can be determined from the liquid holdup occurring at the transition boundary between bubble and slug flow. They assumed that the liquid holdup at the bubble/slug-transition boundary was constant. Therefore, the holdup in the liquid slug also is constant and has the same value as at the transition conditions. Thus, for a concentric annulus the liquid holdup in the liquid-slug zone is $H_{LLS} = 0.80$. Similarly, for a fully eccentric annulus, $H_{LLS} = 0.85$.

Slippage takes place in the liquid-slug zone as the bubbles rise through the liquid phase. The slip velocity can be approximated by the bubble-rise velocity in a bubble swarm as previously given by Eq. 4.177.

Because the total volumetric flow rate is constant at any section in the liquid slug, a mass balance for the liquid-slug region yields

$$(v_{SL} + v_{Sg})A = v_{LLS}H_{LLS}A + v_{gLS}(1 - H_{LLS})A, \quad \dots \quad (4.287)$$

where the flow area for an annulus is

$$A = \frac{\pi}{4}(d_c^2 - d_i^2). \quad \dots \quad (4.288)$$

Combining Eqs. 4.177 and 4.287, the in-situ liquid velocity in the liquid-slug zone becomes

$$v_{LLS} = (v_{SL} + v_{Sg}) - 1.53 \left[\frac{(\rho_L - \rho_g)g\sigma_L}{\rho_L^2} \right]^{1/2} (H_{LL})^{1/2} (1 - H_{LLS}). \quad \dots \quad (4.289)$$

Overall Mass Balances. The flow of gas and liquid within a slug unit was assumed previously to be incompressible. Thus, mass and volume balances are equivalent. An overall volume balance on the liquid phase yields

$$v_{SL} = v_{LLS}H_{LLS}\frac{L_{LS}}{L_{SU}} - v_{LTB}H_{LTB}\frac{L_{LF}}{L_{SU}}, \quad \dots \quad (4.290)$$

where the slug-unit length, L_{SU} , is

$$L_{SU} = L_{LF} + L_{LS}. \quad \dots \quad (4.291)$$

Combining Eqs. 4.290 and 4.291 yields

$$\frac{L_{LS}}{L_{SU}} = \frac{v_{SL} + v_{LTB}H_{LTB}}{v_{LLS}H_{LLS} + v_{LTB}H_{LTB}}. \quad \dots \quad (4.292)$$

A similar procedure can be applied for the gas phase. Because gas in the liquid slug and in the Taylor bubble are both flowing upward, this yields

$$\frac{L_{LS}}{L_{SU}} = \frac{v_{Sg} + (1 - H_{LTB})v_{gTB}}{(1 - H_{LLS})v_{gLS} + (1 - H_{LTB})v_{gTB}}. \quad \dots \quad (4.293)$$

Liquid-Film Zone. The liquid film flowing downward and surrounding the Taylor bubble can be considered as a free-falling film. The free-falling film is assumed to have a thickness and flow-rate relationship at the bottom of the Taylor bubble identical to that for a falling film on the surface of a vertical plane or cylinder. This situation is expected to be valid when the entry region used to develop the velocity profile is less than the length of the film. The relationship between the film thickness and the film velocity for this case is given by

$$v_{LTB} = \frac{\delta^{(1-C_M)/C_M}}{\left\{ C_K \left[\frac{\mu_L^2}{g(\rho_L - \rho_g)\rho_L} \right]^{1/3} \right\}^{1/C_M}} \frac{\mu_L}{4\rho_L}. \quad \dots \quad (4.294)$$

The indices C_K and C_M depend on the flow regime in the film zone. The Reynolds number associated with the liquid-film flow is

$$N_{Re_{LTB}} = \frac{4\rho_L v_{LTB} \delta}{\mu_L}. \quad \dots \quad (4.295)$$

For laminar flow, $N_{Re_{LTB}} < 1,000$, the indices C_K and C_M were analytically determined by Wallis¹⁸ to be 0.9086 and 1/3, respectively. For turbulent flow, $N_{Re_{LTB}} > 1,000$, Fernandes *et al.*³⁹ recommended using $C_K = 0.0682$ and $C_M = 2/3$. Brotz⁴¹ determined these values experimentally.

For a fully developed Taylor bubble, where the film reaches a terminal constant thickness, the liquid holdup in the film zone can be determined from the flow geometry and the film thickness, δ ,

$$H_{LTB} = \frac{4\delta(d_c - \delta)}{d_c^2 - d_i^2}. \quad \dots \quad (4.296)$$

Average Liquid Holdup. The slug-unit average liquid holdup, H_{LSU} , can be determined as

$$H_{LSU} = \left(\frac{L_{LS}}{L_{SU}} \right) H_{LLS} + \left(1 - \frac{L_{LS}}{L_{SU}} \right) H_{LTB}, \quad \dots \dots \dots \quad (4.297)$$

where L_{LS}/L_{SU} is determined from Eq. 4.292 or Eq. 4.293, and H_{LTB} can be determined from Eq. 4.296 for a fully developed Taylor bubble. An iterative procedure on the film thickness, δ , is required.

Pressure Gradient. Because Caetano *et al.* assumed the Taylor bubble to be a constant pressure region, the pressure gradient that occurs in the Taylor bubble and film zone is neglected. Thus, all the pressure gradient for an entire slug unit is assumed to occur in the liquid-slug zone. The pressure-gradient components are determined for the liquid-slug zone and then averaged over the entire slug unit length.

The elevation pressure-gradient component for the slug unit is calculated through the slip density as

$$\left(\frac{dp}{dL} \right)_{el} = \rho_{LS} g \left(\frac{L_{LS}}{L_{SU}} \right), \quad \dots \dots \dots \quad (4.298)$$

where the slip density for the gas/liquid mixture in the liquid slug is

$$\rho_{LS} = \rho_L H_{LLS} + \rho_g (1 - H_{LLS}). \quad \dots \dots \dots \quad (4.299)$$

The acceleration pressure-gradient component is related to the amount of energy required to accelerate the liquid film, which is initially flowing downward, to the existing upward in-situ liquid velocity in the liquid slug.

$$\left(\frac{dp}{dL} \right)_{acc} = \rho_L \frac{H_{LTB}}{L_{SU}} (v_{LTB} + v_{TB})(v_{LTB} + v_{LLS}). \quad \dots \dots \dots \quad (4.300)$$

For a fully developed Taylor bubble, H_{LTB} and v_{LTB} are the average liquid holdup and film velocity in the entire film zone, respectively.

The friction pressure gradient is obtained from

$$\left(\frac{dp}{dL} \right)_f = \frac{2f'}{d_h} \rho_{LS} (v_{sg} + v_{sl})^2 \left(\frac{L_{LS}}{L_{SU}} \right), \quad \dots \dots \dots \quad (4.301)$$

where the Fanning friction factor, f' , is determined by the method presented in Chap. 2. The corresponding Reynolds number for the slug body is determined by Eq. 4.280, where ρ_{TP} is replaced by ρ_{LS} , the slug-body slip density given by Eq. 4.299.

The total pressure gradient for the slug-flow pattern then can be expressed by combining Eqs. 4.298 through 4.301 to obtain

$$\begin{aligned} \left(\frac{dp}{dL} \right)_T &= \left[\frac{2f'}{d_h} \rho_{LS} (v_{sg} + v_{sl})^2 L_{LS} + \rho_{LS} g L_{LS} \right. \\ &\quad \left. + \rho_L H_{LTB} (v_{LTB} + v_{TB})(v_{LTB} + v_{LLS}) \right] \frac{1}{L_{SU}}. \end{aligned} \quad \dots \dots \dots \quad (4.302)$$

Annular Flow. Fig. 4.26 gives a schematic description of annular flow in a concentric annulus. The model is based on equilibrium fully developed flow. The phases are assumed to be incompressible. The two liquid films are assumed to have uniform thickness, but with different values. The gas and liquid droplets flowing in the annulus core are assumed to flow as a homogeneous mixture with the same velocity.

Linear Momentum Equations. The conservation of linear momentum for the outer (casing) liquid film yields

$$\left(\frac{dp}{dL} \right)_{cf} + \tau_c \frac{S_c}{A_{cf}} - \tau_{ci} \frac{S_{ci}}{A_{cf}} + \rho_L g = 0. \quad \dots \dots \dots \quad (4.303)$$

In this equation, $(dp/dL)_{cf}$ is the total pressure gradient for the casing liquid film. τ_c and τ_{ci} are the shear stresses at the casing wall and liquid film core-mixture interface, respectively. S_c and S_{ci} are the wetted

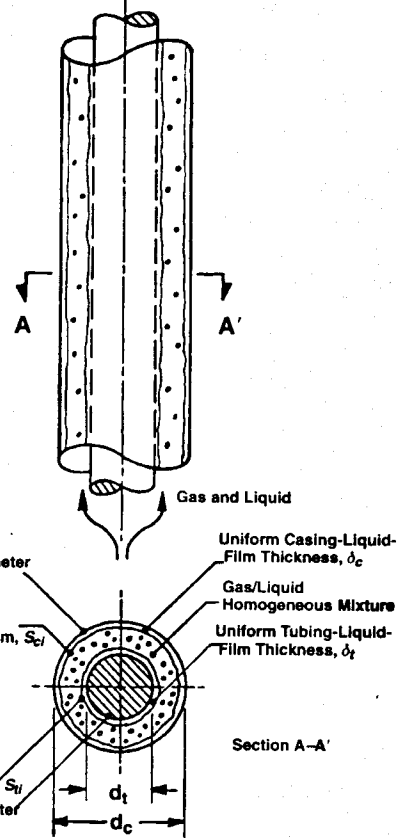


Fig. 4.26—Annular flow in concentric annulus.⁶⁷

liquid perimeters on the casing wall and liquid film core-mixture interface, respectively. A_{cf} is the total area of the casing liquid film.

Similarly, a linear momentum balance for the inner (tubing) film yields

$$\left(\frac{dp}{dL} \right)_f + \tau_i \frac{S_t}{A_{tf}} - \tau_{ii} \frac{S_{ti}}{A_{tf}} + \rho_L g = 0, \quad \dots \dots \dots \quad (4.304)$$

where all the terms have the same meaning as given for similar terms in Eq. 4.303.

A linear momentum balance for the gas/droplets mixture flowing in the core of the annulus yields

$$\left(\frac{dp}{dL} \right)_C + \tau_{ci} \frac{S_{ci}}{A_C} - \tau_{ii} \frac{S_{ti}}{A_C} + \rho_C g = 0, \quad \dots \dots \dots \quad (4.305)$$

where $(dp/dL)_C$ is the total pressure gradient for the mixture in the core, ρ_C is the density of the mixture in the core, and A_C is the area of the core occupied by the mixture.

The gas/liquid interfaces are considered stable; hence, this equilibrium condition exists.

$$\left(\frac{dp}{dL} \right)_{cf} = \left(\frac{dp}{dL} \right)_f = \left(\frac{dp}{dL} \right)_C \quad \dots \dots \dots \quad (4.306)$$

With this equilibrium condition and the linear momentum equations given by Eqs. 4.303 through 4.305, two combined-momentum equations can be written.

$$\begin{aligned} -\tau_c \frac{S_c}{A_{cf}} + \tau_{ci} \frac{S_{ci}}{A_{cf}} + \tau_{ci} \frac{S_{ci}}{A_C} \\ + \tau_{ii} \frac{S_{ti}}{A_C} - (\rho_L - \rho_C)g = 0 \end{aligned} \quad \dots \dots \dots \quad (4.307)$$

and

$$-\tau_i \frac{S_t}{A_{tf}} + \tau_u \frac{S_u}{A_{tf}} + \tau_{ci} \frac{S_{ci}}{A_C} + \tau_u \frac{S_u}{A_C} - (\rho_L - \rho_C)g = 0. \quad (4.308)$$

On the basis of the annulus geometry given in Fig. 4.26 and because the films are considered uniform in thickness, geometrical relationships for the relevant dimensions can be written. The casing-liquid-film area, the tubing-liquid-film area, and the core area for the mixture are, respectively,

$$A_{cf} = \pi \delta_c (d_c - \delta_c), \quad (4.309)$$

$$A_{tf} = \pi \delta_t (d_t + \delta_t), \quad (4.310)$$

and

$$A_C = \frac{\pi}{4} [d_c^2 - d_t^2 - 4\delta_c(d_c - \delta_c) - 4\delta_t(d_t + \delta_t)], \quad (4.311)$$

where δ_c and δ_t = casing-liquid-film thickness and tubing-liquid-film thickness, respectively.

The perimeters associated with the casing-liquid film and tubing-liquid film, for both the wall and interface sides, are

$$S_c = \pi d_c, \quad (4.312)$$

$$S_{ci} = \pi(d_c - 2\delta_c), \quad (4.313)$$

$$S_t = \pi d_t, \quad (4.314)$$

and

$$S_u = \pi(d_t + 2\delta_t). \quad (4.315)$$

By applying the hydraulic-diameter concept to the casing-liquid film, tubing-liquid film, and core and with Eqs. 4.309 through 4.315, the hydraulic diameters associated with each region can be written as

$$d_{ch} = 4\delta_c \left(1 - \frac{\delta_c}{d_c}\right), \quad (4.316)$$

$$d_{gh} = 4\delta_t \left(1 + \frac{\delta_t}{d_t}\right), \quad (4.317)$$

and

$$d_{ch} = \frac{[d_c^2 - d_t^2 - 4\delta_c(d_c - \delta_c) - 4\delta_t(d_t + \delta_t)]}{(d_c - 2\delta_c) + (d_t + 2\delta_t)}. \quad (4.318)$$

The wall shear-stress terms are given by

$$\tau = f' \rho \frac{v^2}{2}, \quad (4.319)$$

where τ is the respective wall shear stress, ρ is the density for the phase which wets the wall, v is the in-situ average phase velocity, and f' is the associated Fanning friction factor, which is evaluated by a Blasius-type expression given by

$$f' = CN_{Re}^n, \quad (4.320)$$

where $n = -1$ for laminar flow and $n = -0.25$ for turbulent flow. The coefficient, C , is evaluated by taking into account the annulus-configuration geometry described in Chap. 2. The Reynolds number in Eq. 4.320 uses either d_{ch} or d_{gh} , depending on the wall shear stress being evaluated.

Neglecting the liquid film velocities in comparison with the core velocity, the interfacial shear stress is approximated by

$$\tau_i = f'_i \rho_C \frac{v_c^2}{2}, \quad (4.321)$$

where τ_i = interfacial shear stress, v_c = in-situ mixture velocity in the core, ρ_C = mixture density in the core, and f'_i = Fanning friction factor associated with the interface. The mixture density and velocity were defined as

$$\rho_C = \rho_L H_{LC} + \rho_g (1 - H_{LC}) \quad (4.322)$$

and

$$v_c = v_{sc} \frac{A}{A_C}, \quad (4.323)$$

where H_{LC} and v_{sc} are given by Eq. 4.332 and Eq. 4.338, respectively; A_C is given in Eq. 4.311; and A = annulus cross section. For flow in an annulus, Caetano *et al.* modified the Wallis interfacial-friction-factor correlation for thin films or high entrainment fractions in annular vertical flow, given by Eqs. 4.220 and 4.221. The resulting casing-film-interface and tubing-film-interface friction factors are, respectively,

$$f'_i = f'_{sc} \left(1 + 300 \frac{\delta_c}{d_c}\right) \quad (4.324)$$

and

$$f'_i = f'_{sc} \left(1 + 300 \frac{\delta_t}{d_t}\right), \quad (4.325)$$

where f'_{sc} = friction factor obtained with Eq. 4.320 for a Reynolds number based on the superficial mixture velocity, mixture density, and hydraulic diameter in the core, given in Eq. 4.318.

With the shear stress and geometrical relationships defined in Eqs. 4.309 through 4.325, the combined linear momentum equation for the casing-liquid film and the mixture in the core, given by Eq. 4.307, can be rewritten as

$$\begin{aligned} & -f'_i \rho_L \frac{v_f^2}{2} \frac{d_c}{\delta_c(d_c - \delta_c)} + \left[f'_{sc} \left(1 + 300 \frac{\delta_c}{d_c}\right) \rho_C \frac{v_c^2}{2} \right] \\ & \times \left\{ \frac{(d_c - 2\delta_c)}{\delta_c(d_c - \delta_c)} \right. \\ & \left. + \frac{4(d_c - 2\delta_c)}{[d_c^2 - d_t^2 - 4\delta_c(d_c - \delta_c) - 4\delta_t(d_t + \delta_t)]} \right\} \\ & + \left[f'_{sc} \left(1 + 300 \frac{\delta_t}{d_t}\right) \rho_C \frac{v_c^2}{2} \right] \\ & \times \frac{4(d_t + 2\delta_t)}{[d_c^2 - d_t^2 - 4\delta_c(d_c - \delta_c) - 4\delta_t(d_t + \delta_t)]} \\ & - (\rho_L - \rho_C)g = 0. \end{aligned} \quad (4.326)$$

Similarly, the combined linear momentum equation for the tubing-liquid film and the mixture in the core, as given by Eq. 4.308, can be rewritten as

$$\begin{aligned} & -f'_i \rho_L \frac{v_f^2}{2} \frac{d_t}{\delta_t(d_t + \delta_t)} + \left[f'_{sc} \left(1 + 300 \frac{\delta_t}{d_t}\right) \rho_C \frac{v_c^2}{2} \right] \\ & \times \left\{ \frac{(d_t + 2\delta_t)}{\delta_t(d_t + \delta_t)} \right\} \end{aligned}$$

$$\begin{aligned}
& + \frac{4(d_t + 2\delta_c)}{[d_c^2 - d_t^2 - 4\delta_c(d_c - \delta_c) - 4\delta_t(d_t + \delta_t)]} \\
& + \left[f_{sc}' \left(1 + 300 \frac{\delta_c}{d_c} \right) \rho_c \frac{v_c^2}{2} \right] \\
& \times \frac{4(d_c - 2\delta_c)}{[d_c^2 - d_t^2 - 4\delta_c(d_c - \delta_c) - 4\delta_t(d_t + \delta_t)]} \\
& - (\rho_L - \rho_c)g = 0. \quad \dots \dots \dots \quad (4.327)
\end{aligned}$$

Phase Continuity Equations. The continuity for the liquid phase, which flows in the form of two films wetting the bounding walls and as droplets entrained in the gas core, yields

$$v_{SL} = v_g H_{Lif} + v_{cf} H_{Lcf} + v_{SL} F_E, \quad \dots \dots \dots \quad (4.328)$$

where H_{Lif} = in-situ liquid holdup in the tubing film, H_{Lcf} = in-situ liquid holdup in the casing film, and F_E = fraction of liquid entrained in the gas core.

The continuity for the gas phase, which flows in the core bounded by the two liquid films, yields

$$v_{Sg} = v_{gc}(1 - H_{L,i}), \quad \dots \dots \dots \quad (4.329)$$

where v_{gc} is the in-situ gas velocity in the core and $H_{L,i}$ is the total in-situ liquid holdup in the annulus.

The liquid holdup for the casing-liquid film is defined as the ratio between the area for this film and the total annulus area. Using Eqs. 4.309 and 4.288 yields

$$H_{Lcf} = \frac{4\delta_c \left(1 - \frac{\delta_c}{d_c} \right)}{d_c(1 - K^2)}, \quad \dots \dots \dots \quad (4.330)$$

where K is the annulus pipe-diameter ratio, d_t/d_c .

Similarly, the in-situ liquid holdup for the tubing-liquid film is given by

$$H_{Lif} = \frac{4\delta_c K \left(1 + \frac{\delta_t}{d_t} \right)}{d_c(1 - K^2)}. \quad \dots \dots \dots \quad (4.331)$$

The in-situ liquid holdup in the core, where the gas/liquid mixture is assumed to be homogeneous, is given by

$$H_{LC} = \frac{v_{SL} F_E}{v_{SL} F_E + v_{Sg}}. \quad \dots \dots \dots \quad (4.332)$$

The total liquid holdup in the annulus is the sum of the liquid holdups in the core and in the two films. Using Eqs. 4.288, 4.309 through 4.311, and 4.330 through 4.332 yields

$$\begin{aligned}
H_{L,i} &= \frac{v_{SL} F_E}{(v_{SL} F_E + v_{Sg})(1 - K^2)} \\
&\times \left[1 - K^2 - \frac{4\delta_c}{d_c} \left(1 - \frac{\delta_c}{d_c} \right) - \frac{4\delta_t K}{d_c} \left(1 + \frac{\delta_t}{d_t} \right) \right] \\
&+ \frac{4}{d_c(1 - K^2)} \left[\delta_c \left(1 - \frac{\delta_c}{d_c} \right) + \delta_t K \left(1 + \frac{\delta_t}{d_t} \right) \right]. \quad \dots \dots \dots \quad (4.333)
\end{aligned}$$

Eqs. 4.208 and 4.209 gave the Wallis¹⁸ correlation, which predicted the liquid fraction entrained in the gas core of long pipes under annular two-phase flow, F_E .

Tubing/Casing-Liquid-Film-Thickness Ratio. A prediction for the ratio between the thicknesses of the tubing film and the casing film was developed by assuming equilibrium between the entrainment and deposition rates of liquid droplets. At equilibrium conditions, the liquid droplets deposition and entrainment rates are equal for each liquid film, resulting in this relationship between the tubing- and casing-liquid-film thicknesses.

$$T = \frac{\delta_t}{\delta_c} = \frac{\langle W'_t \rangle}{(2\pi - \langle W'_t \rangle)K}, \quad \dots \dots \dots \quad (4.334)$$

where $\langle W'_t \rangle$ is the cross-sectional average of the angle of view associated with the tubing deposition area as seen by the entrained droplets. $\langle W'_t \rangle$ can be expressed in terms of geometrical variables by Eqs. 4.335 and 4.336 for concentric and eccentric annuli, respectively.

$$\begin{aligned}
\langle W'_t \rangle &= \frac{16}{(d_c^2 - d_t^2)} \int_{d_t/2}^{d_c/2} \sin^{-1} \left(\frac{d_t}{2r} \right) r dr \\
&= \frac{1}{(1 - K^2)} \left[2 \sin^{-1}(K) + 2K\sqrt{1 - K^2} - K^2\pi \right] \quad \dots \dots \dots \quad (4.335)
\end{aligned}$$

and

$$\begin{aligned}
\langle W'_t \rangle &= \frac{1}{\pi(1 - K^2)} \\
&\times \int_0^\pi \left[8a^2 \sin^{-1} \left(\frac{K}{2a} \right) + 2K\sqrt{4a^2 - K^2} - K^2\pi \right] d\theta, \quad \dots \dots \dots \quad (4.336)
\end{aligned}$$

where the parameter, a , is

$$a = \frac{e}{2}(1 - K) \cos \theta + \frac{1}{2}\sqrt{e^2(1 - K^2)(\cos^2 \theta - 1)} + 1 \quad \dots \dots \dots \quad (4.337)$$

and e is the degree of annulus eccentricity. Note that when $e = 0$ (concentric annulus), a reduces to 0.5. Consequently, the integrand expression in Eq. 4.336 becomes independent of the integration variable, θ , and the integral result is the one given by Eq. 4.335. However, if $e \neq 0$, no analytical solution is found for Eq. 4.336. The integration can be carried out numerically by applying a technique like Simpson's rule.

Fig. 4.27 shows the results found for the tubing/casing-liquid-film-thickness ratio, as given by Eq. 4.334, in terms of the annulus pipe-diameter ratio and degree of eccentricity. During the numerical determination of the average angle of view for an eccentric annulus, singularities were found when the pipe-diameter ratio equaled zero. For a fully eccentric annulus, these singularities also appeared for extremely low values of pipe-diameter ratio. Consequently, the curves in Fig. 4.27 should not be used for liquid-film ratio determination for an eccentric annulus in these singularity regions.

Summary of Governing Equations: Dimensionless Form. The governing equations developed previously for the annular flow model can be presented in dimensionless form. The normalizing variable selected for length is the hydraulic diameter for the annulus configuration, given by Eq. 4.270.

The normalizing variables selected for velocity are the superficial liquid velocity for the in-situ velocities in the liquid films and the core-mixture velocity for the in-situ velocity in this region. This core-mixture velocity is given by

$$v_{SC} = v_{Sg} + F_E v_{SL}, \quad \dots \dots \dots \quad (4.338)$$

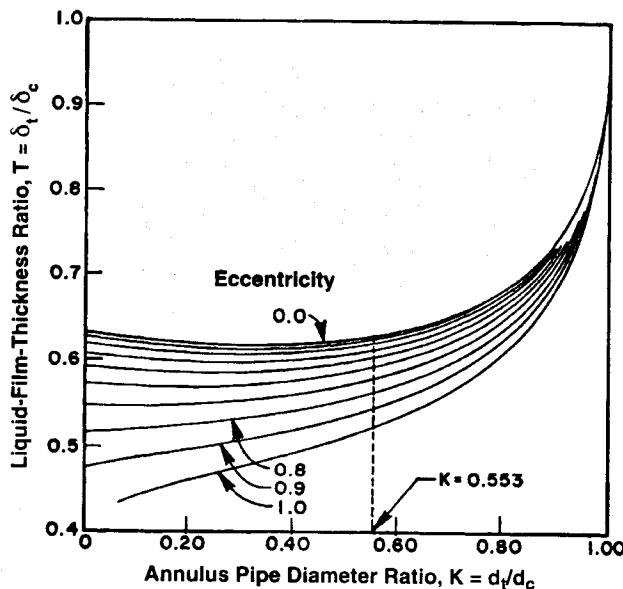


Fig. 4.27—Liquid-film-thickness ratio in annuli.⁶⁷

where F_E = liquid fraction entrained in the core.

Eq. 4.336 in nondimensional form is

$$\begin{aligned} \underline{v}_{cf}^{(2-m)} &= \frac{\underline{\delta}_c [1 - \underline{\delta}_c(1 - K)]}{X_M^2 d_{cf}^{-m}} \left\{ \underline{v}_C^2 [1 + 300\underline{\delta}_c(1 - K)] \right. \\ &\quad \times [1 - 2\underline{\delta}_c(1 - K)] \left(\frac{1}{G_1} - \frac{1}{G_2} \right) \\ &\quad + \underline{v}_C^2 \left(1 + 300\underline{\delta}_c T \frac{1 - K}{K} \right) \\ &\quad \times \left(1 + 2\underline{\delta}_c T \frac{1 - K}{K} \right) \frac{1}{G_3} - 4Y_M \Big\}. \end{aligned} \quad (4.339)$$

Similarly, Eq. 4.327 can be written in nondimensional form as

$$\begin{aligned} \underline{v}_{sf}^{(2-m)} &= \frac{T\underline{\delta}_c [1 + \underline{\delta}_c T(1 - K)/K]}{X_M^2 d_{sf}^{-m}} \left\{ \left(1 + 300\underline{\delta}_c T \frac{1 - K}{K} \right) \right. \\ &\quad \times \underline{v}_C^2 \left(1 + 2\underline{\delta}_c T \frac{1 - K}{K} \right) \left(\frac{1}{G_3} + \frac{1}{G_4} \right) \\ &\quad + \underline{v}_C^2 [1 + 300\underline{\delta}_c(1 - K)] \\ &\quad \times [1 - 2\underline{\delta}_c(1 - K)] \frac{1}{G_2} - 4Y_M \Big\}. \end{aligned} \quad (4.340)$$

In Eqs. 4.339 and 4.340, the modified Lockhart and Martinelli parameter, X_M , and the dimensionless group, Y_M , are

$$X_M = \sqrt{\left(\frac{dp}{dL} \right)_{SL} / \left(\frac{dp}{dL} \right)_{SC}} \quad (4.341)$$

and

$$Y_M = \frac{(\rho_L - \rho_C)g}{\left(\frac{dp}{dL} \right)_{SC}}. \quad (4.342)$$

Also, the dimensionless groups, G_1 , G_2 , G_3 , and G_4 are given by

$$G_1 = \underline{\delta}_c [1 - \underline{\delta}_c(1 - K)], \quad (4.343)$$

$$G_2 = \frac{1 + K}{4} - \underline{\delta}_c [1 - \underline{\delta}_c(1 - K)] \\ - \underline{\delta}_c T \left(1 + \underline{\delta}_c T \frac{1 - K}{K} \right), \quad (4.344)$$

$$G_3 = \frac{1 + K}{4K} - \frac{\underline{\delta}_c}{K} [1 - \underline{\delta}_c(1 - K)] \\ - \underline{\delta}_c T \left(1 + \underline{\delta}_c T \frac{1 - K}{K} \right), \quad (4.345)$$

and

$$G_4 = \underline{\delta}_c T \left(1 + \underline{\delta}_c T \frac{1 - K}{K} \right), \quad (4.346)$$

where

$$\underline{\delta}_c = \frac{\delta_c}{d_h}, \quad (4.347)$$

$$\underline{\delta}_t = \frac{\delta_t}{d_h}, \quad (4.348)$$

$$T = \frac{\delta_t}{\delta_c}, \quad (4.349)$$

$$\underline{v}_{cf} = \frac{v_{cf}}{v_{SL}}, \quad (4.350)$$

$$\underline{v}_{sf} = \frac{v_{sf}}{v_{SL}}, \quad (4.351)$$

$$\underline{v}_C = \frac{v_C}{v_{SC}}, \quad (4.352)$$

$$\underline{d}_{cf} = 4\underline{\delta}_c [1 - \underline{\delta}_c(1 - K)], \quad (4.353)$$

$$\underline{d}_{sf} = 4T\underline{\delta}_c \left[1 + T\underline{\delta}_c \frac{(1 - K)}{K} \right]. \quad (4.354)$$

In Eqs. 4.341 and 4.342, $(dp/dL)_{SL}$ and $(dp/dL)_{SC}$ = superficial pressure gradients of the liquid phase and the core mixture, respectively. Caetano *et al.*⁶⁷ provide additional details on the nondimensionalizing process.

For a given set of phase flow rates, fluid physical property values, and configuration geometry, a solution is obtained for Eqs. 4.339 and 4.340 by use of an iterative procedure to determine the dimensionless casing-liquid-film thickness, $\underline{\delta}_c$. The in-situ velocities and liquid holdups then can be calculated. Finally, the total pressure gradient can be determined by use of any of the linear momentum equations given by Eqs. 4.303 through 4.305.

4.4.2 Hasan and Kabir Method. Hasan and Kabir⁶⁸ investigated two-phase flow in vertical and inclined annuli. The experimental part of their study involved flowing air through a stagnant water column in a vertical annulus. The void fraction in the test section was determined from pressure-drop measurements. An estimated friction pressure drop was subtracted from the measured total pressure drop. The resulting elevation pressure drop was used to calculate the void fraction. The theoretical part included development of a model by use of a drift-flux approach for the slip between phases.

Flow-Pattern-Transition Prediction. As was the case with flow in circular pipes, once again, the four major flow patterns were recognized: bubble, slug, churn, and annular.

Bubble/Slug Transition. Hasan and Kabir suggested that the bubbly/sluggish-transition criterion given by Eq. 4.240 also is applicable for annuli geometry. They recommended the use of Eqs. 4.269 through 4.271 to predict the onset of dispersed-bubble flow in vertical and inclined annuli.

Slug/Churn Transition. Hasan and Kabir²⁵ found that models that predict the slug/churn flow transition on the basis of the "flooding" phenomenon do not appear to be applicable at high pressures. Moreover, Weisman and Kang⁶⁹ identified discrepancies between data and empirical correlations from a number of sources. Therefore, no attempt was made to delineate this transition for annuli. Rather, it was suggested that the model proposed by Brauner and Barnea⁵¹ for circular channels be used for the transition to churn flow, even for flow in annuli. This criterion suggests that the transition to churn flow occurs when the gas void fraction in the liquid slug following the Taylor bubble exceeds 52%.

Transition to Annular Flow. The transition from churn (or slug) to annular flow was not investigated experimentally. Rather, the criterion given by Taitel *et al.*³⁰ in Eq. 4.163 is suggested for flow in annuli.

Flow-Behavior Prediction. Expressions for void fraction in bubble, slug, and churn flow were developed from relationships between the phase velocities. The annular-flow pattern was not investigated.

Bubble Flow. Hasan and Kabir suggested that Eq. 4.246 also can be used in bubbly and dispersed-bubble flow. They concluded that the terminal rise velocity, v_s , was not affected significantly by either the inner pipe or the pipe-deviation angle from the vertical. The influence of pipe diameter becomes significant only when the diameter of the bubble exceeds 20% of the channel diameter. Hasan and Kabir²⁶ demonstrated that a pipe deviation of up to 32° from the vertical did not seem to affect the rise velocity of small bubbles. This also was assumed to be the case for flow in annuli.

Slug Flow. Application of the drift-flux model for slug flow is more complicated than for bubble flow because of the different drift velocity of the small bubbles in the liquid slug compared with that of the Taylor bubbles. Assuming that the liquid slugs do not contain any gas bubbles, Hasan and Kabir^{25,26} arrived at this expression for liquid holdup using v_{TB} for the rise velocity of a Taylor bubble in an annulus.

$$H_{LTB} = 1 - \frac{v_{sg}}{C_1 v_m + v_{TB}}, \quad (4.355)$$

where C_1 is the flow parameter analogous to C_0 in bubble flow.

The approach used for bubble flow to determine the effect of annulus dimension and pipe-inclination angle on the flow parameter can be used for slug flow only if Eq. 4.355 alone is used to estimate the gas void fraction. In Eq. 4.355, $v_{sg}/(1 - H_{LTB})$ varies linearly with v_m , with a slope of C_1 . Although imprecise, this approach indicates that the flow parameter is not influenced significantly by either inner pipe diameter or pipe-inclination angle. Thus, a constant value of 1.2 was proposed for C_1 .

The presence of an inner pipe tends to make the nose of the Taylor bubble sharper, causing an increase in the rise velocity, v_{TB} . Hasan and Kabir⁶⁸ stated that their Taylor-bubble-rise data showed a linear relationship with the diameter ratio, d_i/d_c , suggesting this expression for the Taylor-bubble-rise velocity for vertical annuli

$$v_{TB} = \left(0.345 + 0.1 \frac{d_i}{d_c} \right)$$

$$\times \sqrt{\sin \theta} (1 + \cos \theta)^{1/2} \sqrt{\frac{g d_c (\rho_L - \rho_g)}{\rho_L}}. \quad (4.356)$$

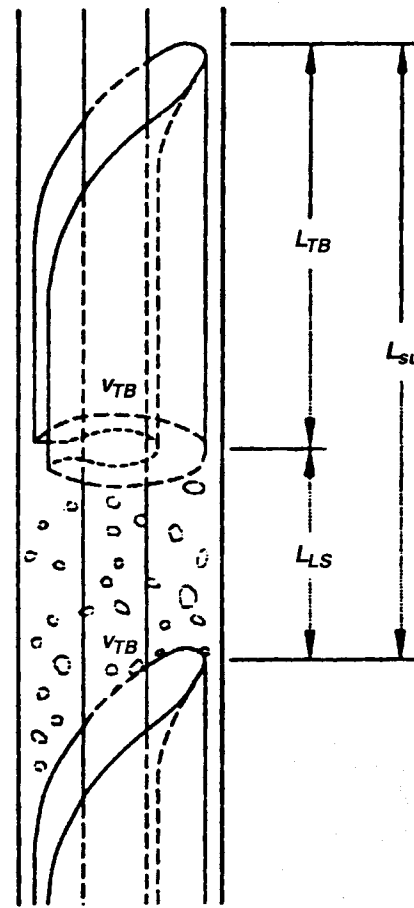


Fig. 4.28—Schematic of slug unit for slug flow in an annulus.⁶⁸ (Reprinted with permission from Elsevier Science.)

Fig. 4.28 shows a slug unit of length L_{SU} , consisting of a Taylor bubble of length L_{TB} and a liquid slug of length L_{LS} . The average holdup for the slug unit can be expressed as

$$H_L = H_{LTB} \frac{L_{TB}}{L_{SU}} + H_{LLS} \frac{L_{LS}}{L_{SU}}. \quad (4.357)$$

Hasan and Kabir⁶⁸ used a simple approach to estimate the liquid-slug void fraction. The circular channel data of Akagawa and Sakanuchi⁷⁰ showed that the average volume fraction of gas in a liquid slug, based on the total slug-unit volume,—i.e., $(1 - H_{LLS})/(L_{LS}/L_{SU})$ —is approximately equal to 0.1 when $v_{sg} > 0.4$ m/s and is equal to 0.25 v_{sg} for lower superficial gas velocities. Assuming that this approximation also applies to flow in an annulus, Eq. 4.357 can be rewritten as

$$(1 - H_L) = (1 - H_{LTB}) \frac{L_{TB}}{L_{SU}} + 0.1 \quad (4.358)$$

if $v_{sg} > 0.4$ m/s and as

$$(1 - H_L) = (1 - H_{LTB}) \frac{L_{TB}}{L_{SU}} + 0.25 v_{sg} \quad (4.359)$$

if $v_{sg} < 0.4$ m/s.

Churn Flow. Hasan and Kabir did not investigate the churn-flow pattern because of its chaotic nature. However, they suggested that the analyses presented for bubble and slug flow can be applicable for the churn-flow pattern. Although the bubble shape is quite different from the classic Taylor bubble, the bubble-rise velocity during churn flow is probably not much different from that for slug flow. In addition, because the mixture velocity is much higher than the bubble-rise velocity during churn flow, a slight error in estimating bubble-rise velocity does not affect void-fraction estimation significantly.

TABLE 4.8—EVALUATION OF CAETANO *et al.* LIQUID-HOLDUP AND PRESSURE-GRADIENT PREDICTIONS FOR TWO-PHASE FLOW IN CONCENTRIC AND FULLY ECCENTRIC ANNULI³⁷

	<i>E</i> ₁		<i>E</i> ₃	
	Air/Water	Air/Kerosene	Air/Water	Air/Kerosene
Bubble				
Concentric <i>H</i> _L	-0.46	-2.17	4.75	5.21
Eccentric <i>H</i> _L	-2.77	—	4.32	—
Concentric <i>d</i> _P / <i>d</i> _L	7.33	-0.61	8.69	3.44
Eccentric <i>d</i> _P / <i>d</i> _L	12.03	—	11.69	—
Dispersed bubble				
Concentric <i>H</i> _L	1.67	-3.84	2.84	2.93
Eccentric <i>H</i> _L	1.12	—	1.11	—
Concentric <i>d</i> _P / <i>d</i> _L	-2.46	-2.89	5.46	1.39
Eccentric <i>d</i> _P / <i>d</i> _L	-3.74	—	2.43	—
Slug				
Concentric <i>H</i> _L	3.94	5.80	7.72	9.97
Eccentric <i>H</i> _L	1.75	—	4.03	—
Concentric <i>d</i> _P / <i>d</i> _L	3.51	8.00	3.32	4.07
Eccentric <i>d</i> _P / <i>d</i> _L	-1.06	—	6.86	—
Annular				
Concentric <i>H</i> _L	10.60	-2.31	8.86	23.17
Eccentric <i>H</i> _L	15.00	—	9.71	—
Concentric <i>d</i> _P / <i>d</i> _L	17.11	66.00	15.94	25.22
Eccentric <i>d</i> _P / <i>d</i> _L	-14.03	—	9.33	—

However, an accurate estimation of C_1 is very important in the prediction of void fraction. The bubble concentration profile in churn flow may be dissimilar to that for slug flow because of the characteristic churning motion of this flow pattern. Using Eq. 4.355, with v_{TB} given by Eq. 4.356 for circular pipes, Hasan^{71,72} analyzed the void-fraction data gathered by Ney⁷³ and Fuentes⁷⁴ for circular pipes in the churn-flow pattern. Hasan concluded that a value of 1.15 was appropriate for the parameter C_1 . The same value was proposed for use in annuli.

4.5 Evaluation of Annulus Liquid-Holdup and Pressure-Gradient-Prediction Methods

Published liquid-holdup and pressure-drop data for two-phase flow through annular geometries are scarce. Caetano³⁷ gathered liquid-holdup, pressure-drop, and flow-pattern data for air/water and air/kerosene two-phase flow through an annulus with 3-in.-ID outer pipe and 1.66-in.-OD inner pipe at a pressure of about 45 psi. Caetano *et al.*⁶⁷ and Hasan and Kabir⁶⁸ used these data to evaluate their respective models.

4.5.1 Caetano *et al.* Method. The model's performance was obtained by comparing the predicted results with measured data. Table 4.8 reports this performance in terms of the average percent error, E_1 , and the percent standard deviation, E_3 , as given by Eqs. 4.256 and 4.259. Results are provided for different flow patterns and for both concentric and fully eccentric annuli.

For bubble flow, Table 4.8 shows that the model's prediction of liquid holdup is very good, with a slight underprediction tendency of less than 3.0%. The degree of scatter about the mean is also good, with a standard deviation of about 5.0%. In general, the model performs very well, independent of either physical properties or annulus configuration. The agreement between the model and experimental results for pressure gradient also is good. The agreement is weaker for the fully eccentric annulus case, with average percent error and standard deviation values slightly higher than 10%. This was caused by the very low superficial phase velocities used when acquiring the data in this configuration. Under these conditions, the

flow was sometimes unstable because of a heading phenomenon, which can cause a lower degree of measurement accuracy.

For dispersed-bubble flow, Table 4.8 shows that the model's prediction of liquid holdup is very good, with a slight overprediction tendency for air/water flow and a slight underprediction tendency for air/kerosene flow. The standard deviation about the mean is below 3.0%. The model performs equally well for either fluid pair or annulus configuration. Although lower values of pressure gradients were encountered in the fully eccentric annulus because of the lower friction losses, the agreement between the model and experimental results is again very good, showing low values of both average percent error and standard deviation.

For slug flow, Table 4.8 shows that the model's prediction of liquid holdup is good, with a slight overprediction for both air/kerosene and air/water mixtures. The standard deviations ranged from 4 to 10%, confirming reasonable scatter about the mean. The model performed slightly better for the air/water mixture. The agreement between the model and experimental results for pressure gradient is also good. As in the liquid-holdup prediction, the model performed slightly better for the air/water mixture. No significant differences were found in model performance for the two annuli, suggesting that the model adequately accounts for eccentricity. The slight overprediction of both the average liquid holdup and pressure gradient might result from treating the liquid holdup in the liquid slug as a constant. However, this value might decrease with an increase in the gas flow rate. Taking into consideration this variation might improve the performance of the model.

For annular flow, Table 4.8 shows that the model's prediction of liquid holdup and pressure gradient is adequate for air/water flow in either annulus type. The model performance is only fair with air/kerosene.

The agreement between experimental results and the annular-flow model's predictions is less satisfactory than for models developed for other flow patterns. However, the accuracy of experimental measurements obtained for the annular-flow pattern must be considered. The quick-closing ball valves used by Caetano³⁷ to measure liquid holdup have a lower accuracy in annular flow than for all other flow patterns. This is because of the low overall holdup values characteristic of annular flow. The actual reported holdup values

TABLE 4.9—EVALUATION OF HASAN AND KABIR LIQUID-HOLDUP PREDICTIONS FOR TWO-PHASE FLOW IN ANNULUS⁶⁸ (Reprinted with permission from Elsevier Science.)

	<i>E</i> ₁		<i>E</i> ₃		<i>E</i> ₄		<i>E</i> ₆	
	Air/Water	Air/Kerosene	Air/Water	Air/Kerosene	Air/Water	Air/Kerosene	Air/Water	Air/Kerosene
Bubble	2.400	1.900	4.070	3.980	0.022	0.013	0.040	0.034
Dispersed Bubble	5.000	0.600	5.020	2.160	0.043	0.003	0.049	0.018
Slug	7.040	9.930	8.100	7.200	0.041	0.047	0.063	0.057
Churn					-0.005	0.026	0.033	0.043

were sometimes less than the accuracy possible with the ball-valve approach. Also, the pressure measurement system used by Caetano may not be adequate for the cross-sectional-dependent and axial-dependent annular-flow pattern. Finally, because of gas compressor limitations, it was not possible for Caetano to acquire data covering a broad region in this flow pattern.

A second major aspect in the annular-flow-model performance is its strong dependence on the entrainment liquid fraction, *FE*. If a large entrainment fraction is predicted because of a high superficial gas velocity, then a small overall liquid-holdup value will be predicted. Wallis¹⁸ reported that viscous liquids normally exhibit a smaller entrainment fraction than predicted by his correlation. The Caetano *et al.*⁶⁷ annular-flow model also showed this.

Film-thickness ratio is the third major aspect to influence the performance. The film-thickness ratio became dependent on the adopted isotropy of scattering and independent of flow interference on the liquid droplets entrained in the gas core. Hutchinson *et al.*⁷⁵ applied the isotropy concept. However, Gardner⁷⁶ reported that the rate of deposition was dependent on mechanisms that account for the existing flow field and are determined by liquid droplet size.

Because no measurements of liquid droplet size were obtained in this investigation, Caetano *et al.* could not use these insights. As a result, a deposition-rate expression was adopted. It is a mass-transfer-process type that does not take into account the particle size and the inherent type of deposition mechanism. Thus, to refine the model, data with more detailed characteristics for this flow pattern would be required.

4.5.2 Hasan and Kabir Model. Hasan and Kabir⁶⁸ reported statistical comparisons between predicted liquid-holdup values and measured values from Caetano³⁷ for flow in a concentric annulus. No comparisons were made on pressure drop. Table 4.9 presents the statistical results.

For bubble flow, general overestimation of the liquid holdup is evident for both fluid systems, although agreement is better for the air/kerosene system. Caetano's air/water bubble-flow data were predicted with an average percentage error of 2.4%. The percentage standard deviation was 4.07%. The Caetano *et al.*⁶⁷ model predicted the same data with an average percentage error and percentage standard deviation of -0.46% and 4.75%, respectively. The Hasan and Kabir model predicted an average percentage error of 1.90% and a percentage standard deviation of 3.98% for the Caetano air/kerosene bubble-flow data, compared with values of -2.17% and 5.21%, respectively, for the Caetano *et al.* model. The general overestimation by Hasan and Kabir suggests that a lower value of *C*_o or a lower value of *v*_s is needed in Eq. 4.246.

For dispersed-bubble flow, the air/water liquid-holdup data are overestimated on the average by 5.0%, compared with an underestimation of 1.67% with the homogeneous model proposed by Caetano *et al.* However, treating the dispersed-bubble flow as homogeneous may not be appropriate because it assumes a value of 1.0 for *C*_o, when most of the bubbles still flow through the channel core. Caetano's air/kerosene data appear to support this contention. The Hasan and Kabir model predicts these data with an average percent error of 0.60% and a standard deviation of 2.16%, compared with values of -3.84% and 2.93%, respectively, for the homogeneous model.

For slug flow, the Hasan and Kabir model overestimates the air/water slug-flow data by 7.04% and the air/kerosene data by 9.93%, while percentage standard deviations for these two sets of data are

8.1 and 7.2%, respectively. These higher percentage-error values reflect the generally lower values of liquid holdup rather than any inaccuracy in predicting the absolute values.

Hasan and Kabir also proposed a simplified approach for slug flow in which all the gas is assumed to have the same drift flux as the Taylor bubble. Considerations of different drift fluxes in the Taylor bubble and the liquid slug reduced the percent standard deviation by only 0.01 for the air/water data and by 0.004 for the air/kerosene data. However, the rigorous Caetano *et al.* slug-flow model predicted the liquid-holdup data for both systems better, with *E*₁ = 3.94% and *E*₃ = 7.72% for the air/water data and *E*₁ = 5.8% and *E*₃ = 9.97% for the air/kerosene data.

Table 4.9 also presents the liquid-holdup predictions of the Hasan and Kabir model vs. Caetano's churn-flow data. The apparent low value of the average error supports the use of a smaller value for the parameter *C*₁. Average percentage error and percentage standard deviation were not reported because liquid-holdup values in this flow pattern were very low, resulting in percentage errors that exaggerated the inaccuracy of the method.

Hasan and Kabir also compared their model predictions with the air/water data of Sadatomi *et al.*⁷⁷ who used a 30-mm-OD, 15-mm-ID annulus. The model predicted an average error of 0.023 and a standard deviation of 0.0214 for the gas void fraction in all flow patterns in this data set. Good agreement also existed between the Sadatomi *et al.* data and Hasan and Kabir predictions for slug- and churn-flow patterns.

4.6 General Observations

Engineers who perform multiphase-flow design calculations for wellbores are clearly faced with an immediate dilemma. Which correlation or model should be used? Many companies have their favorites, often based on experience not documented in the literature. Unfortunately, decisions often are made without awareness of the serious limitations or the availability of more accurate methods. The evaluations presented in Secs. 4.3 and 4.5 are inconclusive and based on a very limited set of data.

Nevertheless, several conclusions can be drawn from published evaluations and experience. Among the empirical correlations presented, the modified Hagedorn and Brown⁴ and Beggs and Brill¹¹ methods appear to be best. The Beggs and Brill method attempts to account for the effect of inclination angle on liquid holdup and, therefore, should perform better than the Hagedorn and Brown method in deviated wells. Although several attempts have been made to create hybrid correlations—i.e., by use of one investigator's flow-pattern map with another's pressure-gradient equation—none has any technical merit and all should be avoided. Any improvements in accuracy are purely accidental.

Mechanistic models offer the most accurate methods to predict pressure gradients in wellbores. Unfortunately, they also are much more complicated and difficult to understand. Among these, the Ansari *et al.*²⁴ comprehensive model has enjoyed great success and is accepted in the petroleum industry. Future models that improve significantly on Ansari *et al.* no doubt will be published. Two models^{28,29} are undergoing peer review. Others, such as the steady-state commercial codes OLGA and TACITE, are proprietary.

No existing comprehensive model properly accounts for all the effects of inclination angle on flow behavior. Although excellent models are available to predict flow patterns at all inclination angles, many of the variables used to predict flow behavior in mechanistic models

are sensitive to inclination angle. The effect of inclination angle on these variables either has not been investigated adequately or has not been incorporated into existing mechanistic models. Included are such phenomena as variation in film thickness with inclination angle, both in annular flow and in the Taylor-bubble region of slug flow; effect of inclination angle on entrainment fraction in annular flow; effect of inclination angle on Taylor-bubble-rise velocity; and effect of coalescence of small bubbles along the upper pipe wall for deviated wells, in both bubbly flow and slug bodies.

Finally, no mechanistic models yet are available to predict the simultaneous flow of gas, oil, and water in wellbores. Successful modeling must begin with two-phase oil/water flow before the more complicated multiphase-flow behavior can be addressed. No proven mechanistic models have been published for oil/water flow in vertical or deviated wellbores. Analogous to gas/liquid flow, the modeling of oil/water flow-pattern transitions must first be accomplished. Only then can improved flow-behavior models be developed to predict pressure gradient. Eventually, mechanistic models will be developed that are sufficiently accurate for a broad range of gas, oil, and water flow rates, inclination angles, oil viscosities, and both diameters and annulus configurations.

References

1. Poettmann, F.H. and Carpenter, P.G.: "The Multiphase Flow of Gas, Oil and Water Through Vertical Flow Strings with Application to the Design and Gas-Lift Installations," *Drill. & Prod. Prac.* (1952) 257.
2. Baxendell, P.B. and Thomas, R.: "The Calculation of Pressure Gradients in High-Rate Flowing Wells," *JPT* (October 1961) 1023; *Trans., AIME*, **222**.
3. Fancher, G.H. Jr. and Brown, K.E.: "Prediction of Pressure Gradients for Multiphase Flow in Tubing," *SPEJ* (March 1963) 59; *Trans., AIME*, **228**.
4. Hagedorn, A.R. and Brown, K.E.: "Experimental Study of Pressure Gradients Occurring During Continuous Two-Phase Flow in Small-Diameter Vertical Conduits," *JPT* (April 1965) 475; *Trans., AIME*, **234**.
5. *User's Manual for API 14B, SSCSV Sizing Computer Program*, second edition, API (1978) Appendix B, 38-41.
6. Asheim, H.: "MONA, An Accurate Two-Phase Well Flow Model Based on Phase Slippage," *SPEPE* (May 1986) 221.
7. Duns, H. Jr. and Ros, N.C.J.: "Vertical Flow of Gas and Liquid Mixtures in Wells," *Proc.*, Sixth World Pet. Cong., Tokyo (1963) 451.
8. Orkiszewski, J.: "Predicting Two-Phase Pressure Drops in Vertical Pipes," *JPT* (June 1967) 829; *Trans., AIME*, **240**.
9. Aziz, K., Govier, G.W., and Fogarasi, M.: "Pressure Drop in Wells Producing Oil and Gas," *J. Cdn. Pet. Tech.* (July-September 1972) **11**, 38.
10. Chierici, G.L., Ciucci, G.M., and Sclocchi, G.: "Two-Phase Vertical Flow in Oil Wells—Prediction of Pressure Drop," *JPT* (August 1974) 927; *Trans., AIME*, **257**.
11. Beggs, H.D. and Brill, J.P.: "A Study of Two-Phase Flow in Inclined Pipes," *JPT* (May 1973) 607; *Trans., AIME*, **255**.
12. Mukherjee, H. and Brill, J.P.: "Pressure Drop Correlations for Inclined Two-Phase Flow," *J. Energy Res. Tech.* (December 1985) **107**, 549.
13. Griffith, P. and Wallis, G.B.: "Two-Phase Slug Flow," *J. Heat Transfer* (August 1961) **83**, 307.
14. Griffith, P.: "Two-Phase Flow in Pipes," special summer program, Massachusetts Inst. of Technology, Cambridge, Massachusetts (1962).
15. Davies, R.M. and Taylor, G.: "The Mechanics of Large Bubbles Rising Through Extended Liquids and Through Liquids in Tubes," *Proc.*, Royal Soc., London (1949) **200A**, 375.
16. Brill, J.P.: "Discontinuities in the Orkiszewski Correlation for Predicting Pressure Gradients in Wells," *J. Energy Res. Tech.* (March 1989) **111**, 34.
17. Govier, G.W., Radford, B.A., and Dunn, J.S.C.: "The Upward Vertical Flow of Air-Water Mixtures, Part 1," *Cdn. J. Chem. Eng.* (1957) **35**, 58.
18. Wallis, G.B.: *One Dimensional Two-Phase Flow*, McGraw-Hill Book Co. Inc., New York City (1969).
19. Al-Najjar, H.S.H. and Al-Soof, N.B.A.: "Alternate Flow-Pattern Maps Can Improve Pressure-Drop Calculations of the Aziz *et al.* Multiphase-Flow Correlation," *SPEPE* (August 1989) 327.
20. Nicklin, D.J., Wilkes, J.O., and Davidson, J.F.: "Two-Phase Flow in Vertical Tubes," *Trans., AIChE* (1962) **40**, 61.
21. Brill, J.P. and Beggs, H.D.: *Two-Phase Flow in Pipes*, U. of Tulsa, Tulsa, Oklahoma (1991).
22. Payne, G.A. *et al.*: "Evaluation of Inclined-Pipe Two-Phase Liquid Holdup and Pressure-Loss Correlations Using Experimental Data," *JPT* (September 1979) 1198; *Trans., AIME*, **267**.
23. Govier, G.W. and Aziz, K.: *The Flow of Complex Mixtures in Pipes*, Van Nostrand Reinhold Publishing Co., New York City (1972).
24. Ansari, A.M. *et al.*: "A Comprehensive Mechanistic Model for Two-Phase Flow in Wellbores," *SPEPF* (May 1994) 143; *Trans., AIME*, **297**.
25. Hasan, A.R. and Kabir, C.S.: "A Study of Multiphase Flow Behavior in Vertical Wells," *SPEPE* (May 1988) 263; *Trans., AIME*, **285**.
26. Hasan, A.R. and Kabir, C.S.: "Predicting Multiphase Flow Behavior in a Deviated Well," *SPEPE* (November 1988) 474.
27. Kabir, C.S. and Hasan, A.R.: "Performance of a Two-Phase Gas/Liquid Model in Vertical Wells," *J. Pet. Sci. & Eng.* (1990) **4**, 273.
28. Chokshi, R.N., Schmidt, Z., and Doty, D.R.: "Experimental Study and the Development of a Mechanistic Model for Two-Phase Flow Through Vertical Tubing," paper SPE 35676 presented at the 1996 Western Regional Meeting, Anchorage, 22-24 May.
29. Petalas, N. and Aziz, K.: "Development and Testing of a New Mechanistic Model for Multiphase Flow in Pipes," paper presented at the 1996 ASME Summer Meeting, Anaheim, California, 11 July.
30. Taitel, Y.M., Barnea, D., and Dukler, A.E.: "Modeling Flow Pattern Transitions for Steady Upward Gas-Liquid Flow in Vertical Tubes," *AIChE J.* (1980) **26**, 345.
31. Barnea, D., Shoham, O., and Taitel, Y.: "Flow Pattern Transition for Vertical Downward Two-Phase Flow," *Chem. Eng. Sci.* (1982) **37**, 741.
32. Barnea, D.: "A Unified Model for Predicting Flow-Pattern Transition for the Whole Range of Pipe Inclinations," *Intl. J. Multiphase Flow* (1987) **13**, 1.
33. Harmathy, T.Z.: "Velocity of Large Drops and Bubbles in Media of Infinite or Restricted Extent," *AIChE J.* (1960) **6**, 281.
34. Scott, S.L. and Kouba, G.E.: "Advances in Slug Flow Characterization for Horizontal and Slightly Inclined Pipelines," paper SPE 20628 presented at the 1990 SPE Annual Technical Conference and Exhibition, New Orleans, 23-26 September.
35. Lockhart, R.W. and Martinelli, R.C.: "Proposed Correlation of Data for Isothermal Two-Phase, Two-Component Flow in Pipes," *Chem. Eng. Prog.* (1949) **45**, 39.
36. Alves, I.N. *et al.*: "Modeling Annular Flow Behavior for Gas Wells," paper presented at the 1988 Annual Winter Meeting of ASME, Chicago, 27 November-2 December.
37. Caetano, E.F.: "Upward Vertical Two-Phase Flow Through an Annulus," PhD dissertation, U. of Tulsa, Tulsa, Oklahoma (1985).
38. Zuber, N. and Hench, J.: "Steady State and Transient Void Fraction of Bubbling Systems and Their Operating Limits. Part 1: Steady-State Operation," Report #62GL100, General Electric Co., Schenectady, New York (1962).
39. Fernandes, R.C., Semait, T., and Dukler, A.E.: "Hydrodynamic Model for Gas-Liquid Slug Flow in Vertical Tubes," *AIChE J.* (1986) **32**, 981.
40. Sylvester, N.D.: "A Mechanistic Model for Two-Phase Vertical Slug Flow in Pipes," *J. Energy Res. Tech.* (December 1987) **109**, 206.
41. Brotz, W.: "Über die Vorausberechnung der Absorptionsgeschwindigkeit von Gasen in Stromenden Flüssigkeitsschichten," *Chem. Ing. Tech.* (1954) **26**, 470.
42. Schmidt, Z.: "Experimental Study of Two-Phase Slug Flow in a Pipeline-Riser Pipe System," PhD dissertation, U. of Tulsa, Tulsa, Oklahoma (1977).
43. Vo, D.T. and Shoham, O.: "A Note on the Existence of a Solution for Two-Phase Slug Flow in Vertical Pipes," *J. Energy Res. Tech.* (June 1989) **111**, 64.
44. McQuillan, K.W. and Whalley, P.B.: "Flow Patterns in Vertical Two-Phase Flow," *Intl. J. Multiphase Flow* (1985) **11**, 161.
45. Barnea, D.: "Effect of Bubble Shape on Pressure Drop Calculations in Vertical Slug Flow," *Intl. J. Multiphase Flow* (1990) **16**, 79.
46. Hewitt, G.F. and Hall-Taylor, N.S.: *Annular Two-Phase Flow*, Pergamon Press, Ltd., Oxford, U.K. (1970).
47. Whalley, P.B. and Hewitt, G.F.: "The Correlation of Liquid Entrainment Fraction and Entrainment Rate in Annular Two-Phase Flow," UKAEA Report, AERE-R9187, Harwell, U.K. (1978).
48. Lopes, J.C.B. and Dukler, A.E.: "Droplet Entrainment in Vertical Annular Flow and its Contribution to Momentum Transfer," *AIChE J.* (1986) **32**, 1500.
49. Hasan, A.R., Kabir, C.S., and Rahman, R.: "Predicting Liquid Gradient in a Pumping-Well Annulus," *SPEPE* (February 1988) 113; *Trans., AIME*, **285**.
50. Barnea, D. and Brauner, N.: "Holdup of the Liquid Slug in Two-Phase Intermittent Flow," *Intl. J. Multiphase Flow* (1985) **11**, 43.
51. Brauner, N. and Barnea, D.: "Slug/Churn Transition in Upward Gas-Liquid Flow," *Chem. Eng. Sci.* (1986) **41**, 159.
52. Steen, D.A. and Wallis, G.B.: AEC report No. NYO-31142-2 (1964).

53. Ansari, A.M. et al.: "Supplement to paper SPE 20630, A Comprehensive Mechanistic Model for Upward Two-Phase Flow in Wellbores," paper SPE 28671 available from SPE, Richardson, Texas (May 1994).
54. Govier, G.W. and Fogarasi, M.: "Pressure Drop in Wells Producing Gas and Condensate," *J. Cdn. Pet. Tech.* (October–December 1975) **14**, 28.
55. Hagedorn, A.R.: "Experimental Study of Pressure Gradients Occurring during Continuous Two-Phase Flow in Small Diameter Vertical Conduits," PhD dissertation, U. of Texas, Austin, Texas (1964).
56. Espanol, H.J.H.: "Comparison of Three Methods for Calculating a Pressure Traverse in Vertical Multi-Phase Flow," MS thesis, U. of Tulsa, Tulsa, Oklahoma (1968).
57. Messulam, S.A.G.: "Comparison of Correlations for Predicting Multiphase Flowing Pressure Losses in Vertical Pipes," MS thesis, U. of Tulsa, Tulsa, Oklahoma (1970).
58. Camacho, C.A.: "Comparison of Correlations for Predicting Pressure Losses in High Gas-Liquid Ratio Vertical Wells," MS thesis, U. of Tulsa, Tulsa, Oklahoma (1970).
59. Pucknell, J.K., Mason, J.N.E., and Vervest, E.G.: "An Evaluation of Recent Mechanistic Models of Multiphase Flow for Predicting Pressure Drops in Oil and Gas Wells," paper SPE 26682 presented at the 1993 Offshore European Conference, Aberdeen, 7–10 September.
60. Salim, P.H. and Stanislav, J.F.: "Evaluation of Methods Describing the Flow of Gas-Liquid Mixture in Wells," *J. Cdn. Pet. Tech.* (January/February 1994) **33**, 58.
61. Baxendell, P.B.: "Producing Wells on Casing Flow—An Analysis of Flowing Pressure Gradients," *JPT* (August 1958) **59**; *Trans., AIME*, **213**.
62. Gaither, O.D., Winkler, H.W., and Kirkpatrick, C.V.: "Single- and Two-Phase Fluid Flow in Small Vertical Conduits Including Annular Configurations," *JPT* (March 1963) **309**; *Trans., AIME*, **228**.
63. Angel, R.R. and Welchon, J.K.: "Low-Ratio Gas-Lift Correlation for Casing-Tubing Annuli and Large-Diameter Tubing," *Drill. & Prod. Prac.* (1964) **100**.
64. Winkler, H.W.: "Single- and Two-Phase Vertical Flow Through 0.996 X 0.625-Inch Fully Eccentric Plain Annular Configuration," PhD dissertation, U. of Texas, Austin, Texas (1968).
65. Ros, N.C.J.: "Simultaneous Flow of Gas and Liquid as Encountered in Well Tubing," *JPT* (October 1961) **1037**; *Trans., AIME*, **222**.
66. Caetano, E.F., Shoham, O., and Brill, J.P.: "Upward Vertical Two-Phase Flow Through an Annulus, Part I: Single-Phase Friction Factor, Taylor Bubble-Rise Velocity and Flow-Pattern Prediction," *J. Energy Res. Tech.* (March 1992) **114**, 1.
67. Caetano, E.F., Shoham, O., and Brill, J.P.: "Upward Vertical Two-Phase Flow Through an Annulus, Part II: Modeling Bubble, Slug and Annular Flow," *J. Energy Res. Tech.* (March 1992) **114**, 14.
68. Hasan, A.R. and Kabir, C.S.: "Two-Phase Flow in Vertical and Inclined Annuli," *Intl. J. Multiphase Flow* (1992) **18**, 279.
69. Weisman, J. and Kang, S.Y.: "Flow Pattern Transitions in Vertical and Upwardly Inclined Lines," *Intl. J. Multiphase Flow* (1981) **7**, 271.
70. Akagawa, K. and Sakaguchi, T.: "Fluctuation of Void Ratio in Two-Phase Flow," *Bulletin, JSME* (1966) **9**, 104.
71. Hasan, A.R.: "Void Fraction in Bubbly, Slug, and Churn Flow in Vertical Two-Phase Up-Flow," *Chem. Eng. Communications* (1988) **66**, 101.
72. Hasan, A.R.: "Inclined Two-Phase Flow: Flow Pattern, Void Fraction, and Pressure Drop in Bubbly, Slug, and Churn Flow," *Particulate Phenomena and Multiphase Transport*, Hemisphere Publishing Co., New York City (1988) **1**, 229–49.
73. Ney, C.: "A Study of the Directional Well," MS thesis, U. of Tulsa, Tulsa, Oklahoma (1968).
74. Fuentes, A.J.: "A Study of Multi-Phase Flow Phenomena in Directional Wells," MS thesis, U. of Tulsa, Tulsa, Oklahoma (1968).
75. Hutchinson, P., Hewitt, G.F., and Dukler, A.E.: "Deposition of Liquid or Solid Dispersions from Turbulent Gas Streams: A Stochastic Model," *Chem. Eng. Sci.* (1971) **26**, 419.
76. Gardner, G.C.: "Deposition of Particles from a Gas Flowing Parallel to a Surface," *Intl. J. Multiphase Flow* (1975) **2**, 213.
77. Sadatomi, M., Sato, Y., and Saruwatari, S.: "Two-Phase Flow in Vertical Noncircular Channels," *Intl. J. Multiphase Flow* (1982) **8**, 641.

Chapter 5

Flow Through Restrictions and Piping Components

5.1 Introduction

The purpose of this chapter is to present the methods used to predict flow behavior through restrictions and piping components commonly encountered in production operations.

The flow of fluids through restrictions is a common occurrence in the petroleum and natural gas industry. It occurs when liquids and/or gas flow rates are measured and when fluids flow through surface or downhole chokes, velocity-controlled subsurface safety valves, tubing centralizers, and any type of surface piping component, such as valves, elbows, and reducers. Restricted flow also can be caused by deposition of paraffin, asphaltenes, or hydrates on pipe walls.

Most published studies on multiphase flow through restrictions involve what is commonly called "critical" or "sonic" flow. This is primarily a consequence of the extensive use of surface chokes, which often operate under critical-flow conditions. However, a few wells still use velocity-controlled subsurface safety valves, which operate under subcritical or subsonic flow conditions.

5.2 Description of Restrictions

Three restrictions commonly found in oil and gas production operations are chokes (or choke beans or positive-flow beans), velocity-controlled subsurface safety valves, and conventional valves and fittings, often called piping components.

Chokes are installed in wells to control flow rates or pressures. They normally have slightly rounded entrances and can be several inches long. For example, the Thornhill-Craver choke beans are about 6 in. long with diameters from $\frac{1}{8}$ to $\frac{3}{4}$ in.¹ Fig. 5.1 shows a typical choke schematic.

The development of offshore and arctic production areas expanded the use of remotely controlled surface chokes. These devices are often called multiple orifice valves (MOV's).

The Willis choke² shown in Fig. 5.2 is an example of an MOV. This choke consists of a stationary ceramic disk and a movable ceramic disk, each with two holes. The size of the opening can be changed by rotating the movable disk relative to the stationary disk, as shown in Fig. 5.3. When changing the opening size, the resulting flow path can cause the fluids to impact on the pipe wall downstream of the valve, potentially causing erosion problems. Erosion concepts are described in Chap. 6.

Subsurface safety valves normally are installed in all offshore wells and frequently are regulated by law.³ Safety valves or storm chokes can operate on various principles, ranging from surface con-

trolled to velocity- or temperature-actuated. All are normally in a "full-open" status unless something causes them to close. Their mechanics can be very complex and are beyond the scope of this monograph. In velocity-controlled devices, the internal configuration through which the fluids must flow can be fairly complex. This configuration differs among the various manufacturers and even for different valves made by the same company. Fig. 5.4 is a diagram of the flow profile for two velocity-controlled subsurface safety valves with locking mandrels and equalizing subs. Chokes within the valves can be short and beveled (Otis-J) or long with only slightly rounded edges (Camco A-3). Sometimes flow through the safety valve follows a tortuous path. Sand erosion, which tends to enlarge the flow opening and can make design calculations only temporarily valid, complicates the selection of an optimum-size safety valve. Failure to consider friction effects on long chokes and subsurface safety valves also can be a design-calculation shortcoming.

A large variety of piping components also are found in surface production facilities. Because of the complex geometries involved, each exhibits a unique flow behavior. For example, pressure drop through an elbow is much different than pressure drop through a partially open gate valve.

5.3 Flow Through Chokes

Most producing wells have some type of surface choke installed near the wellhead to control production rates and/or downstream pressures. Control of flow rates often is necessary to prevent gas or water coning, sand production, or excessive erosion velocities. Chokes may be necessary to limit production to desired or legally imposed quotas. In some cases, pressure measurements at chokes are used to estimate flow rates.

For compressible flow, it is possible for the velocity in the choke throat to reach the speed of sound or the sonic velocity in the fluids. This is true for single-phase gas and multiphase flow. Pressure disturbances travel at sonic velocities. Consequently, if the fluids reach sonic velocity within the choke, the flow behavior becomes independent of conditions downstream from the choke. This condition is called critical flow. If the maximum velocity of fluids in the choke is less than the sonic velocity, the flow is called subcritical flow. Thus, a prediction of the sonic velocity or the boundary between critical and subcritical flow is necessary to describe the flow behavior of compressible fluids through chokes. Fig. 5.5 shows the dependence of flow rate through a choke on the ratio of the downstream to upstream pressure

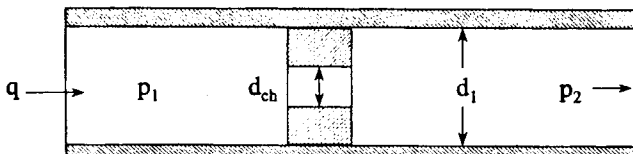


Fig. 5.1—Choke schematic.

for a compressible fluid. As the pressure ratio declines, flow rate increases. When the pressure ratio reaches a critical value, the flow rate through the choke becomes constant.

Prediction of flow behavior for multiphase flow through chokes relies heavily on a knowledge of single-phase flow through restrictions. For this reason, we describe single-phase liquid and gas flow before introducing multiphase flow.

5.3.1 Single-Phase Liquid Flow. Single-phase liquid flow seldom occurs in wellhead chokes because wellhead pressures are almost always below the bubblepoint pressure of the produced fluids. Because sonic velocities are high for single-phase liquids, flow behavior is always subcritical. Eq. 5.1, which can be developed from a combination of Bernoulli's equation⁴ and conservation of mass, describes single-phase flow of an incompressible liquid through a choke.

$$q = CA \sqrt{\frac{2g_c \Delta p}{\rho}} \quad \dots \dots \dots (5.1)$$

In oil field units, this equation becomes

$$q = 22,800 C d_{ch}^2 \sqrt{\frac{\Delta p}{\rho}} \quad \dots \dots \dots (5.2)$$

where q is in B/D and d_{ch} = the choke diameter in inches. Choke diameter is frequently called "bean" size and is measured in 64ths of an inch.

The flow coefficient, C , in Eqs. 5.1 and 5.2 accounts for all irreversibilities, such as friction. C can be determined experimentally and depends primarily on the type of restriction (i.e., venturi, nozzle, orifice, or choke), the ratio of the restriction diameter to the pipe diameter, and the Reynolds number. Fig. 5.6 shows the flow-coefficient behavior for a nozzle.

5.3.2 Single-Phase Gas Flow. For gases, Bernoulli's equation can be combined with an isentropic (adiabatic-frictionless) equation of state. All irreversible losses are accounted for through a discharge coefficient. The resulting Eq. 5.3⁷ is applicable for both critical and subcritical flow. However, for critical flow, the pressure ratio $y = p_2/p_1$ is replaced by the critical-pressure ratio, y_c .

$$q_{sc} = \frac{C_n p_1 d_{ch}^2}{\sqrt{\gamma_g T_1 Z_1}} \sqrt{\left(\frac{k}{k-1}\right)\left(y_c^{\frac{2}{k}} - y_c^{\frac{k+1}{k}}\right)} \quad \dots \dots \dots (5.3)$$

where

$$C_n = \frac{C_f C_D T_{sc}}{p_{sc}} \quad \dots \dots \dots (5.4)$$

Table 5.1 gives values for the constants in Eqs. 5.3 and 5.4 for both customary and SI units.

The critical-pressure ratio for a gas with a ratio of specific heats $k = C_p/C_v$ is given by

$$y_c = \left(\frac{p_2}{p_1}\right)_c = \left(\frac{2}{k+1}\right)^{\frac{k}{k-1}} \quad \dots \dots \dots (5.5)$$

For air and other diatomic gases, k is approximately 1.4 and the critical-pressure ratio from Eq. 5.5 is 0.53. Values of k for hydrocarbon gases at lower pressures are typically between 1.25 and 1.3. For practical reasons, critical flow for gases is often estimated to occur at a pressure ratio of 0.5. Fig. 5.7 shows a typical graph of gas flow rate vs. pressure ratio for different choke sizes, a gas with $k = 1.25$

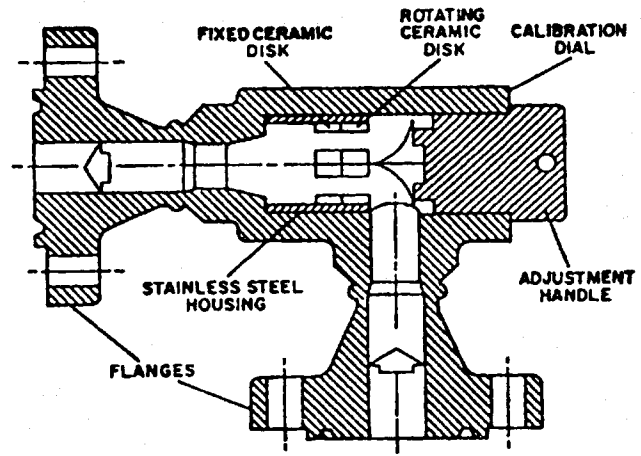


Fig. 5.2—Multiple orifice valve wellhead choke design (after Willis Oil Tool Co.²).

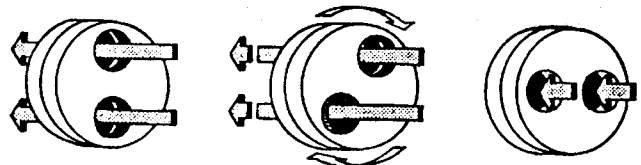


Fig. 5.3—Ceramic choke disk operation (after Willis Oil Tool Co.²).

and for an upstream pressure and temperature of 1,000 psia and 150°F, respectively. Eq. 5.5 predicts a critical-pressure ratio of 0.56 for this gas. For all pressure ratios below y_c , the flow rate is constant for a given choke size.

The correct ratio of specific heats for hydrocarbon gases varies with pressure and temperature.⁶ Fig. 5.8 shows that values as high as $k = 2.0$ are possible for methane at pressures between 2,000 and 4,000 psia and a temperature of 50°F. This can have a significant effect on the predicted critical-pressure ratio and resulting critical-flow rate.

Discharge-coefficient values in Eq. 5.4 depend on the shape of the opening to the restriction, the length of the restriction, and the Reynolds number. Although a value of $C_D = 0.865$ is given in Table 5.1, values between 0.82 and 0.9 are often used.

5.3.3 Multiphase Flow. To predict the flow behavior for multiphase flow through chokes requires that one first predict the boundary between critical and subcritical flow. This is much more difficult than for single-phase gas flow. The proper choice depends on whether calculation is made of the critical-pressure ratio below which total-mass flow rate is constant, or if the sonic velocity of a multiphase mixture is estimated.

TABLE 5.1—CONSTANTS AND UNITS FOR Eqs. 5.3⁷ AND 5.4

Symbol	Customary	SI Metric
q_{sc}	Mscf/D	m ³ /d
d_{ch}	in.	mm
p	psia	kPa
T	°R	K
C_s	27.611	1.6259
C_D	0.865	0.865
p_{sc}	14.696 psia	101.325 kPa
T_{sc}	519.68 °R	273.16 K
C_n	844.57	3.7915

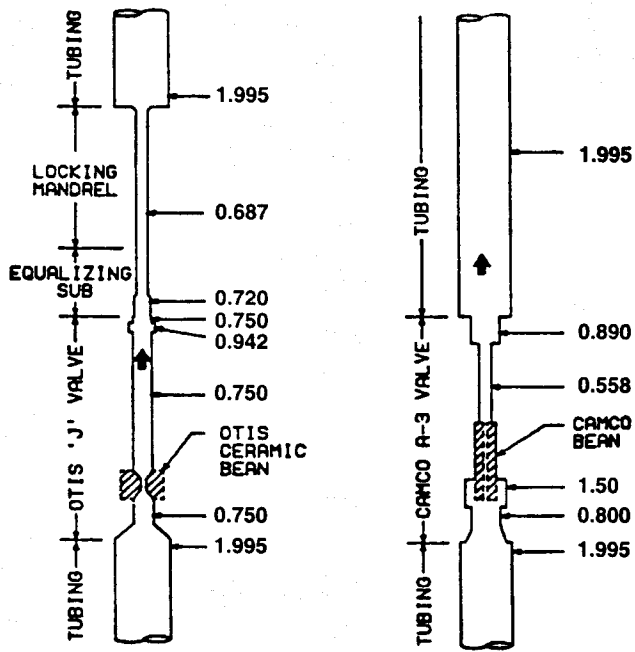


Fig. 5.4—Internal flow paths for velocity-controlled subsurface safety valves (after Brill and Beggs³).

Critical-Flow Boundary. Several authors have developed methods to predict the critical-flow boundary in multiphase flow.

Ashford and Pierce. Ashford and Pierce⁸ developed an expression for total-mass flow rate of a multiphase mixture. They assumed isentropic flow through the restriction, an incompressible liquid, no liquid flashing in the choke, and a homogeneous mixture. Eq. 5.6 assumes the derivative of the flow rate with respect to pressure ratio is zero at the critical boundary.

$$y_c = \frac{\frac{2R_1}{k\left(1+R_1y_c^{-\frac{1}{k}}\right)}\left[\left(\frac{R_1}{b}\right)(1-y_c^b) - y_c + 1\right]y_c^{-e} - 1}{R_1}, \quad (5.6)$$

where

$$b = \frac{k-1}{k}$$

and

$$e = \frac{k+1}{k}.$$

Eq. 5.6 requires an iterative procedure to determine values of y_c as a function of in-situ gas/liquid ratio for different values of k . In-situ gas/liquid ratio at upstream conditions, R_1 , can be calculated easily as the ratio of the superficial gas and liquid velocities determined at conditions immediately upstream of the choke. Fig. 5.9 gives a plot of Eq. 5.6 and shows that at values of R_1 above about 10, the critical-flow boundary is similar to single-phase gas. However, for lower values of R_1 , significantly lower values of y_c are predicted.

Sachdeva et al. Sachdeva et al.¹⁰ performed a combined experimental and theoretical study that resulted in these equations to determine y_c .

$$y_c = \left(\frac{N}{D}\right)^{\frac{1}{k-1}}, \quad (5.7)$$

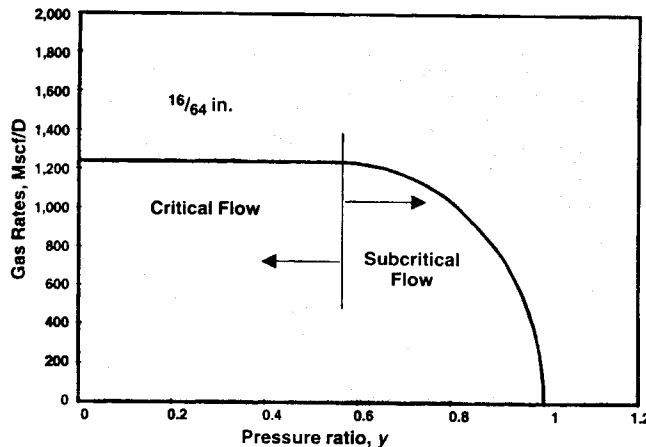


Fig. 5.5—Dependence of choke flow rate on y .

where

$$N = \frac{k}{k-1} + \frac{(1-x_{g1})\rho_{g1}(1-y_c)}{x_{g1}\rho_L} \dots \dots \dots \quad (5.8)$$

and

$$D = \frac{k}{k-1} + \frac{n}{2} + \frac{n(1-x_{g1})\rho_{g2}}{x_{g1}\rho_L} + \frac{n}{2} \left[\frac{(1-x_{g1})\rho_{g2}}{x_{g1}\rho_L} \right] \dots \dots \dots \quad (5.9)$$

In Eqs. 5.8 and 5.9, the parameter n and the upstream in-situ gas mass fraction or quality, x_{g1} , are determined from Eqs. 5.10 and 5.11, respectively.

$$n = 1 + \frac{x_{g1}(C_{pg} - C_{vg})}{x_{g1}C_{vg} + (1-x_{g1})C_L} \dots \dots \dots \quad (5.10)$$

and

$$x_{g1} = \frac{w_{g1}}{w_{g1} + w_{L1}}, \quad (5.11)$$

where

$$w_{g1} = 0.0764\lambda_g q_{Lsc}(R_p - f_o R_{s1}),$$

and

$$w_{L1} = 5.615q_{Lsc}(f_o B_{o1}\rho_{o1} + f_w B_{w1}\rho_{w1}).$$

Eq. 5.7 is dimensionless and any set of consistent units can be used. Determining y_c from Eq. 5.7 requires an iterative procedure. A value of y_c is first assumed in Eq. 5.8. This permits a calculation of y_c . A direct substitution method, in which the calculated value of y_c is used for the next guess until the calculated and guessed values of y_c agree to within a predetermined tolerance, is adequate. A value of 0.5 is a recommended first guess.

Perkins. Perkins⁶ derived an equation to predict the critical-pressure ratio that follows very closely the approach of Ashford and Pierce.⁸ He combined equations for conservation of mass and isentropic expansion of a homogeneous multiphase mixture to arrive at an expression for total mass flow rate. Using the same assumptions as Ashford and Pierce in Eq. 5.6, Perkins developed the expression

$$\left\{ 2C \left[1 - y_c^{\frac{n-1}{n}} \right] + 2\beta_{L1}(1-y_c) \right\}$$

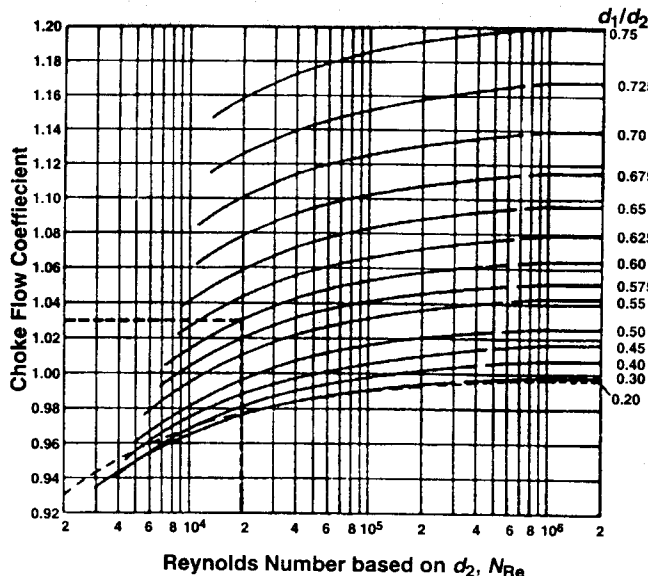


Fig. 5.6—Flow coefficients for liquid flow through a nozzle (after Crane Co. 5).

$$\begin{aligned} & \times \left\{ \left[1 - \left(\frac{A_2}{A_1} \right)^2 \left(\frac{x_{g1} + \beta_{L1}}{x_{g1} y_c^{-1/n} + \beta_{L1}} \right)^2 \right] \left[\frac{x_{g1}}{n} y_c^{-\frac{(1+n)}{n}} \right] \right. \\ & \quad \left. + \left(\frac{A_2}{A_1} \right)^2 \left(\frac{x_{g1}}{n} \right) \frac{\left(x_{g1} + \beta_{L1} \right) y_c^{-\frac{(1+n)}{n}}}{\left(x_{g1} y_c^{-1/n} + \beta_{L1} \right)^2} \right\} \\ & = \left[1 - \left(\frac{A_2}{A_1} \right) \left(\frac{x_{g1} + \beta_{L1}}{x_{g1} y_c^{-1/n} + \beta_{L1}} \right)^2 \right] \left(x_{g1} y_c^{-1/n} + \beta_{L1} \right) \\ & \quad \times \left[C \left(\frac{n-1}{n} \right) y_c^{-1/n} + \beta_{L1} \right], \end{aligned} \quad (5.12)$$

where

$$\beta_{L1} = \rho_{nl} \left(\frac{x_{o1}}{\rho_{o1}} + \frac{x_{w1}}{\rho_{w1}} \right)$$

and

$$C = x_g + \left[\left(x_g C_{vg} + x_o C_{vo} + x_w C_{vw} \right) \frac{M}{ZR} \right].$$

In the Perkins expression, x = weight fraction of a given phase in the flowing stream and C_v = heat capacity at constant volume, (ft-lbf/(lbm-°F)). C presumably can be evaluated at either upstream or downstream conditions. The polytropic expansion exponent for mixtures used in Eq. 5.12 was defined as

$$n = \frac{x_g k C_{vg} + x_o C_{vo} + x_w C_{vw}}{x_g C_{vg} + x_o C_{vo} + x_w C_{vw}}. \quad (5.13)$$

As for the case of Ashford and Pierce and Sachdeva *et al.*, an iterative procedure is required to determine y_c .

Fortunati. Fortunati¹¹ presented an empirical method that can be used to calculate both critical and subcritical multiphase flow through chokes. He assumed a homogeneous mixture and contended that the assumption was valid as long as v_m is greater than 32.8 ft/sec and the mixture Froude number is greater than 600. Using experimental data, Fortunati developed Fig. 5.10, which can be used

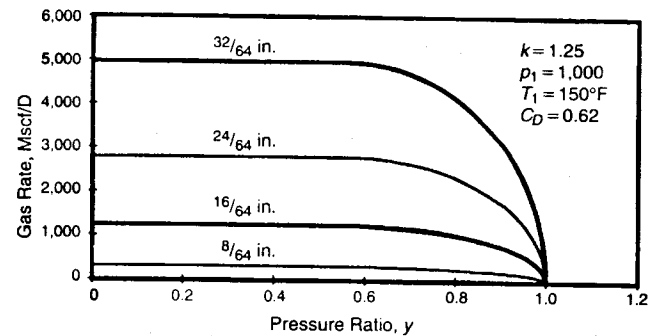


Fig. 5.7—Gas flow performance for different choke sizes.

to define the boundary between critical and subcritical flow. The curves in Fig. 5.10 were based on a downstream pressure of 19.9 psia. Eq. 5.14 should be used to calculate the Fortunati mixture velocity from the actual mixture velocity and downstream pressure.

$$v_{m2} = v_{m2F} \left(\sqrt{\frac{p_2}{p_{2F}}} \right)^\eta, \quad (5.14)$$

where

$$\eta = \left(1 - \lambda_{g2}^3 \right)^{0.38}. \quad (5.15)$$

Fig. 5.9 compares the Fortunati critical-flow boundary with boundaries predicted by Ashford and Pierce.

Wallis Sonic Velocity. In Eq. 5.16, Wallis presented an expression to calculate the sonic or compressibility-wave velocity of a homogeneous mixture.¹²

$$v_m^* = \left[\left(\rho_g \lambda_g + \rho_L \lambda_L \right) \left(\frac{\lambda_g}{\rho_g v_g^{*2}} + \frac{\lambda_L}{\rho_L v_L^{*2}} \right) \right]^{-0.5}. \quad (5.16)$$

The sonic velocity of the homogeneous mixture does not necessarily lie between the sonic velocities of each phase and in some circumstances may be far less than either. For example, an air/water mixture at atmospheric pressure will have an air sonic velocity of 1,100 ft/sec, a density ratio of 0.0012, and a minimum mixture sonic velocity of only 75 ft/sec. Wallis said the sonic velocity of a homogeneous mixture passes through a minimum at a no-slip void fraction of 0.5.

Nguyen *et al.* Sonic Velocities. Nguyen *et al.*¹³ studied sonic velocity in two-phase systems as a function of flow pattern.

For stratified flow, a composite sonic velocity does not exist because each phase is continuous in the axial direction. An effective sonic velocity exists in each phase that is influenced by the other phase. If a pressure pulse is imposed on the liquid and gas simultaneously, the disturbance propagates with different velocities in both phases in the axial direction.

Eq. 5.17 is the effective sonic velocity for the gas phase and shows that the effective sonic velocity is governed primarily by the sonic velocity of the gas phase because the second term in the denominator is small.

$$\frac{v_{Eg}^{*2}}{v_g^{*2}} = \frac{1}{\frac{1}{v_g^{*2}} + \left(\frac{H_L}{1-H_L} \right) \frac{\rho_g}{\rho_L} \frac{1}{v_L^{*2}}}. \quad (5.17)$$

The parallel expression for the effective sonic velocity in the liquid phase is

$$\frac{v_{EL}^{*2}}{v_L^{*2}} = \frac{1}{\frac{1}{v_L^{*2}} + \left(\frac{1-H_L}{H_L} \right) \frac{\rho_L}{\rho_g} \frac{1}{v_g^{*2}}}. \quad (5.18)$$

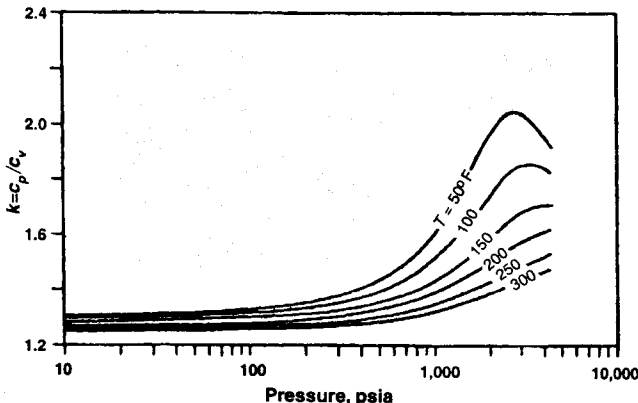


Fig. 5.8—Ratio of specific heats for methane (after Perkins⁶).

ρ_g and v_g^{*2} in the second term of the denominator in Eq. 5.18 are quite small, giving it a larger influence on the effective sonic velocity in the liquid phase.

In contrast to stratified flow, a composite sonic velocity expression was developed for an idealized slug unit. Eq. 5.19 gives the result.

$$v^* = \frac{v_L^* v_g^*}{H_L v_g^* + (1 - H_L) v_L^*}. \quad (5.19)$$

For homogeneous flow, Nguyen *et al.* combined expressions for sonic velocities of each phase flowing within an elastic boundary with a concept that the wave front sequentially passes through zones of liquid and gas within the homogeneous mixture. Eq. 5.20 gives the resulting expression.

$$v^* = \frac{1}{(1 - \alpha) \sqrt{\left(\frac{1-\alpha}{v_L^{*2}} + \frac{\alpha \rho_L}{\rho_g v_g^{*2}} \right)} + \alpha \sqrt{\frac{\alpha}{v_g^{*2}} + \frac{(1-\alpha)\rho_g}{\rho_L v_L^{*2}}}}. \quad (5.20)$$

Subcritical-Flow Behavior. Experimental and field tests confirm that accurate prediction of subcritical flow rates through restrictions is very difficult.

TUFFP Model. Following extensive tests of subcritical two-phase flow through velocity-controlled subsurface safety valves, a simple homogeneous Bernoulli-type equation was adopted. Thus,

$$\Delta p = \frac{\rho_{n1} v_{mB1}^2}{2 g_c C_D^2}. \quad (5.21)$$

Sachdeva *et al.* Sachdeva *et al.*¹⁰ presented the following equation to calculate flow rate through a choke.

$$q_{L_{sc}} = \frac{0.525 C_D d_{ch}^2}{C_{m2}} \times \left\{ p_1 \rho_{m2}^2 \left[\frac{(1-x_{g1})(1-y)}{\rho_{L1}} + \frac{x_{g1} k \left(1 - y^{\frac{k-1}{k}}\right)}{\rho_{g1}(k-1)} \right] \right\}, \quad (5.22)$$

where

$$\rho_{m2} = \left[\frac{x_{g1}}{\rho_{g1} y^{1/k}} + \frac{(1-x_{g1})}{\rho_{L1}} \right]^{-1} \quad (5.23)$$

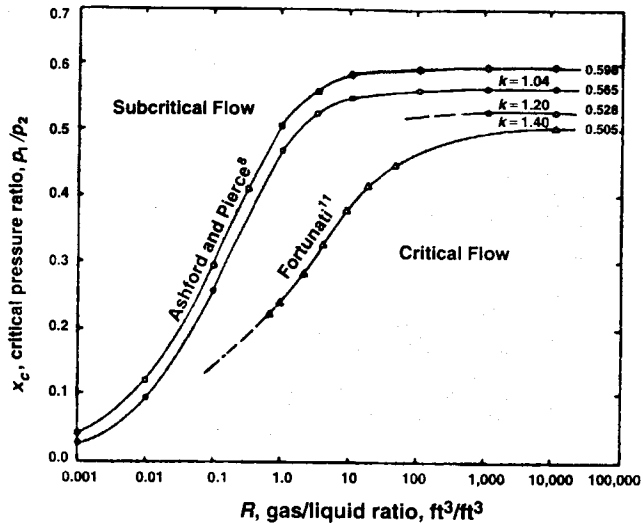


Fig. 5.9—Comparison of critical-flow boundary correlations for multiphase chokes (after Gould⁹). Fortunati¹¹ specifies $p_2 = 19.9$ psia as a basis for correlation.

and

$$C_{m2} = 8.84 \times 10^{-7} \lambda_{g2} (R_p - f_{o2} R_{s2}) + 6.5 \times 10^{-5} (f_{o2} \rho_{o2} B_{o2} + f_{w2} \rho_{w2} B_{w2}). \quad (5.24)$$

Critical-Flow Behavior. Critical flow exists if $y < y_c$ or if $v_m = v^*$.

Omaña *et al.* Omaña *et al.*¹⁴ presented an empirical correlation to predict critical multiphase flow through Thornhill-Craver-type chokes (see Fig. 5.1). A dimensional analysis of the problem of multiphase flow through chokes yielded pertinent dimensionless groups. In the next five equations, these oilfield units should be used: $q_{L_{sc}} = \text{STBL/D}$, $\rho = \text{lbm/ft}^3$, $\sigma_L = \text{dynes/cm}$, $d_{ch} = 64\text{ths of an inch}$, and $p_1 = \text{psia}$.

$$N_p = \rho_g / \rho_L, \quad (5.25)$$

$$N_{p_1} = 1.74 \times 10^{-2} p_1 \left(\frac{1}{\rho_L \sigma_L} \right)^{0.5}, \quad (5.26)$$

$$N_D = 0.1574 d_{ch} \sqrt{\frac{\rho_L}{\sigma_L}}, \quad (5.27)$$

and

$$N_{q_L} = 1.84 q_{L_{sc}} \left(\frac{\rho_L}{\sigma_L} \right)^{1.25} \quad (5.28)$$

Through the application of a least-squares regression-analysis procedure to a series of high-pressure natural gas/water tests, this empirical correlation was developed.

$$N_{q_L} = 0.263 N_p^{-3.49} N_{p_1}^{3.19} \lambda_L^{0.657} N_D^{1.80}. \quad (5.29)$$

Gilbert Type. Nind¹⁵ stated that a generalized expression with some simplifying assumptions for the flow of gas and oil through a knife-edged choke is given by

$$p_1 = \frac{C q_{L_{sc}} R_p^{0.5}}{d_{ch}^2}. \quad (5.30)$$

This expression has been the basis for several modifications by use of experimental and field data. This generalized equation can be used.

$$p_1 = \frac{b q_{L_{sc}} R_p^c}{d_{ch}^a}, \quad (5.31)$$

TABLE 5.2—CHOKE CONSTANTS

Investigator	<i>a</i>	<i>b</i>	<i>c</i>
Ros ¹⁶	2.00	4.25×10^{-3}	0.500
Gilbert ¹⁷	1.89	3.86×10^{-3}	0.546
Baxendell ¹⁸	1.93	3.12×10^{-3}	0.546
Achong ¹⁹	1.88	1.54×10^{-3}	0.650

TABLE 5.3—SUMMARY OF RESULTS

p_2 (psia)	<i>y</i>	Status
200	0.118	Critical
400	0.235	Critical
600	0.353	Critical
800	0.470	Subcritical
1,000	0.588	Subcritical
1,200	0.706	Subcritical

where p_1 is in psi, q_{Lc} is in STBL/D, R_p is in scf/STBL, and d_{ch} is in inches. Table 5.2 gives values of *a*, *b*, and *c* proposed by different investigators.

Sachdeva et al. Sachdeva et al.¹⁰ found that, if the flow is determined to be critical from Eq. 5.7, i.e., $y < y_c$, the flow rate should be calculated from Eq. 5.22 with $y = y_c$ and that all fluid properties in Eq. 5.22 should be evaluated with $p_2 = y_c p_1$.

Example 5.1—Determine Choke Diameters Required To Maintain Well Flow Rates. In Example 3.2, a choke is located immediately downstream of the wellhead. Assume that the wellhead pressure and temperature are 1,700 psia and 180°F, respectively. Determine the choke diameters required to maintain the well flow rates when the separator pressures downstream of the choke are 200, 400, 600, 800, 1,000, and 1,200 psia.

1. Using Eq. 5.6 with $k = 1.3$, determine the critical-pressure ratio, y_c .

$$R_1 = \frac{v_{sg1}}{v_{sl1}} = \frac{3.82}{3.97} = 0.962$$

and

$$k = 1.3.$$

The Eq. 5.6 trial-and-error solution yields $y_c = 0.446$.

Determine the flow status of the given pressure conditions for $p_1 = 1,700$ psia. Table 5.3 summarizes the results.

2. For cases of critical flow, determine d_{ch} using the Gilbert and the Omaña et al. critical-flow correlations.

Gilbert:

$$d_{ch} = \left[\frac{(3.86 \times 10^{-3})(10,000)(1,000)^{0.546}}{1,700} \right]^{1/1.89}$$

$$= 0.993 \text{ in.} = \frac{63.6}{64} \text{ in.}$$

Omaña et al.:

$$R_1 = 0.962,$$

$$N_p = \frac{\rho_g}{\rho_L} = \frac{5.88}{47.61} = 0.1235,$$

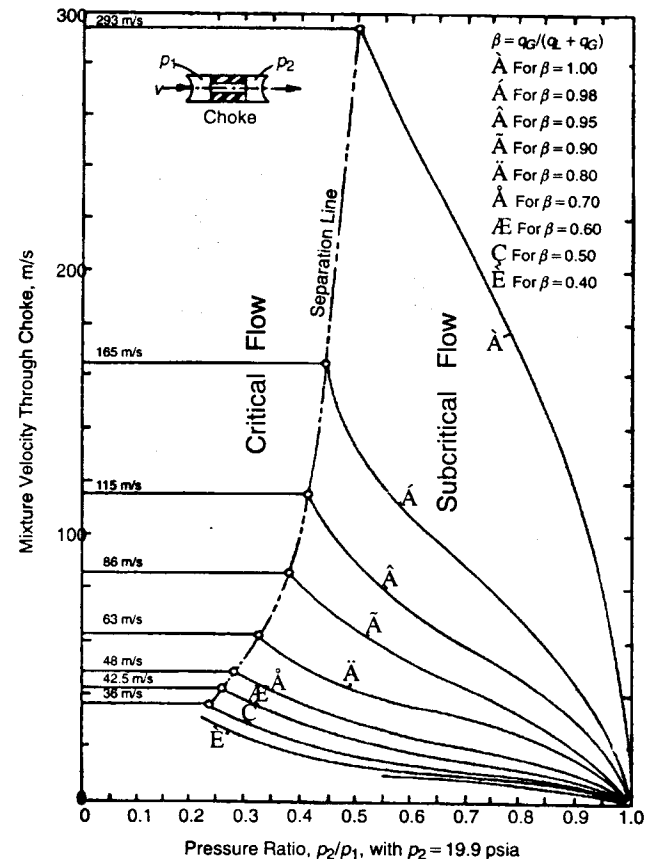


Fig. 5.10—Mixture velocity for critical and subcritical flow (after Fortunati¹¹).

$$N_{p_1} = 1.74 \times 10^{-2} p_1 \left(\frac{1}{\rho_L \sigma_L} \right)^{0.5}$$

$$= (1.74 \times 10^{-2})(1,700) \left(\frac{1}{47.61 \times 8.41} \right)^{0.5}$$

$$= 1.478,$$

$$N_{q_L} = 1.84 q_{Lc} \left(\frac{\rho_L}{\sigma_L} \right)^{1.25}$$

$$= (1.84)(10,000) \left(\frac{47.61}{8.41} \right)^{1.25}$$

$$= 160,674,$$

$$N_D = \left(\frac{N_{q_L}}{0.263 N_p^{-3.49} N_{p_1}^{3.19} \lambda_L^{0.657}} \right)^{1/8} = 18.21,$$

and

$$N_D = 120.872 d_{ch} \left(\frac{\rho_L}{\sigma_L} \right)^{1/2} = 18.21,$$

then

$$d_{ch} = 0.0633 \text{ ft}$$

$$= 0.76 \text{ in.}$$

$$= \frac{48.6}{64} \text{ in.}$$

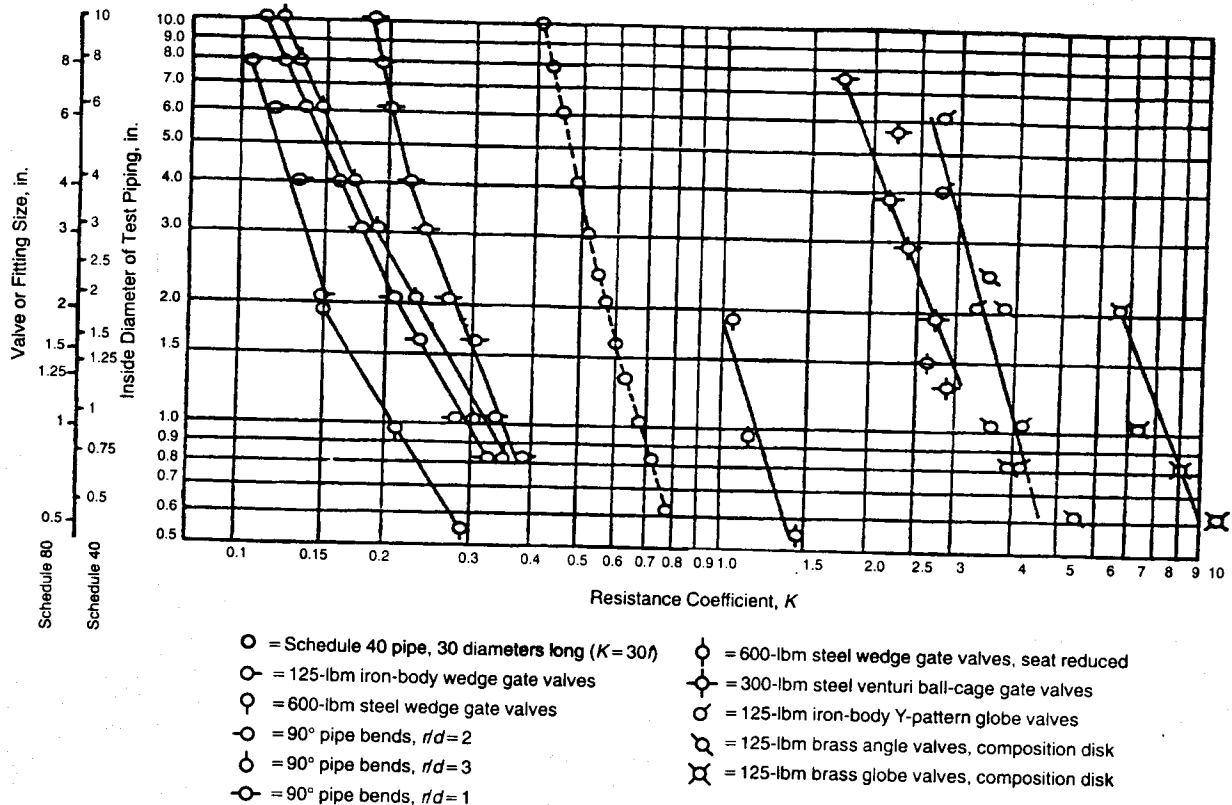


Fig. 5.11—Variation of resistance coefficient K with size and type of selected components (after Crane Co.⁵).

TABLE 5.4—SUMMARY OF RESULTS

p_2 (psia)	d_{ch} (64ths in.)	Status
200	63.6	Critical
400	63.6	Critical
600	63.6	Critical
800	64.4	Subcritical
1,000	68.6	Subcritical
1,200	74.6	Subcritical

3. For cases of subcritical flow, use the TUFFP correlation with a C_D of 0.50. Note that this C_D was selected to force the Gilbert equation and the TUFFP model to yield the same choke diameter at the critical-flow boundary.

$$\Delta p = \frac{\rho_{mb} v_{mb}^2}{2g_c C_D^2(144)} \text{ and } C_D = 0.50.$$

$$q_L = 0.778 \text{ ft}^3/\text{sec} \text{ and } q_g = 0.757 \text{ ft}^3/\text{sec},$$

$$\rho_n = 27.04 \text{ lbm}/\text{ft}^3.$$

At $p_2 = 800$ psia,

$$1,700 - 800 = \frac{(27.04)v_{mb}^2}{2(32.2)(0.50)^2(144)},$$

$$v_{mb} = 277.8 \text{ ft/sec} = \frac{q_L + q_g}{\frac{\pi}{4} d_{ch}^2},$$

$$\text{and } d_{ch} = 0.0838 \text{ ft} = 1.005 \text{ in.} = \frac{64.4}{64} \text{ in.};$$

$$\text{at } p_2 = 1,000 \text{ psia, } d_{ch} = \frac{68.6}{64} \text{ in.};$$

$$\text{and at } p_2 = 1,200 \text{ psia, } d_{ch} = \frac{74.6}{64} \text{ in.}$$

Table 5.4 shows a summary of the results.

Clearly, the Gilbert and Omaña *et al.* correlations give significantly different results for critical flow.

5.4 Flow Through Piping Components

When a single-phase gas or liquid flows through a pipe fitting or piping component, there is generally a higher degree of turbulence in the component than in a straight pipe at the same Reynolds number. When several components occur in a piping system, it is appropriate to calculate the frictional pressure drop or head loss caused by these components. One way to determine the pressure drop across a component is to add an "equivalent length" to the straight pipe. For multiple components, each one is replaced by an equivalent length of pipe that would yield the same pressure drop as the component.

The Darcy-Weisbach equation (Eq. 2.9) can be written as

$$\Delta p = \frac{fL}{d} \frac{\rho v^2}{2g_c} = K \frac{\rho v^2}{2g_c} \quad \dots \dots \dots \quad (5.32)$$

or

$$\frac{fL}{d} = K. \quad \dots \dots \dots \quad (5.33)$$

When solving Eq. 5.33 for the equivalent length of pipe, it is recommended that the fully turbulent friction factor given by Eq. 2.16 be used to account for the increased turbulence in the component.⁴ For multiple components, all the equivalent lengths can be added to the actual pipe length before performing the pressure-drop calculation.

The resistance coefficients, K , for many piping components have been determined experimentally.⁵ Fig. 5.11 gives some of them.

Sookprasong *et al.*²⁰ investigated multiphase flow through several piping components. They concluded that, when Eq. 5.32 is modified for multiphase flow conditions, acceptable results are obtained by use of single-phase, equivalent-length values. Thus, for multiphase flow,

$$\Delta p = \frac{K\rho_n v_m^2}{2g_c} \quad \dots \dots \dots \quad (5.34)$$

They also discovered that, when piping components are located very close to each other, frictional losses are higher than for individual components and undetermined longer equivalent lengths are necessary.

Example 5.2—Estimate the Pressure Drop for Multiphase Flow Through Piping Components. In Example 3.2, five 90° elbows and a gate valve exist next to each other immediately downstream of the well. Estimate the pressure drop across these components.

$$v_m = 7.83 \text{ ft/sec},$$

$$\rho_n = 27.04 \text{ lbm/ft}^3,$$

$$N_{Ren} = 3.15 \times 10^{-5},$$

$$d = 6.0 \text{ in.},$$

and

$$\epsilon = 0.00006 \text{ ft.}$$

From Fig. 5.11, $K=0.15$ for a 6-in.-diameter, 90° elbow and $K=1.8$ for a gate valve.

$$\begin{aligned} \Delta p &= \left(\sum_{i=1}^n K_i \right) \frac{\rho_n v_m^2}{2g_c} = [(5)(0.15) + 1.8] \frac{(27.04)(7.83)^2}{2(32.2)} \\ &= 65.64 \text{ lbf/ft}^2 = 0.46 \text{ psi.} \end{aligned}$$

References

1. Cook, H.L. Jr. and Dotterweich, F.H.: *Report on the Calibration of Positive Flow Beans as Manufactured by Thornhill-Craver Company*.

Houston, Texas, Texas College of Arts and Industries, Kingsville, Texas (1946).

2. *Instructions and Parts List*, Catalog 4230A, Willis Oil Tool Co., Long Beach, California (1971).
3. Brill, J.P. and Beggs, H.D.: *Two-Phase Flow in Pipes*, U. of Tulsa, Tulsa, Oklahoma (1991).
4. Darby, R.: *Chemical Engineering Fluid Mechanics*, Marcel Dekker Inc., New York City (1996).
5. "Flow of Fluids Through Valves, Fittings, and Pipe," Technical Paper 410, Crane Co., New York City (1981).
6. Perkins, T.K.: "Critical and Subcritical Flow of Multiphase Mixtures Through Chokes," *SPEDC* (December 1993) 271.
7. Beggs, H.D.: *Gas Production Operations*, OGCI Publications, Tulsa, Oklahoma (1984).
8. Ashford, F.E. and Pierce, P.E.: "Determining Multiphase Pressure Drops and Flow Capacities in Downhole Safety Valves," *JPT* (September 1975) 1145.
9. Gould, T.L.: "Discussion of An Evaluation of Critical Multiphase Flow Performance Through Wellhead Chokes," *JPT* (August 1974) 849.
10. Sachdeva, R. *et al.*: "Two-Phase Flow Through Chokes," paper SPE 15657 presented at the 1986 SPE Annual Technical Conference and Exhibition, New Orleans, 5–8 October.
11. Fortunati, F.: "Two-Phase Flow Through Wellhead Chokes," paper SPE 3742 presented at the 1972 SPE European Spring Meeting, Amsterdam, 16–18 May.
12. Wallis, G.B.: *One-Dimensional Two-Phase Flow*, McGraw-Hill Book Co. Inc., New York City (1969).
13. Nguyen, D.L., Winter, E.R.F., and Greiner, M.: "Sonic Velocity in Two-Phase Systems," *Int'l. J. Multiphase Flow* (1981) 7, 311.
14. Omaña, R. *et al.*: "Multiphase Flow Through Chokes," paper SPE 2682 presented at the 1969 SPE Annual Fall Meeting, Denver, Colorado 28 September–1 October, 1969.
15. Nind, T.E.W.: *Principles of Oil Well Production*, McGraw-Hill Book Co. Inc., New York City (1964).
16. Ros, N.C.J.: "An Analysis of Critical Simultaneous Gas-Liquid Flow Through a Restriction and Its Application to Flowmetering," *Appl. Sci. Res.* (1960) 9.
17. Gilbert, W.E.: "Flowing and Gas-Lift Well Performance," *Drill. & Prod. Prac.* (1954) 126.
18. Baxendell, P.B.: "Bean Performance—Lake Maracaibo Wells," Internal Company Report, Shell Oil Co., Houston (October 1967).
19. Achong, I.: "Revised Bean Performance Formula for Lake Maracaibo Wells," internal company report, Shell Oil Co., Houston (October 1961).
20. Sookprasong, P., Brill, J.P., and Schmidt, Z.: "Two-Phase Flow in Piping Components," *J. Energy Res. Tech.* (September 1986) 108, 197.

Chapter 6

Well Design Applications

6.1 Introduction

The mechanics of fluid flow in every component in a well's plumbing system affects the flow rate. Accurate well design is the key to achieving optimum flow rate. Consequently, understanding the mechanics of fluid flow through each component, from the reservoir to the first stage of separation, is imperative for accurate well design. The overall objective of this chapter is to present example applications of multiphase-flow theories to well design and optimization. It also provides a brief discussion of the reservoir flow into the wellbore to enable well design calculations.

The well design methods presented in this chapter also are used to troubleshoot well problems. In this context, some of the key constraining phenomena in well design, such as gas-well loading, erosion, and formation of natural gas hydrates, are also discussed.

The plumbing system is an interfacing conduit between the reservoir and the surface handling facilities. Without it, the hydrocarbons cannot become a tangible asset. For optimal production, a well design requires complex engineering considerations that depend on well components. Optimal production yields a maximum return on investment, not a maximum production rate. **Fig. 6.1** shows the major components with substantial pressure losses in a typical well. A production system consists of the following major components.¹⁻⁹

- Porous medium.
 - Completion (stimulation, perforations, and gravel pack).
 - Tubing with safety valve and choke.
 - Artificial lift system (pump and gas-lift valves among others).
 - Flowline with choke and other piping components (valves, elbows, and other such elements) from the wellhead to the first-stage separator.

In an oil or gas production system, the fluids flow from the drainage boundary in the reservoir to the separator at the surface. The average pressure within the drainage boundary is called the average reservoir pressure. This pressure controls the flow through a production system and is assumed to remain constant over a fixed time interval during depletion. When this pressure changes, the well's performance changes and the well may need to be re-evaluated. The average reservoir pressure changes because of normal reservoir depletion or artificial pressure maintenance with water, gas, or chemical injection.

The separator pressure at the surface is designed to optimize production and to retain lighter hydrocarbon components in the liquid phase. This pressure is maintained constant by the use of such mechanical devices as pressure regulators. As the well produces or in-

jects, there is a continuous pressure gradient from the reservoir to the separator. In well design calculations, it is not uncommon to use wellhead pressure for the separator pressure, assuming that the separator is at or very near the wellhead. Such assumptions imply negligible pressure loss in the surface flowline. For long flowlines, especially in hilly terrain, to ignore pressure losses may lead to substantial error in the production-rate calculation.

A node is any point in the production system where the pressure can be calculated as a function of the flow rates. As shown in Fig. 6.2, the two extreme nodes are the reservoir drainage boundary (Node 8) and the separator (Node 1). The pressures at these nodes are called the average reservoir pressure, p_r , and the separator pressure, p_{sep} , respectively. The other two important nodes are the bottomhole (Node 6), where the bottomhole flowing pressure, p_{wf} , is measured by a downhole gauge, and the wellhead (Node 3), where the wellhead pressure, p_{wh} , is measured by a gauge attached to the Christmas tree or the flow arm. If the pressures are measured at each node, the pressure loss between the nodes can be calculated as a function of the flow rate. Some nodes (Nodes 2, 4, and 5) are called functional nodes. These exist where a pressure drop occurs because of a choke, safety valve, or other piping component. For each component, the flow rate, q , is related functionally to the pressure differential, Δp , across the component, as given in Eq. 6.1.

Previous chapters established these mathematical relationships for different component segments of the production system, except for the reservoir system. The following sections discuss parameters that are important for the optimization of production through these components. Production-system analysis combines all component-system design procedures to help in the design and optimization of the total production system.

6.2 Vertical-Flow Performance

Vertical-flow performance² is the well's ability to produce under a constant surface-pressure constraint. In a producing well, this is called tubing intake⁴⁻⁶ or outflow performance. The rate vs. pressure loss in Nodes 1 through 6 are considered to calculate the tubing intake. For deliverability calculations that use any iterative scheme or graphic method, it is convenient to represent the bottomhole flowing pressure in terms of pressure losses through each of the

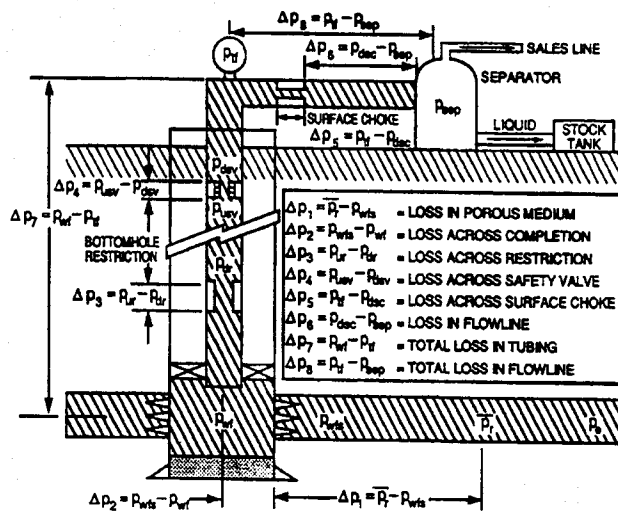


Fig. 6.1—Possible pressure losses in the producing system of a flowing well.⁶

nodes, starting at a fixed wellhead or separator pressure. This relationship can be expressed mathematically as

$$P_{wf} = P_{sep} + \Delta P_h + (\Delta p_{fl} + \Delta p_t + \Delta p_{ch})_f + \Delta P_{acc}, \quad (6.2)$$

where P_{wf} = bottomhole flowing pressure at Node 6, P_{sep} = separator pressure, ΔP_h = total hydrostatic pressure loss, $(\Delta p_{fl}, \Delta p_t, \Delta p_{ch})_f$ = friction pressure losses through the flowline, tubing, choke, or restrictions, and ΔP_{acc} = pressure loss because of acceleration.

Note that, in the absence of flowlines, P_{sep} can be set equal to the wellhead pressure, P_{wh} , and friction loss in the flowline, Δp_{fl} , can be set to zero in Eq. 6.2. The separator or the wellhead pressure normally is known and the methods to determine the pressure losses in each segment were discussed in previous chapters. In this chapter, the plot of P_{wf} vs. q (assuming a fixed wellhead/separator pressure) is called the tubing-intake curve. Fig. 6.3 presents a typical tubing-intake curve for producing wells. It is important to note that the flow condition represented by this curve will be stable only if $dp/dq \geq 0$ at any given point. Flow rates calculated in the unstable flow region indicate intermittent production, heading, or loading up of wells. This should be avoided through proper design and will be discussed in the example problems.

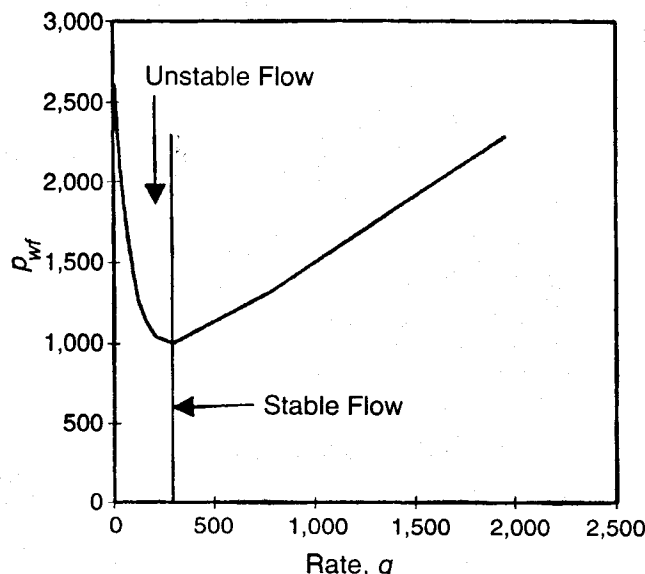


Fig. 6.3—Typical tubing-intake curve for producing wells.

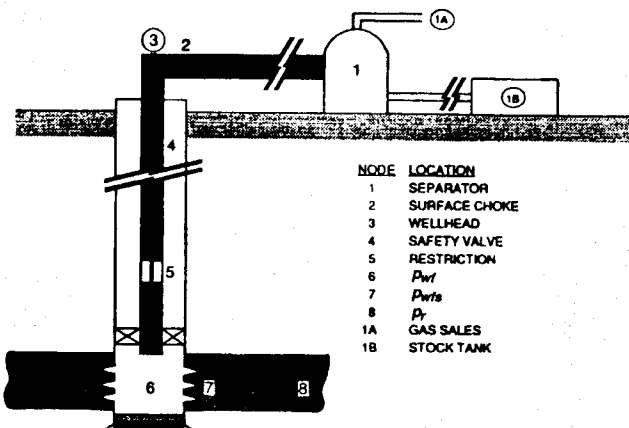


Fig. 6.2—Location of various nodes (from Mach et al.⁶).

The algebraic sign convention to determine pressure losses in Eq. 6.2 is important for production or injection cases. Pressure losses resulting from friction and acceleration always occur in the direction of flow, whereas hydrostatic pressure loss occurs in the direction of elevation gain. In Eq. 6.2, the friction and acceleration terms should be positive for production. For injection, the separator pressure, P_{sep} , in Eq. 6.2 should be replaced by pump discharge pressure; and the friction and acceleration terms should be negative. Consequently, as the injection rate increases, the bottomhole injection pressure decreases. Fig. 6.4 shows a set of typical tubing performance curves for an injection well.

Note that in the case of injection, tubing performance could be called tubing outflow because the fluid is pumped from the tubing into the reservoir. However, during production the tubing intake represents tubing performance. In the rest of this chapter, the tubing performance curve (TPC) is used for both injection and production.

As Fig. 6.5 shows, Eq. 6.2 also can be used to generate gradient curves, or flowing pressure vs. depth curves. Gradient curves are

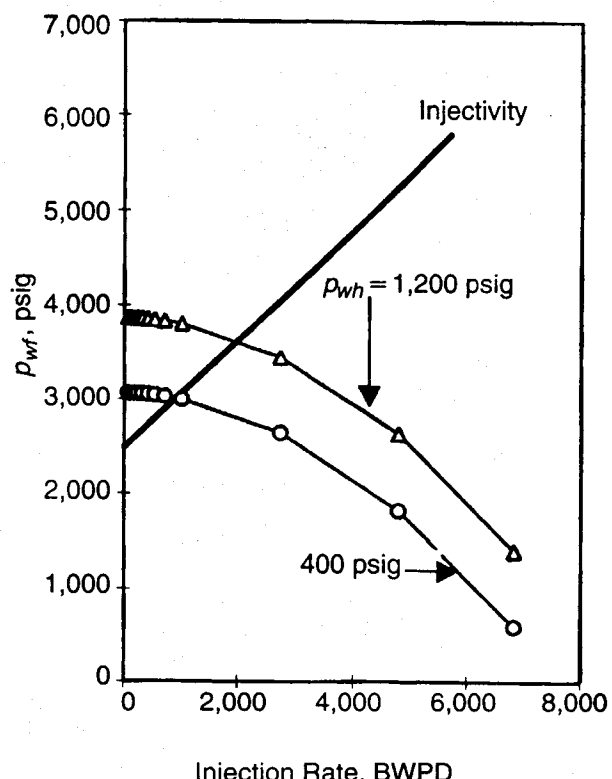


Fig. 6.4—Typical systems graph for injection wells.

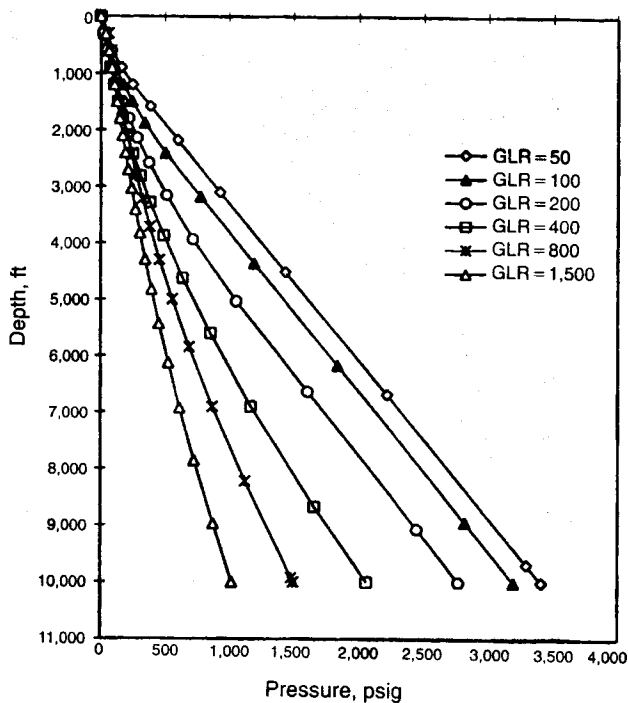


Fig. 6.5—Typical set of gradient curves for different GLR's.

very useful in the design of artificial-lift systems, such as gas lift or bottomhole pumps, as illustrated in Sec. 6.5.

6.3 Inflow Performance

Inflow performance relationship (IPR) is defined as the functional relationship between the production rate from the reservoir and the bottomhole flowing pressure. Gilbert² first proposed well analysis using this relationship. IPR is defined in the pressure range between the average reservoir pressure and atmospheric pressure. The flow rate corresponding to atmospheric bottomhole flowing pressure is defined as the absolute open flow potential (AOFP) of the well, whereas the flow rate is always zero when the bottomhole pressure is the average reservoir pressure, representing a shut-in condition. Fig. 6.6 presents a typical IPR based on Darcy's law for single-phase liquid flow. The actual flowing bottomhole pressure also depends on the separator pressure and the pressure loss in the flow conduits up to the depth of midperforation.

6.3.1 Single-Phase Liquid Flow. For single-phase oil or liquids, the IPR shown in Fig. 6.6 is stated by Darcy's law^{10,11} for radial flow as

$$q_o = \frac{7.08 \times 10^{-3} k_o h (\bar{p}_r - p_{wf})}{\mu_o B_o \left[\ln \left(\frac{r_e}{r_w} \right) - 0.75 + s_t + D q_o \right]}, \quad (6.3)$$

where q_o = oil flow rate into the well, STBO/D; B_o = formation volume factor of oil, bbl/STBO, (see Appendix B); μ_o = viscosity of oil, cp, (see Appendix B); k_o = effective permeability of the formation to oil, md; h = net thickness of the formation, ft; \bar{p}_r = average reservoir pressure, psia; p_{wf} = bottomhole flowing pressure, psia; r_e = radius of drainage, ft = $\sqrt{A/\pi}$, where A is area of circular drainage, ft^2 ; r_w = wellbore radius, ft; s_t = total skin; and $D q_o$ = pseudo-skin caused by turbulence. In oil wells, this term is insignificant, especially for low-permeability reservoirs.

For $r_e = 1,466$ ft, $r_w = 0.583$ ft, $s_t = 0$, and no turbulence, Darcy's law simplifies to

$$q_o = \frac{k_o h}{\mu_o B_o} (\bar{p}_r - p_{wf}), \quad (6.4)$$

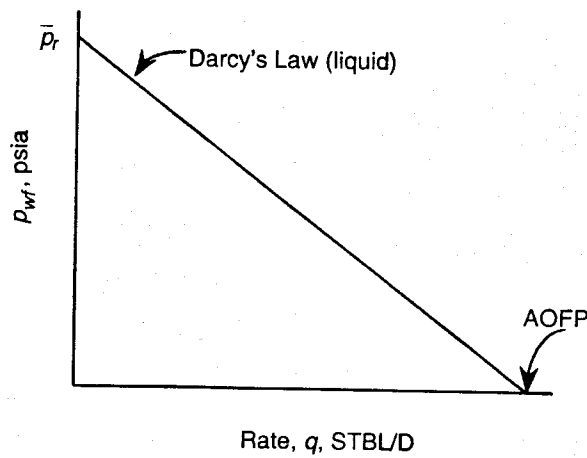


Fig. 6.6—Typical IPR curve.

TABLE 6.1—INPUT DATA FOR EXAMPLE 6.1

Permeability, k_o , md	6
Pay thickness, h , ft	15
Average reservoir pressure, \bar{p}_r , psig	1,000
Water cut	0
Oil viscosity, μ_o , cp	Unknown
Formation volume factor, B_o , bbl/STBO	Unknown
Skin, s	0
Pumped off (negligible fluid column above pump section)	

where k_o is in darcies.

Assuming reasonable reservoir drawdowns, $(\bar{p}_r - p_{wf})$, this simple equation often is used to estimate flow rates from oil wells quickly. Normally, optimized wells flowing naturally or with gas lift should produce with 50 to 80% drawdown. A 60% drawdown can be assumed without any knowledge of the system. A 30% drawdown is common when sand production is suspected. A 90% drawdown is likely when pumps are located just above the top perforations and operated at optimum condition with minimum fluid level above the suction.

Example 6.1—Diagnosing Pumping-Well Problem.

Input Data. Table 6.1 gives the input data.

Solution.

- Estimate production rate assuming a 90% drawdown.

$$\mu_o = 1 \text{ cp},$$

$$B_o = 1 \text{ bbl/STBO},$$

and

$$q_o \equiv \frac{(6)(15)(0.9)(1,000)}{1,000} \cong 81 \text{ STBO/D}.$$

- For a well producing 20 STBO/D, diagnose possible problems.

a. Check actual viscosity under reservoir conditions.

b. If viscosity is not the problem, check fluid level in annulus.

c. If fluid level has risen, increasing the p_{wf} or reducing drawdown, the pump is the problem.

d. If fluid level has not risen, the problem may be caused by skin.

6.3.2 Productivity Index. Fig. 6.7 shows that an IPR based on Darcy's law for oil or liquid is a straight line. AOFP is the maximum flow rate, q_{max} , at which the well can produce with atmospheric pressure at the bottomhole. Productivity index, J , is the absolute val-

TABLE 6.2—INPUT DATA FOR EXAMPLE 6.2

Permeability, k_o , md	30
Oil viscosity, μ_o , cp	0.8
Pay thickness, h , ft	40
Formation volume factor, B_o , bbl/STBO	1.2
Average reservoir pressure, \bar{p}_r , psig	3,000
Drilled hole size (open hole), d , in.	12.25
Reservoir temperature, T_r , °F	200
Well drainage area, A , acres (43,560 ft ² /acre)	160
Skin, s (no turbulence)	0

ue of the slope of the IPR straight line and is a constant for a single-phase liquid reservoir. Thus,

$$J = \frac{q_o}{(\bar{p}_r - p_{wf})}.$$

On the basis of Darcy's law,

$$J = \frac{7.08 \times 10^{-3} k_o h}{\mu_o B_o \left[\ln\left(\frac{r_e}{r_w}\right) - 0.75 + s_t \right]} = \frac{q_o}{(\bar{p}_r - p_{wf})} \cdot \frac{\text{STBO/D}}{\text{psi}}. \quad (6.5)$$

The productivity-index concept is not applicable for gas wells because the IPR for a gas well is nonlinear.

Example 6.2—Oilwell IPR Problem.

Input Data. Table 6.2 provides the input data.

Solution.

1. Calculate drainage radius.

$$r_e = \sqrt{\frac{A \times 43,560}{\pi}} = 1,490 \text{ ft.}$$

Assume $r_w = 0.51$ ft and apply Darcy's law for radial flow.

$$q_o = \frac{7.08 \times 10^{-3} k_o h (\bar{p}_r - p_{wf})}{\mu_o B_o \left[\ln\left(\frac{r_e}{r_w}\right) - 0.75 \right]}.$$

Determine AOPF, $q_{o\max}$.

$$q_{o\max} = \frac{7.08 \times 10^{-3} (30)(40)(3,000 - 0)}{(0.8)(1.2) \left[\ln\left(\frac{1,490}{0.51}\right) - 0.75 \right]} \\ = \frac{26,550}{7.23} = 3,672 \text{ STBO/D.}$$

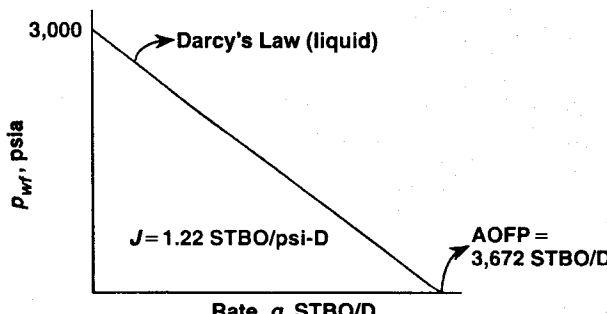


Fig. 6.7—Productivity-index graph.

TABLE 6.3—FACTORS FOR DIFFERENT SHAPES AND WELL POSITIONS IN A DRAINAGE AREA¹⁴

SYSTEM	X
1	$\frac{r_e}{r_w}$
2	$0.571A^{1/2}$
3	$0.585A^{1/2}$
4	$0.604A^{1/2}$
5	$0.610A^{1/2}$
6	$0.678A^{1/2}$
7	$0.688A^{1/2}$
8	$1.368A^{1/2}$
9	$2.066A^{1/2}$
10	$0.884A^{1/2}$
11	$1.485A^{1/2}$
2	$0.986A^{1/2}$
3	$1.44A^{1/2}$
4	$2.208A^{1/2}$
5	$1.925A^{1/2}$
6	$6.50A^{1/2}$
7	$9.36A^{1/2}$
8	$1.724A^{1/2}$
9	$1.794A^{1/2}$
10	$4.072A^{1/2}$
11	$9.529A^{1/2}$
2	$10.135A^{1/2}$

Using Fig. 6.7, plot the IPR curve.

2. Determine productivity index,

$$J = \frac{q_o}{(\bar{p}_r - p_{wf})} = \frac{7.08 \times 10^{-3} k_o h}{\mu_o B_o \left[\ln\left(\frac{r_e}{r_w}\right) - 0.75 \right]} \\ = 1.22 \frac{\text{STBO/D}}{\text{psi}}.$$

6.3.3 Single-Phase Gas Flow.

Darcy's law for single-phase gas is

$$q_g = \frac{7.03 \times 10^{-4} k_g h (\bar{p}_r^2 - p_{wf}^2)}{\bar{\mu}_g \bar{Z} T_r \left[\ln\left(\frac{r_e}{r_w}\right) - 0.75 + s_t + Dq_g \right]}, \quad (6.6)$$

where q_g = gas flow rate, Mscf/D; k_g = effective permeability to gas, md; \bar{Z} = gas compressibility factor determined at average temperature and average pressure, fraction; T_r = average reservoir temperature, °R; and $\bar{\mu}_g$ = gas viscosity calculated at average pressure and average temperature, cp.

6.3.4 Sources of Information. When performing IPR calculations, several information sources are available, including

1. Transient well-test interpretation.^{12,13} For example, buildup and drawdown tests are used to determine kh/μ and s_t . Successful buildup tests also help determine average pressure \bar{p}_r . In injection wells, the buildup test is called a falloff test and the drawdown equivalent test is called an injectivity test.

2. Special well tests, such as extended drawdown or reservoir limit tests, are used to determine the drainage shape and r_e .

3. Well logs and cores also are used to determine k and h .

If properly conducted and interpreted, well-test interpretation methods quite often yield the most representative values of reservoir parameters, such as (kh/μ) , \bar{p}_r , and skin, among others. These values normally are the volumetric average values in the radius of in-

TABLE 6.4—INPUT DATA FOR EXAMPLE 6.3, STEP 1

Permeability, k_o , md	5
Average reservoir pressure, \bar{p}_r , psig	2,500
Pay thickness, h , ft	20
Skin, * s	-5, -1, 0, 1, 5, 10, 50
Oil viscosity, μ_o , cp	1.1
Formation volume factor, B_o , bbl/STBO	1.2
Spacing, acres	80
Wellbore radius, r_w , ft	0.365
*Sensitivity parameter	

vestigation, whereas logs and cores determine the value of k at discrete points around the wellbore.

6.3.5 Boundary Effects. Most reservoir engineering calculations assume radial-flow geometry. Radial geometry implies that the drainage area is circular and the well is located at the center of the drainage circle. In many cases, the drainage area is rectangular or of some other noncircular shape. Applications of equations based on radial geometry to a noncircular drainage area could lead to substantial error. Darcy's law can be modified for a bounded drainage area of different shapes as

$$q_o = \frac{7.08 \times 10^{-3} k_o h (\bar{p}_r - p_{wf})}{B_o \mu_o [\ln(X) - 0.75 + s_t]} \quad \dots \dots \dots \quad (6.7)$$

for oil and

$$q_g = \frac{7.03 \times 10^{-6} k_g h (\bar{p}_r^2 - p_{wf}^2)}{\bar{\mu}_g \bar{Z} T_r [\ln(X) - 0.75 + s_t + D q_g]} \quad \dots \dots \dots \quad (6.8)$$

for gas. The productivity index for oil then is

$$J = \frac{q_o}{\bar{p}_r - p_{wf}} = \frac{7.08 \times 10^{-3} k_o h}{B_o \mu_o [\ln(X) - 0.75 + s_t]}, \quad \dots \dots \dots \quad (6.9)$$

where X is given in Table 6.3 for various drainage shapes and well locations. Note that A is the drainage area and \sqrt{A}/r_w is dimensionless.

Example 6.3—IPR Problems for Oil and Gas Wells.

1. For an oil well, draw IPR's and tabulate skin vs. AOPP, $q_{o\max}$.

Input Data. Table 6.4 gives the input data.

Solution. The drainage radius, r_e , is

$$r_e = \sqrt{\frac{(80)(43,560)}{\pi}} = 1,053 \text{ ft.}$$

AOPP is

$$\begin{aligned} q_{o\max} &= \frac{7.08 \times 10^{-3} k_o h \bar{p}_r}{\mu_o B_o [\ln(r_e/r_w) - 0.75 + s]} \\ &= \frac{7.08 \times 10^{-3} (5)(20)(2,500)}{(1.1)(1.2) \left[\ln\left(\frac{1,053}{0.365}\right) - 0.75 + s \right]} \\ &= \frac{1,341}{7.97 - 0.75 + s} = \frac{1,341}{7.22 + s}. \end{aligned}$$

Table 6.5 gives AOPP values for different skin factors.

Because IPR is linear, the \bar{p}_r and AOPP uniquely define it. Fig. 6.8 shows IPR lines for each skin factor.

TABLE 6.5—EXAMPLE OF SKIN FACTORS AND AOPP's

Skin, s	AOPP (STBO/D)
-5	604
-1	216
0	186
1	163
5	110
10	78
50	23

TABLE 6.6—INPUT DATA FOR EXAMPLE 6.3, STEP 2

Reservoir temperature, T_r , °F	200
Gas permeability, k_g , md	1
Pay thickness, h , ft	200
Average gas viscosity, $\bar{\mu}_g$, cp	0.019
Gas compressibility factor, Z	1.1
Average reservoir pressure, \bar{p}_r , psig	3,500
Spacing, acres	80
Wellbore radius, r_w , ft	0.365
Skin, s	1

2. For a gas well, tabulate and draw the IPR curve. Calculate the AOPP.

Input Data. Table 6.6 gives the input data.

Solution.

From Part 1, for an oil well, $\ln(r_e/r_w) - 0.75 = 7.22$.

From Darcy's law (neglecting turbulence),

$$\begin{aligned} q_g &= \frac{7.03 \times 10^{-6} k_g h (\bar{p}_r^2 - p_{wf}^2)}{\bar{\mu}_g \bar{Z} T_r \left[\ln\left(\frac{r_e}{r_w}\right) - 0.75 + s \right]} \\ &= \frac{7.03 \times 10^{-4}(1)(200)(3,500^2 - p_{wf}^2)}{(0.019)(1.1)(660)(7.22 + 1)} \\ &= 1.24 \times 10^{-3}(3,500^2 - p_{wf}^2). \end{aligned}$$

Fig. 6.9 gives this IPR curve. Table 6.7 gives the IPR data used in this figure.

3. Solve Part 1 for a square drainage area and a skin of zero.

Solution.

$$q_{o\max} = \frac{1,341}{\ln X - 0.75 + s} = \frac{1,341}{\ln X - 0.75}.$$

From Table 6.3,

$$\begin{aligned} X &= \frac{0.571 \sqrt{80 \times 43,560}}{r_w} \\ &= \frac{1,066}{0.365} = 2,920. \end{aligned}$$

$$q_{o\max} = \frac{1,341}{\ln 2,920 - 0.75} = \frac{1,341}{7.98 - 0.75} = 186 \text{ (STBO/D).}$$

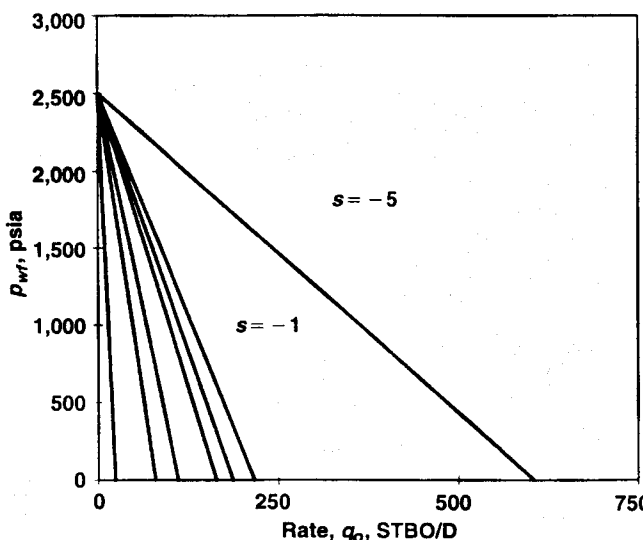


Fig. 6.8—IPR lines for an oil well in Example 6.3 (Part 1).

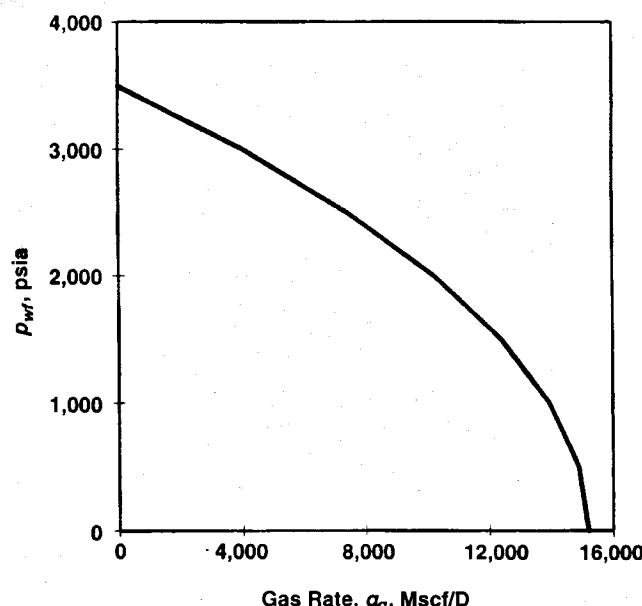


Fig. 6.9—IPR curve for a gas well in Example 6.3 (Part 2).

TABLE 6.7—IPR DATA USED IN FIG. 6.9

P_{wf} (psig)	q_o (Mcscf/D)
3,500	0
3,000	4,030
2,500	7,440
2,000	10,230
1,500	12,400
1,000	13,950
500	14,880
0	15,190

6.3.6 Two-Phase Flow. Darcy's law is applicable only for single-phase flow. For the case of an oil reservoir, single-phase flow occurs when the bottomhole flowing pressure is above the bubblepoint pressure of the reservoir fluid at the reservoir temperature. During reservoir depletion, the pressure continues to drop unless maintained by fluid injection or flooding. Consequently, during depletion, the bottomhole flowing pressure falls below the bubblepoint pressure, resulting in a combination of single- and two-phase flow in the reservoir. The pressure profile in the drainage flow path determines the areas of single- and two-phase flow on the basis of the black-oil phase diagram shown in Fig. 6.10. The IPR of such systems is called a composite IPR. Before discussing composite IPR, hydrocarbon phase behavior is reviewed briefly.

Phase Behavior of Hydrocarbon Fluids. On the basis of fluid samples taken at reservoir conditions, a pressure/volume/temperature (PVT) analysis generates a phase envelope in a pressure-temperature diagram.¹⁵ Fig. 6.10 presents a typical black-oil pressure-temperature diagram showing the physical state of the fluids. When the average reservoir pressure, the bottomhole and wellhead flowing pressures, and the corresponding temperatures are plotted, one can identify the type of reservoir fluid, such as single-phase, two-phase, or a combination. Such information helps determine the type of IPR equation to be used.

For the case of two-phase flow, such as Case E in Fig. 6.10 where \bar{P}_r is below the bubblepoint pressure, either a Vogel¹⁶ or a Fetkovich¹⁷ IPR is recommended. For composite reservoirs shown in Fig. 6.10, Darcy's law is used above the bubblepoint pressure and a Vogel or a Fetkovich IPR is used below the bubblepoint.

Vogel IPR. Through simulation of saturated oil reservoirs, Vogel developed this IPR.

$$\frac{q_o}{q_{o_{max}}} = 1 - 0.2\left(\frac{P_{wf}}{\bar{P}_r}\right) - 0.8\left(\frac{P_{wf}}{\bar{P}_r}\right)^2 \quad \dots \quad (6.10)$$

Flow rate normalization with $q_{o_{max}}$ seemed to make this IPR work in a multiphase system. This IPR can be modified easily for a composite reservoir system, as shown in Eqs. 6.15 through 6.17. A Vogel IPR curve can be generated if either the AOFP, $q_{o_{max}}$, and the reservoir pressure, \bar{P}_r , are known or the reservoir pressure, \bar{P}_r , and a flow rate and the corresponding bottomhole flowing pressure are known. For either case, a buildup test for \bar{P}_r and a flow test with a bottom-hole gauge are needed. Though quite simple to apply, the Vogel IPR is not commonly supported by field data from multirate oilwell tests. The Fetkovich¹⁷ IPR, on the other hand, quite often is supported by field data and is more universally used for both oil and gas wells.

Fetkovich IPR. Multipoint or backpressure testing of gas wells is a common procedure to establish gas-well performance curves or deliverability. Fetkovich applied these tests to oil wells with reservoir pressures above and below the bubblepoint pressure. The general conclusion from these backpressure tests is that, as in gas wells, the IPR in oil wells is of the form

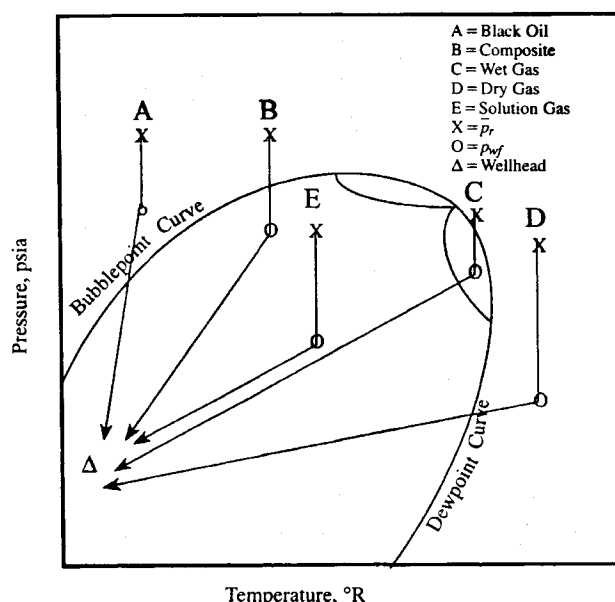


Fig. 6.10—Typical phase diagram for black oil.

TABLE 6.9—INPUT DATA FOR EXAMPLE 6.5

Drainage radius, r_e , ft	2,000
Permeability, k_o , md	1
Average reservoir pressure, \bar{p}_r , psig	2,000
Net pay thickness, h , ft	20
Porosity, ϕ	0.2
Oil viscosity, μ_o , cp	1
Wellbore radius, r_w , ft	0.5
Formation volume factor, B_o , bbl/STBO	1
Skin, s	1.21
Total compressibility, q_f , psi ⁻¹	10 ⁻⁵
Wellbore storage coefficient, c , bbl/psi	0.001
Time, * t , hours	0.1, 10, 100, 1,000, 7,584

*Sensitivity parameter.

transient production period before the onset of the pseudo-steady state flow, defined in Eq. 6.14. As this equation states, the lower the permeability of the rock, the longer the transient period. Consequently, many low-permeability gas reservoirs produce a major part of the recoverable reserve in this transient period, making transient IPR's useful in the prediction of production decline. Earlougher¹² and Agarwal *et al.*¹⁹ presented information on transient IPR.

Infinite Homogeneous Reservoir. For homogeneous reservoirs, the well known infinite-acting semilog approximation for a well with a skin, s , producing at a constant rate, q_o , is given by,

$$q_o = \frac{k_o h (\bar{p}_r - p_{wf})}{162.6 \mu_o B_o \left\{ \left[\log \left(\frac{k_o}{\phi \mu_o c_i r_w^2} \right) - 3.23 + 0.87s \right] + \log(t) \right\}} \quad (6.13)$$

Also known as the transient IPR equation,²⁰ this equation is valid for the transient radial-flow period. It is characterized by flowing times less than t_{pss} when pseudosteady-state flow begins, where

$$t_{pss} = \frac{948 \phi \mu_o c_i r_e^2}{k_o}, \text{ hours.} \quad (6.14)$$

Example 6.5—Transient IPR Problem. Calculate the duration of infinite-acting radial flow and tabulate the AOPP.

Input Data. Table 6.9 gives the input data.

Solution. Duration of infinite-acting radial flow, t_{pss} ,

$$t_{pss} = 948 \frac{0.2 \times 10^{-5} (2,000)^2}{1} = 7,584 \text{ hours (316 days).}$$

AOPP ($p_{wf} = 14.7$ psia or 0 psig) in Eq. 6.13.

$$q_{o\max} =$$

$$\frac{(20)(2,000)}{162.6 \left\{ \left[\log \left(\frac{1}{0.2 \times 10^{-5} (0.5)^2} \right) - 3.23 + 0.87(1.21) \right] + \log t \right\} + \log t} = \frac{246}{4.12 + \log t}.$$

Note that for a single-phase oil reservoir, average reservoir pressure and the AOPP at any time uniquely define the IPR for that time.

TABLE 6.10—TRANSIENT IPR's FOR EXAMPLE 6.5

t (hours)	$q_{o\max}$ (STBO/D)
0.1	79
10	48
100	40
1,000	35
7,584	31

Table 6.10 presents IPR's for five different times to the start of pseudosteady-state flow.

Homogeneous Reservoir With Induced Vertical Fracture. Cinco-L. *et al.*²¹ developed curves for finite-conductivity vertical fractures. Meng and Brown²² modified them for wells with an induced fracture at the center of a reservoir with different closed rectangular drainage areas. The fluid is considered slightly compressible with constant viscosity, μ . For gas flow, the real-gas pseudopressure function²³ is used and gas properties are evaluated at the initial reservoir pressure. The dimensionless variables are defined as follows.

Dimensionless wellbore pressure drop, p_D , for oil and gas, respectively, are

$$p_D = \frac{k_o h [p_i - p_{wf}(t)]}{141.2 q_f \mu_o B_o}$$

and

$$p_D = \frac{k_g h [m(p_i) - m(p_{wf}(t))] }{1,424 q_g T_r};$$

dimensionless time, t_{Dif} , for oil and gas, respectively, are

$$t_{Dif} = \frac{0.000264 k_o t}{\phi \mu_o c_i x_f^2}$$

and

$$t_{Dif} = \frac{0.000264 k_g t}{\phi (\mu_o c_i)_i x_f^2};$$

and dimensionless fracture conductivity, C_{fD} , is

$$C_{fD} = k_f w / k x_f,$$

where w = fracture width and x_f = fracture half-length.

Fig. 6.13 presents a few of these types of curves. It is important to note that the early-time pressure behavior depends on C_{fD} . However, at late times or after depletion starts, the pressure response is influenced by the shape and size of the drainage area.

As in the homogeneous reservoir case, transient IPR curves can be generated for fractured reservoirs by use of curves from Fig. 6.13

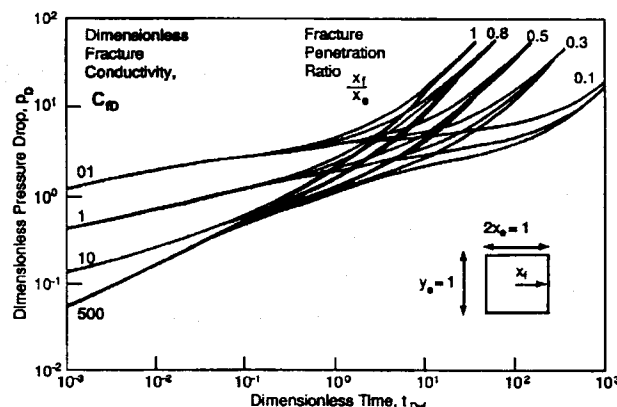


Fig. 6.13—Constant rate type curve for finite-conductivity fracture in a closed-square system.²²

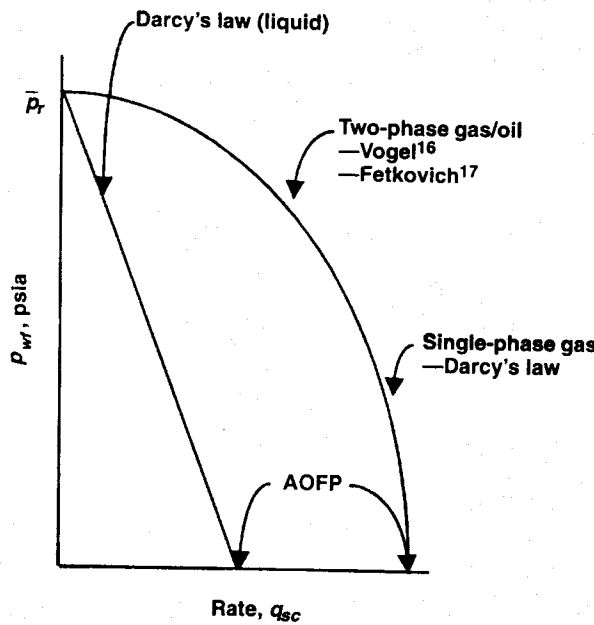


Fig. 6.11—Different forms of IPR's.

$$q_o = C(\bar{p}_r^2 - p_{wf}^2)^n \quad \dots \dots \dots (6.11)$$

This equation is called the oil or gas deliverability equation. The exponent n ranges between 0.5 and 1.0 for both oil and gas wells; n less than 1.0 often is attributed to non-Darcy flow effects. The coefficient C represents the reservoir productivity index and is a strong function of phase mobility. Consequently, this coefficient increases with increasing values of k and decreases with an increasing skin factor. For pseudosteady-state production without rate-dependent skin, C changes as a result of depletion. It also is important to note that for gas wells, this equation is applicable at all stages of depletion. Assuming pseudosteady-state flow, neither C nor n changes. Golan and Whitson⁹ presented a detailed discussion of this IPR. The Fetkovich IPR is customized for a well and is obtained by multipoint backpressure testing, such as flow after flow or isochronal testing.

Horizontal Wells. Darcy's law suggests that the productivity of a vertical well is directly proportional to the net thickness or the productive length of the well. The productive length of a horizontal well can be considerably greater. Unless limited economically, horizontal wells can be very long. However, in horizontal wells, the productivity is not directly proportional to the length. For heterogeneous, naturally fractured reservoirs, these wells can be drilled perpendicular to the natural fracture planes and substantially improve productivity. In Italy's Rosso Mare field, a horizontal well was reported to produce 10 times greater than its vertical neighbors. Such increases also are possible in very thin, low-permeability reservoirs with high vertical permeability. Fig. 6.12 presents a schematic of the drainage region for a horizontal well.

According to Joshi,¹⁸ an IPR for a horizontal well of length, L , located at the middle of the pay thickness, h , is

$$q_o =$$

$$\frac{7.08 \times 10^{-3} k_{oh} h (\bar{p}_r - p_{wf})}{\mu_o B_o \left\{ \ln \left[\frac{a + \sqrt{a^2 - (L/2)^2}}{(L/2)} \right] + \frac{h I_{ani}}{L} \ln \left(\frac{h I_{ani}}{2 r_w} \right) \right\}} \quad \dots \dots \dots (6.12)$$

for $L > h I_{ani}$ and $(L/2) < 0.9 r_{eh}$ and where a is one-half the major axis of a drainage ellipse in a horizontal plane.

TABLE 6.8—INPUT DATA FOR EXAMPLE 6.4

Horizontal permeability, k_h , md	6
Vertical permeability, k_v , md	6
Average reservoir pressure, \bar{p}_r , psia	800
Wellbore radius, r_w , ft	0.21
Reservoir temperature, T_r , °F	80
Gas specific gravity, γ_g	0.65
Net pay thickness, h , ft	16
Horizontal-well length, L , ft	2,770
Drainage radius, r_{eh} , ft	1,490
Calculations (from Appendix B)	
$\frac{\bar{p}_r}{\mu_g}$, cp	0.9
	0.0123

$$a = \frac{L}{2} \left[0.5 + \sqrt{0.25 + \left(\frac{2r_{eh}}{L} \right)^4} \right]^{0.5}$$

for $L/2 < 0.9 r_{eh}$ and I_{ani} , permeability anisotropy = $\sqrt{k_h/k_v}$. Subscripts h and v refer to horizontal and vertical, respectively. All variables are in oilfield units and can be converted easily for a gas-well IPR, as presented in Example 6.4.

Example 6.4—Horizontal-Well Problem. Calculate the flow rate through a horizontal gas well at a bottomhole flowing pressure of 400 psia.

Input Data. Table 6.8 gives the input data.

Solution.

$$q =$$

$$\frac{7.03 \times 10^{-6} h k_h (\bar{p}_r^2 - p_{wf}^2)}{T_r \bar{p}_g \bar{Z} \left\{ \ln \left[\frac{a + \sqrt{a^2 - (L/2)^2}}{(L/2)} \right] + \frac{h I_{ani}}{L} \ln \left(\frac{h I_{ani}}{2 r_w} \right) \right\}}$$

$$x = \frac{703 \times 10^{-6} h}{T_r \bar{p}_g \bar{Z}} = \frac{703 \times 10^{-6} (16)}{(540)(0.0123)(0.9)} = 0.00188.$$

$$a = 1,838; I_{ani} = 1.$$

$$q = \frac{x(\bar{p}_r^2 - p_{wf}^2) k_h}{\ln 2.2 + 0.021} = \frac{5,414}{0.788 + .021} = 6,688 \text{ Mcscf/D.}$$

6.3.7 Transient IPR. These IPR's are used to generate analytical production-decline curves. The decline curves are only valid in the

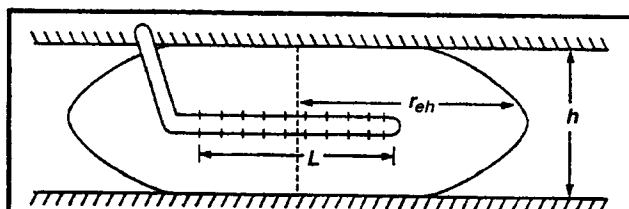


Fig. 6.12—Horizontal-well drainage model (from Joshi¹⁸).

for single-phase oil or gas. For gas, $m(p)$ is used instead of pressure. For oil wells below the bubblepoint pressure, use the Vogel IPR. A step-by-step procedure to calculate transient IPR is presented. Do the following, given k_f , w , k_o , x_f , ϕ , μ_o , and c_t .

1. Calculate the dimensionless fracture conductivity C_{fD} .
2. A drainage geometry x_e/y_e is assumed for a closed reservoir. Calculate the fracture penetration ratio x_f/x_e .
3. Calculate dimensionless time t_{Dx_f} for any assumed time t and for known parameters k_o , ϕ , c_t , and x_f among others
4. From the type curves, determine the dimensionless pressure $p_D(t_{Dx_f}, C_{fD}, x_f/x_e, x_e/y_e)$.

5. Calculate q_{ob} and J at the bubblepoint pressure using

$$q_{ob} = \frac{k_o h (p_i - p_b)}{141.2 B_o \mu_o p_D (t_{Dx_f}, C_{fD}, \frac{x_f}{x_e}, \frac{x_e}{y_e})} \quad \dots \dots \dots \quad (6.15)$$

and

$$J = \frac{q_{ob}}{p_i - p_b},$$

where, p_b = bubblepoint pressure and q_{ob} = oil production rate at the bubblepoint pressure.

6. Calculate q_o , Vogel, where,

$$q_{o,Vogel} = \frac{p_b J}{1.8} \quad \dots \dots \dots \quad (6.16)$$

7. Calculate p_{wf} vs. q_o below the bubblepoint pressure using Vogel's equation.

$$q_o = q_{ob} + q_{o,Vogel} \left[1 - 0.2 \left(\frac{p_{wf}}{p_b} \right) - 0.8 \left(\frac{p_{wf}}{p_b} \right)^2 \right]. \quad \dots \quad (6.17)$$

For gas wells, Steps 1 through 5 are followed in the range of pressures considered to generate IPR curves. Example 6.8 shows how to use transient IPR to generate production decline curves for homogeneous reservoirs, with and without induced hydraulic fractures.

6.4 Production-Systems Analysis

Production-systems analysis is a simple engineering tool to couple IPR with the tubing intake, allowing the determination of surface production rate through the whole production system. Mathematically, such coupling allows the reservoir to produce fluids into the wellbore and enables the piping system to lift these fluids to the separator at the surface. Additional pressure losses in the production system (e.g., through perforations, induced fractures, chokes, and the like) are accounted for by combining these losses with the appropriate total-system losses, such as those in the tubing or reservoir system.

This technique is used widely in the design, economic evaluation, and troubleshooting of oil and gas wells. The graphical presentation of the coupled IPR with the tubing-intake curves often is called the systems graph. The intersection of these curves is the solution point or natural flowing point and determines the producing rate and the pressure.

If these curves do not intersect, the well probably is loading up and artificial-lift methods, such as gas lift or subsurface pumps, may mitigate these problems. Fig. 6.14 elucidates this point graphically before actual problems and sensitivity studies are discussed. This figure shows a typical IPR curve with three hypothetical intake curves. Intake Curve A does not intersect the IPR curve, indicating this well's inability to produce to the surface. However, any artificial-lift method will lower this intake curve by either reducing the total pressure loss in the tubing through aeration of the fluid column or by adding a net positive pressure change, Δp , to the fluid column at the bottom of the tubing string by use of a subsurface pump. The production rate improves to q_{pump} as a result of the new pumped well, Intake Curve C. Intake Curve B is the natural flowing curve with production rate of q_o .

TABLE 6.11—INPUT DATA FOR EXAMPLE 6.6

Reservoir pressure, p_r , psia	4,500
Reservoir temperature, T_r , °F	180
Permeability, k , md	1.0
Pay thickness, h , ft	20
Skin,* s	12 and -4
Wellbore radius, r_w , in.	3.5
Drainage area, r_{eh} , acres	160
IPR	darcy
Perforation interval, ft	20
Perforation shot density, shots/ft	4
Tunnel diameter, D_p , in.	0.35
Tunnel length, L , in.	7
$k_c k_f$	0.8
Water cut, %	0
Oil gravity, °API	35
Gas specific gravity, γ_g	0.65
GOR, scf/STBO	500
Water specific gravity, γ_w	1.07
Wellhead pressure, p_w , psig	100
Perforation top, ft	6,865
Wellhead temperature, T_w , °F	70
Tubing correlation	Hagedorn and Brown
Casing ID, in.	5.012
Tubing ID,* in.	0.824 and 1.5
*Sensitivity parameter	

The system sensitivity study is a major engineering application of production-systems analysis. A system sensitivity is defined as the functional relationship of the production or injection rate with any system parameter, such as tubing internal diameter, gas/oil ratio (GOR), wellhead pressure, permeability, and skin among others. This is accomplished by repeating IPR or intake curves in the system graph for different values of the sensitivity parameter. Once the parameter is optimized, other parameters are considered. This also is called sequential optimization.

Sequential optimization in single-variant steps is a convenient way to learn the procedure and troubleshoot. However, multivariant optimization²⁴ enables one to determine the most profitable well design configuration while considering a number of system parameters simultaneously. A few example systems analyses with a computer program called PERFORM²⁵ will show their importance in optimized production-systems design and troubleshooting. In the input-data

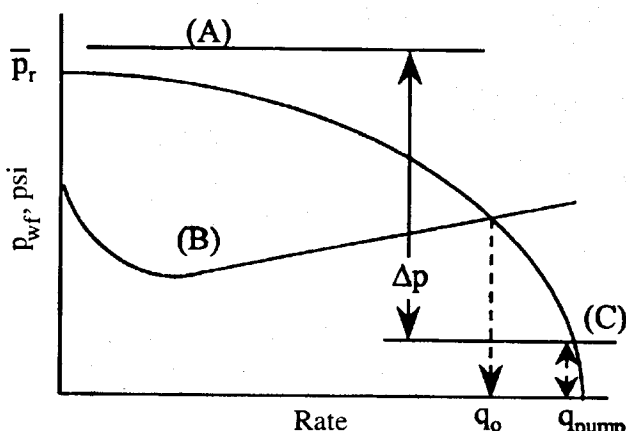


Fig. 6.14—Typical systems graph.

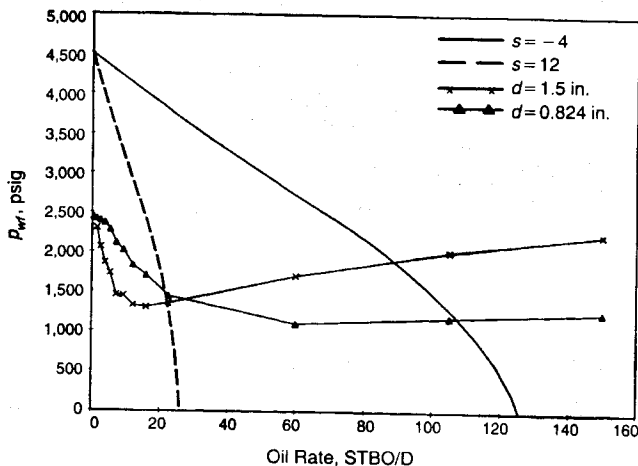


Fig. 6.15—Effects of tubing ID and skin on production performance.

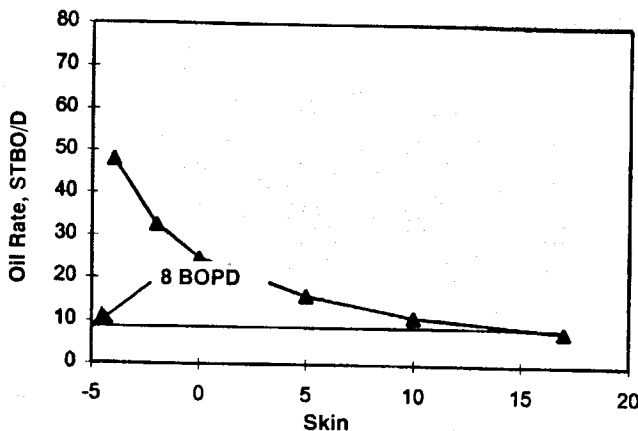


Fig. 6.16—Oil rate sensitivity to total skin.

tables for the following examples, the sensitivity parameters are indicated by an asterisk. As mentioned earlier, optimum production refers to the maximum economic production.

Example 6.6—Production-Systems-Analysis Problem on Effects of Skin and Tubing ID. This problem shows important effects of tubing ID and skin damage on production performance of an oil well.

Input Data. Table 6.11 gives the input data.

Solution. The system graph presented in Fig. 6.15 shows that the damaged well with a high skin of 12 produces about 22 STBO/D with both tubing sizes, although the well surges with the larger 1.5-in. tubing ID. This unstable flow condition is very apparent from the location of the point of intersection between the IPR and the intake curves. For the 1.5-in. tubing ID, the unstable flow condition continues until production reaches about 60 STBO/D. This spread in the flow rate is enough to question the accuracy of the pressure-loss correlation. However, even for the smaller 0.824-in. tubing ID, the well would surge if the calculated rate was 18 STBO/D or less. The rate difference is so marginal that it may need further verification with another method of calculation. However, this well offers excellent opportunity for stimulation. If the source of damage is properly diagnosed, a matrix acid treatment or a fracture treatment can be used to remove skin. A successful fracture stimulation treatment can reduce the skin to -4 or less. Note that this stimulation effect improves the inflow performance to an extent that the potential for surging with any size tubing is eliminated. Additionally, production will range from 89 to 107 STBO/D, depending upon the tubing size. The larger tubing size not only increases the production by a factor of five but also completely stabilizes the production. The

TABLE 6.12—INPUT DATA FOR EXAMPLE 6.7

Reservoir pressure, p_r , psia	3,200
Reservoir temperature, T_r , °F	160
Permeability, k , md	1.5
Pay thickness, h , ft	20
Skin,* s	-4, -2, 0, 10, and 17
Wellbore radius, r_w , in.	3.5
Drainage area, r_{eh} , acres	160
IPR	Darcy
Perforation interval, ft	20
Perforation shot density, shots/ft	4
Tunnel diameter, D_p , in.	0.35
Tunnel length, L , in.	12
$k_c k_f$	0.5
Porosity, ϕ , %	10
Water cut, %	0
Oil gravity, °API	25
Gas specific gravity, γ_g	0.65
GOR, scf/STBO	300
Water specific gravity, γ_w	1.03
Wellhead pressure, p_w , psig	50
Perforation top, ft	8,840
Wellhead temperature, T_w , °F	70
Tubing correlation	Hagedorn and Brown
Casing ID, in.	5.012
Tubing ID, in.	2.75
*Sensitivity parameter	

combination of 1.5-in. tubing ID and a suitable stimulation optimizes the production system design.

Example 6.7—Production-Systems-Analysis Problem on Effect of Skin Improvement by Acidizing an Oil Well. This vertical well produces with a beam pump installed 100 ft above the top perforation. The pump suction pressure is 50 psig. Give a critical review of skin sensitivity analysis and assume the skin caused by damage is 6 out of a total skin of 17.

Input Data. Table 6.12 provides the input data

Solution. On the basis of the sensitivity analysis presented in Fig. 6.16, use of a very efficient matrix acid treatment to remove skin resulting from damage yields a skin of 11 with a very marginal increase in the production rate. Note that hydraulic fractures can remove damage and then impose some negative skin. Thus, if the total skin is reduced to 5 or less through hydraulic fracturing, the well production doubles to about 16 STBO/D, resulting in a more cost-effective treatment.

Example 6.8—Production-Systems-Analysis Problem on Effect of Fracturing a Gas Well. This problem compares the transient rate declines over a year for a fracture-stimulated well vs. a nonfractured gas well.

Input Data. Table 6.13 provides the input data.

Solution. This is a typical low-permeability gas reservoir with very little liquid production. The high reservoir pressure of 6,800 psia makes it a perfect candidate for fracture stimulation. Fig. 6.17 gives rate-decline curves with transient IPR's for a homogeneous reservoir and a finite-conductivity, vertical-fractured reservoir. To study the rate decline, time must be the sensitivity variable. Thus,

TABLE 6.13—INPUT DATA FOR EXAMPLE 6.8

Reservoir pressure, p_r , psia	6,800
Reservoir temperature, T_r , °F	220
Permeability, k , md	0.05
Pay thickness, h , ft	50
Skin, s	2.0
Wellbore radius, r_w , in.	3.5
Drainage area, r_{eh} , acres	160
IPR	Transient
Perforation interval, ft	50
Perforation shot density, shots/ft	4
Tunnel diameter, D_p , in.	0.35
Tunnel length, L , in.	7
$k_c k_f$	0.4
Porosity, ϕ , %	10
Water cut, %	0
Oil gravity, °API	55
Gas specific gravity, γ_g	0.65
Liquid yield, bbl/MMscf	1
Water specific gravity, γ_w	1.07
Wellhead pressure, p_w , psig	600
Perforation top, ft	8,840
Wellhead temperature, T_w , °F	70
Tubing correlation	Cullender and Smith
Casing ID, in.	4.494
Tubing ID, in.	1.995

a transient IPR curve as opposed to a Darcy-type steady-state relationship is used. The well in this problem shows almost a twofold increase in production for the whole year with placement of an infinite-conductivity vertical fracture of 500 ft half-length. To design the fracture, an additional fracture-length-sensitivity analysis for optimization should be performed.

Example 6.9—Production-Systems-Analysis Problem on Effect of Pressure-Gradient-Prediction Method. A dilemma often facing engineers who must solve multiphase-flow problems is how to decide the most suitable pressure-gradient-prediction method to calculate pressure losses in the tubulars. Chap. 4 discusses many methods, and the production rates calculated from them can vary substantially. Errors in production-rate predictions can be caused by other sources, such as the fluid properties calculated from empirical models. Consequently, a judgment based on experience and real data analysis is often the best guide to the selection of the proper or most accurate pressure-gradient method. This example illustrates the discrepancies in pressure-drop calculations for a typical oil well with associated water and gas production. The pressure gradient or the pressure profile in the tubular is calculated with the different methods and presented in Fig. 6.18.

Input Data. Table 6.14 provides the input data

Solution. The gradient curves in Fig. 6.18 show the pressure profiles in the 9,810-ft-deep oil well producing water and associated gas. The bottomhole flowing pressure, calculated by different methods, varies between 2,245 and 2,891 psia. The lower value was calculated by the Orkiszewski method and the higher value by the Aziz *et al.* and Mukherjee and Brill methods. This is a discrepancy of nearly 30%. The Ansari *et al.* method is based on mechanistic modeling of vertical upward flow and comes within 5% of the Beggs and Brill prediction, which is based on an empirical approach. The Orkiszewski and Hagedorn and Brown pressure-loss-calculation

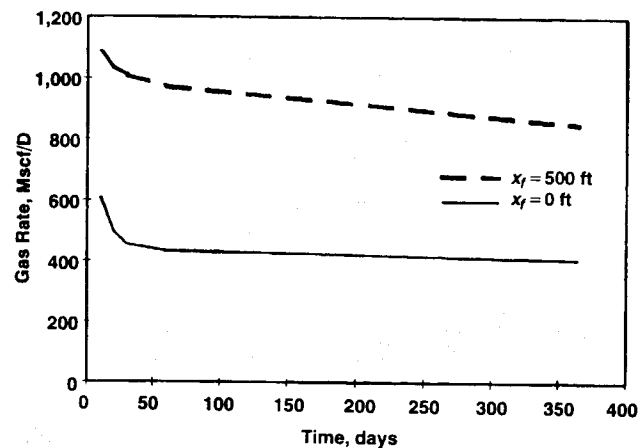


Fig. 6.17—Comparison of production rate decline for fractured vs. nonfractured gas well.

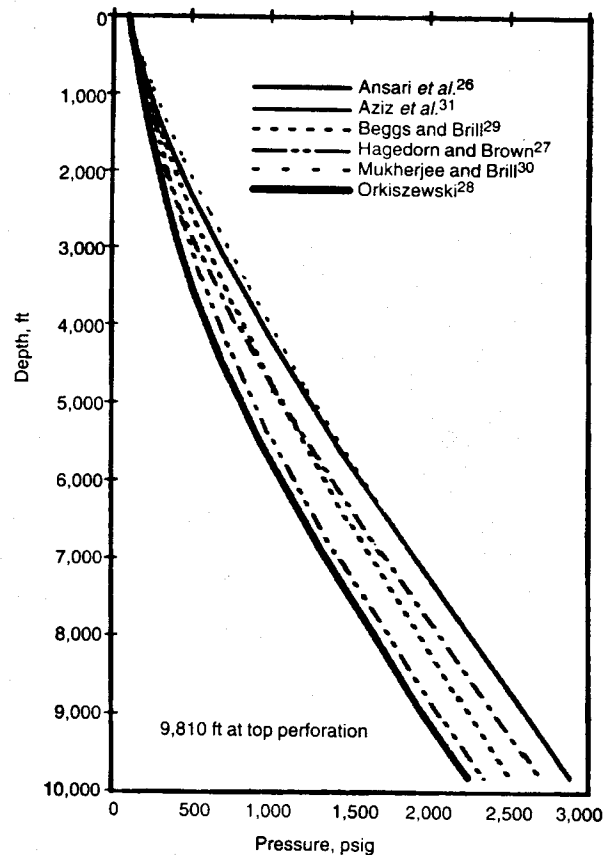


Fig. 6.18—Gradient curves with different pressure-loss methods.

methods predict lighter pressure gradients in the production tubing, resulting in higher fluid deliverability when compared with other methods used in this example. With systems analysis for the well in this example, the Mukherjee and Brill, Aziz *et al.*, Ansari *et al.*, and Beggs and Brill methods predict conservative production rates in that order. These four methods underpredict the rate compared with the Orkiszewski and Hagedorn and Brown methods.

Example 6.10—Production-Systems-Analysis Problem on Effect of Water Cut. This problem is a typical water-cut-sensitivity analysis in an oil well with three-phase oil, water, and gas production. Understanding this problem should clarify any other sensitivity analysis where the same sensitivity parameter is repeated.

TABLE 6.14—INPUT DATA FOR EXAMPLE 6.9

Rate, STBL/D	500
Water cut, %	20
Oil gravity, °API	32
Gas specific gravity, γ_g	0.65
GLR, scf/STBL	360
Water specific gravity, γ_w	1.07
Reservoir temperature, T_r , °F	200
Wellhead pressure, p_w , psig	100
Perforation top, ft	9,810
Wellhead temperature, T_w , °F	70
Casing ID, in.	5.0
Tubing ID, in.	2.441
Wellbore correlations*	Ansari et al. ²⁶ Hagedorn and Brown ²⁷ Okszewski ²⁸ Beggs and Brill ²⁹ Mukherjee and Brill ³⁰ Aziz et al. ³¹

*Sensitivity parameter.

TABLE 6.15—INPUT DATA FOR EXAMPLE 6.10

Reservoir pressure, p_r , psia	5,000
Reservoir temperature, T_r , °F	200
Permeability, k , md	36.0
Pay thickness, h , ft	44
Skin, s	0
Wellbore radius, r_w , in.	3.5
Drainage area, r_{eh} , acres	160
IPR	Darcy/Vogel
Perforation interval, ft	44
Perforation shot density, shots/ft	4
Tunnel diameter, D_p , in.	0.35
Tunnel length, L , in.	6
$k_c k_f$	0.5
Porosity, ϕ , %	10
Water cut, * %	0, 0.1, 0.3, 0.5, 0.7, 0.9
Oil gravity, °API	32
Gas specific gravity, γ_g	0.65
GOR, scf/STBO	300
Water specific gravity, γ_w	1.07
Wellhead pressure, p_w , psig	100
Perforation top, ft	8,650
Wellhead temperature, T_w , °F	70
Tubing correlation	Hagedorn and Brown
Casing ID, in.	5.921
Tubing ID, in.	2.441
*Sensitivity parameter	

Input Data. Table 6.15 gives the input data.

Solution. Fig. 6.19A is the systems graph with tubing-intake curves plotted for each water-cut value considered. The intersections of the tubing-intake curves with the IPR curve give the production rates for each water cut. As the water cut increases, the pressure gradients in the tubing increase because of the density difference between oil and water and also because of the reduction of dissolved gas in the fluid system. As the sensitivity plot in Fig. 6.19B shows, the oil production rate also falls because of the increased water cut. In addition to these problems, formation of oil/water emulsions in the production tubing at higher water cuts may cause increased viscosity and affect the oil production rate more drastically. Appropriate use of artificial-lift methods often may mitigate this problem.

Example 6.11—Production-Systems-Analysis Problem on Effect of Vertical Permeability in Horizontal Well. This example uses an openhole gas well to compare the performance of vertical vs. horizontal wells with vertical permeability as the sensitivity variable. It is important to know that vertical permeability does not affect the production rate from a vertical well when Darcy-type reservoir-flow equations are used, although it affects the rate from a horizontal well quite dramatically.

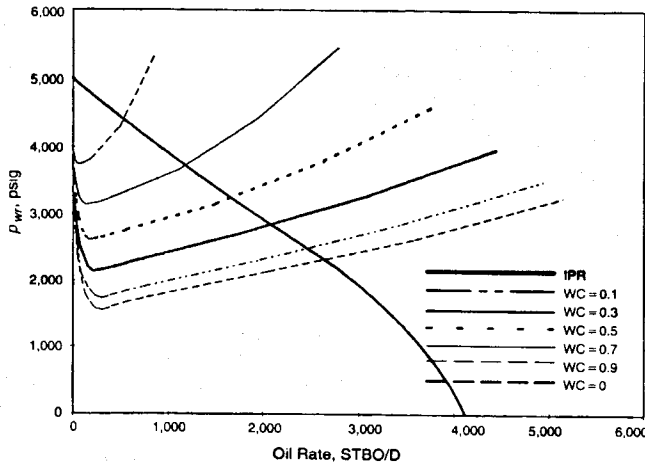


Fig. 6.19A—Systems graph for water-cut sensitivity.

Input Data. Table 6.16 provides the input data.

Solution. The systems graph presented in Fig. 6.20A shows dramatic improvement in productivity in the horizontal well over the vertical well. The vertical permeability increases over a range of 0.001 to 0.1 md. Fig. 6.20B shows that the horizontal-well performance improves substantially as the vertical permeability increases. This is a primary reason for economic successes of horizontal wells in naturally fractured reservoirs with high vertical permeabilities.

Example 6.12—Production-Systems-Analysis Problem on Effect of Choke ID. This is an example of surface-choke-ID sensitivity with the Ashford and Pierce³² correlation.

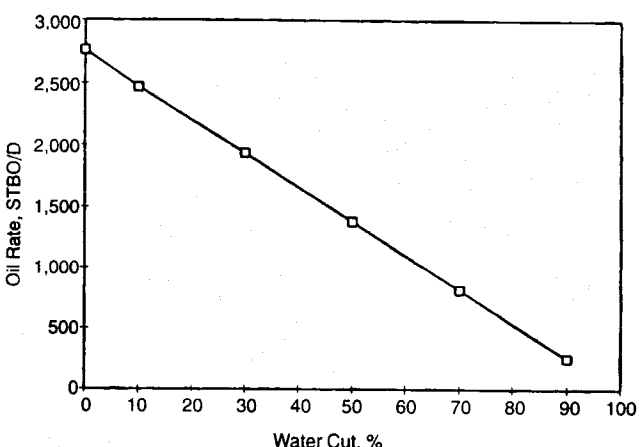


Fig. 6.19B—Water-cut sensitivity.

TABLE 6.16—INPUT DATA FOR EXAMPLE 6.11

Reservoir pressure, p_r , psia	2,500
Reservoir temperature, T_r , °F	140
Horizontal permeability, k_h , md	10
Pay thickness, h , ft	20
Skin, s	0
Wellbore radius, r_w , in.	2.5
Drainage area, r_{eh} , acres	160
IPR	Darcy/Joshi
Porosity, ϕ , %	10
Horizontal-well length, L , ft	2,000
Water cut, %	0
Oil gravity, °API	54
Gas specific gravity, γ_g	0.65
Liquid yield, bbl/MMscf	2.0
Water specific gravity, γ_w	1.07
Vertical permeability,* k_v , md	0.1, 0.03, 0.01, 0.001
Wellhead pressure, p_w , psig	600
Perforation top, ft	5,500
Wellhead temperature, T_w , °F	70
Tubing correlation	Duns and Ros
Casing ID, in.	3.826
Tubing ID, in.	2.441
*Sensitivity parameter	

Input Data. Table 6.17 provides the input data.

Solution. The systems graph in Fig. 6.21A shows the change in tubing-intake curves with differing choke sizes. Fig. 6.21B shows how the choke sizes control the production rates. The larger the choke size, the higher the production rate.

Example 6.13—Production-Systems-Analysis Problem on Effect of Gas/Liquid Ratio (GLR). GLR uniquely affects oilwell production rates. This example demonstrates this sensitivity and provides an introduction to the application of multiphase-flow theory to artificial-lift design, particularly gas lift.

Input Data. Table 6.18 gives the input data.

Solution. Fig. 6.22A is a production-systems graph for GLR sensitivity. Increased GLR reduces the hydrostatic gradient and the mixture density of the fluids in the tubing. As the pressure declines in the direction of flow, the compressible gas phase expands and

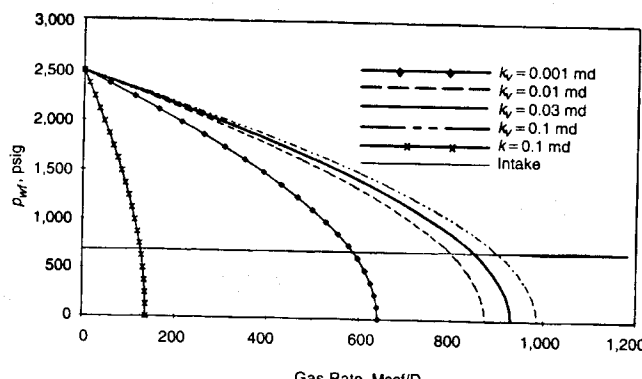


Fig. 6.20A—Systems graphs comparing horizontal vs. vertical well performance with vertical permeability variation in the horizontal well.

TABLE 6.17—INPUT DATA FOR EXAMPLE 6.12

Reservoir pressure, p_r , psia	4,500
Reservoir temperature, T_r , °F	180
Permeability (radial), k , md	30
Pay thickness, h , ft	20
Skin, s	1.0
Wellbore radius, r_w , in.	3.5
Drainage area, r_{eh} , acres	160
IPR	Darcy/Vogel
Water cut, %	30
Oil gravity, °API	30
Gas specific gravity, γ_g	0.65
GLR, scf/STBL	800
Water specific gravity, γ_w	1.07
Perforation shot density, shots/ft	4
Perforation interval, ft	20
Tunnel length, L , in.	7
Tunnel diameter, D_p , in.	0.35
Porosity, ϕ , %	10
$k_h k_v$	0.8
Perforation top, ft	6,865
Separator pressure, p_s , psig	1,000
Vertical well	
Separator temperature, T_s , °F	70
Tubing correlation	Ansari et al.
Casing ID, in.	5.012
Tubing ID, in.	1.867
Horizontal Flowline	
Flowline length, L , ft	400
Flowline correlation	Dukler
Flowline ID, in.	2.9
Choke ID,* in.	0.375, 0.5, 0.75
Choke correlation	Ashford and Pierce
*Sensitivity parameter	

gains velocity, increasing the mixture velocity and the friction losses in the tubing. Thus, the total effect of increasing GLR on the pressure losses in a producing well is the algebraic sum of the reduced hydrostatic gradient and the increased friction gradient. With increasing GLR, there is a threshold GLR above which the reduction in hydrostatic gradient is less than the increase in friction gradient. This often is called the gradient reversal point and happens at about 700 scf/STBL in this example. As Fig. 6.22B shows, this reversal phenomenon causes the dome shape of the liquid rate vs. GLR sensi-

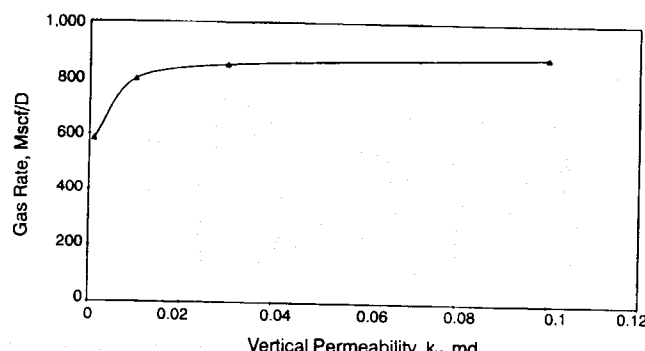


Fig. 6.20B—Horizontal-well performance sensitivity with vertical permeability.

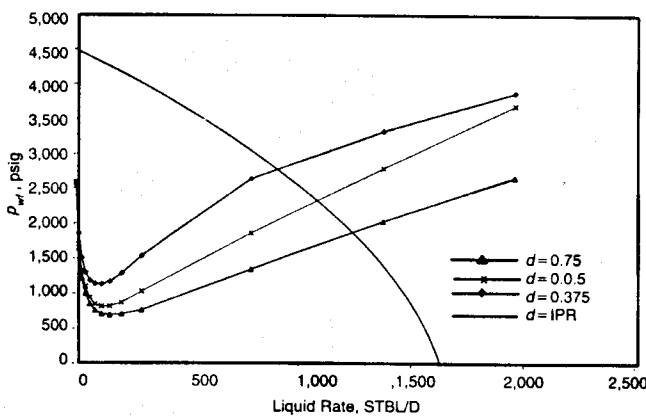


Fig. 6.21A—Systems graph for surface-choke-ID sensitivity.

TABLE 6.18—INPUT DATA FOR EXAMPLE 6.13	
Reservoir pressure, p_r , psia	4,500
Reservoir temperature, T_r , °F	180
Permeability (radial), k , md	30
Pay thickness, h , ft	20
Skin, s	1.0
Wellbore radius, r_w , in.	3.5
Drainage area, r_{eh} , acres	160
IPR	Darcy/Vogel
Water cut, %	30
Oil gravity, °API	30
Gas specific gravity, γ_g	0.65
GLR,* scf/STBL	175, 700, 1,200, 3,000
Water specific gravity, γ_w	1.07
Perforation interval, ft	20
Perforation shot density, shots/ft	4
Tunnel diameter, D_p , in.	0.35
Tunnel length, L , in.	7
$k_c k_f$	0.8
Porosity, ϕ , %	10
Wellhead pressure, p_w , psig	100
Perforation top, ft	6,865
Wellhead temperature, T_w , °F	70
Tubing correlation	Duns and Ros
Casing ID, in.	5.012
Tubing ID, in.	1.867
*Sensitivity parameter	

tivity curve. In this case, the maximum liquid production rate is 983 STBL/D and occurs at the optimum GLR of 700 scf/STBL.

Before any artificial-lift installation, this well produces with a GLR of 175 scf/STBL. If gas is injected into the production string at the lowest possible entry point, the GLR can be increased. For optimized production, the GLR should be increased to 700 scf/STBL, with a resultant increase in the liquid production rate to 983 STBL/D. This is also the basic principle of gas lift.

6.5 Artificial Lift

The previous section introduced artificial-lift diagnostics based on systems analysis principles. This section presents the application of multiphase-flow principles in the design of artificial-lift methods. Artificial-lift methods help manipulate the tubing-gradient curves for a predetermined bottomhole oil or liquid rate, q_o , with a designed flowing

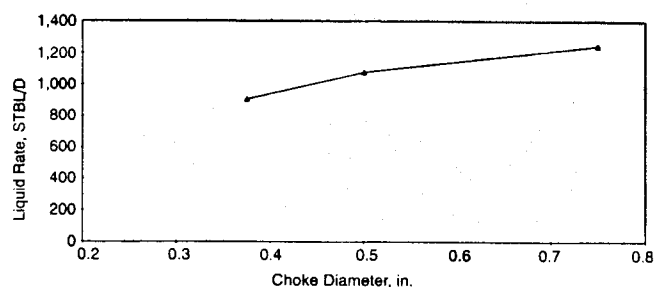


Fig. 6.21B—Choke-ID sensitivity.

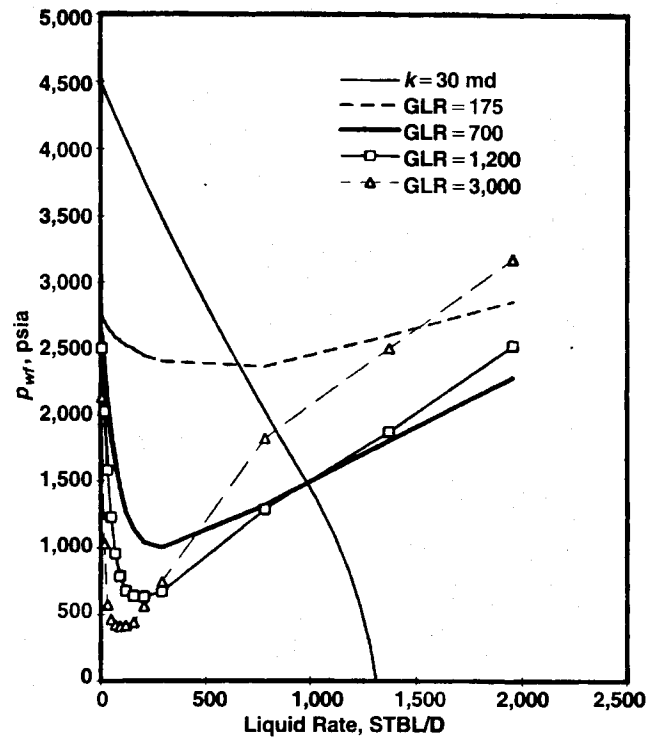


Fig. 6.22A—Production-systems graph for GLR sensitivity.

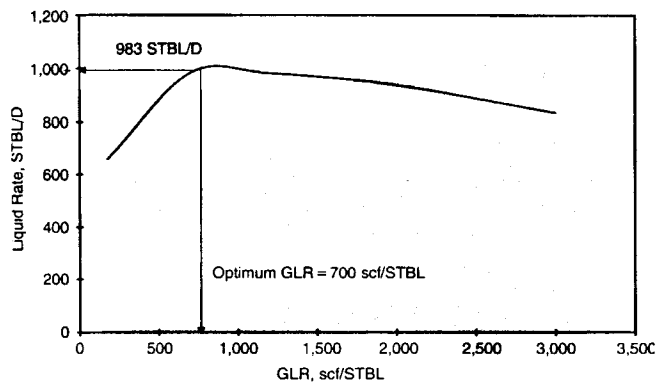


Fig. 6.22B—GLR sensitivity for gas-lift design and optimization.

wellhead pressure, p_{wh} . In many cases, these wells cannot produce to the surface without artificial lift, as Figs. 6.23 and 6.24 show.

6.5.1 Subsurface Pump. Fig. 6.23 presents a typical pressure traverse for a downhole-pumped well. Without the pump this well is dead, with the fluid column at Point A in the tubing. A designed rate, q_o , and the corresponding bottomhole flowing pressure, p_{wf} , are identified from the IPR curve. With the same dead-oil gradient, the oil level in the annulus should be at Point B with the pump suction

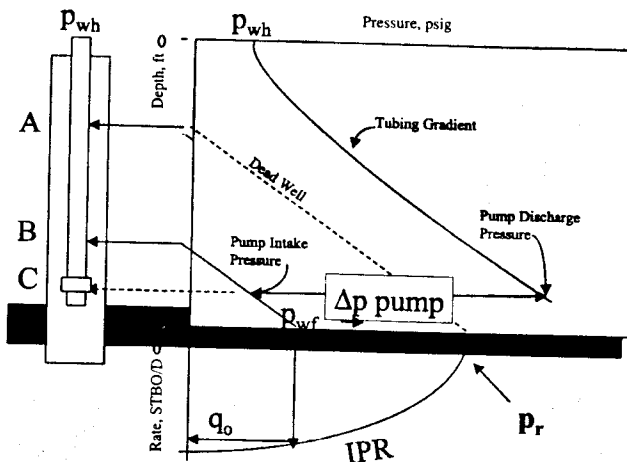


Fig. 6.23—Pressure traverse for bottomhole pumps.

at Point C. As Fig. 6.23 shows, the pump must be designed to provide a pressure boost of Δp_{pump} . This pressure difference is between the pump intake and the pump discharge. When the pump discharges the fluid into the tubing at a rate, q_o , with the discharge pressure at the depth shown, the fluids flow to the surface at the specified wellhead pressure, p_{wh} . This tubing-gradient curve is generated by use of one of the two-phase-flow models with the designed rate, q_o , and designed wellhead pressure, p_{wh} , as in Example 6.9.

6.5.2 Gas Lift. Gas-lift design is optimized based on a GLR sensitivity study, as presented in Example 6.13 (Fig. 6.22B), where the optimum GLR was 700 scf/STBL and the corresponding production rate was 983 STBL/D with a wellhead pressure of 100 psig. Theoretically, gas lift aerates a liquid column with injected gas, allowing the liquid to flow to the surface with a predesigned flowing wellhead pressure.

The gas is injected through a port in the gas-lift valve with a designed differential pressure, Δp , at the port.³³ Fig. 6.24 presents an example gas-lift pressure traverse in the production tubing. For simplicity, this well also is assumed dead before the installation of gas lift. Note that the tubing is packed above the pay zone, which is a precondition to a gas-lift installation that ensures injection into the tubing only through the valve port. If the oil is produced through the annulus, the tubing forms the gas-injection string and needs to be blocked at the bottom.

From the GLR sensitivity study in Example 6.13, the optimum rate, q_o , is calculated for the optimum GLR. At that optimum rate, the bottomhole flowing pressure is obtained from the IPR curve. To calculate the fluid pressure at the point of injection (Point B), a constant fluid gradient is calculated below the point of gas injection. This is particularly important for unloading wells after completion or workover. In Fig. 6.24, the dead-oil gradient is used for simplicity. After determining the flowing fluid pressure in the production string, the injection gas rate is calculated by subtracting the produced gas rate from the optimized gas rate that was calculated from the sensitivity study for the optimum liquid rate and GLR. With the available surface casing injection pressure, p_c , and the calculated gas injection rate through the annulus, the injection gradient or casing gradient is calculated. Any dynamic gas-gradient method can be used. Normally, all the multiphase pressure-loss methods revert to the single-phase-flow case based on superficial gas velocity. The upstream injection pressure is determined from the calculated casing gradient. The pressure difference, Δp , between the casing and the tubing, at the point of injection, is then fixed. The port size of the gas-lift valve then can be determined with the Thornhill-Craver equation⁸ or any type of choke equation for the passage of the designed injection gas rate with the differential pressure, Δp . This should allow lifting the well at rate q_o to the surface at a predesigned wellhead pressure, p_{wh} .

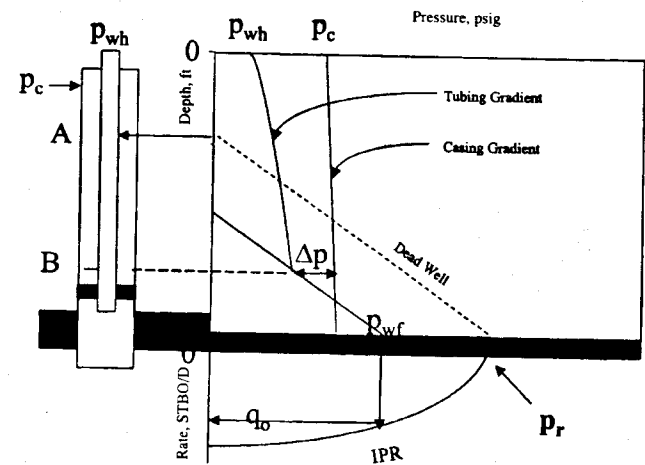


Fig. 6.24—Pressure traverse for gas lift.

6.6 Gas-Well Loading

Gas wells often produce a liquid phase, such as oil, condensates, or even interstitial water. Depending on the phase behavior of the gas, it is even conceivable that a well producing dry gas may have liquid in the wellbore. This problem can be particularly severe in condensate or retrograde condensate reservoirs. If the velocity of the producing gas is sufficiently high, the wellbore liquids are produced to the surface and the well does not accumulate any liquids. However, in low-permeability gas wells, particularly with low reservoir pressures, the gas velocity may not be sufficient to lift the liquid phase to the surface unless the tubing diameter is reduced to attain the liquid unloading velocity. Lower velocities result in accumulation of liquid in the well. This liquid accumulation eventually can create enough hydrostatic pressure in the wellbore to curtail gas production severely, even completely stopping it with time. This phenomenon is called gas-well loading.³⁴⁻⁴² In oil wells with high liquid velocity this may not be a problem. Artificial-lift methods can be used to mitigate the problem. In gas-condensate reservoirs, particularly in the presence of a large retrograde envelope, the effective permeability to gas can be severely reduced if condensation occurs near the wellbore. This may drastically reduce the gas velocity in the wellbore, causing severe well-loading problems.

Gas-well-loading problems often can be diagnosed from production-systems-analysis plots, as shown in Fig. 6.3. The intersection of the IPR curve with the tubing-intake curve in the unstable zone is a good diagnostic of such problems, particularly if the proper PVT relationships given in Appendix B are used. To identify any problem with retrograde-condensation-induced loading, we highly recommend the use of compositional models presented in Appendix C.

This gas-well-loading problem can be mitigated by increasing the gas velocity in the wellbore or by using some form of artificial lift, such as plunger lift or gas lift. Continuous lift of a constant-quality fluid can be achieved only by proper tubing string design. This design generally results in reduction of the production tubing diameter to achieve sufficient gas velocity. This permits complete unloading of liquids from the wellbore, as discussed in Example 6.6. Normally, intermittent gas lift and plunger lift (which is intermittent in nature) are a second choice because of higher cost and associated operational problems. Plunger-lift efficiency also is very sensitive to the volume and pressure of gas in the annulus. The higher the volume and pressure, the greater the plunger-lift efficiency.

Surface production rates and phase characteristics often can be quite deceptive in predicting gas-well-loading problems. Historically, the prediction of the conditions conducive to this problem has been very unreliable.³⁵ Turner *et al.*³⁶ presented the best known procedure to calculate the minimum stable-gas velocity. Unlike with the continuous film model presented earlier by Dukler,³⁷ Turner *et al.* showed that to unload a gas well, the largest droplet in the gas stream must be carried to the surface. Dukler proposed a method to determine the minimum gas velocity required to move the liquid

TABLE 6.19—INPUT DATA FOR EXAMPLE 6.14

Reservoir pressure, p_r , psia	4,000
Reservoir temperature, T_r , °F	160
Permeability, * k , md	1.0, 3.0
Pay thickness, h , ft	20
Skin, s	0
Wellbore radius, r_w , in.	3.0
Drainage area, r_{eh} , acres	160
IPR	Darcy
Completion	Open hole
Water cut, %	0
Oil gravity, °API	54
Gas specific gravity, γ_g	0.65
GOR, scf/STBO	150
Water specific gravity, γ_w	1.03
Wellhead pressure, p_w , psig	200
Perforation top, ft	5,990
Wellhead temperature, T_w , °F	80
Tubing correlation	Gray
Casing ID, in.	4.408
Tubing ID, * in.	0.824, 1.0, 1.6, 2.0, 3.0

*Sensitivity parameter

film on the tubing wall continuously upward. The Turner *et al.* model is accepted as a more reliable method of liquid unloading. These authors suggested that the minimum gas velocity in the well had to equal the terminal velocity of the largest liquid droplet in the flowstream. For a spherical droplet, the terminal velocity is given by the relation developed by Foust *et al.*³⁸

$$v_t = \left[\frac{4(\rho_L - \rho_g)gd_D}{3C_D\rho_g} \right]^{1/2}, \quad (6.18)$$

where v_t = terminal velocity, ft/sec; ρ_L = liquid density, lbm/ft³; ρ_g = gas density, lbm/ft³; g = gravitational acceleration, 32.174 ft/sec²; d_D = droplet diameter, ft; and C_D = drag coefficient for the droplet.

The maximum stable droplet diameter can be determined from the relation³⁵

$$\frac{v_t^2 \rho_g d_D}{\sigma_L} \cong 30, \quad (6.19)$$

where σ_L = surface tension, lbm/sec.²

From Eq. 6.19,

$$d_D = \frac{30\sigma_L}{v_t^2 \rho_g},$$

which can be substituted into Eq. 6.18 to obtain

$$v_t = 5.99 \left[\frac{\sigma_L (\rho_L - \rho_g)}{C_D \rho_g^2} \right]^{1/4}. \quad (6.20)$$

Assuming spherical droplets, Turner *et al.* showed that the drag coefficient for the droplet, C_D , is 0.44. Substituting this value of C_D and converting the units of surface tension, σ , to dynes/cm, the Turner *et al.* drop-terminal-velocity equation can be written as

$$v_t = 1.59 \left[\frac{\sigma_L (\rho_L - \rho_g)}{\rho_g^2} \right]^{1/4}, \quad (6.21)$$

where v_t is in ft/sec, σ_L is in dynes/cm, and ρ_L and ρ_g are in lbm/ft³.

To unload a well, the gas velocity has to exceed this terminal velocity at every point in the tubular until the liquid droplet reaches the surface. Gregory³⁵ reported an error in the coefficient of this equation in the original Turner *et al.*³⁶ paper, which was repeated in other references to this equation. However, the equation presented here has been corrected and does not include the Turner *et al.* arbitrary 16% upward correction to this velocity. Coleman *et al.*^{39,40} concluded from field tests that this 16% upward correction in terminal velocity is not needed to calculate the minimum gas flow rate or critical gas rate required to keep low-pressure gas wells unloaded. Based on the terminal-velocity equation presented here, the critical gas flow rate, q_{gc} , can be calculated as

$$q_{gc} = 3.06pv \frac{A}{TZ}, \quad (6.22)$$

where q_{gc} = critical gas-flow rate, MMscf/D; A = area of cross-section of flow, ft²; p = pressure, psia; T = temperature, °R; and Z = gas compressibility factor.

Turner *et al.* suggested that wellhead conditions controlled the liquid load up in most cases. This was substantiated by Coleman *et al.*³⁹. It is important to note that the critical unloading rate determined from the liquid droplet model may not be applicable to slug flow.³⁹

With the annular transition criteria described in Sec. 4.2.2 for the Ansari *et al.*²⁶ mechanistic model, gas-well loading from downward flow of a liquid film on the tubing wall also can be considered. Gas-well loading does not occur if annular flow is maintained throughout the wellbore. The similarity of Eq. 6.21 to Eq. 4.163, which predicts the transition to annular flow, suggests that gas-well loading will not occur if annular flow is maintained throughout the wellbore.

Example 6.14—Effect of Tubing ID on Gas-Well Unloading and Erosion. The best way to mitigate any flow-related problem is to identify the potential problem before it manifests and design the system around it. This example helps identify a gas-well-loading problem and provides a method of solution. Velocity is the key to liquid unloading. The higher the velocity is, the more efficient the unloading. Velocity depends on permeability and pressure, which are controlled by tubing ID. Consequently, a tubing ID sensitivity study must be performed to optimize tubing size.

Input Data. Table 6.19 gives the input data.

Solution. In this example, two gas wells are studied: one with low permeability and a suspected loading problem and one with higher permeability and a suspected erosion problem. A tubing ID sensitivity analysis is performed. A modified Turner unloading rate is used. The gas-well-unloading and erosion-rate envelopes are superimposed in Fig. 6.25 with the tubing-ID sensitivity plots for two different permeabilities.

As long as the actual predicted production rates are higher than the corresponding unloading rate, the wells are unloaded. In Fig. 6.25, the gas rates for all the tubing ID's considered in the 1-md permeability

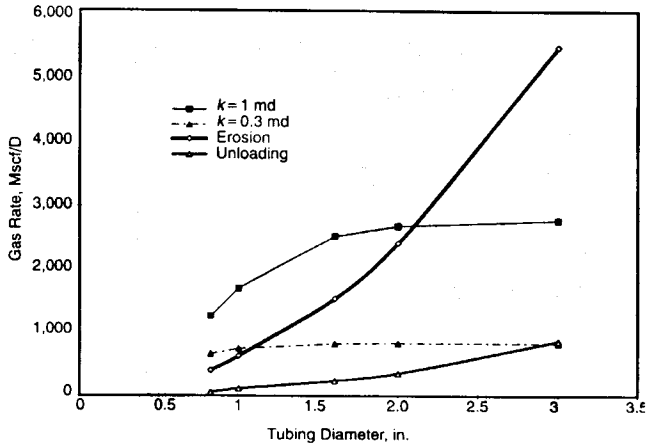


Fig. 6.25—Gas-well-loading erosion envelopes.

case are substantially higher than the corresponding unloading rates, suggesting no imminent chance of a loading problem. However, with normal production decline, the problem may arise in the future. For the low permeability of 0.3 md (as the tubing ID is increased from 1 in.), the gas rate does not improve while the gas velocity in the tubing goes down, causing the well to load in 3-in. tubing. This type of plot should be used as a template for such studies.

6.7 Erosional Velocity

Erosion is the physical removal of pipe material in contact with a flowing fluid. Erosion limits the life of flow strings. Continuous excessive erosion often leads to mechanical failure, leakage, or both. Erosion is caused by cavitation or bubble collapse and by the impingement of liquid or solid particles on the pipe wall. But this subject is very controversial and often not emphasized in design. The mitigation procedure used in this section should be used as guidelines for proper design.

To control erosion, the American Petroleum Inst. (API)⁴³ recommends limiting the maximum velocity in the flow string to a critical value called erosional velocity. To ensure a predesigned life of flow strings, erosional velocity can be calculated from this empirical equation.

$$v_e = \frac{C}{\sqrt{\rho}}, \quad \dots \dots \dots \quad (6.23)$$

where v_e is the erosional velocity in ft/sec, ρ is the density of the flowing fluid in lbm/ft³, and C is an empirical constant. For sand-free flow, the API study recommends C factors of 100 for continuous flow and 150 for intermittent flow. For sand-laden fluids, API recommends an unspecified C value of less than 100. Example 6.14 illustrates the use of Eq. 6.23 to mitigate pipe erosion. This problem uses a value of $C = 100$. In Fig. 6.25, as long as the producing gas rates are lower than the erosion envelope, the problem should not exist. For multiphase mixtures, the erosional velocity is compared with the mixture velocity in a pipe and the no-slip mixture density is used in Eq. 6.23. For the higher permeability of 1 md, erosion problems are predicted to occur for tubing ID's of less than 2 in.

Salama and Venkatesh⁴⁴ reviewed the API equation for erosional velocity and concluded that the form can be justified from a Bernoulli-type relationship. However, assuming a 3,000- to 5,000-psi maximum pressure-drop range in the flow conduit for clean two-phase fluids, the predicted v_e is very conservative. Allowing for a 10 mil/yr erosion rate, they recommended the following relationship to calculate the erosional velocity caused by liquid impingement on a steel surface.

$$v_e = \frac{300}{\sqrt{\rho}}. \quad \dots \dots \dots \quad (6.24)$$

This equation seems to be more reasonable for limiting the designed fluid velocity in tubing to control any erosional damage to the pipe. In producing wells, this results in curtailment of production and, thus, affects the economics. It is often more economic to produce wells at optimum rates, allowing for some acceptable penetration rates resulting from erosion. Because Eqs. 6.23 and 6.24 are independent of penetration rate, they cannot be used for such calculations. In fact, the only parameter considered in these equations is density, suggesting that the erosional velocity can be increased by reducing the density of the flowing fluid or decreased by increasing the density of the flowing fluid. This does not agree with experimental observations for sand-laden fluids. Sand in gases with lower densities causes more erosion than sand in liquids with higher densities.⁴⁵

The presence of sand in the flowing fluid results in erosion damage caused by abrasive wear mechanism.^{46,47} Rabinowicz,^{48,49} has shown that the volume of ductile metal eroded from the surface because of solid particle impingement is directly proportional to the total weight of impinging solids. Thus, in the case of pipe flow, elbows will be more susceptible to erosion because more solids will impinge on the projected area of the incoming pipe. It is estimated^{50,51} that for low-density gas systems, 100% of these solids will impinge on the pipe. As the density increases, this percentage

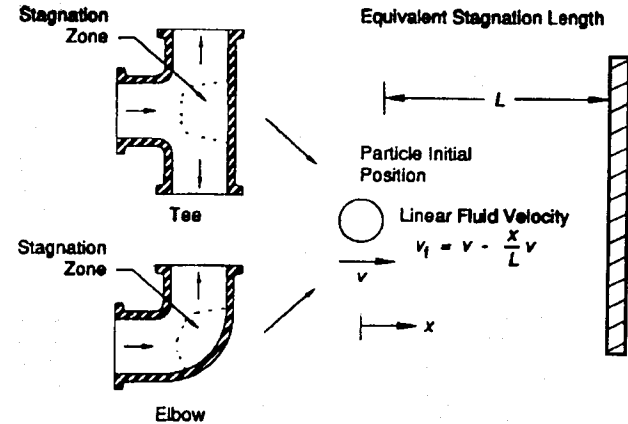


Fig. 6.26—Concept of equivalent stagnation length.⁴⁵

will decrease to 30% for liquids because most of the fluids will be carried in the center of the flow stream without impacting the wall of the elbow. This means that for solid-laden gases, the erosional velocity will be lower than for liquids carrying solids.

The prediction of erosional velocity is based on penetration rates in an elbow geometry. Elbows are a common piping component and are affected the most by erosion damage. Salama and Venkatesh⁴⁴ developed this model to predict the penetration rate for an elbow.

$$h = 496,920 [q_{sd}v_p^2/(Td^2)], \quad \dots \dots \dots \quad (6.25)$$

where h = erosion penetration rate, mil/yr; q_{sd} = sand production rate, ft³/D; v_p = particle impact velocity, ft/sec; T = elbow metal hardness, psi; and d = elbow diameter, in.

Salama and Venkatesh obtained this expression for erosional velocity in ft/sec. Assuming particle impact velocity equals flow stream velocity in Eq. 6.25.

$$v_e = 1.73d/\sqrt{q_{sd}}. \quad \dots \dots \dots \quad (6.26)$$

This equation assumes hardness $T = 1.55 \times 10^5$ psi and an allowable penetration rate of $h = 10$ mil/year.

However, Salama and Venkatesh suggested that the applicability of Eq. 6.26 be limited to gas flow only, noting that the particle-impact velocity in gas flows (with low density and viscosity) nearly equals the flow-stream velocity. This assumption is not valid for liquid flow, where the particle-impact velocity is lower than the flow-stream velocity. In this case, the sand flow rate, q_{sd} , must be adjusted for the number of particles actually impinging on the pipe wall. This adjustment is necessary because with high fluid density and viscosity most of the sand grains may pass through the core of the elbow without impinging on the wall, thus reducing erosion. This flow-regime dependence of erosion calls for consideration of fluid properties, such as the density, viscosity, and composition.

Shirazi *et al.*⁴⁵ presented a new, more rigorous mechanistic model that accounts for a number of variables, including flow geometry, pipe size, pipe material, sand density, particle size, sand-particle sharpness, flow-stream velocity, fluid viscosity, and fluid density. The model to compute the maximum penetration rate in elbows for carbon-steel material is

$$h = AF_s F_p [q_{sd}\rho_p v_p^{1.73}/(B^{0.59} d^2)], \quad \dots \dots \dots \quad (6.27)$$

where A = empirical constant (0.9125 for carbon steel); B = Brinell hardness; F_p = penetration factor for steel based on 1-in. pipe diameter, in./lbm; F_s = sand sharpness factor (empirical); and ρ_p = particle density, lbm/ft³.

The other variables were defined previously. This equation is based on extensive empirical information gathered by Shirazi *et al.*⁴⁵ and others.^{52,53} Unlike the previous equations, this one is more general because v_p is the true characteristic impact velocity on the pipe wall and not the flow-stream velocity. Consequently, this ve-

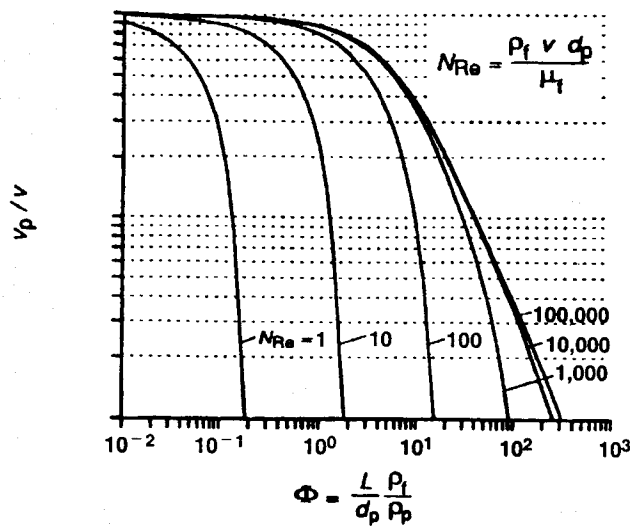


Fig. 6.27—Dimensionless impact velocity nomograph.⁴⁵

lacity depends on such factors as pipe geometry and size, sand size and density, flow regime, fluid velocity, and fluid properties.

The characteristic impact velocity is calculated based on a simple model^{54,55} that defines a stagnation zone presented in Fig. 6.26. To impinge on the target wall, the sand particles must penetrate the fluid layer. The distance of penetration in the stagnation zone, also called the equivalent stagnation length, L (in.), is a function of the elbow internal diameter, d (in.), and is determined from this relationship, where $L_0 = 1.28$ in.

$$L = L_0 [1 - 1.27 \tan^{-1}(1.01d^{-1.89}) + d^{1.29}] \quad (6.28)$$

On the basis of this equivalent stagnation length and assuming the sand particle is traveling in a one-dimensional flow field, McLaury⁵⁴ presented a graphical relationship to calculate the characteristic impact velocity. Fig. 6.27 presents this graphical relationship with three dimensionless groups.

1. Dimensionless impact velocity, a ratio of characteristic impact velocity to the flow-stream velocity (v_p/v).

2. Particle Reynolds number, N_{Re} , based on the flow-stream or the fluid velocity, v (ft/sec), and the particle diameter, d_p (in.)

$$N_{Re} = 124 \rho_f v d_p / \mu_f \quad (6.29)$$

where fluid viscosity, μ_f , is in centipoise and fluid density, ρ_f , is in lbm/ft.³

3. A dimensionless parameter, Φ , proportional to the ratio of the mass of fluid being displaced by the particle to the mass of the impacting particle

$$\Phi = \frac{L}{d_p} \frac{\rho_f}{\rho_p} \quad (6.30)$$

The following procedure should be used to calculate the maximum penetration rate caused by erosion damage in elbows for a given sand-flow rate, q_{sd} (ft³/D),

1. Calculate the equivalent stagnation length, L , from Eq. 6.28.
2. Calculate N_{Re} and Φ from Eqs. 6.29 and 6.30.
3. Determine the dimensionless impact velocity, v_p/v , from Fig. 6.27.
4. Determine the characteristic impact velocity, v_p , for the known flow-stream velocity, v .
5. Select particle sharpness factor, F_s , from Table 6.20 and a penetration factor, F_p , from Ref. 52 (or use 3.68 in./lbm for steel elbows and tees).
6. Compute the maximum penetration rate, h , from Eq. 6.27.
7. To calculate the erosional velocity for an allowed yearly penetration rate, repeat Steps 1 through 6 for different assumed velocities and plot h vs. v over the range of allowed h values. Select the

TABLE 6.20—SAND-SHARPNESS FACTOR⁵⁶

Description	F_s
Sharp corners, angular	1.0
Semirounded, rounded corners	0.53
Rounded, spherical glass beads	0.20

flow-stream velocity, v , for the actual allowed h value from this plot. This is an iterative calculation and can be programmed easily on the basis of this procedure. Shirazi *et al.*⁵⁵ and McLaury *et al.*⁵⁶ also presented this procedure in detail.

6.8 Special Problems

This section is intended to alert the reader to some of the potential pipe-flow-related problems in permafrost and marine environments.

6.8.1 Permafrost/Marine Environment. Permafrost is the frozen or semifrozen alluvial formation found in arctic climates. Depending on the geographical area, permafrost thickness may exceed 2,000 ft. Because of permafrost on Alaska's North Slope, some unusual production problems have been reported.^{57,58} Many of them are related to the abnormal geothermal gradients in the area. The permafrost zone is abnormally cold with low geothermal gradients (0.8 to 3.1°F/100 ft, on the basis of a study of 34 wells by Godbole and Ehlig-Economides⁵⁷), whereas the geothermal gradient below the base of permafrost was found by those authors and Lachenbruch *et al.*⁵⁸ to be in the range of 1.4 to 5.4°F/100 ft. There is also a significant difference in the flowing and static temperature gradients in these zones.

Similar problems⁶⁰⁻⁶² caused by abnormal temperature gradients also have been observed in marine pipelines, where a negative hydrothermal gradient⁶⁰ in sea water follows a positive geothermal gradient below the seabed. Thus, in a marine environment with sub-sea wells, wax deposition and hydrate problems⁶² may be expected, depending on the characteristics of the produced fluid.

Fig. 6.28 illustrates the unique geothermal and hydrothermal gradients found in permafrost, marine environment, and normal earth's crust. The hydrate-forming temperature also is marked to locate the potential zone or depth interval of hydrate formation.

Because the phase behavior of hydrocarbon fluids is highly temperature-dependent, an accurate knowledge of temperature gradient is absolutely necessary for multiphase-flow-related design calculations. The difference in temperature gradients under flowing and static conditions is particularly instrumental in most of the reported production problems. These problems are related to the low temperatures in the permafrost or marine environment, cooling tubulars during startup, or the initial flow period after a shutdown.

Before a shutdown, these problems can be avoided with such proper precautions as inhibitor injection, pipe insulation, or both. Depending on the duration of shut-in in such environments, the tubulars cool down to the low ambient temperature. This leads to solidification of fluids if the temperature in the affected tubulars falls below the pour point and wax-appearance temperature in waxy crude.⁶²

The problem may be particularly severe if there is a gas-lift casing or pressure valve, subsurface pumps, subsurface safety valve, or other restrictive (choke) devices within or near the low-temperature zone. Hanson⁵⁹ presents a case study, where the gas-lift pressure valve just below the permafrost will not close during unloading, thus preventing the transfer of gas to the next lower valve. These pressure valves are very sensitive to the temperature of the nitrogen-charged dome. Because the pressure of nitrogen in the dome actuates these valves, they will not close if the actual operating or closing pressure of the dome is lower than the test-rack setting of this pressure. Hanson mentions that the valve was set to close at the flowing temperature at valve depth, which was 50 to 60°F higher than the actual static temperature during cold startup. As a result, the nitrogen pressure in the dome was substantially lower than the set valve closure pressure. This problem could be mitigated by use of a fluid valve that is insensitive to temperature. However, if possible, prior production through the well immediately before unloading to establish a flowing temperature gradient also could solve this problem.

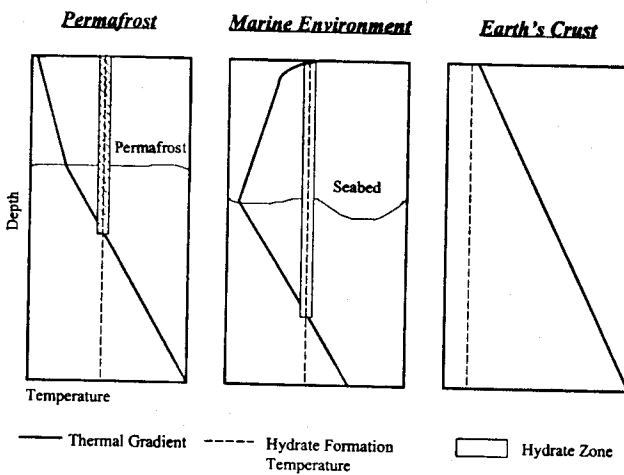


Fig. 6.28—Geothermal and hydrothermal gradient in different environments.

To avoid or mitigate these problems,

- Determine the geothermal and hydrothermal gradients before the pipeline design.
- Determine the flowing temperature gradient in the well or pipeline before the pipeline design.
- Determine the phase behavior of the flowing fluids in the operating minimum and maximum pressure and temperature range experienced between the reservoir and first stage of separator.
- After combining the information in the first three steps, generation of a gas-hydrate envelope in a pressure/temperature phase diagram, as shown in Fig. 6.29, can identify pipe segments ideal for hydrate formation during cold startup. Similar phase envelopes can be drawn for wax deposition.
- Displace the pipe segments identified in Step 4 with chemical inhibitors, such as diesel, methanol, etc., during any shutdown.
- To mitigate these problems, the oil and gas industry uses properly insulated pipeline segments or hot oil pumping when the problem occurs. Economics permitting, permanent chemical injection lines also are used for mitigation.

6.8.2 Gas Hydrates. The formation of gas hydrates is another very common problem, particularly in a high-pressure and low-temperature operation.⁶⁰⁻⁶⁴ Gas hydrates (also called clathrates for encaging) are crystalline compounds that result when water forms a cage-like molecular structure around very specific smaller guest molecules. They are commonly composed of water and a combination of methane, ethane, propane, normal butane, iso-butane, nitrogen, carbon dioxide, and hydrogen sulfide.⁶¹

Gas hydrates are crystalline solid compounds resembling dirty ice in appearance. Unlike ice, however, hydrates form anywhere water and the guest hydrocarbon molecules come in contact at temperatures above or below 32°F and at elevated pressures dictated by the composition-dependent phase behavior. Being solid, hydrates are a nuisance in flowing wells or pipelines, where they can totally or partially block fluid passage. Subsurface restrictions, such as chokes or safety valves, are particularly susceptible to hydrate blockage even during normal operation because of Joule-Thompson cooling.

Hydrates also concentrate hydrocarbons. One cubic foot of hydrate may contain as much as 180 scf of gas. In high-pressure oil and gas wells, hydrates often form during the startup phase. Although the very low temperature of a permafrost environment provides the perfect condition for gas-hydrate formation, they are found anywhere in the world, especially in high-pressure and marine environments. Ideal situations for gas-hydrate formation include

- High-pressure gas wells or flowlines, where the gas contains moisture or free water or load-water produced during post-fracture cleanup.
- In marine pipelines, riser pipes, and high-pressure oil and gas wells.
- In arctic wells, especially near the permafrost zone.

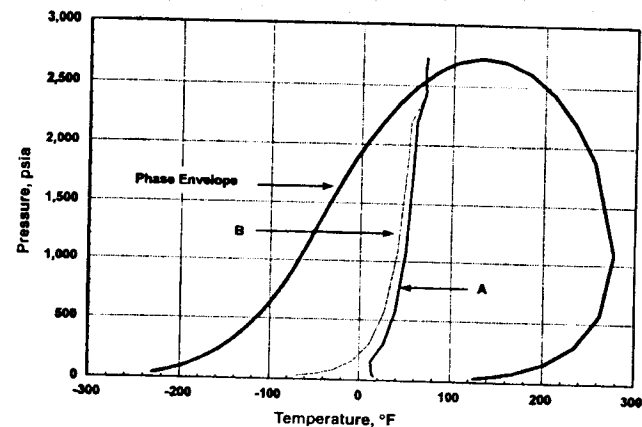


Fig. 6.29—Gas-hydrate envelope in a pressure/temperature phase diagram.

4. At or near subsurface safety valves or other choke devices where Joule-Thompson cooling is present.

5. During cold startup of producing wells after shut-ins for well testing, workover, or routine surface-facility maintenance.

Gas-hydrate phase behavior and kinetics are well understood. Sloan⁶¹ presented a very comprehensive review of these processes. Formation of solid gas hydrates in oil and natural gas wells or transmission pipelines⁶³ causes physical blockages to flow and is a major nuisance. When designing gas or multiphase-flow pipelines in gas-hydrate-prone systems, consider the phase behavior of gas hydrates and, if possible, avoid the formation of gas hydrates or hydrate plugging. If a hydrate-free system cannot be designed, hydrate-related blockage in the pipeline should be considered while troubleshooting flow or production problems, especially after shutdowns or during cold startups.

Inhibition/Dissociation. The common method of hydrate inhibition is by inducing thermodynamic instability to the hydrate phase, also known as thermodynamic inhibition. This is accomplished by the following method.

- Heating the system above the hydrate-formation temperature at system pressure.
- Reducing the system pressure below hydrate stability at system temperature.
- Changing composition or removing one of the components of hydrate, such as the hydrocarbon or the water.
- Adding or injecting an inhibitor, such as methanol or glycol, to the hydrate system to reduce its stability at the system pressure and temperature.

The injection of inhibitors moves the hydrate stability conditions toward higher pressures and lower temperatures.^{65,65} New inhibi-

TABLE 6.21—EXAMPLE OF GAS COMPOSITION

Component	Mole Fraction
Methane	0.6741
Ethane	0.0842
Propane	0.0460
Iso-butane	0.0063
n-butane	0.0171
Iso-pentane	0.0051
n-pentane	0.0077
Hexane	0.0093
Heptane	0.0677
Nitrogen	0.0024
CO ₂	0.0801

tors, called kinetic inhibitors, are being developed that allow the system to exist in the hydrate thermodynamic stability region, inhibiting the agglomeration of smaller hydrate nuclei to larger masses. Inhibition of hydrates by pumping hot oil into the hydrate system is commonly practiced to mitigate any existing problems during cold startup. However, chemical inhibitor injection with pipe insulation (if necessary) is a more common method to prevent hydrate formation. Davalath and Barker⁶⁰ presented a detailed review of design considerations for gas-hydrate prevention in deepwater gas-well completions. The following example illustrates the hydrate-phase envelope with respect to a typical North Sea gas-phase envelope. Table 6.21 gives the gas composition.

A phase envelope for this gas in a feed stream with 1,000 lbm-mol/hr dry gas and 2 lbm-mol/hr water was generated with the Peng-Robinson equation of state from Appendix C and is presented in Fig. 6.29. Note that the hydrate equilibrium line (Line A) in the middle of the gas/liquid phase envelope determines the thermodynamic stability conditions of pressure and temperature. The area to the left of this curve provides the ideal stable-gas-hydrate envelope. If the pressure and temperature in this gas well lie on the left side of this envelope during cold startup, hydrates may cause blockage to the line. Injection of inhibitor moves this curve to the left, requiring higher pressure and/or lower temperature to form hydrates. With the same gas/water stream, injection of 3.607 lbm-mol/hr, 80 wt% methanol in water moves the hydrate equilibrium line to the left, as shown by Line B. This shows a little shrinkage of the hydrate-phase envelope with the addition of methanol. The extent of control of the hydrate-phase envelope depends on the composition of the producing hydrocarbons and the type and amount of hydrate inhibitor added. Thus, an understanding of such hydrate-phase behavior forms the basis of its thermodynamic inhibition and is highly recommended for troubleshooting and solving hydrate-related problems.

References

1. Versluis, J.: "Mathematical Development of the Theory of Flowing Oil Wells," *Trans., AIME* (1930) **86**, 192.
2. Gilbert, W.E.: "Flowing and Gas-Lift Well Performance," *Drill. & Prod. Prac.* (1954) 126.
3. Nind, T.E.W.: *Principles of Oil Well Production*, McGraw-Hill Book Co. Inc., New York City (1964).
4. Proano, E.A., Mach, J.M., and Brown, K.E.: "Systems Analysis as Applied to Producing Wells," paper 3.1 presented at the 1979 Congreso Panamericano de Ingeniería del Petróleo, Mexico City, 19–23 March.
5. Crouch, E.C. and Pack, K.J.: "Systems Analysis Use for the Design and Evaluation of High-Rate Gas Wells," paper SPE 9424 presented at the 1980 SPE Annual Technical Conference and Exhibition, Dallas, 21–24 September.
6. Mach, J.M., Proano, E.A., and Brown, K.E.: "Application of Production System Analysis to Determine Completion Sensitivity on Gas Well Production," paper presented at the 1981 ASME Energy Sources Technical Conference and Exhibition, Houston, 18–22 January.
7. Mach, J.M.: "Apply NODAL™ Analysis to Production Systems," *Well Servicing* (January/February 1981) 38.
8. Brown, K.E. et al.: "Production Optimization of Oil and Gas Wells by NODAL™ Systems Analysis," *Technology of Artificial Lift Methods*, PennWell Publishing Co., Tulsa, Oklahoma (1984) Chap. 4.
9. Golani, M. and Whitson, C.H.: *Well Performance*, Prentice-Hall Book Co. Inc., Englewood Cliffs, New Jersey (1991).
10. Darcy, H.: *Les fontaines publiques de la ville de Dijon* (1856).
11. Muskat, M.: *The Flow of Homogeneous Fluids Through Porous Media*, McGraw-Hill Book Co. Inc., New York City (1937); reprinted by SPE, Richardson, Texas (1982); copyrighted by Intl. Human Resources Development Corp., Boston (1982).
12. Earlougher, R.C. Jr.: *Advances in Well Test Analysis*, Monograph Series, SPE, Richardson, Texas (1977) 5.
13. Matthews, C.S. and Russell, D.G.: *Pressure Buildup and Flow Tests in Wells*, Monograph Series, SPE, Richardson, Texas (1967) 1.
14. Dietz, D.N.: "Determination of Average Reservoir Pressure From Build-Up Surveys," *JPT* (August 1965) 955; *Trans., AIME*, **234**.
15. Ahmed, T.H.: *Hydrocarbon Phase Behavior*, Gulf Publishing Co., Houston (1989).
16. Vogel, J.V.: "Inflow Performance Relationships for Solution-Gas Drive Wells," *JPT* (January 1968) 83; *Trans., AIME*, **243**.
17. Fetkovich, M.J.: "The Isochronal Testing of Oil Wells," paper SPE 4529 presented at the 1973 SPE Annual Meeting, Las Vegas, Nevada, 30 September–3 October.
18. Joshi, S.D.: "Augmentation of Well Productivity With Slant and Horizontal Wells," *JPT* (June 1988) 729; *Trans., AIME*, **285**.
19. Agarwal, R.G., Al-Hussainy, R., and Ramey, H.J. Jr.: "An Investigation of Wellbore Storage and Skin Effect in Unsteady Liquid Flow: I. Analytical Treatment," *SPEJ* (September 1970) 279; *Trans., AIME*, **249**.
20. Odeh, A.S.: "Pseudosteady-State Flow Capacity of Oil Wells With Limited Entry and an Altered Zone Around the Wellbore," *SPEJ* (August 1977) 271; *Trans., AIME*, **270**.
21. Cinco-L., H., Samaniego-V., F., and Dominguez-A., N.: "Transient Pressure Behavior for a Well With a Finite-Conductivity Vertical Fracture," *SPEJ* (August 1978) 253.
22. Meng, H.Z. and Brown, K.E.: "Coupling of Production Forecasting, Fracture Geometry Requirements, and Treatment Scheduling in the Optimum Hydraulic Fracture Design," paper SPE 16435 presented at the 1987 SPE Low Permeability Reservoirs Symposium, Denver, Colorado, 18–20 May.
23. Al-Hussainy, R. and Ramey, H.J. Jr.: "Application of Real Gas Flow Theory to Well Testing and Deliverability Forecasting," *JPT* (May 1966) 637; *Trans., AIME*, **237**.
24. Carroll, J.A. III and Horne, R.N.: "Multivariate Optimization of Production Systems," *JPT* (July 1992) 782; *Trans., AIME*, **293**.
25. "PERFORM" Well Performance Analysis Program," Dwight's Energydata Inc., Dallas (1995).
26. Ansari, A.M. et al.: "A Comprehensive Mechanistic Model for Two-Phase Flow in Wellbores," *SPEPF* (May 1994) 143; *Trans., AIME*, **297**.
27. Hagedorn, A.R. and Brown, K.E.: "Experimental Study of Pressure Gradients Occurring During Continuous Two-Phase Flow in Small-Diameter Vertical Conduits," *JPT* (April 1965) 475; *Trans., AIME*, **234**.
28. Orkiszewski, J.: "Predicting Two-Phase Pressure Drops in Vertical Pipes," *JPT* (June 1967) 829; *Trans., AIME*, **240**.
29. Beggs, H.D. and Brill, J.P.: "A Study of Two-Phase Flow in Inclined Pipes," *JPT* (May 1973) 607; *Trans., AIME*, **255**.
30. Mukherjee, H. and Brill, J.P.: "Pressure Drop Correlations for Inclined Two-Phase Flow," *J. Energy Res. Tech.* (December 1985) **107**, 549.
31. Aziz, K., Govier, G.W., and Fogarasi, M.: "Pressure Drop in Wells Producing Oil and Gas," *J. Cdn. Pet. Tech.* (July–September 1972) **11**, 38.
32. Ashford, F.E. and Pierce, P.E.: "Determining Multiphase Pressure Drops and Flow Capacities in Down-Hole Safety Valves," *JPT* (September 1975) 1145.
33. Mach, J.M. et al.: "A New Concept in Continuous-Flow Gas-Lift Design," *SPEJ* (December 1983) 885; *Trans., AIME*, **275**.
34. Lea, J.F.: "Avoid Premature Liquid Loading in Tight Gas Wells Using Prefrac and Postfrac Test Data," *Oil & Gas J.* (20 September 1982) 123.
35. Gregory, G.A.: "Comments on the Prediction of Minimum Unloading Velocities for Wet Gas Wells," Technical Note No. 14, Neotechnology Consultants Ltd., Calgary (December 1989).
36. Turner, R.G., Hubbard, M.G., and Dukler, A.E.: "Analysis and Prediction of Minimum Flow Rate for the Continuous Removal of Liquids From Gas Wells," *JPT* (November 1969) 1475; *Trans., AIME*, **246**.
37. Dukler, A.E.: "Fluid Mechanics and Heat Transfer in Vertical Falling Film Systems," *Chem. Eng. Prog.* (1960) **56**.
38. Foust, A.S. et al.: *Principles of Unit Operations*, second edition, John Wiley & Sons, New York City (1980).
39. Coleman, S.B. et al.: "A New Look at Predicting Gas-Well Loadup," *JPT* (March 1991) 329; *Trans., AIME*, **291**.
40. Coleman, S.B. et al.: "Understanding Gas-Well Load-Up Behavior," *JPT* (March 1991) 334; *Trans., AIME*, **291**.
41. Oudeeman, P.: "Improved Prediction of Wet-Gas-Well Performance," *SPEPE* (August 1990) 212; *Trans., AIME*, **289**.
42. Upchurch, E.R.: "Expanding the Range for Predicting Critical Flow Rates of Gas Wells Producing From Normally Pressured Waterdrive Reservoirs," *SPEPE* (August 1989) 321; *Trans., AIME*, **287**.
43. RP14E, *Recommended Practice for Design and Installation of Offshore Production Platform Piping System*, third edition, API, Washington, DC (1981).
44. Salama, M.M. and Venkatesh, E.S.: "Evaluation of API RP14E, Erosional Velocity Limitations for Offshore Wells," paper SPE 12531 presented at the 1983 Offshore Technology Conference, Houston, 2–5 May.
45. Shirazi, S.A. et al.: "Generalization of the API RP14E Guideline for Erosive Services," *JPT* (August 1995) 693.
46. Thompson, T.L. and Aude, T.C.: "Slurry Pipeline Design and Operation Pitfalls to Avoid," *Trans., ASME* (1976).

47. Benchaita, M.T., Griffith, P., and Rabinowicz, E.: "Erosion of a Metallic Plate by Solid Particles Entrained in a Liquid," *J. Eng. Ind.* (1983) **105**, No. 3, 215; *Trans.*, ASME.
48. Rabinowicz, E.: "The Wear Equation for Erosion of Metals by Abrasive Particles," *Proc.*, Fifth Intl. Conference on Erosion by Liquid and Solid Impact, Cambridge, U.K. (1979).
49. Rabinowicz, E.: "Factors Modifying the Erosive Wear Equations for Metals," *Israel J. Tech.* (1980) **18**, 193.
50. Benchaita, M.T.: "Erosion of a Two-Dimensional Channel Bend by a Solid/Liquid Stream," *Trans.*, CSME (1985) **9**, No. 2, 98.
51. Blanchard, D., Griffith, P., and Rabinowicz, E.: "Erosion of a Pipe Bend by Solid Particles Entrained in Water," *J. Eng. Ind.* (1984) **106**, No. 3, 213; *Trans.*, ASME.
52. Tolle, G. and Greenwood, D.R.: "Design of Fittings to Reduce Wear Caused by Sand Erosion," API Offshore Safety and Anti Pollution Research (OSAPR) Project No. 6, Texas A&M Research Foundation, College Station, Texas (May 1977).
53. Weiner, P.D. and Tolle, G.: "Detection and Prevention of Sand Erosion of Production Equipment," API OSAPR Project No. 2, Texas A&M Research Foundation, College Station, Texas (March 1976).
54. McLaury, B.S.: "A Model to Predict Solid Particle Erosion in Oilfield Geometries," MS thesis, U. of Tulsa, Tulsa, Oklahoma (1993).
55. Shirazi, S.A. *et al.*: "A Procedure to Predict Solid Particle Erosion in Elbows and Tees," *Codes and Standards in Global Environment*, Pressure Vessels and Piping Div., ASME, New York City (1993) **259**, 159.
56. McLaury, B.S. *et al.*: "A Particle Tracking Method to Predict Sand Erosion Threshold Velocities in Elbows and Tees," *Liquid-Solid Flows*, Fluid Engineering Div., ASME, New York City (1994) **189**, 145.
57. Godbole, S.P. and Ehlig-Economides, C.: "Natural Gas Hydrates in Alaska: Quantification and Economic Evaluation," paper SPE 13593 presented at the 1985 SPE California Regional Meeting, Bakersfield, California, 27-19 March.
58. Lachenbruch, A.H. *et al.*: "Permafrost, Heat Flow and Geothermal Regime at Prudhoe Bay, Alaska," *J. Geo. Res.*, **87**, B11, 9301.
59. Hanson, E.S.: "Pilot Gas-Lift System at Prudhoe Bay," paper SPE 13635 presented at the 1985 SPE California Regional Meeting, Bakersfield, California, 27-29 March.
60. Davalath, J. and Barker, J.W.: "Hydrate Inhibition Design for Deepwater Completions," *SPEDC* (June 1995) 115.
61. Sloan, E.D. Jr.: "Natural Gas Hydrates," *JPT* (December 1991) 1414; *Trans.*, AIME, **291**.
62. Hartley, R. and Jadid, M.B.: "Use of Laboratory and Field Testing To Identify Potential Production Problems in the Troll Field," *SPEPE* (February 1989) 34.
63. Sira, J.H., Patil, S.L., and Kamath, V.A.: "Study of Hydrate Dissociation by Methanol and Glycol Injection," paper SPE 20770 presented at the 1990 SPE Annual Technical Conference and Exhibition, New Orleans, 23-26 September.
64. Sloan, E.D. Jr.: *Clathrate Hydrates of Natural Gases*, Marcel Dekker Inc., New York City (1990).
65. Ng, J.J., Chen, C.J., and Robinson, D.B.: "Hydrate Formation and Equilibrium Phase Compositions in the Presence of Methanol: Selected Systems Containing Hydrogen Sulfide, Carbon Dioxide, Ethane or Methane," RR-87, Project 825-85, Gas Processors Suppliers Assn., Tulsa, Oklahoma (1985).

Appendix A

Nomenclature and

SI Metric Conversion Factors

a = abscissa
 A = Helmholtz energy, mL^2/t^2
 A = pipe cross-sectional area, L^2
 A = well drainage area, L^2
 \bar{A} = parameter defined in Eq. 4.196
 B_g = formation volume factor of gas, L^3/L^3
 B_o = formation volume factor of oil, L^3/L^3
 B_t = total formation volume factor, L^3/L^3
 B_w = formation volume factor of water, L^3/L^3
 c = compressibility, L^2/m
 c = wellbore storage coefficient, $\text{L}^4\text{t}^2/\text{m}$
 C = correction factor
 C = flow coefficient in Eqs. 5.1 and 5.2
 C = liquid-holdup parameter in Eq. 4.117
 C = specific heat, $\text{L}^2/\text{t}^2\text{T}$
 C_D = discharge coefficient, drag coefficient
 C_{FD} = dimensionless fracture conductivity
 C_K, C_M = film indices in Eq. 4.294
 C_L = specific heat of liquid, $\text{L}^2/\text{t}^2\text{T}$
 C_o = flow coefficient in Eqs. 4.240 and 4.241
 C_p = specific heat at constant pressure, $\text{L}^2/\text{t}^2\text{T}$
 C_v = specific heat at constant volume, $\text{L}^2/\text{t}^2\text{T}$
 d = pipe diameter, L
 D = dimensionless parameter in Eqs. 5.7 and 5.9
 D = turbulence coefficient
 D_{BC} = distance between pipe centers, L
 e = eccentricity of annulus, L/L
 e = intrinsic specific energy, L^2/t^2
 e = error
 e_r = relative error
 E_k = dimensionless kinetic-energy pressure gradient in Eqs. 4.9 and 4.53
 E_1 = average percent error in Eq. 4.256
 E_2 = absolute average percent error in Eq. 4.258
 E_3 = percent standard deviation in Eq. 4.259
 E_4 = average error in Eq. 4.260
 E_5 = absolute average error in Eq. 4.262
 E_6 = standard deviation in Eq. 4.263
 f = Moody or Darcy-Weisbach friction factor
 f = no-slip volume fraction, L^3/L^3
 f' = Fanning friction factor
 f = fugacity, $\text{m}/\text{L}^2\text{t}^2$

F = friction geometry parameter for annulus
 F = moles of feed mixture, mol
 F = formation resistivity factor
 F_E = liquid entrainment fraction, L^3/L^3
 F_p = penetration factor, L/m
 F_{rp} = relative performance factor in Eq. 4.264
 F_s = sand sharpness factor
 g = acceleration of gravity, L/t^2
 g_c = gravitational conversion factor
 g_G = geothermal temperature gradient, T/L
 h = convective film coefficient, $\text{m}/\text{t}^3\text{T}$
 h = specific enthalpy, L^2/t^2
 h = net reservoir thickness, L
 h = erosion penetration rate, L/t
 h_L = liquid interface height, L
 H = enthalpy, mL^2/t^2
 H_L = slip gas/liquid volume fraction (liquid holdup), L^3/L^3
 H_{LF} = liquid holdup from liquid film, L^3/L^3
 H_R = holdup ratio in Eq. 4.140
 i = injection rate, L^3/t
 I_{ani} = permeability anisotropy
 J = mechanical equivalent of heat
 k = thermal conductivity, $\text{mL}/\text{t}^3\text{T}$
 k = ratio of specific heats, C_p/C_v
 k = effective permeability, L^2
 K = pipe diameter ratio for annulus, L/L
 K = piping component factor in Eq. 5.33
 K = equilibrium constant, mol/mol
 K_W = Watson characterization factor
 K' = power-law consistency index in Eq. 2.29
 L = pipe length, L
 L = liquid mole fraction, mol/mol
 L = moles of liquid, mol
 L = horizontal well length, L
 L_B = parameter in Eq. 4.59
 L_v = latent heat of vaporization, L^2/t^2
 m = mass, m
 m = parameter in Eq. 4.96
 $m(p)$ = real-gas pseudopressure function
 M = molecular weight, m
 M = volumetric heat capacity, $\text{mL}/\text{t}^2\text{T}$
 n = number of moles

n	= parameter in Eqs. 5.9 and 5.10	x_e	= drainage boundary length, L
n	= polytropic expansion exponent in Eq. 5.13	x_f	= fracture half length, L
n_c	= number of components	X_M	= Lockhart and Martinelli parameter in Eq. 4.167
n'	= power-law flow behavior index in Eq. 2.29	y	= mole fraction of component in vapor phase
n'	= bubble-swarm parameter in Eq. 4.177	y	= parameter in Eq. 4.124
N	= dimensionless parameter in Eqs. 5.7 and 5.8	y	= parameter in Eq. 4.132
N_d	= pipe-diameter number in Eq. 4.5	y	= ratio of downstream to upstream pressure
N_D	= dimensionless diameter numbers in Eqs. 4.13 and 5.27	y_c	= critical pressure ratio
N_E	= dimensionless number in Eq. 4.97	y_e	= drainage boundary width, L
N_{Fr}	= Froude number in Eq. 4.109	Y_M	= Lockhart and Martinelli parameter in Eq. 4.168
N_{gv}	= gas-velocity number in Eq. 4.4	z	= mole fraction of component in feed mixture, mol/mol
N_{Gr}	= Grashof number in Eq. 2.93	z	= parameter in Eq. 4.134
N_L	= liquid-viscosity number in Eq. 4.6	Z	= gas compressibility factor, L^3/L^3
N_{LC}	= corrected liquid-viscosity number in Figs. 4.2 and 4.3	Z	= vertical distance, L
N_{Lv}	= liquid-velocity number in Eq. 4.3	Z	= interfacial friction parameter in Eqs. 4.221 and 4.222
N_{Nu}	= Nusselt number in Example 2.4	α	= thermal diffusivity, L^2/t
N_{p1}	= dimensionless pressure number in Eq. 5.26	α	= void fraction
N_{Pr}	= Prandtl number in Eq. 2.94	β	= coefficient of thermal expansion, $1/T$
N_{qL}	= dimensionless liquid flow rate number in Eq. 5.28	β	= ratio of Taylor bubble to slug unit length
N_{Re}	= Reynolds number	δ	= subtended angle by interface chord
N_v	= dimensionless velocity number in Eq. 4.12	$\underline{\delta}$	= dimensionless film thickness
N_{We}	= Weber number in Eq. 4.47	δ_{mn}	= minimum dimensionless film thickness
N_x	= flow-pattern coordinate in Eq. 4.85 and Fig. 4.14, L/t	δ_L	= liquid film thickness, L
N_y	= flow-pattern coordinate in Eq. 4.86 and Fig. 4.14, L/t	Δ	= difference
N_μ	= liquid viscosity number in Eq. 4.48	ϵ	= absolute pipe roughness, L
N_ν	= dimensionless number in Eq. 4.98	ϵ	= convergence tolerance
N_p	= dimensionless density ratio in Eq. 5.25	ϕ	= parameter in Eqs. 2.53 and 2.103
p	= pressure, m/Lt ²	ϕ	= parameter in Eqs. 4.231 and 4.232
p_D	= dimensionless wellbore pressure drop	ϕ	= porosity
P	= perimeter, L	Φ	= fugacity coefficient
P_{ch}	= parachor	γ	= specific gravity
	q = volumetric flow rate, L^3/t	γ_{API}	= oil gravity, °API
	q = heat flow rate, mL^2/t^3	γ	= shear rate, 1/t
q_{\max}	= absolute-open-flow potential, L^3/t	Γ	= liquid distribution coefficient in Eqs. 4.72 through 4.81
q_{sc}	= volumetric flow rate at standard conditions, L^3/t	η	= Joule-Thompson coefficient, $T Lt^2/m$
Q	= heat flux, m/t^3	λ	= no-slip gas/liquid volume fraction, L^3/L^3
r	= radius, L	λ	= thermal conductivity, mL/t^3
r_d	= drainage radius, L	μ	= absolute viscosity, m/Lt
r_w	= well radius, L	v	= kinematic velocity, L^2/t
R	= annulus concentricity parameter in Eq. 2.63, L/L	θ	= inclination angle from horizontal
R	= gas constant, mL^2/t^2T	θ	= reduced boiling point
R	= gas/oil ratio, L^3/L^3	ρ	= density, m/L^3
R	= in-situ gas/liquid volume ratio, L^3/L^3	σ	= surface tension, m/t^2
R_p	= producing gas/oil ratio, L^3/L^3	σ	= percent standard deviation
s	= skin factor	τ	= shear stress, m/Lt^2
s	= parameter in Eqs. 4.122, 4.123, and 4.125	w	= Pitzer acentric factor
S	= slip velocity number	ψ	= parameter in Fig. 4.4
S	= surface area, L^2	Ψ	= liquid-holdup inclination angle correction in Eq. 4.116
S	= saturation		
S	= entropy, mL^2/t^2T		
t	= time, t		
T	= temperature, T		
T	= metal hardness, m/Lt^2		
u	= specific internal energy, L^2/t^2		
U	= overall heat-transfer coefficient, m/t^3T		
v	= velocity, L/t		
v^*	= sonic velocity, L/t		
v_E^*	= effective sonic velocity, L/t		
v_s	= specific volume, L^3/m		
V	= vapor mole fraction, mol/mol		
V	= volume, L^3		
V	= moles of vapor, mol		
w	= mass flow rate, m/t		
w	= fracture width, L		
W'	= angle of view average in Eqs. 4.335 and 4.336, rad		
W_i	= interface chord length, L		
x	= mass fraction		
x	= mole fraction of component in liquid phase, mol/mol		
x	= parameter in Eq. 4.129		

Subscripts

1	= upstream conditions
2	= downstream conditions
a	= air, atmospheric, apparent
acc	= acceleration
an	= annulus
b	= bubble, boiling point, bulk
bf	= bubble in flowing liquid
bs	= bubble in static liquid
B/S	= bubble/slug boundary
c	= casing, circular, critical
$calc$	= calculated
cem	= cement
ch	= choke
ci	= inside casing
co	= outside casing
$crit$	= critical
C	= calculated, corrected, gas core
CA	= concentric annulus

d = dewpoint, dissolved, dead, differential, dry, deposits, downstream
 D = droplet
 D_w = dimensionless at wellbore
 e = environment, earth, erosional, emulsion
 el = elevation
 est = estimated
 E = effective
 EA = eccentric annulus
 EP = equiperipheral
 f = film, fluid, friction, free, formation, flash, fracture
 fc = forced convection
 fl = flowline
 F = film, Fortunati
 FC = friction-concentric annulus
 FE = friction-eccentric annulus
 g = gas
 h = hydraulic, hydrostatic, horizontal
 HT = heat transfer in Eqs. 2.74 and 2.75
 i = inlet, interface, initial, inner
 I = interfacial
 k = kinetic
 L = liquid
 LF = liquid film
 LS = liquid slug
 m = mixture, minerals
max = maximum
meas = measured
 mf = midpoint flowing
min = minimum
M-R = Metzner and Reed
 n = no-slip, normalizing
NC = noncircular
 o = oil
 p = pipe, producing, particle
 pc = pseudocritical
 pr = pseudoreduced
 pss = pseudosteady state
 q = at Inclination Angle q , quartz
 r = rough pipe, reservoir, reduced, restriction
 s = smooth pipe, solution, slip, static, steam, sandface
sc = standard conditions, surface choke
 sd = sand
sep = separator
sv = safety valve
SC = superficial core
 Sg = superficial gas
SL = superficial liquid
SM = slug/mist boundary
S/Tr = slug/transition boundary
SU = slug unit
 t = total, tubing, transition, terminal
 tf = wellhead flowing
 ti = inside tubing
 to = outside tubing
TB = Taylor bubble
TP = two-phase

Tr/M = transition/mist boundary
 u = upstream
 v = vertical
 vp = vapor pressure
 V = vapor
 w = water, wellbore, wall
 wf = bottomhole flowing
 wh = wellhead
 σ = solid

Superscripts

A = assumed
 C = calculated
 L = liquid
 V = vapor
 0 = ideal
 $\bar{}$ = average

SI Metric Conversion Factors

$^{\circ}\text{API}$	$141.5/(131.5 + ^{\circ}\text{API})$	$= \text{g/cm}^3$
bbl	$\times 1.589\ 873$	$E - 01 = \text{m}^3$
bbl/psi	$\times 2.305\ 916$	$E - 02 = \text{m}^3/\text{kPa}$
Btu	$\times 1.055\ 056$	$E + 00 = \text{kJ}$
Btu/ft ³ - $^{\circ}\text{F}$	$\times 2.069\ 942$	$E + 01 = \text{kJ/m}^3\text{K}$
Btu/hr	$\times 2.930\ 711$	$E - 04 = \text{kW}$
Btu/hr-ft ²	$\times 3.154\ 591$	$E - 03 = \text{kW/m}^2$
Btu/hr-ft ² - $^{\circ}\text{F}/\text{ft}$	$\times 5.678\ 263$	$E - 03 = \text{kW/m}^2/\text{K}$
Btu/(hr-ft ² - $^{\circ}\text{F}/\text{ft}$)	$\times 1.730\ 735$	$E + 00 = \text{W/mK}$
Btu/lbm	$\times 2.326$	$E + 00 = \text{kJ/kg}$
Btu/lbm- $^{\circ}\text{F}$	$\times 4.186^*$	$E + 00 = \text{kJ/kg-K}$
Btu/R	$\times 7.536\ 240$	$E + 00 = \text{kJ/K}$
cp	$\times 1.0^*$	$E - 03 = \text{Pa}\cdot\text{s}$
dyne/cm	$\times 1.0^*$	$E + 00 = \text{mN/m}$
$^{\circ}\text{F}$	$(^{\circ}\text{F} - 32)/1.8$	$= ^{\circ}\text{C}$
$^{\circ}\text{F}$	$(^{\circ}\text{F} + 459.67)/1.8$	$= \text{K}$
$^{\circ}\text{F}/\text{ft}$	$\times 1.822\ 689$	$E + 00 = \text{K/m}$
$^{\circ}\text{F}\cdot\text{in.}^2/\text{lbf}$	$\times 8.057\ 652$	$E - 02 = \text{K/kPa}$
ft	$\times 3.048^*$	$E - 01 = \text{m}$
ft/sec	$\times 3.048^*$	$E - 01 = \text{m/s}$
ft/sec ²	$\times 3.048^*$	$E - 01 = \text{m/s}^2$
ft ²	$\times 9.290\ 304$	$E - 02 = \text{m}^2$
ft ³	$\times 2.831\ 685$	$E - 02 = \text{m}^3$
ft ³ /lbm	$\times 6.242\ 796$	$E - 02 = \text{m}^3/\text{kg}$
ft ³ /sec	$\times 2.831\ 685$	$E - 02 = \text{m}^3/\text{s}$
in.	$\times 2.54^*$	$E + 01 = \text{mm}$
in./lbm	$\times 1.152\ 125$	$E + 00 = \text{m/kg}$
lbm	$\times 4.535\ 924$	$E - 01 = \text{kg}$
lbm mol	$\times 4.535\ 924$	$E - 01 = \text{kg mol}$
lbm/ft ³	$\times 1.601\ 846$	$E + 01 = \text{kg/m}^3$
lbm/hr	$\times 1.259\ 979$	$E + 04 = \text{kg/s}$
md	$\times 9.869\ 233$	$E - 04 = \mu\text{m}^2$
mil/yr	$\times 2.54^*$	$E + 01 = \text{mm/a}$
psi	$\times 6.894\ 757$	$E + 00 = \text{kPa}$
scf/D	$\times 2.831\ 685$	$E - 02 = \text{std m}^3/\text{d}$
scf/STBO	$\times 1.801\ 175$	$E - 01 = \text{std m}^3/\text{std m}^3$

*Conversion factor is exact.

Appendix B

Fluid and Rock Properties

B.1 Introduction

Integration of the pressure-gradient equation requires determination of individual phase velocities, densities, viscosities, and, in some cases, surface tension at different pressures and temperatures. In dynamic conditions of multiphase flow in pipes, the pressure and temperature of the fluids change continuously. Consequently, very active mass transfer occurs between the liquid and the gas phases. As the pressure decreases in the direction of flow below the bubble-point, gas evolves from solution in the oil, increasing the gas velocity and the oil density and viscosity. Such flow and fluid property changes can be predicted with either compositional or black-oil models. The compositional models presented in Appendix C can represent the mass-transfer phenomena more accurately and are applicable universally.

This appendix presents methods to determine fluid physical properties required in the black-oil model. The assumptions in the black-oil model are that, at any fixed temperature, pressure, API gravity of the liquid phase and specific gravity of gas, the liquid phase has a fixed gas solubility and formation volume factor. These assumptions imply that the composition of the oil and gas do not change with pressure and temperature. This constant composition assumption may be valid for the oil phase, but can cause errors in predicting the physical properties of the gas phase.

Gas solubility is defined as the volume of gas dissolved per unit volume of liquid at a fixed temperature and pressure. Formation volume factor determines the change in the volume of a phase at different pressures and temperatures. This appendix presents a detailed discussion of these black-oil parameters. An important limitation of the black-oil model is its inability to predict retrograde condensation phenomena. The black-oil model should be avoided for very volatile or light crude oils or gas condensates. Compositional models are recommended for these cases.

Most black-oil-model-related fluid physical properties¹⁻²⁸ can be determined by use of pressure/volume/temperature (PVT) cells. These are often called PVT properties. This appendix presents the most widely used and reliable fluid and rock physical property correlations. These correlations are very useful in determining the fluid and rock physical properties required in the application of the multiphase flow theories presented in this monograph. However, the correlations should be used with proper caution. Most of these correlations are empirical in nature and are based on a limited quantity of representative samples of data. Some of these PVT properties are developed from reservoir fluid samples belonging to particular geographical areas and may not be applicable in other areas where reservoir fluid composition is very different. Although PVT property correlations are very widely used in the petroleum industry world-

wide, the use of laboratory data measured on representative samples taken from the reservoir is strongly recommended whenever available.

Most of the fluid and rock properties included in this appendix have been reported previously.¹⁻⁵ However, we decided to incorporate some of these materials, in some cases verbatim or with minor changes, and to provide supplementary information when necessary.

B.2 Hydrocarbon Physical Properties

Crude oils and natural gases contain several pure organic and inorganic chemical components, each with its own properties. Table B-1 presents selected physical properties of several of these individual components. Refs. 6 and 7 present more complete data.

Table B-1 shows a very wide range of molecular weights, boiling points, phase densities, and critical temperatures and pressures among the components constituting reservoir fluids (crude oils or natural gases). Clearly, the physical properties of reservoir fluids are pressure- and temperature-dependent. The critical pressure and temperature of a multicomponent mixture are called pseudocritical pressure, p_{pc} , and pseudocritical temperature, T_{pc} , respectively. In this appendix, these pseudocritical properties are used as correlating parameters in many empirical correlations. If the mixture composition is known, these quantities may be estimated from

$$T_{pc} = \sum_{j=1}^{n_c} y_j T_{cj} \quad \dots \dots \dots \quad (B-1)$$

and

$$p_{pc} = \sum_{j=1}^{n_c} y_j p_{cj}, \quad \dots \dots \dots \quad (B-2)$$

where n_c = number of components in the mixture; y_j = mole fraction of Component j ; T_{cj} = critical temperature of Component j , °R, and p_{cj} = critical pressure of Component j , psia.

If the system composition is not known, Figs. B-1 through B-3 can be used to estimate T_{pc} and p_{pc} . Fig. B-1 provides a way to estimate these quantities for undersaturated oil at reservoir pressure; the oil specific gravity corrected to 60°F (the value normally reported) is used. "The specific gravity of a petroleum oil and of mixtures of petroleum products with other substances is the ratio of the weight of a given volume of the material at a temperature of 60°F... to the weight of an equal volume of distilled water at the same temperature, both weights being corrected for the buoyancy of air."⁹ This often is referred to as γ_o at 60°F/60°F. Sometimes the weight of the

TABLE B-1—PHYSICAL PROPERTIES OF HYDROCARBONS AND SELECTED COMPOUNDS⁶

Constituent	Molecular Weight	Normal Boiling Point (°F)	Normal Boiling Point (°R)	Liquid Density (lbm/ft ³)	Gas Density at 60°F, 1 atm (lbm/ft ³)	Critical Temperature (°R)	Critical Pressure (psia)
Methane, CH ₄	16.04	-258.7	201.0	19*	0.04228	343.1	668
Ethane, C ₂ H ₆	30.07	-127.5	332.2	22.22**	0.07924	549.8	708
Propane, C ₃ H ₈	44.10	-43.7	416.0	31.66**	0.1162	665.7	616
Isobutane, C ₄ H ₁₀	58.12	10.9	470.6	35.12**	0.1531	734.7	529
n-butane, C ₄ H ₁₀	58.12	31.1	490.8	36.44**	0.1531	765.3	551
Isopentane, C ₅ H ₁₂	72.15	82.1	541.8	38.96	—	828.8	490
n-pentane, C ₅ H ₁₂	72.15	96.9	556.6	39.35	—	845.4	489
n-hexane, C ₆ H ₁₄	86.18	155.7	615.4	41.41	—	913.4	437
n-heptane, C ₇ H ₁₆	100.20	209.2	668.9	42.92	—	972.5	397
n-octane, C ₈ H ₁₈	114.23	258.2	717.9	44.08	—	1,023.9	361
n-nonane, C ₉ H ₂₀	128.26	303.5	763.2	45.01	—	1,070.4	332
n-decane, C ₁₀ H ₂₂	142.29	345.5	805.2	45.79	—	1,112	304
Nitrogen, N ₂	28.01	-320.4	139.3	—	0.07380	227.3	493
Air (O ₂ + N ₂)	28.96	-317.6	142.1	—	0.07630	238.4	547
Carbon dioxide, CO ₂	44.01	-109.3	350.4	51.5**	0.1160	547.6	1,071
Hydrogen sulfide, H ₂ S	34.08	-76.6	383.1	49.3**	0.08977	672.4	1,306
Water	18.02	212.0	671.7	62.37	—	1,365.3	3,208
Hydrogen, H ₂	2.02	-423.0	36.7	—	0.005313	59.9	181
Oxygen, O ₂	32.00	-297.4	162.3	—	0.08432	278.6	737
Carbon monoxide, CO	28.01	-313.6	146.1	—	0.07380	240	507

*Apparent density in liquid phase.

**Density at saturation pressure.

© 1972 Gas Processors Suppliers Assn.

oil is not determined at 60°F, in which case the specific gravity is either corrected to 60°F to give γ_o at 60°F/60°F or is reported as γ_o at the given temperature. The pressure at which the liquids are weighed is not specified. In Fig. B-1, the specific gravity at reservoir pressure corrected to 60°F is the ratio of the oil density at reservoir pressure and temperature corrected to 60°F to the density of distilled water at 60°F and 1 atm. Fig. B-2 applies to bubblepoint liquids by use of the specific gravity corrected to 60°F. Fig. B-3 applies to condensate well fluids and natural gases. To use Fig. B-3, the gas gravity must be known. T_{pc} and p_{pc} normally are used to estimate the pseudoreduced temperature, T_{pr} , and pressure, p_{pr} .

$$T_{pr} = \frac{T}{T_{pc}} \quad \dots \dots \dots \quad (B-3)$$

and

$$p_{pr} = \frac{p}{p_{pc}}, \quad \dots \dots \dots \quad (B-4)$$

where T = temperature of interest, °R, and p = pressure of interest, psia. In Eqs. B-1 through B-4, temperature and pressure must be absolute.

B.3 Oil Physical Property Correlations

Oil, in the absence of gas in solution, is called dead oil. The physical properties of dead oil are a function of the API gravity of the oil, γ_{API} , pressure, and temperature. API gravity of oil is defined as

$$\gamma_{API} = \frac{141.5}{\gamma_o} - 131.5, \quad \dots \dots \dots \quad (B-5)$$

with γ_o at 60°F. In Eq. B-5, γ_o = specific gravity of stock tank or dead oil at 60°F/60°F. If the oil gravity is reported at other than 60°F, it can be corrected to 60°F by use of the technique described in Ref. 9. (In Ref. 9, Table 5 is used for hydrometer measurements at other than 60°F; Table 7 allows the correction of volume at a given temperature to volume at 60°F.) The API gravity of water is 10.

With gas in solution, oil physical properties also depend on gas solubility, in addition to the pressure, temperature, and API gravity of oil.

B.3.1 Gas Solubility. Gas solubility is defined as the volume of gas dissolved in one stock tank barrel of oil at a fixed pressure and temperature. Gas solubility in oil increases as the pressure increases, up to the bubblepoint pressure of the oil. Above the bubblepoint pressure, gas solubility stays constant (Fig. B-4) and crude oil is often called undersaturated. In black-oil models, gas solubility determines the mass transfer between the liquid and gas phases.

This parameter fails to predict any retrograde condensation effects. For light oils or condensates, where retrograde condensation

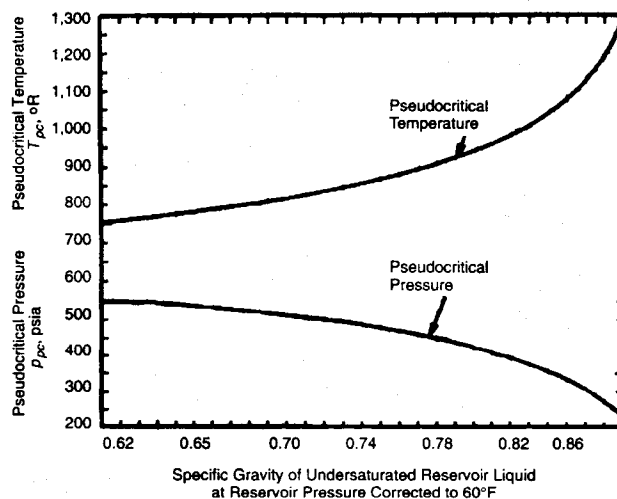


Fig. B-1—Approximate correlation of liquid pseudocritical pressure and temperature with specific gravity (after Trube⁸).

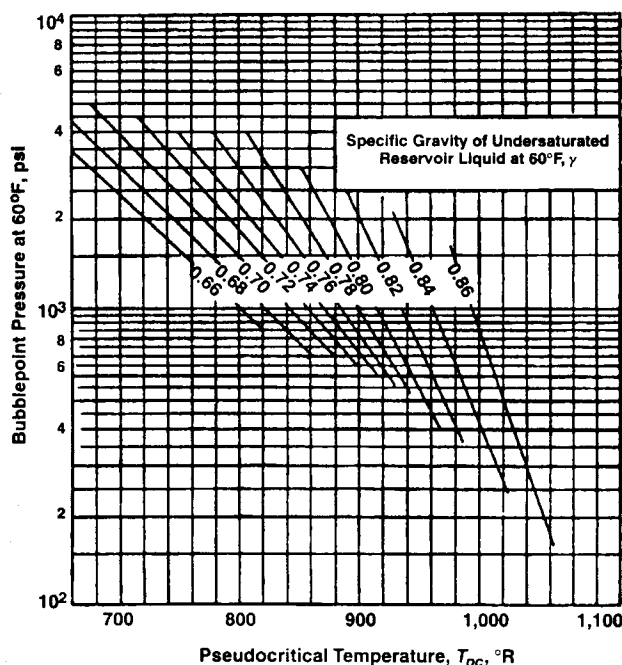


Fig. B-2—Correlation of liquid pseudocritical temperature with specific gravity and bubblepoint (after Trube⁸).

effects are suspected, use of this parameter may lead to substantial error in calculations. In this case, the amount and composition of each phase should be predicted by flash-vaporization calculations presented in Appendix C.

In the flash-vaporization process, the gas liberated from the oil in a PVT cell during pressure decline remains in contact with the oil from which it was liberated. This is quite different from the differential-vaporization process,¹⁹ which is considered to be more representative of the separation process experienced in the reservoir flow system. This is because of the higher transmissibility of gas, leading to faster flow of gas, and leaving behind the oil from which it was liberated. Consequently, the differential-vaporization process is defined as the separation of the solution gas that is liberated from an oil sample as a result of a change in pressure and/or temperature, with continuous removal from contact with the source oil before establishing equilibrium with the liquid phase. Fig. B-4 compares gas solubility with these two types of vaporization processes.

Several empirical correlations to determine gas solubility are presented. They assume a flash-vaporization process.

Standing Correlation. The Standing correlation²¹ states

$$R_s = \gamma_g \left[\left(\frac{p}{18.2} + 1.4 \right) 10^{0.0125\gamma_{API} - 0.000917} \right]^{1.2048}, \quad \dots \quad (B-6)$$

where γ_g = specific gravity of gas (air = 1.0); T = temperature, °F; p = system pressure, psia; and γ_{API} = gravity of oil, °API. It is often convenient to calculate the gas solubility from the nomograph presented in Fig. B-5.

Lasater Correlation. Lasater¹² presented the empirical relationship to calculate the solution gas/oil ratio or gas solubility as

$$R_s = \left(\frac{132,755\gamma_o}{M_o} \right) \left(\frac{\gamma_g}{1 - \gamma_g} \right), \quad \dots \quad (B-7)$$

where γ_o = specific gravity of oil; M_o = effective molecular weight of tank oil obtained from Fig. B-6; and γ_g = mole fraction of gas, a correlating parameter obtained from Fig. B-7.

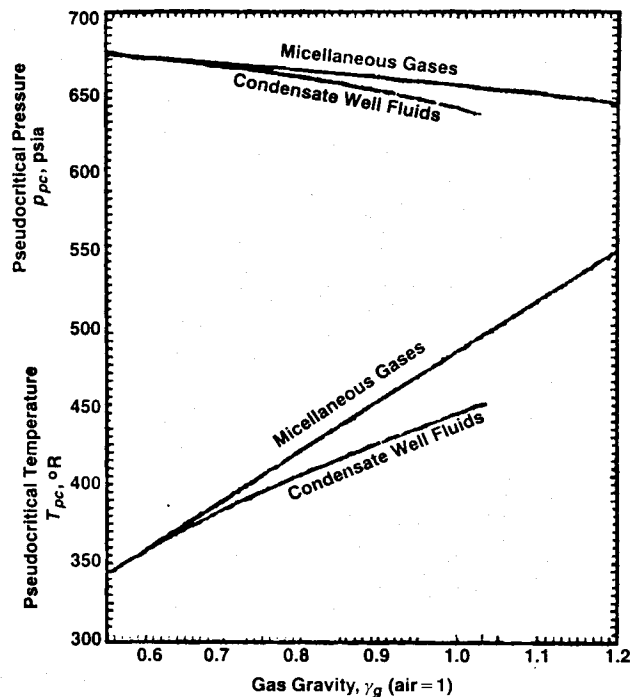


Fig. B-3—Correlation of pseudocritical properties of condensate well fluids and miscellaneous natural gases with gas gravity (after Brown et al.¹⁰).

TABLE B-2—COEFFICIENTS FOR VAZQUEZ AND BEGGS¹³ CORRELATION

Coefficient	$\gamma_{API} \leq 30$	$\gamma_{API} > 30$
C_1	0.0362	0.0178
C_2	1.0937	1.1870
C_3	25.7245	23.931

Vazquez and Beggs Correlation. Vazquez and Beggs¹³ presented an improved empirical correlation to estimate gas solubility, R_s , which can be written as

$$R_s = C_1 \gamma_{g100} p^{C_2} \exp \left[C_3 \left(\frac{\gamma_{API}}{T + 460} \right) \right], \quad \dots \quad (B-8)$$

where the values for the coefficients are presented in Table B-2.

The gas specific gravity, γ_{g100} , refers to a separator pressure of 100 psig and can be calculated from

$$\gamma_{g100} = \gamma_g \left(1.0 + 5.912 \times 10^{-5} \gamma_{API} T_{sep} \log \frac{p_{sep}}{114.7} \right), \quad \dots \quad (B-9)$$

where γ_{g100} = gas gravity at the reference separator pressure of 100 psig; γ_g = gas gravity at the actual separator conditions of p_{sep} and T_{sep} ; p_{sep} = actual separator pressure, psia; and T_{sep} = actual separator temperature, °F. If the specified gas gravity, γ_g , is at any pressure other than 100 psi, it should be adjusted to γ_{g100} with Eq. B-9.

Glasø Correlation. This correlation¹⁴ is based on North Sea crude-oil data. The mathematical form is

$$R_s = \gamma_g \left(\frac{\gamma_{API}^{0.989}}{T^{0.172}} p_b^* \right)^{1.2255}, \quad \dots \quad (B-10)$$

where T is in °F and $p_b^* = 10^{2.8869 - [14.1811 - 3.3093 \log(p)]^{0.5}}$.

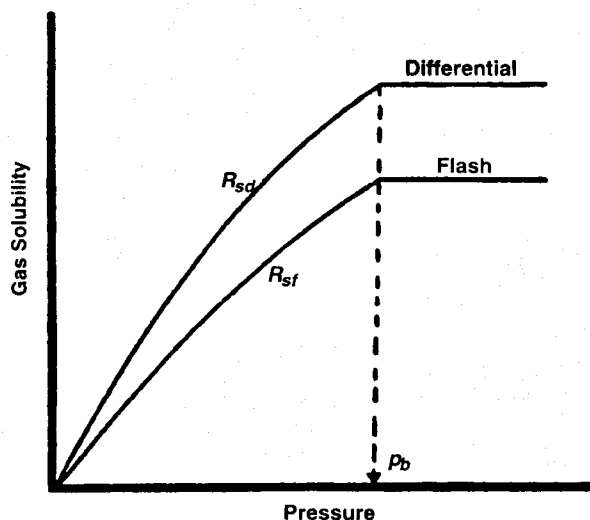


Fig. B-4—Idealized comparison of flash and differential gas solubilities.

The accuracy of this correlation is believed to decrease for solution gas/oil ratios exceeding 1,400 scf/STBO.¹⁸ Analysis of the expression for p_b^* shows that the correlation cannot be used for pressures in excess of 19,285 psi.

Al-Marhoun Correlation. Al-Marhoun¹⁵ presented this correlation based on Middle East crude oils. It can be expressed as

$$R_s = (a\gamma_g^b \gamma_o^c T^d p)^e, \quad \dots \dots \dots \quad (\text{B-11})$$

where γ_g = gas specific gravity; γ_o = stock-tank oil specific gravity; T = temperature, °R; $a = 185.843208$; $b = 1.877840$; $c = -3.1437$; $d = -1.32657$; and $e = 1.398441$.

Kartoatmodjo and Schmidt Correlation. This correlation¹⁶ is based on a wide range of data covering Southeast Asia (including Indonesia), North and South America, and the Middle East. Kartoatmodjo and Schmidt evaluated all the correlations presented in this section to determine gas solubility and found the Vazquez and Beggs correlation to be the most accurate. They used it to correlate data into two groups on the basis of API gravity, γ_{API} .

For $\gamma_{\text{API}} \leq 30$,

$$R_s = 0.05958 \gamma_{100}^{0.7972} p^{1.0014} 10^{13.1405 \gamma_{\text{API}} / (T + 460)}. \quad \dots \dots \dots \quad (\text{B-12a})$$

For $\gamma_{\text{API}} > 30$,

$$R_s = 0.03150 \gamma_{100}^{0.7587} p^{1.0937} 10^{11.289 \gamma_{\text{API}} / (T + 460)}. \quad \dots \dots \dots \quad (\text{B-12b})$$

where T is in °F.

On the basis of their large data base, Kartoatmodjo and Schmidt observed that the mean separator pressure, p_{sep} , was 101.6, or very close to the Vazquez and Beggs¹³ reference pressure of 100 psig. This observation led to the adoption of 100 psig as their reference pressure for specific gravity of gas, γ_{g100} . Kartoatmodjo and Schmidt also proposed an empirical equation to correct specific gravity referred at any other separator pressure and temperature.

$$\gamma_{g100} = \gamma_g \left(1.0 + 0.1595 \gamma_{\text{API}}^{0.4078} T_{\text{sep}}^{-0.2466} \log \frac{p_{\text{sep}}}{114.7} \right). \quad \dots \dots \dots \quad (\text{B-13})$$

B.3.2 Oil Formation Volume Factor and Bubblepoint Pressure. The volume in barrels occupied by one stock tank barrel of oil with the dissolved gas at any specified pressure and temperature is defined as the formation volume factor of oil, B_o . The oil formation volume factor is measured in reservoir barrels per stock tank barrel. This is a measure of the volumetric shrinkage of oil from the reser-

voir to surface conditions. Thus, the formation volume factor is always equal to or greater than 1.0. A mathematical definition is

$$B_o = \frac{(V_o)_{p,T}}{(V_o)_{sc}}, \quad \dots \dots \dots \quad (\text{B-14})$$

where B_o = oil formation volume factor, bbl/STBO; $(V_o)_{p,T}$ = volume of oil at pressure, p , and temperature, T , bbl; and $(V_o)_{sc}$ = volume of oil at standard conditions, STB.

The oil formation volume factor increases continuously with pressure as more gas dissolves in the oil until the pressure reaches the bubblepoint or the saturation pressure. As the pressure increases above the bubblepoint pressure, the oil stops dissolving more gas and the formation volume factor decreases because of the compressibility of the liquid. Fig. B-8 describes this behavior. It is important to note that the oil formation volume factors are determined by use of different equations above and below the bubblepoint pressure. Consequently, it also is imperative to determine the bubblepoint pressure before the oil formation volume factor is determined. There are different correlations to calculate the oil formation volume factor and the bubblepoint pressure. A few of the more commonly used correlations are presented here. The bubblepoint pressures are calculated from the solution gas/oil ratio correlations given in Sec. B.3.1 by setting R_s equal to the producing gas/oil ratio, R_p , and solving for the corresponding pressure.

Standing Correlation. This is the oldest and most commonly used empirical correlation.²¹ It was developed primarily from California crude oils. The Standing correlation can be expressed in this mathematical form below the bubblepoint pressure.

$$B_o = 0.9759 + 0.00012 \left[R_s \left(\frac{\gamma_g}{\gamma_o} \right)^{0.5} + 1.25T \right]^{1.2}, \quad \dots \dots \dots \quad (\text{B-15})$$

where T = temperature, °F; γ_o = specific gravity of the stock-tank oil; γ_g = specific gravity of the solution gas; and R_s = solution gas/oil ratio, scf/STBO.

Standing also presented Eq. B-15 in graphical form as Fig. B-9. For noncomputer determination of the formation volume factor, this is very convenient. The gas solubility, R_s , in Eq. B-15 should be obtained from Eq. B-6 or Fig. B-5. To calculate the formation volume factor of oil, B_{ob} , above the bubblepoint pressure, p_b , use

$$B_o = B_{ob} \exp[-c_o(p - p_b)]. \quad \dots \dots \dots \quad (\text{B-16})$$

B_{ob} can be calculated from the Standing correlation (Fig. B-9 or Eq. B-15), replacing R_s with the produced gas/oil ratio, R_p . The isothermal compressibility, c_o , in Eq. B-16 can be calculated with one of several methods, including the Vazquez and Beggs correlation from Eq. B-19. The bubblepoint pressure, p_b , can be calculated by solving Eq. B-6 for pressure after replacing R_s with R_p , as presented by Standing.²¹

$$p_b = 18.2 \left[\left(\frac{R_p}{\gamma_g} \right)^{0.83} 10^{(0.00091T - 0.0125\gamma_{\text{API}})} - 1.4 \right]. \quad \dots \dots \dots \quad (\text{B-17})$$

Vazquez and Beggs Correlation. Based on empirical correlation of 6,000 measured data values for the formation volume factor of oil below the bubblepoint pressure, Vazquez and Beggs proposed this mathematical expression.

$$B_o = 1.0 + C_1 R_s + (T - 60) \left(\frac{\gamma_{\text{API}}}{\gamma_{g100}} \right) (C_2 + C_3 R_s), \quad \dots \dots \dots \quad (\text{B-18})$$

where R_s = gas solubility, scf/STBO; T = temperature, °F; and γ_{g100} = gas specific gravity at 100 psig. Table B-3 gives values for the coefficients C_1 , C_2 , and C_3 .

Above the bubblepoint pressure or for undersaturated crudes, Eq. B-16 can be used to determine the formation volume factor where

Example

Required: Bubblepoint pressure at 200°F of liquid with a gas/oil ratio (GOR) of 350 ft³/bbl, a gas gravity of 0.75, and a tank-oil gravity of 30°API.

Procedure: Starting at the left side of the chart, proceed horizontally along the 350-ft³/bbl line to a gas gravity of 0.75. From that point, drop vertically to the 30°API line. Proceed horizontally from the tank-oil-gravity scale to the 200°F line. The required pressure is found to be 1,930 psia.

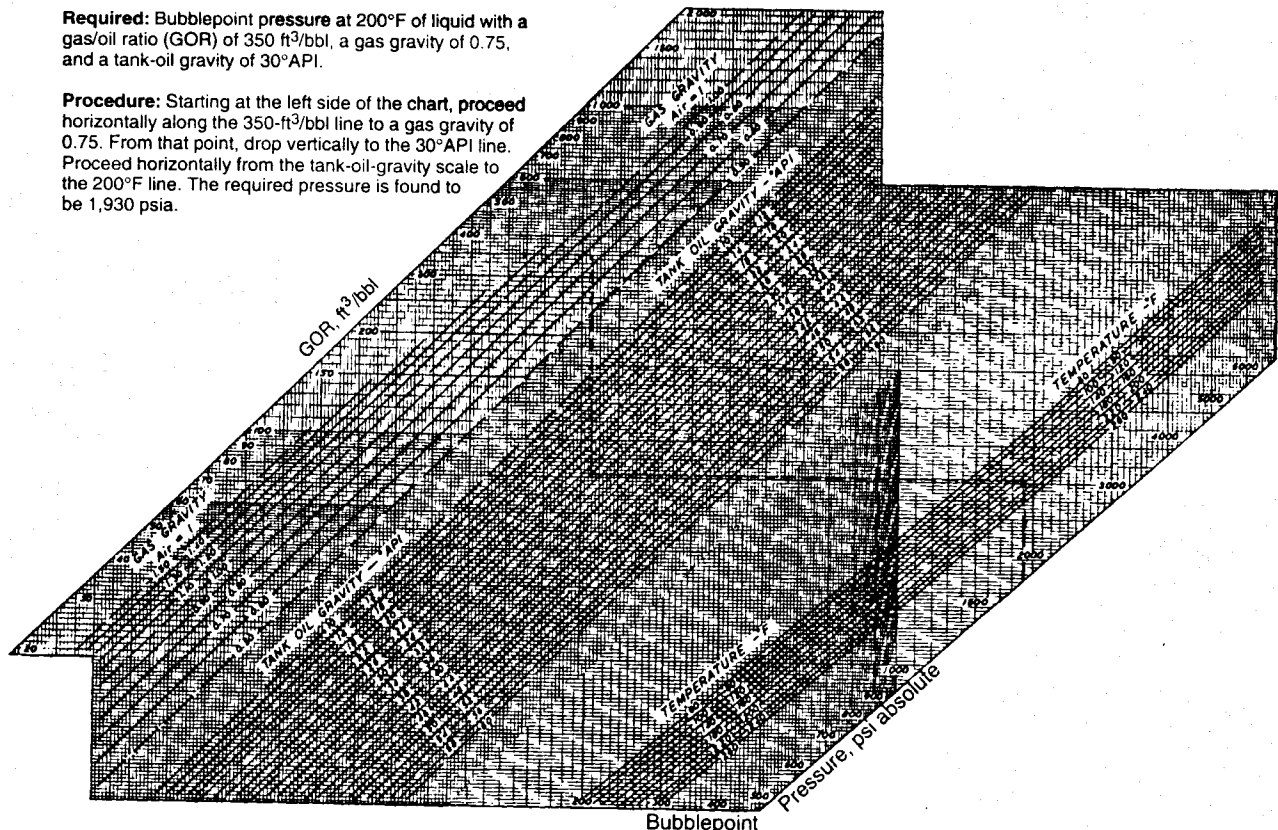


Fig. B-5—Properties of natural mixtures of hydrocarbon gas and liquids at bubblepoint pressure (after Standing²¹).

TABLE B-3—COEFFICIENTS FOR THE VAZQUEZ AND BEGGS CORRELATION¹³

Coefficient	$\gamma_{\text{API}} \leq 30$	$\gamma_{\text{API}} > 30$
C_1	4.677×10^{-4}	4.670×10^{-4}
C_2	1.751×10^{-5}	1.100×10^{-5}
C_3	-1.811×10^{-8}	1.337×10^{-9}

TABLE B-4—COEFFICIENT VALUES FROM VAZQUEZ AND BEGGS MODIFICATION¹³

Coefficient	$\gamma_{\text{API}} \leq 30$	$\gamma_{\text{API}} > 30$
C_1	27.62	56.18
C_2	0.914328	0.84246
C_3	11.172	10.393

the isothermal compressibility of oil, c_o , can be determined from this Vazquez and Beggs empirical correlation.

$$c_o = \frac{-1,433 + 5R_s + 17.2T - 1,180\gamma_{g100} + 12.61\gamma_{\text{API}}}{10^5 p} \quad (\text{B-19})$$

Gas specific gravity, γ_{g100} , can be calculated from Eq. B-9. p is the pressure at which formation volume factor is to be calculated.

Vazquez and Beggs modified Eq. B-8 to solve for bubblepoint pressure by replacing R_s with R_p , and presented this mathematical expression.

$$p_b = \left[\left(\frac{C_1 R_p}{\gamma_{g100}} \right) 10^a \right]^{C_2}, \quad (\text{B-20})$$

where $a = -C_3 \gamma_{\text{API}}/T$. Table B-4 tabulates the values of coefficients C_1 , C_2 , and C_3 in Eq. B-20.

Glasø Correlation. The Standing¹⁷ PVT correlations are widely used in the oil industry, although they are based primarily on California crude oils. These correlations do not correct for other oil types or nonhydrocarbon content. Glasø¹⁴ modified the Standing correlations to make them independent of oil type and suggested ap-

propriate corrections for nonhydrocarbon content and paraffinicinity. The Glasø correlations were developed and validated against North Sea crude oils. Glasø's oil formation volume factor correlation can be expressed mathematically as

$$B_v = 1.0 + 10^A, \quad (\text{B-21a})$$

where

$$A = -6.58511 + 2.91329 \log B_{ob}^* - 0.27683(\log B_{ob}^*)^2 \quad (\text{B-21b})$$

and B_{ob}^* is a "correlating number" defined by

$$B_{ob}^* = R_s \left(\frac{\gamma_g}{\gamma_o} \right)^{0.526} + 0.9687. \quad (\text{B-21c})$$

Glasø also presented a bubblepoint-pressure correlation and suggested a procedure to account for the presence of nonhydrocarbon content of the crude oil system. The proposed bubblepoint-pressure correlation¹⁹ can be expressed as

$$\log p_b = 1.7669 + 1.7447 \log p_b^* - 0.30218(\log p_b^*)^2, \quad (\text{B-22a})$$

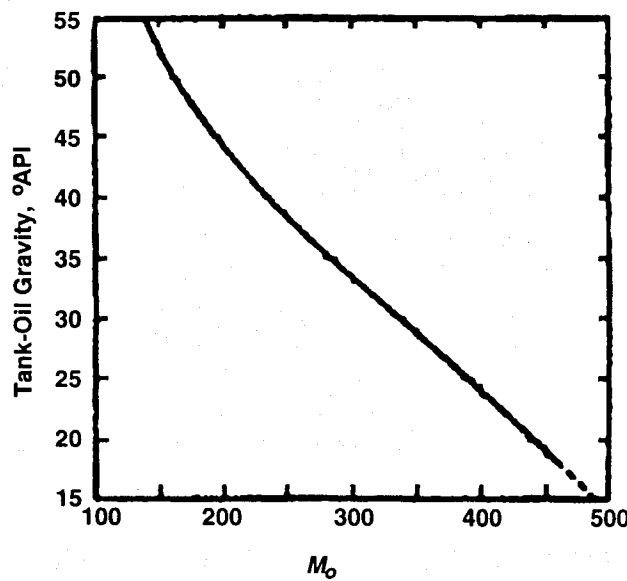


Fig. B-6—Molecular weight vs. tank-oil gravity (after Lasater¹²).

with p_b^* a "correlating number" defined by

$$p_b^* = \left(\frac{R_s}{\gamma_g} \right)^a T^b / \gamma_{\text{API}}^c, \quad (\text{B-22b})$$

where R_s = gas solubility, scf/STBO; T = temperature, °F; γ_g = average specific gravity of the total surface gases, and a, b, c = coefficients with respective values of 0.816, 0.172, and 0.989. For volatile oils, $b = 0.130$. For nonhydrocarbon content, Glasø suggested these corrections to the bubblepoint pressure, p_b .

$$(p_b)_c = p_b C_{N_2} C_{CO_2} C_{H_2S}, \quad (\text{B-23})$$

where C = correction factor; and $(p_b)_c$ = corrected bubblepoint pressure, psia. Correction factors, C , for N_2 , CO_2 , and H_2S are calculated by

$$C_{N_2} = 1.0 + [(a_1 \gamma_{\text{API}} + a_2)T + a_3 \gamma_{\text{API}} - a_4] y_{N_2} \\ + (a_5 \gamma_{\text{API}}^a T + a_6 \gamma_{\text{API}}^b - a_8) y_{N_2}^2, \quad (\text{B-24a})$$

where y_{N_2} = mole fraction of nitrogen in total surface gases, and a_1 through a_8 = coefficients of the correlation with the following values:

$$a_1 = -2.65 \times 10^{-4},$$

$$a_2 = 5.5 \times 10^{-3},$$

$$a_3 = 0.0391,$$

$$a_4 = 0.8295,$$

$$a_5 = 1.954 \times 10^{-11},$$

$$a_6 = -4.699,$$

$$a_7 = 0.027,$$

and

$$a_8 = 2.366.$$

$$C_{CO_2} = 1.0 - 593.8 y_{CO_2} T^{-1.553}, \quad (\text{B-24b})$$

where y_{CO_2} = mole fraction of CO_2 in total surface gases.

$$C_{H_2S} = 1.0 - (0.9035 + 0.0015 \gamma_{\text{API}}) y_{H_2S} \\ + 0.019(45 - \gamma_{\text{API}}) y_{H_2S}^2, \quad (\text{B-24c})$$

where C_{H_2S} = H_2S correction factor and y_{H_2S} = mole fraction of H_2S in total surface gases.

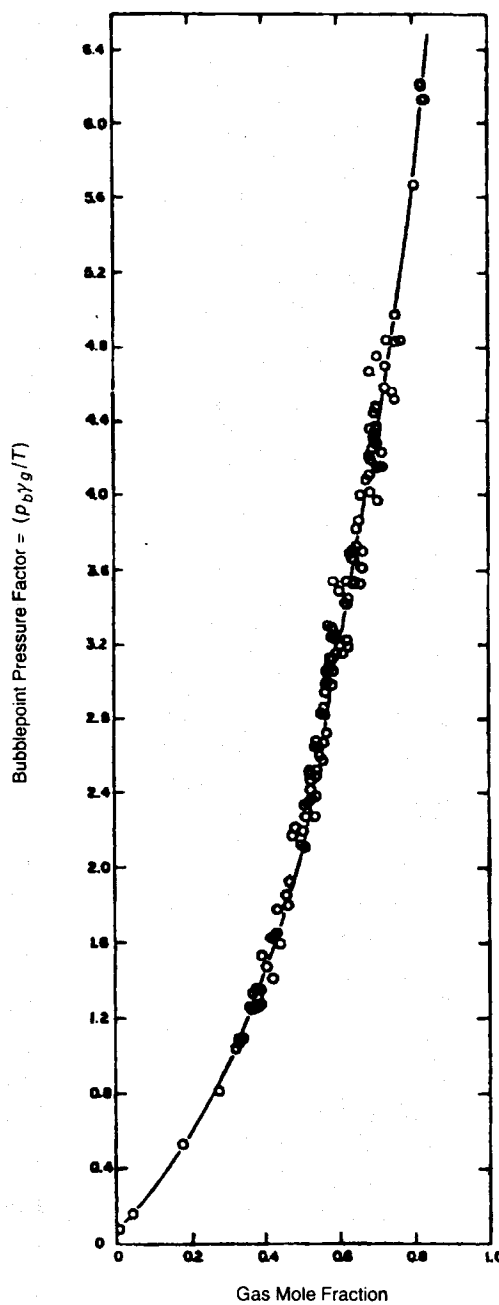


Fig. B-7—Bubblepoint pressure factor vs. gas mole fraction (after Lasater¹²).

Al-Marhoun Correlation. Al-Marhoun¹⁵ developed his formation volume factor correlation on the basis of crude oils from the Middle East and proposed this empirical relationship.

$$B_o = 0.497069 + 0.862963 \times 10^{-3}T + 0.182594 \times 10^{-2}F \\ + 0.318099 \times 10^{-5}F^2, \quad (\text{B-25})$$

where $F = R_s^a \gamma_g^b \gamma_o^c$, where the coefficients are $a = 0.742390$, $b = 0.323294$, and $c = 1.202040$.

Al-Marhoun's bubblepoint-pressure correlation can be expressed as

$$p_b = a R_s^b \gamma_g^c \gamma_o^d T^e, \quad (\text{B-26})$$

where T = temperature, °R; γ_o = stock-tank-oil gravity, $a = 5.38088 \times 10^{-3}$, $b = 0.715082$, $c = -1.87784$, $d = 3.1437$, and $e = 1.32657$.

Kartoatmodjo and Schmidt Correlation. Kartoatmodjo and Schmidt¹⁶ proposed a formation volume factor correlation at and

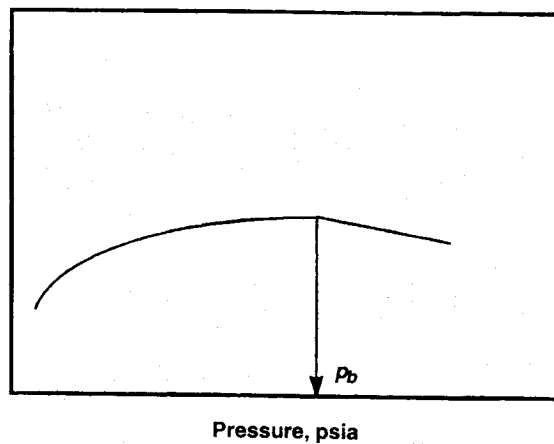


Fig. B-8—Variation of formation volume factor isotherm with pressure at constant temperature, T ; P_b = bubblepoint pressure.

below the bubblepoint pressure that can be expressed mathematically as

$$B_o = 0.98496 + 0.0001F^{1.50}, \quad \dots \dots \dots \quad (B-27)$$

where $F = R_s^{0.755} \gamma_{g100}^{0.25} \gamma_o^{-1.50} + 0.45T$, where T = temperature, °F; γ_{g100} = specific gravity of gas at 100 psig, and γ_o = specific gravity of stock-tank oil. This formation volume factor is recommended for the flash-vaporization process normally encountered in pipe flow. For application to reservoir flow, such as in inflow performance relationship (IPR), a differential-vaporization formation volume factor

is recommended. Eq. B-90 gives an empirical conversion factor between flash- and differential-vaporization formation volume factors.

The formation volume factor above the bubblepoint pressure can be calculated with Eq. B-16. In this case, B_{ob} is estimated from Eq. B-27 and the isothermal oil compressibility, c_o , is calculated from this empirical relationship.

$$c_o = \frac{6.8257 \times 10^{-6}}{P} R_s^{0.5002} \gamma_{API}^{0.3613} T^{0.76606} \gamma_{g100}^{-0.35505}, \quad \dots \dots \dots \quad (B-28)$$

where p is in psia.

The bubblepoint-pressure correlation is presented in two ranges of API gravity oil.

For $\gamma_{API} \leq 30$,

$$P_b = \left[\frac{R_p}{0.05958 \gamma_{g100}^{0.7972} 10^{13.1405 \gamma_{API}/(T+460)}} \right]^{0.9986} \quad \dots \dots \dots \quad (B-29a)$$

For $\gamma_{API} > 30$,

$$P_b = \left[\frac{R_p}{0.03150 \gamma_{g100}^{0.7587} 10^{11.289 \gamma_{API}/(T+460)}} \right]^{0.9143} \quad \dots \dots \dots \quad (B-29b)$$

Note that Eqs. B-29a and B-29b are identical to Eqs. B-12a and B-12b, but solve for p with R_s equal to the produced gas/oil ratio, R_p . These correlations were developed with nonlinear regression analysis.

B.3.3 Oil Density. The density for saturated crude oils below the bubblepoint pressure can be calculated at a given pressure and tem-

Example

Required: Formation volume at 200°F of bubblepoint liquid with a GOR of 350 ft³/bbl, a gas gravity of 0.75, and a tank-oil gravity of 30°API.

Procedure: Starting at the left side of the chart, proceed horizontally along the 350-ft³/bbl line to a gas gravity of 0.75. From that point, drop vertically to the 30°API line. Proceed horizontally from the tank-oil-gravity scale to the 200°F line. The formation volume is found to be 1.22 bbl/bbl of tank oil.

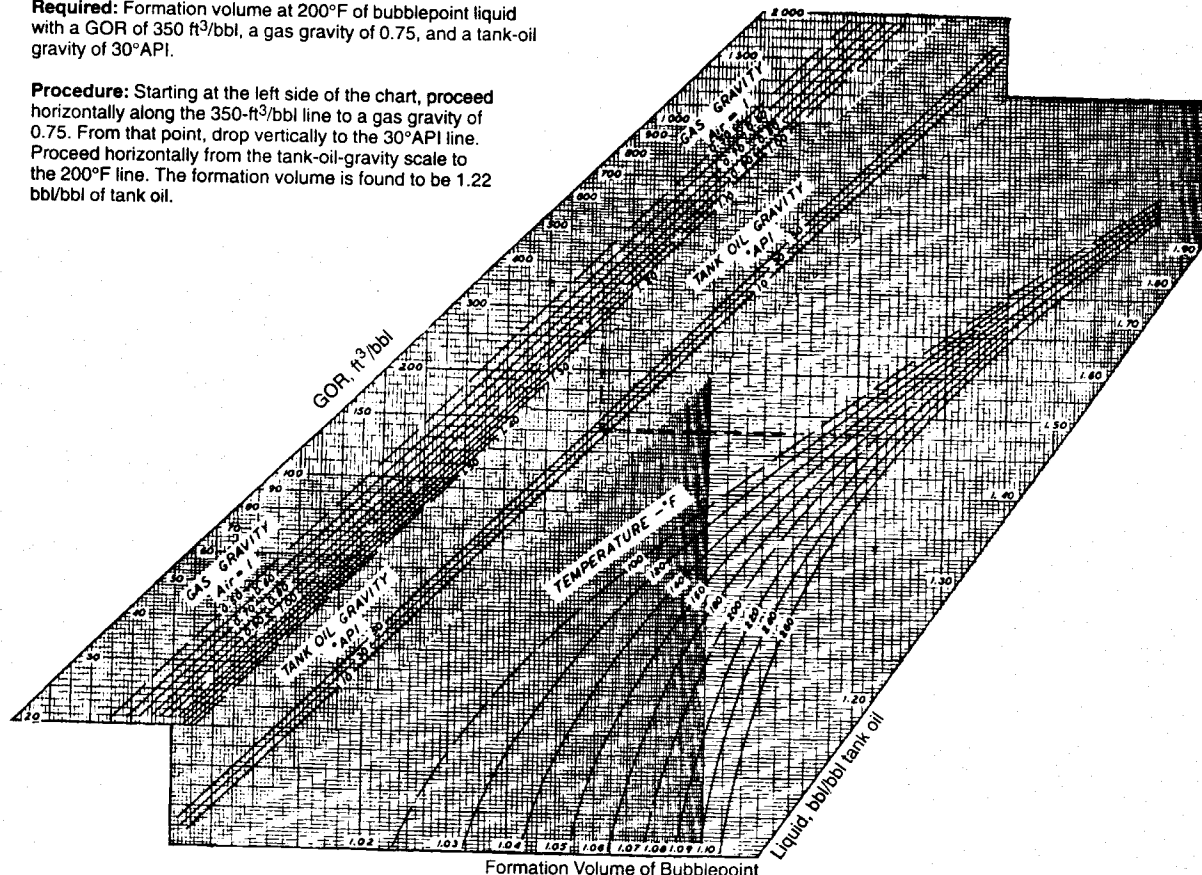


Fig. B-9—Chart to determine oil formation volume factor with the Standing correlation.²¹

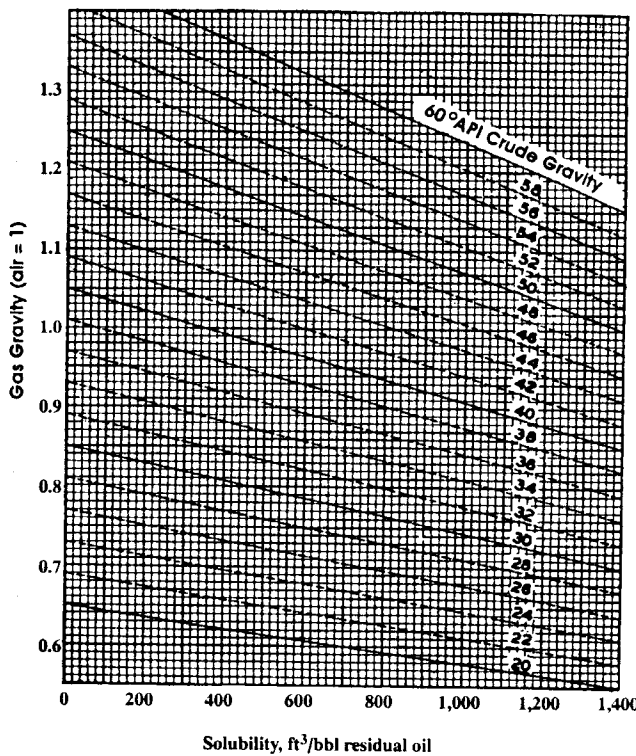


Fig. B-10—Dissolved-gas gravity correlation. (After Katz *et al.*²⁶ Reproduced with permission of the McGraw-Hill Cos.)

perature if the solution gas/oil ratio, R_g , the formation volume factor, B_o , and the specific gravity of the dissolved gas, γ_{gd} , are known.

$$\rho_o = \frac{62.4\gamma_o + 0.0136R_g\gamma_{gd}}{B_o}, \quad (B-30)$$

where γ_o = stock-tank oil specific gravity and γ_{gd} = dissolved-gas gravity described in Sec. B.3.4.

For saturated oils above the bubblepoint, oil density can be calculated by first determining the density at the bubblepoint pressure,

$$\rho_{ob} = \frac{62.4\gamma_o + 0.0136R_p\gamma_{gt}}{B_{ob}}. \quad (B-31)$$

Then, given the oil compressibility, Eq. B-32 can be used for density when $p > p_b$.

$$\rho_o = \rho_{ob}e^{c_o(p - p_b)}. \quad (B-32)$$

B.3.4 Specific Gravity of Free and Dissolved Gas. In thermodynamically stable mixtures of oil and gas, as the equilibrium is disturbed with change in pressure under isothermal conditions, the composition of each phase changes. Methane is the first hydrocarbon component to evolve into the free-gas phase at or below the bubblepoint pressure. Heavier hydrocarbon components vaporize with further lowering of pressure. Such sequential vaporization increases the specific gravity of both the free and the dissolved gas. Katz *et al.*²⁶ used Fig. B-10 to predict the dissolved-gas gravity, γ_{gd} , as a function of the API gravity of the crude oil and the gas solubility of the oil phase. Because methane is the lightest component in natural gas, with specific gravity of 0.56, both the free and the dissolved-gas gravity must be greater than 0.56. However, while the upper limit of the free-gas gravity is the average specific gravity of the total separated gas, γ_{gt} , expressed at standard conditions, this also forms the lower limit of the dissolved-gas gravity. These limits can be expressed mathematically as

$$\gamma_{gt} \leq \gamma_{gd} \geq 0.56 \quad (B-33)$$

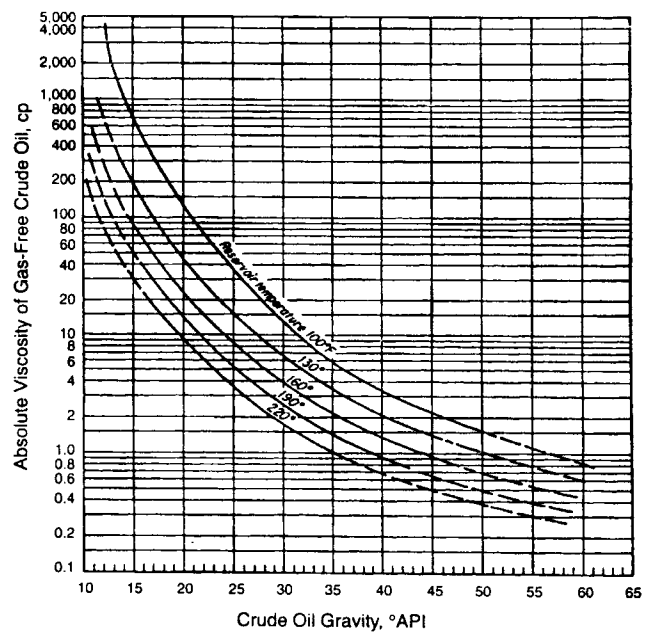


Fig. B-11—Gas-free crude viscosity as a function of temperature and oil gravity at 60°F and atmospheric pressure (after Beal²⁰).

and

$$\gamma_{gt} \geq \gamma_{gf} \geq 0.56. \quad (B-34)$$

On the basis of a simple material balance, the free-gas gravity can be calculated by

$$\gamma_{gf} = \frac{R_p\gamma_{gt} - R_s\gamma_{gd}}{R_p - R_s}, \quad (B-35)$$

where produced gas/oil ratio, R_p , is calculated as the gas solubility at or above the bubblepoint pressure. In gas/oil, two-phase-flow calculations, the physical properties of the free gas, such as density and viscosity, should be calculated based on the free-gas gravity, γ_{gf} , as functions of pressure and temperature, which changes the gas solubility and the specific gravity of the dissolved gas. Most commercial computer programs fail to account for the changing composition of the free and dissolved gas as pressure and temperature change.

B.3.5 Oil Viscosity. The viscosity of crude oil with dissolved gas is an important parameter in pressure-loss calculations for flow in pipes or in porous media. Whenever possible, the oil viscosity should be determined in the laboratory for the required pressure and temperature ranges. This section presents empirical correlations to calculate the oil viscosity based on frequently available hydrocarbon-system parameters, such as temperature, pressure, oil gravity, gas gravity, and gas solubility.

B.3.5.1 Dead-Oil Viscosity Correlations. For empirical correlations, the dead-oil viscosity is determined first. The dead oil is defined at atmospheric pressure and at any fixed system temperature without dissolved gas. This dead-oil viscosity then is corrected for the system pressure condition. Normally dead-oil viscosity is determined in the laboratory whenever PVT analysis is done.

Beal Correlation. Beal²⁰ presented a graphical correlation in Fig. B-11 to determine dead-oil viscosity if the API gravity of the crude oil and the temperature are known. Standing²¹ presented this mathematical equation to represent Beal's correlation for dead-oil viscosity, μ_{od} , at 1-atm pressure and temperature, T , in °R.

$$\mu_{od} = \left(0.32 + \frac{1.8 \times 10^7}{\gamma_{API}^{4.53}} \right) \left(\frac{360}{T - 260} \right)^a, \quad (B-36)$$

where $a = 10^{(0.43 + 8.33/\gamma_{API})}$.

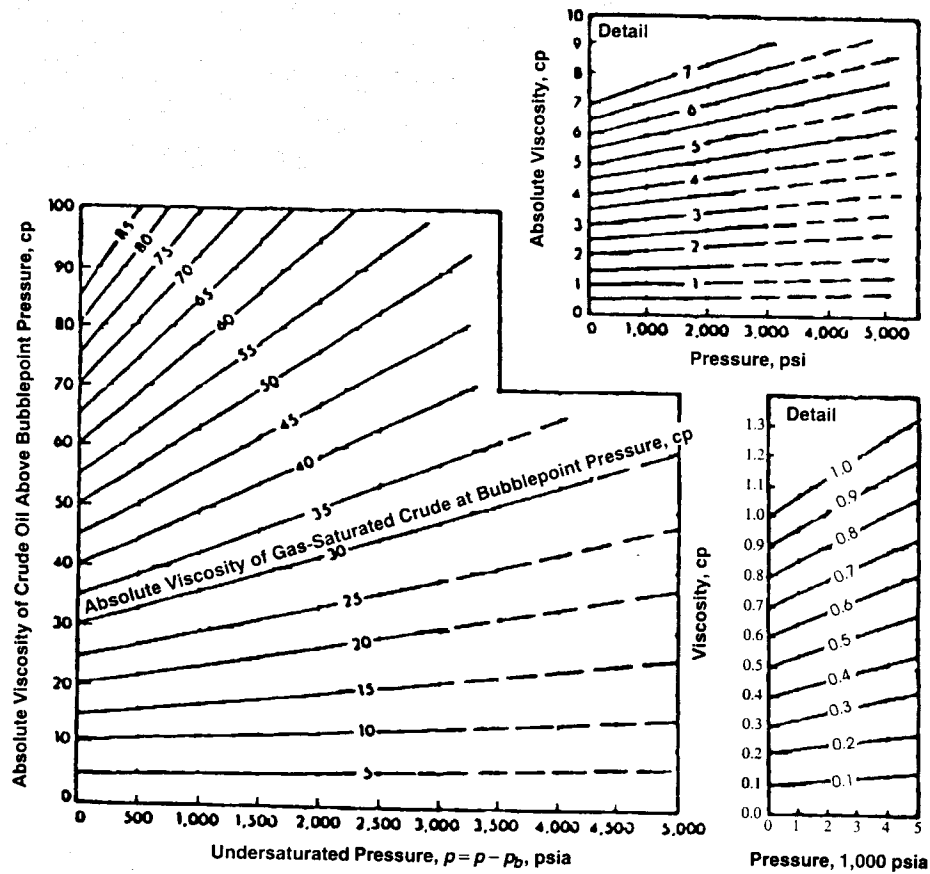


Fig. B-12—Variation of oil viscosity with pressure.²⁰

Beggs and Robinson Correlation. Beggs and Robinson²² proposed a different empirical correlation to determine the dead-oil viscosity. It is based on 460 dead-oil viscosity measurements and can be expressed mathematically as

$$\mu_{od} = 10^x - 1, \quad \dots \quad (B-37)$$

where

$$x = \frac{10^{(3.0324 - 0.02023y_{API})}}{T^{1.163}}$$

and T is in °F.

Glasø Correlation. Glasø¹⁴ presented an empirical correlation based on North Sea data. Sutton and Farshad¹⁸ found this correlation to be the most accurate dead-oil viscosity correlation among the three described here. This correlation can be expressed as

$$\mu_{od} = (3.141 \times 10^{10})T^{-3.444}(\log y_{API})^a, \quad \dots \quad (B-38)$$

where $a = 10.313 \log T - 36.447$; T = system temperature, °F; and y_{API} = gravity of oil system, °API.

Eq. B-38 was developed for data in the following ranges of temperature and API gravity, respectively: $50 \leq T \leq 300$ and $20.1 \leq y_{API} \leq 48.1$.

Kartoatmodjo and Schmidt Correlation. In its empirical form, this correlation¹⁶ is a combination of all three previous ones and can be expressed as

$$\mu_{od} = (16.0 \times 10^8)T^{-2.8177}(\log y_{API})^{5.7520 \log(T) - 26.9718} \quad \dots \quad (B-39)$$

B.3.5.2 Saturated Crude Oil Viscosity. The reservoir oil viscosity depends on the solution-gas content. Oil viscosity decreases with rising pressure as the solution gas increases, up to the bubblepoint pressure. There are few empirical correlations to determine the viscosity of saturated or undersaturated crude oil systems.

Beggs and Robinson Correlation. This correlation²² is based on 2,073 saturated oil viscosity measurements. The empirical form of this equation is

$$\mu_o = [10.715(R_s + 100)^{-0.515}] \mu_{od}^b, \quad \dots \quad (B-40)$$

where

$$b = 5.44(R_s + 150)^{-0.338}.$$

This correlation was developed from these ranges of data:

pressure = 132 to 5,265 psia,

temperature = 70 to 295°F,

oil gravity = 16 to 58°API, and

gas solubility = 20 to 2,070 scf/STBO.

Kartoatmodjo and Schmidt Correlation. This correlation¹⁶ recommends the following correction of the dead-oil viscosity presented in Eq. B-39 to determine the live-oil viscosity, μ_o ,

$$\mu_o = -0.06821 + 0.9824f + 0.0004034f^2, \quad \dots \quad (B-41)$$

where

$$f = (0.2001 + 0.8428 \times 10^{-0.000845R_s}) \mu_{od}^{(0.43 + 0.5165y)}$$

and

$$y = 10^{-0.00081R_s}$$

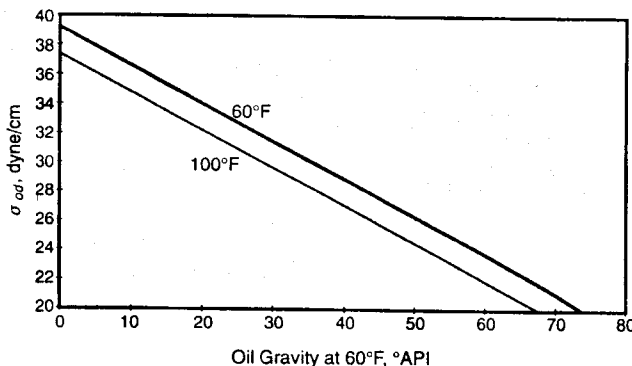


Fig. B-13—Surface tension of crude oils at atmospheric pressure (after Baker and Swerdluff²³).

B.3.5.3 Undersaturated Crude Oil Viscosity. Above the bubble-point pressure, rising pressure increases the viscosity of oil because of its compressibility. Fig. B-12 presents this viscosity vs. pressure relationship.

Vazquez and Beggs Correlation. Vazquez and Beggs¹³ proposed this correction to the saturated crude oil viscosity at the bubblepoint pressure for pressures above the bubblepoint pressure.

$$\mu_o = \mu_{ob} \left(\frac{p}{p_b} \right)^m, \quad \dots \dots \dots \quad (B-42)$$

where

$$m = 2.6 p^{1.187} 10^a$$

and

$$a = -(3.9 \times 10^{-5}) p^{-5}.$$

This correlation is based on data in the following ranges:

pressure = 141 to 9,515 psia,
gas solubility = 90.3 to 2,199 scf/STBO,
viscosity = 0.117 to 148 cp,
gas specific gravity = 0.511 to 1.351, and
oil gravity = 15.3 to 59.5°API.

Kartoatmodjo and Schmidt Correlation. This correlation¹⁶ allows correction of the saturated crude oil viscosity at the bubblepoint, μ_{ob} , based on Eq. B-41 for undersaturated pressure, p .

$$\mu_o = 1.00081\mu_{ob} + 0.001127(p - p_b) \\ \times (-0.006517\mu_{ob}^{1.8148} + 0.038\mu_{ob}^{1.590}), \quad \dots \dots \dots \quad (B-43)$$

where μ_o = viscosity of undersaturated oil, cp.

B.3.6 Surface Tension. Surface tension²³⁻²⁶ is a measure of the imbalance in the interfacial molecular forces for two phases in contact. In multiphase pipe flow, gas/liquid and liquid/liquid surface or interfacial tension values are used to determine flow patterns and liquid holdup.

The empirical work of Baker and Swerdluff,²³ presented in Fig. B-13, commonly is used to estimate the surface tension of crude oil at atmospheric pressure (dead oil), σ_{od} . In this figure, the surface tension of dead oil is correlated vs. temperature and the API gravity of the oil. Because the precise effects of temperature on dead-oil surface tension is unknown, extrapolation beyond the data presented in Fig. B-13 is not recommended.

The surface tension of live oil with dissolved gas, σ_o , can be obtained with an appropriate correction to σ_{od} for the dissolved gas. Fig. B-14 presents this correction to the surface tension of the dead oil as a percentage reduction of the dead-oil surface tension, as a function of pressure. The effect of increasing pressure is to increase gas solubility, thus decreasing surface tension. The effect of pressure on surface tension of oil with dissolved gas can be determined from Eq. B-44.

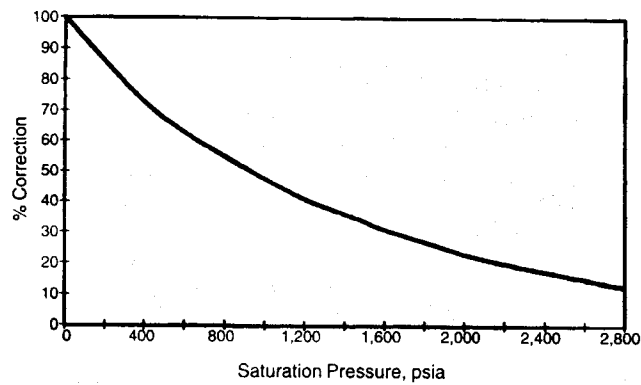


Fig. B-14—Correction to dead-oil surface tension.²³

$$\sigma_o = \sigma_{od}(x/100), \quad \dots \dots \dots \quad (B-44)$$

where x = percent correction from Fig. B-14.

B.4 Water Physical Properties

Water is often a very important liquid component in the oil and gas production system.²⁹ Consequently, the physical properties of water play an important role in multiphase flow calculations. Among the physical properties of water, gas solubility, formation volume factor, viscosity, surface tension, and compressibility are of particular interest. Specific gravity or density of water is also an important property and is normally readily available from an oilfield water analysis.

B.4.1 Water Density. The density of pure water at standard conditions is 62.4 lbm/ft³. Neglecting gas solubility in water, the density of water can be calculated from

$$\rho_w = \frac{\rho_{wsc}}{B_w} = \frac{62.4\gamma_{wsc}}{B_w}, \quad \dots \dots \dots \quad (B-45)$$

where ρ_w = density of water at any pressure and temperature, lbm/ft³; ρ_{wsc} = density of water at standard conditions, lbm/ft³; B_w = formation volume factor of water; and γ_{wsc} = specific gravity of water at standard conditions.

B.4.2 Gas Solubility in Water. The solubility of hydrocarbon gas components is inversely proportional to their molecular weights. Thus, methane is more soluble than ethane, ethane is more soluble than propane, and so forth. McCain²⁷ states that the solubility of each component is two to three times greater than that of the next heavier paraffinic component. Methane is the most soluble component of natural gas in water. The solubility of methane in water can be used to estimate the solubility of natural gas in pure water with an accuracy of 5% or better. Fig. B-15 can be used to estimate methane solubility in pure water.²⁸

To account for the effect of water salinity, Dodson and Standing³¹ suggested the corrections presented in Fig. B-16.

Ahmed¹⁹ recommends the use of this gas-solubility correlation for water.

$$R_{sw} = A + Bp + Cp^2, \quad \dots \dots \dots \quad (B-46)$$

where $A = 2.12 + (3.45 \times 10^{-3})T - (3.59 \times 10^{-5})T^2$, $B = 0.0107 - (5.26 \times 10^{-5})T + (1.48 \times 10^{-7})T^2$, and $C = -(8.75 \times 10^{-7}) + (3.9 \times 10^{-9})T - (1.02 \times 10^{-11})T^2$. The gas solubility is corrected for the effect of water salinity.

$$(R_{sw})_b = R_{sw}C_S, \quad \dots \dots \dots \quad (B-47)$$

where T is in °F and $(R_{sw})_b$ = gas solubility in brine, scf/STBW; R_{sw} = gas solubility in pure water; C_S = salinity correction factor = $1.0 - [0.0753 - 0.000173T]S$, where S = salinity of water, weight percent of NaCl.

Ref. 19 is the source of this gas-solubility correlation.

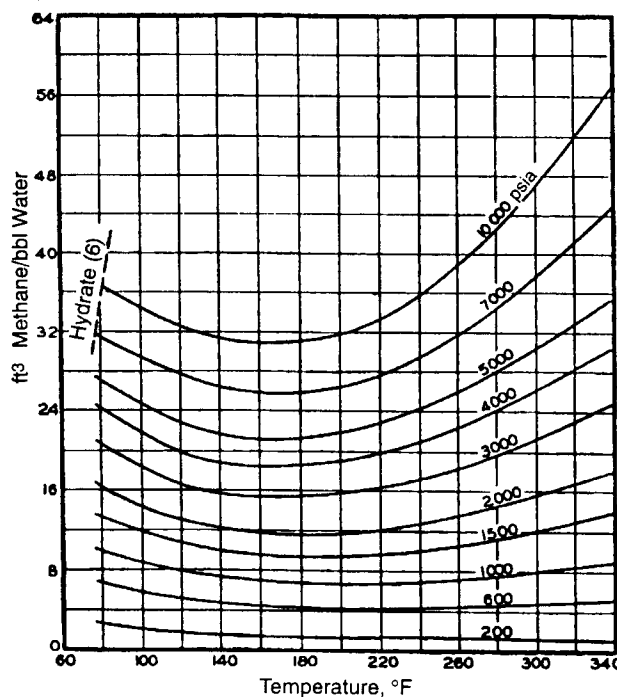


Fig. B-15—Solubility of methane in pure water (after Culberson and McKetta²⁸).

B.4.3 Water Formation Volume Factor. Because gas solubility is very low in water compared to that in oil, it is common practice to neglect compressibility and gas solubility of water. Assuming negligible thermal expansion, water formation volume factor is assumed to be 1.0. In actual field situations, water shows gas solubility and, thus, shrinks under pressure reduction. Gould³⁰ presented an empir-

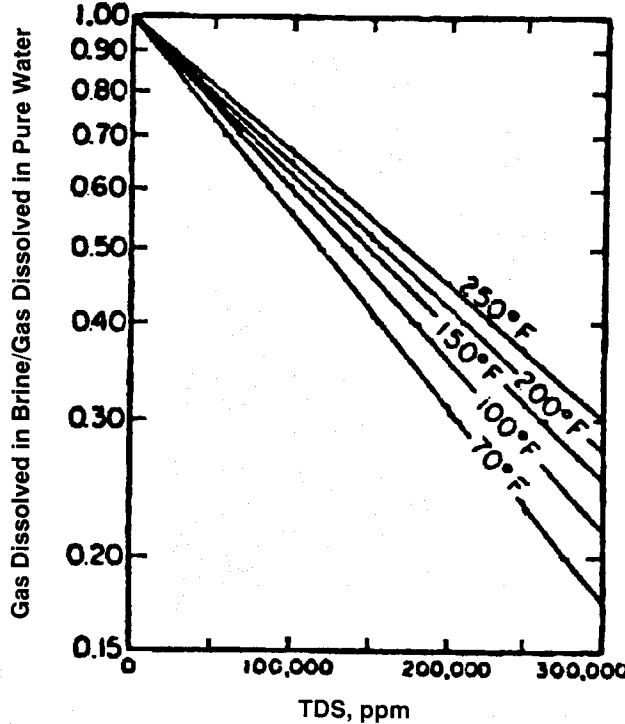


Fig. B-16—Effect of salinity on gas solubility: TDS = total dissolved solids (after Dodson and Standing³¹).

ical polynomial relation to determine the formation volume factor of water.

$$B_w = 2.0 + 1.2 \times 10^{-4} T_x + 1.0 \times 10^{-6} T_x^2 - 3.33 \times 10^{-6} p, \quad \dots \quad (B-48)$$

where B_w = formation volume factor of water, bbl/STBW; T = system temperature, °F; $T_x = T - 60$; and p = system pressure, psia.

Water formation volume factor above the bubblepoint pressure changes as a result of the compressibility.

$$B_w = B_{wb} \exp[-c_w(p - p_b)], \quad \dots \quad (B-49)$$

where B_w = water formation volume factor above bubblepoint pressure, p_b ; B_{wb} = water formation volume factor at the bubblepoint pressure; c_w = water compressibility, psi^{-1} ; and p = system pressure ($p > p_b$), psia.

The compressibility of water with natural gas in solution can be estimated from Fig. B-17.³¹ The top graph yields c_w for pure water while the bottom graph is used to determine a correction factor for c_w to correct for the effects of gas solubility.

Meehan³² presented an empirical correlation to determine the isothermal compressibility coefficient of gas-free and gas-saturated water. For gas-free water, this empirical relationship is proposed.

$$(c_w)_f = 10^{-6}(A + BT + CT^2), \quad \dots \quad (B-50)$$

where $(c_w)_f$ = isothermal compressibility coefficient of the gas-free water, psi^{-1} ; $A = 3.8546 - 0.000134 p$; $B = -0.01052 + (4.77 \times 10^{-7})p$; $C = (3.9267 \times 10^{-5}) - (8.8 \times 10^{-10})p$; p = pressure, psia; and T = temperature, °F.

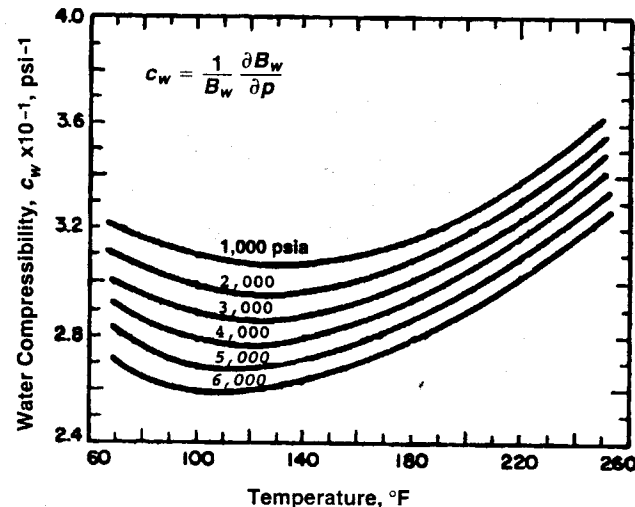


Fig. B-17—Compressibility of pure water, including effects of gas in solution (after Dodson and Standing³¹).

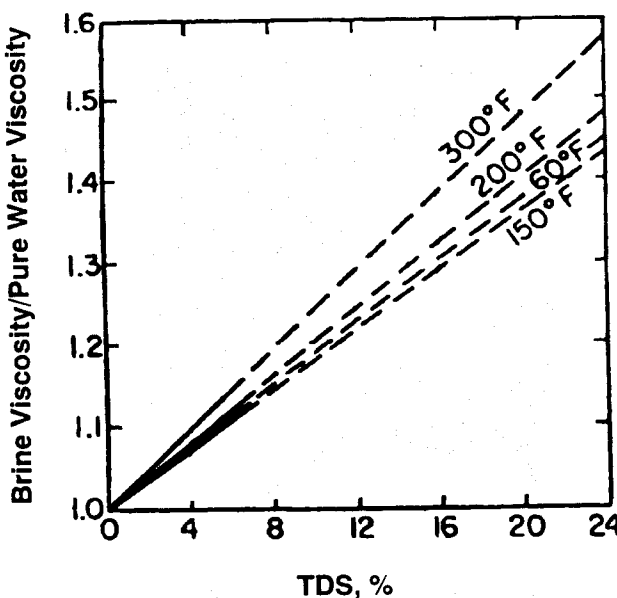


Fig. B-18—Ratio of brine viscosity to pure water viscosity vs. salinity (after Frick³⁵).

Meehan also proposed a correlation to determine the isothermal compressibility of gas-saturated water.

$$(c_w)_g = (c_w)_f (1.0 + 8.9 \times 10^{-3} R_{sw}), \quad \dots \dots \dots \quad (\text{B-51a})$$

where $(c_w)_g$ = isothermal compressibility coefficient of the gas-saturated water, psi^{-1} , and R_{sw} = gas solubility in water, scf/STBW .

To account for the salinity of water, this adjustment is suggested.

$$c_w = (c_w)_g C_S, \quad \dots \dots \dots \quad (\text{B-51b})$$

where c_w = isothermal compressibility coefficient of the brine, psi^{-1} , and C_S = salinity correction factor.

Numbere *et al.*³³ proposed this mathematical expression for the salinity correction factor.

$$C_S = 1.0 + (-0.052 + 2.7 \times 10^{-4} T - 1.14 \times 10^{-6} T^2 + 1.121 \times 10^{-9} T^3) S^{0.7}, \quad \dots \dots \dots \quad (\text{B-52})$$

where S = salinity of the water, weight percent of NaCl, and T = temperature, °F.

B.4.4 Water Viscosity. Data on the viscosity of oilfield water are very scarce. Water viscosity increases with pressure and dissolved solids and decreases with increased gas solubility. No data are available on the effects of gas solubility. However, van Wingen³⁴ reported the effect of temperature on water viscosity. His empirical correlation relating water viscosity with temperature in °F is presented as

$$\mu_w = \exp(1.003 - 1.479 \times 10^{-2} T + 1.982 \times 10^{-5} T^2). \quad \dots \dots \dots \quad (\text{B-53})$$

For large dissolved-solids content in water, apply Frick's³⁵ correction chart in Fig. B-18 to estimate brine viscosity.

Fig B-19 shows the kinematic viscosity, ν , of water at saturated condition vs. temperature. Matthews and Russell¹ presented Fig. B-20 to estimate water viscosity as a function of salinity and temperature. This figure also provides a method to correct for pressure.

It is important to note that the production of oil and water mixtures often causes emulsions to form in the well. A volume fraction weighted mixture viscosity calculation procedure does not work in this case.

As discussed in Chap. 3, the viscosity of an oil/water emulsion can be many times greater than the viscosity of either constituent liquid phase. Thus, actual laboratory viscosity data should be used in this case.

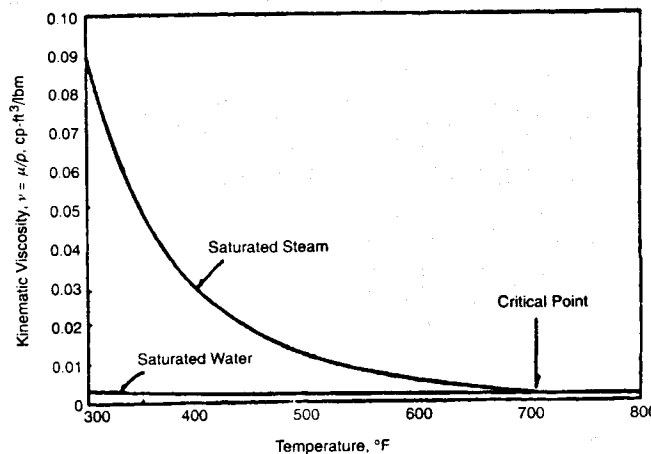


Fig. B-19—Kinematic viscosity of steam and water as a function of temperature (after Prats⁵).

uid phase. Thus, actual laboratory viscosity data should be used in this case.

B.4.5 Surface Tension of Water. Hocott³⁶ and Hough *et al.*³⁷ investigated the surface tension of water/gas systems. Katz *et al.*²⁶ combined their works into a single diagram (Fig. B-21).

Although these results,^{26,36,37} suggest that all experiments have been valid, their approach is highly questionable in its prediction of water surface tension as a function of such variables as water salinity and gas composition. Nevertheless, from the work of Hough *et al.* one can linearly interpolate between the curves for 74°F and 280°F and obtain acceptable estimates of the surface tension of water.

B.5 Gas Physical Properties

A gas is defined as a homogeneous fluid of low density and viscosity without a definite volume. Gas occupies the volume of its container without regard to shape or size. According to the kinetic theory of gases, gas is composed of a large number of molecules of insignificant volume compared to the total volume of the container. These molecules are assumed to have no attractive or repulsive forces between them, and they collide at random. These intermolecular collisions are perfectly elastic. An equation of state is a mathematical relationship between pressure, volume, and temperature for a fixed mass of gas and is expressed mathematically for n moles of gas as

$$pV = nRT. \quad \dots \dots \dots \quad (\text{B-54})$$

This equation is called the ideal gas law, where p = absolute pressure, psia; V = volume of gas (gas container), ft^3 ; T = absolute temperature, °R; n = number of moles of gas; m = mass of gas, lbm; M = molecular weight of gas; and R = universal gas constant.

Hydrocarbons or natural gases are not pure or single-component gases. These are mixtures of multicomponent gases and are called real gases. For real gases, the basic assumptions of negligible intermolecular forces and insignificant volume of molecules compared with the volume occupied by the gas are not valid. Based on empirical studies, the equations of state are modified for real gases to include the gas deviation factor or compressibility factor, often called the Z factor.

$$pV = ZnRT, \quad \dots \dots \dots \quad (\text{B-55})$$

where the compressibility factor, Z , is an empirically determined constant. This equation of state is called the real gas law.

B.5.1 Gas Density. Gas density is defined as the mass per unit volume of gas. From the real gas law,

$$\rho_g = \frac{m}{V} = \frac{pM_g}{ZRT}, \quad \dots \dots \dots \quad (\text{B-56})$$

where ρ_g is the density of gas, m = weight of gas, and V = volume of gas. The other parameters in this equation have been defined pre-

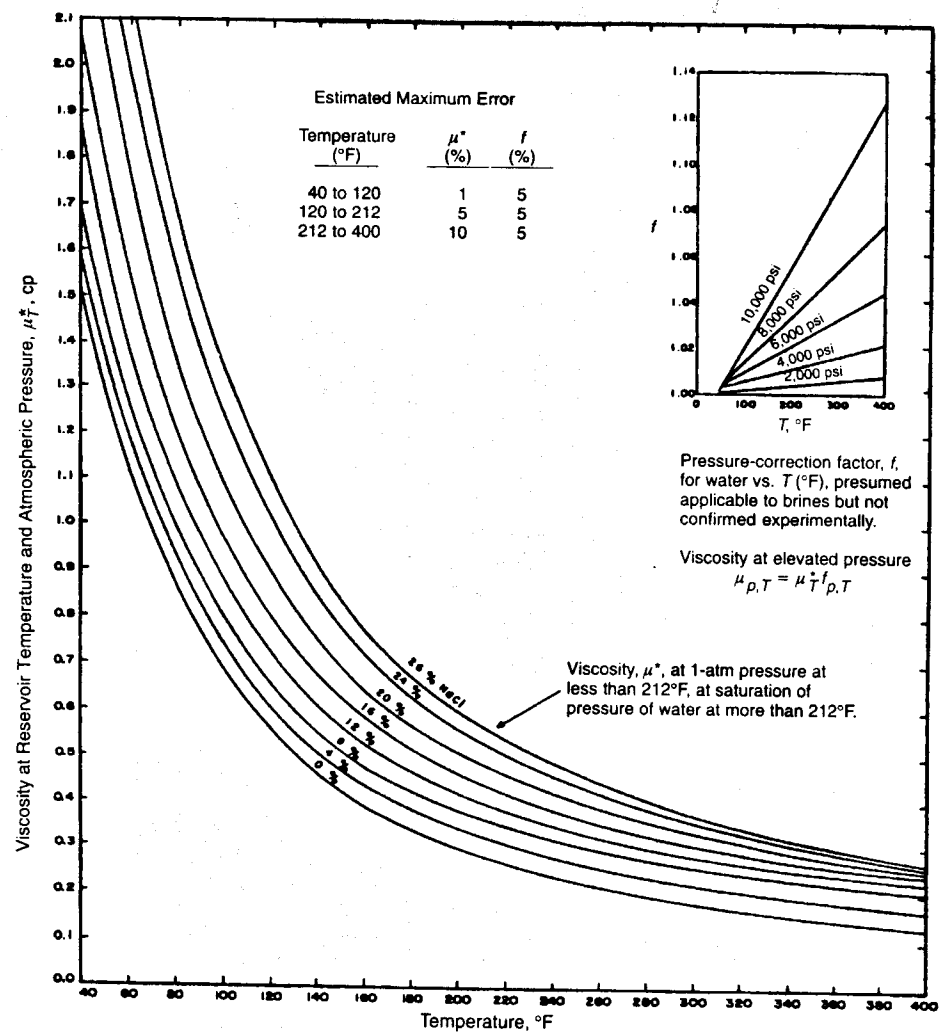


Fig. B-20—Water viscosities at various salinities and temperatures (after Matthews and Russell¹).

viously. The specific gravity of gas, γ_g , is defined as the ratio of the gas density to that of air, ρ_a , at standard conditions, expressed mathematically as

$$\gamma_g = \left(\frac{\rho_g}{\rho_a} \right)_{sc} = \frac{M_g}{M_a} \quad \dots \dots \dots \quad (B-57)$$

The molecular weight of air, M_a , is 28.96 and its specific gravity is 1.

Thus, the specific gravity of gas is

$$\gamma_g = \frac{M_g}{28.96} \quad \dots \dots \dots \quad (B-58)$$

Gas density in lbm/ft³ can be determined easily by combining the real gas law with the definition of specific gravity of gas.

$$\rho_g = 2.7 \gamma_g \frac{p}{ZT}, \quad \dots \dots \dots \quad (B-59)$$

where γ_g = specific gravity of free gas (air = 1); p = pressure of gas, psia; T = absolute temperature of gas, °R; Z = real-gas deviation factor; and $R = 10.73$, psia ft³/lbm-mol °R.

The specific gravity of free gas is a function of pressure and temperature because it depends on the composition and quantity of gas transferred between the liquid and the free-gas phase. Thus, γ_g , in Eq. B-59 should be replaced by $\gamma_{g,f}$ as defined in Eq. B-35.

B.5.2 Real-Gas Deviation Factor. The real-gas deviation factor is a very important variable used to calculate gas density and gas formation volume factor. To determine this parameter, Standing and Katz¹¹ used the law of corresponding states. This law states that at the same reduced pressure and temperature, all hydrocarbon gases have the same gas deviation factor. Eqs. B-1 through B-4 define the critical and reduced pressures and the critical and reduced temperatures.

Brown *et al.*¹⁰ correlated the pseudocritical pressure and temperature with the specific gravity of gas (Fig. B-3). If the specific gravity of the natural gas exceeds 0.75 a correction for high molecular-weight gas should be applied.¹⁹ Stewart *et al.*³⁸ proposed adjustments to the pseudocritical pressure and temperature for high-molecular-weight natural gases. Note that the term "pseudo" is used

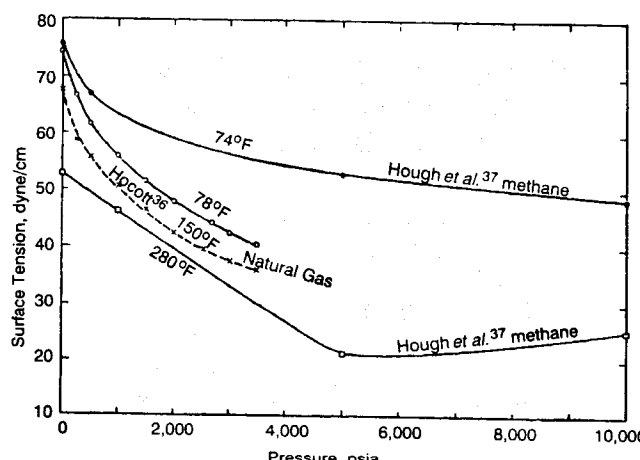


Fig. B-21—Effect of pressure and temperature on surface tension of water (after Katz *et al.*²⁶).

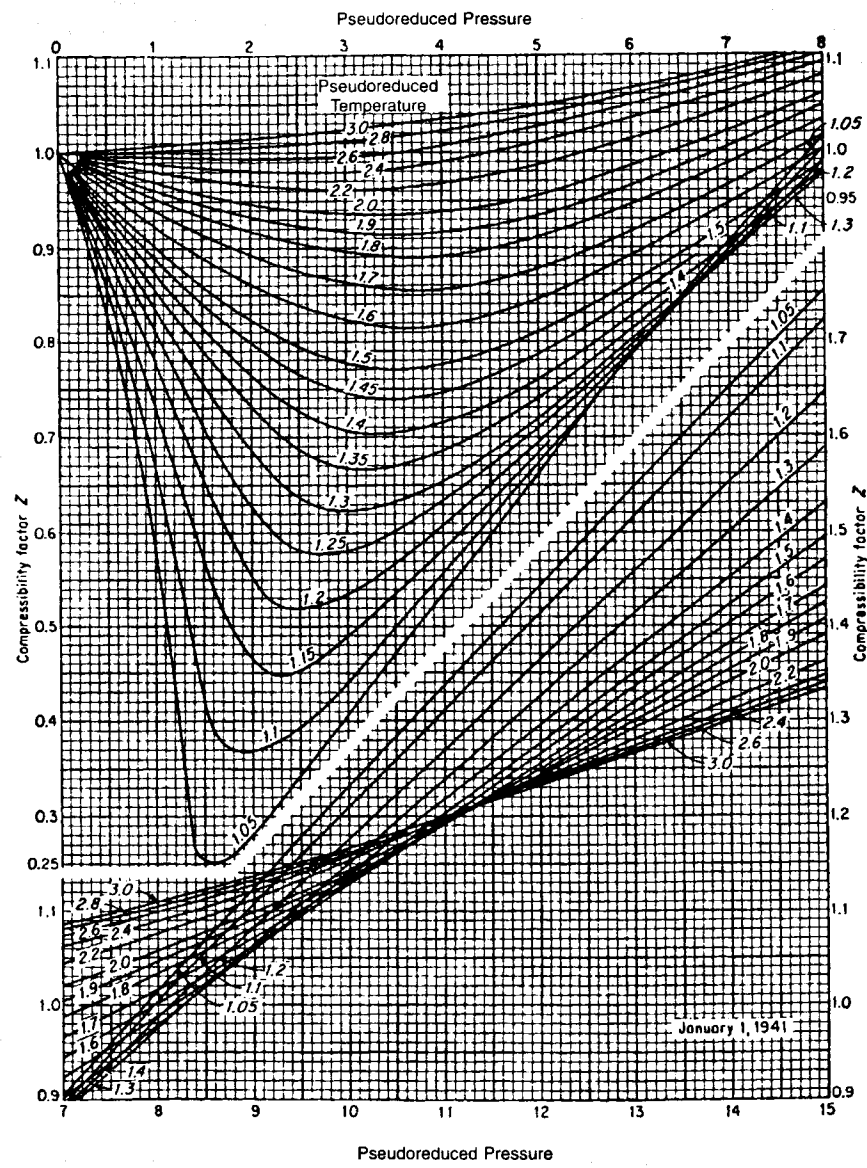


Fig. B-22—Real-gas deviation factor for natural gases as a function of pseudoreduced pressure and temperature.¹¹

to represent the properties of pure gas mixtures, such as hydrocarbon or natural gases. Standing²¹ presented a set of empirical equations to determine the pseudocritical pressure and temperature to approximate the curves in Fig. B-3.

Case 1: Natural Gas Systems.

$$T_{pc} = 168 + 325\gamma_g - 12.5\gamma_g^2 \quad \dots \quad (B-60)$$

and

$$P_{pc} = 677 + 15.0\gamma_g - 37.5\gamma_g^2 \quad \dots \quad (B-61)$$

Case 2: Gas Condensate Systems.

$$T_{pc} = 187 + 330\gamma_g - 71.5\gamma_g^2 \quad \dots \quad (B-62)$$

and

$$P_{pc} = 706 - 51.7\gamma_g - 11.1\gamma_g^2, \quad \dots \quad (B-63)$$

where T_{pc} = pseudocritical temperature, °R; P_{pc} = pseudocritical pressure, psia; and γ_g = specific gravity of the gas mixture (air = 1).

After determining the pseudocritical pressure and temperature, Eqs. B-3 and B-4 can be used to calculate the reduced pressure and temperature. Then, the gas deviation factor can be obtained from Fig. B-22.

Several empirical correlations are available, representing the Standing and Katz¹¹ Z-factor nomogram (Fig. B-22). For ease of calculation with computer programs, these mathematically expressed correlations are convenient for Z-factor determination. The Dranchuk and Abu-Kassem correlation³⁹ is presented for the sake of completeness. It is an 11-constant empirical equation used to fit Z-factor curves in Fig. B-22, and can be expressed as

$$\begin{aligned} Z = & \left(A_1 + \frac{A_2}{T_{pr}} + \frac{A_3}{T_{pr}^2} + \frac{A_4}{T_{pr}^3} + \frac{A_5}{T_{pr}^4} \right) \rho_r \\ & + \left(A_6 + \frac{A_7}{T_{pr}} + \frac{A_8}{T_{pr}^2} \right) \rho_r^2 - A_9 \left(\frac{A_7}{T_{pr}} + \frac{A_8}{T_{pr}^2} \right) \rho_r^5 \\ & + A_{10} \left(1 + A_{11} \rho_r^2 \right) \frac{\rho_r^2}{T_{pr}^3} \exp \left(- A_{12} \rho_r^2 \right) + 1.0, \quad \dots \quad (B-64) \end{aligned}$$

where ρ_r = reduced gas density and is defined by

$$\rho_r = \frac{0.27 p_{pr}}{Z T_{pr}} \quad \dots \dots \dots \quad (\text{B-65})$$

The 11 constants, A_1 through A_{11} were determined from nonlinear regression on 1,500 data points from the Standing and Katz¹¹ Z-factor chart.

$$\begin{aligned} A_1 &= 0.3265, \\ A_2 &= -1.0700, \\ A_3 &= -0.5339, \\ A_4 &= 0.01569, \\ A_5 &= -0.05165, \\ A_6 &= 0.5475, \\ A_7 &= -0.7361, \\ A_8 &= 0.1844, \\ A_9 &= 0.1056, \\ A_{10} &= 0.6134, \end{aligned}$$

and

$$A_{11} = 0.7210.$$

Eq. B-64 is implicit in Z and must be solved by some iterative method, such as the Newton-Raphson iteration technique. This correlation represents the Standing and Katz Z-factor chart within 0.585% average absolute error and is applicable over the ranges, $0.2 \leq p_{pr} < 30$ and $1.0 \leq T_{pr} \leq 3.0$. Although presented for p_{pr} up to 15, the Standing and Katz Z-factor chart can be extrapolated beyond that reduced pressure because of the linear relationship of Z vs. p_{pr} at constant T_{pr} for $p_{pr} > 15$.

B.5.3 Correction for Nonhydrocarbons. Standing and Katz developed their Z-factor correlation based on mixtures of hydrocarbon gases with molecular weights less than 40. Natural gases often contain nonhydrocarbon components, such as carbon dioxide, nitrogen, and hydrogen sulfide. At nonhydrocarbon gas-content values below 5%, there is negligible effect on the Z factor. Higher concentrations of nonhydrocarbon gases can cause substantial error when calculating the compressibility factor and, thus, require correction. Wichert and Aziz⁴⁰ presented a simple gas compressibility correction procedure to compensate for the presence of hydrogen sulfide and carbon dioxide in natural gases. This method suggests the following adjustments to the pseudocritical properties used to determine the Z factor from the Standing and Katz chart.

$$T'_{pc} = T_{pc} - \epsilon \quad \dots \dots \dots \quad (\text{B-66})$$

and

$$p'_{pc} = \frac{p_{pc} T'_{pc}}{T_{pc} + y_{H_2S}(1 - y_{H_2S})\epsilon}, \quad \dots \dots \dots \quad (\text{B-67})$$

where T_{pc} = pseudocritical temperature, °R; p_{pc} = pseudocritical pressure, psia; T'_{pc} = corrected pseudocritical temperature, °R; p'_{pc} = corrected pseudocritical pressure, psia; y_{H_2S} = mole fraction of hydrogen sulfide in the gas mixture; and ϵ = pseudocritical temperature adjustment factor, defined mathematically by

$$\epsilon = 120(A^{0.9} - A^{1.6}) + 15(y_{H_2S}^{0.5} - y_{H_2S}^{4.0}), \quad \dots \dots \dots \quad (\text{B-68a})$$

where the Coefficient A is the sum of the mole fractions of hydrogen sulfide and carbon dioxide in the gas mixture or

$$A = y_{H_2S} + y_{CO_2}. \quad \dots \dots \dots \quad (\text{B-68b})$$

B.5.4 Gas Formation Volume Factor. The formation volume factor of gas can be calculated from the real gas law.

$$B_g = 0.0283 \frac{ZT}{p}, \quad \dots \dots \dots \quad (\text{B-69})$$

where B_g = gas formation volume factor, ft³/scf; p = pressure, psia; and T = absolute temperature, °R.

B.5.5 Gas Viscosity. The viscosity of a fluid is defined as the ratio of shear stress to shear rate. The commonly used oilfield unit for viscosity is centipoise, where 1 poise is defined as a viscosity of 1 dyne-s/cm².

Carr *et al.*⁴¹ presented a widely used method to estimate natural gas viscosity. It requires knowledge of the gas composition and the viscosity of each component at atmospheric pressure and in-situ temperature. The viscosity of the gas mixture at atmospheric pressure is estimated from

$$\mu_{ga} = \frac{\sum_{j=1}^n y_j \mu_j \sqrt{M_j}}{\sum_{j=1}^n y_j \sqrt{M_j}}, \quad \dots \dots \dots \quad (\text{B-70})$$

where μ_{ga} = viscosity of the gas mixture at the desired temperature and atmospheric pressure, cp; n = number of components in the gas; y_j = mole fraction of Component j ; μ_j = viscosity of Component j at the desired temperature and atmospheric pressure; and M_j = molecular weight of Component j from Table B-1.

If the gas composition is not known, Fig. B-23 can be used with the gas molecular weight or gas gravity to estimate the gas viscosity at reservoir temperature and atmospheric pressure. Molecular weight is related to gas gravity by

$$M_g = 28.97 \gamma_g. \quad \dots \dots \dots \quad (\text{B-71})$$

The gas viscosity at reservoir pressure is estimated by determining the ratio μ_g/μ_{ga} at the appropriate temperature and pressure from Fig. B-24. Then, that ratio is applied to μ_{ga} , obtained from either Eq. B-70 or Fig. B-23. The pseudoreduced temperatures and pressures for use in Fig. B-24 are estimated from Eqs. B-3 and B-4 and Fig. B-3.

In the presence of nonhydrogen gases, such as nitrogen, carbon dioxide, and hydrogen sulfide, the gas viscosity at atmospheric pressure and desired temperature must be corrected by use of the inserts in Fig. B-23.

Lee *et al.*⁴² presented a semiempirical equation to calculate gas viscosity. This equation, which cannot be used for sour gases, can be presented as

$$\mu_g = 10^{-4} K \exp \left[X \left(\frac{\rho_g}{62.4} \right)^Y \right], \quad \dots \dots \dots \quad (\text{B-72})$$

where $K = (9.4 + 0.02 M_g) T^{1.5} / (209 + 19 M_g + T)$; $X = 3.5 + (986/T) + 0.01 M_g$; $Y = 2.4 - 0.2 X$; ρ_g = gas density at reservoir pressure and temperature, lbm/ft³; T = reservoir temperature, °R; and M_g = apparent molecular weight of the gas mixture.

B.5.6 Gas Compressibility. Isothermal gas compressibility can be defined as the change in volume per unit volume of gas for a unit change in pressure,¹³ expressed mathematically as

$$c_g = -\frac{1}{V} \left(\frac{\partial V}{\partial p} \right)_T. \quad \dots \dots \dots \quad (\text{B-73})$$

With the real gas law to replace volume in the previous equations and after proper differentiation,

$$c_g = \frac{1}{p} - \frac{1}{Z} \left(\frac{dZ}{dp} \right)_T, \quad \dots \dots \dots \quad (\text{B-74})$$

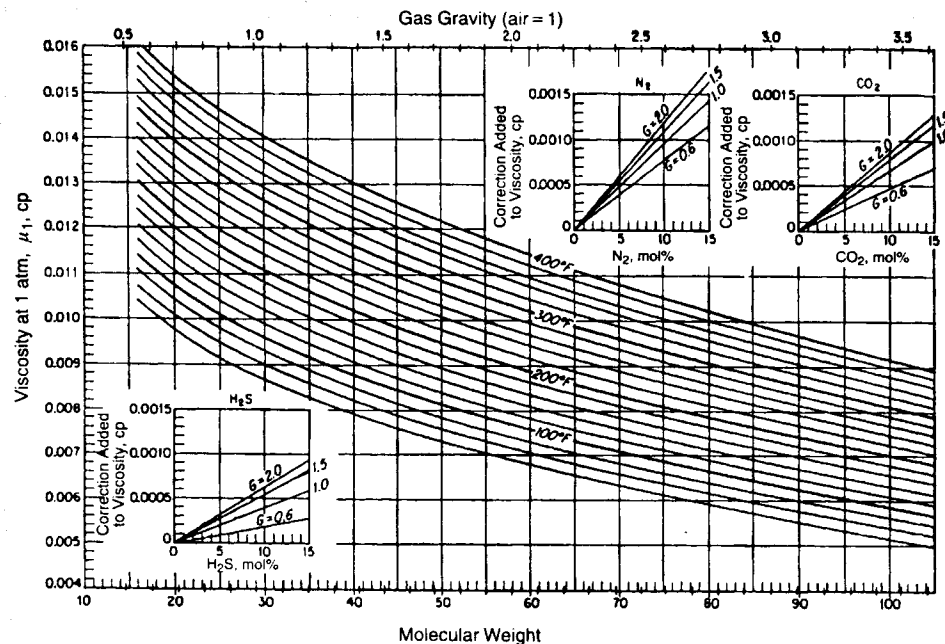


Fig. B-23—Viscosity of natural gases at 1 atm (after Carr et al.⁴¹).

where Z = gas deviation factor at absolute pressure, p , in psia and absolute temperature, T , in °R. Note that for an ideal gas, $Z = 1$, and

$$c_g = \frac{1}{p} \quad \dots \dots \dots \quad (B-75)$$

Trube⁴⁴ presented a correlation to estimate gas compressibility. He defined isothermal gas compressibility, c_g , as the ratio of pseudoreduced compressibility, c_{pr} , to the pseudocritical pressure, p_{pc} , as

$$c_g = \frac{c_{pr}}{p_{pc}} \quad \dots \dots \dots \quad (B-76)$$

To estimate the gas compressibility, Trube presented correlations to estimate the pseudoreduced compressibility as a function of pseudoreduced pressure and temperature (Figs. B-25 and B-26). Note that these two correlations are similar. They present pseudoreduced compressibility at two different ranges of compressibility values.

Example B.1—Calculate Black-Oil-Model Mass-Transfer Parameters and Physical Properties. A crude oil and natural gas mixture is flowing through a wellbore. Determine the black-oil-model mass-transfer parameters and the physical properties of the gas and oil phases at a location in the well where the pressure is 1,700 psia and the temperature is 180°F. Also given are $\gamma_g = 0.75$ at $p_{sep} = 14.7$ psia and $T_{sep} = 60^\circ\text{F}$, $\gamma_{\text{API}} = 33^\circ$, and $R_p = 1,000 \text{ scf/STBO}$.

Solution Gas/Oil Ratio (from Vazquez and Beggs).

From Eq. B-9,

$$\begin{aligned} \gamma_{g100} &= \gamma_g \left\{ 1.0 + 5.912 \times 10^{-5} (33)(60) \log \left[\frac{14.7}{114.7} \right] \right\} \\ &= (0.75)(0.896) \\ &= 0.672. \end{aligned}$$

From Eq. B-8 for $\gamma_{\text{API}} > 30^\circ$,

$$R_s = (0.0178)(0.672)(1,700)^{1.187}$$

$$\times \exp \left[(23.931) \left(\frac{33}{180 + 460} \right) \right]$$

$$= 281 \text{ scf/STBO.}$$

Oil Formation Volume Factor (from Vazquez and Beggs).

From Eq. B-18,

$$B_o = 1.0 + 4.677 \times 10^{-4} (281)$$

$$\begin{aligned} &+ (180 - 60) \left(\frac{33}{0.672} \right) [1.1 \times 10^{-5} + 1.337 \times 10^{-9} (281)] \\ &= 1.0 + 0.131 + 0.067 \\ &= 1.197 \text{ bbl/STBO}. \end{aligned}$$

Specific Gravity of Dissolved Gas (from Katz).

From Fig. B-10, $\gamma_{gd} = 0.88$.

Specific Gravity of Free Gas.

From Eq. B-35,

$$\gamma_{gf} = \frac{(1,000)(0.75) - (281)(0.88)}{1,000 - 281} = 0.70.$$

Oil Density.

From Eq. B-5,

$$\gamma_o = \frac{141.5}{131.5 + 33} = 0.86.$$

From Eq. B-30,

$$\begin{aligned} \rho_o &= \frac{(62.4)(0.86) + (0.0136)(281)(0.88)}{1.197} \\ &= \frac{53.66 + 3.36}{1.197} \\ &= 47.61 \text{ lbm/ft}^3. \end{aligned}$$

Pseudocritical Pressure and Temperature (from Standing).

From Eq. B-61,

$$\begin{aligned} p_{pc} &= 677 + (15)(0.7) - (37.5)(0.7)^2 \\ &= 669 \text{ psia}. \end{aligned}$$

From Eq. B-60,

$$\begin{aligned} T_{pc} &= 168 + (325)(0.7) - (12.5)(0.7)^2 \\ &= 389^\circ\text{R}. \end{aligned}$$

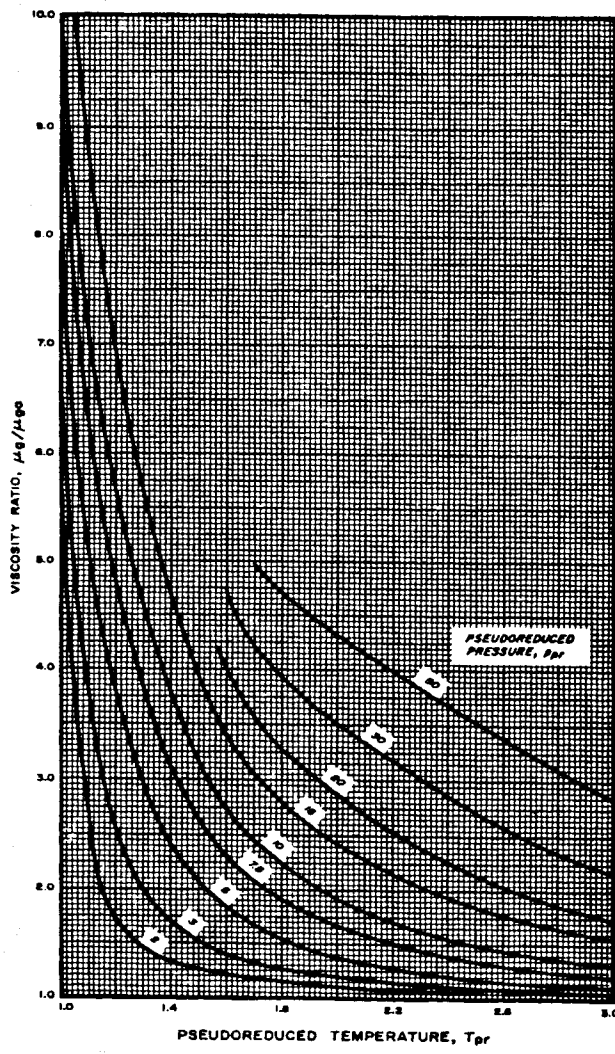


Fig. B-24—Effect of temperature and pressure on gas viscosity.⁴¹

Gas Compressibility Factor (from Standing and Katz).

From Eq. B-3,

$$T_{pr} = \frac{180 + 460}{389} = 1.65.$$

From Eq. B-4,

$$P_{pr} = \frac{1,700}{669} = 2.54.$$

From Fig. B-22,

$$Z = 0.853.$$

Gas Formation Volume Factor.

From Eq. B-69,

$$B_g = 0.0283 \frac{ZT}{P} = (0.0283) \frac{(0.853)(180 + 460)}{(1,700)} \\ = 0.0091 \text{ ft}^3/\text{scf}.$$

Gas Density.

From Eq. B-59,

$$\rho_g = \frac{(2.7)(0.7)(1,700)}{(0.853)(180 + 460)} = 5.88 \text{ lbm}/\text{ft}^3.$$

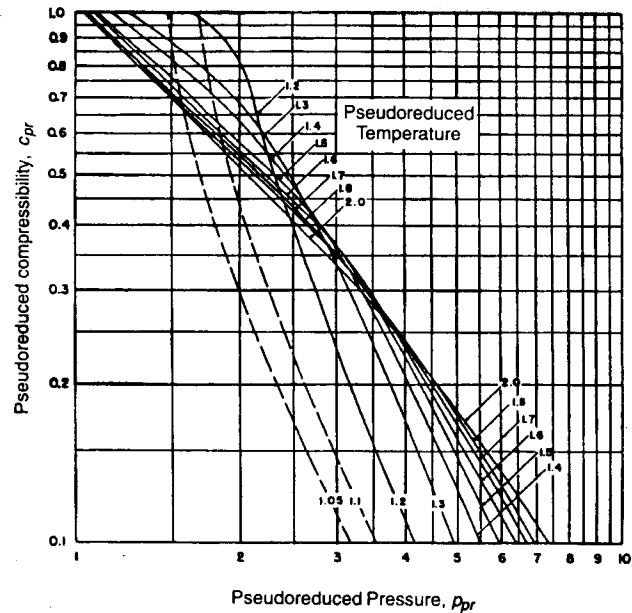


Fig. B-25—Correlation of pseudoreduced compressibility for natural gases (after Trube⁴⁴).

Oil Viscosity (from Beggs and Robinson).

$$x = \frac{10^{[3.0324 - (0.02023)(33)]}}{180^{1.163}} = 0.552$$

and

$$b = 5.44(281 + 150)^{-0.338} = 0.7.$$

From Eq. B-37,

$$\mu_{od} = 10^{0.552} - 1 = 2.56 \text{ cp.}$$

From Eq. B-40,

$$\mu_o = [10.715(281 + 100)^{-0.515}](2.56)^{0.7} = 0.97 \text{ cp.}$$

Gas Viscosity (from Lee et al.).

From Eq. B-71,

$$M_g = (28.97)(0.7) = 20.28 \text{ lbm/lbm-mol.}$$

$$K = \frac{[9.4 + (0.02)(20.28)](640)^{1.5}}{209 + (19)(20.28) + 640} = 128.7,$$

$$X = 3.5 + \frac{986}{640} + (0.01)(20.28) = 5.243,$$

and

$$Y = 2.4 - (0.2)(5.243) = 1.351.$$

From Eq. B-72,

$$\mu_g = (10)^{-4}(128.7) \exp \left[(5.243) \left(\frac{5.88}{62.4} \right)^{1.351} \right] = 0.016 \text{ cp.}$$

Surface Tension (from Baker and Swerdlow).

From Fig. B-13,

$$\sigma_{od} = 29 \text{ dynes/cm.}$$

From Fig. B-14,

$$\% = 29.$$

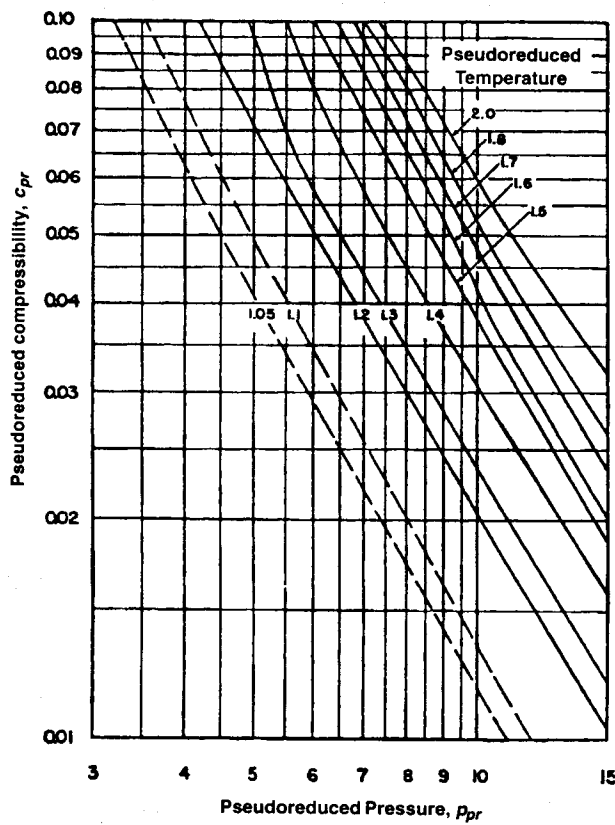


Fig. B-26—Correlation of pseudoreduced compressibility for natural gases (after Trube⁴⁴).

From Eq. B-44,

$$\sigma_o = (29) \left(\frac{29}{100} \right) = 8.41 \text{ dynes/cm.}$$

B.6 Composite Fluid Properties

Individual phase properties for formation volume factor and compressibility can be combined into composite properties.

B.6.1. Total Formation Volume Factor. It is often convenient to express the formation volume factor below the bubblepoint pressure in terms of total formation volume factor, independent of the number of phases present. Total formation volume factor is defined as the ratio of the total volume of hydrocarbons per unit stock-tank barrel of oil at the prevailing pressure and temperature. This can be expressed mathematically as

$$B_t = B_o + (R_{sb} - R_s)B_g, \quad \dots \dots \dots \quad (B-77)$$

where B_o = formation volume factor of oil, bbl/STBO; R_{sb} = gas solubility at bubblepoint, scf/STBO; R_s = gas solubility at system conditions, scf/STBO; and B_g = gas formation volume factor, bbl/scf.

Glasø¹⁴ presented an empirical correlation to calculate the total formation volume factor, which also is known as the two-phase formation volume factor. This correlation can be expressed mathematically as

$$\log B_t = 0.080135 + 0.47257 \log B_t^* + 0.17351 (\log B_t^*)^2, \quad \dots \dots \dots \quad (B-78a)$$

where B_t^* = a correlating number and is defined as

$$B_t^* = R_s \frac{T^{0.5}}{\gamma_g^{0.3}} \gamma_o^c p^{-1.1089}, \quad \dots \dots \dots \quad (B-78b)$$

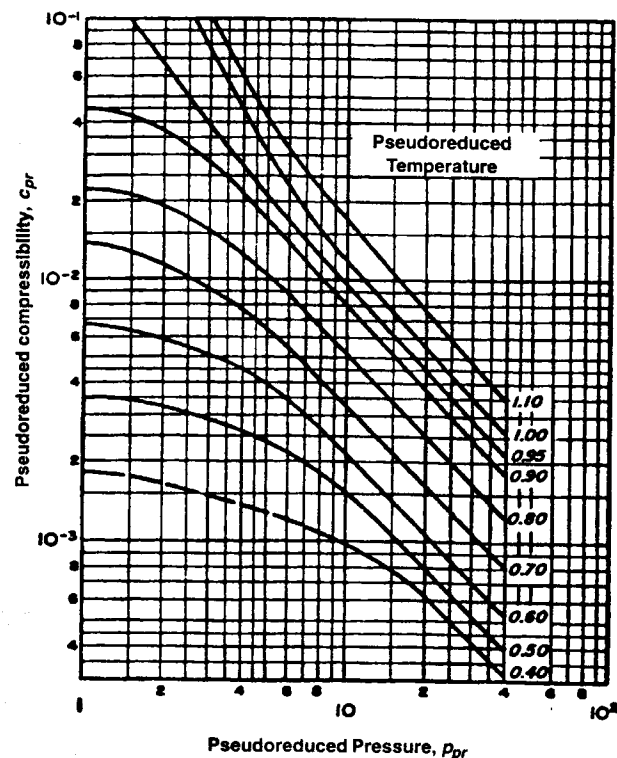


Fig. B-27—Correlation of pseudoreduced compressibility for an undersaturated oil (after Trube⁸).

where $C = 2.9 \times 10^{-0.00027R}$; T = temperature, °F; p = system pressure, psia; and γ = phase specific gravity.

Al-Marhoun Correlation. This empirical correlation¹⁵ to determine the total formation volume factor can be expressed mathematically as

$$B_t = 0.314693 + 0.106253 \times 10^{-4}F + 0.18883 \times 10^{-10}F^2, \quad \dots \dots \dots \quad (B-79)$$

where $F = R_s^a \gamma_g^b \gamma_o^c T^d p^e$, and $a = 0.644516$, $b = -1.079340$, $c = 0.724874$, $d = 2.00621$, and $e = -0.761910$.

B.6.2 Total Compressibility. Compressibility, c , is defined as the change in volume per unit volume for unit change in pressure at constant temperature.

$$c = \frac{1}{V} \left(\frac{\partial V}{\partial p} \right)_T \quad \dots \dots \dots \quad (B-80)$$

The unit of compressibility is reciprocal of pressure (1/psi).

In this appendix, different methods to determine individual fluid compressibilities already have been presented. In all transient fluid-flow calculations in porous media, the total isothermal compressibility, denoted as c_t , must be calculated. The total rock/fluid system compressibility can be expressed mathematically as

$$c_t = S_o c_o + S_w c_w + S_g c_g + c_f, \quad \dots \dots \dots \quad (B-81)$$

where c_t = total system compressibility, psi⁻¹; S_o = average oil saturation; c_o = isothermal compressibility coefficient of the oil phase, psi⁻¹; S_w = water saturation; c_w = isothermal compressibility coefficient of the water phase, psi⁻¹; S_g = gas saturation; c_g = isothermal compressibility coefficient of the gas phase, psi⁻¹; c_f = formation or rock compressibility, psi⁻¹; and $S_o + S_w + S_g = 1$.

By definition, the isothermal compressibility coefficient of Phase i is

$$c_i = \frac{-1}{B_i} \left(\frac{\partial B_i}{\partial p} \right)_T, \quad \dots \dots \dots \quad (B-82)$$

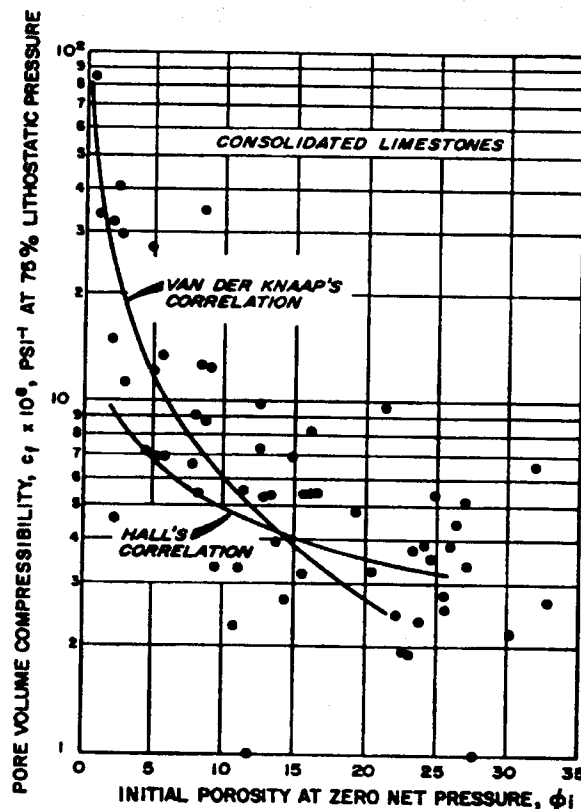


Fig. B-28—Pore-volume compressibility at 75% lithostatic pressure vs. initial sample porosity for limestones (after Newman⁴⁵).

where B_i = formation volume factor of Phase i .

Accordingly, c_o , c_w , and c_g in Eq. B-81 can be replaced by the previous expression to yield

$$c_t = S_o \left(\frac{-1}{B_o} \frac{\partial B_o}{\partial p} \right)_T + S_w \left(\frac{-1}{B_w} \frac{\partial B_w}{\partial p} \right)_T + S_g \left(\frac{-1}{B_g} \frac{\partial B_g}{\partial p} \right)_T + c_f, \quad (B-83)$$

where B_w = water formation volume factor, bbl/STBW; B_o = oil formation volume factor, bbl/STBO; and B_g = gas formation volume factor, bbl/scf.

Eq. B-83 can be modified slightly to include the effects of solution gas on the change in liquid phase volumes and presented as

$$c_t = S_o \left[\left(\frac{-1}{B_o} \frac{\partial B_o}{\partial p} \right)_T + \frac{B_g}{B_o} \left(\frac{\partial R_s}{\partial p} \right)_T \right] \times S_w \left[\left(\frac{-1}{B_w} \frac{\partial B_w}{\partial p} \right)_T + \frac{B_g}{B_w} \left(\frac{\partial R_{sw}}{\partial p} \right)_T \right] + S_g \left(\frac{-1}{B_g} \frac{\partial B_g}{\partial p} \right)_T + c_f, \quad (B-84)$$

where R_s and R_{sw} = gas solubilities in oil and water, respectively.

Oil Compressibility. The isothermal compressibility of an undersaturated oil (above the bubblepoint pressure) can be defined as

$$c_o = -\frac{1}{V_o} \left(\frac{\partial V_o}{\partial p} \right)_T = \frac{1}{\rho_o} \left(\frac{\partial \rho_o}{\partial p} \right)_T = -\frac{1}{B_o} \left(\frac{\partial B_o}{\partial p} \right)_T. \quad (B-85)$$

Oil compressibility is always positive because the volume of an undersaturated liquid decreases as the pressure increases. Oil com-

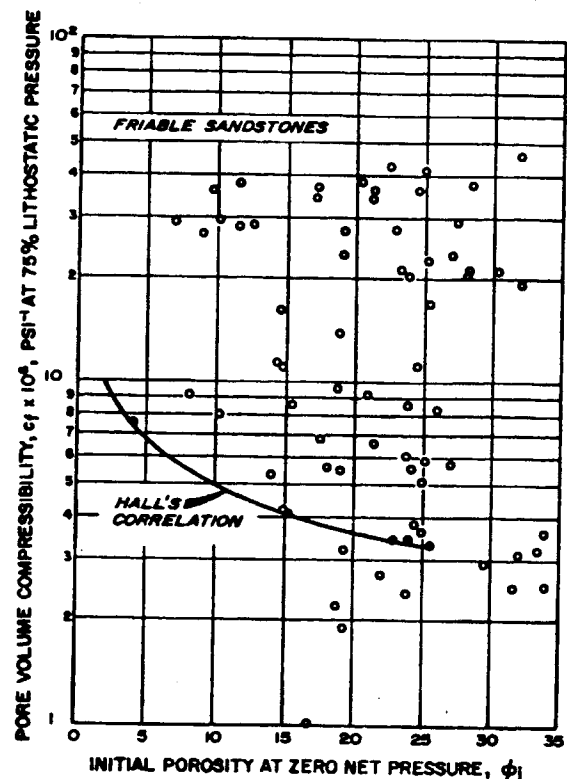


Fig. B-29—Pore-volume compressibility at 75% lithostatic pressure vs. initial sample porosity for friable sandstones (after Newman⁴⁵).

pressibility can be determined from laboratory experiments, from the correlations presented earlier in this section, or from the Trube correlation⁸ shown in Fig. B-27. Trube correlated pseudoreduced compressibility, c_{pr} , with pseudoreduced pressure, p_{pr} , and pseudoreduced temperature, T_{pr} . The oil compressibility then can be estimated from

$$c_o = c_{pr}/p_{pc}, \quad (B-86)$$

where p_{pc} = pseudocritical pressure from Fig. B-1 and T_{pc} = pseudocritical temperature from Fig. B-1.

Taking into account the gas in solution, the apparent compressibility of oil, c_{oa} , below the bubblepoint pressure can be calculated by

$$c_{oa} = c_o + \frac{R_s}{(0.83p + 21.75)} \left(\frac{B_g}{B_o} \right). \quad (B-87)$$

Water Compressibility. For an isothermal condition, the compressibility of oilfield water can be defined as

$$c_w = -\frac{1}{B_w} \left(\frac{\partial B_w}{\partial p} \right)_T, \quad (B-88)$$

where B_w = formation volume factor of water.

Dodson and Standing³¹ presented a correlation to estimate the compressibility of water (Fig. B-17). Because the gas solubility in water is very low, the effect of gas solubility can be ignored. However, Meehan³² presented a correlation that includes the effects of gas solubility (Eqs. B-50 and B-51a).

Formation Compressibility. Rock or formation compressibility under isothermal conditions can be defined as

$$c_f = \frac{1}{V_p} \left(\frac{\partial V_p}{\partial p} \right)_T, \quad (B-89)$$

where V_p = pore volume.

There are different correlations for rock compressibility, each for a fixed type of rock. Figs. B-28 through B-31 present the rock compressibility correlation after Newman.⁴⁵ It is strongly recom-

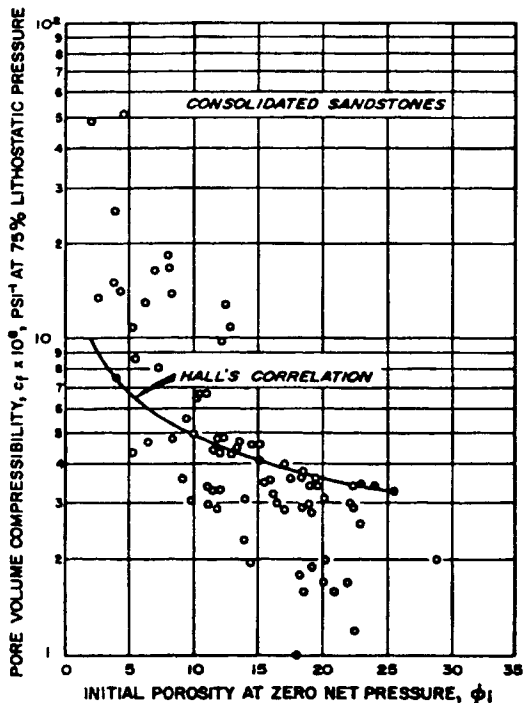


Fig. B-30—Pore-volume compressibility at 75% lithostatic pressure vs. initial sample porosity for consolidated sandstones (after Newman⁴⁵).

mended that laboratory data for this parameter be used wherever possible. From Figs. B-28 through B-31, it is clear that these correlations are questionable, at best. However, for well-performance calculations, rock compressibility, c_f , is needed in Eq. B-81.

Sec. B.5.6 presented a detailed discussion of gas compressibility. However, it is important to note that the gas compressibility is at least an order of magnitude higher than the rock or liquid compressibility. While the gas compressibility is on the order of 10^{-4} , the liquid or rock compressibilities are typically on the order of 10^{-5} or 10^{-6} . In gas reservoirs, it often is assumed that $c_f \approx c_g$.

B.7 Flash vs. Differential Liberation of Gas

Accurate determination of rock and fluid physical properties is very important for any pipe flow calculations used in oil and gas production engineering. As the fluid produces from the reservoir through the well and flowlines, gas evolves from the liquid, increasing the volumetric flow rate of the gas and continuously changing the liquid and gas physical properties. Depending on the type of gas liberation, such as flash or differential liberation, the fluid physical properties vary.¹⁶ Fluid physical properties based on flash liberation are more appropriate for use in tubing and flowline calculations. The differential-liberation process more accurately represents gas liberation from liquid during flow through a porous rock or reservoir. Most of the fluid physical property correlations presented in this appendix were developed with flash data, although this often was not reported. Moses⁴⁶ has shown that the error resulting from the use of flash data for a differential-liberation case, or differential liberation for a flash-data case, can be up to 20%.

Kartoatmodjo and Schmidt¹⁶ presented an empirical method to convert flash-liberation oil formation volume factors to differential-liberation oil formation volume factors based on tank oil gravity, separator gas gravity, separator pressure, separator temperature, and reservoir temperature. The conversion factor, F_C , is given as

$$F_C = B_{of}/B_{od} \\ = 0.7264\gamma_o^{0.3202} - 0.3126\gamma_{gsep}^{-0.02087} + 0.6459\left(\frac{T_{sep}}{T}\right)^{0.5596}, \quad (B-90)$$

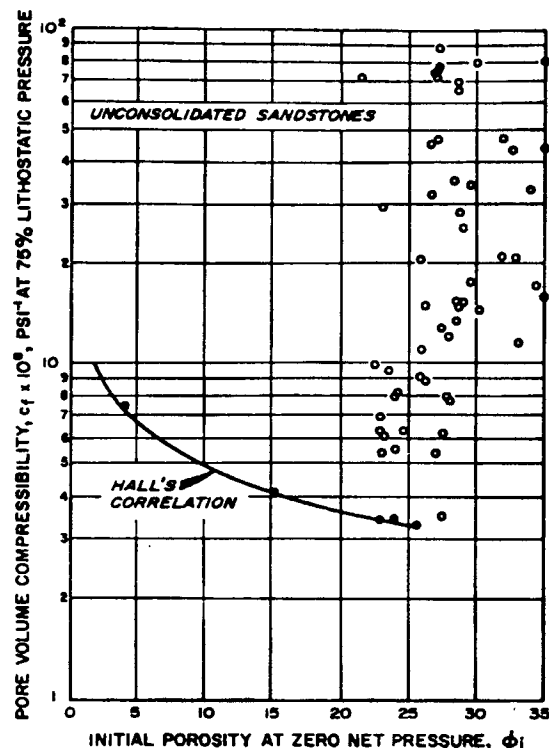


Fig. B-31—Pore-volume compressibility at 75% lithostatic pressure vs. initial porosity for unconsolidated sandstones (after Newman⁴⁵).

where T = temperature, °R; B_{of} = flash formation volume factor from Eq. B-27; and B_{od} = differential formation volume factor.

Eq. B-90 also can be used to convert formation volume factor at the bubblepoint pressure obtained from Eq. B-15, B-18, B-21a, B-25, or B-27. Formation volume factors above the bubblepoint pressure then can be obtained from Eq. B-16 by use of oil compressibility, c_o , calculated from Eq. B-19 or B-28. However, the differential-solution gas/oil ratio cannot be converted by application of this method.

B.8 Enthalpy

Enthalpy is the property of a fluid that determines the heat required to raise or lower its temperature.

B.8.1 Crude Oils and Fractions. Kesler and Lee⁴⁷ and others^{6,7,48,49} have investigated and reported on the enthalpy of crude oil fractions for liquids and vapors. The Kesler and Lee correlations involve obtaining base values of the enthalpy at zero pressure (denoted by h^o) and then correcting these for pressure effects according to the relation

$$h = h^o - \Delta h. \quad (B-91)$$

This correction, also called the enthalpy correction factor, can be calculated by equations of state (see Appendix C). An empirical method for correction of base enthalpies for pressure follows. Figs. B-32 through B-39 give the base enthalpies and require information on the API gravity and the Watson characterization factor of the crude (or crude fraction), K_w . K_w is defined as

$$K_w = \frac{(\bar{T}_b)^{1/3}}{\gamma_o}, \quad (B-92)$$

where \bar{T}_b = average cubed boiling point and γ_o = oil specific gravity.

The pressure correction Δh is determined as

$$\Delta h = \left\{ \left[\left(\frac{\Delta h}{RT_{pc}} \right)^{(0)} + \omega \left(\frac{\Delta h}{RT_{pc}} \right)^{(1)} \right] \frac{RT_{pc}}{M} \right\}_{p_r}$$

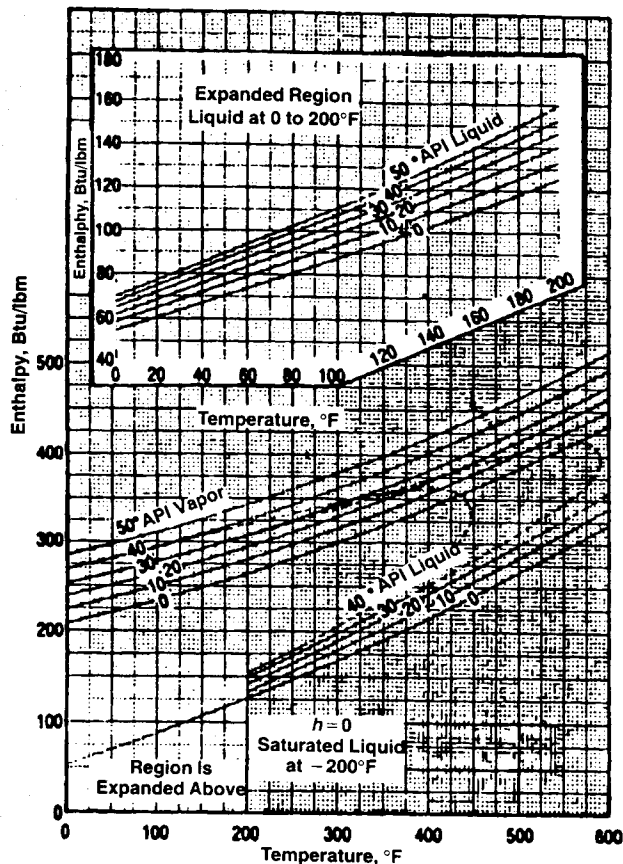


Fig. B-32—Enthalpy of petroleum fractions ($K_w = 10$, $T = 0$ to 600°F , after Kesler and Lee⁴⁷).

$$-\left\{\left[\left(\frac{\Delta h}{RT_{pc}}\right)^{(0)} + \omega\left(\frac{\Delta h}{RT_{pc}}\right)^{(1)}\right]\frac{RT_{pc}}{M}\right\}_{p_r=1}, \quad (\text{B-93})$$

where $(\Delta h/RT_{pc})^{(0)}$ is found in Fig. B-40, $(\Delta h/RT_{pc})^{(1)}$ is found in Figs. B-41 and B-42, and the quantities T_{pc} , p_{pc} , ω , and RT_{pc}/M are found in Fig. B-43. The second term of Eq. B-93 is omitted when the reduced temperature is less than 0.8.

The corrections for pressure given in Figs. B-40 through B-42 depend on the reduced temperature and pressure, defined by Eqs. B-3 and B-4, and are independent of the Watson characterization factor, K_w , and acentric factor, ω . If they are not available from measurements or other sources, the values of K_w and ω may be estimated from Fig. B-43, when the API gravity and the pseudocritical temperature or pressure of the crude are known. Kesler and Lee⁴⁷ provide additional details. The base enthalpies, h^0 , are referred to a value $h^0 = 0$ at $T = -200^\circ\text{F}$. Enthalpies calculated by this procedure take into account changes in the isobaric specific heat, C_{po} , with temperature and of the latent heat of condensation and evaporation of the crude fractions. Average specific heats, \bar{C}_{po} , of the liquid and vapor phases can be estimated by taking the chord secant of the enthalpies over the desired temperature range.

$$\bar{C}_{po} = \frac{h_{T_1} - h_{T_2}}{T_1 - T_2}. \quad (\text{B-94})$$

When only the density or API gravity of the crude is known, its heat capacity may be estimated from the Gambill⁵⁰ relationship.

$$C_{po} = \frac{0.388 + 0.00045T}{\sqrt{\gamma_o}}, \quad (\text{B-95})$$

where T is less than 300°F .

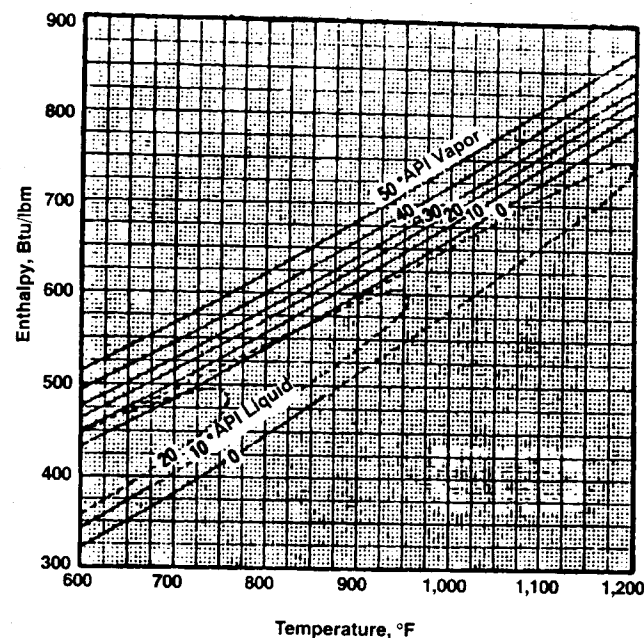


Fig. B-33—Enthalpy of petroleum fractions ($K_w = 10$, $T = 600$ to $1,200^\circ\text{F}$, after Kesler and Lee⁴⁷).

Fig. B-44 gives heat capacities of selected hydrocarbon and non-hydrocarbon gases and vapors at atmospheric pressure; Fig. B-45 corrects for pressure. Fig. B-46 gives heat capacities of saturated liquids. Sec. B-8.2 discusses the liquid and vapor enthalpies of water.

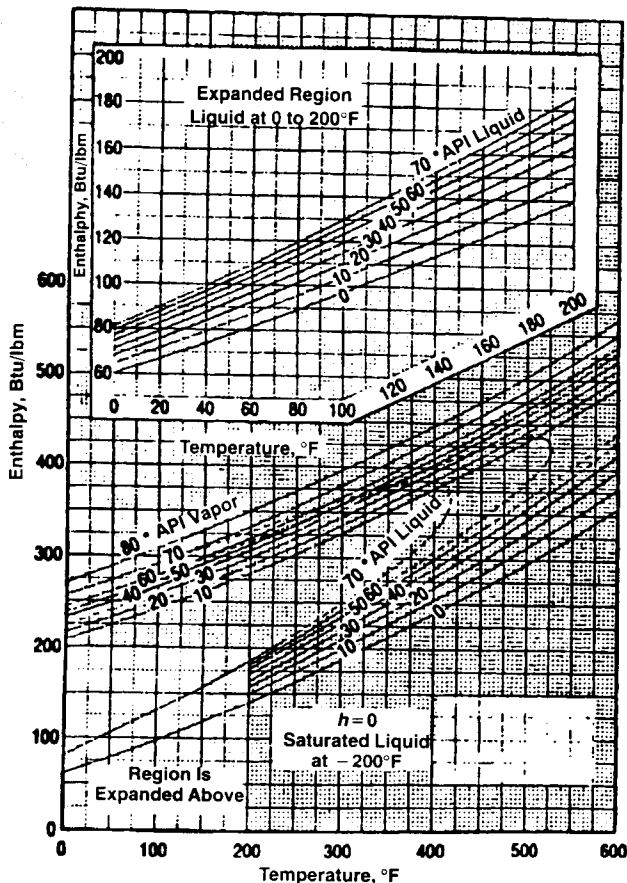


Fig. B-34—Enthalpy of petroleum fractions ($K_w = 11$, $T = 0$ to 600°F , after Kesler and Lee⁴⁷).

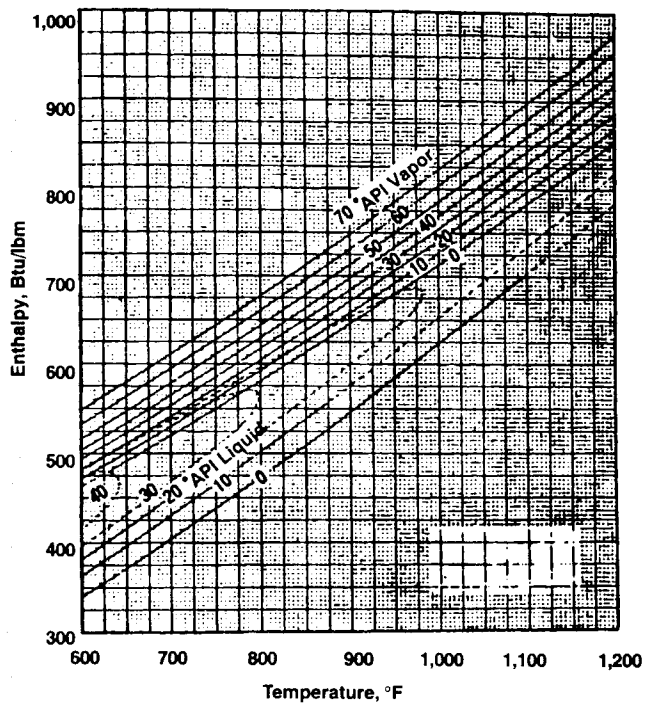


Fig. B-35—Enthalpy of petroleum fractions ($K_w = 11$, $T = 600$ to $1,200^\circ\text{F}$, after Kesler and Lee⁴⁷).

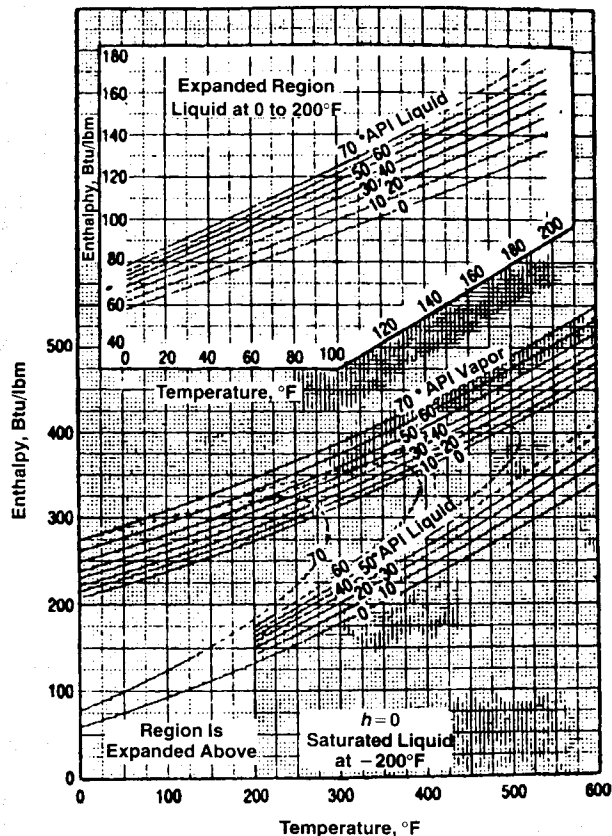


Fig. B-36—Enthalpy of petroleum fractions ($K_w = 11.8$, $T = 0$ to 600°F , after Kesler and Lee⁴⁷).

B.8.2 Water and Steam. Table B-5 presents the enthalpy of water and steam at the saturation pressure and temperature. The difference between these two quantities represents the heat required to convert water from liquid to its vapor (steam) and is called the latent heat of evaporation.

$$L_v = h_s - h_w \quad \dots \quad (\text{B-96})$$

TABLE B-5—ENTHALPY OF WATER AND STEAM AT SATURATED CONDITIONS⁵³

Temperature (°F)	Absolute Pressure (psia)	Enthalpy (Btu/lbm)		
		Liquid h_w	Vapor h_s	Latent Heat L_v (Btu/lbm)
101.76	1	69.72	1,105.2	1,035.5
150	3.716	117.87	1,125.7	1,007.8
162.25	5	130.13	1,130.8	1,000.7
193.21	10	161.17	1,143.3	982.1
200	11.525	167.99	1,145.8	977.8
212	14.696	180.07	1,150.4	970.3
250	29.82	218.48	1,163.8	945.3
300	67.01	269.60	1,179.7	910.1
327.83	100	298.43	1,187.3	888.9
350	134.62	321.64	1,192.6	871.0
358.43	150	330.53	1,194.4	863.9
381.82	200	355.40	1,198.7	843.3
400	247.25	374.97	1,201.2	826.2
400.97	250	376.04	1,201.4	825.4
417.33	300	393.85	1,203.2	809.3
420	308.82	396.78	1,203.5	806.7
431.71	350	409.70	1,204.4	794.7
440	381.59	418.91	1,204.8	785.9
460	466.97	441.42	1,205.0	763.6
467.00	500	449.40	1,204.9	755.5
480	566.12	464.37	1,204.2	739.8
486.21	600	471.59	1,203.6	732.0
500	680.80	487.80	1,202.0	714.2
520	812.68	511.9	1,198.4	686.5
540	962.80	536.6	1,193.3	656.7
544.56	1,000	542.4	1,191.9	649.5
560	1,133.4	562.2	1,186.3	624.1
580	1,326.1	588.9	1,177.0	588.1
596.20	1,500	611.4	1,167.7	556.3
600	1,543.2	616.8	1,165.2	548.4
620	1,787.0	646.5	1,150.2	503.7
635.78	2,000	671.7	1,135.2	463.5
640	2,060.3	678.7	1,130.7	452.0
660	2,366.2	714.4	1,104.9	390.5
680	2,708.4	757.2	1,067.2	310.0
695.37	3,000	802.6	1,019.3	216.7
700	3,094.1	823.9	995.6	171.7
705.34*	3,206.2*	910.3	910.3	0

* Critical properties.

Figs. B-47 and B-48 give the enthalpies of water and steam at saturation pressures and temperatures.

At temperatures higher than its boiling point, steam is said to be superheated. The additional enthalpy of superheated steam, above its saturation value as given in Table B-5, is found by multiplying the mean specific heat, \bar{C}_s , given in Fig. B-49, by the excess temperature above the saturation value, T_s . This product is called superheat.

$$\Delta h_s = \bar{C}_s(T - T_s), T \geq T_s \quad \dots \quad (\text{B-97})$$

Note that the mean specific heat of steam at atmospheric pressure over a temperature range indicated in Fig. B-49 is somewhat lower

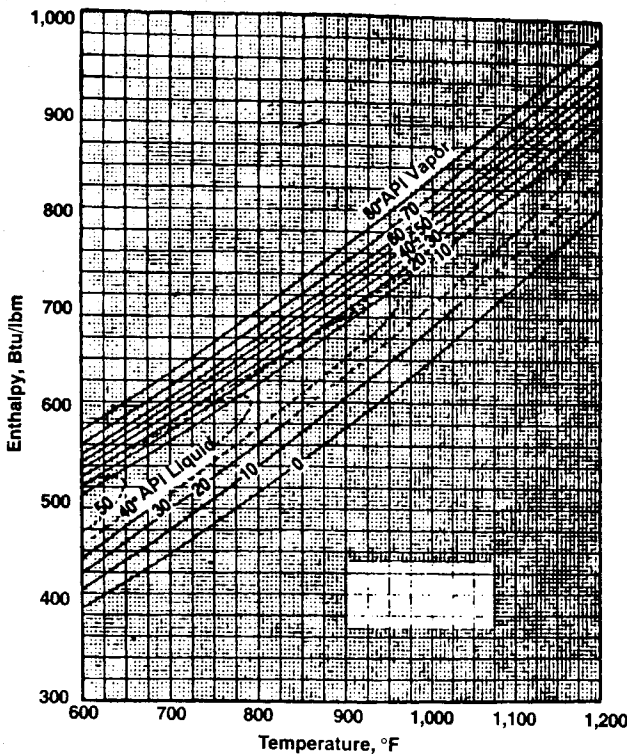


Fig. B-37—Enthalpy of petroleum fractions ($K_w = 11.8$, $T = 600$ to $1,200^{\circ}\text{F}$, after Kesler and Lee⁴⁷).

than the actual specific heat of superheated steam at a given temperature, shown in Fig. B-44. Fig. B-46 shows the specific heat of saturated water.

B.8.3 Reservoir Rocks and Minerals. Somerton⁵⁴ provided data in Figs. B-50 and B-51 and Table B-6 on the heat capacity of dry reservoir rocks. Fig. B-51 also shows the calculated heat capacity corresponding to the porosities of Samples 1 and 8 of Table B-7. Those calculated heat capacities are based on reported heat capaci-

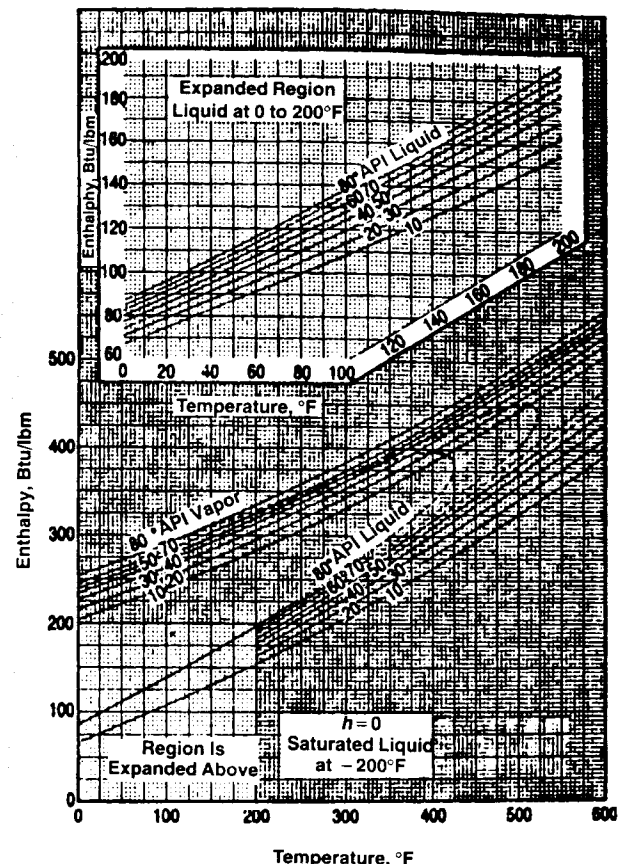


Fig. B-38—Enthalpy of petroleum fractions ($K_w = 12.5$, $T = 0$ to 600°F , after Kesler and Lee⁴⁷).

ties of pure quartz and pure calcite. They agree rather well with the experimental values of the two samples. This is an example of the rule that the heat capacity of a mixture is the mass average of that of its constituents. For fluid-saturated rocks, the heat capacity may be estimated from

$$C_f = \frac{M_f}{\rho_f} \quad \dots \dots \dots \quad (\text{B-98})$$

where M_f = effective volumetric heat capacity of the rock in terms of the rock and fluid properties. Prats prescribed this as

$$M_f = (1 - \phi)M_o + \phi S_o M_o + \phi S_w M_w$$

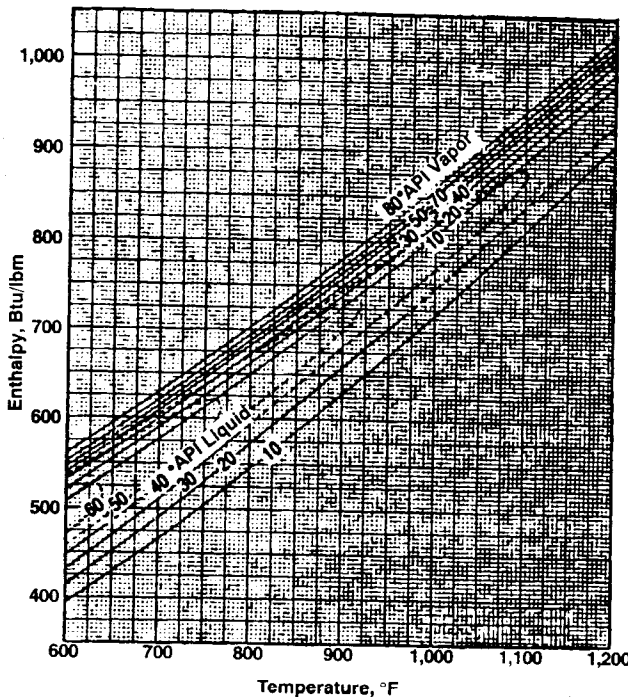


Fig. B-39—Enthalpy of petroleum fractions ($K_w = 12.5$, $T = 600$ to $1,200^{\circ}\text{F}$, after Kesler and Lee⁴⁷).

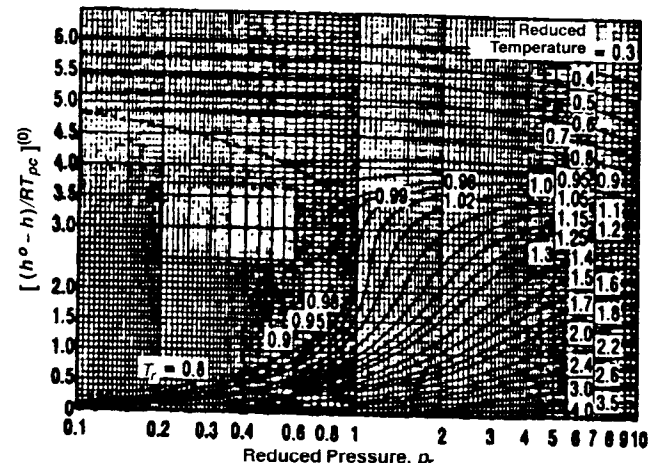


Fig. B-40—Enthalpy departure from zero-pressure simple-fluid function (after Kesler and Lee⁴⁷).

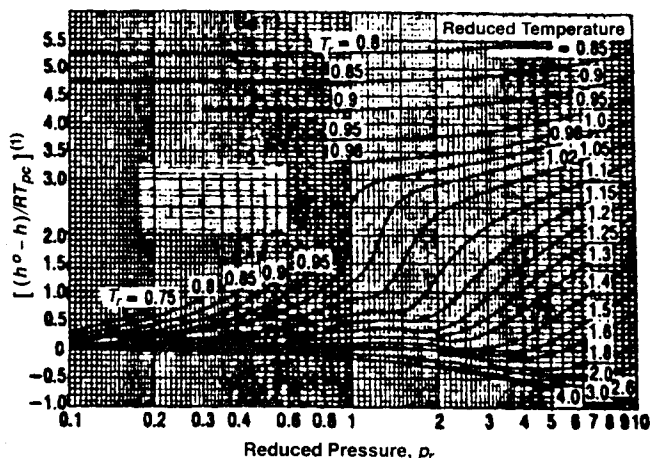


Fig. B-41—Enthalpy departure from zero-pressure-deviation function high-temperature part (from Kesler and Lee⁴⁷).

$$+ \phi S_g \left[f M_g + (1-f) \left(\frac{\rho_s L_v}{\Delta T} + \rho_w C_w \right) \right], \dots \dots \quad (B-99)$$

where ϕ = formation or rock porosity; S = saturation of fluid phases (oil, water and gas); M_o = isobaric volumetric heat capacity of solid; M_o = isobaric volumetric heat capacity of oil; M_w = isobaric volumetric heat capacity of water; M_g = isobaric volumetric heat capacity of gas; f = volume fraction of noncondensable gases in the vapor phase; ρ_s = steam density; L_v = latent heat of vaporization of water; C_w = isobaric heat capacity of water per unit mass; and ΔT = temperature change under isobaric condition. The average density, ρ_f , of the fluid-saturated rock in Eq. B-98 is the volumetric average of the densities of its constituents.

$$\rho_f = \rho_o(1-\phi) + \phi(S_o\rho_o + S_w\rho_w + S_g\rho_g), \dots \dots \quad (B-100)$$

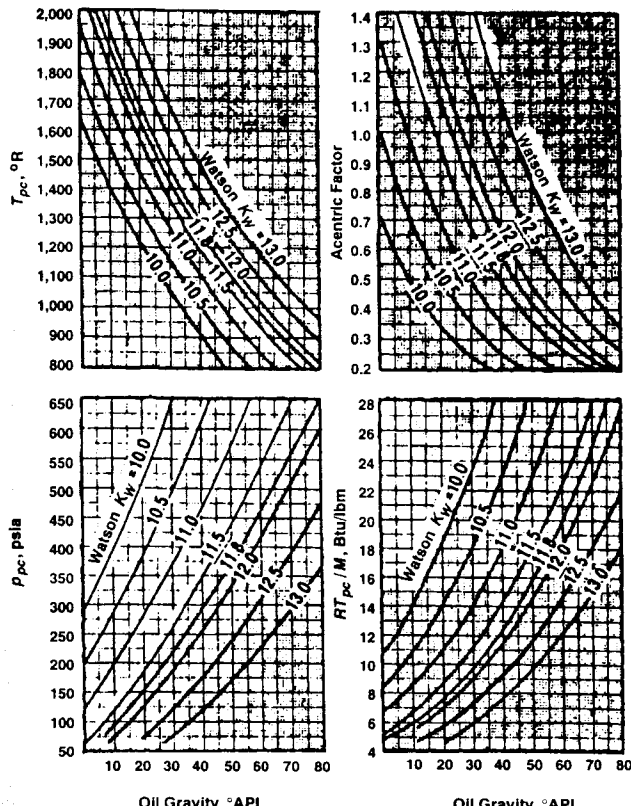


Fig. B-43— T_{pc} , p_{pc} , ω and R_{pc}/M as functions of oil gravity and Watson's characterization factor, K_w (after Kesler and Lee⁴⁷).

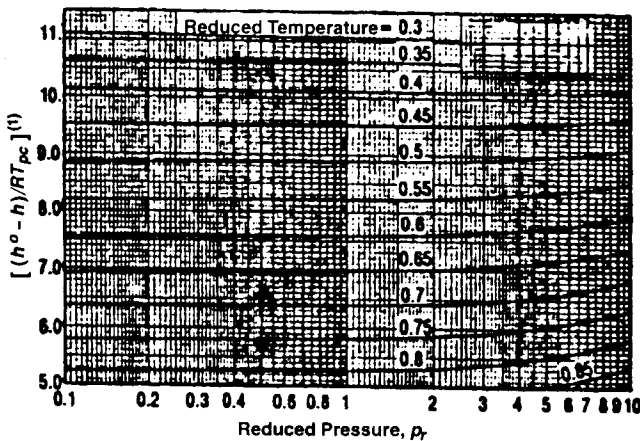


Fig. B-42—Enthalpy departure from zero-pressure-deviation function low-temperature part (after Kesler and Lee⁴⁷).

where ρ_o , ρ_o , ρ_w , and ρ_g = densities of the solid (rock), oil, water, and gas phases, respectively. The solid density, ρ_o , is the volumetric average density of the solid constituents of the rock matrix.⁵⁷⁻⁵⁹

Table B-6 gives the calculated heat capacities for the first eight samples in Table B-7, when those samples are saturated with methane or water at 620°F and several pressures between 14.7 and 3,000 psia. Note that the water is in the liquid state only at the highest pressure.

Helgeson⁵⁶ provides coefficients to calculate isobaric heat capacities, as a function of temperature, of several minerals, including calcite, dolomite, anhydrite, micas, and clays in cal/mol·°K. Touhoukian *et al.*⁶⁰ provide both tables and graphs of isobaric heat capacities in cal/g·°K for nonmetallic solids, including elements, oxides, sulfides, carbonates, sulfates, and other oxygen compounds.

Table B-8 provides thermophysical properties of selected materials.

B.9 Thermal Conductivity

Thermal conductivity is a property of substances that controls the rate of heat transfer by a conductive process.

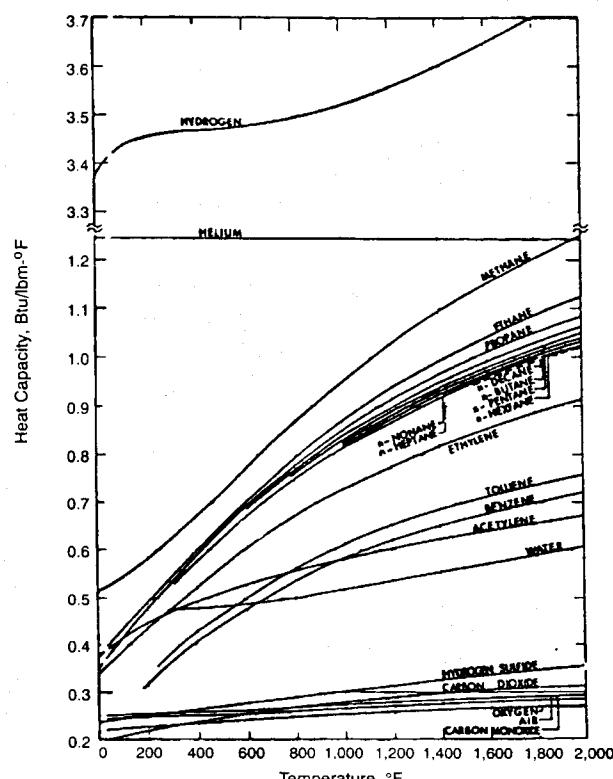


Fig. B-44—Heat capacity of gases at 1 atm (after Touhoukian *et al.*⁵¹).

TABLE B-6—CALCULATED HEAT CAPACITIES OF FLUID-SATURATED ROCKS⁵⁴
(heat capacity at 620°F and pressure in Btu/ft³·°F)

Sample	Rock	14.7 psia			500 psia			1,500 psia			3,000 psia	
		Dry	Methane	Water	Methane	Water	Methane	Water	Methane	Water	Methane	Water
1	Sandstone	34.0	34.0	34.0	34.1	34.1	34.3	34.9	34.6	45.9		
2	Sandstone	32.9	32.9	32.9	33.0	33.0	33.3	34.0	33.7	47.6		
3	Silty sand	35.6	35.6	35.6	35.7	35.7	36.0	36.5	36.3	49.1		
4	Silty sand	33.5	33.5	33.5	33.5	33.6	33.9	34.5	34.3	48.3		
5	Siltstone	32.0	32.0	32.0	32.1	32.1	32.5	33.2	32.9	48.7		
6	Siltstone	33.6	33.6	33.6	33.7	33.7	34.0	34.6	34.3	47.7		
7	Shale	39.6	39.6	39.6	39.6	39.6	39.7	40.0	39.9	40.1		
8	Limestone	35.4	35.4	35.4	35.5	35.5	35.7	36.2	36.0	46.8		

TABLE B-7—DESCRIPTION OF TEST SAMPLES⁵⁴

Sample	Rock	Description	Principal Minerals		
			Porosity (%)	Quartz (%)	Clay Mineral
1	Sandstone	Well consolidated, medium-coarse grain	0.196	80	Trace kaolinite
2	Sandstone	Poorly consolidated, medium-fine grain	0.273	40	Illite(?)
3	Silty sand	Poorly consolidated, poorly sorted	0.207	20	Kaolinite type
4	Silty sand	Medium hard, poorly sorted	0.225	20	Kaolinite type
5	Siltstone	Medium hard, broken	0.296	20	Kaolinite type
6	Siltstone	Hard	0.199	25	Illite
7	Shale	Hard, laminated	0.071	40	Illite/kaolinite
8	Limestone	Granular, uniform texture	0.186		
9	Sand	Unconsolidated, fine-grained	0.38	100	
10	Sand	Unconsolidated, coarse-grained	0.34	100	Calcium carbonate

B.9.1 Liquids. Thermal conductivities of saturated organic liquids decrease with increasing temperature. Plotted in Fig. B-52 are values for some pure organic liquids. For petroleum fractions and hydrocarbon mixtures, Cragoe⁶¹ proposes the relationship

$$\lambda_o = 1.62[1 - 3(T - 32)10^{-4}]/\gamma_o, \quad \dots \quad (B-101)$$

to estimate the thermal conductivity in Btu/D-ft·°F. For $0.78 < \gamma_o < 0.95$ and $32°F < T < 392°F$, Eq. B-101 gave "average and maximum errors of 12 and 39%."

Lenoir⁶² gives the ratio of two liquid thermal conductivities at the same temperature but different pressures as

$$(\lambda_1/\lambda_2) = (\varepsilon_1/\varepsilon_2), \quad \dots \quad (B-102)$$

where ε is given in Fig. B-53. As can be seen in that figure, values for organic liquids are not very sensitive to changes in pressure, except at low values of reduced pressure and high values of reduced temperature. Comparing measured values with predicted values, based on Lenoir's work⁶² shown in Fig. B-53, revealed an arithmetic deviation of 1.6% with a maximum deviation of 4.2%.

The thermal conductivity of saturated water, shown in Fig. B-52, is several times larger than that of pure hydrocarbons and exhibits a maximum at about 260°F.

B.9.2 Gases. Thermal conductivities of gases at atmospheric pressure are plotted vs. temperature in Figs. B-54 and B-55. Touhoukian *et al.*⁶⁰ reviewed methods to estimate the thermal conductivity of mixtures of gases, $\bar{\lambda}$, from those of constituents, λ_j , and suggest that the following relation be used "because of its simplicity and moderate reliability" for "approximate engineering calculations."

$$\bar{\lambda} = \frac{1}{2} \left\{ \sum_{j=1}^{n_c} y_j \lambda_j + \left[\sum_{j=1}^{n_c} \left(\frac{y_j}{\lambda_j} \right) \right]^{-1} \right\}, \quad \dots \quad (B-103)$$

where y_j = mole fraction of the j th gas component.

Lenoir and Comings⁶³ and Eckert and Drake⁶⁴ presented thermal conductivities of superheated steam vs. temperature at several values of pressure and for the saturated vapor.

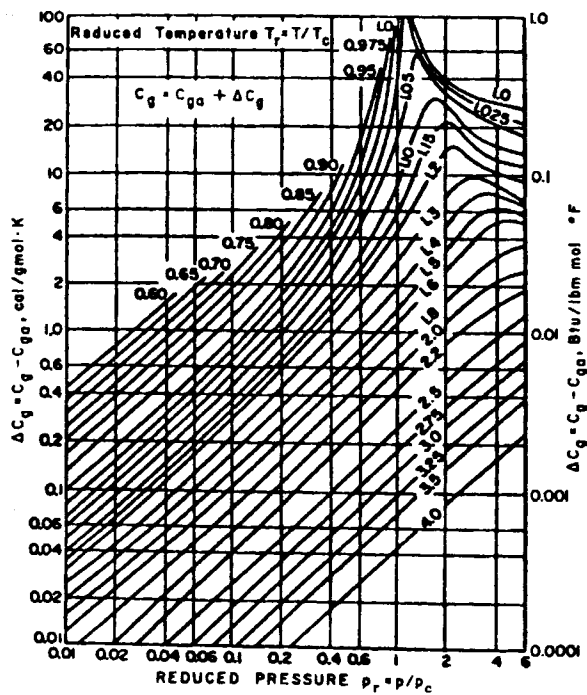


Fig. B-45—Pressure correction to the molar heat capacity of gases (after *Chemical Engineers' Handbook*⁶²).

TABLE B-8—THERMOPHYSICAL PROPERTIES OF SELECTED MATERIALS⁵

	Density ρ (lbm/ft ³)	Isobaric Heat Capacity C_p (Btu/lbm·°F)		Thermal Conductivity λ (Btu/D-ft·°F)			Thermal Diffusivity a (ft ² /D)
		At 68°F	At 68°F	At 68°F	At 212°F	At 1,112°F	
Metals and Alloys							
Aluminum, pure	169	0.214		2,830	2,860		87.96
Brass (70% Cu, 30% Zn)	532	0.092		1,500	1,800		31.73
Copper, pure	559	0.0915		5,350	5,260	4,900	104.5
Concrete	119 to 144	0.21		11 to 19			0.45 to 0.65
Iron							
Pure	493	0.108		1,000	940	550	18.8
Cast (C ~ 4%)	454	0.10		720			16.0
Wrought (C < 0.5%)	490	0.11		820	790	500	15.2
Lead, pure	710	0.031		480	463		22.2
Nickel							
Pure (99.9%)	556	0.1065		1,200	1,200		21.1
Impure (99.2%)	556	0.106		960	890	770	16.2
Steel, mild, 1% C	487	0.113		600	600	460	10.8
Stainless steel (18 Cr, 8 Ni)	488	0.11		230	240	310	4.13
Tin, pure	456	0.054		890	820		36.12

©1961 Prentice-Hall Inc.

B.9.3 Reservoir Rocks and Other Solids. Somerton *et al.*⁶⁶ and Anand *et al.*⁶⁸ have reported extensively on the thermal conductivity of reservoir rocks, including the effects of fluid and mineral content, particle size, temperature, and pressure. For unconsolidated quartzitic sands saturated with water and oil, the thermal conductivity at 125°F is given by

$$\lambda_f = 0.735 - 1.30\phi + 0.390\lambda_m \sqrt{S_w}, \quad \dots \quad (B-104)$$

where the thermal conductivity may be estimated from

$$\lambda_m = 4.45f_q + 1.65(1 - f_q), \quad \dots \quad (B-105)$$

for quartzitic sands unless the mineral thermal conductivity can be estimated from its composition. f is the fractional volume of quartz in the sand. Eqs. B-104 and B-105 are correlations based on samples having porosities between 0.28 and 0.37 and fluids and minerals

corresponding to those in Kern River oil sands. In these expressions, no distinction is made about the fluids other than the brine.

The effect of temperature is given by

$$\lambda_f(T) = \lambda_f - 1.28 \times 10^{-3}(T - 125)(\lambda_f - 0.82), \quad \dots \quad (B-106)$$

where λ_f is given by Eq. B-103, and the effect of pressure, which is generally minor, is estimated from

$$\Delta\lambda_f = \Delta p \times 10^{-5}(0.50\rho_b\phi + 5.75\phi - 0.37k^{0.10} + 0.12F), \quad \dots \quad (B-107)$$

where k = permeability in millidarcies, F = formation resistivity factor, and ρ_b = bulk density in grams per cubic centimeter. Values of $\Delta\lambda_f$ are added to the value of λ_f at the base pressure. The data points

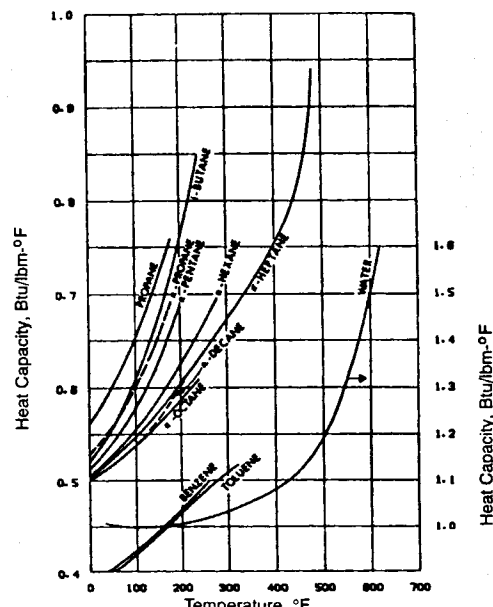


Fig. B-46—Heat capacity of saturated pure liquids (after Touloukian *et al.*⁵¹).

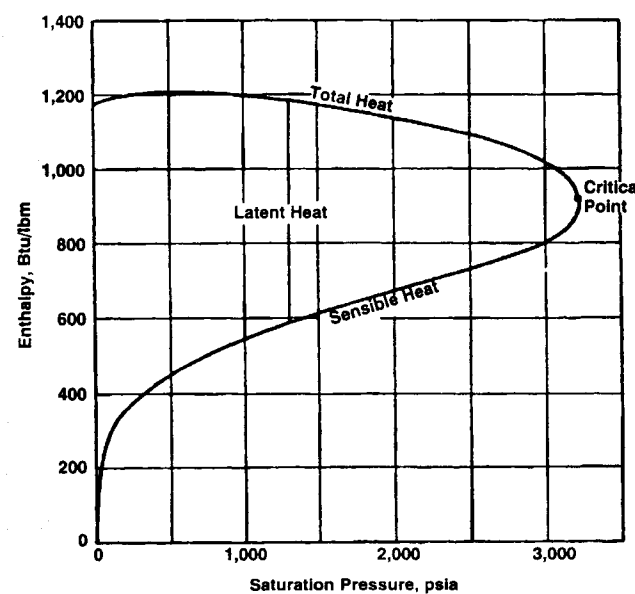


Fig. B-47—Enthalpies of water and steam as a function of the saturation pressure (reference temperature is 32°F).⁵³

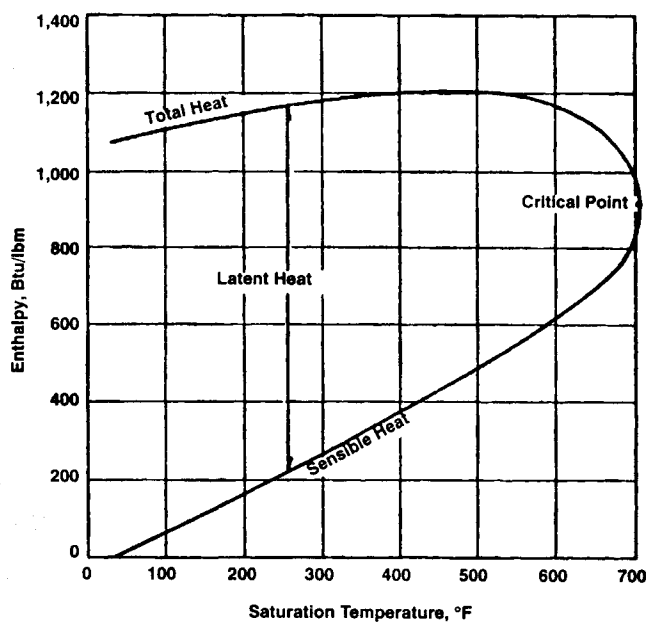


Fig. B-48—Enthalpies of water and steam as a function of the saturation temperatures (reference temperature is 32°F).⁵³

in Fig. B-56 show the typical effects of fluid content and porosity on the thermal conductivity of unconsolidated oil sands.

For consolidated sands, Anand *et al.*⁶⁸ give the relation

$$\frac{\lambda_{f,l}}{\lambda_{f,d}} = 1.0 + 0.3 \left(\frac{\lambda_l}{\lambda_a} - 1.0 \right)^{1/3} + 4.57 \left(\frac{\phi}{1 - \phi} \frac{\lambda_l}{\lambda_{f,d}} \right)^{0.48m} \left(\frac{\rho_{f,l}}{\rho_{f,d}} \right)^{-4.30} \quad \dots \dots \dots \quad (B-108)$$

for the thermal conductivities of sandstones at 68°F fully saturated with one liquid. In this equation, the subscript *f,l* refers to the reservoir rock at full liquid saturation, *f,d* refers to dry reservoir rock, *l* refers to liquid, *a* refers to air, and *m* is Archie's cementation factor.

The thermal conductivity of the dry consolidated sandstone at 68°F may be estimated from

$$\lambda_{f,d} = 0.340\rho_{f,d} - 3.20\phi + 0.530k^{0.10} + 0.0130F - 0.031. \quad \dots \dots \dots \quad (B-109)$$

The agreement between values of thermal conductivity reported in the literature and those calculated by Eq. B-108 is said to be with-

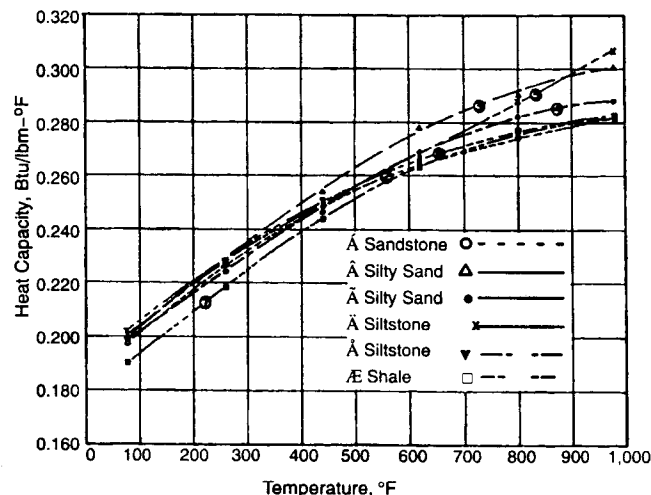


Fig. B-50—Heat capacities of some reservoir rocks (after Somerton⁵⁴).

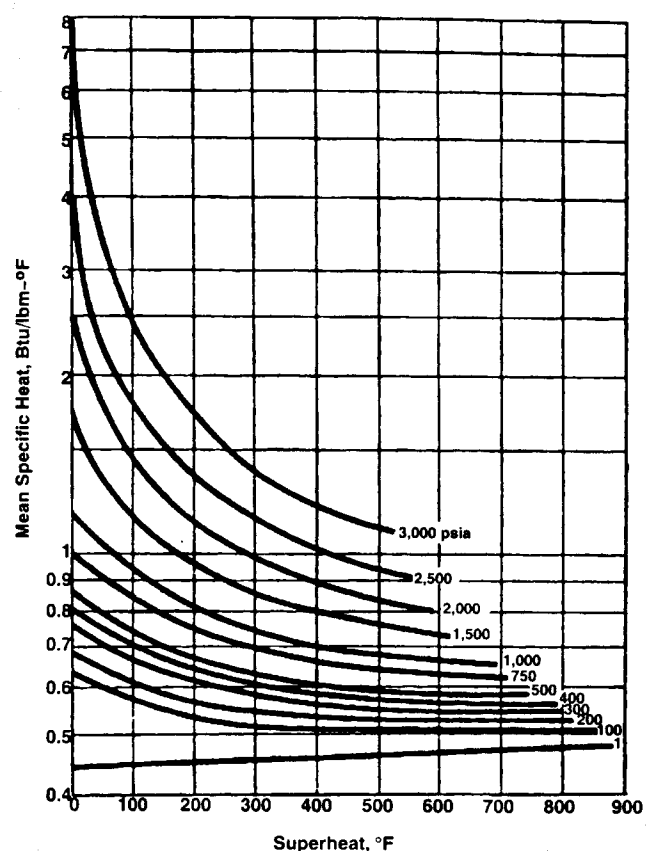


Fig. B-49—Mean specific heat of superheated steam. Heat added (Btu/lbm) = mean specific heat × superheat (°F).⁵³

in 15% for 85% of the values when the ratio $\lambda_{f,l}/\lambda_{f,d}$ is within the range of 1.20 to 2.30.

The effect of temperature on the thermal conductivity of liquid-saturated sandstones is given by

$$\lambda_{f,l}(T) = \lambda_{f,l} - 0.71 \times 10^{-3}(T - 528)(\lambda_{f,l} - 0.80) \times \left[\lambda_{f,l}(T \times 10^{-3})^{-0.55\lambda_{f,l}} + 0.74 \right], \quad \dots \dots \dots \quad (B-110)$$

where $\lambda_{f,l}$ is given by Eq. B-108, and *T* is in °R. The effect of stress on the thermal conductivity of consolidated sandstones is to increase the thermal conductivity value by "1 to 2% per 17,000 psi increase in effective stress."⁶⁸

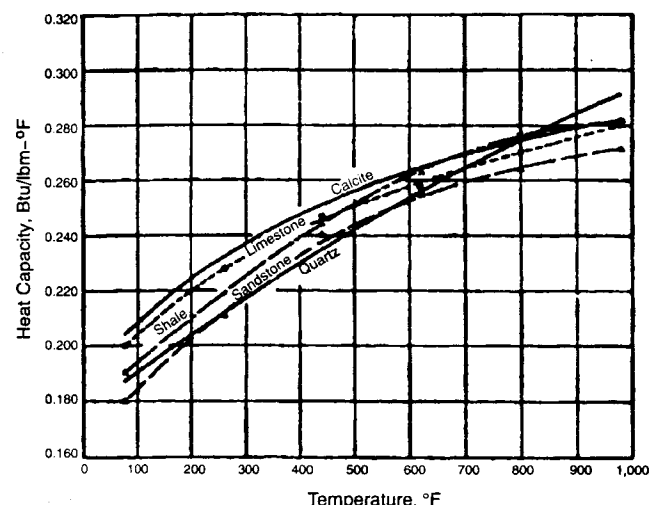


Fig. B-51—Comparison of calculated heat capacities of reservoir rocks and principal constituents (after Somerton⁵⁴).

TABLE B-9—THERMAL CHARACTERISTICS OF TEST SAMPLES⁷⁰

Sample	Bulk Density (lbm/ft ³)		Thermal Diffusivity Unsteady State (ft ² /D at 200°F)		Thermal Diffusivity Steady State (ft ² /D)		Thermal Conductivity Unsteady State (Btu/D·ft·°F at 200°F)		Thermal Reactions
	Initial	Repeat	Initial	Repeat	90°F	275°F	Initial	Repeat	
Bandera sandstone	134.2	131.8	0.816	0.660	0.895	0.660	2.16	16.6	$\alpha-\beta$ quartz 1,015°F, clay
Berea sandstone	134.8	126.0	0.821	0.581	0.948	0.665	21.8	15.7	$\alpha-\beta$ quartz 1,020°F, clay
Boise sandstone	118.9	116.0	0.833	0.492	0.694	0.624	19.5	11.8	$\alpha-\beta$ quartz 1,040°F, clay
Limestone	140.2	78.5	0.780	0.497	0.780	0.643	21.7	13.9	$\text{CaCO}_3\text{-CaO}$ $+\text{CO}_2, 1,530^\circ\text{F}$
CaO (after reaction)	78.5	—	0.924	—	—	—	—	—	
Shale	137.1	128.2	0.936	0.516	0.950	0.698	26.2	13.9	$\alpha-\beta$ quartz 1,045°F, clay
Rock salt	135.0	128.0	2.96	—	1.7	1.5	8.30	8.30	Dehydration, 864°F
Tuffaceous sandstone	115.3	107.2	0.444	—	0.504	—	9.55	9.55	$\alpha-\beta$ quartz 1,035°F

TABLE B-10—DESCRIPTION OF SAMPLES USED IN TABLE B-11⁷⁰

Sample	Description	Principal Minerals			
		Quartz	Feldspar	Other	Porosity
Bandera sandstone	Well consolidated, very fine grained	35	25	Calcite, clay	0.200
Berea sandstone	Well consolidated, fine grained	65	10	Calcite, sericite, clay	0.205
Boise sandstone	Well consolidated, medium grained	40	35	Clay, sericite	0.265
Limestone	Small vugs, medium-coarse grained	—	—	Ca CO_3	0.186
Shale	Hard, laminated, very fine grained	50	—	Clay, iron oxides, biotite	0.170
Rock salt	Crystalline	—	—	Halite	0.010
Tuffaceous sandstone	Well consolidated, large to very fine grained	10	60	Clay, pumice lapilli, calcite	0.280

Fig. B-57 shows the measured thermal conductivity of Berea sandstone vs. temperature when the sample is saturated with four different fluids. Thermal conductivities of reservoir rocks containing several fluids are treated differently. Average values may be estimated from figures, such as Fig. B-57, or from the values obtained with the equations given previously. Such averages must consider the relative volumes of the fluids present in the reservoir rock. According to Anand *et al.*,⁶⁸ the conductivity of the wetting phase has the dominant effect. The liquid conductivity used in Eq. B-107 should be biased accordingly.

Table B-9 presents data on the thermal conductivity of several dry consolidated rock samples, calculated from thermal diffusivities and densities measured at 200°F. Repeat values were generally lower because of reactions that occurred in the samples as they were heated to temperatures of 1,800°F. Thus, the temperature history of a sample may have a significant effect on thermal properties. Fig. B-58 shows the effect of temperature on the thermal conductivities. Tables B-9 and B-10 give initial sample properties.

In the absence of specific data, it appears that Eq. B-108 could be used, together with thermal conductivities of dry saturated rocks given in Table B-9 and Fig. B-58, to estimate thermal conductivities of saturated consolidated rocks other than sandstones. Errors in this approach should be recognized as being potentially significant. The following approximate averaging procedure is useful to estimate the value of the thermal conductivity of a porous medium containing water, oil, and gas when the thermal conductivity of the brine-saturated sample is available.

$$\lambda_f = \lambda_{f,w} \left(\frac{\lambda_o}{\lambda_{f,w}} \right)^{\phi S_o} \left(\frac{\lambda_g}{\lambda_{f,w}} \right)^{\phi S_g} \quad \dots \quad (\text{B-111})$$

where the value of $\lambda_{f,w}$ may be estimated from Eq. B-108 or consolidated samples, and λ_o and λ_g are the thermal conductivities of the oil and gas phases, respectively. A similar volumetrically weighted geometric mean may be used to approximate any average value when no better procedure is available.

Table B-11 gives thermal conductivities of selected minerals found in reservoir rocks. Table B-8 reported the thermal conductivities of some metallic and nonmetallic materials. Fluid flow increases the apparent thermal conductivity of porous rocks.

B.9.4 Thermal Diffusivity. Thermal diffusivities are related to the thermal conductivity and volumetric heat capacity by the relationship

$$\alpha = \lambda/M \quad \dots \quad (\text{B-112})$$

Values calculated in this manner are quite adequate for engineering applications. Because of difficulties in the measurement techniques, calculated values actually may be better than directly measured values.

Table B-9 presents information on the thermal diffusivities of several dry consolidated rock samples at 200°F, measured by use of two different techniques. Repeat measurements were always lower because of reactions that occurred as the samples were heated to temperatures of 1,800°F. Fig. B-59 shows the effect of temperature on the thermal diffusivity of dry consolidated rocks. Tables B-9 and B-10 give the initial sample properties.

B.9.5 Coefficients of Heat Transfer. For condensing steam, the film coefficient of heat transfer, h_f , is large and generally adequate.⁶⁹

$$h_f = 48,000 \text{ Btu}/\text{ft}^2\cdot\text{D}\cdot^\circ\text{F}, \text{ when } N_{\text{Re}} > 2,100, \quad \dots \quad (\text{B-113})$$

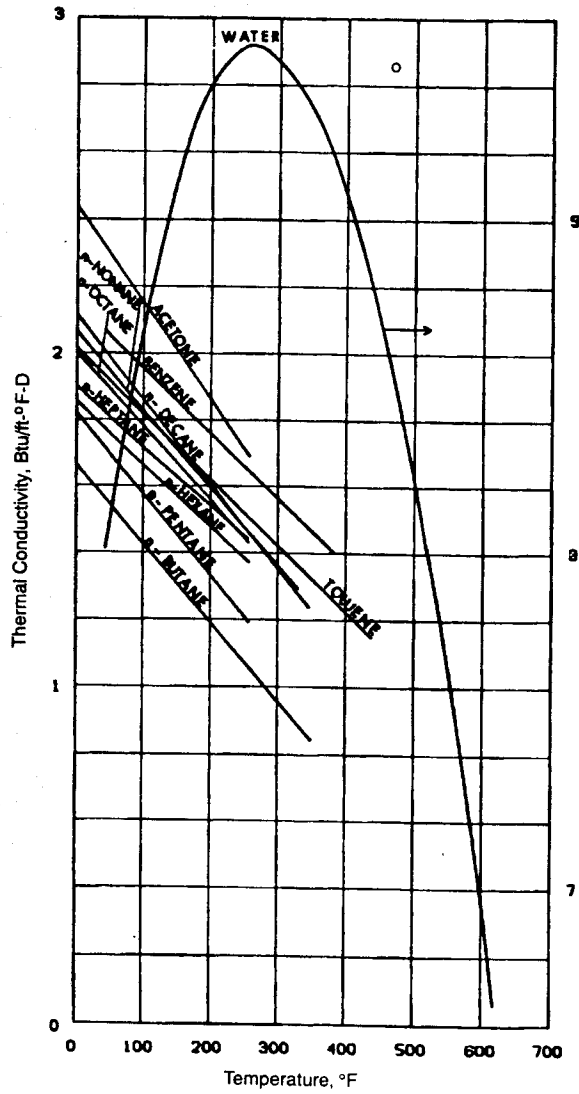


Fig. B-52—Thermal conductivity of saturated pure liquids (after Touloukian *et al.*⁶⁰).

where the Reynolds number, N_{Re} , is defined as

$$N_{Re} = \left[\frac{\pi}{2} (0.0616) \right] \frac{2i_w \rho_{w,sc}}{\pi \mu_s r_i}, \quad (B-114)$$

where i_w = steam-equivalent injection rate as condensed water in barrels per day, $\rho_{w,sc}$ = density of water at standard conditions (62.4 lbm/ft³), μ_s = viscosity of steam at the injection temperature in centipoise, and r_i = inner radius of the conduit in feet.

Because the viscosity of saturated steam over typical temperature ranges is approximately 0.018 cp, turbulence prevails ($N_{Re} > 2,100$) whenever i_w is greater than $9.85r_i$.

For hot water, the film coefficient of heat transfer is found from⁷⁰

$$h_f = 0.0115 \frac{\lambda_w}{r_i} N_{Re}^{0.8} N_{Pr}^{0.4}, \quad (B-115)$$

when N_{Re} exceeds 2,100. N_{Re} also is given by Eq. B-114; λ_w is the thermal conductivity of water in Btu/ft·D·°F. The dimensionless Prandtl number is

$$N_{Pr} = 58.1(C\mu/\lambda)_w, \quad (B-116)$$

where C_w = specific heat of water at constant pressure in Btu/lbm·°F and μ_w = viscosity of the hot water in centipoise. In the temperature range of 350 to 600°F, the value of factors representing the water properties $[(\lambda_w/\mu_w^{0.8})N_{Pr}^{0.4}]$ does not vary by more than ± 10%. Accordingly, the approximate film coefficient is derived as

$$h_f = 1.6i_w^{0.8} r_i^{-1.8}, \quad (B-117)$$

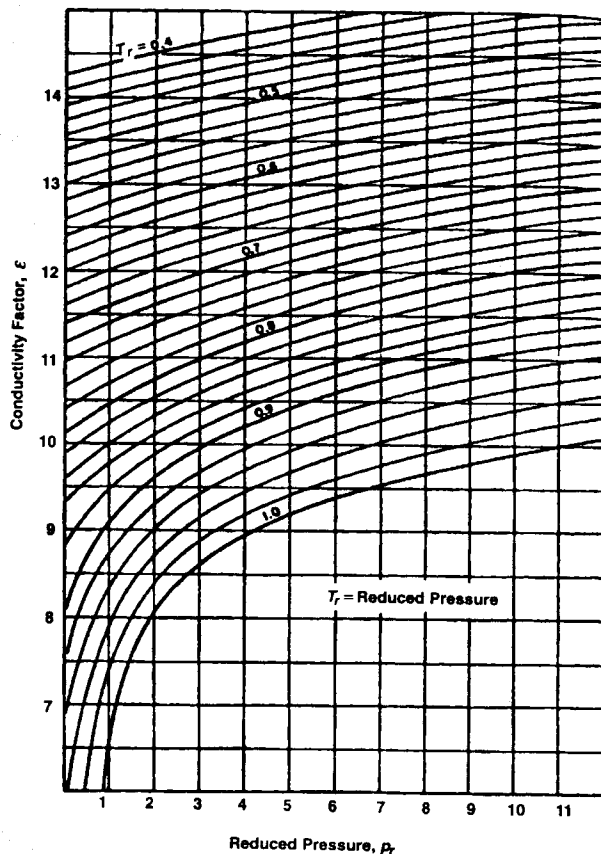


Fig. B-53—Generalized chart for liquid thermal conductivities and effect of pressure (after Lenoir⁶²).

TABLE B-11—THERMAL CONDUCTIVITY OF ROCK-FORMING NATURAL MINERALS⁵

Mineral	Density (lbm/ft ³)	Thermal Conductivity (Btu/ft·°F·D)
Calcite	169.9	49.8
Dolomite	178.4	76.35
Siderite	237.9	41.7
Aragonite	176.5	31.0
Anhydrite	185.9	65.97
Gypsum		17.4
Halite		84.7
Quartz	165.2	106.6
Chert	159.8	51.4
Pyrite	306.8	266.2
Hornblende	198.7	38.9
Albite	163.8	29.7
Microcline	159.7	34.2
Orthoclase	161.3	32.1
Kaolinite		38**
Illite	181.3	30.49
Montmorillonite	176.6	112.8
Chlorite	171.8	71.36
Biotite	186.1	28.0
Muscovite	178.1	32.2

*Except for kaolinite, all data are from Horai⁶⁵ and were obtained by use of naturally occurring minerals at room temperatures and pressures.

**Value used by Somerton *et al.*⁶⁶

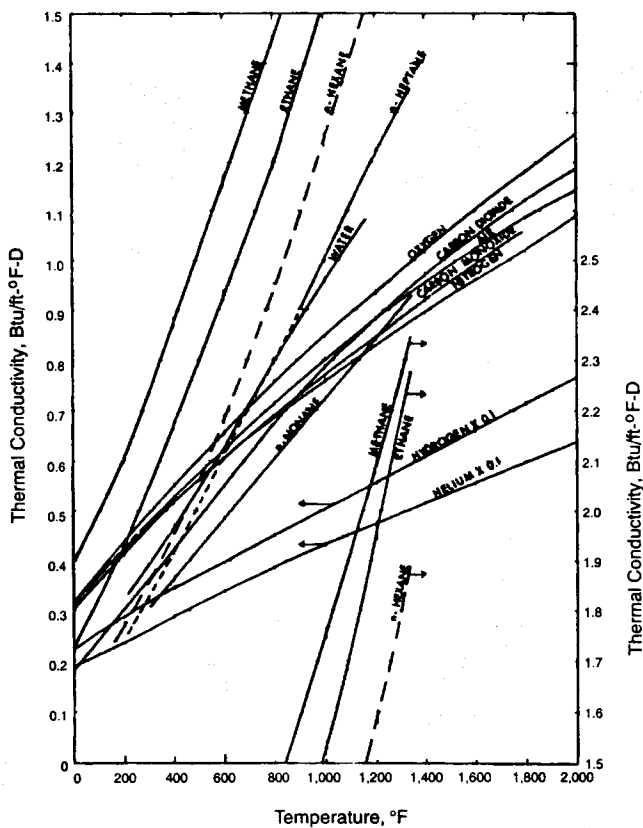


Fig. B-54—Thermal conductivities of gases at 1 atm (after Toulioukian *et al.*⁶⁰).

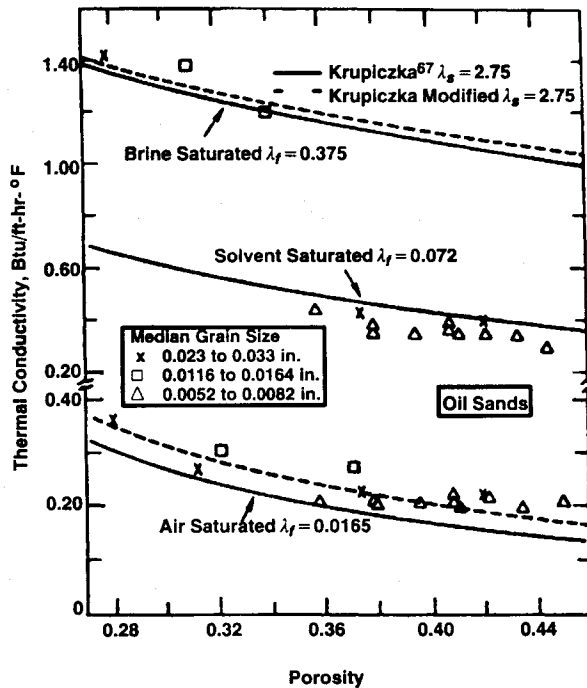


Fig. B-56—Thermal conductivity of unconsolidated oil sands (after Somerton *et al.*⁶⁶).

when $350^{\circ}\text{F} < T < 600^{\circ}\text{F}$, $i_{w,sc} > r_i$, and the subscript sc refers to standard conditions. Fig. B-60 shows a plot of the results calculated from Eq. B-117.

For hot gases, the film coefficient is found by evaluating Eq. B-115 for gas properties. For gases, it generally is found that $N_{Pr}^{0.4} = 0.92 \pm 0.07$ and the Reynolds number, including the conversion factor associated with the oilfield units for gas, is given by

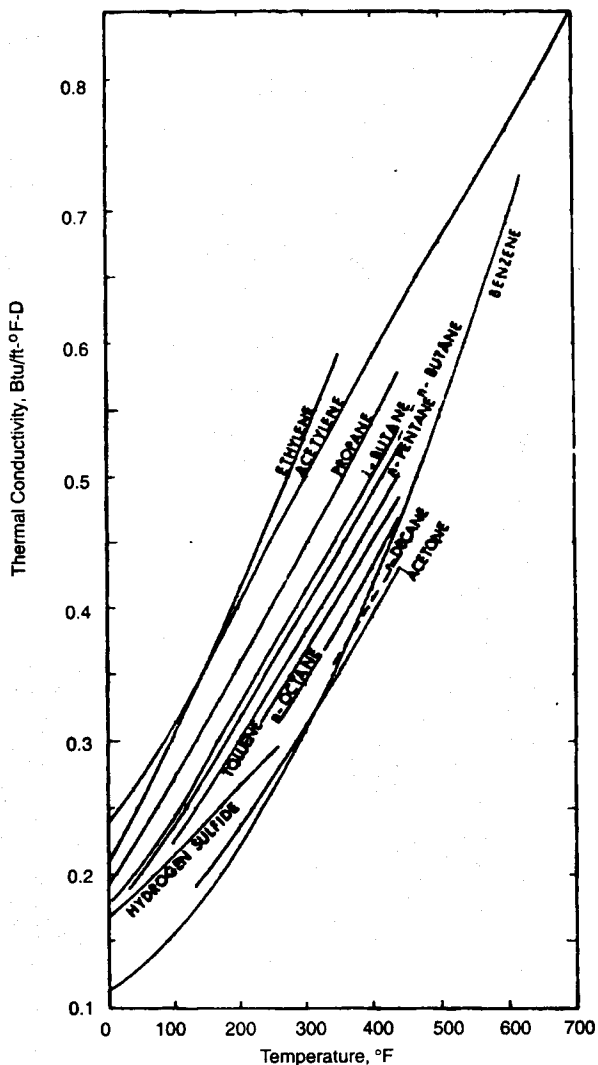


Fig. B-55—Thermal conductivities of gases at 1 atm (after Toulioukian *et al.*⁶⁰).

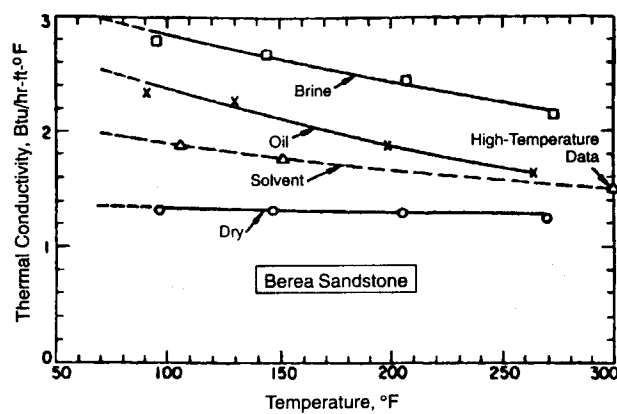


Fig. B-57—Thermal conductivity of Berea sandstone—effects of temperature and fluid saturant (after Anand *et al.*⁶⁸).

$$N_{Re} = [\pi(0.01096)/2] \frac{2}{\pi} \frac{w_g}{\mu_g r_i} \quad \dots \dots \dots \quad (\text{B-118})$$

Accordingly, the film coefficient is given by

$$h_f \approx 2.86 \times 10^{-4} \frac{\lambda_g}{r_i} \left(\frac{w_g}{\mu_g r_i} \right)^{0.8} \quad \dots \dots \dots \quad (\text{B-119})$$

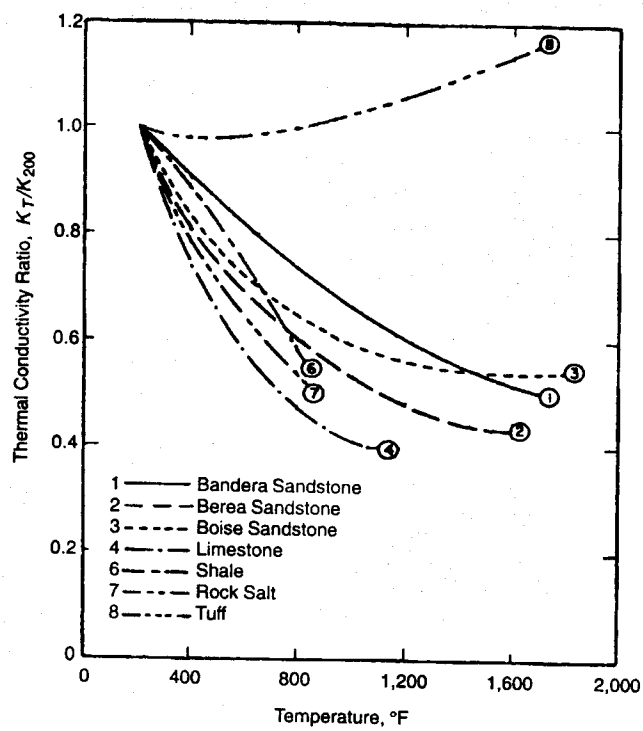


Fig. B-58—Thermal conductivity relative to that at 200°F—samples subjected to increasing temperatures (after Somerton and Boozer⁷⁰).

when $w_g > 192\mu_g r_i$ and $w_g = i\rho$, 10³ lbm/D; i = injection rate, Mscf/D; ρ = density, lbm/ft³; μ_g = viscosity, cp; λ_g = thermal conductivity, Btu/ft-D-°F; and r_i = inner radius of the conduit, ft.

Fig. B-61 shows the values of h_f for hot-gas injection obtained from Eq. B-119.

Values of h_d . Values of the coefficient of heat transfer caused by deposits of scale and dirt, h_d , seldom are known with any degree of confidence. Often values are specific to the project and seldom available unless measurements are made. McAdams⁶⁹ used a typical value of 48,000 Btu/ft²-D-°F. This value is recommended in the absence of better information. In injection and production lines, where low heat losses are desired, a significant scale deposit between pipe and insulation is an asset, because it results in a relatively high resistance to heat flow. A scale deposit on the inside wall of the pipe also would be an asset if there were no danger of the deposit

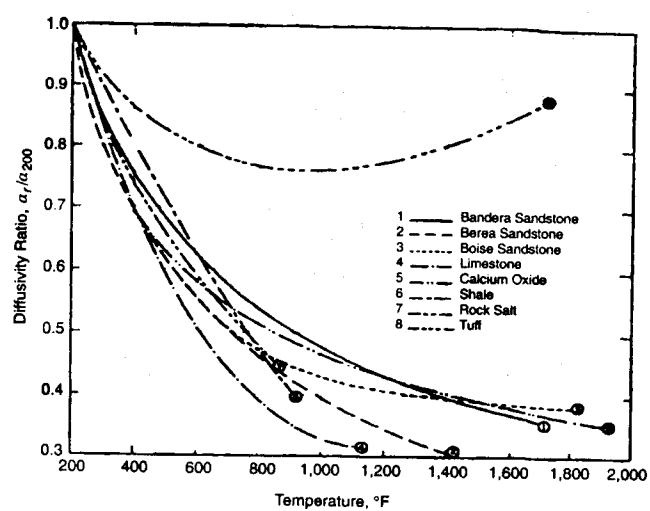


Fig. B-59—Thermal diffusivity relative to that at 200°F—samples subjected to increasing temperatures (after Somerton and Boozer⁷⁰).

being dislodged, thus possibly plugging the injection wellbore or other parts of the flow system.

Values of h_{fc} . For surface injection lines exposed to winds, McAdams⁶⁹ gave the coefficient of heat transfer caused by forced convection (air currents) at the outer surface of a conduit, h_{fc} , as

$$h_{fc} = \frac{0.12\lambda_a}{r_e} N_{Re}^{0.6}, \quad \dots \dots \dots \quad (B-120)$$

for $1,000 < N_{Re} < 50,000$, where λ_a = thermal conductivity of air, Btu/ft-D-°F; r_e = external radius of the conduit exposed to air, ft; $N_{Re} = [1/2(4,364)](2r_e v_w \rho_{a,sc}/\mu_a)$; v_w = wind velocity normal to the pipe, mile/hr; $\rho_{a,sc}$ = density of air, lbm/ft³; and μ_a = viscosity of air, cp.

For the surface temperatures at r_e of about 200°F, McAdams⁶⁹ gave the approximate film coefficient as

$$h_{fc} = \frac{18}{r_e} (r_e, v_w)^{0.6}, \quad \dots \dots \dots \quad (B-121)$$

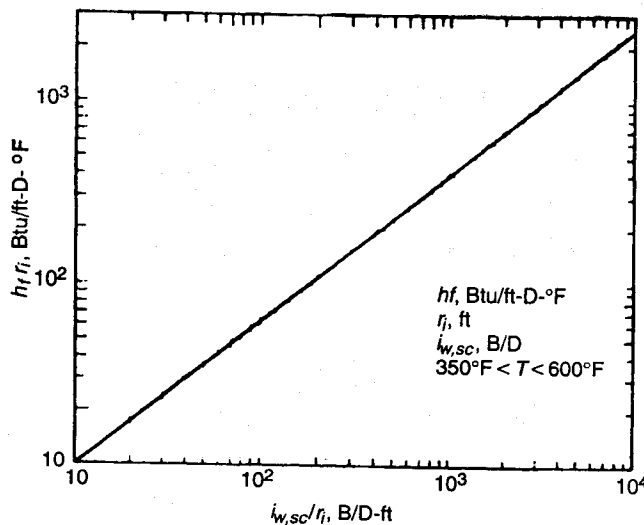


Fig. B-60—Correlation to estimate film coefficient of heat transfer for water.⁵

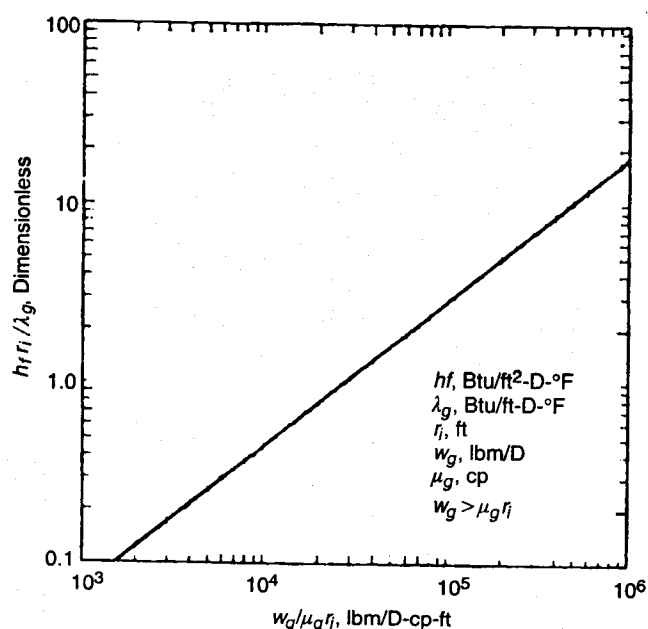


Fig. B-61—Correlation to estimate film coefficient of heat transfer for gas flow at high velocities.⁵

when the given units are used. Although strictly speaking Eqs. B-119 and B-120 are valid only for wind velocities that are normal to the pipes, they generally are applied irrespective of wind direction because there is no easy way to correct for differences in the wind direction. Radiation effects may be important for uninsulated exposed pipes carrying high-temperature fluids. McAdams,⁶⁹ Willhite,⁷¹ and Allen and Roberts⁷² have provided additional data on radiation effects.

References

1. Matthews, C.S. and Russell, D.G.: *Pressure Buildup and Flow Tests in Wells*, Monograph Series, SPE, Richardson, Texas (1967) 1.
2. Craig, F.F. Jr.: *The Reservoir Engineering Aspects of Waterflooding*, Monograph Series, SPE, Richardson, Texas (1971) 3.
3. Earlougher, R.C. Jr.: *Advances in Well Test Analysis*, Monograph Series, SPE, Richardson, Texas (1977) 5.
4. Farouq Ali, S.M.: *Oil Recovery by Steam Injection*, Producers Publishing Co., Inc., Bradford, Pennsylvania (1970).
5. Prats, M.: *Thermal Recovery*, Monograph Series, SPE, Richardson, Texas (1982) 7.
6. *Engineering Data Book*, ninth edition, Gas Processors Suppliers Assn., Tulsa, Oklahoma (1972) Sec. 16.
7. Edminster, W.C.: *Applied Hydrocarbon Thermodynamics*, Gulf Publishing Co., Houston (1961).
8. Trube, A.S.: "Compressibility of Undersaturated Hydrocarbon Reservoir Fluids," *Trans., AIME* (1957) 210, 341.
9. Standard 2500, *Measuring, Sampling, and Testing Crude Oil*, API, Dallas; reproduced in *Petroleum Production Handbook*, McGraw-Hill Book Co. Inc., New York City (1962) 1, Chap. 16.
10. Brown, G. et al.: "Natural Gasoline and the Volatile Hydrocarbons," Natural Gasoline Assn. of America, Tulsa, Oklahoma (1948).
11. Standing, M.B. and Katz, D.L.: "Density of Natural Gases," *Trans., AIME* (1942) 146, 140.
12. Lasater, J.A.: "Bubblepoint Pressure Correlation," *Trans., AIME* (1958) 213, 379.
13. Vazquez, M. and Beggs, H.D.: "Correlations for Fluid Physical Property Prediction," *JPT* (June 1980) 968; *Trans., AIME*, 269.
14. Glasø, Ø.: "Generalized Pressure-Volume-Temperature Correlations," *JPT* (May 1980) 785; *Trans., AIME*, 269.
15. Al-Marhoun, M.A.: "PVT Correlation for Middle East Crude Oils," *JPT* (May 1988) 650; *Trans., AIME*, 285.
16. Kartootmodjo, T. and Schmidt, Z.: "New Correlations for Crude Oil Physical Properties," paper SPE 23556 available from SPE, Richardson, Texas (June 1991).
17. Standing, M.B.: "A Pressure-Volume-Temperature Correlation for Mixtures of California Oils and Gases," *Drill. & Prod. Pract.* (1957) 275.
18. Sutton, R.P. and Farshad, F.: "Evaluation of Empirically Derived PVT Properties for Gulf of Mexico Crude Oils," *SPERE* (February 1990) 79.
19. Ahmed, T.H.: *Hydrocarbon Phase Behavior*, Gulf Publishing Co., Houston (1989).
20. Beal, C.: "The Viscosity of Air, Water, Natural Gas, Crude Oils and Its Associated Gases at Oil Field Temperatures and Pressures," *Trans., AIME* (1946) 165, 94.
21. Standing, M.B.: *Volumetric and Phase Behavior of Oil Field Hydrocarbon Systems*, ninth edition, SPE, Richardson, Texas (1981).
22. Beggs, H.D. and Robinson, J.R.: "Estimating the Viscosity of Crude Oil Systems," *JPT* (September 1975) 1140.
23. Baker, O. and Swerdloff, W.: "Finding Surface Tension of Hydrocarbon Liquids," *Oil & Gas J.* (2 January 1956) 125.
24. Reid, R.C., Prausnitz, J.N., and Poling, B.E.: *The Properties of Gases and Liquids*, fourth edition, McGraw-Hill Book Co. Inc., New York City (1987).
25. Weintraub, C. and Katz, D.L.: "Surface Tension of Methane-Propane Mixtures," *Ind. Eng. Chem.* (1943) 25, 35.
26. Katz, D.L. et al.: *Handbook of Natural Gas Engineering*, McGraw-Hill Book Co. Inc., New York City (1959).
27. McCain, W.D. Jr.: *The Properties of Petroleum Fluids*, Petroleum Publishing Co., Tulsa, Oklahoma (1973).
28. Culberson, O.L. and McKetta, J.J. Jr.: "Phase Equilibria in Hydrocarbon-Water Systems: III—Solubility of Methane in Water at Pressures to 10,000 psia," *Trans., AIME* (1951) 192, 223.
29. Adamson, D.K. et al.: "The Impact of Hurricanes on Technical Conferences and Exhibitions," Keynote Address presented at the 1998 SPE Annual Technical Conference and Exhibition, New Orleans, 27–30 September.
30. Gould, T.L.: "Vertical Two Phase Steam-Water Flow in Geothermal Wells," *JPT* (August 1974) 833.
31. Dodson, C.R. and Standing, M.B.: "Pressure-Volume-Temperature and Solubility Relations for Natural Gas Water Mixtures," *Drill. & Prod. Pract.* (1944) 173.
32. Meehan, D.N.: "A Correlation for Water Compressibility," *Pet. Eng. Intl.* (November 1980) 125.
33. Numbere, D., Brigham, W., and Standing, M.B.: *Correlations for Physical Properties of Petroleum Reservoir Brines*, Petroleum Research Inst., Stanford U., Palo Alto, California (November 1977) 17.
34. van Wingen, N.: *Recovery of Oil in the United States*, API, New York City (1950) 127.
35. Frick, T.C.: *Petroleum Production Handbook*, SPE, Richardson, Texas (1962) II.
36. Hocott, C.R.: "Interfacial Tension Between Water and Oil Under Reservoir Conditions," *Trans., AIME* (1939) 132, 184.
37. Hough, E.W., Rzasa, M.J., and Wood, B.B.: "Interfacial Tensions at Reservoir Pressures and Temperatures; Apparatus and the Water-Methane System," *Trans., AIME* (1951) 192, 57.
38. Stewart, W.F., Burkhard, S.F., and Voo, D.: "Prediction of Pseudo-Critical Parameters for Mixtures," paper presented at the 1959 AIChE Meeting, Kansas City, Missouri.
39. Dranchuk, P.M. and Abu-Kassem, J.H.: "Calculation of Z-Factors for Natural Gases Using Equations-of-State," *J. Cdn. Pet. Tech.* (July–September 1975) 14, 34.
40. Wichert, E. and Aziz, K.: "Calculation of Z's for Sour Gases," *Hydrocarbon Processing* (May 1972) 119.
41. Carr, N.L., Kobayashi, R., and Burrows, D.B.: "Viscosity of Hydrocarbon Gases Under Pressure," *Trans., AIME* (1954) 201, 264.
42. Lee, A.L., Gonzalez, M.H., and Eakin, B.E.: "The Viscosity of Natural Gases," *JPT* (August 1966) 997; *Trans., AIME*, 237.
43. Hankinson, R.W., Thomas, L.K., and Phillips, K.A.: "Predict Natural Gas Properties," *Hydrocarbon Processing* (April 1969) 106.
44. Trube, A.S., "Compressibility of Natural Gases," *Trans., AIME* (1957) 210, 355.
45. Newman, G.H.: "Pore-Volume Compressibility of Consolidated, Frangible, and Unconsolidated Reservoir Rocks Under Hydrostatic Loading," *JPT* (February 1973) 129.
46. Moses, P.L.: "Engineering Applications of Phase Behavior of Crude Oil and Condensate System," *JPT* (July 1986) 715.
47. Kesler, M.G. and Lee, B.I.: "Improve Prediction of Enthalpy of Fractions," *Hydrocarbon Processing* (March 1976) 153.
48. *Technical Data Book*, API, New York City (1964).
49. Tarakad, R.R. and Danner, R.P.: "A Comparison of Enthalpy Prediction Methods," *AIChE J.* (1976) 22, 409.
50. Gambill, W.R.: "You Can Predict Heat Capacities," *Chem. Eng.* (June 1957).
51. Touloukian, Y.S. et al.: "Specific Heat—Nonmetallic Liquids and Gases," *Thermophysical Properties of Matter*, IFI/Plenum, New York City (1970) Chap. 6.
52. *Chemical Engineers' Handbook*, R.H. Perry and C.H. Chilton (eds.), fifth edition, McGraw-Hill Book Co. Inc., New York City (1973).
53. *Steam Tables. Properties of Saturated and Superheated Steam*, third edition, Combustion Engineering Inc., Windsor, Connecticut (1940).
54. Somerton, W.H.: "Some Thermal Characteristics of Porous Rocks," *Trans., AIME* (1958) 213, 375.
55. Touloukian, Y.S. et al.: "Specific Heat-Nonmetallic Solids," *Thermophysical Properties of Matter*, IFI/Plenum, New York City (1970) Chap. 5.
56. Helgeson, H.C.: "Thermodynamics of Hydrothermal Systems at Elevated Temperatures and Pressures," *Amer. J. Science* (1967) 267, 729.
57. Keenan, J.H. and Keyes, F.G.: *Thermodynamic Properties of Steam*, John Wiley & Sons Inc., New York City (1936).

58. Grim, R.F.: *Clay Mineralogy*, McGraw-Hill Book Co. Inc., New York City (1968).
59. *Handbook of Physical Constants*, S.P. Clark Jr. (ed.), revised edition, Geological Soc. of America, Boulder, Colorado (1966) 97.
60. Touloukian, Y.S. et al.: "Thermal Conductivity—Nonmetallic Liquids and Gases," *Thermophysical Properties of Matter*, IFI/Plenum, New York City (1970) Chap. 3.
61. Cragoe, C.S.: Miscellaneous Publication No. 97, U.S. Bureau of Standards, Washington, DC (1929).
62. Lenoir, J.M.: "Effect of Pressure on Thermal Conductivity of Liquids," *Petroleum Refiner* (1956) 35, No. 8, 162.
63. Lenoir, J.M. and Comings, E.W.: "Thermal Conductivity of Gases, Measurements at High Pressure," *Chem. Eng. Prog.* (1951) 47, 223.
64. Eckert, E.R.G. and Drake, R.M. Jr.: *Heat and Mass Transfer*, McGraw-Hill Book Co. Inc., New York City (1959).
65. Horai, K.-I.: "Thermal Conductivity of Rock-Forming Minerals," *J. Geophysical Research* (1971) 76, No. 5, 1278.
66. Somerton, W.H., Keese, J.A., and Chu, S.L.: "Thermal Behavior of Unconsolidated Oil Sands," *SPEJ* (October 1974) 513.
67. Krupiczka, R.: "Analysis of Thermal Conductivity in Granular Materials," *Intl. Chem. Eng.* (1967) 7, 122.
68. Anand, J., Somerton, W.H., and Gomaa, E.: "Predicting Thermal Conductivities of Formations From Other Known Properties," *SPEJ* (October 1973) 267.
69. McAdams, W.H.: *Heat Transmission*, third edition, McGraw-Hill Book Co. Inc., New York City (1954).
70. Somerton, W.H. and Boozer, G.D.: "Thermal Characteristics of Porous Rocks at Elevated Temperatures," *Trans., AIME* (1960) 219, 418.
71. Willhite, G.P.: "Overall Heat Transfer Coefficients in Steam and Hot Water Injection Wells," *JPT* (May 1967) 607.
72. Allen, T.O. and Roberts, A.P.: *Production Operations, Oil & Gas Consultants Intl. Inc.*, Tulsa, Oklahoma (1978) 1.

Appendix C

Vapor-/Liquid-Phase Equilibrium

C.1 Introduction

A complex mixture of hydrocarbon compounds flows in producing oil and gas wells. This mixture continuously changes its phase composition during the production cycle, as it flows to the surface and enters the first stage of separation. A phase is defined as that part of a mixture that is uniform in physical and chemical properties, homogeneous in composition, and separated from other coexisting phases by well-defined boundary surfaces.^{1,2} Depending on the composition, pressure, and temperature, the hydrocarbon system may exist as a single-phase gas, a single-phase liquid, or a mixture of gas and liquid. In petroleum production fluids, water often is present as an additional liquid phase.

Unlike a single-component fluid, a multicomponent mixture exhibits a phase envelope rather than a distinct monotonic phase transition between gas and liquid phases defined uniquely by pressure and temperature. Within the two-phase region bounded by the phase envelope for multicomponent systems, both liquid and gas phases exist in equilibrium at constant pressures and temperatures. The shape of the phase envelope and the location of the critical point are unique properties of the fluid composition.

Fig. C-1 permits a qualitative classification of the types of reservoirs that are encountered in oil and gas production systems. Typical oil reservoirs have temperatures below the critical temperature of the hydrocarbon mixture. Volatile oil and condensate reservoirs normally have temperatures between the critical temperature and the cricondentherm for the hydrocarbon mixture. Dry gas reservoirs have temperatures above the cricondentherm.

Many condensate fluids exhibit retrograde condensation, a phenomenon in which condensation occurs during pressure reduction. In Fig. C-1, this abnormal (or retrograde) behavior occurs within the two-phase envelope between the critical point and the cricondentherm or cricondenbar.

When volatile oils and condensate fluids flow through pipes, their phase behavior is best predicted with a variable composition model. The procedure requires a series of vapor/liquid equilibrium or "flash" calculations. These calculations are based on the concept of an equilibrium constant, otherwise known as the distribution coefficient or K value.

C.2 Equilibrium Constant

For a multicomponent system, such as petroleum fluids, the composition, pressure, and temperature uniquely define the system phase behavior. The equilibrium constant, K_i , of a Component i is defined as the ratio of the mole fraction of the component in the gas

phase, y_i , to the mole fraction of the same component in the liquid phase, x_i . Expressed mathematically,

$$K_i = \frac{y_i}{x_i} \quad \dots \dots \dots \quad (C-1)$$

For ideal solutions at low pressures (typically below 75 psia), an ideal equilibrium constant can be derived by combining Raoult's law and Dalton's law. This can be expressed mathematically for a fixed temperature as

$$K_i = \frac{y_i}{x_i} = \frac{P_{vi}}{P}, \quad \dots \dots \dots \quad (C-2)$$

where P_{vi} = vapor pressure of Component i , psia, and P = total system pressure, psia.

The vapor pressure of any pure hydrocarbon is a unique function of temperature. Eq. C-2 assumes the liquid phase behaves as an ideal solution following Raoult's law and the gas phase behaves as an ideal solution following Dalton's law.

For a real solution, the equilibrium constants are not only functions of pressure and temperature but also of the composition of the hydrocarbon phases. In compositional modeling, the engineering objective is to determine the physical properties of the individual gas and liquid phases. Consequently, the equilibrium constants (indicating partitioning of each component between the liquid and gas phases) must be known. Sec. C.7 provides a detailed discussion on determination of equilibrium constants by use of equations of state (EOS's). An alternative method to determine approximate equilibrium constants uses charts for pure components, such as those given in Fig. C-2. However, it is appropriate at this time to introduce flash calculation techniques to determine the mole fractions of each component in each equilibrium phase.

C.3 Flash Calculations

Flash calculations are based on simple overall and component molal balances. It is important to define the variables required in the material balance:

F = number of moles of feed,

L = number of moles of liquid,

V = number of moles of vapor,

z_i = mole fraction of Component i in feed,

x_i = mole fraction of Component i in liquid phase,

y_i = mole fraction of Component i in vapor phase, and

n = total number of components in the feed.

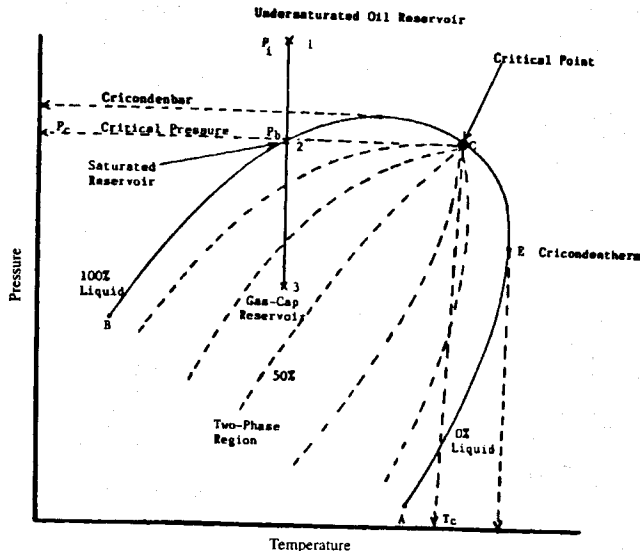


Fig. C-1—Typical phase diagram.²

The overall material balance is

$$F = L + V. \quad \dots \dots \dots \quad (C-3)$$

Individual component balances are

$$z_i F = x_i L + y_i V. \quad \dots \dots \dots \quad (C-4)$$

Eq. C-3 may be rewritten as

$$\frac{L}{F} = 1 - \frac{V}{F}. \quad \dots \dots \dots \quad (C-5)$$

C3.1 Liquid Phase. Solving Eq. C-4 for x_i , and replacing y_i and L/F with Eqs. C-1 and C-5, respectively, results in

$$x_i = \frac{z_i F - y_i V}{L} = \frac{z_i - y_i \frac{V}{F}}{\frac{L}{F}} = \frac{z_i - x_i K_i \frac{V}{F}}{1 - \frac{V}{F}}. \quad \dots \dots \dots \quad (C-6)$$

On further simplification, this equation to determine the mole fraction of the i th component in the liquid phase can be written as

$$x_i = \frac{z_i}{1 + \frac{V}{F}(K_i - 1)}. \quad \dots \dots \dots \quad (C-7)$$

C3.2 Vapor Phase. Similarly, solving Eq. C-4 for y_i and using Eqs. C-1 and C-5 gives

$$y_i = \frac{z_i F - x_i L}{V} = \frac{z_i F - \frac{x_i}{K_i}}{V}. \quad \dots \dots \dots \quad (C-8)$$

Eq. C-8 can be simplified as

$$y_i = \frac{z_i K_i}{1 + \frac{V}{F}(K_i - 1)}. \quad \dots \dots \dots \quad (C-9)$$

C3.3 Solution Procedure. It is important to note that the solutions for x_i and y_i , based on Eqs. C-7 and C-9, respectively, require the determination of the V/F value. To solve for V/F , Eqs. C-7 and C-9 are combined by use of this definition of mole fractions.

$$\sum_{i=1}^n x_i = \sum_{i=1}^n y_i = 1.0$$

OR

$$\sum_{i=1}^n (y_i - x_i) = 0.$$

Therefore, combining Eqs. C-7 and C-9 gives

$$\begin{aligned} \sum_{i=1}^n (y_i - x_i) &= \sum_{i=1}^n \frac{z_i(K_i - 1)}{(K_i - 1)\frac{V}{F} + 1} \\ &= f\left(\frac{V}{F}\right) = 0. \quad \dots \dots \dots \quad (C-10) \end{aligned}$$

This equation is often called the Rachford and Rice equation. It is implicit in V/F . To solve it, K values must be known. Note that K values are themselves phase-composition-dependent. Because phase compositions are unknown in flash calculations, so are the dependent variables for which a solution is needed. This imposes a second level of implicitness in Eq. C-10. Therefore, solution of Eq. C-10 is computation intensive.

This section presents a solution scheme for the Rachford and Rice equation, assuming K values can be calculated at each iteration step for V/F .

A second-order Newton-Raphson convergence scheme⁴ can be used to solve the Rachford and Rice equation for V/F with a reasonable (10^{-6}) convergence tolerance.² The procedure requires that these variables be known:

- Number of components, n .
- Mole fraction of each component in the feed mixture, z_i .
- Equilibrium constant for each component, K_i .
- A first guess for the mole ratio, $(V/F)_j$, where the subscript j refers to the iteration step count.

Given a first guess, for instance 0.5 for $(V/F)_j$, an improved value of (V/F) can be estimated from

$$\left(\frac{V}{F}\right)_{j+1} = \left(\frac{V}{F}\right)_j - \frac{f\left(\frac{V}{F}\right)_j}{f'\left(\frac{V}{F}\right)_j}, \quad \dots \dots \dots \quad (C-11)$$

where the derivative, $f'(V/F)$, is obtained by differentiating Eq. C-10 with respect to V/F .

$$f'\left(\frac{V}{F}\right)_j = - \sum_{i=1}^n \frac{z_i(K_i - 1)^2}{\left[(K_i - 1)\left(\frac{V}{F}\right)_j + 1\right]^2}. \quad \dots \dots \dots \quad (C-12)$$

Convergence is achieved when

$$\left| \left(\frac{V}{F}\right)_{j+1} - \left(\frac{V}{F}\right)_j \right| < 1.0 \times 10^{-6}. \quad \dots \dots \dots \quad (C-13)$$

Once convergence is obtained for V/F , the composition of each phase can be determined from Eq. C-7 and either Eq. C-1 or C-9.

The previous procedure requires values for K_i at the pressure, temperature, and composition of each phase. As mentioned earlier, several methods exist to determine K values, including use of charts, such as those given in Fig. C-2. The recommended way to determine K values, however, is from EOS's. Sec. C.9 gives this procedure.

C.4 Bubblepoint and Dewpoint Curves

For temperatures less than the critical temperature, the bubblepoint curve separates a single-phase liquid from the two-phase region. Thus, a bubblepoint pressure is the minimum pressure at which a liquid will not vaporize. At the bubblepoint pressure, there is no vapor and all feed is in the saturated-liquid phase. Thus, $V=0$ and $z_i \approx x_i$. Therefore, Eq. C-9 simplifies to $y_i = z_i K_i$ and

$$\sum_{i=1}^n y_i = \sum_{i=1}^n z_i K_i = 1. \quad \dots \dots \dots \quad (C-14)$$

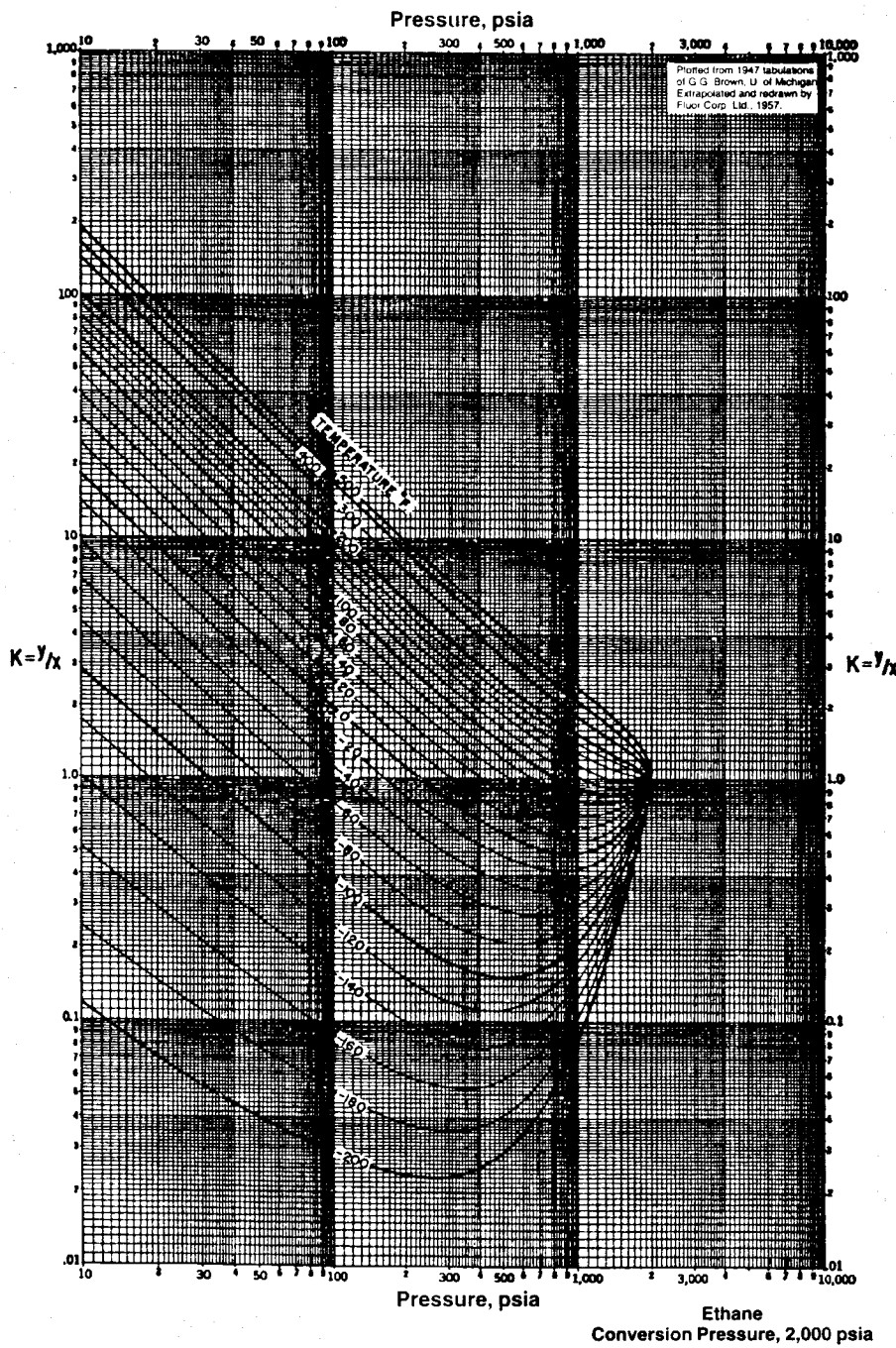


Fig. C-2—Example K-value chart. (After Katz *et al.*³ Reproduced with permission of the McGraw-Hill Cos.)

The dewpoint curve in Fig. C-1 separates the single-phase gas and two-phase regions. At a given temperature, two dewpoint pressures can exist. At a dewpoint pressure, $L = 0$, $V = F$, and $z_i \approx y_i$.

Therefore, Eq. C-7 simplifies to

$$x_i = \frac{z_i}{K_i} \quad \dots \quad (C-15a)$$

and

$$\sum_{i=1}^n x_i = \sum_{i=1}^n \frac{z_i}{K_i} = 1. \quad \dots \quad (C-15b)$$

Bubblepoint and dewpoint pressures also are calculated with iterative methods. This procedure is iterative in pressure at any temperature below the critical point. Note that, at the bubblepoint or

dewpoint pressure, the hydrocarbon mixture exists in a single phase. The known feed composition is also the phase composition. The problem is to determine iteratively the pressure and the K values of each component in the feed at that calculated pressure to satisfy Eq. C-14 or C-15, depending on whether a bubblepoint or a dewpoint pressure is to be calculated. The Wilson⁵ correlation can be used to estimate K values initially. Wilson proposed this simplified thermodynamic expression to estimate K values.

$$K_i = \frac{p_{ci}}{p} \exp \left[5.37(1 + \omega_i) \left(1 - \frac{T_{ci}}{T} \right) \right], \quad \dots \quad (C-16)$$

where p_{ci} = critical pressure of Component i , psia; p = system pressure, psia; T_{ci} = critical temperature of Component i , °R; T = system temperature, °R; and ω_i = acentric factor of Component i .

The acentric factor, ω , for a pure component is defined as⁶

$$\omega = -\log p_{vp}/(at T_r = 0.7) - 1.0, \quad \dots \dots \dots \quad (C-17)$$

where p_{vpr} = reduced vapor pressure ($= p_{vp}/p_c$) and p_{vp} = vapor pressure. To determine ω , the reduced vapor pressure at a reduced temperature $T_r (= T/T_c)$ of 0.7 is required. ω represents the acentricity or nonsphericity of a molecule. For monatomic gases, ω is essentially zero. For methane it is very small. For higher molecular-weight hydrocarbons, ω increases. Acentric factors for pure components can be determined experimentally. The acentric factor also can be determined from the Lee and Kesler⁷ vapor-pressure relationships as

$$\omega = \frac{\alpha}{\beta}, \quad \dots \dots \dots \quad (C-18)$$

where $\alpha = -\ln p_c - 5.97214 + 6.09648 \theta^{-1} + 1.28862 \ln \theta - 0.169374 \theta^6$ and $\beta = 15.2518 - 15.6875 \theta^{-1} - 13.4721 \ln \theta + 0.43577 \theta^6$, where $\theta = T_b/T_c$ = reduced boiling point; p_c = critical pressure, in atmospheres; T_c = critical temperature, °R; and T_b = normal boiling point at 1 atm, °R.

For hypothetical or pseudocomponents, such as those used to characterize the heavy ends (C_{7+}) in a multicomponent hydrocarbon mixture, the acentric factors also can be estimated from the Edmister⁸ correlation as

$$\omega = \frac{3}{7} T_b \left[\frac{\log p_c - 1.167}{T_c - T_b} \right] - 1.0. \quad \dots \dots \dots \quad (C-19)$$

C.5 Bubblepoint Pressure

Bubblepoint-pressure calculations can be initialized with the Wilson correlation (Eq. C-16) for K_i . At the bubblepoint, the system pressure is denoted by p_b . A good starting value for p_b can be obtained from

$$p_b = \sum_{i=1}^n \left\{ z_i p_{ci} \exp \left[5.37 \left(1 + \omega_i \right) \left(1 - \frac{T_{ci}}{T} \right) \right] \right\}. \quad \dots \dots \dots \quad (C-20)$$

Starting with a first guess of bubblepoint pressure from Eq. C-20, K values are determined by use of EOS's. These K values are substituted into Eq. C-14. If Eq. C-14 is satisfied within a reasonable tolerance, then the iteration is stopped and the last assumed bubblepoint pressure is accepted as the solution. Otherwise, a new bubblepoint pressure is assumed based on these criteria:

During the iterative process, if

$$\sum_{i=1}^n (z_i K_i) < 1, \quad \dots \dots \dots \quad (C-21a)$$

then the assumed bubblepoint pressure is high and the next guess must be a lower pressure. If

$$\sum_{i=1}^n (z_i K_i) > 1, \quad \dots \dots \dots \quad (C-21b)$$

then the assumed bubblepoint pressure is low and the next guess must be a higher pressure.

C.6 Dewpoint Pressure

The first guess of dewpoint pressure can be obtained by combining Eqs. C-15 and C-16 as

$$p_d = \sum_{i=1}^n \left\{ \frac{p_{ci} \exp \left[5.37 \left(1 + \omega_i \right) \left(1 - \frac{T_{ci}}{T} \right) \right]}{z_i} \right\}. \quad \dots \dots \dots \quad (C-22)$$

With this initial guess for dewpoint pressure, K values are calculated with EOS's. These K values then are substituted into Eq. C-15 to check if this equation is satisfied within a reasonable tolerance. If it is, the iteration is stopped. Otherwise, a new dewpoint pressure is assumed based on the following criteria. The iteration is continued until convergence within the pre-set tolerance is achieved. If

$$\sum_{i=1}^n \frac{z_i}{K_i} > 1, \quad \dots \dots \dots \quad (C-23a)$$

then the assumed dewpoint pressure is higher than the actual dewpoint pressure. If

$$\sum_{i=1}^n \frac{z_i}{K_i} < 1, \quad \dots \dots \dots \quad (C-23b)$$

then the assumed dewpoint pressure is lower than the actual dewpoint pressure.

C.7 Equilibrium Constants From EOS's

For most applications in the multiphase flow of hydrocarbon mixtures in pipes, the ideal assumptions used in deriving Eq. C-2 are unrealistic. A hydrocarbon/liquid mixture at any point in the pipe is in equilibrium with a vapor mixture at the local pressure and temperature. The important parameters controlling the phase behavior are pressure, temperature, and the composition of both phases. An important objective in flash calculations is to determine the individual phase compositions, given the pressure and temperature at the computation node and the overall mixture composition. The equilibrium constants, or K values, thus depend on all these parameters; i.e.,

$$K = f(p, T, z_i). \quad \dots \dots \dots \quad (C-24)$$

These equilibrium constants can be calculated based on the thermodynamics of vapor/liquid equilibria. Such equilibrium depends on the fugacity of each component in each of the phases. Physically, equal fugacities of a component in each phase implies zero net mass transfer of that component between the phases, resulting in thermodynamic equilibrium of phases. Thus, the criteria for thermodynamic vapor/liquid equilibrium is that the fugacities of every component in each phase must be equal, or

$$f_i^V = f_i^L, \quad i = 1, \dots, n, \quad \dots \dots \dots \quad (C-25)$$

where f = fugacity, V = vapor phase, L = liquid phase, and n = number of components in the system.

Mathematically, the fugacity of a pure component is defined as

$$f = p \exp \left[\int_0^p \left(\frac{Z-1}{P} \right) dp \right], \quad \dots \dots \dots \quad (C-26)$$

where f = fugacity, psia; p = system pressure, psia; and Z = compressibility factor.

It is evident from this definition that fugacity has units of pressure. Fugacity also can be considered as vapor pressure modified to represent the escaping tendency of molecules from one phase into the other. The ratio of the fugacity to the system pressure is called the fugacity coefficient, Φ , and is calculated from Eq. C-26 for pure components.

For a hydrocarbon/liquid/gas mixture in equilibrium, the fugacity coefficient of Component i in each phase is a function of the system pressure, phase composition, and temperature. In mixtures, the fugacity coefficient of any component is defined for vapors as

$$\Phi_i^V = \frac{f_i^V}{(y_i p)} \quad \dots \dots \dots \quad (C-27a)$$

TABLE C-1—CONSTANTS FOR FOUR COMMON EOS's (After Reid *et al.*¹ Reproduced with permission of the McGraw-Hill Cos.)

Equation	<i>u</i>	<i>w</i>	<i>b</i>	<i>a</i>
van der Waals	0	0	$\frac{RT_c}{8p_c}$	$\frac{27}{64} \frac{R^2 T_c^2}{p_c}$
Redlich-Kwong	1	0	$\frac{0.08664 RT_c}{p_c}$	$\frac{0.42748 R^2 T_c^{2.5}}{p_c \sqrt{T}}$
Soave	1	0	$\frac{0.08664 RT_c}{p_c}$	$\frac{0.42748 R^2 T_c^2}{p_c} [1 + k\omega(1 - T_r^{1/2})]^2$, where $k\omega = 0.48 + 1.574\omega - 0.176\omega^2$
Peng-Robinson	2	-1	$\frac{0.07780 RT_c}{p_c}$	$\frac{0.45724 R^2 T_c^2}{p_c} [1 + k\omega(1 - T_r^{1/2})]^2$, where $k\omega = 0.37464 + 1.54226\omega - 0.26992\omega^2$

and for liquids as

$$\Phi_i^L = \frac{f_i^L}{(x_i p)}, \quad \dots \dots \dots \quad (C-27b)$$

where Φ_i^V = fugacity coefficient of Component *i* in the vapor phase and Φ_i^L = fugacity coefficient of Component *i* in the liquid phase.

It is clear from the definition of mixture fugacity coefficient that, because at thermodynamic vapor/liquid equilibrium $f_i^V = f_i^L$, the equilibrium constant may be found with

$$K_i = \frac{y_i}{x_i} = \frac{\Phi_i^L}{\Phi_i^V}. \quad \dots \dots \dots \quad (C-28)$$

The fugacity coefficients for each component in each phase are defined by use of EOS's.

C.8 Cubic EOS's

An EOS is an analytical expression relating the pressure to the temperature and molar volume of fluids. The ideal and real gas laws presented in Appendix B are two EOS's. Ideal gas laws assume that the volume of molecules is insignificant compared to the volume of the container, and that there are no attractive or repulsive forces between the molecules.

Cubic EOS's have been developed that do not use these restrictive assumptions. Thus, it is possible to apply these equations to both vapor and liquid phases. The term cubic EOS implies that the volume terms in it can be cubic. A generalized form for a cubic EOS is

$$p = \frac{RT}{V - b} - \frac{a}{V^2 + ubV + wb^2}. \quad \dots \dots \dots \quad (C-29)$$

An alternative form in terms of the compressibility factor, *Z*, replacing molar volume, *V*, from the real gas law is

$$Z^3 - (1 + B^* - uB^*)Z^2 + (A^* + wB^{*2} - uB^* - uB^{*2})Z - A^*B^* - wB^{*2} - wB^{*3} = 0, \quad \dots \dots \dots \quad (C-30)$$

where $A^* = ap/R^2T^2$; $B^* = bp/RT$; p = system pressure, psia; T = system temperature, °R; R = gas constant, 10.73 psi·ft³/lbmol·°R; and V = molar volume, ft³/mol. Parameters *a* and *b* characterize the molecular properties of the individual components. Parameter *a* is a measure of the intermolecular attractive forces between the molecules. Parameter *b* is the covolume and reflects the volume of molecules.

There are four well-known cubic EOS's⁹⁻¹⁴: van der Waals, Redlich-Kwong (RK), Soave-Redlich-Kwong (SRK), and Peng-Robinson (PR).

For these EOS's, Parameters *u* and *w* in Eqs. C-29 and C-30 are integers and are presented in Table C-1, as are the constants for the four EOS's. Parameters *a* and *b* are calculated based on van der Waals⁹ observations that the critical isotherm has a zero slope and an inflection point at the critical point. This results in the following mathematical criteria at the critical point:

$$\left(\frac{\partial p}{\partial V}\right)_{T_c} = 0 \quad \dots \dots \dots \quad (C-31a)$$

and

$$\left(\frac{\partial^2 p}{\partial V^2}\right)_{T_c} = 0. \quad \dots \dots \dots \quad (C-31b)$$

Soave¹¹ and Peng and Robinson¹² used these criteria to determine Parameter *a* and then modified the resulting expression empirically by use of the acentric factor to reproduce pure hydrocarbon vapor pressures. In Table C-1, *T_c* and *p_c* are the critical temperature and critical pressure of the pure component, respectively, and *T_r* is the reduced temperature. ω is the acentric factor of the pure component. Alternative forms of these EOS's, in terms of compressibility factor, are used often to calculate phase compressibility factors and fugacity coefficients.

Secs. C.8.1 and C.8.2 present the SRK and PR EOS's, the two most widely used in terms of the phase compressibility factors. Both have been modified with suggested mixing rules recommended by Soave¹¹ and Peng and Robinson.¹² These modifications allow the use of SRK and PR EOS's for mixtures of hydrocarbons, such as volatile oils and gas condensates.

C.8.1 SRK EOS. Eqs. C-32a and C-32b give the alternatives for liquid and vapor phases, respectively, from the SRK EOS.

$$Z_L^3 - Z_L^2 + Z_L(A_L - B_L - B_L^2) - A_L B_L = 0 \quad \dots \dots \dots \quad (C-32a)$$

and

$$Z_V^3 - Z_V^2 + Z_V(A_V - B_V - B_V^2) - A_V B_V = 0, \quad \dots \dots \dots \quad (C-32b)$$

where *Z_L* and *Z_V* = liquid-phase and gas- or vapor-phase compressibility factors, respectively. Combining this EOS with the definition of fugacity coefficient presented earlier, Soave¹¹ derived these relationships to calculate the fugacity coefficients for each component in the liquid and gas phases.

$$\ln \Phi_i^L = \left(\frac{b_i}{b}\right)_L (Z_L - 1) - \ln(Z_L - B_L)$$

$$- \frac{A_L}{B_L} \left[2\left(\frac{a_i}{a}\right)_L^{0.5} - \left(\frac{b_i}{b}\right)_L \right] \ln\left(1 + \frac{B_L}{Z_L}\right) \quad \dots \dots \dots \quad (C-33a)$$

and

$$\ln \Phi_i^V = \left(\frac{b_i}{b}\right)_V (Z_V - 1) - \ln(Z_V - B_V)$$

$$- \frac{A_V}{B_V} \left[2\left(\frac{a_i}{a}\right)_V^{0.5} - \left(\frac{b_i}{b}\right)_V \right] \ln\left(1 + \frac{B_V}{Z_V}\right). \quad \dots \dots \dots \quad (C-33b)$$

The next nine equations define variables used in Eqs. C-33a and C-33b.

$$\left(\frac{a_i}{\bar{a}}\right)_L^{0.5} = \frac{\alpha_i^{0.5} T_{ci}/p_{ci}^{0.5}}{\sum_{i=1}^n x_i \alpha_i^{0.5} T_{ci}/p_{ci}^{0.5}}, \quad \dots \quad (C-34)$$

$$\left(\frac{a_i}{\bar{a}}\right)_V^{0.5} = \frac{\alpha_i^{0.5} T_{ci}/p_{ci}^{0.5}}{\sum_{i=1}^n y_i \alpha_i^{0.5} T_{ci}/p_{ci}^{0.5}}, \quad \dots \quad (C-35)$$

$$\left(\frac{b_i}{b}\right)_L = \frac{T_{ci}/p_{ci}}{\sum_{i=1}^n x_i T_{ci}/p_{ci}}, \quad \dots \quad (C-36)$$

$$\left(\frac{b_i}{b}\right)_V = \frac{T_{ci}/p_{ci}}{\sum_{i=1}^n y_i T_{ci}/p_{ci}}, \quad \dots \quad (C-37)$$

$$A_L = C_a \frac{p}{T^2} \left[\sum_{i=1}^n x_i T_{ci} \left(\frac{\alpha_i}{p_{ci}} \right)^{0.5} \right]^2, \quad \dots \quad (C-38)$$

$$A_V = C_b \frac{p}{T^2} \left[\sum_{i=1}^n y_i T_{ci} \left(\frac{\alpha_i}{p_{ci}} \right)^{0.5} \right]^2, \quad \dots \quad (C-39)$$

$$B_L = C_a \frac{p}{T} \sum_{i=1}^n x_i T_{ci}/p_{ci}, \quad \dots \quad (C-40)$$

$$B_V = C_b \frac{p}{T} \sum_{i=1}^n y_i T_{ci}/p_{ci}, \quad \dots \quad (C-41)$$

and

$$\alpha_i = [1 + f\omega_i (1 - T_{ri}^{0.5})]^2, \quad \dots \quad (C-42)$$

where $C_a = 0.42748$ and $C_b = 0.08664$. The function $f\omega_i$ can be calculated on the basis of the equation for Soave presented in Table C-1. The equilibrium constants, K_i , can be calculated from Eq. C-28.

C.8.2 PR EOS. Eqs. C-43a and C-43b give cubic equations for the liquid and vapor phases, respectively, based on the PR EOS's.¹²⁻¹⁴

$$Z_L^3 - (1 - B_L)Z_L^2 + (A_L - 3B_L^2 - 2B_L)Z_L - (A_L B_L - B_L^2 - B_L^3) = 0 \quad \dots \quad (C-43a)$$

and

$$Z_V^3 - (1 - B_V)Z_V^2 + (A_V - 3B_V^2 - 2B_V)Z_V - (A_V B_V - B_V^2 - B_V^3) = 0, \quad \dots \quad (C-43b)$$

where Z_L and Z_V = liquid-phase and gas-phase compressibility factors, respectively. The fugacity coefficients are calculated with Eqs. C-33 through C-42, as previously discussed for the SRK EOS. Only the C_a , C_b , and $f\omega_i$ values are different. For the PR EOS, these are $C_a = 0.45724$, $C_b = 0.07780$, and $f\omega_i = 0.37464 + 1.54226\omega_i - 0.26992\omega_i^2$. The equilibrium constants, K_i , are calculated with Eq. C-28.

C.9 Solution Algorithm

To determine the compressibility factor, Z , in the liquid or gas phase, the appropriate EOS can be solved either by direct or iterative methods. These equations are cubic equations that yield a single real root

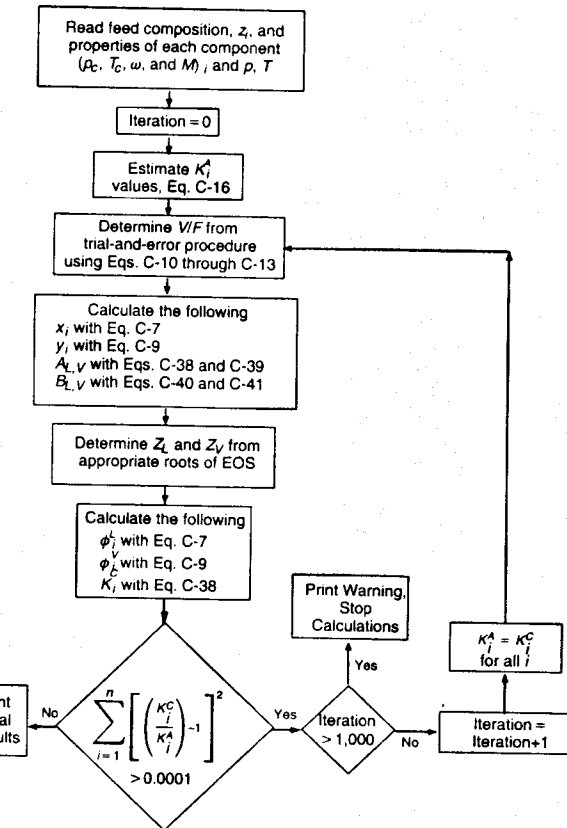


Fig. C-3—Algorithm to perform vapor/liquid equilibrium calculations.

in the single-phase region and three real roots in the two-phase region. The largest root for the vapor cubic equations corresponds to the compressibility factor of the vapor phase, Z_V , and the smallest root for the liquid cubic equations corresponds to that of the liquid phase, Z_L .

It is important to note that the compressibility factors used in the fugacity coefficient for each phase are phase-composition-dependent. Thus, the equilibrium constants also are composition-dependent. Consequently, the solution procedures for mixture equilibrium constants are highly iterative. The following is a step-by-step algorithm² to calculate the equilibrium constants.

1. The input data required for this calculation are the system pressure, p , temperature, T , and the overall system composition, z_i , for each component.

2. On the basis of Eq. C-16, estimate or assume K_i^A values for each component.

3. On the basis of assumed K_i^A values from Eq. C-16 and the known z_i values, use Eq. C-10 to perform flash calculations.

4. With appropriate EOS's, the compositions of the liquid and gas phases obtained from flash calculations can be used to determine the fugacity coefficients of each component in each phase, Φ_i^L and Φ_i^V .

5. Using fugacity coefficient ratios from Eq. C-28, calculate the equilibrium constants or K_i^C values for each component.

6. Compare the equilibrium constants in Step 2 with the calculated values in Step 5 using the following convergence criteria:

$$\sum_{i=1}^n \left(\frac{K_i^C}{K_i^A} - 1 \right)^2 \leq \epsilon, \quad \dots \quad (C-44)$$

where ϵ = preassigned convergence tolerance ($\leq 10^{-4}$) and n = number of components in the system.

7. If the convergence criterion in Step 6 is satisfied for all components, the values of the equilibrium constants are used to calculate phase compositions required in determining phase physical properties. Otherwise, these calculated values are used as the new guesses, and Steps 3 through 6 are repeated until convergence is achieved.

TABLE C-2—PARAMETERS FOR V^* CORRELATION
 (After Hankinson and Thomson.¹⁸ Reproduced with permission of
 American Inst. of Chemical Engineers.)

	<i>a</i>	<i>b</i>	<i>c</i>	Average Absolute Error (%)
Paraffins	0.2905331	-0.08057958	0.02276965	1.23
Olefins and diolefins	0.3070619	-0.2368581	0.2834693	1.43
Cycloparaffins	0.6564296	-3.391715	7.442388	1.00
Aromatics	0.2717636	-0.05759377	0.05527757	0.58
All hydrocarbons	0.2851686	-0.06379110	0.01379173	1.89
Sulfur compounds	0.3053426	-0.1703247	0.1753972	1.98
Fluorocarbons	0.5218098	-2.346916	5.407302	0.82
Cryogenic liquids	0.2960998	-0.05468500	-0.1901563	0.85
Condensable gases	0.2828447	-0.1183987	0.1050570	3.65

Fig. C-3 is a computer flow chart to perform a flash calculation with the algorithm.

Soave¹¹ suggested some modifications to calculations of the *A* and *B* parameters. These parameters consider molecular interactions. The modifications were based on an empirically determined correction factor called the binary interaction coefficient.¹⁵ Soave¹¹ and Grubbski and Daubert¹⁶ suggested that these corrections are not necessary for pure hydrocarbon systems. In the presence of associated non-hydrocarbons, such as H₂S and CO₂, this correction can greatly improve the volumetric- and phase-behavior predictions.

C.10 Densities

Once the compressibility factors of each phase are determined, the vapor and liquid densities can be determined from

$$\rho_v = \frac{p \sum_{i=1}^n x_i M_i}{Z_v RT} \quad \dots \quad (C-45)$$

and

$$\rho_L = \frac{p \sum_{i=1}^n x_i M_i}{Z_L RT}, \quad \dots \quad (C-46)$$

where, M_i = molecular weight of the *i*th component.

Liquid densities calculated from Eq. C-46 are usually not sufficiently accurate. Alani and Kennedy¹⁷ also developed an equation similar to the van der Waals equation to determine the molal liquid volume. A better approach is to use the correlation proposed by Hankinson and Thomson.¹⁸

C.10.1. Hankinson and Thomson Correlation. This correlation was developed for the saturated-liquid densities of pure compounds and their mixtures.¹⁸ The method can be applied to a variety of liquids with sufficient accuracy and reliability. From Eq. C-46, the liquid density can be defined as

$$\rho_L = M_L / V_s, \quad \dots \quad (C-47)$$

where the apparent molecular weight of the liquid, M_L , can be calculated from

$$M_L = \sum_{i=1}^n x_i M_i \quad \dots \quad (C-48)$$

V_s in Eq. C-47 is the molal liquid volume. Hankinson and Thomson proposed this empirical model to calculate molal liquid volume.

$$V_s = V^* \left\{ V_R^{(o)} \left[1 - \omega_{SRK} V_R^{(\delta)} \right] \right\}, \quad \dots \quad (C-49)$$

where V^* is the characteristic molal volume of the liquid and $V_R^{(o)}$ and $V_R^{(\delta)}$ are two correlating parameters given by

$$V_R^{(o)} = 1 - 1.52816(1 - T_r)^{1/3} + 1.43907(1 - T_r)^{2/3} \\ - 0.81446(1 - T_r) + 0.190454(1 - T_r)^{4/3}, \quad \dots \quad (C-50a)$$

where $0.25 < T_r < 0.95$, and

$$V_R^{(\delta)} = (-0.296123 + 0.386914T_r - 0.0427258T_r^2 \\ - 0.0480645T_r^3)/(T_r - 1.00001), \quad \dots \quad (C-50b)$$

where $0.25 < T_r < 1.0$, and $T_r = T/T_c$.

Hankinson and Thomson¹⁸ provided the values of V^* and ω_{SRK} for a list of organic and inorganic pure components relevant to hydrocarbon fluids. ω_{SRK} is the acentric factor derived from the SRK EOS.¹¹ It can be calculated, independent of any EOS, by methods proposed by Lee and Kesler⁷ and presented in Sec. C.4. Thus, ω_{SRK} can be replaced in Eq. C-49 by ω from a more general source. The relevant independent variables in Eq. C-49 are calculated with the following mixing rules.

$$T_c = \frac{\sum_{i=1}^n \sum_{j=1}^n X_i X_j V_{ij}^* T_{cij}}{V^*}, \quad \dots \quad (C-51)$$

$$\omega = \sum_{i=1}^n x_i \omega_i, \quad \dots \quad (C-52)$$

and

$$V^* = \frac{1}{4} \left[\sum_{i=1}^n x_i V_i^* + 3 \left(\sum_{i=1}^n x_i V_i^{*2/3} \right) \right. \\ \left. \times \left(\sum_{i=1}^n x_i V_i^{*1/3} \right) \right], \quad \dots \quad (C-53)$$

where

$$V_{ij}^* T_{cij} = \sqrt{V_i^* T_{ci} V_j^* T_{cj}} \quad \dots \quad (C-54)$$

If nitrogen and/or hydrogen are present, T_c and ω are calculated with the following expressions.

$$T_c = \frac{\sum_{i=1}^n x_i V_i^* T_{ci}}{\sum_{i=1}^n x_i V_i^*}, \quad \dots \quad (C-55)$$

and

$$\omega = \frac{\sum_{i=1}^n x_i V_i^* \omega_i}{\sum_{i=1}^n x_i V_i^*} \quad \dots \dots \dots \quad (\text{C-56})$$

Hankinson and Thomson¹⁸ also presented a correlation to calculate the characteristic volume, V^* , if data are not readily available,

$$V^* = \frac{RT_c}{p_c} (a + b\omega + c\omega^2), \quad \dots \dots \dots \quad (\text{C-57})$$

where a , b , and c are determined from Table C-2. The last resort in determining the characteristic molal volume, V^* , is to equate it to the critical volume, V_c ; i.e.,

$$V^* = V_c \quad \dots \dots \dots \quad (\text{C-58})$$

C.11 Viscosity

Based on compositional models, gas viscosity can be calculated with the methods of Carr *et al.*¹⁹ or Lee *et al.*²⁰ described in Appendix B.

There are few methods to determine liquid viscosity based on compositional models. Like any other intensive property, viscosity is a function of pressure, temperature, and composition of the hydrocarbon fluid. This relationship for liquids can be mathematically expressed as

$$\mu = f(p, T, x_i), i = 1, \dots, n. \quad \dots \dots \dots \quad (\text{C-59})$$

To determine the viscosity of hydrocarbon liquids, one must know the composition of the liquid, expressed in terms of methane through heptane-plus components, hydrogen sulfide, nitrogen, and carbon dioxide, together with the molecular weight and specific gravity of the heptane-plus component. System pressure and temperature also must be known.

C.11.1 Lohrenz, Bray, and Clark Correlation. Lohrenz *et al.*²¹ developed this empirical correlation to determine the viscosity of saturated or live oil from its composition.

$$\mu = \mu_{oL} + \left(\xi_m \right)^{-1} \left[(a_0 + a_1 \rho_r + a_2 \rho_r^2 + a_3 \rho_r^3 + a_4 \rho_r^4) - 0.0001 \right]. \quad \dots \dots \dots \quad (\text{C-60})$$

where the mixture viscosity parameter, ξ_m , is defined mathematically as

$$\xi_m = \frac{5.4402(T_{pc})^{1/6}}{(M_a)^{0.5}(p_{pc})^{2/3}}, \quad \dots \dots \dots \quad (\text{C-61})$$

μ_{oL} = live oil viscosity at system temperature and atmospheric pressure, cp; $a_0 = 0.1023$; $a_1 = 0.023364$; $a_2 = 0.058533$; $a_3 = -0.040758$; $a_4 = 0.0093724$; T_{pc} = pseudocritical temperature of the crude, °R; p_{pc} = pseudocritical pressure of the crude, psia; M_a = apparent molecular weight of the liquid mixture, from Eq. C-48; and ρ_r = reduced oil density, defined by

$$\rho_r = \frac{\rho_o}{M_a} \left[\sum_{\substack{i=1 \\ i \neq C_{7+}}}^n (x_i M_i V_{ci}) + (x_{C_{7+}} V_{C_{7+}}) \right], \quad \dots \dots \dots \quad (\text{C-62})$$

where ρ_o = oil density at the prevailing system condition, lbm/ft³; x_i = mole fraction of Component i ; M_i = molecular weight of Component i ; V_{ci} = critical volume of Component i , ft³/lbm; $x_{C_{7+}}$ = mole fraction of C_{7+} ; $V_{C_{7+}}$ = critical molar volume of C_{7+} , ft³/lbm-mol; and n = number of components in the mixture.

TABLE C-3—PARACHORS FOR PURE SUBSTANCES
(After Weinaug and Katz.²³ Reproduced with permission of the American Chemical Soc.)

Component	Parachor
CO ₂	78.0
N ₂	41.0
C ₁	77.0
C ₂	108.0
C ₃	150.3
i-C ₄	181.5
n-C ₄	189.9
i-C ₅	225.0
n-C ₅	231.5
n-C ₆	271.0
n-C ₇	312.5
n-C ₈	351.5

Lohrenz *et al.*²¹ proposed this equation to calculate $V_{C_{7+}}$.

$$V_{C_{7+}} = 21.573 + 0.015122M_{C_{7+}} - 27.656\gamma_{C_{7+}} + 0.070615M_{C_{7+}}\gamma_{C_{7+}}, \quad \dots \dots \dots \quad (\text{C-63})$$

where $M_{C_{7+}}$ = molecular weight of C_{7+} and $\gamma_{C_{7+}}$ = specific gravity of C_{7+} .

Lohrenz *et al.* used Herning- and Zipperer-type equations to determine the viscosity of the live oil.

$$\mu_{oL} = \frac{\sum_{i=1}^n (x_i \mu_i M_i^{0.5})}{\sum_{i=1}^n (x_i M_i^{0.5})}, \quad \dots \dots \dots \quad (\text{C-64})$$

where μ_i = viscosity of Component i at atmospheric pressure and system temperature. This viscosity is calculated from these equations. For $T_{ri} \leq 1.5$,

$$\mu_i = \frac{34(10^{-5})(T_{ri})^{0.94}}{\xi_i}, \quad \dots \dots \dots \quad (\text{C-65})$$

and for $T_{ri} > 1.5$,

$$\mu_i = \frac{17.78(10^{-5})(4.58T_{ri} - 1.67)^{0.625}}{\xi_i}, \quad \dots \dots \dots \quad (\text{C-66})$$

where T_{ri} = reduced temperature of Component i ; T/T_{ci} and ξ_i = mixture viscosity parameter of Component i , given by

$$\xi_i = \frac{5.4402(T_{ci})^{1/6}}{(M_i)^{0.5}(p_{ci})^{2/3}}. \quad \dots \dots \dots \quad (\text{C-67})$$

The viscosity of C_{7+} used in this correlation can be calculated by any of the dead-oil-viscosity correlations presented in Appendix B. Ahmed² observed that the Lohrenz *et al.*²¹ correlation is very sensitive to the density of the oil and the critical molar volume of the C_{7+} fraction. If observed viscosity data are available, the critical molar volume of the C_{7+} fraction should be adjusted to validate this correlation.

C.12 Surface Tension

Surface tension is a measure of imbalance in the interfacial molecular forces for two phases in contact. In multiphase pipe flow, gas/liquid and liquid/liquid surface- or interfacial-tension values are used to determine flow regimes and liquid holdup.

The surface tension of a liquid in equilibrium with its own vapor decreases as the temperature of the system decreases. At the critical point, the surface tension becomes zero as the phase interface vanishes. There are a few empirical correlations to predict surface ten-

sion of pure liquids and their mixtures. For pure liquids in equilibrium with their own vapor, Sugden²² suggested the use of Macleod's relation¹ between the surface tension of liquid and the phase densities. This relationship can be expressed mathematically as

$$\sigma = \left[\frac{P_{ch}(\rho_L - \rho_V)}{M} \right]^4, \quad \dots \dots \dots \quad (C-68)$$

where σ = surface tension and P_{ch} = a temperature-independent parameter called the parachor.

A parachor is a constant. In Eq. C-68, the liquid- and vapor-phase densities, ρ_L and ρ_V , are expressed in g/cm.³ The surface tension is calculated in dynes/cm. Weinaug and Katz²³ presented parachor values of a selected set of pure components, shown in Table C-3.

The parachor of hydrocarbon mixtures can be calculated from this Weinaug and Katz²³ empirical relationship.

$$(P_{ch})_{C+} = a_1 + a_2(M)_{C+} + a_3(M)_{C+}^2 + a_4/(M)_{C+}, \quad \dots \dots \dots \quad (C-69)$$

where $(P_{ch})_{C+}$ = parachor of the plus fraction or the hydrocarbon mixture; $(M)_{C+}$ = molecular weight of the plus fraction; and a_1 through a_4 = coefficients with the following values: $a_1 = -4.6148734$, $a_2 = 2.558855$, $a_3 = 3.4004065(10^{-4})$, and $a_4 = 3.767396(10^3)$.

For complex hydrocarbon mixtures, Katz *et al.*³ used the Macleod-Sugden equations to calculate the surface tension of liquid.

$$\sigma^{1/4} = \sum_{i=1}^n [(P_{ch})_i (Ax_i - By_i)], \quad \dots \dots \dots \quad (C-70)$$

with

$$A = \frac{\rho_o}{62.4(M_{aL})} \quad \dots \dots \dots \quad (C-71a)$$

and

$$B = \frac{\rho_g}{62.4(M_{ag})}, \quad \dots \dots \dots \quad (C-71b)$$

where ρ_o = density of the oil phase, lbm/ft³; M_{aL} = apparent molecular weight of the oil phase; ρ_g = density of the gas phase, lbm/ft³; M_{ag} = apparent molecular weight of the gas phase; x_i = mole fraction of Component i in the oil phase; y_i = mole fraction of Component i in the gas phase; and n = total number of components in the system.

C.13 Thermodynamic Properties¹

In this section, we present a method based on EOS's to estimate the enthalpy and entropy departure from ideality. These variables are very useful thermodynamic properties¹ and often can be related to well-operating variables, such as temperature change in the fluid. It is important to estimate thermodynamic-property variations as the other independent variables (pressure, temperature, and other such parameters) in the system change.

The variation of thermodynamic properties between two equilibrium states is independent of the path chosen from one state to the other, as long as the pressure and temperature at each of the states are known. For example, the enthalpy of a fluid system, H , can be represented at any pressure, p , and temperature, T , as $H = f(p, T)$.

Between two states at (p_1, T_1) and (p_2, T_2) the enthalpy change can be represented as

$$\Delta H = H_2 - H_1 = \int_{p_1}^{p_2} \left(\frac{\partial H}{\partial p} \right)_{T_1} dp + \int_{T_1}^{T_2} \left(\frac{\partial H}{\partial T} \right)_{p_2} dT$$

$$\begin{aligned} &= \int_{p_1}^{p_0} \left(\frac{\partial H}{\partial p} \right)_{T_1} dp + \int_{T_1}^{T_2} C_p^0 dT + \int_{p_0}^{p_2} \left(\frac{\partial H}{\partial p} \right)_{T_2} dp \\ &= (H^0 - H_{p1})_{T_1} + \int_{T_1}^{T_2} C_p^0 dT - (H^0 - H_{p2})_{T_2}, \end{aligned} \quad \dots \dots \dots \quad (C-72)$$

where the constant-pressure heat capacity, C_p^0 , is defined as

$$C_p^0 = \left(\frac{dH}{dT} \right)_{p^0}. \quad \dots \dots \dots \quad (C-73)$$

The superscript 0 indicates the fluid is an ideal gas. The terms $(H^0 - H_{p1})_{T_1}$ and $(H^0 - H_{p2})_{T_2}$ are called the departure functions (from ideality). They relate any thermodynamic property (enthalpy, in this case) at any state represented by p , T to a reference state ($p=0$, in this case) at the same temperature, T . Thus, enthalpy at (p_1, T_1) can be found from $H_{p1}, T_1 = H^0 - \Delta H$, where ΔH is enthalpy departure from the ideal condition calculated from the EOS.

All departure functions can be calculated from an EOS. For example, Reid *et al.*¹ derive the departure function for Helmholtz energy as

$$A - A^0 = - \int_s^V \left(p - \frac{RT}{V} \right) dV - RT \ln \frac{V}{V^0}, \quad \dots \dots \dots \quad (C-74)$$

where A = Helmholtz energy at any specified state, (J/mol); A^0 = Helmholtz energy at any reference state or an ideal gas state; p = system pressure; T = system temperature; V = system volume; and V^0 = reference volume.

The entropy departure function, S , can be calculated as

$$S - S^0 = - \frac{d}{dT} (A - A^0) V = \int_s^V \left[\left(\frac{dp}{dT} \right)_V - \frac{R}{V} \right] dV + R \ln \frac{V}{V^0}, \quad \dots \dots \dots \quad (C-75)$$

where S^0 = entropy at reference state, (J/mol - K).

The departure function for enthalpy, H , is presented as

$$H - H^0 = (A - A^0) + T(S - S^0) + RT(Z - 1). \quad \dots \dots \dots \quad (C-76)$$

Note that the SRK EOS¹⁰ can be presented as

$$p = \frac{RT}{V - b} - \frac{a}{V(V + b)}, \quad \dots \dots \dots \quad (C-77)$$

where the values of Parameters a and b are presented in Table C-1. With the SRK EOS, it can be shown that the departure functions for the Helmholtz free energy, entropy, and enthalpy for a pure material or for a mixture of constant composition can be written as

$$A - A^0 = - RT \ln \frac{V - b}{V} - \frac{a}{b} \ln \frac{V + b}{V} - RT \ln \frac{V}{V^0}, \quad \dots \dots \dots \quad (C-78a)$$

$$S - S^0 = R \ln \frac{V - b}{V} - \frac{a}{2bT} \ln \frac{V + b}{V} + R \ln \frac{V}{V^0}, \quad \dots \dots \dots \quad (C-78b)$$

and

$$H - H^0 = \frac{bRT}{V - b} - \frac{a}{(V + b)} - \frac{1.5a}{b} \ln \left(\frac{V + b}{V} \right). \quad \dots \dots \dots \quad (C-78c)$$

It is important to note that both of the departure functions, $(A - A^0)$ and $(S - S^0)$, depend on V^0 or the reference-state molar volume. The reference-state molar volume can be calculated from

$$V^0 = \frac{RT}{p^0}, \quad \dots \dots \dots \quad (\text{C-79})$$

where the reference-state pressure, p^0 , can be set to unity at any chosen unit system and R is chosen consistently. The reference state also can be chosen as the system pressure of $p^0 = p$. Then, $V/V^0 = Z$ is the compressibility factor.

References

1. Reid, R.C., Prausnitz, J.N., and Poling, B.E.: *The Properties of Gases and Liquids*, fourth edition, McGraw-Hill Book Co. Inc., New York City (1987).
2. Ahmed, T.H.: *Hydrocarbon Phase Behavior*, Gulf Publishing Co., Houston (1989).
3. Katz, D.L. et al.: *Handbook of Natural Gas Engineering*, McGraw-Hill Book Co. Inc., New York City (1959).
4. Carnahan, B., Luther, H.A., and Wilkes, J.O.: *Applied Numerical Methods*, John Wiley & Sons, New York City (1969).
5. Wilson, G.: "A Modified Redlich-Kwong EOS Application to General Physical Data Calculations," paper 15C presented at the 1968 AIChE Annual Meeting, Cleveland, Ohio, 4-7 May.
6. Pitzer, K.S.: "The Volumetric and Thermodynamic Properties of Fluids," *J. Am. Chem. Soc.* (1955) **77**, No. 13, 3427.
7. Lee, B.I. and Kesler, M.G.: "A Generalized Thermodynamics Correlation Based on Three-Parameter Corresponding States," *AIChE J.* (1975) **21**, 510.
8. Edmister, W.C.: "Applied Hydrocarbon Thermodynamics, Part 4: Compressibility Factors and Equations of State," *Petroleum Refiner* (1958) **37**, No. 4, 173.
9. van der Waals, J.D.: "On the Continuity of the Liquid and Gaseous State," PhD dissertation, Sighoff, Leiden, The Netherlands (1873).
10. Redlich, O. and Kwong, J.: "On the Thermodynamics of Solutions. An Equation of State. Fugacities of Gaseous Solutions," *Chemical Reviews* (1949) **44**, 233.
11. Soave, G.: "Equilibrium Constants From a Modified Redlich-Kwong Equation of State," *Chem. Eng. Sci.* (1972) **27**, 1197.
12. Peng, D. and Robinson, D.B.: "A New Two Constant Equation of State," *Ind. Eng. Chem. Fund.* (1976) **15**, 59.
13. Peng, D. and Robinson, D.B.: "Two and Three Phase Equilibrium Calculations for Systems Containing Water," *Cdn. J. Chem. Eng.* (1976) **54**, 595.
14. Peng, D. and Robinson, D.B.: "Two and Three Phase Equilibrium Calculations for Coal Gasification and Related Processes," *Thermodynamics of Aqueous Systems with Industrial Applications*, Symposium Series, American Chemical Soc., Washington, DC (1980) No. 133.
15. Slot-Petersen, C.: "A Systematic and Consistent Approach To Determine Binary Interaction Coefficients for the Peng-Robinson Equation of State," *SPEER* (November 1989) 488.
16. Graboski, M.S. and Daubert, T.E.: "A Modified Soave Equation of State for Phase Equilibrium Calculations I: Hydrocarbon System," *Ind. Eng. Chem. Proc. Des. Dev.* (1978) **17**, 443.
17. Alani, G.H. and Kennedy, H.T.: "Volume of Liquid Hydrocarbons at High Temperatures and Pressures," *Trans., AIME* (1960) **219**, 288.
18. Hankinson, R.W. and Thomson, G.H.: "A New Correlation for Saturated Densities of Liquids and Their Mixtures," *AIChE J.* (1979) **25**, 653.
19. Carr, N.L., Kobayashi, R., and Burrows, D.B.: "Viscosity of Hydrocarbon Gases Under Pressure," *Trans., AIME* (1954) **201**, 264.
20. Lee, A.L., Gonzalez, M.H., and Eakin, B.E.: "The Viscosity of Natural Gases," *JPT* (August 1966) 997; *Trans., AIME*, **237**.
21. Lohrenz, J., Bray, B.G., and Clark, C.R.: "Calculating Viscosities of Reservoir Fluids From Their Compositions," *JPT* (October 1964) 1171; *Trans., AIME*, **231**.
22. Sugden, S.: "The Variation of Surface Tension, VI. The Variation of Surface Tension with Temperature and Some Related Functions," *J. Chem. Soc.* (1924) **125**, 32.
23. Weintraub, C. and Katz, D.L.: "Surface Tension of Methane-Propane Mixtures," *Ind. Eng. Chem.* (1943) **25**, 35.

Appendix D

Tubing and Casing Properties

Tables D-1 and D-2 provide the standard tubing and casing information required for pipe-flow calculations. The information is taken

from *Production Operations* by T.O. Allen and A.P. Roberts, Oil & Gas Consultants Intl. Inc., Tulsa, Oklahoma (1978).

TABLE D-1—TUBING MINIMUM PERFORMANCE PROPERTIES

Tubing Size	Nominal Weight			Threaded and Coupled (T&C)			Integral Joint		Joint Yield Strength					
				Drift Diameter (in.)	Coupled Outside Diameter									
					Non-Upset (in.)	Upset Regular (in.)	Upset Spec. (in.)							
Nominal OD (in.)	T & C Non-Upset (lbf/ft)	T & C Upset (lbf/ft)	Integral Joint (lbf/ft)	Grade	Wall Thickness (in.)	Inside Diameter (in.)	Drift Diameter (in.)	Non-Upset (in.)	Upset Regular (in.)	Upset Spec. (in.)	Drift Diameter (in.)	Box OD (in.)		
											Collapse Resistance (psi)	Internal Yield Pressure (psi)		
1/4	1.050	1.14	1.20	H40	0.113	0.824	0.730	1.313	1.660		7,680	7,530		
	1.050	1.14	1.20	J55	0.113	0.824	0.730	1.313	1.660		10,560	10,360		
	1.050	1.14	1.20	C75	0.113	0.824	0.730	1.313	1.660		14,410	14,120		
	1.050	1.14	1.20	N80	0.113	0.824	0.730	1.313	1.660		15,370	15,070		
1	1.315	1.70	1.80	H40	0.133	1.049	0.955	1.660	1.900	0.955	1.550	7,270	7,270	
	1.315	1.70	1.80	J55	0.133	1.049	0.955	1.660	1.900	0.955	1.550	10,000	10,000	
	1.315	1.70	1.80	C75	0.133	1.049	0.955	1.660	1.900	0.955	1.550	13,640	13,640	
	1.315	1.70	1.80	N80	0.133	1.049	0.955	1.660	1.900	0.955	1.550	14,550	14,160	
1 1/4	1.660	2.30	2.40	H40	0.125	1.410	1.286	2.054	2.200	1.286	1.880	5,570	5,270	
	1.660	2.30	2.40	J55	0.140	1.380	1.286	2.054	2.200	1.286	1.880	6,80	5,900	
	1.660	2.30	2.40	C75	0.125	1.410	1.286	2.054	2.200	1.286	1.880	7,660	7,250	
	1.660	2.30	2.40	N80	0.140	1.380	1.286	2.054	2.200	1.286	1.880	8,500	8,120	
	1.660	2.30	2.40	H40	0.140	1.380	1.286	2.054	2.200	1.286	1.880	11,580	11,070	
	1.660	2.30	2.40	J55	0.140	1.380	1.286	2.054	2.200	1.286	1.880	12,360	11,810	
	1.660	2.30	2.40	C75	0.140	1.380	1.286	2.054	2.200	1.286	1.880	31,060	28,480	
	1.660	2.30	2.40	N80	0.140	1.380	1.286	2.054	2.200	1.286	1.880	31,060	28,480	
1 1/2	1.900	2.75	2.90	H40	0.125	1.650	1.516	2.200	2.500	1.516	2.110	4,920	4,610	
	1.900	2.75	2.90	J55	0.145	1.610	1.516	2.200	2.500	1.516	2.110	5,640	5,340	
	1.900	2.75	2.90	C75	0.125	1.650	1.516	2.200	2.500	1.516	2.110	6,640	6,330	
	1.900	2.75	2.90	N80	0.145	1.610	1.516	2.200	2.500	1.516	2.110	7,750	7,350	
	1.900	2.75	2.90	H40	0.145	1.610	1.516	2.200	2.500	1.516	2.110	10,750	10,020	
	1.900	2.75	2.90	J55	0.145	1.610	1.516	2.200	2.500	1.516	2.110	11,280	10,680	
2 1/16	2.063		3.25	H40	0.156	1.751				1.657	2.325	5,590	5,290	
	2.063		3.25	J55	0.156	1.751				1.657	2.325	7,690	7,280	
	2.063		3.25	C75	0.156	1.751				1.657	2.325	10,480	9,920	
	2.063		3.25	N80	0.156	1.751				1.657	2.325	11,180	10,590	
2 3/8	2.375	4.00	4.70	H40	0.167	2.041	1.947	2.875				5,230	4,920	
	2.375	4.60	4.70	H40	0.190	1.995	1.901	2.875	3.063	2.910		5,890	5,600	
	2.375	4.00		J55	0.167	2.041	1.947	2.875				7,190	6,770	
	2.375	4.60	4.70	J55	0.190	1.995	1.901	2.875	3.063	2.910		8,100	7,700	
	2.375	4.00		C75	0.167	2.041	1.947	2.875				9,520	9,230	
	2.375	4.60	4.70	C75	0.190	1.995	1.901	2.875	3.063	2.910		11,040	10,500	
	2.375	5.80	5.95	C75	0.254	1.867	1.773	2.875	3.063	2.910		14,330	14,040	
	2.375	4.00		N80	0.167	2.041	1.947	2.875				9,980	9,840	
	2.375	4.60	4.70	N80	0.190	1.995	1.901	2.875	3.063	2.910		11,780	11,200	
	2.375	5.80	5.95	N80	0.254	1.867	1.773	2.875	3.063	2.910		15,280	14,970	
	2.375	4.60	4.70	P105	0.190	1.995	1.901	2.875	3.063	2.910		15,460	14,700	
	2.375	5.80	5.95	P105	0.254	1.867	1.773	2.875	3.063	2.910		20,060	19,650	
2 7/8	2.875	6.40	6.50	H40	0.217	2.441	2.347	3.500	3.668	3,460		5,580	5,290	
	2.875	6.40	6.50	J55	0.217	2.441	2.347	3.500	3.668	3,460		7,680	7,260	
	2.875	6.40	6.50	C75	0.217	2.441	2.347	3.500	3.668	3,460		10,470	9,910	
	2.875	8.60	8.70	C75	0.308	2.259	2.165	3.500	3.668	3,460		14,350	14,060	
	2.875	6.40	6.50	N80	0.217	2.441	2.347	3.500	3.668	3,460		11,160	10,570	
	2.875	8.60	8.70	N80	0.308	2.259	2.165	3.500	3.668	3,460		15,300	15,000	
	2.875	6.40	6.50	P105	0.217	2.441	2.347	3.500	3.668	3,460		14,010	13,870	
	2.875	8.60	8.70	P105	0.308	2.259	2.165	3.500	3.668	3,460		20,090	19,960	

TABLE D-1—TUBING MINIMUM PERFORMANCE PROPERTIES (continued)

SAW CUT & SWELLED (continued)																		
Tubing Size		Nominal Weight		Threaded and Coupled (T&C)						Integral Joint		Joint Yield Strength						
						Coupled Outside Diameter												
Nominal (in.)	OD (in.)	T & C Non- Upset (lbf/ft)	T & C Upset (lbf/ft)	Integral Joint (lbf/ft)	Grade	Wall Thickness (in.)	Inside Diameter (in.)	Drift Diameter (in.)	Non- Upset (in.)	Upset Regular (in.)	Upset Spec. (in.)	Drift Diameter (in.)	Box OD (in.)	Collapse Resistance (psi)	Internal Yield Pressure (psi)	T & C Non- Upset (lbf)	T & C Upset (lbf)	Integral Joint (lbf)
3½	3.500	7.70	9.30	H40	0.216	3.068	2.943	4.250	4.500	4.180	4.180	4.250	4.320	65,070	65,070	103,610		
	3.500	9.20		H40	0.254	2.992	2.867	4.250				5.380	5,080	79,540				
	3.500	10.20		H40	0.289	2.992	2.797	4.250				6,060	5,780	92,550				
	3.500	7.70		J55	0.216	3.068	2.943	4.250				5,970	5,940	89,470				
	3.500	9.20		J55	0.254	2.992	2.867	4.250				7,400	6,980	109,370				
	3.500	10.20		J55	0.289	2.992	2.797	4.250				8,330	7,950	127,250				
	3.500	7.70		C75	0.216	3.068	2.943	4.250				7,540	8,100	122,010				
	3.500	9.20		C75	0.254	2.992	2.867	4.250				10,040	9,510	149,140				
	3.500	10.20		C75	0.289	2.992	2.797	4.250				11,360	10,840	173,530				
	3.500	12.70		C75	0.375	2.750	2.625	4.250				14,350	14,060	230,990				
	3.500	7.70		N80	0.216	3.068	2.943	4.250				7,870	8,640	130,140				
4	3.500	9.20	9.30	N80	0.254	2.992	2.867	4.250				10,530	10,160	159,090				
	3.500	10.20		N80	0.289	2.992	2.797	4.250				12,120	11,560	185,100				
	3.500	12.70		N80	0.375	2.750	2.625	4.250				15,310	15,000	246,390				
	3.500	9.20		P105	0.254	2.992	2.867	4.250				13,050	13,330	208,800				
	3.500	12.70		P105	0.375	2.750	2.625	4.250				20,090	19,690	323,390				
	4.000	9.50	11.00	H40	0.226	3.548	3.423	4.750	5.000	5.000	5.000	4,060	3,960	72,000				
	4.000	9.50		H40	0.262	3.476	3.351	4,900				4,580	123,070					
	4.000	9.50		J55	0.226	3.548	3.423	4.750				5,110	5,440	99,010				
	4.000	9.50		J55	0.262	3.476	3.351	6,590				6,300	169,220					
	4.000	9.50		C75	0.226	3.548	3.423	4.750				6,350	7,420	135,010				
	4.000	11.00		C75	0.262	3.476	3.351	8,410				8,600	230,750					
	4.000	9.50		N80	0.226	3.548	3.423	4.750				6,590	7,910	144,010				
	4.000	11.00		N80	0.262	3.376	3.351	8,800				9,170	246,140					
4½	4.500	12.60	12.75	H40	0.271	3.958	3.833	5.200	5.563			4,500	4,220	104,360	144,020			
	4.500	12.60	12.75	J55	0.271	3.958	3.833	5.200	5.563			5,720	5,800	143,500	298,030			
	4.500	12.60	12.75	C75	0.271	3.958	3.833	5.200	5.563			7,200	7,900	195,680	270,040			
	4.500	12.60	12.75	N80	0.271	3.958	3.833	5.200	5.563			7,500	8,430	208,730	288,040			

TABLE D-2—CASING MINIMUM PERFORMANCE PROPERTIES

Dimensions						Minimum Collapse Pressure (psi)				Minimum Internal Yield Pressure (psi)				Joint Yield Strength (1,000 lbf)								
														Short Thread			Long Thread					
OD Size (in.)	Nominal Weight (lbf/ft)	Wall (in.)	ID (in.)	Drift (in.)	Coupling OD (in.)	H40	J55	N80	P110	H40	J55	N80	P110	H40	J55	N80	P110	J55	N80	P110		
4½	9.50	0.205	4.090	3.965	5.000	2,770	3,310			3,190	4,380			77	101			162	223	279		
	11.60	0.250	4.000	3.875	5.000		4,960	6,350	7,560			5,350	7,780	10,690			9,020	12,410				
	13.50	0.290	3.920	3.795	5.000			8,540	10,670								14,320					
	15.10	0.337	3.826	3.701	5.000																162	220
5	11.50	0.220	4.560	4.435	5.563		3,060				4,240				133				182	223	388	
	13.00	0.253	4.494	4.369	5.563			4,140			4,870				169							
	15.00	0.296	4.408	4.283	5.563		5,550	7,250	8,830		5,700	8,290	11,400		207							
	18.00	0.362	4.276	4.151	5.563			10,490	13,450				10,140	13,940					311	396	495	
5½	14.00	0.244	5.012	4.887	6.050		2,630	3,120			3,110				130	172			217	247	445	
	15.50	0.275	4.950	4.825	6.050			4,040			4,270				202							
	17.00	0.304	4.892	4.767	6.050			4,910	6,280		7,460	4,810	7,740	10,640								
	20.00	0.361	4.778	4.653	6.050				8,830		11,080	5,320	9,190	12,640					348	428	548	
6½/8	14.00	0.244	5.012	4.887	6.050				11,160		14,520		9,880	13,580					502	643	643	
	20.00	0.288	6.049	5.924	7.390	2,520	2,970			3,040	4,180			184	245							
	24.00	0.352	5.921	5.796	7.390		4,560	5,760	6,710		5,110	7,440	10,230									
	28.00	0.417	5.791	5.666	7.390			8,170	10,140		10,320	13,200	8,810	12,120					266	340	481	
7	20.00	0.475	5.675	5.550	7.390					10,040		13,800							586	781	904	
	17.00	0.231	6.538	6.413	7.656	1,450				2,310				122								
	20.00	0.272	6.456	6.331	7.656	1,980	2,270			2,720	3,740			176	234							
	23.00	0.317	6.366	6.241	7.656		3,270	3,830			4,360	6,340			284							
7½/8	26.00	0.362	6.276	6.151	7.656		4,320	5,410	6,210			4,980	7,240	9,960					313	367	693	
	29.00	0.408	6.184	6.059	7.656			7,020	8,510				8,160	11,220					442	519	693	
	32.00	0.453	6.094	5.969	7.656			8,600	10,760				9,060	12,460					597	672	897	
	35.00	0.498	6.004	5.879	7.656			10,180	13,010				9,240	12,700					746	814	996	
8½/8	38.00	0.540	5.920	5.795	7.656			11,390	15,110				9,240	12,700					814	1,087		
	24.00	0.300	7.025	6.900	8.500	2,040				2,750	4,140			212				346	490	769		
	26.40	0.328	6.969	6.844	8.500		2,890	3,400			6,020				315							
	29.70	0.375	6.875	6.750	8.500			4,790	5,340			6,890	9,470					575	674	901		
8½/8	33.70	0.430	6.765	6.640	8.500			6,560	7,850				7,900	10,860					798	798	1,066	
	39.00	0.500	6.625	6.500	8.500			8,810	11,060				9,180	12,620								
8½/8	24.00	0.264	8.097	7.972	9.625			1,370			2,470	2,950			244				417	486	688	
	28.00	0.304	8.017	7.892	9.625	1,640				2,860	3,930			233								
	32.00	0.352	7.921	7.796	9.625	2,210	2,530			4,460		6,490			372							
	36.00	0.400	7.825	7.700	9.625		3,450	4,100			5,510	6,380			434				798	887	1,055	
8½/8	40.00	0.450	7.715	7.600	9.625						6,950	8,400							887	997	1,186	
	44.00	0.500	7.625	7.500	9.625						8,570	10,720							997	1,335		
	49.00	0.557	7.511	7.386	9.625								9,040	12,430								

TABLE D-2—CASING MINIMUM PERFORMANCE PROPERTIES (continued)

Dimensions						Minimum Collapse Pressure (psi)				Minimum Internal Yield Pressure (psi)				Joint Yield Strength (1,000 lbf)							
														Short Thread				Long Thread			
OD Size (in.)	Nominal Weight (lbf/ft)	Wall (in.)	ID (in.)	Drift (in.)	Coupling OD (in.)	H40	J55	N80	P110	H40	J55	N80	P110	H40	J55	N80	P110	J55	N80	P110	
9 ⁵ / ₈	32.30	0.312	9.001	8.845	10.625	1,400	1,740	2,020		2,270	2,560	3,520		254	294	394		453	520	737	
	36.00	0.352	8.921	8.765	10.625		2,570		3,090	3,950	5,750	6,330	8,700		452				825	1,106	
	40.00	0.395	8.835	8.679	10.625				3,810	4,430			6,870	9,440				905	1,213		
	43.50	0.435	8.755	8.599	10.625				4,750	5,310			7,930	10,900				1,062	1,422		
	47.00	0.472	8.681	8.525	10.625				6,820	7,930											
	53.50	0.545	8.535	8.379	10.625																
10 ¹ / ₂	32.75	0.279	10.192	10.036	11.750	870	1,420	1,580		1,820	2,280	3,130		205	314	420					
	40.50	0.350	10.050	9.894	11.750			2,090		3,580				493							
	45.50	0.400	9.950	9.794	11.750			2,700	3,220	3,670	4,030	5,860	8,060		565	804	1,080				
	51.00	0.450	9.850	9.694	11.750				4,020	4,630		6,450	8,860		895	1,203					
	55.50	0.495	9.760	9.604	11.750					5,860			9,760			1,338					
	60.70	0.545	9.660	9.504	11.750					7,490			10,650			1,472					
11 ¹ / ₄	42.00	0.333	11.084	10.928	12.750	1,070				1,980				307							
	47.00	0.375	11.000	10.844	12.750			1,510		3,070				477							
	54.00	0.435	10.880	10.724	12.750			2,070		3,560				568							
	60.00	0.489	10.772	10.616	12.750			2,660	3,180	4,010	5,830			649	924						
13 ³ / ₈	48.00	0.330	12.715	12.559	14.375	740				1,730				322							
	54.50	0.380	12.615	12.459	14.375			1,130		2,730				514							
	61.00	0.430	12.515	12.359	14.375			1,540		3,090				595							
	68.00	0.480	12.415	12.259	14.375			1,950		3,450				675							
16	72.00	0.514	12.347	12.191	14.375				2,670			5,380				1,040					
	65.00	0.375	15.250	15.062	17.000	630				1,640				439							
	75.00	0.438	15.124	14.936	17.000			1,020		2,630				710							
	84.00	0.495	15.010	14.822	17.000			1,410		2,980				817							
18 ⁵ / ₈	87.50	0.435	17.755	17.567	19.625	650	630			1,630	2,250			559	754						
	94.00	0.438	19.124	18.936	21.000	520	520			1,530	2,110			581	784						
	106.50	0.500	19.000	18.812	21.000			770		2,410				913				907			
20	133.00	0.635	18.730	18.542	21.000			1,500		3,060				1,192				1,057			
																		1,380			